

Anthony L. Peratt

# Physics of the Plasma Universe

*Second Edition*



Springer

# Physics of the Plasma Universe



Anthony L. Peratt

# Physics of the Plasma Universe

Second Edition



Springer



Anthony L. Peratt  
Los Alamos, NM, USA

ISBN 978-1-4614-7818-8      ISBN 978-1-4614-7819-5 (eBook)  
DOI 10.1007/978-1-4614-7819-5  
Springer New York Heidelberg Dordrecht London

Library of Congress Control Number: 2014940735

© Springer Science+Business Media New York 1992, 2015

This work is subject to copyright. All rights are reserved by the Publisher, whether the whole or part of the material is concerned, specifically the rights of translation, reprinting, reuse of illustrations, recitation, broadcasting, reproduction on microfilms or in any other physical way, and transmission or information storage and retrieval, electronic adaptation, computer software, or by similar or dissimilar methodology now known or hereafter developed. Exempted from this legal reservation are brief excerpts in connection with reviews or scholarly analysis or material supplied specifically for the purpose of being entered and executed on a computer system, for exclusive use by the purchaser of the work. Duplication of this publication or parts thereof is permitted only under the provisions of the Copyright Law of the Publisher's location, in its current version, and permission for use must always be obtained from Springer. Permissions for use may be obtained through RightsLink at the Copyright Clearance Center. Violations are liable to prosecution under the respective Copyright Law.

The use of general descriptive names, registered names, trademarks, service marks, etc. in this publication does not imply, even in the absence of a specific statement, that such names are exempt from the relevant protective laws and regulations and therefore free for general use.

While the advice and information in this book are believed to be true and accurate at the date of publication, neither the authors nor the editors nor the publisher can accept any legal responsibility for any errors or omissions that may be made. The publisher makes no warranty, express or implied, with respect to the material contained herein.

Printed on acid-free paper

Springer is part of Springer Science+Business Media ([www.springer.com](http://www.springer.com))

# Preface

## Physics of the Plasma Universe, Second Edition

Twenty years have passed since the printing of the first book on this topic, *Physics of the Plasma Universe*. As the first printing was soon exhausted, there became a need for a new printing or a new book. At this time, I had organized several IEEE sanctioned *International Workshops on Plasma Cosmology* and was hesitant to simply reprint the first book because of the growing amount of new data whose inclusion would enhance a second book. But with the cessation of all nuclear testing in July 1993, I was reassigned to the Department of Energy in Washington D.C., 1995–1999, where I was tasked in representation of Los Alamos, Sandia, and Livermore National Laboratories, experiments and simulations. Nevertheless, in spite of several exciting posts, International Conferences on *Plasma Cosmology* were held world-wide. Two new books were published, *Plasma Astrophysics and Cosmology*, Kluwer, 1995 and *Advanced Topics on Astrophysical and Space Plasmas*, Kluwer, 1997 as well as other research papers. In addition, Professors Alv Egeland and William Burke had published their book on *Kristian Birkeland, The First Space Scientist*, an edition filled with details as to how the study of space plasma came to be.

Over the decades we have been fortunate to have access to institutes possessing the fastest computers at the time: The Magnetic Fusion Energy Computational Center (MFECC), Lawrence Livermore National Laboratory, Los Alamos National Laboratory, NASA's Jet Propulsion Laboratory of the California Institute of Technology, Sandia National Laboratories, and support from the Mission Research Corporation, NASA's Goddard Space Flight Center, Greenbelt, Maryland, and the U.S. Air Force Office of Scientific Research, Virginia, whose encouragement proved invaluable.

Countering the growth of faster computers, better diagnostics, and nuclear research facilities has been the encroachment of those not schooled in plasma science, computer science, physics, astrophysics, or high-power electrical, pulsed energy, and nuclear engineering. Without exception they rail at barriers placed to insure sound scientific technique and methodology. In times past, their 'achievements' were limited to hand-written, mimeographed, or in-house notes. Peer-reviewed

papers in print in archived journals or even short letters in their town OpEd page were beyond their reach. However, now the internet or World Wide Web allows anyone, even cults, to present their cacaphony to the world, often citing unsuspecting researchers as ‘colleagues’ for false endorsement. As Hannes Alfven, Harold Urey, and myself, during our tenure at the New Astrophysics lectures at the University of California, San Diego, 1979–1981, said, ‘they deserve no attention’. Indeed, as if a topic of psuedoscience, the subject was never even raised.

As in the first edition, this book could not have been written without the encouragement and support of colleagues and collaborators, who in addition to those listed above include: Drs. Emil Wolf, D. F. W. James, E. Witalis, A. K. T. Assis, M. C. C. Neves, W. G. Tifft, H. Arp, M. Marconi, T. Miller, Kevin Healy (VLA), J. Kanipe, D. Roscoe, J. Brandenburg, Bogdan Wszolek, T. Venturi, G. Giovannini, C. Whitney, B. Chargeishvili, Jun-Ichi Sakai, S. Goldstein, Daniel Wells, M. Birkenshaw, D. Biskamp, D. Melrose, A.C.-L. Chian, Reuven Opher, Elisabete de Gouveia Dal Pino, Gustavo Tanco, P. Bustamante Diaz, S.-I. Akasofu, S. Leifer, J. Wang, I. Potapenko, B. Trubnikov, V. Rantsev-Kartinov, A. Kukushin, L. Marmet, C. Gallo, B. Coppi, A. Brynjolfsson, C. Pedersen, P. Whitley, B. Whitley, J. McGovern, Charles Pearce, G. Strait, G. Chenevert, R. DeWitt, A. Cox, M. Mostrom, J. Taylor, J. Hammel, J. Mack, D. Scudder, R. Leeper, P. VanDevender, K. Matzen, D. Cook, M. Sweeney, I. Alexeff, R. Barker, S. Gold, S. T. Lai, Torsten Neubert, M. Mostrom, G. Verschuur, and to Wing Fay Yao whose extensive knowledge of Asian cosmology and history proved invaluable and whose perserverance insured I would finish the Second Edition.

Los Alamos, USA

Anthony L. Peratt

# Acknowledgements

I am indebted to Prof. Hannes Alfvén, University of Southern California, whose instruction started me on an unexpected path of the study of space and cosmic plasmas, for which we collaborated in Los Angeles, La Jolla, and Stockholm for the next 23 years.

I am equally indebted to Prof. O. Buneman, STAR Laboratory, Stanford University. It was Oscar, 'Father of the Particle Simulation of Plasmas', from whom I was taught this discipline on supercomputers during a 12-year collaboration. It is fitting that Oscar's last plenary talk at the IEEE International Conference in Vancouver, 1993, was to have been "Simulation From Electron Devices to Cosmic Plasma."

## Physics of the Plasma Universe, First Edition

The purpose of this book is to address the growing recognition of the need for plasma physics in astrophysics. In fact, astrophysics has contributed to the growth of plasma physics, especially in the field of plasma waves. During the last decade plasma physics, or more appropriately, plasma science, has witnessed an explosive growth in two areas: pulsed-power technology and space physics. Both have led to knowledge that is mutual and complementary, and the material in this book largely derives from these new discoveries and their application to astrophysics. With the passage of the *Voyager* spacecraft in 1989, Neptune was transformed from an astronomical object to a space science object. In our solar system only Pluto remains unvisited. In this decade of exploration, the solar system has become recognized as the primary plasma laboratory in which plasma processes of great generality and astronomical significance can be studied in situ. By the 1960s, with the discovery of the earth's natural plasmas, the Van Allen radiation belts, and the solar wind, it was already clear that future understanding of the earth and sun would be expressed in terms of plasmas. Today plasma is recognized as the key element to understanding the generation of magnetic fields in planets, stars, and galaxies; phenomena occurring in stellar atmospheres, in the interstellar and intergalactic media,

in radio galaxies and quasars, and in active galactic nuclei; and the acceleration and transport of cosmic rays (Fälthammar 1988). There are convincing arguments for the view that the clouds out of which galaxies form and stars condense are ionized: The problem of the formation and structure of these clouds and bodies, therefore, naturally belongs to the field of cosmic plasmas as well as astrophysics. Each has traditionally been pursued independently. Only recently has there been a tendency to view them as a unified discipline. Together these problems form what is called The Plasma Universe, the basis for the book. The material presented dwells basically on the known properties of matter in the plasma state. Some of the interesting topics in contemporary astrophysics such as discordant redshifts and other cosmological issues are not discussed here. The interested reader will be referred to the *IEEE Transactions on Plasma Science*, Special Issues on Space and Cosmic Plasmas (December 1986, April 1989, and February 1990) and *Laser and Particle Beams* (August 1988). This book is organized into eight chapters. Chapter 1 is an introduction to the fundamental physics of cosmic plasmas. An attempt is made to review the known properties of plasmas from the laboratory scale to the Hubble distance. Chapter 2 starts the application of basic plasma theory to astrophysical plasmas in the study of magnetic-field-aligned (Birkeland) currents and charged particle beams. Chapter 3 covers magnetism in plasma and the Biot-Savart force law, while Chap. 4 concentrates on electric fields in space and cosmic plasmas. Chapters 5–7 survey double layers, synchrotron radiation, and energy transport in plasmas, respectively. Chapters 10 and 11 cover the particle-in-cell simulation of astrophysical plasmas. Found throughout the book are examples that apply the material of the chapter or section to specific problems. At the end of the book are appendixes highlighting topics that are often not covered in plasma physics or in astrophysics texts, or else are well documented to the point that a short condensation suffices. Appendix A covers transmission line concepts in space plasmas. Appendix B is a condensation of the polarization properties of plasma waves. In Appendix C dusty and grain plasmas are discussed. A list of references is given for each chapter. These are divided into parts: General references give a list of papers and books that cover the general aspects and often give a more thorough treatment of the subjects covered, and special or specialized references document the sources for specific topics. As far as possible, the equations are written to conform to SI regulations, but since this book deals with the plasma universe whose elements transcend many disciplines, from laboratory controlled fusion experiments to cosmology, a multitude of non-SI units are used. For example, it is customary in the laboratory to state densities in particles per cubic centimeter and magnetic induction in gauss, rather than in per cubic meter and tesla, as used in space plasmas. Likewise, units of light-years and parsecs are more meaningful to describe the dimensions of galaxies and clusters of galaxies than are meters. To aid visualization, both SI and familiar units are often given in the text. This book could not have been written without the help and encouragement of many friends and colleagues. I am grateful to my collaborators at the Royal Institute of Technology, Stockholm, whose work I have freely drawn upon: Drs. Carl-Gunne Fälthammar, Pers Carlqvist, Michael Raadu, Lars Block, Nils Brenning, Steffan Torvén, Lennart Lindberg, and Martin Bohm. I am appreciative to my

colleagues at Los Alamos: Drs. Steve Gitomer, George Nickel, Ricky Faehl, Rick Shannahan, Art Greene, Rhon Keinigs, Michael Jones, Galen Gisler, Joe Borovsky, Bruce Freeman, Erick Lindman, Art Cox, and Don Lemons. Thanks are also due to Drs. Hans Kuehl, Alex Dessler, Tom Potemra, Norman Rostocker, Grote Reber, Rainer Beck, Paul Marmet, John Kierein, Tim Eastman, Jean-Paul Vigier, Winston Bostick, Vittorio Nardi, Fausto Gratton, Boris Meierovich, André Crusius-Wätzel, Eric Witalis, Eric Wollman, and Nikos Salingaros. I am especially indebted to Oscar Buneman, Jim Green, Charles Snell, Bill Peter, Eric Lerner, and Hannes Alfvén for their constant encouragement. Last, my wife, Glenda, and children Sarah, Galvin, and Mathias should not be forgotten for the time given to complete this book.

Los Alamos, USA

Anthony L. Peratt



# Contents

<b>1</b>	<b>Cosmic Plasma Fundamentals</b>	<b>1</b>
1.1	Plasma	1
1.2	The Physical Sizes and Characteristics of Plasmas in the Universe	3
1.2.1	Plasmas on Earth	3
1.2.2	Near-Earth Plasmas	5
1.2.3	Plasmas in the Solar System	8
1.2.4	Transition Regions in the Solar System	8
1.2.5	Solar, Stellar, and Interstellar Plasmas	11
1.2.6	Galactic and Extragalactic Plasmas	16
1.3	Regions of Applicability of Plasma Physics	17
1.4	Power Generation and Transmission	20
1.5	Electrical Discharges in Cosmic Plasma	22
1.6	Particle Acceleration in Cosmic Plasma	25
1.6.1	Acceleration of Electric Charges	25
1.6.2	Collective Ion Acceleration	25
1.7	Plasma Pinches and Instabilities	26
1.7.1	The Bennett Pinch	26
1.7.2	The Force-Free Configuration	26
1.7.3	The Diocotron Instability	27
1.7.4	Critical Ionization Velocity	28
1.8	Diagnosing Cosmic Plasmas	32
1.8.1	The Electromagnetic Spectrum	32
1.8.2	In Situ Space Probes	36
	References	37
<b>2</b>	<b>Birkeland Currents in Cosmic Plasma</b>	<b>41</b>
2.1	History of Birkeland Currents	41
2.2	Field-Aligned Currents in Laboratory Plasma	46
2.3	Field-Aligned Currents in Astrophysical Plasmas	46
2.4	Basic Equations of Magnetohydrodynamics	47
2.4.1	General Plasma Fluid Equations	47
2.4.2	Magnetic Reynolds and Lundquist Numbers	49



2.5	The Generalized Bennett Relation	50
2.5.1	The Bennett Relation	52
2.5.2	Alfvén Limiting Current	53
2.5.3	Charge Neutralized Beam Propagation	54
2.5.4	Current Neutralized Beam Propagation	54
2.5.5	Discussion	55
2.5.6	Beam Propagation Along an External Magnetic Field	55
2.5.7	Schönherr Whirl Stabilization	56
2.5.8	The Carlqvist Relation	56
2.5.9	The Cylindrical Pinch	57
2.5.10	The Sheet Pinch	59
2.6	Application of the Carlqvist Relation	59
2.6.1	Birkeland Currents in Earth's Magnetosphere	59
2.6.2	Currents in the Solar Atmosphere	61
2.6.3	Heliospheric Currents	61
2.6.4	Currents in the Interstellar Medium	62
2.6.5	Currents in the Galactic Medium	63
2.6.6	Currents in the Intergalactic Medium	64
2.7	Basic Fluid and Beam Instabilities	64
2.7.1	Jeans Condition for Gravitational Instability	64
2.7.2	Two-Stream (Buneman) Instability	66
2.7.3	Sausage and Kink Instabilities	68
2.8	Laboratory Simulation of Cosmic Plasma Processes	68
2.8.1	High-Current Plasma Pinches	69
2.8.2	Laboratory Aurora Simulations	72
2.9	The Particle-in-Cell Simulation of Beams and Birkeland Currents	73
2.9.1	Charge and Current Neutralized Beam Propagation in Plasma	75
2.9.2	Relativistic and Mildly Relativistic Beam Propagation in Plasma	76
2.9.3	Propagation of a Relativistic Beam Bunch Through Plasma	77
2.9.4	Beam Filamentation	78
2.9.5	Dynamical Evolution of a Narrow Birkeland Filament	79
2.9.6	Vortex Formation in Thin Cylindrical Electron Beams Propagating Along a Magnetic Field	82
2.9.7	Charge-Neutralized Relativistic Electron Beam Propagation Along a Magnetic Field	86
2.9.8	Numerical Aurora Simulations	87
	References	88
<b>3</b>	<b>Biot-Savart Law in Cosmic Plasma</b>	<b>93</b>
3.1	History of Magnetism	93
3.2	The Magnetic Interaction of Steady Line Currents	94

3.3	The Magnetic Induction Field	95
3.3.1	Field from an Infinite Conductor of Finite Radius	97
3.3.2	Force Between Two Infinite Conductors	97
3.4	The Vector Potential	98
3.4.1	Field from a Circular Loop and Force Between Two Circular Loops	99
3.4.2	Force Between Two Circular Loops Lying in a Plane	101
3.5	Quasi-stationary Magnetic Fields	101
3.5.1	Faraday's Law	101
3.5.2	Motion Induced Electric Fields	102
3.5.3	Faraday Disk Dynamo	103
3.6	Inductance	104
3.7	Storage of Magnetic Energy	105
3.7.1	Energy in a System of Current Loops	105
3.7.2	In Situ Storage in Force Free Magnetic Field Configurations	106
3.8	Forces as Derivatives of Coefficients of Inductance	107
3.9	Measurement of Magnetic Fields in Laboratory Plasmas	108
3.10	Particle-in-Cell Simulation of Interacting Currents	109
3.10.1	Simulation Setup	110
3.10.2	Initial Motion of Current Filaments	111
3.10.3	Polarization Forces	113
3.10.4	Magnetic Energy Distribution and Magnetic Isobars	114
3.10.5	Net Motion	115
3.10.6	"Doubleness" in Current-Conducting Plasmas	119
3.11	Magnetic Fields in Cosmic Dimensioned Plasma	121
3.11.1	Measurement of Galactic Magnetic Fields	121
3.11.2	Milky Way Galaxy	123
3.11.3	Spiral Galaxies	124
3.11.4	Rotational Velocities of Spiral Galaxies	128
3.11.5	Elliptical Galaxies	131
3.11.6	Intergalactic Magnetic Fields	134
	References	134
<b>4</b>	<b>Electric Fields in Cosmic Plasma</b>	<b>139</b>
4.1	Electric Fields	140
4.2	Measurement of Electric Fields	140
4.3	Magnetic Field Aligned Electric Fields	145
4.3.1	Collisionless Thermoelectric Effect	145
4.3.2	Magnetic Mirror Effect	146
4.3.3	Electrostatic Shocks	146
4.3.4	Electric Double Layers	147
4.4	Magnetospheric Electric Fields	148
4.4.1	The Plasmasphere	148
4.4.2	The Plasmasheet	149

4.4.3	The Neutral Sheet .....	150
4.4.4	The Magnetotail .....	151
4.4.5	The Magnetopause .....	151
4.4.6	The Auroral Acceleration Region .....	151
4.4.7	Global Distributions of Auroral Electric Fields .....	153
4.5	Outstanding Questions .....	155
4.6	Phenomena Associated with Electric Fields .....	156
4.6.1	Surface Discharges .....	156
4.6.2	Plasma Gun Arc Discharges .....	158
4.6.3	Marklund Convection and Separation of Elements .....	167
4.6.4	Particle Acceleration and Runaway .....	168
4.6.5	Field-Aligned Electric Fields as the Source of Cosmic Rays .....	171
	References .....	172
<b>5</b>	<b>Double Layers in Astrophysics .....</b>	<b>175</b>
5.1	General Description of Double Layers .....	175
5.2	The Time-Independent Double Layer .....	177
5.2.1	One-Dimensional Model .....	177
5.2.2	Ratio of the Current Densities .....	179
5.2.3	The Potential Drop .....	179
5.2.4	Structure of the Double Layer .....	180
5.2.5	Kinetic Description .....	180
5.3	Particle-in-Cell Simulation of Double Layers .....	183
5.3.1	Simulations of the Two-Stream Instability .....	184
5.3.2	Simulations of Double Layers .....	186
5.4	Double Layers in Current Filaments .....	187
5.5	Basic Properties of Double Layers .....	189
5.5.1	Double Layers as a Surface Phenomena .....	189
5.5.2	Noise and Fluctuations in Double Layers .....	190
5.5.3	Exploding Double Layers .....	190
5.5.4	Oblique Double Layers .....	191
5.6	Examples of Cosmic Double Layers .....	192
5.6.1	Double Layers in the Auroral Circuit .....	192
5.6.2	Solar Flares .....	195
5.6.3	Double Radio Galaxies and Quasars .....	200
5.6.4	Double Layers as a Source of Cosmic Radiation .....	200
	References .....	201
<b>6</b>	<b>Synchrotron Radiation .....</b>	<b>205</b>
6.1	Theory of Radiation from an Accelerated Charge .....	206
6.1.1	The Induction Fields .....	208
6.1.2	The Radiation Fields .....	209
6.1.3	Radiation of an Accelerated Electron in a Magnetic Field .....	214
6.1.4	Angular Distribution of the Radiation .....	218
6.1.5	Frequency Distribution of the Radiation .....	220

6.2	Field Polarization	224
6.2.1	Polarization in the Plane of Rotation	224
6.2.2	Polarization for Arbitrary Angles of Observation	226
6.3	Radiation from an Ensemble of Electrons	227
6.3.1	Velocity-Averaged Emissivity	227
6.3.2	Emission from an Ensemble of Electrons	229
6.4	Synchrotron Radiation from Z Pinches	232
6.4.1	X Ray Emission	232
6.4.2	X Ray Spectroscopy	233
6.4.3	Morphology of the Thermal X Ray Source	234
6.5	Particle-in-Cell Simulation of Synchrotron Processes	236
6.5.1	Simulated Z Pinches	236
6.5.2	Synchrotron Bursts from Simulated Z Pinches	237
6.5.3	Synchrotron Source Radiation Patterns	238
6.6	Synchrotron Radiation from Cosmic Sources	240
6.6.1	Gross Radio Properties of Galaxies	240
6.6.2	Double Radio Galaxies	243
6.6.3	“Jets” and Superluminosity	247
6.6.4	Quasars and Active Galaxy Nuclei	249
6.6.5	X Ray and Gamma-Ray Sources	255
	References	256
<b>7</b>	<b>Transport of Cosmic Radiation</b>	<b>259</b>
7.1	Energy Transport in Plasma	260
7.1.1	Group Velocity	263
7.1.2	Time Rate of Decay of Wave Oscillations	267
7.2	Applications of Geometrical Optics	267
7.2.1	Basic Principle and Limitations of Geometrical Optics	268
7.2.2	Equation of Transfer	272
7.3	Black Body Radiation	275
7.4	The Source Function and Kirchoff’s Law	276
7.4.1	Classical Limit of the Emission, Absorption, and Source Functions	277
7.5	Self Absorption by Plasma Filaments	278
7.6	Large-Scale, Random Magnetic Field Approximation	282
7.6.1	Plasma Effects	283
7.6.2	Monoenergetic Electrons	284
7.7	Anisotropic Distribution of Velocities	285
	References	286
<b>8</b>	<b>Critical Ionization Effect in Interstellar Clouds</b>	<b>289</b>
8.1	Critical Ionization Velocity	289
8.2	The CIV Process in Laboratory Experiments	289
8.3	The CIV Process in Interstellar Space	290
8.4	Neutral Hydrogen Emission Line Data	293

8.5	The Relationship Between Observed HI Emission and CIV Data . . .	295
	References . . . . .	298
<b>9</b>	<b>Neutral Hydrogen Filaments and Dynamics</b>	
	<b>of Galactic Bennett Pinches</b> . . . . .	299
9.1	Interstellar Filaments . . . . .	299
9.2	Interstellar Filaments as Tracers of Current Flow . . . . .	304
	References . . . . .	308
<b>10</b>	<b>Particle-in-Cell Simulation of Cosmic Plasma</b> . . . . .	311
10.1	“In-Situ” Observation of Cosmic Plasmas via Computer Simulation . . . . .	311
10.2	The History of Electromagnetic Particle-in-Cell Simulation . . . . .	312
10.3	The Laws of Plasma Physics . . . . .	314
10.4	Multidimensional Particle-in-Cell Simulation . . . . .	315
	10.4.1 Sampling Constraints in Multidimensional Particle Codes . .	315
	10.4.2 Discretization in Time and Space . . . . .	316
	10.4.3 Spectral Methods and Interpolation . . . . .	318
10.5	Techniques for Solution . . . . .	319
	10.5.1 Leap-Frogging Particles Against Fields . . . . .	320
	10.5.2 Particle Advance Algorithm . . . . .	321
	10.5.3 Field Advance Algorithm . . . . .	322
10.6	Issues in Simulating Cosmic Phenomena . . . . .	323
	10.6.1 Boundary Conditions . . . . .	323
	10.6.2 Relativity . . . . .	324
	10.6.3 Compression of Time Scales . . . . .	324
	10.6.4 Collisions . . . . .	325
10.7	Gravitation . . . . .	327
10.8	Scaling Laws . . . . .	327
10.9	Data Management . . . . .	328
	References . . . . .	329
<b>11</b>	<b>Further Developments in Plasma Simulation</b> . . . . .	331
11.1	Updates in Three-Dimensional, Electromagnetic Particle Simulation Models . . . . .	331
11.2	Astrophysical Plasma and Plasma Cosmology . . . . .	331
11.3	Advancement in Particle/Field Methodology . . . . .	332
11.4	Simulation Results . . . . .	333
	11.4.1 Advances in the Setup of Geometries for Plasmas in Interstellar Space . . . . .	336
	References . . . . .	338

<b>12 Dynamics of Field–Aligned Currents in the Laboratory, Aurorae, and Galactic Space</b>	341
12.1 Formation and Dynamics of Laboratory Currents	341
12.1.1 Formation and Evolution of Plasma Currents	341
12.1.2 Evolution of Field–Aligned Currents	343
12.2 Dense Plasma Focus (DPF)	347
12.3 Evolution of Plasma Filaments via the Biot-Savart Force	348
12.4 Birkeland’s Terrella Experiments	349
12.5 Birkeland’s Trips to Egypt	352
12.6 Macro–Terrella Experiments	354
12.7 Properties of a Strong Aurora	354
12.8 Temporal Occurrence and Properties of Intense Auroras	354
12.9 The Carrington Event	355
12.10 THEMIS Mission	357
References	358
<b>13 Plasma Astrophysics</b>	361
13.1 The Cosmic–Triple–Jump	361
13.2 Near-Earth Plasma Astrophysics	362
13.2.1 “Earth–Currents”	362
13.2.2 View of Birkeland Currents from Ica and Palpa, Peru	363
13.2.3 Mandalas or Concentric Circles in the Southern Hemisphere	364
13.3 The Cosmic Nebula and Interstellar Clouds	365
13.4 Galaxies in Plasma Cosmic Space	367
13.4.1 Double Radio Galaxies	367
13.4.2 Spiral Galaxies	368
References	370
<b>A Transmission Lines</b>	373
A.1 Cosmic Filaments as Transmission Lines	373
A.2 Definition of the State of the Line at a Point	374
A.3 Primary Parameters	374
A.4 General Equations	375
A.4.1 The General Case	375
A.4.2 The Special Case of the Lossless Line	376
A.5 Heaviside’s Operational Calculus (The Laplace Transform)	377
A.5.1 The Propagation Function	377
A.6 Characteristic Impedance	379
A.7 Reflection Coefficients	379
A.8 Time-Domain Reflectometry	380
A.8.1 Cosmic Transmission-Line	381
References	382

**B Polarization of Electromagnetic Waves in Plasma** ..... 383

    References ..... 389

**C Dusty and Grain Plasmas** ..... 391

    C.1 Dusty Plasma ..... 392

    C.2 Grain Plasma ..... 392

    References ..... 395

**D Some Useful Units and Constants** ..... 397

**Index** ..... 401

# Prologue

This is a book about high-energy-density plasma (HEDP). In particular, HEDP applied to astrophysics and cosmology. The contents are a result of 37 years research at Livermore and Los Alamos National Laboratories, all associated with experiments and simulations in the Applied Physics Division, Physics Division, the Associate Laboratory Directorate for Experiments and Simulations, and Defense Programs, U.S. Department of Energy.

The work was carried out within laboratory facilities and at the Nevada Test Site (NTS), usually a few kilometers downhole or within tunnels onsite at Rainer Mesa.

Only in this way could I have access to the energies outlined in Chap. 13, taught me by my mentors, Profs. Hans Kuehl (USC), Hannes Alfvén (Royal Institute of Technology and USC), and Oscar Buneman (Stanford). To these names I add those listed in the Preface without whose guidance, insights, and contributions this book would not be possible.

To be sure, nothing expected was ever encountered; only the unexpected but readily recognizable from a standpoint of HEDP in astrophysics and cosmology, to which I might add earth sciences. These were done jointly at NTS with Russian counterparts under the Threshold Test Ban Treaty (TTBT) during the early 2000s.

The terms ‘Plasma Universe’ and ‘Plasma Cosmology’<sup>1</sup> were first used to describe the 1.4-megaton (MT) 400-km altitude Starfish Event (Fig. 1.4) above Johnston Island in the Pacific, with ground and satellite diagnostics (Brown et al. 1963). The first ‘full-up’, heavily diagnosed HEDP tests were carried out underground at NTS with yields coincidentally slightly less than the TTBT limit.

To the names above I must add Charles Snell, a prime mover in studying the records of over 100 U.S. and British nuclear tests at NTS and the Moruroa archipelago nuclear tests in French Polynesia. In addition to this information was the knowledge picked up by designing and executing intense particle beam experiments, both marx-bank and high-explosive driven.

---

<sup>1</sup> We coined these names in the mid- and late 1980s. Plasma Cosmology does require an understanding of broad-band explosive electromagnetic radiation as outlined in Chap. 6, some nuclear experience, and of course radio astronomy.



On the simulation side, my work with Oscar and his student Jim Green began on the Magnetic Fusion Energy Cray's. I had just rejoined Alfvén, who under the invitation of Harold Urey, discoverer of deuterium, had moved to the University of California, San Diego (UCSD), to organize the La Jolla New Astrophysics seminars. At the time, the Cray-2 (Fig. 10.1, 1980) was the fastest machine available and it was this machine that could model the simplest realistic plasma configuration that Oscar, Jim, and I could think of: Two adjacent ion-electron filaments. These were set up on Oscar's code TRISTAN (Chap. 10). Oscar insisted that these simulations be fully three-dimensional, relativistic, and fully electromagnetic (gravity is included).<sup>2</sup> Once the plasma parameters were set, sizes, and density, magnetic and electric field strengths and directions were chosen, nothing could be changed except run time. The code was run from 1980 to 2012 on ever faster computers as the years went by, and the findings are those given in this book. None of the results were ever expected nor could they be changed.

My special thanks are due to Prof. Timothy Eastman, who was always able to keep my research tied to the achievements reported at IEEE conferences on Plasma Astrophysics and Cosmology and the American Physical Society Topical Group on Plasma Astrophysics, and Prof. Gerrit Verschuur, whose work extended the experimental/simulation results greatly.

---

<sup>2</sup> The Tristan Prime code is sometimes confused with the very much smaller student desktop Tristan learning code given in the First Edition.

# Chapter 1

## Cosmic Plasma Fundamentals

### 1.1 Plasma

Plasma consists of electrically charged particles that respond collectively to electromagnetic forces. The charged particles are usually clouds or beams of electrons, ions, and neutrals or a mixture of electrons ions, and neutrals but also can be charged grains or dust particles. Plasma is also created when a gas is brought to a temperature that is comparable to or higher than that in the interior of stars. At these temperatures, all light atoms are stripped of their electrons, and the gas is reduced to its constituent parts: positively charged bare nuclei and negatively charged free electrons. The name plasma is also properly applied to ionized gases at lower temperatures where a considerable fraction of neutral atoms or molecules are present. However, the subject matter in this book is concerned primarily, but not exclusively, with energetic or highly ionized plasmas.

While all matter is subject to gravitational forces, the positively charged nuclei, or ions, and the negatively charged electrons of plasmas react strongly to electromagnetic forces, as formulated by Oliver Heaviside (1850–1925),<sup>1</sup> but now called Maxwell's Equations, after James Clerk Maxwell (1831–1879),<sup>2</sup>

$$\frac{\partial \mathbf{B}}{\partial t} = -\nabla \times \mathbf{E} \quad (1.1)$$

$$\frac{\partial \mathbf{D}}{\partial t} = \nabla \times \mathbf{H} - \mathbf{j} \quad (1.2)$$

$$\nabla \bullet \mathbf{D} = \rho \quad (1.3)$$

$$\nabla \bullet \mathbf{B} = 0 \quad (1.4)$$

---

<sup>1</sup> Oliver Heaviside was the first to reduce Maxwell's 20 equations in 20 variables to the two Eqs. (1.1) and (1.2) in vector field notation. For some years Eqs. (1.1)–(1.4) were known as the Hertz-Heaviside Equations, and later A. Einstein called them the Maxwell-Hertz Equations. Today, only Maxwell's name is mentioned (Nahin 1988).

<sup>2</sup> These are "rewritten" in update form ideal for programming. This also emphasizes the causality correctly:  $\nabla \times \mathbf{E}$  is the cause of changes in  $\mathbf{B}$ ,  $\nabla \times \mathbf{H}$  is the cause of changes in  $\mathbf{D}$ .

and the equation of motion due to Hendrik Antoon Lorentz (1853–1928),

$$\frac{d}{dt}(mv) = q(E + v \times B); \quad \frac{dr}{dt} = v; \quad (1.5)$$

The quantities  $\mathbf{D} = \epsilon \mathbf{E}$  and  $\mathbf{B} = \mu \mathbf{H}$  are the constitutive relations between the electric field  $\mathbf{E}$  and the displacement  $\mathbf{D}$  and the magnetic induction  $\mathbf{B}$  and magnetic intensity  $\mathbf{H}$ ,  $\mu$  and  $\epsilon$  are the permeability and permittivity of the medium, respectively, and  $\rho$  and  $\mathbf{j}$  are the charge and current densities, respectively.<sup>3</sup> The mass and charge of the particle obeying the force law (1.5) are  $m$  and  $q$ , respectively.

Because of their strong interaction with electromagnetism, plasmas display a complexity in structure and motion that far exceeds that found in matter in the gaseous, liquid, or solid states. For this reason, plasmas, especially their electrodynamic properties, are far from understood. Irving Langmuir; (1881–1957), the electrical engineer and Nobel chemist, coined the term plasma in 1923, probably borrowing the term from medical science to describe the collective motions that gave an almost lifelike behavior to the ion and electron regions with which he experimented. Langmuir was also the first to note the separation of plasma into cell-like regions separated by charged particle sheaths. Today, this cellular structure is observed wherever plasmas with different densities, temperatures, or magnetic field strengths come in contact.

Plasmas need not be neutral (i.e., balanced in number densities of electrons and ions). Indeed, the study of pure electron plasmas and even positron plasmas, as well as the electric fields that form when electrons and ions separate, are among the most interesting topics in plasma research today. In addition to cellular morphology, plasmas often display a filamentary structure. This structure derives from the fact that plasma, because of its free electrons, is a good conductor of electricity, far exceeding the conducting properties of metals such as copper or gold. Wherever charged particles flow in a neutralizing medium, such as free electrons in a background of ions, the charged particle flow or current produces a ring of magnetic field around the current, pinching the current into filamentary strands of conducting currents.

Matter in the plasma state can range in temperature from hundreds of thousands of electronvolts (1 eV = 11,605° absolute) to just 100th of an electronvolt. In density, plasmas may be tenuous, with just a few electrons present in a million cubic centimeters, or they may be dense, with more than  $10^{20}$  electrons packed per cubic centimeter (Fig. 1.1). Nearly all the matter in the universe exists in the plasma state, occurring predominantly in this form in the Sun and stars and in interstellar space. Auroras, lightning, and welding arcs are also plasmas. Plasmas exist in neon and fluorescent tubes, in the sea of electrons that moves freely within energy bands in the crystalline structure of metallic solids, and in many other objects.

Plasmas are prodigious producers of electromagnetic radiation.

---

<sup>3</sup> In free space  $\epsilon = \epsilon_0 = 8.8542 \sim 10^{-12} \text{ F m}^{-1}$  and  $\mu = \mu_0 = 4\pi \sim 10^{-7} \text{ H m}^{-1}$ .

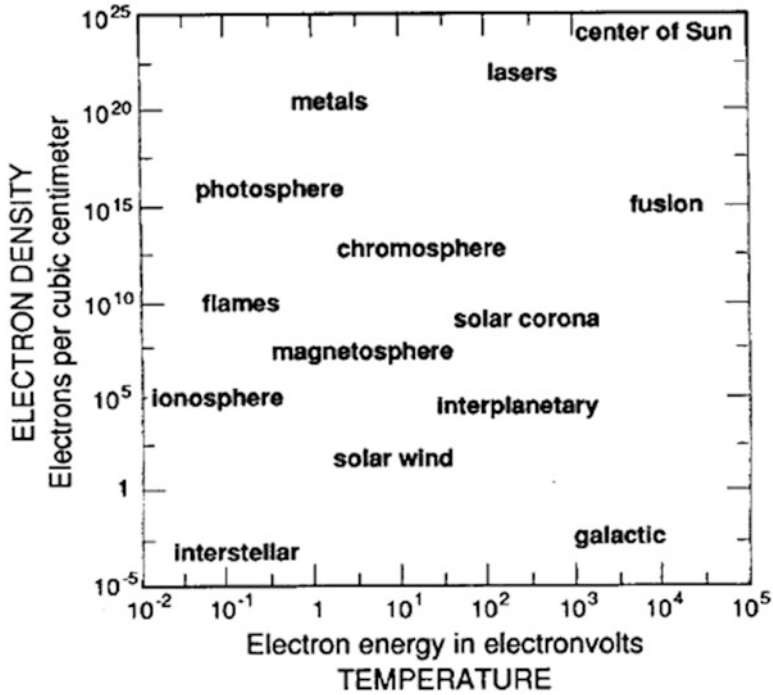


**Fig. 1.1** The remarkable range of temperatures and densities of plasmas is illustrated by this chart. In comparison, solids, liquids, and gases exist over a very small range of temperatures and pressures. In “solid” metals, the electrons that carry an electric current exist as a plasma within the more rigid crystal structure

## 1.2 The Physical Sizes and Characteristics of Plasmas in the Universe

### 1.2.1 Plasmas on Earth

On the earth, plasmas are found with dimensions of microns to meters, that is, sizes spanning six orders of magnitude. The magnetic fields associated with these plasmas range from about 0.5 G (the earth’s ambient field) to megagauss field strengths. Plasma lifetimes on earth span 12–19 orders of magnitude: Laser produced plasmas have properties measurable in picoseconds, pulsed power plasmas have nanosecond to microsecond lifetimes (Fig. 1.2), and magnetically confined fusion oriented plasmas persist for appreciable fractions of a second. Quiescent plasma sources, including fluorescent light sources, continuously produce plasmas whose lifetimes may be measured in hours, weeks, or years, depending on the cleanliness of the ionization system or the integrity of the cathode and anode discharge surfaces ([Jursa 1985](#)).

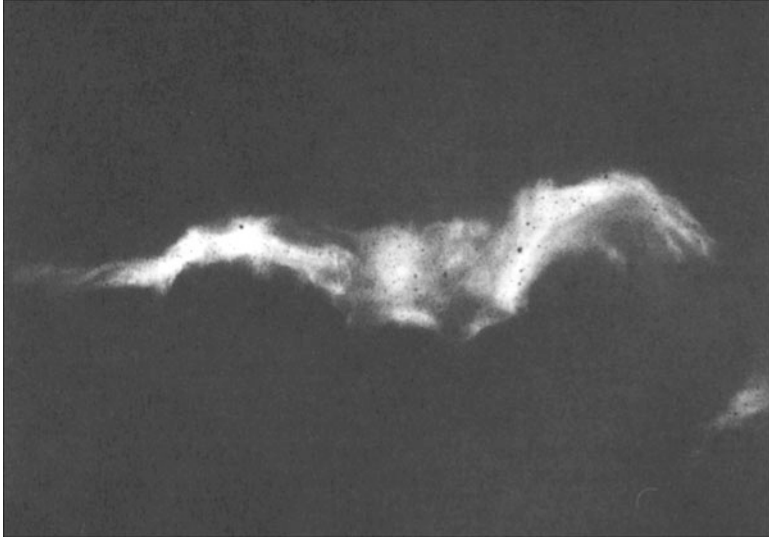


**Fig. 1.2** Filamentary plasma structure produced by “exploding” titanium wires within a 10 TW pulsed-power generator (The photograph was taken with a pin-hole X ray camera)

Lightning is a natural plasma resulting from electrical discharges in the earth’s lower troposphere (Fig. 1.3). Such flashes are usually associated with cumulonimbus clouds but also occur in snow and dust storms, active volcanos, nuclear explosions, and ground fracturing. The maximum time duration of a lightning flash is about 2 s in which peak currents as high as 200 kA can occur. The conversion from air molecules to a singly ionized plasma occurs in a few microseconds, with hundreds of megajoules of energy dissipated and plasma temperatures reaching 3 eV. The discharge channel avalanches at about one-tenth the speed of light, and the high current carrying core expands to a diameter of a few centimeters. The total length of the discharge is typically 2–3 km, although cloud-to-cloud discharges can be appreciably longer (Willett et al. 1990). Lightning has been observed on Jupiter, Saturn, Uranus, and Venus (Borucki 1989). The energy released in a single flash on earth, Venus, and Jupiter is typically  $6 \times 10^8$  J,  $2 \times 10^{10}$  J, and  $2.5 \times 10^{12}$  J, respectively.

Nuclear driven atmospheric plasmas were a notable exception to the generally short-lived energetic plasmas on earth. For example, the 1.4 Mt ( $5.9 \times 10^{15}$  J) Starfish detonation, 400 km above Johnston Island, on July 9, 1962, generated plasma from which artificial Van Allen belts of electrons circulating the earth were created (Ness 1963). These electrons, bound at about 1.2 earth-radii in a 0.175 G field, produced synchrotron radiation whose decay constant exceeded 100 days (Fig. 1.4).

### 1.2.2 Near-Earth Plasmas

The earth's ionosphere and magnetosphere constitute a cosmic plasma system that is readily available for extensive and detailed in situ observation and even active experimentation. Its usefulness as a source of understanding of cosmic plasmas is enhanced by the fact that it contains a rich variety of plasma populations with densities ranging from more than  $10^6 \text{ cm}^{-3}$  to less than  $10^{-2} \text{ cm}^{-3}$ , and temperatures from about 0.1 eV to more than 10 keV.

The earth's magnetosphere is that region of space defined by the interaction of the solar wind with the earth's dipole-like magnetic field. It extends from approximately 100 km above the earth's surface, where the proton neutral atom collision frequency is equal to the proton gyrofrequency, to about ten earth radii ( $\sim 63,800 \text{ km}$ ) in the sunward direction and to several hundred earth radii in the anti-sunward direction. It is shown schematically in Fig. 1.5.

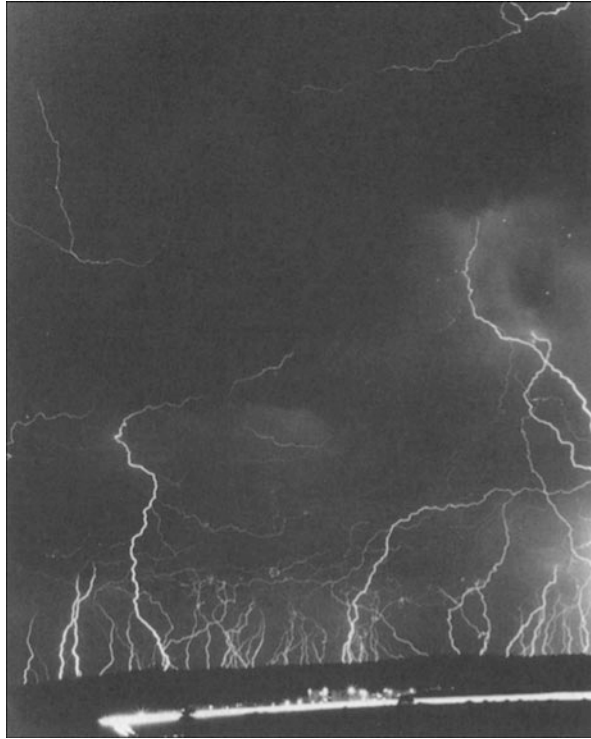


**Fig. 1.3** Cloud to ground lightning on earth (5 min exposure). The discharge channel may be 20 % ionized plasma. The potential difference between the lower portion of the cloud and earth is in excess of 10 MV. The *bright line* at the lower right is the Santa Fe-Los Alamos highway (Courtesy of Henry Ortega, Santa Fe, New Mexico)



**Fig. 1.4** Starfish event. Artificial aurora produced by plasma particles streaming along the earth's magnetic field lines. Picture taken from a Los Alamos KC-135 aircraft 3 min after the July 9, 1962, 1.4-Mt 400-km-altitude nuclear detonation above Johnston Island. The event produced a degradation of radio communications over large areas of the Pacific and an intense equatorial tube of synchrotron emitting electrons having a decay constant of 100 days. The brightest background object (mark) at the top, left-hand corner is the star Antares, while the right-hand-most object is  $\theta$ -Centauri. The burst point is two-thirds of the way up the lower plasma striation

First detected by radio waves and then by radar, the ionosphere is a layered plasma region closest to the surface of the earth whose properties change continuously during a full day (Fig. 1.6). First to be identified was a layer of molecular ionization, called the *E* layer. This region extends over a height range of 90–140 km and may have a nominal density of  $10^5 \text{ cm}^{-3}$  during periods of low solar activity. A *D* region underlies this with a nominal daytime density of  $10^3 \text{ cm}^{-3}$ . Overlying the *E* region is the *F* layer of ionization, the major layer of the ionosphere, starting at about 140 km. In the height range 100–150 km, strong electric currents are generated by a process analogous to that of a conventional electric generator, or dynamo. The region, in consequence, is often termed the dynamo region and may have densities of  $10^6 \text{ cm}^{-3}$ . The *F* layer may extend 1,000 km in altitude where it eventually merges with the plasmas of the magnetopause and solar wind.

The interaction of the supersonic solar wind with the intrinsic dipole magnetic field of the earth forms the magnetosphere whose boundary, called the magnetopause, separates interplanetary and geophysical magnetic fields and plasma environments. Upstream of the magnetopause a collisionless bow shock is formed in the solar wind-magnetosphere interaction process. At the bow shock the solar wind becomes thermalized and subsonic and continues its flow around the magnetosphere as magnetosheath plasma, ultimately rejoining the undisturbed solar wind.

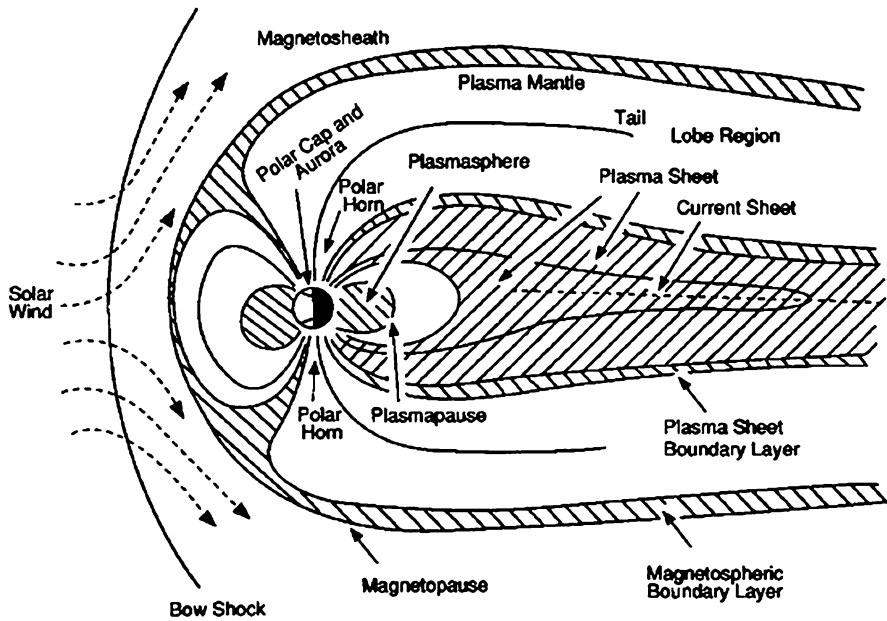


**Fig. 1.5** Earth's magnetosphere. Ions and electrons in the solar wind (*left*) impinge against the magnetosphere, distorting the field lines and creating a bow shock and the various regions shown

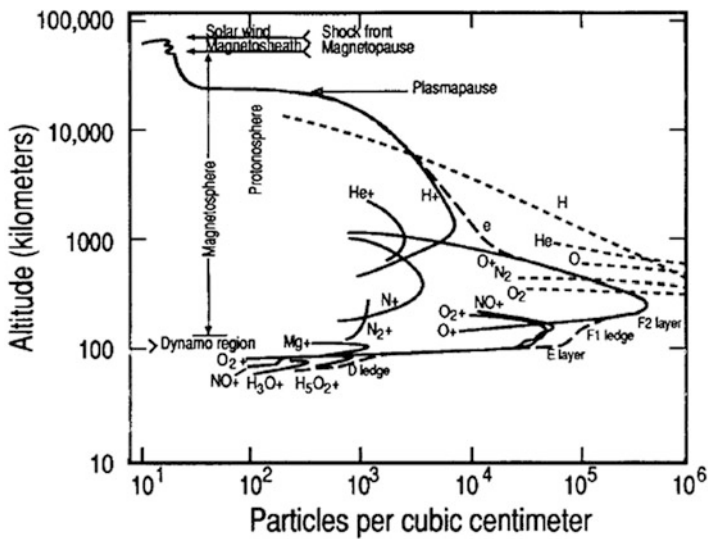


**Fig. 1.6** Daytime ionosphere at low latitudes and low solar activity



In the anti-solar direction, observations show that the earth's magnetic field is stretched out in an elongated geomagnetic tail to distances of several hundred earth radii. The field lines of the geomagnetic tail intersect the earth at high latitudes ( $\approx 60^\circ$ – $75^\circ$ ) in both the northern and southern hemisphere (polar horns), near the geomagnetic poles. Topologically, the geomagnetic tail roughly consists of oppositely directed field lines separated by a “neutral” sheet of nearly zero magnetic field. Surrounding the neutral sheet is a plasma of “hot” particles having a temperature of 1–10 keV, density of  $\approx 0.01$ – $1 \text{ cm}^{-3}$ , and a bulk flow velocity of a few tens to a few hundreds of  $\text{km s}^{-1}$ .

Deep within the magnetosphere is the plasmasphere, a population of cold ( $\leq 1 \text{ eV}$ ) ionospheric ions and electrons corotating with the earth. Table 1.1 lists some typical values of parameters in the earth's magnetosphere.

### ***1.2.3 Plasmas in the Solar System***

The space environment around the various planetary satellites and rings in the solar system is filled with plasma such as the solar wind, solar and galactic cosmic rays (high energy charged particles), and particles trapped in the planetary magnetospheres. The first in situ observations of plasma and energetic particle populations in the magnetospheres of Jupiter, Saturn, Uranus, Neptune, and Titan were made by the Voyager 1 and 2 spacecraft from 1979 to 1989. Interplanetary spacecraft have identified magnetospheres around Mercury, Venus, Jupiter, Saturn, Uranus, and Neptune (e.g., Fig. 1.7).

Comets also have “magnetospheres” as depicted in Fig. 1.8. The comet-to-sheath, a region extending about  $1.1 \times 10^6 \text{ km}$  (for Comet Halley), consists of decelerated plasma of density and temperature  $T_e \sim 1.5 \text{ eV}$ . The peak magnetic field strength found in Comet Halley was 700–800 mG.

Excluding the Sun, the largest organized structures found in the solar system are the plasma tori around Jupiter and Saturn. The Jupiter-Io plasma torus (Fig. 1.9) is primarily filled with sulphur ions at a density of  $3 \times 10^3 \text{ cm}^{-3}$  (Sect. 4.6.2). An immense weakly ionized hydrogen plasma torus has been found to encircle Saturn, with an outer diameter 25 times the radius of the planet and an inner diameter of about 15 Saturn radii (Book 1987, Lang 1974).

### ***1.2.4 Transition Regions in the Solar System***

Examples of transition regions include the boundary layers found in planetary and comet magnetospheres (Table 1.2). Transition regions between plasmas of different densities, temperatures, magnetization, and chemical composition offer a rich variety of plasma phenomena in the solar system (Eastman 1990).

**Table 1.1** Typical values of some parameters in the earth's magnetosphere (Adapted from A.T.Y. Lui 1987)

	Inner side of					Plasma-sheet		Central
	Magnetosheath	Magnetopause	boundary layer	Plasma mantle	Tail lobe	boundary layer	plasma sheet	
Characteristics								
Number density	$n$ (cm <sup>-3</sup> )	5	20	1	1	10 <sup>-2</sup>	0.1	0.5
Ion temperature	$T_i$ (KeV)	0.1	0.8	4	0.1	0.1	1	5
Electron temperature	$T_e$ (KeV)	0.05	0.08	0.15	0.05	0.05	0.5	1
Magnetic field	$B$ (nT)	5	25	40	25	25	20	10
Electric field	$E$ (mV/m)	1			1	0.1	300	0.01
Lengths								
Debye length	$\lambda_D$ (m)	18	10		40	400	400	280
Plasma skin depth	$\lambda_E$ (m)	$2.4 \times 10^3$			$5.3 \times 10^3$	$5.3 \times 10^4$	$1.7 \times 10^4$	$7.5 \times 10^3$
Electron gyroradius	$rL_e$ ( $R_e$ )	$4.9 \times 10^{-4}$	$1.1 \times 10^{-4}$	$1.1 \times 10^{-4}$	$9.8 \times 10^{-5}$	$9.8 \times 10^{-5}$	$3.9 \times 10^{-4}$	$1.1 \times 10^{-3}$
Ion gyroradius	$rL_i$ ( $R_e$ )	$3.0 \times 10^{-2}$	$2.2 \times 10^{-2}$	$2.5 \times 10^{-2}$	$5.9 \times 10^{-3}$	$5.9 \times 10^{-3}$	$2.3 \times 10^{-2}$	$1.0 \times 10^{-1}$
Frequencies								
Electron cyclotron	$f_{ce}$ (Hz)	$1.4 \times 10^2$	$7.0 \times 10^2$	$6.0 \times 10^2$	$7.0 \times 10^2$	$7.0 \times 10^2$	$5.6 \times 10^2$	$2.8 \times 10^2$
Ion cyclotron	$f_{ci}$ (Hz)	$7.6 \times 10^{-2}$	$4.0 \times 10^{-1}$	$6.0 \times 10^{-1}$	$3.8 \times 10^{-1}$	$3.8 \times 10^{-1}$	$3.0 \times 10^{-1}$	$1.5 \times 10^{-1}$
Electron plasma	$f_{pe}$ (Hz)	$2.0 \times 10^4$	$4.0 \times 10^4$	$9.0 \times 10^3$	$9.0 \times 10^3$	$9.0 \times 10^2$	$2.8 \times 10^3$	$6.3 \times 10^3$
Ion plasma	$f_{pi}$ (Hz)	$4.7 \times 10^2$	$1.0 \times 10^3$	$2.0 \times 10^2$	$2.1 \times 10^2$	$2.1 \times 10^1$	$6.6 \times 10^1$	$1.5 \times 10^2$
Frequency ratio	$\omega_{pe}/\omega_{ce}$	$1.4 \times 10^2$	$5.7 \times 10^1$	$1.5 \times 10^1$	$1.3 \times 10^1$	$1.3 \times 10^0$	$5.0 \times 10^0$	$4.5 \times 10^1$
Velocities								
Ion sound	$c_g$ (km/s)	83			83	83	260	370
Alfvén	$v_A$ (km/s)	49	122	870	550	5,500	1,400	300
Electron thermal	$v_{the}$ (km/s)	2,800			2,800	2,800	8,700	$1.2 \times 10^4$
Ion thermal	$v_{thi}$ (km/s)	91	277	619	91	91	290	640
Convection	$v_E$ (km/s)	200	250	50	4	4	5	1
Miscellaneous								
Thermal/magnetic energy ratio	$\beta_p$	6.9	10.0	1.0	0.056	$5.6 \times 10^{-4}$	0.87	8.8
Magnetic energy density	(J m <sup>-3</sup> )	$9.9 \times 10^{-18}$			$2.5 \times 10^{-16}$	$2.5 \times 10^{-16}$	$1.6 \times 10^{-16}$	$4.0 \times 10^{-17}$
								$1.6 \times 10^{-18}$

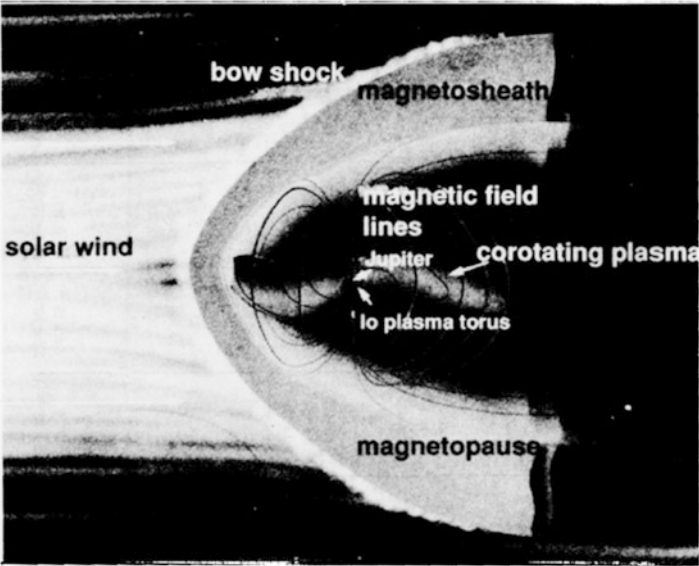


**Fig. 1.7** Jupiter’s magnetosphere. Io’s plasma torus contains energetic sulfur and oxygen ions arising from the moon’s active discharges

**Table 1.2** Plasma transition regions within the solar system

Transition region	$n(\text{cm}^{-3})$	$T(\text{eV})^a$	$v(\text{km/s})$	$B(\mu\text{G})^b$
<i>Earth’s Magnetosphere</i>				
Plasmapause	5–1,000	1–1,000	0–0.1	500–5,000
Bow shock	10–50	5–100 (ions) 10–40( $e^-$ )	100–500	50–300
Magnetopause and boundary layer	0.5–30	500–1,600 (ions) 25–200( $e^-$ )	25–350	100–600
Plasma sheet boundary layer	0.02–1	300–2,000(ions) 30–500( $e^-$ )	0–1,500	10–500
<i>Other Transition Regions</i>				
Jovian boundary layer	0.01–1	10–30 keV (ions) 50–3,000eV( $e^-$ )	100–800	1–15
Cometary boundary layer	10–100	1–50	20–300	50–300
Heliopause	0.00001–1	0.1–100	10–100	0.1–200

<sup>a</sup> Temperature associated with  $1\text{ eV} = 1.602 \times 10^{-19}\text{ J} = 11,600^\circ\text{K}$

<sup>b</sup>  $1\text{ }\mu\text{G} = 0.1\text{ nT}$



**Fig. 1.8** Comet Kohoutek. The filamentary structure of the tail is typical of the structure of plasmas at all scale (December 7, 1973. Source: NASA)

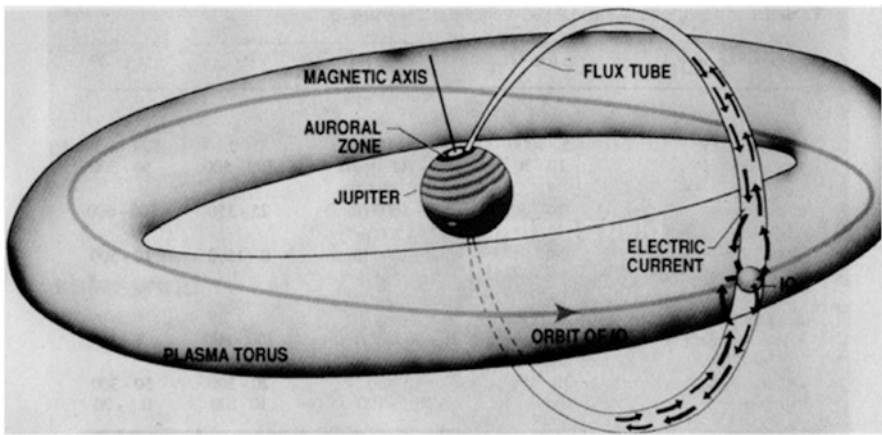


**Fig. 1.9** The Jupiter-Io plasma torus. The diagram shows the megaampere Birkeland currents flowing between Jupiter and Io

### 1.2.5 Solar, Stellar, and Interstellar Plasmas

The nuclear core of the Sun is a plasma at about a temperature of 1.5 keV. Beyond this, our knowledge about the Sun's interior is highly uncertain. Processes which govern the abundance of elements, nuclear reactions, and the generation mechanism and strength of the interior magnetic fields, are incompletely known.

We do have information about the Sun's surface atmospheres that are delineated as follows: the photosphere, the chromosphere, and the inner corona. These plasma layers are superposed on the Sun like onion skins. The photosphere ( $T \sim 0.5$  eV) is only a very weakly ionized atmosphere, the degree of ionization being  $10^{-4}$ – $10^{-5}$  in the quiet regions and perhaps  $10^{-6}$ – $10^{-7}$  in the vicinity of sunspots. The chromosphere ( $T \sim 4$  eV) extends 5,000 km above the photosphere and is a transition region to the inner corona. The highly ionized inner corona extends some  $10^5$  km above the photosphere. From a plasma physics point of view, the corona is perhaps the

most interesting region of the Sun. The corona is the sight of explosively unstable magnetic-field configurations, X ray emission (Fig. 1.10), and plasma temperatures in the range 70–263 eV (Table 1.3).<sup>4</sup> The source of this heating is uncertain.<sup>5</sup>

**Table 1.3** Parameters associated with the Sun

<i>Density</i>	
At center	$(10^{26} \text{ cm}^{-3}) 160 \text{ g/cm}^3$
At surface	$(10^{15} \text{ cm}^{-3}) 10^{-9} \text{ g/cm}^3$
In corona	$(10^7 \text{ cm}^{-3}) 10^{16} \text{ g/cm}^3$
<i>Temperature</i>	
At center	1.5 keV
At surface	0.5 eV
In sunspots	0.37 eV
In chromosphere	0.38 – 4.5 eV
In corona	70 eV – 263 eV
<i>Emission</i>	$3.826 \times 10^{26} \text{ W}$
<i>Magnetic field strengths</i>	
In sunspots	→ 3.5 kG
Elsewhere on Sun	1 – 100 G

Solar flares resulting from coronal instabilities raise temperatures to 10–30 keV and produce relativistic streams of electrons and protons. Particles accelerated outward produce radio interference at the earth. Protons accelerated inward collide with ions in the Sun’s atmosphere to produce nuclear reactions, whose gamma rays and neutrons have been detected from spacecraft. Solar flares consist of plasma at a temperature of about 1–10 keV. Although flares represent the most intense energy

<sup>4</sup> One of the Sun’s outstanding problems is the temperature of the corona. The temperature rises steadily in the chromosphere, then jumps abruptly in the corona to a level 300 times hotter than the surface. That the Sun is a plasma and not just a hot gaseous object is illustrated by the fact that the temperature increases away from its surface, rather than cooling as dictated by the thermodynamic principle for matter in the nonplasma state.

<sup>5</sup> For decades the preferred explanation has been that energy flows from the Sun’s surface to the corona in the form of sound waves generated by convective upswelling motions. However, space-based ultraviolet observations proved that sound waves do not carry energy as high as the corona. One mechanism that may produce coronal heating is electron beams produced in double layers in coronal loops (Chap. 5). These are expected to accelerate electrons to energies comparable to those in the corona. Generally, the term acceleration refers to the preferential gain of energy by a population of electrons and ions, while heating is defined as the bulk energization of the ambient plasma. Paraphrasing Kirchoff that “heating is a special kind of acceleration,” one may argue, since heating and acceleration are always present in flares and in laboratory relativistic electron beams, that electron beam instabilities (Sect. 1.7.3) may be the source of coronal heating.



**Fig. 1.10** Solar Dynamics Observatory photograph of solar prominence features of the Sun (Credit: NASA)

dissipation of any form of solar activity, releasing energy in the form of gamma rays, X rays, and microwaves, the active sun has many other plasma manifestations.

These include sunspots, photospheric faculae, chromospheric and transition region plages, large coronal loops, and even larger scale coronal streamers and occasional coronal mass ejections. In addition, prominences (referred to as filaments when seen in  $H_\alpha$  absorption on the disk) frequently form between opposite magnetic polarities in active regions of the sun. These phenomena are dynamic, on time scales ranging from seconds to the complete solar magnetic cycle of 22 years.

The outer corona and solar wind form the heliosphere (Fig. 1.11). At one astronomical unit the solar wind has a plasma density  $5 \leq n \leq 60 \text{ cm}^{-3}$  and a velocity of  $200 \leq v_{sw} \leq 800 \text{ km s}^{-1}$ . Its temperature can be as high as 50 eV, while  $B$  may reach 200 mG. The outer heliosphere has a plasma density, a temperature, and a magnetic field strength  $\sim 1 \text{ mG}$ . The local interstellar medium is characterized by  $10^{-2} \leq n \leq 1 \text{ cm}^{-3}$ , a temperature of order 1 eV, and magnetic field strength  $1 \leq B \leq 20 \mu\text{G}$ . Table 1.4 lists some of the parameter values found in the solar system.

The rotating sun, coupled with its continual radial ejection of plasma, twists its magnetic field (that is referred to as the interplanetary magnetic field or IMF) into a classical Archimedean spiral, as depicted in Fig. 1.12a, b. Measurements have confirmed that the interplanetary magnetic field is directed toward the sun in certain regions of the solar system and away from the sun in other regions. These regions are separated by a very sharp boundary layer that is interpreted as a current layer.

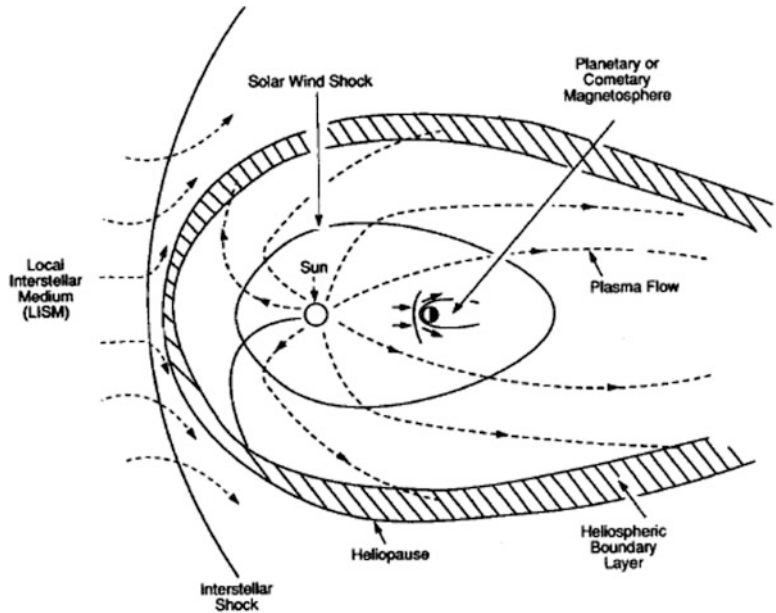


**Fig. 1.11** The heliosphere

This layer is depicted in Fig. 1.12b which shows “ripples” in the sheet. In this situation, the planets find themselves sometimes in a region where the field has a strong northward component and sometimes where it has a strong southward component (Priest 1985).

**Table 1.4** Solar system plasmas

Parameter	Solar wind at 1 AU	Outer heliosphere	Local interstellar medium	Planetary boundary layers
$n_i = n_e(\text{cm}^{-3})$	5–60	0.001–0.1	0.01–1	0.05–50
$kT_{i,e}(\text{eV})$	1–50	0.1–10	0.1–10	5–5,000
$v(\text{km/s})$	200–800	10–100	1–30	10–1,500
$B(\mu\text{G})$	10–200	$< 1$ –1	$< 1$ –20	10–500

Stellar plasmas have not only the dimension of the star,  $0.3 \times 10^6$ – $10^8$  km, but also the stellar magnetospheres, a remnant of the interstellar plasma that the star and its satellites condensed out of. The surface temperatures vary from about 0.3–3 eV. Estimates of the magnetic fields range from a few gauss to tens of kilogauss or more for magnetic variable stars.

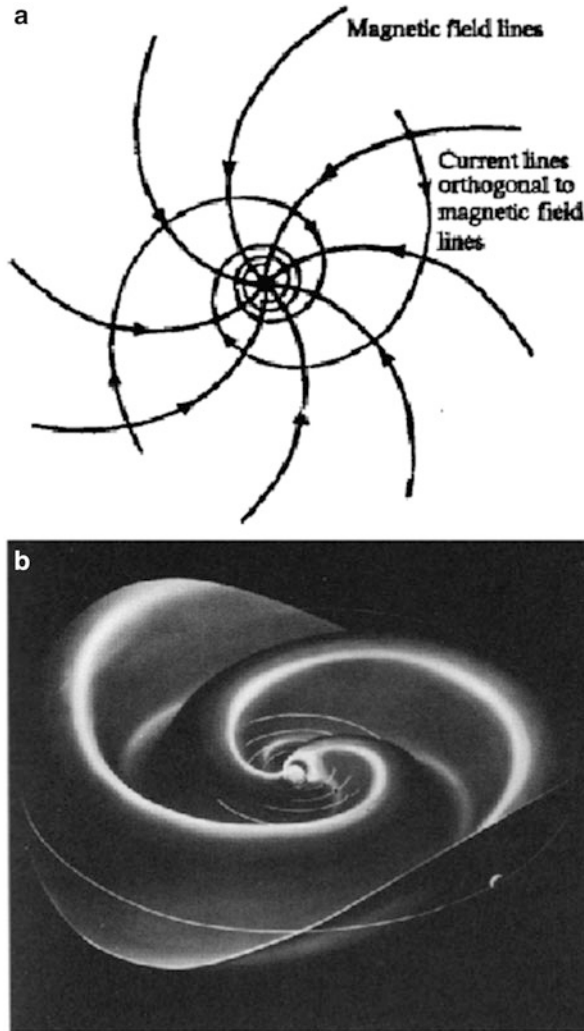


**Fig. 1.12** (a) Magnetic field lines of the sun which are bent into Archimedean spirals owing to the rotation of the sun and the radial emission of plasma (which carries the magnetic field). This is a view over the north pole of the sun looking downward at the field lines slightly above the sun's equatorial plane. Close below the equatorial plane, the field lines have the same geometry but opposite direction. The shapes of the associated current lines are also shown. (b) An artist's view of the solar current sheet in the equatorial plane. [Alfvén \(1981\)](#) has proposed that the sheet develops ripples like the skirt of a ballerina. As this system rotates, the planets find themselves in different regions so that the interplanetary magnetic field can assume a variety of orientations, e.g., directed toward or away from the sun and northward or southward (Courtesy of T. Potemra)



Stellar winds occur in stars of many types, with wind properties probably connected with stellar magnetism (Table 1.5).

**Table 1.5** Parameters associated with the interstellar medium

Parameter	Stellar wind	Hot ionized medium	Warm ionized medium	Warm neutral medium	Cool neutral medium	Filaments, cloud edges, shock interfaces
Neutral density ( $\text{cm}^{-3}$ )	$< 1$	0	$< 1$	$10^{-1} - 10^1$	$10^0 - 10^4$	$10^1 - 10^4$
$n_i = n_e (\text{cm}^{-3})$	$10^{-1} - 10^3$	$< 10^{-3} - 10^1$	$10^{-1} - 10^1$	$10^{-2} - 10^0$	$10^{-2} - 10^2$	$10^0 - 10^3$
$kT_{i,e} (\text{eV})$	$10^0 - 10^2$	$10^1 - 10^4$	$0.5 - 1$	$10^{-1} - 10^0$	$10^{-2} - 10^{-1}$	$10^0 - > 10^3$
$v (\text{km/s})$	200–1,000	1–20	1–20	1–20	1–100	20–1,500
$B (\mu\text{G})$	5–500	$< 1 - 100$	1–50	1–50	$< 1 - 20$	1–1,000

### 1.2.6 Galactic and Extragalactic Plasmas

Dark clouds within our Galaxy have dimensions of  $10^8$  km and microgauss strength magnetic fields (Fig. 1.13).

The Galactic plasma has an extent equal to the dimensions of our Galaxy itself;  $\sim 35$  kpc or  $10^{21}$  m. The most salient feature of the Galactic plasma are  $10^{-3}$  G poloidal-toroidal plasma filaments extending nearly 250 light years (60 pc,  $1.8 \times 10^{18}$  m) at the Galactic center (Fig. 1.14). The vast regions of nearly neutral hydrogen (HI regions) found in the Galaxy and other galaxies are weakly ionized plasmas. These regions extend across the entire width of the galaxy and are sometimes found between interacting galaxies. They are detected by the 21 cm radiation they emit.

Galaxies may have bulk plasma densities of  $10^{-1} \text{ cm}^{-3}$ ; groups of galaxies,  $3 \times 10^{-2} \text{ cm}^{-3}$ ; and rich clusters of galaxies,  $3 \times 10^{-3} \text{ cm}^{-3}$ .

By far the single largest plasmas detected in the Universe are those of double radio galaxies. In size, these sources extend hundreds of kiloparsecs ( $10^{21}$ – $10^{22}$  m) to a few megaparsecs ( $10^{22}$ – $10^{23}$  m). Double radio galaxies are thought to have densities of  $10^{-3} \text{ cm}^{-3}$  and magnetic fields of the order of  $10^{-4}$  G (Fig. 1.15).



**Fig. 1.13** The Veil nebula in Cygnus (Credit: NASA)

### 1.3 Regions of Applicability of Plasma Physics

The degree of ionization in interplanetary space and in other cosmic plasmas may vary over a wide range, from fully ionized to degrees of ionization of only a fraction of a percent.<sup>6</sup> Even weakly ionized plasma reacts strongly to electromagnetic fields since the ratio of the electromagnetic force to the gravitational force is 39 orders of magnitude. For example, although the solar photospheric plasma has a degree of ionization as low as  $10^{-4}$ , the major part of the condensable components

---

<sup>6</sup> The degree of ionization is defined as  $n_p / (n_0 + n_p)$  where  $n_p$  is the plasma density and  $n_0$  is the density of neutral particles.

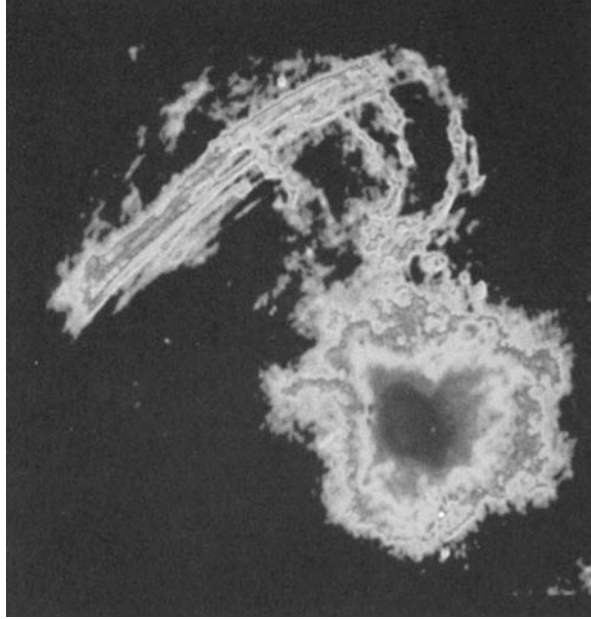


**Fig. 1.14** VLA radiograph of large-scale, 20-cm radio emission features within  $\sim 60$  pc (20 arcmin) of the Galactic nucleus. The galactic plane runs from *top-left* to *bottom-right*, through the lower diffuse structure. The contrast is chosen to bring out radio features brighter than 15 mJy per beam area (the half-power beam width is  $5 \times 9$  arcsec) (Courtesy F. Yusef-Zadeh et al. 1984)

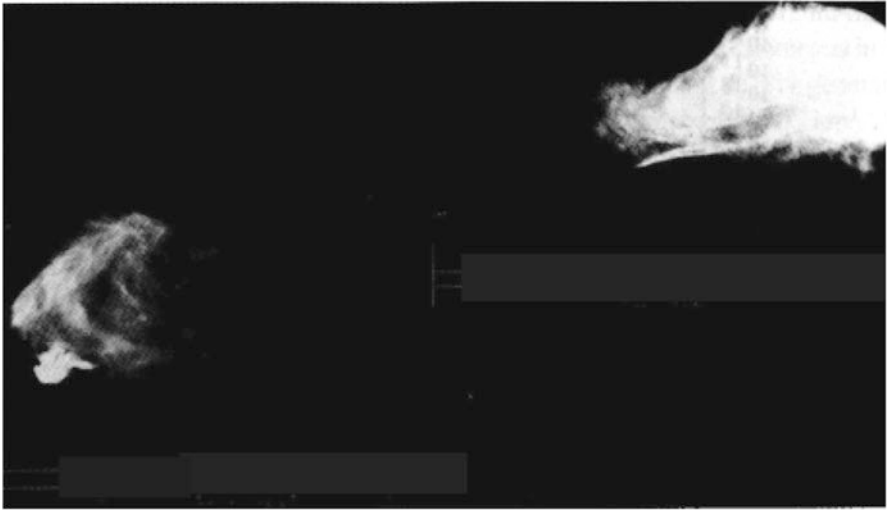


**Fig. 1.15** Photographic representation of Cygnus A at 6 cm wavelength with  $0.4''$  resolution. The east-west extent of the radio emission is  $127''$ . The bars beneath each radio lobe denote the receiver sensitivity: The left-hand lobe is at about 5 mJy/pixel, while the right-hand lobe is 1.5 mJy/pixel. The plasma associated with this radio galaxy is thought to have  $n \approx 2 - 3 \times 10^{-3} \text{ cm}^{-3}$  and  $B \approx 1 - 2 \times 10^{-4} \text{ G}$

is still largely ionized. The “neutral” hydrogen (HI) regions around galaxies are also plasmas, although the degree of ionization is only  $10^{-4}$ . Most of our knowledge about electromagnetic waves in plasmas derives from laboratory plasma experiments where the gases used have a low degree of ionization,  $10^{-2}$ – $10^{-6}$ .

Because electromagnetic fields play such an important role in the electrodynamics of plasmas, and because the dynamics of plasmas are often the sources of electromagnetic fields, it is desirable to determine where within the universe a plasma approach is necessary. We first consider the magnetic field. The criterion for neglecting magnetic effects in the treatment of a problem in gas dynamics is that the Lundquist parameter (Sect. 2.4.2) is much less than unity,

**Table 1.6** Characteristics quantities for laboratory and cosmic plasmas (Adapted from [Alfvén and Fälthammar 1963](#))

	$l_c$ (m)	$B$ (T)	$\rho_m$ (kg/m <sup>3</sup> )	$\sigma$ (S/m)	$V_A$ (m/s)	$L_u$
<i>Laboratory experiments</i>						
Mercury	0.1	1	$10^4$	$10^6$	7.7	1
Sodium	0.1	1	$10^3$	$10^7$	30	37
Hydrogen	0.1	1	$10^{-7}$	$5 \times 10^4$	$2.8 \times 10^6$	$2 \times 10^4$
<i>Cosmic plasmas</i>						
Earth's interior	$10^6$	$10^{-3}$ (?)	$10^4$	$8 \times 10^5$	$10^{-2}$	$10^4$
Sunspots	$10^7$	0.2	$10^{-1}$	$4.4 \times 10^4$	20	$10^8$
Solar granulation	$10^6$	$10^{-2}$	$10^{-4}$	$8 \times 10^3$	$10^3$	$10^7$
Magnetic variable stars	$10^{10}$	1	$10^3$ (?)	$8 \times 10^5$	30	$3 \times 10^{11}$
Interstellar space	$10^{20}$	$10^{-9}$ (?)	$10^{-21}$ (?)	$8 \times 10^2$ (?)	$3 \times 10^4$	$3 \times 10^{21}$
Interplanetary space	$10^{11}$	$10^{-8}$	$10^{-20}$	$8 \times 10^4$ (?)	$10^5$	$10^{15}$
Solar corona	$10^9$	$10^{-4}$ (?)	$10^{-15}$ (?)	$8 \times 10^5$ (?)	$3 \times 10^6$	$3 \times 10^{15}$
Dark clouds	$10^{11}$	$10^{-10}$	$10^{-17}$	$5 \times 10^2$	30	$2 \times 10^9$

$$L_u = \frac{u^{1/2} \sigma B l_c}{\sqrt{\rho_m}} \ll 1 \quad (1.6)$$

where  $l_c$  is a characteristic length of the plasma and  $\rho_m$  is the mass density. As the conductivity of known plasmas generally varies only over about four orders of magnitude, from  $10^2$  to  $10^6$  S/m, the value of  $L_u$  is largely dependent on the strength of  $B$  in the plasma as delineated in Table 1.6.

The variation of  $B$  in plasmas can be 18 orders of magnitude, from microgauss strengths in intergalactic space to perhaps teragauss levels in the magnetospheres of neutron sources. On earth, magnetic field strengths can be found from about 0.5 G ( $0.5 \times 10^{-4}$  T) to  $10^7$  G ( $10^3$  T) in pulsed-power experiments; the outer planets have magnetic fields reaching many gauss, while the magnetic fields of stars are 30–40 kG (3–4 T). Large scale magnetic fields have also been discovered in distant cosmic

objects. The center of the Galaxy has milligauss magnetic field strengths stretching 60 pc in length. Similar strengths are inferred from polarization measurements of radiation recorded for double radio galaxies. No rotating object in the universe, that is devoid of a magnetic field, is known.

In cosmic problems involving planetary, interplanetary, interstellar, galactic, and extragalactic phenomena, is usually of the order  $10^{15}$ – $10^{20}$  (Fig. 1.16). In planetary ionospheres falls below unity in the *E* layer. Neglecting lightning, planetary atmospheres and hydrospheres are the only domains in the universe where a nonhydromagnetic treatment of fluid dynamic problems is justified.

## 1.4 Power Generation and Transmission

On earth, power is generated by nuclear and nonnuclear fuels, hydro and solar energy, and to a much lesser extent, by geothermal sources and magnetohydrodynamic generators. Always, the location of the supply is not the location of major power usage or dissipation. Transmission lines are used to convey the power generated to the load region. As an example, abundant hydroelectric resources in the Pacific Northwest of the United States produce power ( $\sim 1,500$  MW) that is then transmitted to Los Angeles, 1,330 km away, via 800 kV high-efficiency dc transmission lines. In optical and infrared emission, only the load region, Los Angeles, is visible from the light and heat it dissipates in power usage. The transmission line is invisible (Fig. 1.17).

This situation is also true in space. With the coming of the space age and the subsequent discovery of magnetospheric-ionospheric electrical circuits, Kirchoff's circuit laws (Appendix A) were suddenly catapulted to dimensions eight orders of magnitude larger than that previously investigated in the laboratory and nearly four orders of magnitude greater than that associated with the longest power distribution systems on earth.

On earth, transmission lines consist of metallic conductors or waveguides in which energy is made to flow via the motion of free electrons (currents) in the metal or in displacement currents in a time varying electric field. Often strong currents within the line allow the transmission of power many orders of magnitude stronger than that possible with weak currents. This is because a current associated with the flow of electrons produces a self-magnetic field that helps to confine or pinch the particle flow. Magnetic-insulation is commonly used in pulsed-power technology to transmit large amounts of power from the generator to the load without suffering a breakdown due to leakage currents caused by high electric potentials (Di Capua 1983).

There is a tendency for charged particles to follow magnetic lines of force and this forms the basis of transmission lines in space (Appendix A). In the magnetosphere-ionosphere, a transmission line 7–8 earth radii in length ( $R_e = 6,350$  km) can convey tens of terawatts of power, that derives from the solar

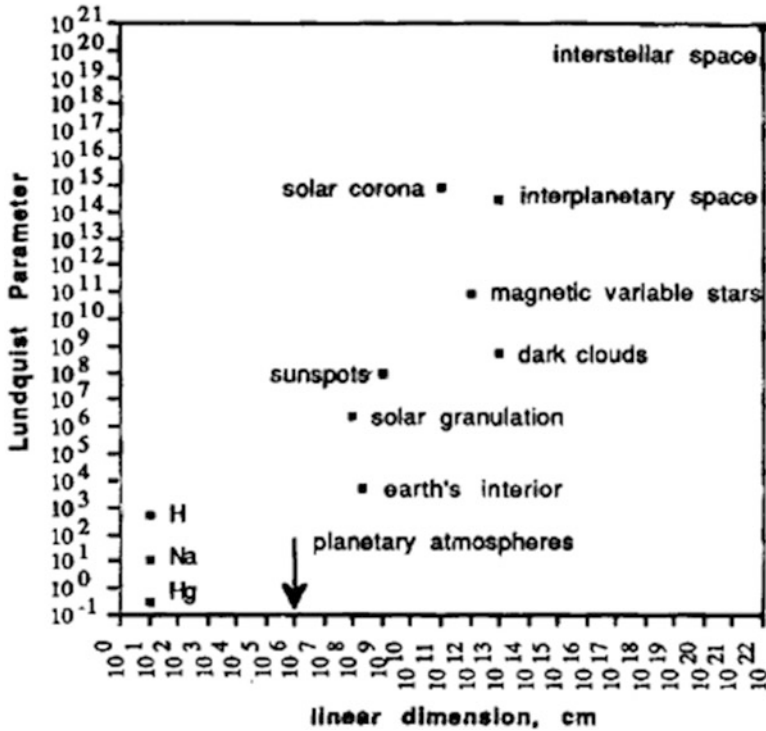


**Fig. 1.16** The Lundquist parameter  $L_u$  vs linear dimension for a variety of laboratory, space, and astronomical plasmas

wind-magnetosphere coupling,<sup>7</sup> to the lower atmosphere. The transmission line is the earth's dipole magnetic field lines along which electrons and ions are constrained to flow. The driving potential is solar-wind induced plasma moving across the magnetic field lines at large radii. The result is an electrical circuit in which electric currents cause the formation of auroras at high latitude in the upper atmosphere on earth. This aurora mechanism is observed on Jupiter, Io, Saturn, Uranus, and is thought to have been detected on Neptune and perhaps, Venus.

Only the aurora discharge is visible at optical wavelengths to an observer. The source and transmission line are invisible (Fig. 1.18). Before the coming of space probes, in situ measurement was impossible and exotic explanations were often given of auroras. This is probably true of other non in situ cosmic plasmas today. The existence of a megaampere flux tube of current, connecting the Jovian satellite Io to its mother planet (Fig. 1.9), was verified with the passage of the Voyager spacecraft.

<sup>7</sup> It is not known how the energy carried by the solar wind is transformed into the energy of the aurora. It has been demonstrated that the southward-directed interplanetary magnetic field is an essential ingredient in causing auroral substorms so that energy transformation appears to occur through interactions between the interplanetary and geomagnetic fields (Akasofu 1981).

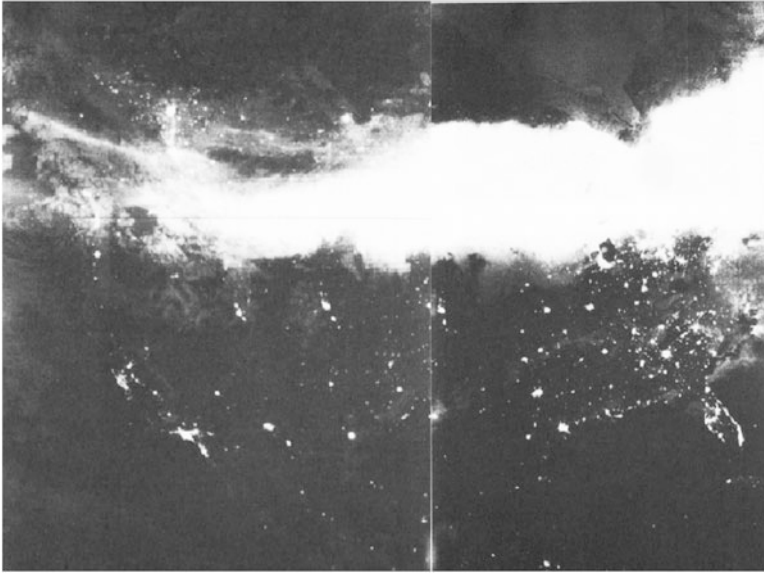


**Fig. 1.17** White light view of the United States at night. Satellite images of visible light radiation defines major metropolitan areas, while other land features are illuminated by moonlight. This composite image was obtained around June 27, 2011 (Credit: NASA, GSFC)

## 1.5 Electrical Discharges in Cosmic Plasma

An electrical discharge is a sudden release of electric or magnetic stored energy. This generally occurs when the electromagnetic stress exceeds some threshold for breakdown that is usually determined by small scale properties of the energy transmission medium. As such, discharges are local phenomena and are usually accompanied by violent processes such as rapid heating, ionization, the creation of pinched and filamentary conduction channels, particle acceleration, and the generation of prodigious amounts of electromagnetic radiation.

As an example, multi-terawatt pulsed-power generators on earth rely on strong electrical discharges to produce intense particle beams, X rays, and microwaves. Megajoules of energy are electrically stored in capacitor banks, whose volume may encompass  $250 \text{ m}^3$ . This energy is then transferred to a discharge region, located many meters from the source, via a transmission line. The discharge region, or load, encompasses at most a few cubic centimeters of space, and is the site of high-variability, intense, electromagnetic radiation (Fig. 1.2).

On earth, lightning is another example of the discharge mechanism at work where electrostatic energy is stored in clouds whose volume may be of the order of  $3,000 \text{ km}^3$ . This energy is released in a few cubic meters of the discharge channel.

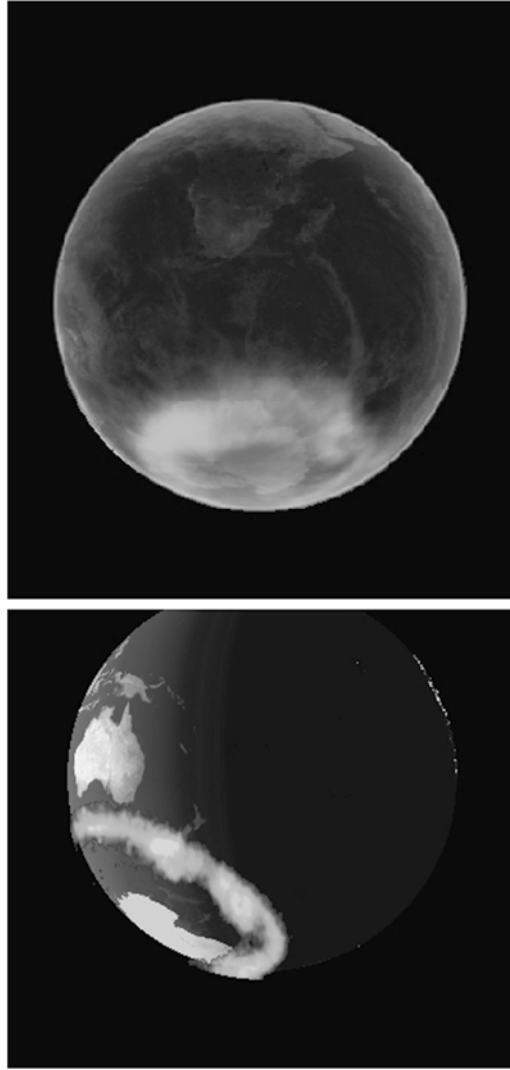


**Fig. 1.18** Solar Dynamics Observatory photograph of Earth's southern aurora (Credit: NASA)

The aurora is a discharge caused by the bombardment of atoms in the upper atmosphere by 1–20 keV electrons and 200 keV ions spiralling down the earth's magnetic field lines at high latitudes. Here, the electric field accelerating the charged particles derives from plasma moving across the earth's dipole magnetic field lines many earth radii into the magnetosphere. The potential energy generated by the plasma motion is fed to the upper atmosphere by multi-megaampere Birkeland currents (Chap. 2) that comprise a transmission line, 50,000 km in length, as they flow into and out of the discharge regions at the polar horns (Fig. 1.5). The generator



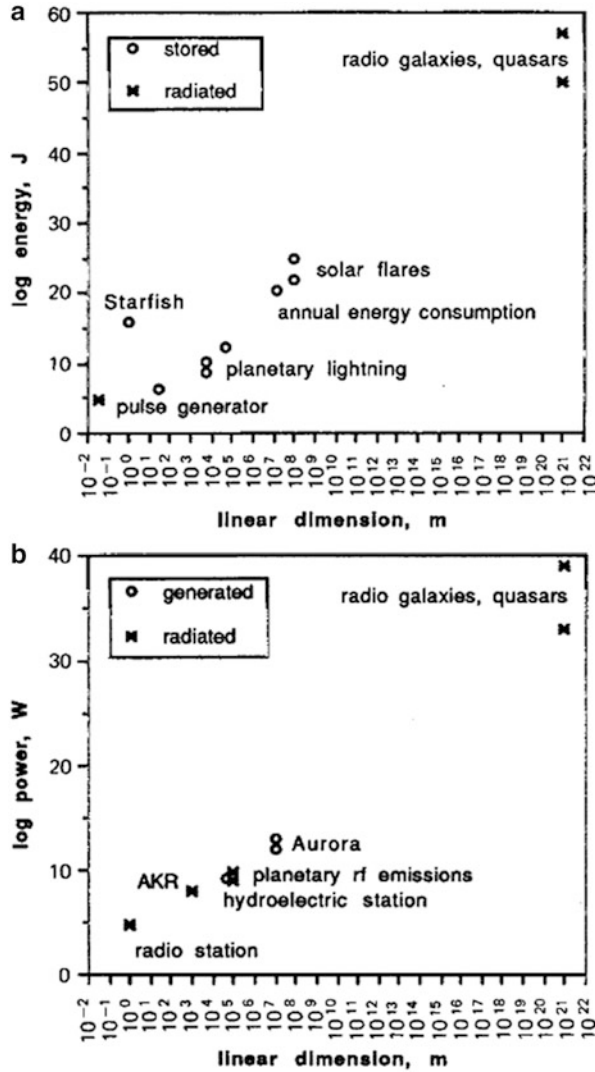


**Fig. 1.19** (a) Stored and radiated energies from man-made and natural plasmas versus linear dimension. Mankind's total energy consumption in 1989 is shown for comparison. (b) Generated and radiated power versus linear dimension

region may encompass  $10^{12}$ – $10^{13}$  km<sup>3</sup> while the total discharge volume can be  $10^9$ – $10^{10}$  km<sup>3</sup>. The stored or generated and radiated energies and powers versus linear dimension (approximately, the cube root of the volume) of several cosmic plasma discharge objects are shown in Fig. 1.19.

## 1.6 Particle Acceleration in Cosmic Plasma

### 1.6.1 Acceleration of Electric Charges

The acceleration of a charged particle  $q$  in an electromagnetic field is mathematically described by the Lorentz equation (1.5),

$$F = ma = q(e + v \times B) \quad (1.7)$$

The electric field vector  $\mathbf{E}$  can arise from a number of processes (Chaps. 4 and 5) that include the motion of plasma with velocity  $\mathbf{v}$  across magnetic fields lines  $\mathbf{B}$ , charge separation, and time varying magnetic fields via Eq. (1.1).

Acceleration of charged particles in laboratory plasmas is achieved by applying a potential gradient between metallic conductors (cathodes and anodes); by producing time varying magnetic fields such as in betatrons; by radio frequency (RF) fields applied to accelerating cavities as in linear accelerators (LINACS); and by beat frequency oscillators or wake-field accelerators that use either the electric field of lasers or charged particle beams to accelerate particles.

The magnetospheric plasma is essentially collisionless. In such a plasma, electric fields aligned along the magnetic field direction (Chap. 3) freely accelerate particles. Electrons and ions are accelerated in opposite directions, giving rise to a current along the magnetic field lines (Chap. 2).

### 1.6.2 Collective Ion Acceleration

The possibility of producing electric fields by the space-charge effect to accelerate positive ions to high energies was first discussed by [Alfvén and Wernholm \(1952\)](#). They were unsuccessful in their attempt to experimentally accelerate ions in the collective field of clouds of electrons, probably because of the low intensity of electron beam devices available then. However, proof of principle came in 1961 when [Plyutto et al. \(1965\)](#) reported the first successful experiment in which ions were collectively accelerated. By 1975, the collective acceleration of ions had become a wide-spread area of research. [Luce \(1975\)](#) reported collectively accelerating both light and heavy ions to multi-MeV energies, producing an intense burst of D-D neutrons and nuclear reactions leading to the identification of several radioisotopes. Luce used a plasma-focus device in the pinched plasma (Sect. 1.7). Subsequently, [Destler et al. \(1979\)](#) collectively accelerated carbon ions to energies in excess of 170 MeV using a 6 MeV electron beam.

Individual ion energies up to several GeV using pulsed-power generators have been suggested in particle-in-cell simulations of collective ion acceleration processes ([Faehl and Godfrey 1978](#); [Shanahan and Faehl 1981](#); [Katsouleas 1987](#)).

Collective acceleration as a mechanism for creating high energy ions in astrophysical plasmas were investigated by Bostick (1986).

Refer also to Chap. 10 in this book.

## 1.7 Plasma Pinches and Instabilities

### 1.7.1 The Bennett Pinch

In cosmic plasma the perhaps most important constriction mechanism is the electromagnetic attraction between parallel currents. A manifestation of this mechanism is the pinch effect as first studied by Bennett (1934). Phenomena of this general type also exist on a cosmic scale and lead to a bunching of currents and magnetic fields to filaments. This bunching is usually accompanied by the accumulation of matter, and it may explain the observational fact that cosmic matter exhibits an abundance of filamentary structures.

Consider a fully ionized cylindrical plasma column of radius  $r$ , in an axial electric field  $E_z$ , that produces an axial current density  $j_z$ . Associated with  $j_z$  is an azimuthal magnetic field  $B_\phi$ . The current flowing across its own magnetic field exerts a  $j \times B$ , radially inward, pinch force. In the steady-state, the balance of forces is

$$\nabla p = \nabla(p_e + p_i) = j \times B \quad (1.8)$$

By employing Eq. (1.2),  $\nabla \times B = \mu_0 j$ , and the perfect gas law  $p = NkT$ , we arrive at the Bennett relation

$$2Nk(T_e + T_i) = \frac{\mu_0}{4\pi} I^2 \quad (1.9)$$

where  $N$  is the number of electrons per unit length along the beam,  $T_e$  and  $T_i$  are the electron and ion temperatures,  $I$  is the total beam current, and  $k$  is Boltzmann's constant.

### 1.7.2 The Force-Free Configuration

Sheared magnetic fields are a characteristic of most plasmas. Here, the sheared field is considered a nonpotential field that is caused by shear flows of plasma. A nonpotential field tends to settle into a particular configuration called a “force-free” field, namely

$$(\nabla \times B) \times B = 0 \quad (1.10)$$

or

$$j \times B = 0 \quad (1.11)$$

since  $\mathbf{j} = \nabla \times B\mu_0^{-1}$ , showing that the electric current tends to flow along  $\mathbf{B}$ . Substituting (1.11) into (1.8) gives  $F = \nabla p = 0$ , hence the name “force-free”. Force-free fields tend to have a twisted or “sheared” appearance. Examples of force-free fields are chromospheric fibrils and penumbral structures near active sunspots (Sects. 3.7.2 and 5.6.2).

The condition (1.10) can be satisfied in three ways:  $\mathbf{B} = \mathbf{0}$  (trivial), (i.e.,  $\mathbf{j} = \mathbf{0}$ ), or

$$\nabla \times \mathbf{B} = \alpha \mathbf{B} \quad (1.12)$$

where the scalar  $\alpha = \alpha(r)$  in general. The essence of a force-free field is simply that electric currents flow parallel to magnetic field lines. Such currents are often called “field-aligned” currents (Chap. 2).

The force-free fields with constant  $\alpha$  represent the lowest state of magnetic energy that a closed system may attain. This has two important consequences. It proves the stability of force-free fields with constant  $\alpha$ , and shows that in a system in which the magnetic forces are dominant and in which there is a mechanism to dissipate the fluid motion, force-free fields with constant  $\alpha$  are the natural end configuration. In astrophysical plasmas, the dissipation mechanism may be the acceleration of charged particles to cosmic ray energies.

### 1.7.3 The Diocotron Instability

One of the outstanding problems in the propagation of electron beams along an axial magnetic field is the breakup of the beam into discrete vortex-like current bundles when a threshold determined by either the beam current or distance of propagation is surpassed. The phenomena observed, closely resembles that associated with the Kelvin-Helmholtz fluid dynamical shear instability, in which vortices develop throughout a fluid when a critical velocity in the flow is exceeded, with a large increase in the resistance to flow (Chandrasekhar 1961).

While structural changes in the azimuthal direction are observed in solid, annular, or sheet beams, it is with thin electron beams that the vortex phenomenon is most pronounced. Since thin annular beams are easily produced and are capable of conducting intense currents, they have found widespread application in microwave generation and accelerators. Conversely, in many applications a cold beam is desired and the heating of the beam by the onset of instabilities is an undesired property.

The instability leading to the filamentation of the beam is known as the “slipping steam” or “diocotron”<sup>8</sup> and occurs when charge neutrality is not locally maintained, for example, when electrons and ions separate. In the steady state equation (1.3) in cylindrical coordinates is

$$r^{-1} \frac{d(rE_r)}{dr} = -\frac{e}{\epsilon_0} (n_e - n_i) \quad (1.13)$$

---

<sup>8</sup> The term diocotron derives from the Greek  $\delta\iota\omega\kappa\epsilon\iota\nu$ , meaning “pursue.”

which gives rise to a shear in the drift velocity. The shear (precisely, the axial component of the vorticity) is given by

$$\omega_s = (\nabla \times v)_z = \frac{1}{r} \frac{\partial (rE_r/B_z)}{\partial r} \quad (1.14)$$

where

$$q = \omega_p^2 / \omega_\gamma^2 \quad (1.15)$$

is called the cross-field electron beam parameter (Buneman et al. 1966),  $\omega_p^2 = n_e e^2 / m \gamma \epsilon_0$ , and  $\omega_\gamma = \omega_b / \gamma = -eB / m_e \gamma$ , where  $\gamma$  is the Lorentz factor  $\gamma = (1 - \beta_z^2)^{-1/2}$ , and  $\beta_z = v_z / c$  for a beam of axial velocity  $v_z$ . The factor  $f_e = Zn_i / n_e$  represents the degree of charge neutralization. For strong magnetic field “low-density” beams ( $q < 0.1$ ) of thickness  $\Delta r$ , the instability occurs at long wavelengths

$$\lambda = (\pi/0.4) \Delta r \quad (1.16)$$

or at wavelengths about eight times the beam thickness.

Equations (1.13)–(1.15) are exactly the magnetron equations (cf. “Buneman Small Amplitude Theory” in Collins, Microwave Magnetrons 1948), except that  $n_i = 0$  in a properly vacuum-pumped magnetron.

Figure 1.20 depicts both the vortices of a 90 kA electron beam etched onto a carbon witness plate and those of a 58- $\mu$ A electron beam detected by a sensitive fluorescent screen. Therefore, in the laboratory, well-defined vortices are found to occur over some 12 orders of magnitude in beam current. This mechanism was first introduced to explain auroral curtains (Fig. 1.21) by Alfvén (1950). The diocotron instability as the cause of the auroral curtains is discussed in Sect. 2.9.8.

#### 1.7.4 Critical Ionization Velocity

If both a plasma and a neutral gas are so thin that collisional momentum exchange is negligible, one would expect them to move through each other without appreciable interaction. That this need not be so was suggested by Alfvén (1942) in his theory of the origin of the planets and satellites. He introduced the hypothesis that if the relative velocity exceeds a certain critical value, a strong interaction and rapid ionization of the neutral gas would take place. He further assumed that this “critical velocity”  $v_c$  was given by the velocity at which the neutral gas particles with mass  $M$  have a kinetic energy equal to their ionization energy  $eV_i$ :

$$\frac{1}{2} M v_c^2 = eV_i \quad (1.17)$$

Table 1.7 summarizes the critical ionization velocity parameters for many elements while Fig. 1.22 illustrates the gravitational potential energy versus ionization potential (Alfvén and Arrhenius 1976).

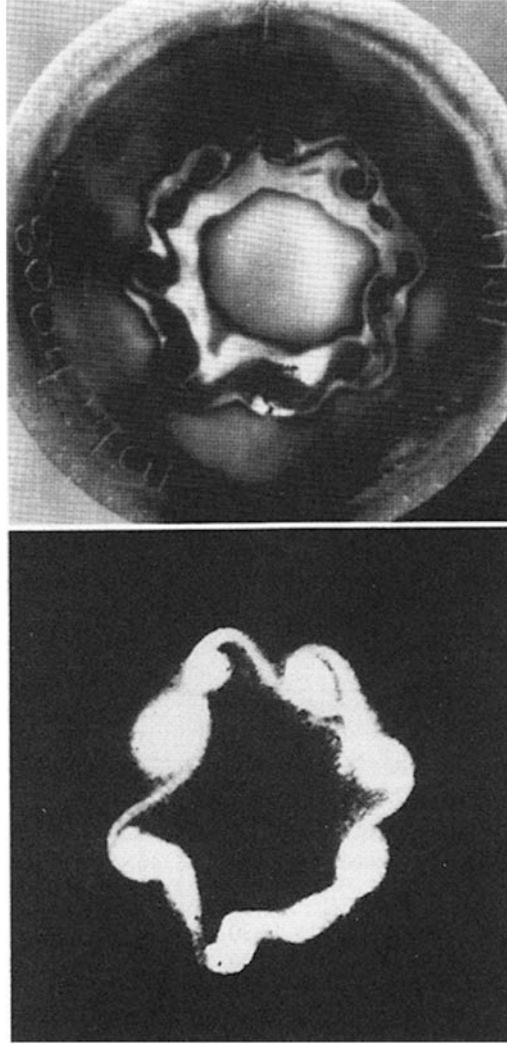


**Fig. 1.20** (Top) Vortices of a 90-kA electron beam etched onto a carbon witness plate (Courtesy of H. Davis). (Bottom) Vortices of a 58- $\mu$ A electron beam photographed on a fluorescent screen (Courtesy of H. F. Webster)

At the time Eq. (1.17) was proposed, there was no known reason why such a relation should hold. Nevertheless, the hypothesis was confirmed later in a laboratory experiment (Fahleson 1961). For many years it remained a mystery, but experiments have now clarified the phenomenon at least in general terms (Lai et al. 1989). What is involved is an instability that transfers energy from ions to electrons, so that they become capable of ionizing. Still, important questions remain (Brenning and Axnäs 1988).

**Table 1.7** Parameters associated with the critical ionization velocity

Element <sup>a</sup>	Ionization potential (Y)	Average atomic mass (amu)	Gravitational potential energy ((log) g/cm)	Atomic abundance <sup>b</sup> Si = 10 <sup>6</sup>	Critical velocity (10 <sup>5</sup> cm/s) (km/s) (mm/μs)	Band
H	13.5	1.0	20.29	$2 \times 10^{10}$	50.9	I
He	24.5	4.0	19.94	$2 \times 10^9$	34.3	I
Ne	21.5	20.2	19.18	$2 \times 10^6$	14.3	II
N	14.5	14.0	19.18	$2 \times 10^6$	14.1	II
C	11.2	12.0	19.11	$1 \times 10^7$	13.4	II
O	13.5	16.0	19.08	$2 \times 10^7$	12.7	II
(F)	17.42	19.0	19.11	$4 \times 10^3$	13.3	II
(B)	8.3	10.8	19.08	$1 \times 10^2$	12.1	II
[Be]	9.32	9.0	19.18	$8 \times 10^{-1}$	14.1	II
[Li]	5.39	6.9	19.04	$5 \times 10^1$	12.2	II
Ar	15.8	40.0	18.78	$1 \times 10^5$	8.7	III
P	10.5	31.0	18.70	$1 \times 10^4$	8.1	III
S	10.3	32.1	18.70	$5 \times 10^5$	7.8	III
Mg	7.6	24.3	18.60	$1 \times 10^6$	7.7	III
Si	8.1	28.1	18.60	$1 \times 10^6$	7.4	III
Na	5.12	23.0	18.30	$6 \times 10^4$	6.5	III
Al	5.97	27.0	18.48	$8 \times 10^4$	6.5	III
Ca	6.09	40.1	18.30	$7 \times 10^4$	5.4	III
Fe	7.8	55.8	18.30	$9 \times 10^5$	5.2	III
Mn	7.4	54.9	18.30	$1 \times 10^4$	5.1	III
Cr	6.8	52.9	18.30	$1 \times 10^4$	5.0	III
Ni	7.6	58.7	18.30	$5 \times 10^4$	5.0	III
(Cl)	13.0	35.5	18.70	$2 \times 10^3$	8.4	III
(K)	4.3	39.1	18.30	$2 \times 10^3$	4.6	III

<sup>a</sup> Minor elements (abundance  $10^2 - 10^4$ ) are indicated by parentheses; trace elements (abundance  $< 10^2$ ) are indicated by brackets

<sup>b</sup> The very fact separation processes are active interstellar and circumstellar space makes it difficult to specify relative abundances of elements except by order of magnitude and for specific environments (such as the solar photosphere, the solar wind at a given point in time, the lunar crust). The abundances are the average estimated by Urey (1972). Most values are based on carbonaceous chondrites of Type II which form a particularly well analyzed set, apparently unaffected by the type of differentiation which is characteristic of planetary interiors. Supplementary data for volatile elements are based on estimates for the solar photosphere and trapped solar wind. All data are normalized to silicon, arbitrarily set at  $10^6$

Meanwhile, critical ionization velocity phenomena have been observed in space plasma (Haerendel 1982; Torbert 1988). The phenomenon has been invoked in several cosmical applications, such as the formation of an ionosphere at the Jovian satellite Io (Cloutier et al. 1978), the interaction of the solar wind with gas clouds (Lindeman et al. 1974; Gold and Soter 1976), with comets (Haerendel 1986; Galeev et al. 1986), with planetary atmospheres (Luhmann 1988), and with the interstellar medium (Petelski et al. 1980; Petelski 1981). Thus, the phenomenon may have important astrophysical implications. However, these cannot be evaluated in detail



**Fig. 1.21** Auroral vortices observed in the magnetic zenith, College, Alaska, 31 January 1973. The exposure time is 0.1 s and the field of view is  $12 \times 16^\circ$ . The image was obtained from a low-light level television system with a broad-band filter (Courtesy T. Hallinan)

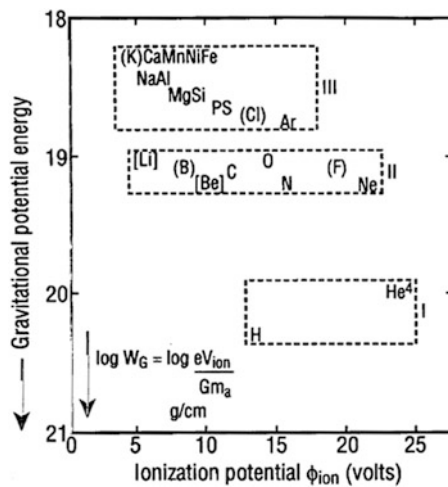


**Fig. 1.22** The gravitational energy  $W_G$  and ionization potential of the most abundant elements. Roman numerals refer to row in the periodic table, with “III” including the fourth row. All elements in a band have approximately the same gravitational energy and ionization potential as discussed by [Alfvén and Arrhenius \(1976\)](#)



until a full understanding of the phenomenon has been achieved, which is the goal of rocket experiments. Because the existence of this anomalous interaction has been so definitely documented plus the fact that it has been so successfully applied to the cosmogonic process, should make it interesting to keep in mind in cosmological contexts, too.

## 1.8 Diagnosing Cosmic Plasmas

### 1.8.1 The Electromagnetic Spectrum

For millennia our knowledge of the universe has been based on information received in the visual octave, 400–800 nm, supplemented during the last half-century by infrared and radio observations (Fig. 1.23). During the 1970s and 1980s, however, space research has opened the full spectrum, including the entire infrared region and the ultraviolet, X ray, and  $\gamma$  ray regions (Fig. 1.24). The full electromagnetic spectrum is delineated into bands, which generally are designated as follows:

**Gamma Ray and X ray.** Most emission at these wavelengths is likely to be produced by electrons with energies in excess of  $10^2$  eV. We know that processes in magnetized plasmas, especially concerning electric fields aligned by magnetic fields, accelerate auroral electrons to keV energies. Similar plasma processes in solar flares produce energies of 1–10 GeV. Under cosmic conditions, relativistic double layers (Chap. 5) may generate even higher energies in magnetized cosmic plasmas.

Therefore we can assume with some confidence that the X rays and  $\gamma$  rays we observe derive mainly from magnetized plasmas with energies in excess of  $10^2$  eV. Therefore, we call the picture we get from these wavelengths the high-energy-plasma universe, or simply, the plasma universe.

High energy magnetized plasmas not only emit X rays and  $\gamma$  rays, but also synchrotron radiation that often falls in lower energy bands, including the optical and radio regions.

The energy densities of radiation in the  $\gamma$  ray and X ray bands are  $\sim 10^{-18}$  and  $\sim 10^{-16}$  J m $^{-3}$ , respectively, and may arise from the total contribution of discrete sources (Sect. 6.6.5). The isotropy of the X ray background is  $\Delta T/T < 10^{-2}$ .

**Ultraviolet.** Ultraviolet astronomy satellites have discovered various circumstellar plasma distributions in association with a variety of stellar objects, from protostars to highly evolved red giants. The energy density of the cosmic diffuse ultraviolet background is estimated to be  $\sim 10^{-15}$  J m $^{-3}$ .

**Visible.** Visible light comes from solid bodies such as planets, but to a much larger extent comes from stellar photospheres, which are typically plasmas with low energies – less than 10 eV. Hence the visual universe is almost synonymous with the low-energy plasma universe (Urey 1959). The energy density of visible light in the universe is  $\sim 10^{-15}$  J m $^{-3}$ .

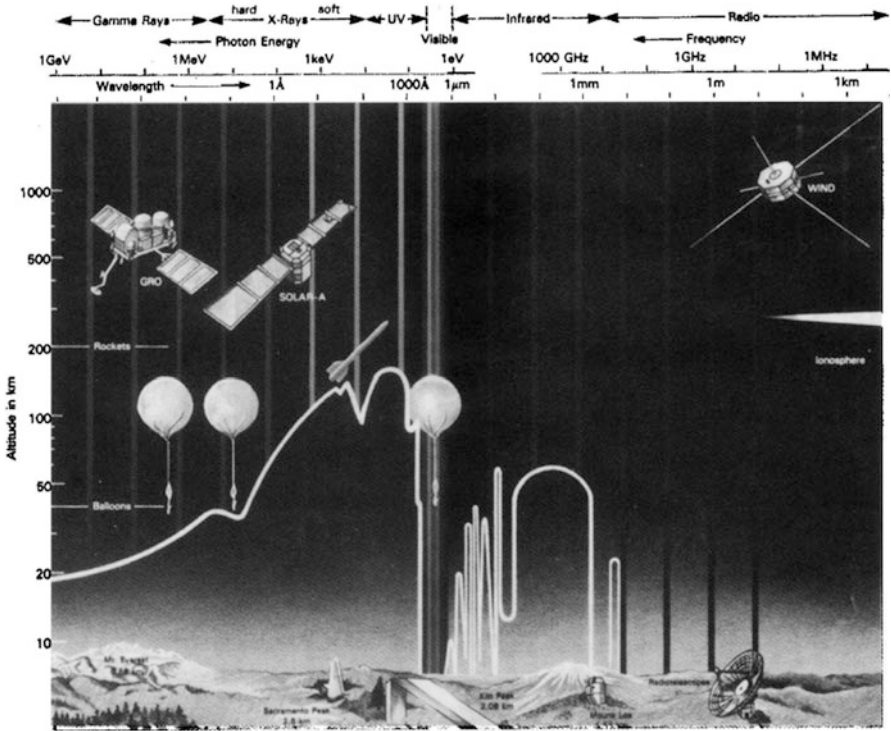


**Fig. 1.23** (Opposite) Cross section through the earth's atmosphere showing the altitude and the approximate wavelength coverage of the different *spacecraft, rockets, balloons,* and ground-based observatories that make the observations. The *solid white line* shows the altitude as a function of wavelength where the intensity of the solar radiation is reduced to half its original value (From Max 91/courtesy of B. Dennis and R. Canfield (1988) NASA-GSFC)

**Infrared.** Infrared radiation is emitted from the photospheres of stars. For example, 52 % of the electromagnetic radiation emitted by the Sun falls between 100 and 1 mm. The energy density of radiation in the infrared approaches  $10^{-14} \text{ J m}^{-3}$ . The infrared background radiation is a component of the cosmic background radiation that also includes the submillimeter and microwave backgrounds.

**Submillimeter and Microwave.** High-power microwave generation on earth belongs exclusively to devices using relativistic electron beams. The microwaves derive from naturally occurring beam instabilities or from electromagnetic-induced beam instabilities caused by cavities or slow-wave structures placed near the beam. For example, the diocotron instability (Sect. 1.7.3) is responsible for microwave generation in magnetrons and magnetically-insulated transmission-line oscillators (Felch 1985). Microwaves from beam interactions with slow-wave structures or cavities is the mechanism used by backward-wave oscillators and relativistic-klystron oscillators (Sect. 2.7.2).

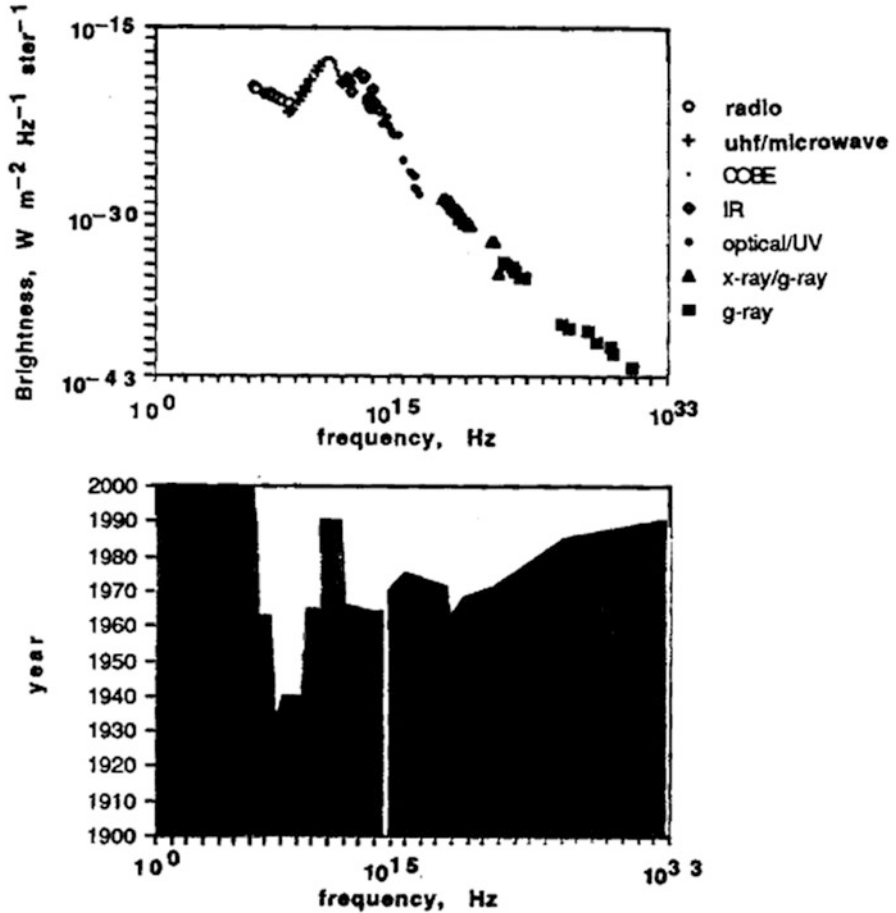


**Fig. 1.24** (Top) Spectrum of the cosmic background radiation from  $10^6$  to  $10^{31}$  Hz. (Bottom) The approximate year when new technology made possible observation in the different regions of the electromagnetic spectrum. As shown, most of the spectrum was not accessible until the mid-1970s

In addition high-power microwaves are generated via the Barkhausen-Kurz, or reflex, mechanism whenever the current carried by the relativistic electrons exceeds the space charge limiting current (Sect. 2.5.3) causing the formation of virtual cathodes or virtual anodes (double layers) (Peratt 1985). A relativistic electron beam that does not produce microwave radiation is unknown.

These same basic mechanisms are likely to have their natural analogs in cosmic plasmas. Coronal loops conducting electric currents on the Sun produce microwaves, as do electric currents in the lobes of double radio galaxies. The nuclei of spiral galaxies radiate at microwave frequencies and are even sites of MASER (microwave amplification by stimulated emission of radiation) action (Moran 1984).

In our Galaxy water-vapor masers occur in the dusty plasma surrounding newly formed massive stars.

Measurements in the frequency range 400 MHz–600 GHz show a cosmic microwave background (CMB) that can be fitted to a black body spectrum (Sect. 7.3) at temperature of 2.73 K (Fig. 1.25).

In the Rayleigh-Jeans region ( $<120$  GHz) the radiation is isotropic with a precision approaching (and in some cases better than) in a scale of  $1^\circ$  at  $\lambda = 7.6$  cm (Berlin et al. 1983). The isotropy is  $\Delta T/T < 10^{-4}$  over all angular scales (Fig. 1.26) (Periiskii and Korolkov 1986).

The energy density of microwaves in the universe is  $\sim 4.5 \times 10^{-14} \text{ J m}^{-3}$ .

**Radio Wave.** The radio wave portion of the electromagnetic spectrum is further divided into sub-classifications.

Like Jupiter and Saturn, the earth is an intense source of long (kilometer) wavelength radio waves. These waves were discovered by satellites above the ionosphere. Since their frequency  $\omega \ll \omega_p$ , where  $\omega_p$  is the maximum angular plasma frequency in the ionosphere, they cannot penetrate the ionosphere and so cannot be detected at ground level. The radiation derives from the polar aurora at high altitudes (auroral kilometric radiation or AKR). The mean intensity of AKR from earth is 100 MW, with peak intensities as high a gigawatt.

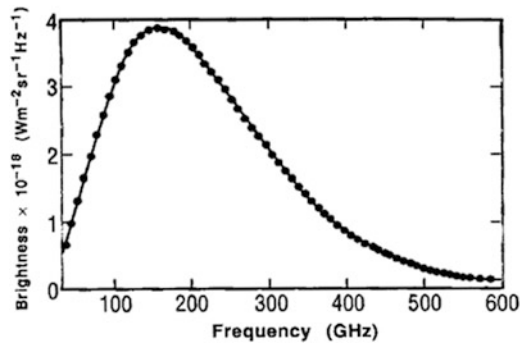


**Fig. 1.25** Spectral brightness vs frequency for the cosmic microwave background measured by COBE at the north galactic pole. The solid curve is a  $2.735 \pm 0.06$  K blackbody spectrum

Both Jupiter and Saturn radiate at kilometric, hectometric, and decametric wavelengths via the synchrotron process (Chap. 6). The average power radiated by Jupiter between 500 and 40 kHz is 6 GW while Saturn produces an average power of 1 GW between 3 kHz and 1.2 MHz. The planetary radio emissions are superimposed onto a cosmic radio background (Kaiser and Desch 1984).

At VHF frequencies (178 MHz), the radio background radiation has a nonthermal, isotropic component whose brightness temperature (Sect. 7.3) is  $65 \pm 5$  K (Bridle 1967). Reber (1986) has surveyed the southern sky at 2.085 MHz (144 m) and reports a bright background corresponding to a  $3.5 \times 10^6$  K blackbody (Fig. 1.27).

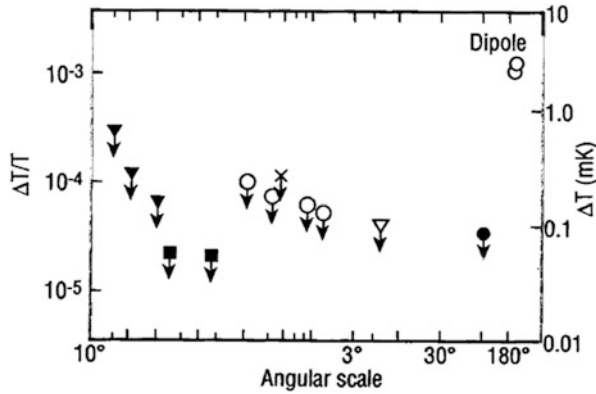


**Fig. 1.26** Isotropy observations in the cosmic microwave background on all angular scales. Except for the dipole effect at  $180^\circ$  all results are upper levels. Symbols indicate the sources of the data: (closed triangles) Very Large Array interferometer, Socorro, New Mexico; (closed squares) 140' telescope, Green Bank, West Virginia; (open circles) RATAN-600 telescope in Zelenchukskaya, USSR; (crosses) Testa Grigia alpine station, Italy; (open triangles) balloon launched from Sicily; (closed circles) balloons launched from Palestine, Texas, and São José dos Campos, Brazil

Because of the uncertainties in radio intensity at ultra-low frequencies, the energy density of radio waves in the universe is unknown but, nevertheless, appreciable.

### 1.8.2 In Situ Space Probes

Until the early 1970s, almost everything we knew about the universe had been obtained from information brought to the observer by electromagnetic radiation. Only a very small part of our knowledge stemmed from material information carriers, be they in the form of meteorites hitting the surface of the earth, cosmic ray particles, or material collected by manned or unmanned satellites or from lunar and planetary landings.

With the advent of earth and interplanetary space probes, this knowledge has been augmented by in situ measurements in our own solar system. These measurements have often resulted in discoveries that were unsuspected or misinterpreted from information contained in the electromagnetic spectrum alone. For example, prior to space probe measurements, it was universally assumed that the outer magnetosphere was populated by hydrogen plasma from the solar wind, and therefore ultimately from the sun. In contrast to this, we now know that the magnetosphere is

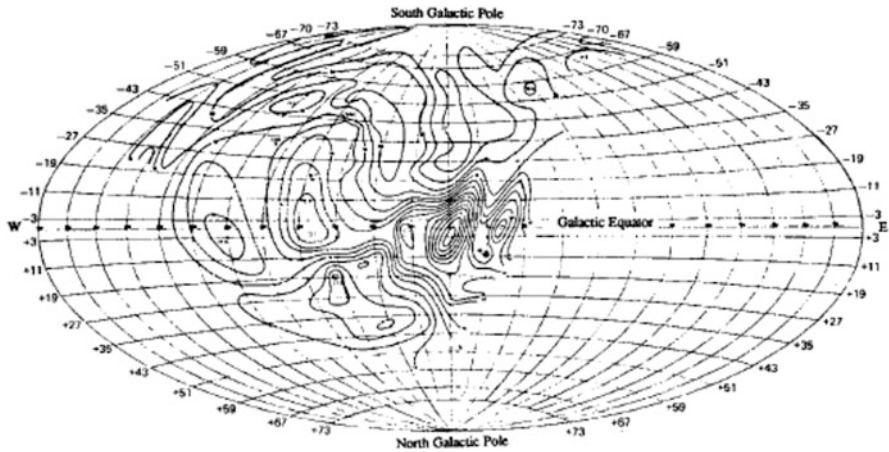


**Fig. 1.27** Map of southern sky at 144 m wavelength (2.085 MHz). This map shows a bright background (corresponding to  $3.5 \times 10^6$  K black body) with dimming at the center of the Galaxy and along the Milky Way (Courtesy of G. Reber)

sometimes dominated by oxygen plasma originating in the earth's own atmosphere. Electric fields within the near-earth plasma were generally not thought possible until space probes measured them directly. Their existence was either not inferable by means of electromagnetic radiation or they have radiation signatures at frequencies far below that currently measurable on earth.

It is a sobering fact that even after hundreds of satellites had circled the earth, the generally accepted picture of our space environment was fundamentally wrong in aspects as basic as the origin and chemical composition of matter in the earth's own neighborhood and the existence and role of electric fields in the magnetosphere (Fälthammar 1990). This must inspire caution in making assertions about the composition and properties of other invisible cosmic objects, whether they be stellar interiors, interstellar plasma, pulsar magnetospheres, or intergalactic cosmic rays. The danger of misconception is particularly great for distant astrophysical objects that will forever remain inaccessible to in situ observation. To avoid this danger, it is essential to utilize the empirical knowledge of plasma behavior that has been, and will continue to be, gathered from plasmas in the laboratory and accessible regions of space.

## References

- Alfvén, H.: On the cosmogony of the solar system. Stockh. Obs. Ann. I. **14**(2), 8 (1942)
- Alfvén, H.: *Cosmical Electrodynamics*. Oxford University Press, New York (1950)
- Alfvén, H.: *Cosmic Plasma*. D. Reidel, Dordrecht (1981)

- Alfvén, H., Arrhenius, G.: *Evolution of the Solar System*. NASA Publication, SP-345. NASA, Washington, DC (1976)
- Alfvén, H., Fälthammar, C.-G.: *Cosmical Electrodynamics*. Oxford, London (1963)
- Alfvén, H., Wernholm, O.: A new type of accelerator. *Ark. För Fys.* **15**, 175 (1952)
- Akasofu, S.-I.: Energy coupling between the solar wind and the magnetosphere. *Space Sci. Rev.* **28**, 121 (1981)
- Bennett, W.H.: Magnetically self-focussing streams. *Phys. Rev.* **45**, 890 (1934)
- Berlin, A.B., Bulaenko, E.N., Vitkivskii, V.V., Pariiskii, Y.N., Petrov, Z.E.: Search for small scale anisotropy of the 3K emission of the universe. In: Abell, G.O., Chincarini, G.L. (eds.) *Early Evolution of the Universe and its Present Structure*. IAU Symposium, Kolymbari, 104, pp. 121–124. D. Reidel, Dordrecht (1983)
- Book, D.L.: *Plasma Formulary*. NRL Publication 0084–4040. Naval Research Laboratory, Washington, DC (1987)
- Borucki, W.J.: Planetary lightning: a short review of extraterrestrial lightning characteristics. In: Kikuchi, H. (ed.) *Laboratory and Space Plasmas*. Springer, Berlin (1989)
- Bostick, W.H.: What laboratory-produced plasma structures can contribute to the understanding of cosmic structures both large and small. *IEEE Trans. Plasma Sci.* **1**, 703 (1986)
- Brenning, N., Axnäs, I.: Critical ionization velocity interactions: some unsolved problems. *Astrophys. Space Sci.* **144**, 15 (1988)
- Bridle, A.H.: The spectrum of the radio background between 13 and 404 MHz. *Mon. Not. R. Astro. Soc.* **136**, 219 (1967)
- Brown, W.C., Ness, W.N., Van Allen, J.A.: Collected papers on the artificial radiation belt from the July 9, 1962, nuclear detonation. *J. Geophys. Res.* **68**, 605 (1963)
- Buneman, O., Levy, R.H., Linson, L.M.: Stability of crossed-field electron beams. *J. Appl. Phys.* **37**, 3203 (1966)
- Chandrasekhar, S.: *Hydrodynamic and Hydromagnetic Stability*. Clarendon, Oxford (1961)
- Cloutier, P.A., Daniell, R.E., Dessler, A.J., Hill, T.J.: A cometary ionosphere model for Io. *Astrophys. Space Sci.* **55**, 93 (1978)
- Collins, G.B.: *Microwave Magnetrons*. McGraw-Hill, New York (1948)
- Dennis, B., Canfield, R.: *Max'91*. NASA Goddard Space Flight Center, Greenbelt (1988)
- Destler, W.W., Hoerberling, R.F., Kim, H., Bostick, W.H.: Collective acceleration of carbon ions to 170 MeV. *Appl. Phys. Lett.* **35**, 296 (1979)
- Di Capua, M.S.: Magnetic insulation. *IEEE Trans. Plasma Sci.* **11**, 205 (1983)
- Eastman, T.: Transition regions in solar system and astrophysical plasmas. *IEEE Trans. Plasma Sci.* **18**, 18 (1990)
- Faehl, R.J., Godfrey, B.B.: Collective ion acceleration through temporal modulation of relativistic-electron beam energy. *Phys. Rev. Lett.* **40**, 1137 (1978)
- Fälthammar, C.-G.: Laboratory and near-earth space plasma as a key to the plasma universe. *Laser Part. Beams* **6**, 437 (1988)

- Fälthammar, C.-G.: Electrodynamics of cosmical plasmas: some basic aspects of cosmological importance. *IEEE Trans. Plasma Sci.* **18**, 11 (1990)
- Fahleson, U.: Experiments with plasma moving through neutral gas. *Phys. Fluids* **4**, 123 (1961)
- Felch, K.L.: Introduction to the special issue on high-power microwave generation. *IEEE Trans. Plasma Sci.* **13**, 361 (1985)
- Galeev, A.A. et al.: Critical ionization velocity effects in the inner coma of Comet Halley: measurements by Vega-2. *Geophys. Res. Lett.* **13**, 845 (1986)
- Gold, T., Soter, S.: Cometary impact and the magnetization of the moon. *Planet. Space Sci.* **24**, 45 (1976)
- Haerendel, G.: Alfvén's critical velocity effect tested in space. *Z. Naturforsch.* **37a**, 728 (1982)
- Haerendel, G.: Plasma flow and critical velocity ionization in cometary comae. *Geophys. Res. Lett.* **13**, 255 (1986)
- Jursa, A.S.: Handbook of Geophysics and the Space Environment. National Technical Information Service. U.S. Department of Commerce, Springfield (1985)
- Kaiser, M.L., Desch, M.D.: Radio emissions from the planets Earth, Jupiter, and Saturn. *Rev. Geophys. Space Phys.* **22**, 373 (1984)
- Katsouleas, T.: Introduction to the special issue on plasma-based high-energy accelerators. *IEEE Trans. Plasma Sci.* **15**, 85 (1987)
- Lai, S.T., Murad, E., McNeil, W.J.: An overview of atomic and molecular processes in critical ionization velocity. *IEEE Trans. Plasma Sci.* **17**, 124 (1989)
- Lang, K.: *Astrophysical Formulae*. Springer, New York (1974)
- Lindeman, R.A., et al.: The interaction between an impact-produced neutral gas cloud and the solar wind at the lunar surface. *J. Geophys. Res.* **79**, 2287 (1974)
- Luce, J.S.: Neutrons and radioisotopes produced by collective effect acceleration. *Ann. N. Y. Acad. Sci.* **251**, 217 (1975)
- Luhmann, J.: An assessment of the conditions for critical velocity ionization at the weakly ionized planets. In: Paper XIII.1.6 at the XXVIIth COSPAR Meeting, Helsinki (1988)
- Lui, A.T.Y. (ed.): *Magnetotail Physics*. The Johns Hopkins University Press, Baltimore (1987)
- Miller, R.B.: *Intense Charged Particle Beams*. Plenum, New York (1982)
- Moran, P.: Masers in the nuclei of galaxies. *Nature* **310**, 270 (1984)
- Nahin, P.J.: *Oliver Heaviside: Sage in Solitude*. IEEE, New York (1988)
- Ness, W.N.: Collected papers on the artificial radiation belt from the July 9, 1962, nuclear detonation. *J. Geophys. Res.* **68**, 605 (1963)
- Peratt, A.L.: A high-power reflex triode microwave source. *IEEE Trans. Plasma Sci.* **13**, 498 (1985)
- Periškii, Y.N., Korolkov, D.V.: Experiment cold: the first deep sky survey with the Ratan-600 radio telescope. *Sov. Sci. Rev. E. Astrophys. Space Phys.* **5**, 39 (1986)
- Petelski, E.F.: Viability of the critical ionization velocity concept in selected space situations. In: Kikuchi, H. (ed.) *Relation Between Laboratory and Space Plasmas*. D. Reidel, Dordrecht (1981)



- Petelski, E.F., Fahr, H.J., Ripken, H.W., Brenning, N., Axnäs, I.: Enhanced interaction of the solar wind and the interstellar neutral gas by virtue of a critical velocity effect. *Astron. Astrophys.* **87**, 20 (1980)
- Plyutto, A.A., Ryzhkov, V.N., Kapin, A.T.: High Speed Plasma Streams in Vacuum Arcs. *Sov. Phys. JETP* **20**, 328 (1965)
- Priest, E.R.: *Solar System Magnetic Fields*. D. Reidel, Dordrecht (1985)
- Reber, G.: Intergalactic plasma. *IEEE Trans. Plasma Sci.* **14**, 678 (1986)
- Rose, D.J., Clark, M.: *Plasmas and Controlled Fusion*. MIT, Cambridge (1961)
- Shanahan, W.R., Faehl, R.J.: Collective ion acceleration. Los Alamos National Laboratory Report LA-8961-PR (1981); Suess, S.T., Dessler, A.J.: Probing the local interstellar medium. *Nature* **317**, 702 (1985)
- Torbert, R.: Review of ionospheric CIV experiments. In: Paper XIII.2.1 at the XXVIIth COSPAR Meet, Helsinki (1988)
- Urey, H.C.: The atmosphere of the planets. In: *Handbuch der Physik*, vol. 52, p. 363. Springer, Berlin (1959)
- Urey, H.C.: Abundances of the elements, part IV: abundances of interstellar molecules an laboratory Spectroscopy. *Ann. N. Y. Acad. Sci.* **194**, 35 (1972)
- Urey, H.C., Alfvén, H.: Testimony on the California Nuclear Initiative. *Energy*. **1**(1), 105–108 (1976)
- Willett, J.C., Bailey, J.C., Leteinturier, C., Krider, E.P.: Lightning electromagnetic radiation field spectra in the interval from 0.2 to 20 MHz. *J. Geophys. Res.* **95**, 20367 (1990)
- Yusef-Zadeh, F., Morris, M., Chance, D.: Large, highly organized radio structures near the galactic centre. *Nature* **310**, 557 (1984)

## Chapter 2

# Birkeland Currents in Cosmic Plasma

### 2.1 History of Birkeland Currents

An electromotive force  $\phi = \int \mathbf{v} \times \mathbf{B} \cdot d\mathbf{l}$  giving rise to electrical currents in conducting media is produced wherever a relative perpendicular motion of plasma and magnetic field lines exist (Sect. 3.5.2). An example of this is the sunward convective motion of the magnetospheric plasma that cuts the earth's dipole field lines through the equatorial plane, thereby producing a Lorentz force that drives currents within the auroral circuit. The tendency for charged particles to follow magnetic lines of force and therefore produce field-aligned currents has resulted in the widespread use of the term "Birkeland Currents" in space plasma physics. Their discovery in the earth's magnetosphere in 1974 has resulted in a drastic change of our understanding of aurora dynamics, now attributed to the filamentation of Birkeland charged-particle sheets following the earth's dipole magnetic field lines into vortex current bundles. In anticipation of the importance of Birkeland currents in astrophysical settings, Fälthammar (1986) states:

A reason why Birkeland currents are particularly interesting is that, in the plasma forced to carry them, they cause a number of plasma physical processes to occur (waves, instabilities, fine structure formation). These in turn lead to consequences such as acceleration of charged particles, both positive and negative, and element separation (such as preferential ejection of oxygen ions). Both of these classes of phenomena should have a general astrophysical interest far beyond that of understanding the space environment of our own Earth.

Birkeland currents have a long and colorful history. Inspired by his famous terrella experiments at the beginning of the twentieth century (Fig. 2.1) and by his extensive studies of geomagnetic data recorded during magnetic storms, the Norwegian scientist Kristian Birkeland (1867–1917) suggested that the aurora was associated with electric "corpuscular rays" emanating from the sun and deflected to the polar regions of the earth by the geomagnetic field. Birkeland recognized that the magnetic disturbances recorded on the earth's surface below the auroral region were due to intense currents flowing horizontally above. He suggested that these currents, now called "auroral electrojet" currents, were coupled to vertical currents that flowed along

geomagnetic field lines into and away from the lower ionosphere. The system of field-aligned currents suggested by Birkeland is shown in Fig. 2.2a.

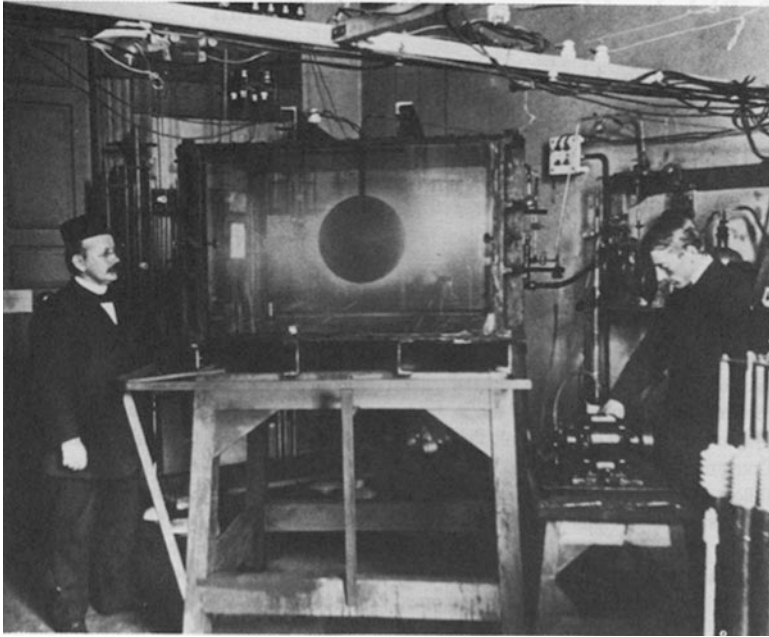


**Fig. 2.1** Birkeland (*left*), the founder of experimental astrophysics, is shown here with his assistant, K. Devik, and his “terrella,” a magnetized globe representing the earth

The existence of magnetic field-aligned “Birkeland” currents was disputed because it is not possible to distinguish unambiguously between current systems that are field-aligned and those that are completely ionospheric from a study of surface magnetic field measurements. Sydney Chapman, the noted British geophysicist, developed mathematically elegant models of currents that were contained completely within the earth’s ionosphere that could adequately account for ground-based magnetic field observations obtained during magnetic storms. Figure 2.2b shows the “atmospheric current system” developed by Chapman in 1927 (Egeland and Holtet 1968; Hill 1984; Dessler 1984).

Hannes Alfvén, the Swedish engineer and physicist, advocated the idea of Birkeland currents and developed a theory for the generation of these currents by the solar wind (Alfvén 1939). Figure 2.2c shows Alfvén’s diagram for these currents.

The first satellite measurements of Birkeland currents were provided by Zmuda et al. (1966, 1967) with a single axis magnetometer on board the navigation satellite 1963–1938C at an altitude of  $\sim 1,100$  km. The magnetic disturbances observed were initially interpreted as hydromagnetic waves, but it was soon realized that their latitudinal extent was not appropriate for waves and they were interpreted as being due to Birkeland currents (Cummings and Dessler 1967). Today, Birkeland currents are routinely measured by a variety of rocket and satellite instruments.

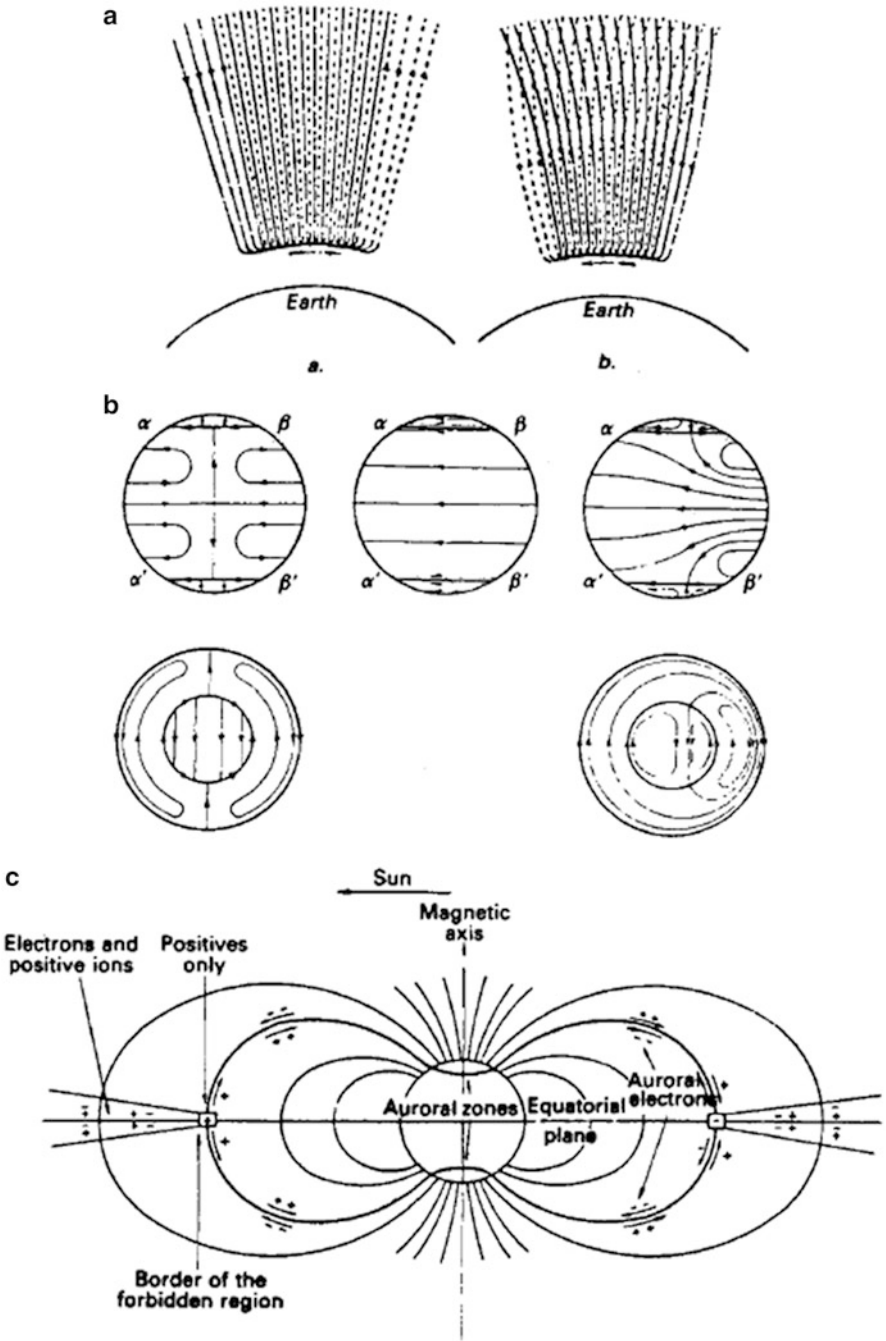
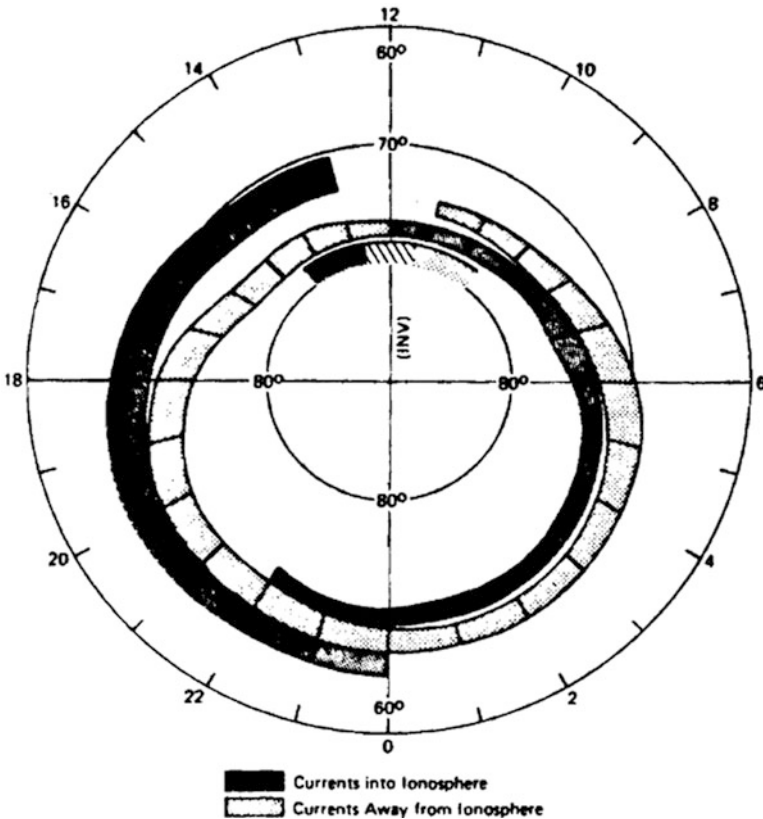


Fig. 2.2 Historical diagrams of auroral current systems from: (a) Birkeland (1908), (b) Chapman (1927), (c) Alfvén (1939)

The location, flow direction, and intensity of Birkeland currents have been studied by several satellites, and a statistical map is provided in Fig. 2.3. This distribution, plotted on an invariant (magnetic) latitude and geomagnetic local time polar dial, was determined from hundreds of orbits of the TRIAD satellite over the polar regions (Iijima and Potemra 1976). It shows that there are well defined patterns of these currents, and these patterns coincide approximately with the auroral zone. The inflowing currents are at latitude  $70^\circ$  and the outflowing currents are at  $74^\circ$ – $78^\circ$  from about noon to midnight, then reverse directions from midnight to noon.

The magnitude and flow direction of Birkeland currents are determined from the magnetic field observations with Maxwell's equation (1.2),  $j = (1/\mu_0) \nabla \times \Delta B$  (where  $\Delta B$  is the magnetic perturbation). For currents flowing parallel to the geomagnetic field and in sheets aligned in the east-west direction (with infinite extent), this vector formula reduces to the scalar gradient,  $j_z = (1/\mu_0) \partial (\Delta B_y) / \partial x$  where  $j_z$



**Fig. 2.3** Distribution of Birkeland currents at earth's north pole as determined by TRIAD satellite magnetic field observations. The *dark areas* denote currents into the ionosphere while the *shaded areas* denote currents away from the ionosphere. The hatched area near noon indicates confused current directions (Courtesy T. Potemra)

is the current flowing along the main geomagnetic field (in the  $z$  direction),  $\Delta B_y$  is the perturbation in the eastward ( $y$ ) direction, and  $x$  is the northward direction.

Birkeland currents not only heat the upper atmosphere, increasing the drag on low altitude earth circling satellites, but cause substantial density depletions. Electric fields along the dipole magnetic field lines can give rise to field-aligned currents that reduce the ionospheric topside electron and ion densities (Block and Fälthammar 1969). In the topside there is then an excess of ionization in contrast to low altitudes where recombination dominates. The net effect is an upward flux of neutral particles that are ionized at high altitudes. Auroral primary particles are charged particles with the proper sign that have been accelerated downward. Closure of the global circuit is accomplished by particles with the opposite sign, that move out of the magnetosphere and precipitate in another region of the ionosphere with reversed polarity. Current measurements suggest that the supply of plasma from the solar wind is negligible in relation to the supply of plasma from the closed loop ionospheric/magnetospheric system.

As an example of a manmade “Birkeland current,” a charged-particle beam in space undergoing a helical motion along the Earth’s magnetic field is shown in Fig. 2.4. The physics of this beam behavior are examined in Sects. 2.5.3 and 2.9.7.

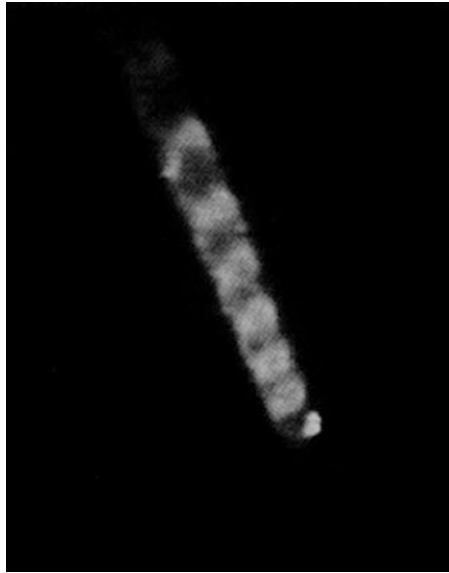


**Fig. 2.4** A glowing beam of electrons spirals upwards along the earth’s magnetic field. This television image was taken during the Echo 7 sounding-rocket experiment. The view shows a portion of the corkscrew beam several hundred meters long from top to bottom and 17 m across. The small, bright glow at the lower end of the beams is the accelerator that produced the energetic particles (Courtesy John R. Winckler, University of Minnesota)

## 2.2 Field-Aligned Currents in Laboratory Plasma

In the laboratory, filamentary and helical structure is a common morphology exhibited by energetic plasmas. X ray pinhole photographs, optical streak and framing camera photographs, and laser holograms often show a filamentary, magnetic “rope-like” structure from plasmas produced in multi-terawatt pulse power generators or in dense plasma focus machines (Fig. 1.2). Often, the cross-sectional patterns from filamentation in hollow electron beams are recorded onto observing screens or witness plates. Regardless of size or current, the patterns are those of vortices (Figs. 1.20–1.21). In the dense plasma focus the vortices have dimensions of a few microns while in laboratory electron beams the vortices may be a few centimeters in diameter. This size variation of 4 orders of magnitude is extended to nearly 9 orders of magnitude when auroral vortex recordings are directly compared to the laboratory data. With regard to actual current magnitudes; filamentation occurs over nearly 12 orders of magnitude while coarser resolution experiments show that the phenomena probably transcends at least 14 orders of magnitude, from microampere to multi-megaampere electron beams.

## 2.3 Field-Aligned Currents in Astrophysical Plasmas

As far as we know, most cosmic low density plasmas also depict a filamentary structure. For example, filamentary structures are found in the following cosmic plasmas, all of which are observed or are likely to be associated with electric currents:

1. In the aurora, filaments parallel to the magnetic field are often observed. These can sometimes have dimensions down to about 100 m (Fig. 1.21).
2. Inverted V events and the in-situ measurements of strong electric fields in the magnetosphere ( $10^5$ – $10^6$  A,  $10^8$  m) demonstrate the existence of filamentary structures.
3. In the ionosphere of Venus, “flux ropes”, whose filamentary diameters are typically 20 km, are observed.
4. In the sun, prominences ( $10^{11}$  A), spicules, coronal streamers, polar plumes, etc., show filamentary structure whose dimensions are of the order  $10^7$ – $10^8$  m (Fig. 1.10).
5. Cometary tails often have a pronounced filamentary structure (Fig. 1.8).
6. In the interstellar medium and in interstellar clouds there is an abundance of filamentary structures (e.g., the Veil nebula (Fig. 1.13), the Lagoon nebula, the Orion nebula, and the Crab nebula).
7. The center of the Galaxy, where twisting plasma filaments, apparently held together by a magnetic field possessing both azimuthal and poloidal components, extend for nearly 60 pc ( $10^{18}$  m) (Fig. 1.14).
8. Within the radio bright lobes of double radio galaxies, where filament lengths may exceed 20 kpc ( $6 \times 10^{20}$  m) (Fig. 1.15).

Regardless of scale, the motion of charged particles produces a self-magnetic field that can act on other collections of particles or plasmas, internally or externally. Plasmas in relative motion are coupled via currents that they drive through each other. Currents are therefore expected in a universe of inhomogeneous astrophysical plasmas of all sizes.

## 2.4 Basic Equations of Magnetohydrodynamics

### 2.4.1 General Plasma Fluid Equations

Fundamental equations for the plasma velocity, magnetic field, plasma density, electric current, plasma pressure, and plasma temperature can be derived from macroscopic averages of currents, fields, charge densities, and mass densities. In this “fluid” treatment, the Maxwell-Hertz-Heaviside equations (1.1)–(1.4) are coupled to the moments of the Boltzmann equation for a highly ionized plasma.

The evolution of the distribution function  $f(r, p, t)$  for particles with charge  $q$  and mass  $m$  is described by the Boltzmann equation

$$\left[ \frac{\partial}{\partial t} + \mathbf{v} \cdot \frac{\partial}{\partial \mathbf{r}} + q(\mathbf{E} + \mathbf{v} \times \mathbf{B}) \cdot \frac{\partial}{\partial \mathbf{p}} \right] f(r, p, t) = \left( \frac{\partial f}{\partial t} \right)_{\text{collisions}} \quad (2.1)$$

which is an expression of Liouville’s theorem for the incompressible motion of particles in the six-dimensional phase space  $(r, t)$ . In the fluid description the particle density, mean velocity, momentum, pressure, and friction are defined by

$$n(r, t) \equiv \int d^3 p f(r, p, t) \quad (2.2)$$

$$n(r, t) \bar{\mathbf{v}}(r, t) \equiv \int d^3 p \mathbf{v} f(r, p, t) \quad (2.3)$$

$$n(r, t) \bar{p}(r, t) \equiv \int d^3 p p f(r, p, t) \quad (2.4)$$

$$\mathbf{P}(r, t) \equiv \int d^3 p [\bar{\mathbf{p}} - \mathbf{p}(r, t)] [\bar{\mathbf{v}} - \mathbf{v}(r, t)] f(r, p, t) \quad (2.5)$$

$$\mathbf{R}(r, t) \equiv \int d^3 p [\bar{\mathbf{p}} - \mathbf{p}(r, t)] \left( \frac{\partial f}{\partial t} \right)_{\text{collisions}} \quad (2.6)$$

where the momentum  $p$  and velocity  $\mathbf{v}$  are related by

$$\mathbf{p} = m\gamma\mathbf{v} \quad (2.7)$$



The fields  $E(r, t)$  and  $B(r, t)$  in Eq. (2.1) are self-consistently solved from Eqs. (1.1) to (1.4) with

$$\rho(r, t) \equiv e \int d^3 p f(r, p, t) \quad (2.8)$$

$$j(r, t) \equiv e \int d^3 p v f(r, p, t) \quad (2.9)$$

Taking the moments  $\int d^3 p$  and  $\int d^3 p \mathbf{p}$  of the Boltzmann equation yields the two-fluid equations (Rose and Clark 1961; Alfvén and Carlqvist 1967; Chen 1984) for ions and electrons  $\alpha = i, e$ ,

$$\frac{\partial n_\alpha}{\partial t} + \nabla \cdot (n_\alpha \bar{v}_\alpha) = 0 \quad (2.10)$$

$$n_\alpha \frac{dp_\alpha}{dt} = q_\alpha n_\alpha (E + v_\alpha \times B) - \nabla \cdot P_\alpha + R_\alpha - n_\alpha m_\alpha \nabla \phi_G \quad (2.11)$$

These are called the continuity and momentum equations, respectively. The continuity equation, as written, is valid if ionization and recombination are not important. Conservation of linear momentum dictates that

$$R_i + R_e = 0 \quad (2.12)$$

The two fluid equations are the moments, or averages, of the kinetic plasma description and no longer contain the discrete particle phenomena such as double layers from charge separation and synchrotron radiation. Nevertheless, this approach is useful in studying bulk plasma flow and behavior. A single fluid hydromagnetic force equation may be obtained by substituting into Eq. (2.11) and adding to get,

$$\rho_m \frac{\partial v_m}{\partial t} = \rho E + j \times B - \nabla p - \rho_m \nabla \phi_G \quad (2.13)$$

which relates the forces to mass and acceleration for the following averaged quantities:

$$\begin{aligned} \rho_m &= n_e m_e + n_i m_i && \text{mass density} \\ j_m &= n_e m_e \bar{v}_e + n_i m_i \bar{v}_i && \text{mass current} \\ v_m &= j_m / \rho_m && \text{averaged velocity} \\ \rho &= n_e q_e + n_i q_i && \text{charge density} \\ j &= n_e q_e \bar{v}_e + n_i q_i \bar{v}_i && \text{current density} \end{aligned} \quad (2.14)$$

The first term in Eq. (2.14) is caused by the electric field, the second term derives from the motion of the current flow across the magnetic field, the third term is due to the pressure gradient (Eq. (2.14) is valid for an isotropic distribution  $\nabla \cdot P \rightarrow \nabla p$ , where  $p \equiv nkT$ ), and the fourth term is due to the gravitational potential  $\phi_G$ . The near absence of excess charge  $\rho = e(n_i - n_e) \approx 0$ , for  $q_{i,e} = \pm e$ , is a characteristic

of the plasma state; however, this does not mean that electrostatic fields (e.g., those deriving from Eq. (1.3)) are unimportant.<sup>1</sup>

Completing the single fluid description is the equation for mass conservation,

$$\frac{\partial \rho_m}{\partial t} + \nabla \cdot (\rho_m \mathbf{v}_m) = 0 \quad (2.15)$$

In addition to Eqs. (2.13) and (2.15), we find it useful to add the equation for magnetic induction,

$$\frac{\partial \mathbf{B}}{\partial t} = \nabla \times (\mathbf{v}_m \times \mathbf{B}) + \frac{1}{\mu \sigma} \nabla^2 \mathbf{B} \quad (2.16)$$

obtained by taking the curl of Ohm's law

$$\mathbf{j} = \sigma (\mathbf{E} + \mathbf{v} \times \mathbf{B})$$

where  $\sigma$  is the electrical conductivity (Table 1.6).

### 2.4.2 Magnetic Reynolds and Lundquist Numbers

The significance of Eq. (2.16) in which  $(\mu \sigma)^{-1}$  is the magnetic diffusivity, is that changes in the magnetic field strength are caused by the transport of the magnetic field with the plasma (as represented by the first term on the right-hand-side), together with diffusion of the magnetic field through the plasma (second term on the right-hand-side). In order of magnitude, the ratio of the first to the second term is the *magnetic Reynolds number*

$$R_m = \mu \sigma V_c l_c \quad (2.17)$$

in terms of a characteristic plasma speed  $V_c$  and a characteristic scale length  $l_c$ . A related quantity is the Lundquist parameter

$$L_u = \mu \sigma V_A l_c \quad (2.18)$$

where

$$V_A = \frac{B}{\sqrt{\mu \rho_m}} \quad (2.19)$$

is the Alfvén speed. It may be written as the ratio

$$L_u = \frac{\tau_d}{\tau_A} \quad (2.20)$$

---

<sup>1</sup> According to Chen (1985): "In a plasma, it is usually possible to assume  $n_i = n_e$  and  $\nabla \cdot \mathbf{E} \neq 0$  at the same time. We shall call this the *plasma approximation*. It is a fundamental trait of plasmas, one which is difficult for the novice to understand. *Do not use Poisson's equation to obtain  $E$  unless it is unavoidable!*"

of the *magnetic diffusion time*

$$\tau_d = \mu \sigma l_c^2 \quad (2.21)$$

to the *Alfvén travel time*

$$\tau_A = l_c / V_A \quad (2.22)$$

## 2.5 The Generalized Bennett Relation

A generalized Bennett relation follows directly from Eq. (2.13) and Eqs. (1.1)–(1.4). Consider a current-carrying, magnetic-field-aligned cylindrical plasma of radius  $a$  which consists of electrons, ions, and neutral gas having the densities  $n_e$ ,  $n_i$ , and  $n_n$ , and the temperatures  $T_e$ ,  $T_i$ , and  $T_n$ , respectively. A current of density  $j_z$  flows in the plasma along the axis of the cylinder which coincides with the  $z$ -axis. As a result of the axial current a toroidal magnetic field  $B_\phi$  is induced (Fig. 2.5). An axial electric field is also present. Thus, there exists the electric and magnetic fields

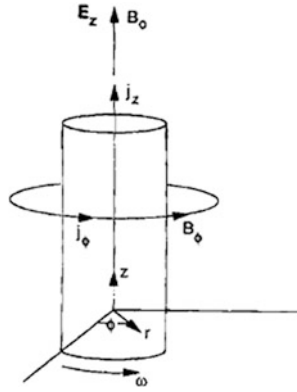


**Fig. 2.5** A current-carrying plasma pinch undergoing rotation at angular frequency  $\omega$

$$E = (E_r, E_\phi, E_z)$$

$$B = (0, B_\phi, B_z)$$

The derivation of the generalized Bennett relation for this plasma is straightforward, but lengthy (Witalis 1981), and the final result is

$$\begin{aligned} \frac{1}{4} \frac{\partial^2 J_0}{\partial r^2} = W_\perp + \Delta W_{E_z} + \Delta W_{B_z} + \Delta W_k \\ - \frac{\mu_0}{8\pi} I^2(a) - \frac{1}{2} G \bar{m}^2 N^2(a) + \frac{1}{2} \pi a^2 \epsilon_0 \left( E_r^2(a) - E_\phi^2(a) \right) \end{aligned} \quad (2.23)$$

where

$$J_0 = \int_0^{2\pi} \int r^2 \rho_m r dr d\phi = \int_0^a r^2 \rho_m 2\pi r dr \quad (2.24)$$

is the total moment of inertia with respect to the  $z$  axis. (As the mass  $m$  of a particle or beam is its resistance to linear acceleration,  $J_0$  is the beam resistance to angular displacement or rotation.) The quantities  $\Delta W$  are defined by

$$\Delta W_{E_z} \equiv W_{E_z} - \frac{1}{2} \epsilon_0 E_z^2(a) \pi a^2 \quad (2.25)$$

$$\Delta W_{B_z} \equiv W_{B_z} - \frac{1}{2\mu_0} B_z^2(a) \pi a^2 \quad (2.26)$$

$$\Delta W_k \equiv W_k - p(a) \pi a^2 \quad (2.27)$$

where  $E_z(a)$ ,  $B_z(a)$ , and  $p(a)$  denote values at the boundary  $r = a$ . The individual energies  $W$  are defined as follows. The kinetic energy per unit length due to beam motion transverse to the beam axis:

$$W_{\perp kin} \equiv \frac{1}{2} \int_0^a \rho_m(r) [v_\phi^2 + v_r^2] 2\pi r dr \quad (2.28)$$

The self-consistent  $B_z$  energy per unit length:

$$W_{B_z} \equiv \frac{1}{2\mu_0} \int_0^a B_z^2(r) 2\pi r dr \quad (2.29)$$

The self-consistent  $E_z$  energy per unit length:

$$W_{E_z} \equiv \frac{\epsilon_0}{2} \int_0^a E_z^2(r) 2\pi r dr \quad (2.30)$$

The thermokinetic energy per unit length:

$$W_k \equiv \int_0^a p(r) 2\pi r dr \quad (2.31)$$

The axial current inside the radius  $a$ :

$$I(a) \equiv \int_0^a j_z(r) 2\pi r dr \quad (2.32)$$

The total number of particles per unit length:

$$N(a) \equiv \int_0^a n(r) 2\pi r dr \quad (2.33)$$

where  $n = n_i + n_e + n_n$  is the total density of ions, electrons, and neutral particles. The mean particle mass is  $\bar{m} = n_i m_i + n_e m_e + n_n m_n$ . The self-consistent electric field can be determined from Eq. (1.13)

$$r^{-1} \frac{d(rE_r)}{dr} = -\frac{e}{\epsilon_0} (n_e - n_i)$$

and is given by

$$E_r(r) = \frac{-en_e(1-f_e)}{2\epsilon_0} r, \quad 0 \leq r \leq a$$

$$E_r(r) = \frac{-en_e(1-f_e)}{2\epsilon_0} \frac{a^2}{r}, \quad r \geq a$$

Neglecting the displacement current, the self-consistent magnetic field can be determined from Ampère's law Eq. (1.2) (also see Sect. 3.3.1),

$$r^{-1} \frac{d(rB_\phi)}{dr} = \mu_0 j$$

and is given by

$$B_\phi(r) = \frac{\mu_0 I}{2\pi} \frac{r}{a^2}, \quad 0 \leq r \leq a$$

$$= \frac{\mu_0 I}{2\pi r}, \quad r \geq a$$

The positive terms in Eq. (2.23) are expansional forces while the negative terms represent beam compressional forces. In addition, it is assumed that the axially directed kinetic energy is

$$W_{||kin} = \frac{1}{2} \gamma m N \beta^2 c^2 \quad (2.34)$$

Since Eq. (2.23) contains no axially directed energy, it must be argued that there are conversions or dissipation processes transferring a kinetic beam of energy of magnitude  $W_{||kin}$  into one or several kinds of energy expressed by the positive  $W$  elements in Eq. (2.23):

$$W_{||kin} = W_{\perp kin} + W_{E_z} + W_{B_z} + W_k \quad (2.35)$$

### 2.5.1 The Bennett Relation

Balancing the thermokinetic and azimuthal compressional (pinch) energies in Eq. (2.23),

$$W_k - \frac{\mu_0}{8\pi} I^2 = 0 \quad (2.36)$$

yields the Bennett relation equation (1.9),

$$\frac{\mu_0}{4\pi} I^2 = 2NkT \quad (2.37)$$

If there is a uniform temperature  $T = T_e + T_i$  and if the current density is uniform across the current channel cross-section, Eqs. (2.32), (2.33), and (2.37) yield a parabolic density distribution

$$n(r) = \frac{\mu_0 I^2}{4\pi^2 a^2 kT} \left( 1 - \frac{r^2}{a^2} \right)$$

### 2.5.2 Alfvén Limiting Current

Equating the parallel beam kinetic energy to the pinch energy

$$W_{\perp \text{ kin}} - \frac{\mu_0}{8\pi} I^2 = 0 \quad (2.38)$$

yields the Alfvén limiting current

$$I_A = 4\pi\epsilon_0 m_e c^3 \beta \gamma / e = 17\beta \gamma \text{ kiloamperes} \quad (2.39)$$

for an electron beam. This quantity was derived (Alfvén 1939) in order to determine at what current level in a cosmic ray beam the self-induced pinch field would turn the forward propagating electrons around. It should be noted that this limit is independent of any physical dimensions.

Lawson's (1959) interpretation of Eq. (2.39) is that the electron trajectories are beam-like when  $I < I_A$  and they are plasma-like when  $I > I_A$ . In laboratory relativistic electron beam (REB) research, Budker's parameter

$$v_{Bud} = \pi a^2 n_b e^2 / mc^2 = Ne^2 / mc^2 \quad (2.40)$$

where  $n_b$  is the electron density of the beam, finds wide application in beam and plasma accelerators. Yonas (1974) has interpreted the particle trajectories as beam-like for  $v_{Bud} < \gamma$  and plasma-like for  $v_{Bud} > \gamma$ . The relationship between  $I_A$  and  $v_{Bud}$  is

$$v_{Bud} / \gamma = I / I_A \quad (2.41)$$

The Alfvén limiting current Eq. (2.39) is a fundamental limit for a uniform beam, charge-neutralized ( $f_e = 1$ ), with no magnetic neutralization ( $f_m = 0$ , Sect. 2.5.4), no rotational motion ( $v_\phi = 0$ ), and no externally applied magnetic field ( $B_z = 0$ ). By modifying these restrictions, it is possible, under certain circumstances, to propagate currents in excess of  $I_A$ .

### 2.5.3 Charge Neutralized Beam Propagation

Balancing the parallel kinetic, pinch, and radial electric field energies in Eq. (2.23) gives

$$W_{\perp \text{ kin}} - \frac{\mu_0}{8\pi} I^2 + \frac{1}{2} \pi a^2 \epsilon_0 E_r^2(a) = 0 \quad (2.42)$$

which yields<sup>2</sup>

$$I_{\max} = I_A \beta^2 \left[ \beta^2 - (1 - f_e)^2 \right]^{-1}, \quad 0 \leq f_e \leq 1 \quad (2.43)$$

Depending on the amount of neutralization, the denominator in Eq. (2.43) can become small, and  $I_{\max}$  can exceed  $I_A$ . However, the unneutralized electron beam cannot even be injected into a drift space unless the space charge limiting current condition is satisfied. For a shearless electron beam this is (Bogdankevich and Rukhadze 1971)

$$I_{sc} = \frac{17 (\gamma^{2/3} - 1)^{3/2}}{1 + 2 \ln(b/a)} \text{ kiloamperes} \quad (2.44)$$

where  $b$  is the radius of a conducting cylinder surrounding the drift space. Thus, in free space  $I_{sc} \rightarrow 0$  and an unneutralized electron beam will not propagate but, instead, builds up a space charge cloud of electrons (a virtual cathode) which repels any further flow of electrons as a beam. Moreover, the space charge limiting current is derived under the assumption of an infinitely large guide field  $B_z$ ; no amount of magnetic field will improve beam propagation.

### 2.5.4 Current Neutralized Beam Propagation

For beam propagation in plasma, the electrostatic self-field  $E_z$  built up by the beam, efficiently drives a return current through the plasma, thus moderating the compressional term  $\mu_0 I^2 / 8\pi$  in Eq. (2.23), so that

$$W_{\perp \text{ kin}} - \frac{\mu_0}{8\pi} I^2 (1 - f_m) + \frac{1}{2} \pi a^2 \epsilon_0 E_r^2(a) = 0 \quad (2.45)$$

where the magnetic neutralization factor is

$$f_m \equiv |I_{\text{return}} / I| \quad (2.46)$$

From Eq. (2.45) the maximum current is

$$I_{\max} = I_A \beta^2 \left[ \beta^2 (1 - f_m) - (1 - f_e)^2 \right]^{-1}, \quad 0 \leq f_e \leq 1, \quad 0 \leq f_m \leq 1. \quad (2.47)$$

<sup>2</sup> This equation differs from the Alfvén-Lawson limiting current,  $I_{\max} = I_A \beta^2 / [\beta^2 - 1 + f_e]$ , because of the differing ways in describing charge neutralization (Witalis 1981).

Thus, depending on the values of  $f_e$  and  $f_m$ , the denominator in Eq. (2.47) can approach zero and the maximum beam current can greatly exceed  $I_A$ . The effect of current neutralization is examined further in Sect. 2.9.1.

### 2.5.5 Discussion

When a charged particle beam propagates through plasma, the plasma ions can neutralize the beam space charge. When this occurs,  $E_r \rightarrow 0$  and, as a result, the beam constricts because of its self-consistent pinch field  $B_\phi$ . For beam currents in excess of the Alfvén limiting current,  $B_\phi$  is sufficient to reverse the direction of the beam electron trajectories at the outer layer of the beam. However, depending on the plasma conductivity  $\sigma$ , the induction electric field at the head of the beam (due to  $dB/dt$   $dI/dt$  in Eq. (1.1)) will produce a plasma current  $I_p = -I_b$ . Hence, the pinch field

$$B_\phi(r) = \frac{\mu_0}{2\pi r} [I_b(r) + I_p] \quad (2.48)$$

can vanish allowing the propagation of beam currents  $I_b$  in excess of  $I_A$ .

Because of the finite plasma conductivity, the current neutralization will eventually decay in a magnetic diffusion time  $\tau_d$  given by Eq. (2.21). During this time a steady state condition exists in which no net self-fields act on the beam particles. While in a steady state, beam propagation is limited only by the classic macro-instabilities such as the sausage instability and the hose (kink) instability.

When the beam undergoes a small displacement, the magnetic field lags behind for times of the order  $\tau_d$ . This causes a restoring force to push the beam back to its original position, leading to the well-known  $m = 1$  (for a  $e^{im\phi}$  azimuthal dependency) kink instability.

### 2.5.6 Beam Propagation Along an External Magnetic Field

An axially directed guide field  $B_z$  produces an azimuthal current component  $I_\phi$  through Eq. (1.2). This modification to the conducting current follows by balancing the energies

$$W_{\perp kin} - \frac{1}{2\mu_0} B_z^2 \pi a^2 - \frac{\mu_0}{8\pi} I^2 + \frac{1}{2} \epsilon_0 E_r^2(a) \pi a^2 = 0 \quad (2.49)$$

In the absence of any background confining gas pressure  $p(a)$ , the maximum current is

$$I_{\max} = I_\phi \beta^2 \left[ \beta^2 - (1 - f_e)^2 \right]^{-1} \quad (2.50)$$



For the case of an axial guide field, the axial current  $I_z$  is not limited to  $I_A$  and depends only on the strength of the balancing  $I_z$  ( $B_z$ ) current (magnetic field). In terms of the magnetic fields, the current flows as a beam when

$$B_z \gg \frac{\left[(1 - f_e)^2 - \beta^2\right]^{1/2}}{\beta} B_\phi \quad (2.51)$$

Note that Eq. (2.44) still holds; that is, a cylindrical conductor around the electron beam is necessary for the beam to propagate.

Equation (2.51) finds application in accelerators such as the high-current betatron (Hammer and Rostocker 1970). In spite of the high degree of axial stabilization of a charged particle beam because of, appreciable *azimuthal* destabilization and filamentation can occur because of the diocotron effect (Sect. 1.7.3) (Levy 1965; Levy and Hockney 1968). This can be alleviated by bringing the metallic wall close to the beam.

### 2.5.7 Schönherr Whirl Stabilization

The transverse kinetic energy term  $W_{\perp kin}$  in Eq. (2.23) explains an observation made long ago (Schönherr 1909). High-current discharges conduct more current if the discharge is subject to an externally impressed rotation  $v_\phi$ . This phenomena can also be expected in astronomical situations if the charged particle beam encounters a nonaxial component of a magnetic field line that imparts a spin motion to the beam or if a gas enters transversely to an arc discharge-like plasma.

### 2.5.8 The Carlqvist Relation

An expression having broad applicability to cosmic plasmas, due to Carlqvist (1988), may be obtained from Eq. (2.23) if the beam is taken to be cylindrical and in a rotationless and steady-state condition:

$$\frac{\mu_0}{8\pi} I^2(a) + \frac{1}{2} G \bar{m}^2 N^2(a) = \Delta W_{B_z} + \Delta W_k \quad (2.52)$$

Thus, in a straightforward and elegant way, the gravitational force has been included in the familiar Bennett relation. Through Eq. (2.52), the Carlqvist Relation, the relative importance of the electromagnetic force and the gravitational force may be determined for any given cosmic plasma situation. This relation will now be applied to the two commonest pinch geometries—the cylindrical pinch and the sheet pinch.

### 2.5.9 The Cylindrical Pinch

Consider the case of a dark interstellar cloud of hydrogen molecules ( $\bar{m} = 3 \times 10^{-27}$  kg and  $T = T_i = T_e = T_n = 20$  K). Carlqvist (1988) has given a graphical representation of the solution to Eq. (2.52) for these values and this is shown in Fig. 2.6 for discrete values of  $\Delta W_{B_z}$ . Several physically different regions are identified in this figure.

The region in the upper left-hand part of the figure is where the pinching force due to  $I$  and the magnetic pressure force due to  $B_z$  constitute the dominating forces. Equation (2.52) in this region reduces to

$$\frac{\mu_0}{8\pi} I^2(a) \approx \Delta W_{B_z} \quad (2.53)$$

representing a state of almost force-free magnetic field (Sect. 1.7.2).

Another important region is demarked by negative values of  $\Delta W_B$ . In this region an outwardly directed kinetic pressure force is mainly balanced by an inwardly directed magnetic pressure force. Hence the total pressure is constant and Eq. (2.52) is approximately given by

$$NkT + \Delta W_{B_z} \approx 0 \quad (2.54)$$

For yet larger negative values of  $\Delta W_B$ , the magnetic pressure force is neutralized by the gravitational force so that Eq. (2.52) reduces to

$$\frac{1}{2} G \bar{m}^2 N^2(a) \approx \Delta W_{B_z} \quad (2.55)$$

Another delineable region is where  $\Delta W_B = 0$ , where Eq. (2.52) reduces to the Bennett relation,

$$\frac{\mu_0}{8\pi} I^2(a) \approx \Delta W_k(n, T) \quad (2.56)$$

Another region of some interest is where the classic Bennett relation line turns over into an almost vertical segment. Here, the pinching force of the current may be neglected, leaving the kinetic pressure force to balance only the gravitational force so that

$$\frac{1}{2} G \bar{m}^2 N^2(a) \approx NkT \quad (2.57)$$

This is the Jeans's criterion in a cylindrical geometry.

The size or radius of the cylindrical pinch depends on the balancing forces. For the Bennett pinch equation (2.56) the equilibrium radius is

$$a \approx \frac{I}{2\pi} \sqrt{\frac{\mu_0}{2nkT}} \quad (2.58)$$

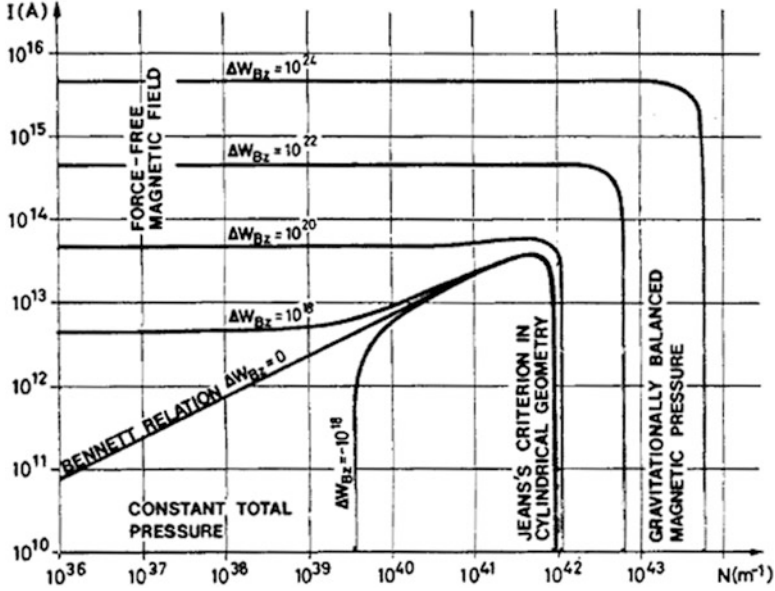


**Fig. 2.6** The total current  $I$  in a generalized Bennett pinch of cylindrical geometry as a function of the number of particles per unit length  $N$ . The temperature of the plasma is  $T = 20$  K while the mean particle mass is  $\bar{m} = 3 \times 10^{-27}$  kg. It is assumed that the plasma does not rotate ( $\omega = 0$ ) and that the kinetic pressure is much smaller at the border of the pinch than in the inner parts. The parameter of the curves is  $\Delta W_{Bz}$ , representing the excess magnetic energy per unit length of the pinch due to an axial magnetic field  $B_z$  (Courtesy of P. Carlqvist)

Küppers (1973) has investigated the case of a REB propagating through plasma. Space charge neutralization ( $E_r = 0$ ) is maintained when  $n_e + n_b = n_i$ . For this case, the replacements  $n \rightarrow n_b$  and  $T \rightarrow T_b - T_e$  are made to  $\Delta W_k(n, T)$ , where  $T_b$  is the beam temperature and  $T_e$  is the background plasma electron temperature. For the space charge neutralized REB,

$$a \approx \frac{I_b}{2\pi} \sqrt{\frac{\mu_0}{2n_b k (T_b - T_e)}} \quad (2.59)$$

Note that physically acceptable solutions for the equilibrium radius are obtained only when the beam temperature (in the axial direction for a cold beam) exceeds the plasma electron temperature.

From Eq. (2.53), the equilibrium radius of a pinch balanced by an internal field  $B_z$  is

$$a \approx \frac{\mu_0 I}{2\pi B_z} \quad (2.60)$$

### 2.5.10 The Sheet Pinch

The sheet pinch, which is the plane parallel analog of the cylindrical pinch, is a geometry of considerable importance in astrophysical plasmas. A current of density  $j_z(x)$  flows in the  $z$ -direction in a symmetrical slab limited by the planes  $x = \pm d$  (orthogonal coordinates  $x, y, z$  are adopted). This current induces a magnetic field  $B_y(x)$ . There also exists a magnetic field in the  $z$ -direction,  $B_z(x)$ , consistent with the current density  $j_y(x)$ . All quantities are supposed to vary with the  $x$ -coordinate only.

In a similar way as Eq. (2.52) was derived, Carlqvist (1988) uses the force equation (without the centrifugal term) to obtain the relation

$$\mu_0 I^2(d) + 4\pi G \bar{m}^2 N^2(d) = 8(\Delta p_k + \Delta p_{Bz}) \quad (2.61)$$

for the one-dimensional, charge neutral pinch where

$$I(d) = 2 \int_0^d j_z dx \quad (2.62)$$

is the current per unit length of the slab, and

$$N(d) = 2 \int_0^d (n_e + n_i + n_n) dx \quad (2.63)$$

is the number of particles per unit area of the slab. The kinetic pressure and magnetic pressure difference terms in the slab are, respectively, given by

$$\Delta p_k = p_k(0) - p_k(d) \quad (2.64)$$

$$\Delta p_{Bz} = p_{Bz}(0) - p_{Bz}(d) \quad (2.65)$$

Equation (2.61) is the one-dimensional analog of (2.52) and Fig. 2.7 is its graphical solution using the same parameter values as in Fig. 2.6. Comparison of Figs. 2.6 and 2.7 reveals a striking similarity between the behavior of cylindrical and sheet pinches.

By means of the theory discussed in Sect. 2.5, in the next section we shall study the physical conditions in a few different, current-carrying, cosmic plasmas.

## 2.6 Application of the Carlqvist Relation

### 2.6.1 Birkeland Currents in Earth's Magnetosphere

Magnetometer measurements from rockets and satellites show that Birkeland currents often exist in sheets in the auroral zones, where the current density may be

as large as  $j_{||} \approx 10^{-4} \text{ A m}^{-2}$ . The thickness of such sheets is found to range from a few kilometers to several hundred kilometers. Often the sheets exist in pairs with oppositely directed currents.

Consider a model of a Birkeland current with a current density  $j_z \approx 3 \times 10^{-5} \text{ A m}^{-2}$  flowing in a magnetospheric plasma slab of half-thickness  $d = 10^4 \text{ m}$  (Carlqvist 1988). The mean mass of the electrons and protons in the slab is taken to be  $\bar{m} \approx 10^{-27} \text{ kg}$ . At an altitude of a few thousand kilometers above the earth,  $n_e = n_i \approx 10^{10} \text{ m}^{-3}$ ,  $T \approx 2 \times 10^3 \text{ K}$ , and  $B_z \approx 4 \times 10^{-5} \text{ T}$ . Substituting these values into Eqs. (2.62) and (2.63), gives

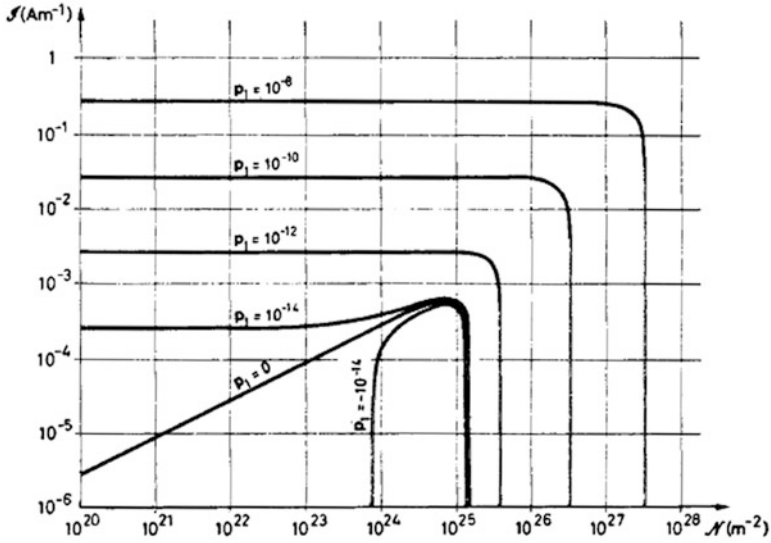


**Fig. 2.7** The current per unit length  $I$  as a function of the number of particles  $N$  in a generalized Bennett pinch of plane parallel geometry forming a slab. The temperature and mean particle mass are the same as in Fig. 2.6. It is assumed that  $n(0) \approx N/d$ . The parameter of the curves is  $p_1 = \Delta p_{B_z} - p_k(d)$  where  $p_k(d)$  is the kinetic pressure at the border of the slab while  $\Delta p_{B_z}$  denotes the difference of the magnetic pressure due to  $B_z$  between the center of the slab and the borders (Courtesy of P. Carlqvist)

$$I(d) \approx 6 \times 10^{-1} \text{ A m}^{-1}$$

$$N(d) \approx 4 \times 10^{14} \text{ m}^{-2}$$

Under steady state conditions, Eq. (2.61) is applicable and its terms have the magnitudes:

$$\mu_0 I^2(d) \approx 5 \times 10^{-7} \text{ Pa}$$

$$4\pi G \bar{m}^2 N^2(d) \approx 1 \times 10^{-34} \text{ Pa}$$

$$8\Delta p_k < 8p_k(0) \approx 4 \times 10^{-9} \text{ Pa}$$

$$8\Delta p_{B_z} < 8p_{B_z}(0) \approx 5 \times 10^{-3} \text{ Pa}$$

Hence, the gravitational and kinetic pressure terms may be neglected with respect to the pinching current and  $B_z$  pressure. These values for  $N(d)$  and  $\Delta p_{B_z}$  pertain to the lower far-left region in Fig. 2.7, corresponding to the force-free magnetic field configuration (Sect. 1.7.2).

For a strong circular aurora, 5,000 km in diameter (Fig. 1.18a), the total current is  $I = I(d)2\pi r \approx 7$  MA.

### 2.6.2 Currents in the Solar Atmosphere

The solar atmosphere consists of a highly conducting plasma in which vertical currents of about  $10^{11} - 10^{12}$  A are common in active regions where solar flares occur. For a current of  $I = 3 \times 10^{11}$  A flowing in a filament of radius  $a \leq 10^6$  m,  $j_z \approx 0.1 \text{ Am}^{-2}$ . The length of the filament is  $l \leq 10^8$  m and passes mainly through the lower corona in a loop connecting two foot-prints in the photosphere. The coronal plasma density and temperature is taken to be  $n_e = n_i \leq 10^{16} \text{ m}^{-3}$  and  $T \leq 100 \text{ eV}$  ( $10^6 \text{ K}$ ) (Table 1.3) and uniformly distributed across the filament so that differential kinetic pressure term  $\Delta W_k(a)$  is negligible. Hence,

$$I(a) \approx 3 \times 10^{11} \text{ A}$$

$$N(a) \approx 6 \times 10^{28} \text{ m}^{-1}$$

Applying Eq. (2.52), the magnitudes of the remaining terms are

$$\mu_0 I^2 / 8\pi \approx 4 \times 10^{15} \text{ J m}^{-1}$$

$$G\bar{m}^2 N^2 / 2 \approx 3 \times 10^{-8} \text{ J m}^{-1}$$

$$\Delta W_{B_z}(a) < W_{B_z} \approx 1 \times 10^{17} \text{ J m}^{-1}$$

for a magnetic field  $B_z \approx 0.1 \text{ T}$  within the filament. Gravity is negligible and a force-free magnetic field configuration exists.

### 2.6.3 Heliospheric Currents

The heliospheric current system (Alfvén 1981) consists of the sun as a unipolar generator with axial currents flowing out of (or into, depending on the polarity of the sun) the solar polar regions. These currents fan out and close at great distances from the sun, probably near the heliopause. The return current flows back towards (or away from) the sun in a thin and wavy layer near the equatorial plane, eventually dividing and terminating at high latitudes on the northern and southern hemispheres, where the currents are then conducted across the sun (Fig. 2.8). The magnitude of the total current in each of the polar regions is  $I_p \approx 1.5 \times 10^9 \text{ A}$ .

Whether or not the polar current is diffuse or filamentary is an important problem for cosmic plasmas.

**Example 2.1. Polar currents balanced by axial magnetic fields.** Consider the case of  $M$  filamentary currents each containing an axial magnetic field  $B_z \approx 30 \times 10^{-4}$  T (Table 1.3). Each current conducts  $I/M$  amperes so that, if  $M = 1,000$ , a filamental current is  $I = 1.5 \times 10^6$  A. According to Eq. (2.60), the radius of each filament is  $a \approx 100$  m. If the filaments are approximately equally spaced a diameter's distance from one another, they form a tube of radius of the order of 5 km, each with a current density  $j_z \approx 20$  A/m<sup>2</sup>. If, on the other hand  $M = 1$ ,  $I = 1.5 \times 10^9$  A and  $a \approx 100$  km. For this diffuse current case,  $j_z \approx 0.05$  A/m<sup>2</sup>.

**Example 2.2. Polar currents in an axial magnetic field balanced by the thermokinetic plasma.** Consider the conducting path to be plasma with  $n = 2 \times 10^{15}$  m<sup>-3</sup> and  $T = 100$  eV ( $10^6$  K) (Table 1.3). For this case,  $M = 1,000$  filaments each of which conducts  $1.5 \times 10^6$  A and, according to Eq. (2.58), each has a Bennett radius  $a \approx 1.5$  km. The filaments fill a tube of radius of the order of 50 km and each has a current density  $j_z \approx 0.2$  A/m<sup>2</sup>. If  $M = 1$ ,  $I = 1.5 \times 10^9$  A and  $a \approx 1,500$  km. For this diffuse current case,  $2 \times 10^{-4}$  A/m<sup>2</sup>.

#### 2.6.4 Currents in the Interstellar Medium

Currents in the interstellar medium may be one or two orders of magnitude stronger than solar currents. Consider first a single interstellar cloud of density  $n \approx 10^7$  m<sup>-3</sup>, linear extent  $l_C \sim 10^{16}$  m, and temperature  $T \approx 10$  K. The total mass  $M_C \approx 2 \times 10^{32}$  kg corresponds to a single solar mass. Hence, representative values for current and number density per unit length are

$$I \approx 10^{13} \text{ A}$$

$$N \approx 10^{39} \text{ m}^{-1}$$

Under steady state conditions, the magnitude of the terms in Eq. (2.52) are

$$\mu_0 I^2 / 8\pi \approx 5 \times 10^{18} \text{ J m}^{-1}$$

$$G\bar{m}^2 N^2 / 2 \approx 3.3 \times 10^{13} \text{ J m}^{-1}$$

$$\Delta W_k(a) < W_k \approx 1.4 \times 10^{17} \text{ J m}^{-1}$$

so that the Bennett relation Eq. (2.56) is applicable. Consider now an interstellar cloud of density  $n \approx 10^8$  m<sup>-3</sup>, linear extent  $l_C \sim 10^{17}$  m, and temperature  $T \approx 10$  K. These values are typical of the Orion nebula, where the total mass  $MC \approx 2 \times 1,032$  kg corresponds to a 100 solar masses. Hence,

$$I \approx 10^{14} \text{ A}$$

$$N \approx 10^{42} \text{ m}^{-1}$$

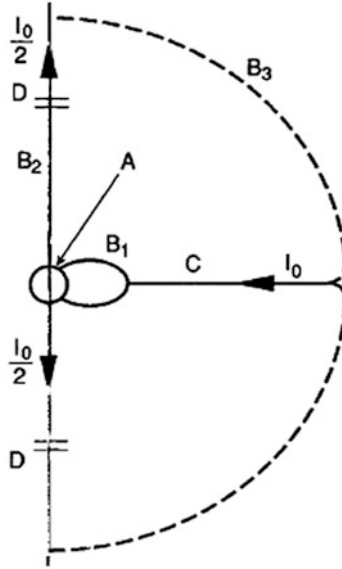


**Fig. 2.8** Heliospheric circuit. The sun acts as a unipolar inductor producing a current which goes outward along both the axes and inward in the equatorial plane C and along the magnetic field lines B1. The current closes at large distances B3

Under steady state conditions, the magnitude of the terms in Eq. (2.52) are as follows:

$$\mu_0 I^2 / 8\pi \approx 5 \times 10^{20} \text{ J m}^{-1}$$

$$G \bar{m}^2 N^2 / 2 \approx 3.3 \times 10^{19} \text{ J m}^{-1}$$

$$\Delta W_k(a) < W_k \approx 1.4 \times 10^{20} \text{ J m}^{-1}$$

That is, the pinch, gravitational, and kinetic forces are approximately balanced. The two cases illustrated above are representative of particular values found in Fig. 2.6.

### 2.6.5 Currents in the Galactic Medium

By extrapolating the size and strength of magnetospheric currents to galaxies, [Alfvén \(1977\)](#) suggests a number of confined current regions that flow through interstellar clouds and assist in their formation. For example, a galactic magnetic field of the order  $B_G \sim 10^{-9} - 10^{-10} \text{ T}$  associated with a galactic dimension of  $10^{20} - 10^{21} \text{ m}$  suggests the galactic current be of the order  $I_G = 10^{17} - 10^{19} \text{ A}$ . As a natural extension of the size hierarchy in cosmic plasmas, these currents are thought to have an axial component parallel to an axial galactic magnetic field, in addition to



the ring or azimuthal current component, so that the galactic currents are galactic-dimensional Birkeland currents (Peratt and Green 1983). From Sect. 1.2.6 (also see Example 6.3),  $n_e = 2 \times 10^3 \text{ m}^{-3}$ ,  $T_\perp = 3 \text{ keV}$  ( $3 \times 10^7 \text{ K}$ ), and  $B_z = 2 \times 10^{-8}$ . The radius is  $a \approx 17 \text{ kpc}$  ( $0.5 \times 10^{21} \text{ m}$ ). Hence,

$$I \approx 2.5 \times 10^{19} \text{ A}$$

$$N \approx 2.9 \times 10^{45} \text{ m}^{-1}$$

Under steady state conditions, the magnitude of the terms in Eq. (2.52) are

$$\mu_0 I^2 / 8\pi \approx 3 \times 10^{31} \text{ J m}^{-1}$$

$$G\bar{m}^2 N^2 / 2 \approx 2.6 \times 10^{26} \text{ J m}^{-1}$$

$$\Delta W_k(a) < W_k \approx 1.3 \times 10^{30} \text{ J m}^{-1}$$

where it has been assumed that the galactic currents are imbedded in  $B_z$  so that  $\Delta W_{B_z}$  is negligible. Hence, the galactic pinch is balanced by the thermokinetic pressure of the plasma it contains and, to a lesser extent, by gravity.

For a galactic field  $B \sim 10^{-8} \text{ T}$  over a volume  $V \sim 10^{63} \text{ m}^3$  ( $l_G \sim a_G \sim 10^{21} \text{ m}$ ), the magnetostatic energy Eq. (3.41) is  $W_B \sim 10^{53} \text{ J}$ .

### 2.6.6 Currents in the Intergalactic Medium

One of the most compelling pieces of evidence for the existence of supercluster-sized Birkeland currents comes from the discovery of faint supercluster-scale radio emission at 326 MHz between the Coma cluster of galaxies and the Abell 1367 cluster (Kim et al. 1989). The radiation's synchrotron origin implies the existence of a large-scale intercluster magnetic field with an estimated strength of  $0.3\text{--}0.6 \times 10^{-10} \text{ T}$  ( $0.3\text{--}0.6 \text{ mG}$ ). For the linear dimension  $l$  of the source,  $\sim 1.5 \text{ Mpc}$ , the current to produce a field of this magnitude is  $I \sim lB/\mu_0 \sim 0.5 \times 10^{19} \text{ A}$ . Further evidence for such currents is examined in Chaps. 3, 6, and 7.

## 2.7 Basic Fluid and Beam Instabilities

### 2.7.1 Jeans Condition for Gravitational Instability

Consider matter in the gaseous, rather than plasma, state. Further assume that the gas is nonmagnetized, static, and uniform. Take the zero-order velocity  $v_0$  to be zero, and the mass density  $\rho_0$  and pressure  $p_0$  to be constant. Next assume a density

perturbation of strength  $\rho_1/\rho_0$  such that the mass density is  $\rho_m = \rho_0 + \rho_1$  and the velocity  $v = v_1$ . Under these assumptions, Eqs. (2.15) and (2.13) may be linearized to obtain

$$\frac{\partial \rho_1}{\partial t} + \rho_0 \nabla \cdot v_1 = 0 \quad (2.66)$$

$$\rho_0 \frac{\partial v_1}{\partial t} = -\nabla p_1 - \rho_0 \nabla \phi_{G1} \quad (2.67)$$

For an isothermal process in an ideal gas  $p_1 = kT\rho_1/M$ , where  $M$  is the total mass of the molecular gas. From Poisson's equation

$$\nabla^2 \phi_{G1} = 4\pi G \rho_1 \quad (2.68)$$

Equations (2.66)–(2.68) may be combined to form a wave equation

$$\frac{\partial^2 \rho_1}{\partial t^2} = \frac{kT}{M} \nabla^2 \rho_1 + 4\pi G \rho_0 \rho_1 \quad (2.69)$$

Equation (2.69) has the plane wave solution

$$\rho_1 = \rho_0 \exp i(kr - \omega t) \quad (2.70)$$

where  $k = 2\pi/\lambda$  is the wavenumber and the frequency  $\omega$  is given by

$$\omega^2 = k^2 v_s^2 - 4\pi G \rho_0 \quad (2.71)$$

where

$$v_s^2 = \sqrt{kT/M} \quad (2.72)$$

is identified as the velocity of sound in the gas.

One of the roots of Eq. (2.71) is positive imaginary

$$\omega = +i\sqrt{4\pi G \rho_0 - k^2 v_s^2} \quad (2.73)$$

so that Eq. (2.70) is an exponentially growing perturbation with growth rate

$$\Gamma = \sqrt{4\pi G \rho_0 - k^2 v_s^2} \quad (2.74)$$

when

$$k^2 v_s^2 = \left(\frac{2\pi}{\lambda}\right)^2 v_s^2 < 4\pi G \rho_0 \quad (2.75)$$

That is, the gas is unstable to density fluctuations with a wavelength  $\lambda$  greater than the critical wavelength (Jeans 1902)

$$\lambda_J = \sqrt{\frac{\pi kT}{GM\rho_0}} \quad (2.76)$$

The velocity of propagation  $V_j$  of the density perturbation is given by (Jeans 1902)

$$V_j = k\omega = v_s^2 \sqrt{1 - \frac{G\rho_0\lambda^2}{\pi v_s^2}} \quad (2.77)$$

Based on the assumption leading to Eqs. (2.66) and (2.67), Jeans found that a spherical gas distribution whose diameter was larger than  $\lambda_j$ , would contract continuously due to  $G$ . The critical mass of such a sphere of gas is  $M_J = \pi\rho_0\lambda_j^3/6$ . It should be noted that these results are only applicable for a medium in which the Lundquist parameter Eq. (1.6) is of order unity or less.

### 2.7.2 Two-Stream (Buneman) Instability

Consider a plasma in which the ions are stationary  $v_{i0} = 0$  and the electrons have a velocity  $V_0$  relative to the ions. Let the plasma be cold,  $T = T_e = T_i = 0$  and assume  $B_0 = 0$ . Under these assumptions, Eqs. (2.15) and (2.13) may be linearized to yield

$$\frac{\partial n_{i1}}{\partial t} + n_0 \nabla \cdot v_{i1} = 0 \quad (2.78)$$

$$\frac{\partial n_{e1}}{\partial t} + n_0 \nabla \cdot v_{e1} + (V_0 \cdot \nabla) n_{e1} = 0 \quad (2.79)$$

$$n_0 m_i \frac{dv_{i1}}{dt} = n_0 m_i \frac{\partial v_{i1}}{\partial t} = en_0 E_1 \quad (2.80)$$

$$n_0 m_e \frac{dv_{e1}}{dt} = n_0 m_e \left[ \frac{\partial v_{e1}}{\partial t} + (V_0 \cdot \nabla) v_{e1} \right] = -en_0 E_1 \quad (2.81)$$

where  $n_{i0} = n_{e0} = n_0$ . Note that in Eq. (2.78) use has been made of  $\nabla n_0 = v_{i0} = 0$  while in Eq. (2.80)  $(v_{i0} \cdot \nabla) v_{i1} = 0$ . For electrostatic waves  $E_1 = \hat{z} E e^{i(kz - \omega t)}$ , and Eqs. (2.78)–(2.81) may be written as

$$-i\omega n_{i1} + ikn_0 v_{i1} = 0 \quad (2.82)$$

$$(-i\omega + ikV_0) n_{e1} + ikn_0 v_{e1} = 0 \quad (2.83)$$

$$-i\omega n_0 m_i v_{i1} = en_0 E_1 \quad (2.84)$$

$$n_0 m_e (-i\omega + ikV_0) = -en_0 E_1 \quad (2.85)$$

Solving Eqs. (2.82)–(2.85) for the velocities and densities gives

$$v_{i1} = \frac{ie}{m_i \omega} E_1 \quad (2.86)$$

$$v_{e1} = \frac{ie}{m_e \omega} E_1 \quad (2.87)$$

$$n_{i1} = \frac{ien_0k}{m_i\omega^2}E_1 \quad (2.88)$$

$$n_{e1} = \frac{-ien_0k}{m_e} \frac{E_1}{(\omega - kV_0)^2} \quad (2.89)$$

Because the unstable waves are high-frequency plasma oscillations, the plasma approximation (Sect. 2.4.1) cannot be used, and the electrostatic field must be obtained from Poisson's equation (1.3):

$$\epsilon_0 \nabla \cdot E_1 = e(n_{i1} - n_{e1}) \quad (2.90)$$

Substituting  $\nabla \cdot E_1 = ikE_1$ , Eq. (2.88), Eq. (2.89) into Eq. (2.90), yields the dispersion relation,

$$1 = \frac{\omega_{pi}^2}{\omega^2} + \frac{\omega_{pe}^2}{(\omega - kV_0)^2} \quad (2.91)$$

Equation (2.91) has four roots and, under certain conditions, two of these are complex conjugate. The location of the complex root having a positive imaginary component is given by (Krall and Trivelpiece 1973)

$$\omega' = kV_0 \left[ \frac{(\omega_{pe}/\omega_{pi})^{2/3}}{(\omega_{pe}/\omega_{pi})^{2/3} + 1} \right] \quad (2.92)$$

The condition for instability is that the right-hand side of Eq. (2.91) be greater than 1 at  $\omega = \omega'$ , and is

$$|kV_0|^2 < \omega_{pe} \left[ 1 + (\omega_{pi}/\omega_{pe})^{2/3} \right]^3 \quad (2.93)$$

This is the *two-stream*, or *Buneman*, instability (Buneman 1959). Since the sign of the charge does not appear, Eq. (2.93) can be equally well applied to two electron streams in a fixed neutralizing ion background, replacing  $\omega_{pi}/\omega_{pe}$  by  $\omega_{pe1}/\omega_{pe2}$ .<sup>3</sup> The introduction of thermal effects becomes important only if the thermal velocities are of the order of  $V_0$ , in which case the flow can hardly be classified a beam.

The physical interpretation of Eq. (2.91) is that, because of the Doppler shift of the plasma oscillations, the ion and electron plasma frequencies can coincide in the laboratory frame only if it has the proper value. The ion and electron density fluctuations can then satisfy Poisson's equation. The electron oscillations have negative energy; they draw energy from the kinetic energy of the electrons.<sup>4</sup> Therefore, the negative energy electron waves and the positive energy ion waves both can grow while the total energy of the system remains constant. This type of instability finds application in high-power microwave generation in relativistic klystrons

<sup>3</sup> The dispersion relation for a beam of electrons propagating through a plasma is simply  $1 = \omega_p^2/\omega^2 + \omega_b^2/(\omega - kV_b^2)$ . If the beam is relativistic  $\omega_b^2$  is replaced by  $\omega_b^2/\gamma^3$ .

<sup>4</sup> In the prescription for Landau damping (Chen 1984), if the electrons are traveling slower than and in the same direction as the wave, they take energy from it.

(Godfrey and Thode 1975). A REB is velocity modulated by an rf signal, thereby producing bunches of accelerated electrons that pass through the slower velocity or deaccelerated electrons. This produces a two-stream condition. As the bunches pass through a microwave resonator, they excite the natural mode of the cavity to produce microwave power.

In space and cosmic plasmas, the two stream condition often exists to produce electromagnetic radiation (albeit at efficiencies far less than laboratory devices), and may also be the source of double layers in Birkeland currents (Chap. 5).

### 2.7.3 Sausage and Kink Instabilities

The simple pinch has a number of serious instabilities (Shrafranov 1957). The sausage ( $m = 0$ ) instability occurs periodically along the pinch where the magnetic pressure becomes greater. This causes bulges to appear which result in even greater inward pressure between them. Ultimately, if the axial current is strong enough, the pinch can collapse into force-free magnetic plasmoids.

The kink ( $m = 1$ ) instability produces a helical mode in the pinch. This most often occurs when a strong axial magnetic guide field is present, that is, the pinched plasma is a Birkeland current. The simulated time evolution of the kink instability is discussed in Sect. 2.9.2.

## 2.8 Laboratory Simulation of Cosmic Plasma Processes

The rapid development of high-voltage pulsed power technology in the 1970s and 1980s has made it possible, for the first time, to investigate the intense currents, high voltages, and energetic particles found in space and cosmic plasma. Megaamperes of current in pulsed beams of electrons and ions with particle kinetic energies in the range from  $\sim 100$  keV to several hundred MeV have been achieved. Although this technology was originally developed for materials testing, X radiography, and nuclear weapon effects simulation, it has found widespread use in such diverse fields as thermonuclear fusion, high-power microwave generation, collective ion acceleration, laser excitation, and laboratory astrophysics.

A multi-terawatt pulsed-power generator may typically consist of an array of capacitor banks (called a “Marx bank”), or many kilograms of high explosive on a magnetic-compression-generator, driving a coaxial pulseline (Fig. 2.9).<sup>5</sup> A diode consisting of an outer anode and a cathode (terminating the inner coaxial conductor) is attached to the water pulseline through a coaxial vacuum transmission line. The purpose of the pulseline is to shorten the microseconds-long-pulse generated by

---

<sup>5</sup> The dielectric medium of the Marx bank may be 300,000 L of transformer oil while the pulseline may contain 400,000 L of deionized water.

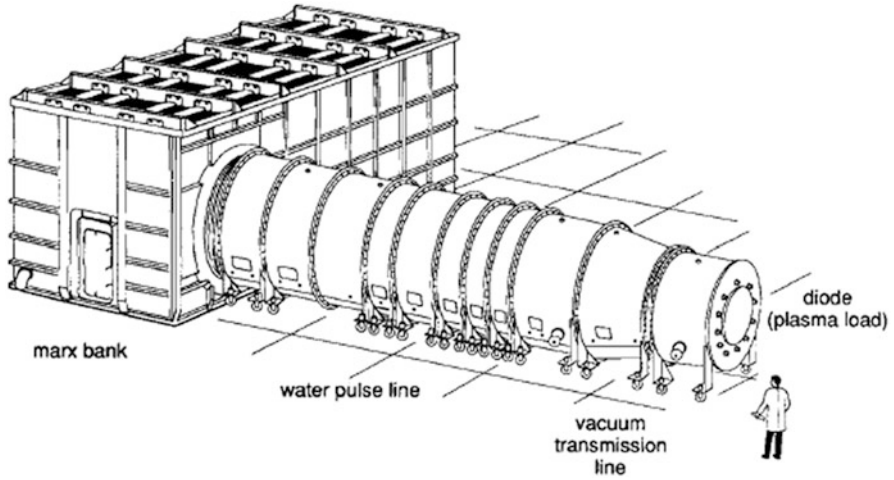


**Fig. 2.9** A multi-terawatt pulsed-power generator. The diode, that contains the plasma load, is located at the end of the cylindrical, coaxial, pulse shaping line

the Marx bank, which may contain megajoules of energy, to a 30–60 nanosecond-long-pulse at the diode, thereby producing a power amplification (watts = joules per second). In this way, space and astrophysical magnitude quantities are generated: megaamperes of current, megavolts of potential differences, megaelectronvolt particle energies, and terawatts of power.

### 2.8.1 High-Current Plasma Pinches

A plasma pinch can be created by attaching thin (few microns thick) wires or thin cylindrical foils between the cathode and anode, or else injecting gas between the cathode and anode at the time of pulse arrival.

Unlike most astrophysical pinches, the laboratory pinch is available to in situ measurement and study. The magnetohydrodynamic evolution is recorded using streak and framing cameras to record the bulk plasma motion, pulsed-laser holography and shadowgraphy to study time resolved morphology, and Faraday rotation measurements to plot magnetic field vectors (Fig. 2.10). The radiation history is recorded using X ray detectors, spectrum analyzers, pin-hole X ray cameras, and microwave antennas (Fig. 2.11).

Figure 2.12 shows the time history of a jet of argon gas injected through the cathode. At time 7 ns the gas is ionized by the arrival of the MV pulse. The images, recorded in soft X rays, show the flaring out of the hollow gas towards the anode. At 14 ns the gas is fully ionized and the plasma conduction current is nearly 4 MA, causing the plasma to pinch. The inward compression of plasma is halted when the

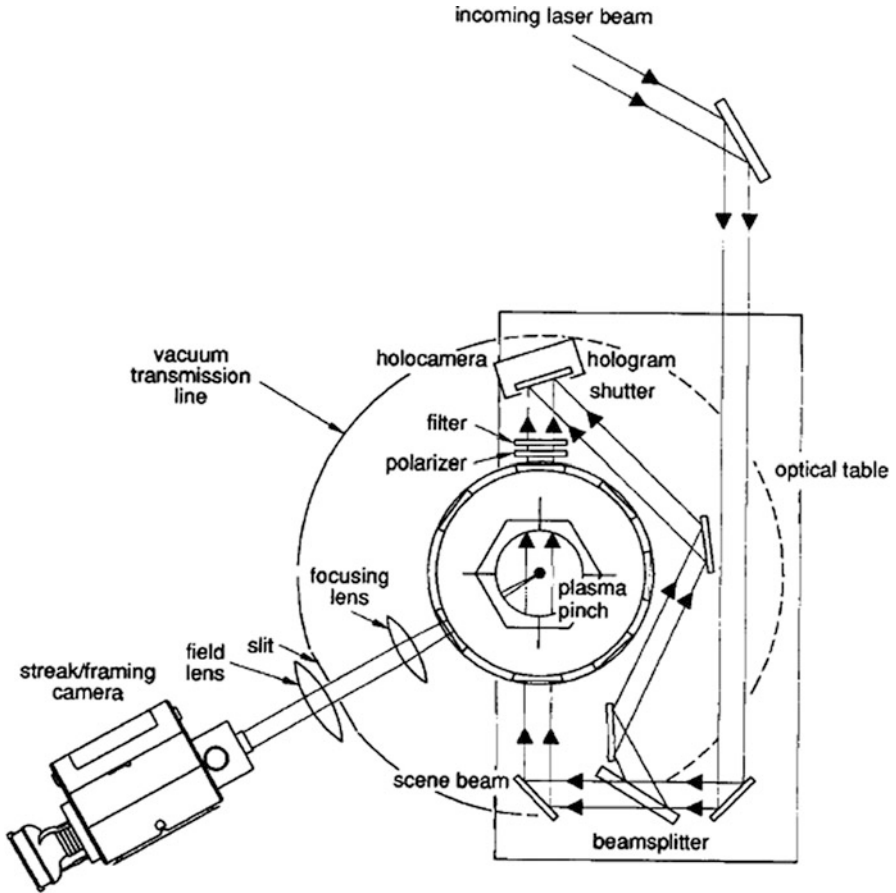


**Fig. 2.10** Diagnostics setup on pulsed-power generator diode. Shown are the pulsed-laser holography and framing camera setups

pinch undergoes a transformation to a force-free state, producing the “plasmoids” recorded at 21 ns.<sup>6</sup> These plasmoids then pair together, sometimes producing spiral configurations such as that (barely discernible) at 28 ns.

A detailed study of plasmoid interaction was carried out by Bostick (1956, 1957). Figure 2.13 shows the time history of spiral formation from plasmoids produced by plasma guns (Sect. 4.6.2) fired at each other across a magnetic field.

The unique possibility of plasma pinches to create ultradense matter, such as that in the interiors of stars, is investigated in some detail by Meierovich (1984).

<sup>6</sup> The term “plasmoid” was coined by W. Bostick (1956) to describe the force-free self-magnetic field carrying entities he experimented with.

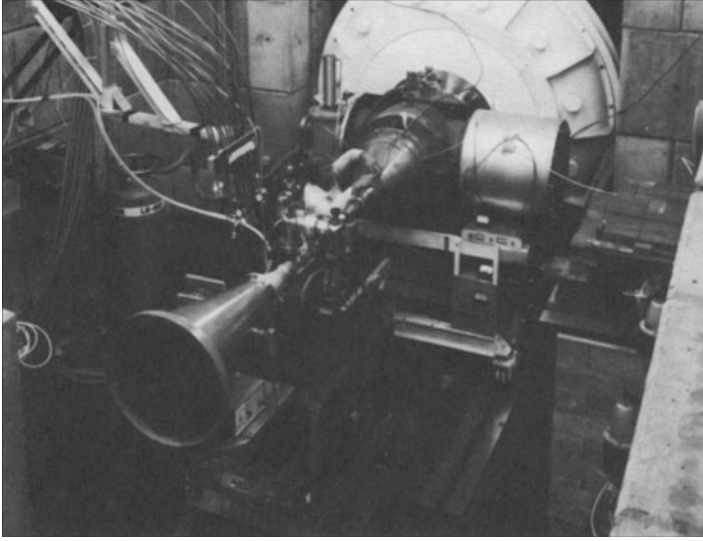


**Fig. 2.11** Diagnostics setup to study microwave emission. The microwave horn is attached to the generator diode

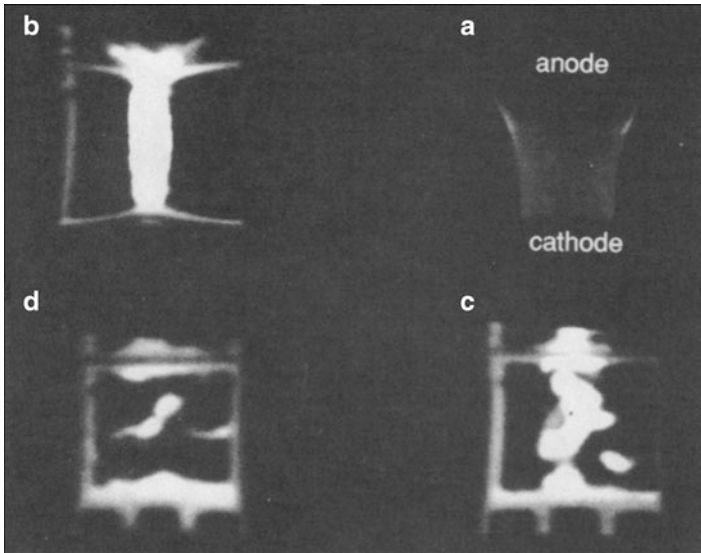


**Fig. 2.12** Evolution of a plasma pinch produced by fully ionized argon gas. These photos were recorded in soft X rays by a framing camera. The cathode is at the *bottom* of each frame while the anode is at the *top*





**Fig. 2.13** The evolution of two plasmoids fired at each other across a magnetic field (Courtesy W. Bostick)

### 2.8.2 Laboratory Aurora Simulations

The magnetized sheet electron beam has been studied in some detail in a very careful set of experiments carried out by Webster (1957). Webster was able to produce laboratory analogs of the polar aurora in a small, vacuum, anode-cathode arrangement in which currents as low as  $58 \mu\text{A}$  were conducted and detected (Fig. 1.20). The experimental setup consisted of a small vacuum tube (Fig. 2.14) that launched a  $0.1 \times 1.2 \text{ cm}$  flat sheet electron beam by means of a slotted grid disk in front of the cathode. The beam traveled  $9.2 \text{ cm}$  parallel to a  $71 \text{ G}$  axial magnetic field until it struck a fluorescent screen anode. The fluorescent screen was made of a thin coating ( $1 \text{ mg/cm}^2$ ) of  $\text{ZnO}$  phosphor.

Figure 2.15 depicts a series of single-frame photographs of the phosphor screen showing the beam shape at the anode as the beam voltage was increased. Here we see that the sheet beam rotates as a rigid rod through an angle of about  $30^\circ$ . Beyond this angle, the beam begins to fold into charge bunches, producing vortex patterns on the phosphorus plate. At a certain critical voltage, the vortices disrupt, produc-

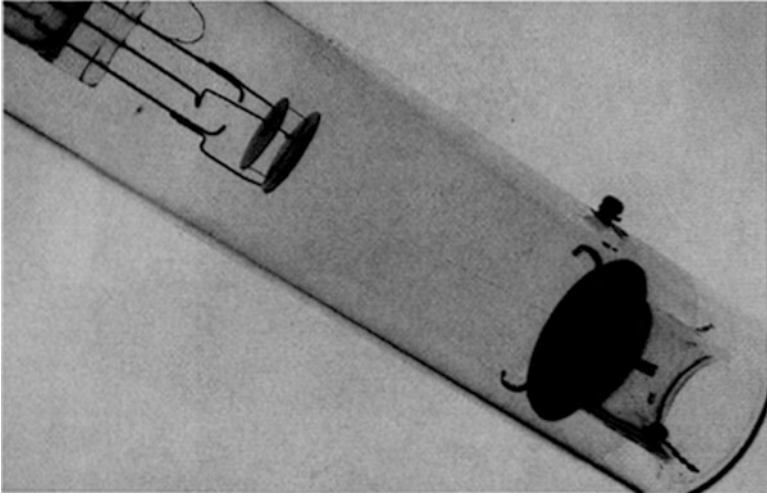


**Fig. 2.14** Vacuum electron tube used to simulate the aurora. The total length of the tube is about 20 cm (Courtesy of H. Webster)

ing a violent oscillation. These oscillations have a complex waveform indicating a rather broadband frequency distribution. The bandwidth increases rapidly with beam voltage.

## 2.9 The Particle-in-Cell Simulation of Beams and Birkeland Currents

Even before its application to plasmas, the particle-in-cell technique was applied to the study of electron beams in vacuum (Chap. 10). This section is concerned with the particle-in-cell simulation of electron beams, in the presence or absence of an external magnetic field, propagating through plasma. The beam may be a solid or hollow cylinder, or a planar sheet, a geometry that happens to be of particular interest to the study of the aurora or of vacuum devices. Thin sheet beams produced by electrons ejected from cathodes along magnetic lines of force have found a multiple applications on earth (e.g., in cross-field microwave generators, backward-wave amplifiers, and in multi-gapped particle accelerators). Furthermore, solid cylindrical beams of electrons traveling a sufficient distance along a magnetic field line can become cylindrical-sheet beams due to a hollowing instability (Ekdahl 1987). For these applications, the particle-in-cell simulation (PIC) technique has been often used to study the dynamics of sheets of charged particles (Hallinan 1976; Jones and Mostrom 1981; Mostrom and Jones 1983). This offers an opportunity to benchmark the simulation against physical data.



**Fig. 2.15** Laboratory simulated aurora. Voltage (current) increases continuously from top to bottom in each column, and the beam pinches only at the edge. In contrast, cold beams with a radius of a few are noncurrent neutralized and exhibit strong pinching

A simulation of complex phenomenon is generally given little credence until it is “benchmarked” against physical measurements. For this reason, laboratory measurements and the PIC approach often create a synergism in understanding the problem at hand. This approach works best when high quality diagnostics methods are available to guide the simulation.

The beams and Birkeland filaments simulated in Sect. 2.9 will be found to exhibit a number of properties which will be pursued throughout the remainder of this book (Chap. 10): pinching of plasma in the presence of a field-aligned electric field (Chaps. 4 and 5), uniform bulk rotation of the plasma particles indicative of force-

free plasma interiors (when the external fields are turned off or become negligible), and the release of electromagnetic radiation via the synchrotron process (Chap. 6).

### 2.9.1 Charge and Current Neutralized Beam Propagation in Plasma

Consider a cold plasma of electrons and ions of density  $n_p = 0.28 \text{ cm}^{-3}$ . A beam of electrons of radius  $a = 100 \text{ km}$  at density  $n_b/n_p = 0.003$  and a risetime of 7 ms propagates from the left in a simulation region of dimension  $500 \times 300 \text{ km}$ . This problem was simulated with the particle code ISIS (Fig. 2.16). (For this problem the plasma skin depth parameter  $\lambda_E = c/\omega_p$  is 10 km.) The beam is mildly-relativistic with  $\beta\gamma = 0.2$ . Because of the background plasma, the beam is charge neutralized so that  $f_e = 1$  and the beam propagates without diverging.

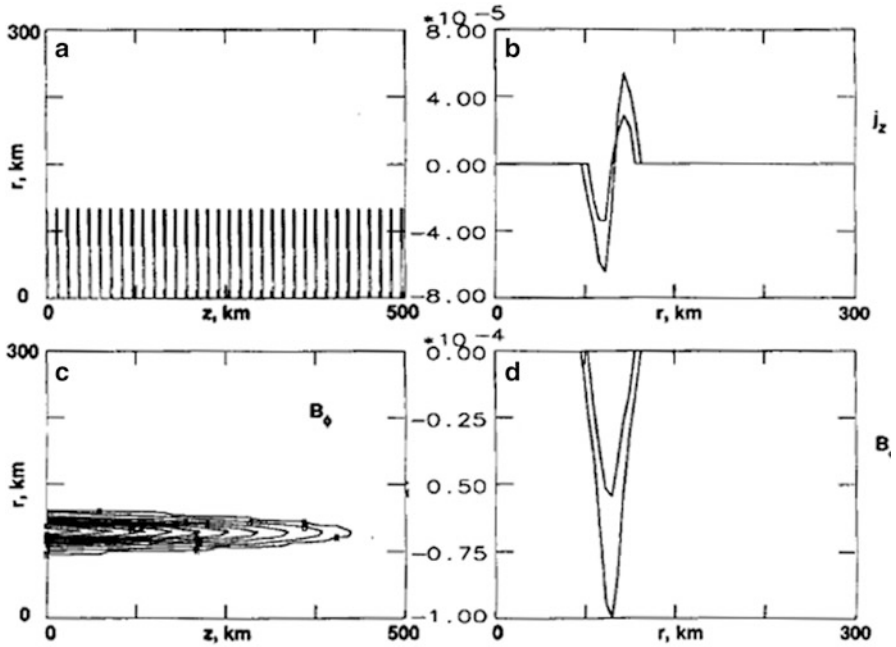


**Fig. 2.16** (a) Electron beam profile along the axial dimension. The beam propagates from left to right through a plasma background. (b) Current density versus radius. The ordinate is in units of  $= 1.35 \times 10^{-5} \text{ A/m}^2$ . The return current is equal to the beam current out to a radius of 75 km. (c) Self magnetic field profiles. (d) Self field versus radius. The ordinate is in units of which corresponds to 0.17 nT. The two curves (b) and (d) are slices at  $z = 100$  and 200 km, respectively, at  $t = 10 \text{ ms}$

As the beam propagates, a return current is set up within the beam by the plasma electrons. (The electron beam flow is to the right so the beam current is to the left, i.e., a negative value. The return current has a positive value.) Because of the return current, the beam is very nearly current neutralized,  $f_m \approx 1$ . The nonneutralized part of the axial current  $j_z$  and the nonzero azimuthal field  $B_\phi$  are largely localized within a few plasma skin depths  $\lambda_E$  at the beam edge (Fig. 2.16c, d)

### 2.9.2 Relativistic and Mildly Relativistic Beam Propagation in Plasma

Consider a cold plasma of electrons and ions of density  $n_p = 1 \text{ cm}^{-3}$ . A beam of electrons of radius  $a = 100 \text{ km}$  at density  $n_b/n_p = 8 \times 10^{-4}$  and a risetime of  $0.2 \text{ ms}$  propagates from the left in a simulation region of dimension  $1,000 \times 300 \text{ km}$  (Fig. 2.17). The beam is mildly-relativistic with  $\beta\gamma = 0.2$ . For these values the beam current is  $I = 200 \text{ A}$ , and since the Alfvén current  $I_A = 17\beta\gamma = 2.5 \text{ kA}$ , the beam propagates unhindered, electrically neutralized by the plasma ions (Fig. 2.17a).

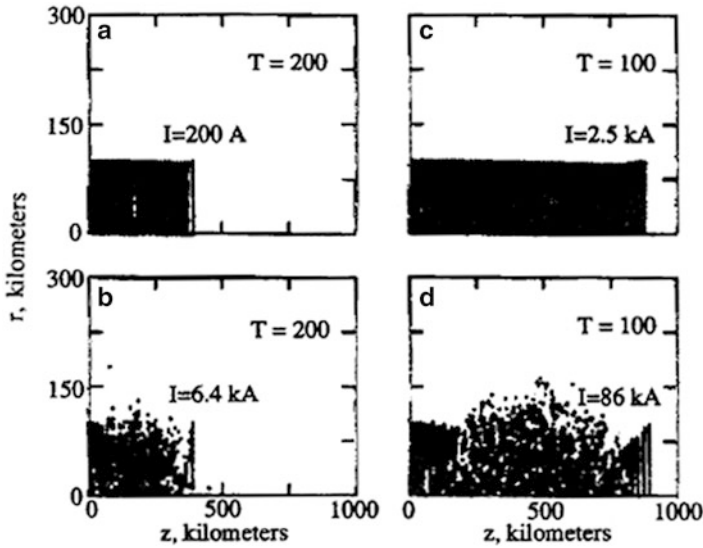


**Fig. 2.17** Electron beam propagating through a plasma background. The “comb” structure in the incoming beam is an artifact of every 24th particle being plotted

If the beam current is increased to  $I = 6.4 \text{ kA}$  ( $n_b/n_p = 0.1$ ), it exceeds  $I_A$  and no longer propagates as a beam by time  $t = 6.6 \text{ ms}$  (Fig. 2.17b).

If the beam is relativistic with  $\gamma = 2$  and  $n_b/n_p = 0.003$ ,  $I = 2.6 \text{ kA}$  and  $I_A = 34 \text{ kA}$ . The beam propagates as shown in Fig. 2.17c. A slight pinching of the beam

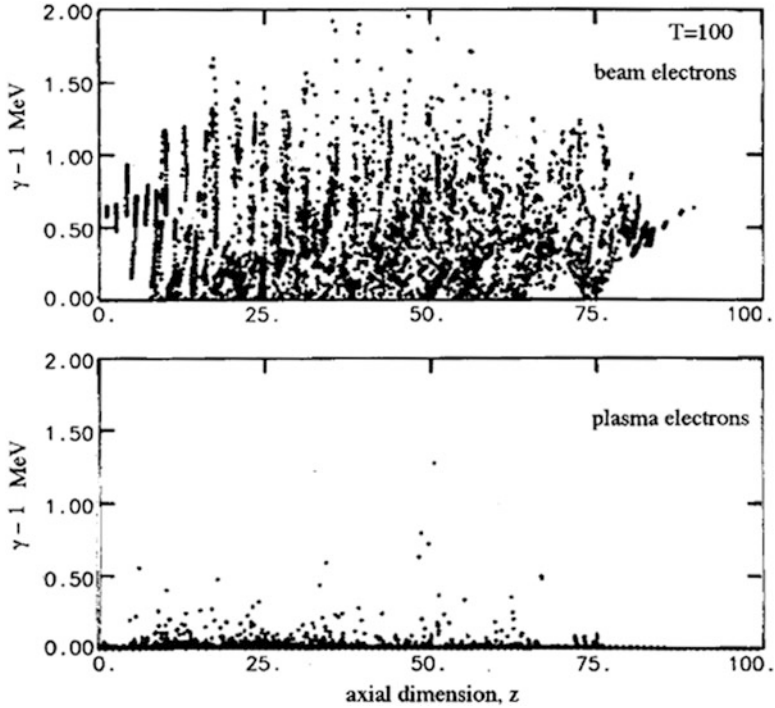


**Fig. 2.18** (Top, a) Kinetic energy of beam electrons at  $t = 100\omega_p^{-1}$ . (Bottom, b) Kinetic energy of plasma electrons at  $t = 100\omega_p^{-1}$

front is seen as the current builds up during risetime and before any return current neutralization can be established.

If the beam current is increased to  $I = 86 \text{ kA}$  ( $n_b/n_p = 0.1$ ), it rapidly pinches, converting axial momentum into radial momentum (Fig. 2.17d). Some of the kinetic energy of the beam electrons (Fig. 2.18 (top)) is transferred to the plasma electrons, causing the background to be heated. Some of the initially cold plasma electrons attain energies as high as 1.5 MeV (Fig. 2.18 (bottom)).

### 2.9.3 Propagation of a Relativistic Beam Bunch Through Plasma

Consider a cold plasma of electrons and ions of density  $n_p = 0.28 \text{ cm}^{-3}$ . A pulse or bunch of  $\gamma = 40$  electrons of radius  $a = 20 \text{ km}$ , length  $l = 8 \text{ km}$ , and density  $n_b/n_p = 0.02$  propagates from the left to right, as shown at time  $t = 0.5 \text{ ms}$  in Fig. 2.19.

The beam pulse produces a “wake field” condition (Keinigs and Jones 1987): The production of negative and positive plasma electron momenta with a concomitant alternating electric field in the wake of the pulse. The peak strength of the induced

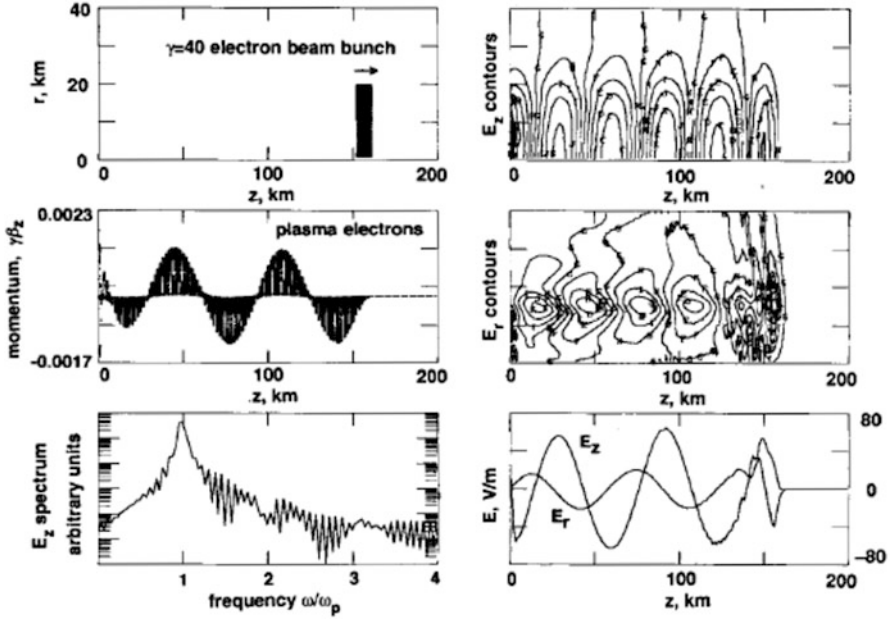


Fig. 2.19 Particle, field, and frequency data for a pulsed beam propagating in a plasma

fields  $E_z$  and  $E_r$  are 60 and 20 V/m, respectively. The frequency spectrum of the wake field is sharply peaked at the plasma frequency (4.8 kHz), as is also the case for much longer beam lengths.

### 2.9.4 Beam Filamentation

Large radius beams ( $a \gg \lambda_E$ ) propagating through plasma are susceptible to a filamentation instability (Molvig et al. 1978; Shannahan 1986; Lee and Thode 1983). The filamentation instability most readily occurs for large currents. In addition, relativistic beams are more susceptible to this instability since the time to filamentation scales as  $\gamma^{1/2}$  (Molvig 1975).

Consider a relativistic beam ( $\gamma = 20$ ) of radius  $a = 20\lambda_E$  and  $n_b/n_p = 0.2$ . For this case, the beam current is approximately the same as the Alfvén current (340 kA) so that filamentation is expected.

Figure 2.20 shows the evolution of the beam. As predicted, initially the pinching occurs only near the beam edge. At later time the beam undergoes a strong filamentation instability. The solid beam therefore pinches into current carrying filaments whose thicknesses are of the order of  $\lambda_E$ . The actual width is determined by the factors outlined in Eq. (2.23).

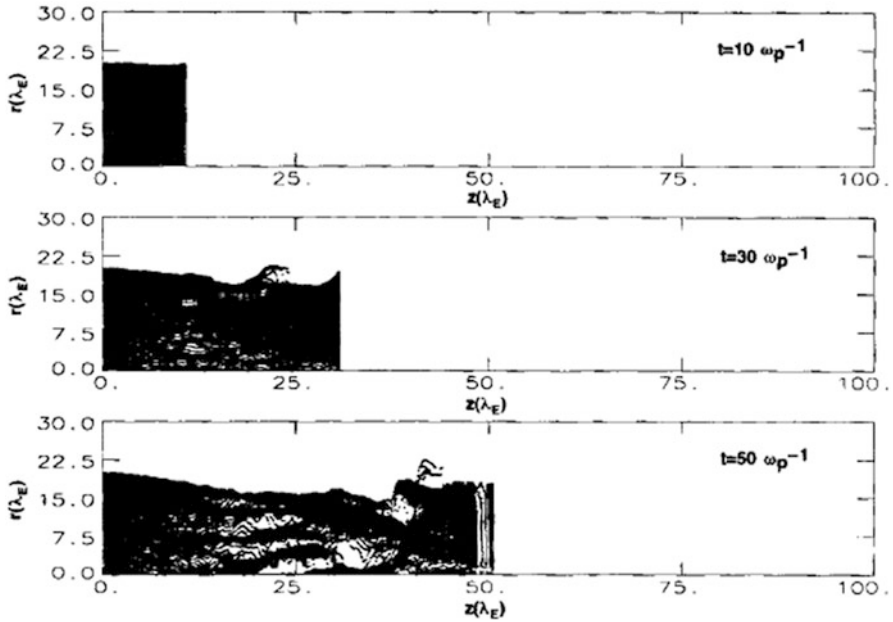


**Fig. 2.20** Filamentation of a thick ( $20\lambda_E$ ), relativistic ( $\gamma = 20$ ), current neutralized beam in a plasma

Strong magnetic fields can inhibit beam filamentation, however in most cosmic plasmas  $\omega_b \leq \omega_p$  so that filamentation is expected.

### 2.9.5 Dynamical Evolution of a Narrow Birkeland Filament

Since [Bennett \(1934\)](#), the dynamic evolution of astrophysical plasma: filamentation and rotation, has been the topic of a great many physicists, driven by the experiments of Birkeland. These include [Lehnert \(1952, 1955\)](#), [Webster \(1955\)](#), [Webster and Hallinan \(1973\)](#), [Murty \(1961\)](#), [Yu et al. \(1965\)](#), [Knauer \(1966\)](#), [Knauer and Poeschel \(1966\)](#), [Bostick et al. \(1966\)](#), [Egeland and Holtet \(1968\)](#), [Carmel and Nation \(1973\)](#), [Davis and Hallinan \(1976\)](#), [Friedman and Hammar \(1972\)](#), [Hallinan \(1970\)](#), [Küppers et al. \(1973\)](#), [Kapetanacos et al. \(1973\)](#), [Kapetanacos \(1974\)](#), [Nardi et al. \(1980\)](#), [Peratt et al. \(1980\)](#), [Browne \(1980\)](#), [Ivanov et al. \(1981\)](#), [Hill \(1984\)](#), [Wagner et al. \(1983\)](#), [Potemra \(1984\)](#), [Dessler \(1984\)](#), [Peratt and Snell \(1985\)](#), [Ek-dahl et al. \(1985\)](#), [Witalis \(1986\)](#), [Lerner \(1986\)](#), [Bhavsar and Ling \(1988\)](#), [Salin-garos \(1988\)](#), and [Pereira et al. \(1989\)](#).

Consider a columnar plasma filament with a Gaussian radial density profile ([Nielsen et al. 1979](#)). A large external magnetic field  $\beta_p \approx 0.1$  Eq. (10.20) is applied uniformly throughout the plasma column and the simulation region with the field



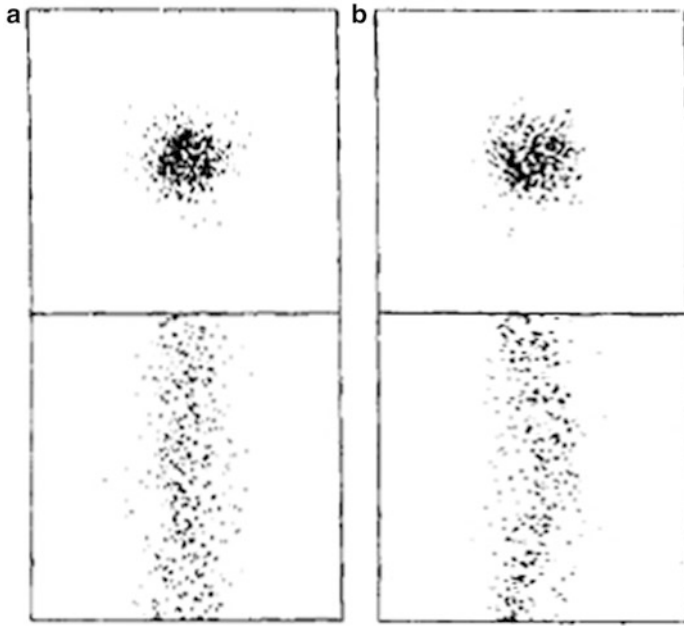


**Fig. 2.21** Cross-sectional and axial views of the electron distributions in the simulated Birkeland filament (5 % of the electrons are plotted). (a) Before instability,  $t = 150\omega_p^{-1}$ ; (b) After helix formation,  $t = 164\omega_p^{-1}$

lines parallel to the axis of the column. Additionally, a strong uniform electric field is applied along the column so that significant currents are generated ( $B_0/B^{self} \approx 4.5$ ). The simulation is periodic in space so that a particle which moves out of one side of the simulation domain is returned at the opposite side with its same velocity. Computer economy forces a time compression by setting  $m_i/m_e = 16$  (Sect. 10.6.3). The number of superparticles per Debye cube is  $n\lambda_D^3$ . This problem was simulated with the 3D code SPLASH (Chap. 10).

After an initial current buildup, accompanied by visible pinching, a sudden a dramatic helical mode developed (Fig. 2.21). At this point the ratio of externally applied magnetic field to self-generated magnetic field was about 2.5:1. The effect of the instability was a transport of plasma across  $B$ , resulting in a column of radius somewhat larger than the original radius. The magnetostatic energy  $W_B$  reaches its peak at  $t = 160\omega_p^{-1}$  (Fig. 2.22a). The onset of the instability converts this into electrostatic energy  $W_E$  (Fig. 2.22b). The peak of  $W_E$  occurs at  $t = 184\omega_p^{-1}$ . This energy is subsequently radiated away (Fig. 2.22c, d) as electromagnetic waves. The frequency of radiation is the bulk rotation frequency which for this simulation is less than . Since there are still relatively few Debye lengths across the column ( $a/\lambda_D \approx 12$ ), it is probable that the entire column, not just the surface, participates in a synchrotron radiation process.

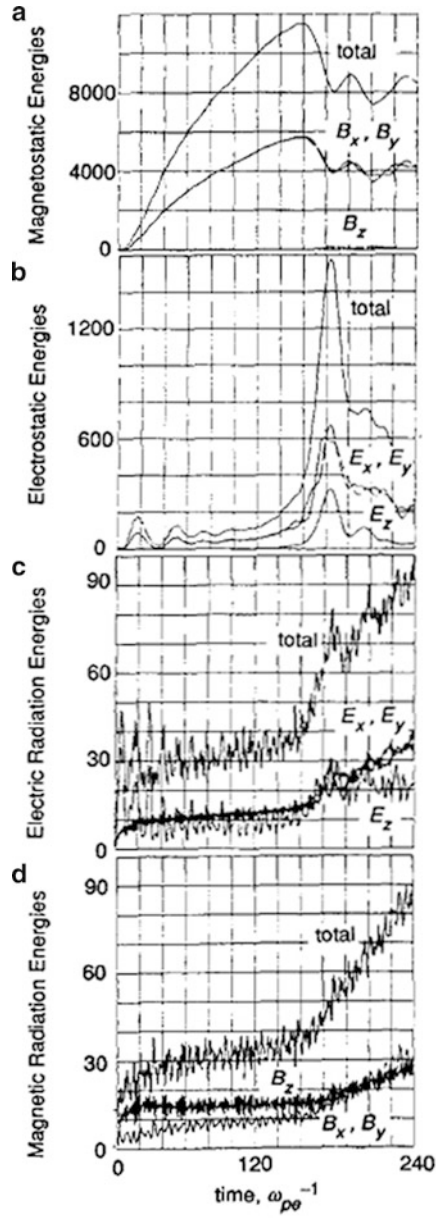


**Fig. 2.22** Magnetostatic, electrostatic, electric and magnetic radiation energies vs. time in  $\omega_p^{-1}$ . The energies are given in arbitrary energy units



**Fig. 2.23** Cross-sectional view of a 2.1 mA electron beam

### ***2.9.6 Vortex Formation in Thin Cylindrical Electron Beams Propagating Along a Magnetic Field***

Historically, vortex structure and vortex interactions in charged particle beams have been known since the turn of the nineteenth century when Birkeland first photographed the passage of particle beams through low vacuum in his terrella cathode experiments. [Cutler \(1956\)](#), starting with a perfectly circular 2.1 mA electron beam was able to record the vortex structure shown in [Fig. 2.23](#) after the beam had propagated for 300 cm along a 34 G field.

The circular beam employed by Cutler was simulated with SPLASH where  $q = 0.04$  Eq. (1.15), and  $\omega_p dt = 0.25$  ([Peratt 1985](#)). The simulation used 250,000 electrons, 1 % of which are plotted in [Fig. 2.24](#). This figure shows the time evolution of the diocotron instability over 190 plasma periods and is in good agreement with the measured beam pattern.

The  $e$ -folding length for instability buildup is ([Kyhl and Webster 1956](#); [Pierce 1956](#))

$$L = \lambda C B_z V / I \quad (2.94)$$

where  $C$  is the beam circumference,  $B_z$  is the magnetic field,  $V$  is the voltage, and  $I$  is the beam current. [Figure 2.25](#) plots the current required to initiate the instability, the formation of simple vortex patterns, and the onset of vortex interactions as a function of the beam length  $L$  for a number of experimental and simulation cases.

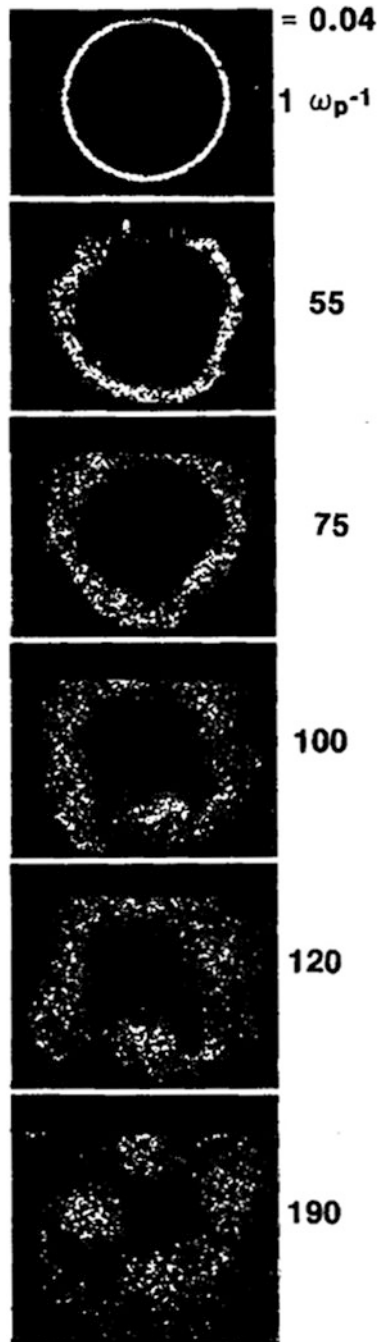


**Fig. 2.24** (Opposite) Cross-sectional views of simulated beam corresponding to the experimental conditions of Fig. 2.23 at various time steps. One percent of the electrons are plotted. The vorticity is clockwise for the outwardly directed  $B_z$

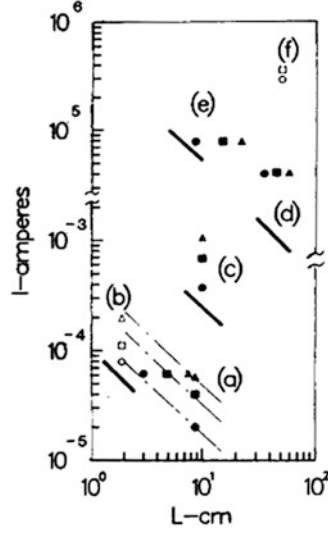


**Fig. 2.25** Beam current vs. distance for instability onset (circles), simple vortex patterns (squares), and vortex interactions (triangles). Experiment (solid symbols), simulation (open symbols), and Eq. (2.94) (dark lines). (a)  $q = 2.5 \times 10^{-3}$ , 80 V,  $l = 10$ ; (b)  $q = 0.04$ , 50 V,  $l = 4$ ,  $n_i = 0$ ; (c)  $q = 7.3 \times 10^{-3}$ , 80 V,  $l = 10$ ,  $p = 10^{-5}$  T; (d)  $q = 0.39$ , 400 kV,  $l = 4$ ,  $p = 0.2$  T; (e)  $q = 0.59$ , 1.9 MV,  $l = 10$ ,  $p = 0.3$  T; (f)  $q = 0.11$ , 10 MV,  $l = 16$ ,  $n_i = n_e$

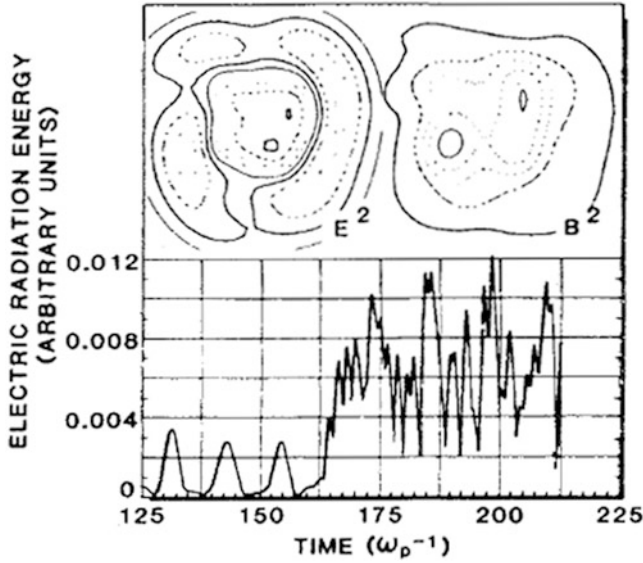


**Fig. 2.26** Transverse electric field radiation energy vs. time in  $\omega_p^{-1}$ . Inset: Contours of  $E^2$  and  $B^2$  at  $175 \omega_p^{-1}$

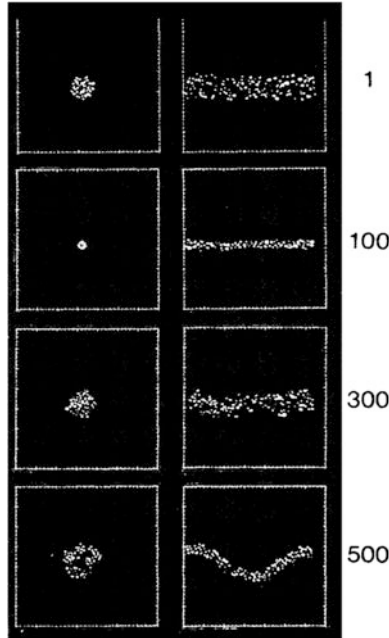


**Fig. 2.27** Evolution of a non-magnetically neutralized 7.5 MeV electron current in a plasma

Also plotted is the linear-theory prediction for instability onset Eq. (2.94). As shown, the linear theory underestimates the onset by a factor of 2–3.

As shown in Fig. 2.24, the onset of instability occurs when  $\Delta r \approx 10\lambda_D$  (after expansion from an initial  $2.5\lambda_D$  beam thickness) for a beam of circumference  $314\lambda_D$ . Thus, the number of vortices expected is  $l = C/\lambda \approx 4$ , as found in the simulation.

Microwaves from the following radiation mechanism are observed in the simulations. The initially concentric ring contours of the electrostatic field  $E_r(r)$  and the induced magnetic field  $B_\phi(r)$  form cross-sectional “islands” as the nonlinear state evolves (Fig. 2.26, inset). The helical electron flow in a vortex can be generalized into axial and azimuthal current components, thereby producing both long-range attractive and short-range repulsive forces between neighboring vortices (Sect. 3.10.2), in addition to the electrostatic line-charge repulsive force

$$F \approx +n_e e (1 - f_e) / r \quad (2.95)$$

These forces causes the most neighborly filaments to spiral together in coalescence (when  $f_e \approx 1$ ) and also produce microwaves from the rapid changes in the electromagnetic fields during this process (Fig. 2.26).



**Fig. 2.28** Simulated aurora. Current increases continuously from *top* to *bottom* in each column. The simulated beam is analogous to the experimental conditions leading to the data shown in Fig. 2.15

### 2.9.7 Charge-Neutralized Relativistic Electron Beam Propagation Along a Magnetic Field

Consider the propagation of beam of 7.5 MeV electrons through a plasma of equal numbers of electrons and ions in the presence of an axial magnetic field. To simulate this case, we choose  $\omega_p dt = 0.25$ ,  $\lambda_D/\Delta = 0.1$ ,  $m_i/m_e = 40$ ,  $T_i/T_e = 1.0$ , and an axial magnetic field of strength  $\omega_c = 1.0\omega_p$ . The beam radius is  $r_b = 3\Delta$  and the beam density is  $n_b/\Delta^3 = 3.0$ . For 7.5 MeV electrons,  $\gamma = 1 + 7.5 \text{ MeV}/0.511 \text{ MeV} = 15.8$  and  $\beta_z = 0.998$ .

For the background plasma we choose  $r_p = 5\Delta$  and ion and electron densities  $n_i/\Delta^3 = n_e/\Delta^3 = 0.4$ . Both the beam and background plasmas are given Gaussian density profiles.

Figure 2.27 shows the end and side views of the beam and plasma evolution versus timestep number. The first frame ( $1\omega_p$ ) depicts the initial simulation setup. Because the background plasma is tenuous and the beam is thin, the beam is not current neutralized and pinches to a minimum radius  $r_b \approx \Delta$  within  $25\omega_p^{-1}$ . Once

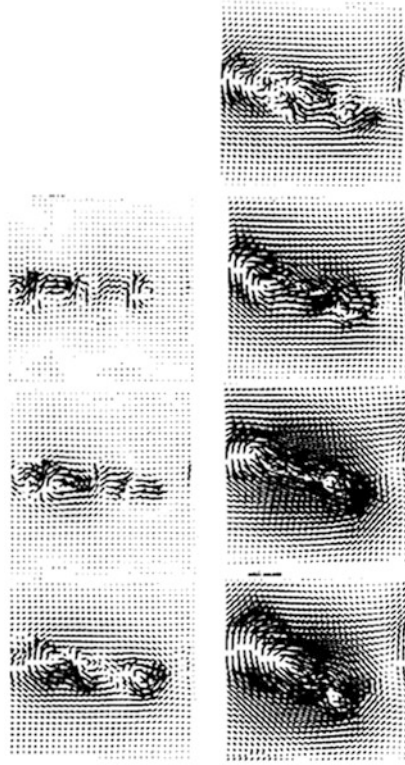


**Fig. 2.29** “Magnetic storm” produced by self-generated transverse magnetic field during beam vorticing. The length of the arrows indicate relative field strength while direction gives the polarization. These frames coincide with those of Fig. 2.28

this “steady state” is reached, small amplitude long wavelength perturbation growth sets in, causing the beam to go unstable. This instability leads to a well-defined helical mode shown in the last frame at  $125\omega_p^{-1}$ .

### 2.9.8 Numerical Aurora Simulations

A simulation of the laboratory aurora experiment of Sect. 2.8.2 is shown in Fig. 2.28. The parameters used in this simulation are  $q = 0.04$ ,  $\omega_p dt = 0.25$ , and  $w/\Delta x$ , where  $w$  is the width of the beam. To simulate the continuously increasing voltage applied to the beam, the acceleration parameter  $E_z/cB_z$  was set to 0.05. The constant electric field causes the electrons to accelerate in the  $-z$  direction and the ions to accelerate in the  $+z$  direction, thereby producing a time-increasing beam current, in mimicry of increasing the voltage in the laboratory experiment. The simulated beam patterns shown in Fig. 2.28 are to be compared to Fig. 2.15. Here we again see an essentially rigid rotor rotation predicted by linear theory until vortices develop on the beam.



The simulation allows an in-depth study of the other beam parameters and Fig. 2.29 shows the time evolution of the self-consistent magnetic field produced by the beam. The “magnetic storm” shown corresponds to the beam profiles of Fig. 2.28.

## References

- Alfvén, H.: Magnetic storms and the aurorae. *Proc. R. Swed.-Acad. Sci. (Kungliga Svenska Vetenskapakademiens Handlingar)* **18**, 139 (1939)
- Alfvén, H.: Electric currents in cosmic plasma. *Rev. Geophys. Space Phys.* **15**, 271 (1977)
- Alfvén, H.: *Cosmic Plasma*. D. Reidel, Dordrecht (1981)
- Bennett, W.H.: Magnetically self-focussing streams. *Phys. Rev.* **45**, 890 (1934)
- Bogdankevich, L.S., Rukhadze, A.A.: Stability of relativistic electron beams in a plasma and the problem of critical currents. *Sov. Phys. Usp.* **14** 163–179 (1971)
- Block, L.P., Fälthammar, C.-G.: Field-aligned currents and auroral precipitation. In: McCormac, B.M. (ed.) *Atmospheric Emissions*, p. 285. Van Nostrand Reinhold, New York (1969)
- Bostick, W.H.: Experimental study of ionized matter projected across a magnetic field. *Phys. Rev.* **104**, 292 (1956)
- Bostick, W.H.: Simulation of astrophysical processes in the laboratory. *Nature* **179**, 214 (1957)
- Bostick, W.H., Prior, W., Grunberger, L., Emmert, G.: *Phys. Fluids* **9**, 2078 (1966)
- Buneman, O.: A toroidal magnetron. *Proc. Phys. Soc. Lond.* **1363**, 278 (1949)
- Buneman, O.: Ribbon beams. *J. Electron. Control* **3**, 507 (1957)
- Buneman, O., Levy, R.H., Linson, L.M.: Stability of crossed-field electron beams. *J. Appl. Phys.* **37**, 3203 (1966)
- Carlqvist, P.: Cosmic electric currents and the generalized Bennett relation. *Astro-phys. Space Sci.* **144**, 73 (1988)
- Carmel, Y., Nation, J.A.: Instability of an unneutralized relativistic electron beam. *Phys. Rev. Lett.* **31**, 286 (1973)
- Cutler, C.C.: Instability in hollow and strip electron beams. *J. Appl. Phys.* **27**, 1028 (1956)
- Cummings, W., Dessler, A.J.: Field-aligned currents in the magnetosphere. *J. Geophys. Res.* **72**, 1007 (1967)
- Davis, T.N., Hallinan, T.J.: Aurora spirals 1. Observations. *J. Geophys. Res.* **81**, 3953 (1976)
- Dessler, A.: Evolution of arguments regarding existence of field aligned currents. In: Potemra, T.A. (ed.) *Magnetospheric Currents*. Geophysical Monograph, vol. 28. American Geophysical Union, Washington, DC (1984)
- Egeland, A., Holtet, J.: *The Birkeland Symposium on Aurora and Magnetic Storms*, Sandefjord. Centre National de la Recherche Scientifique, Paris (1968)

- Ekdahl, C.A., Freeman, J.R., Leifste, G.T., Miller, R.B., Stygar, W.A., Godfrey, B.B.: Axisymmetric hollowing instability of an intense relativistic electron beam propagating in air. *Phys. Rev. Lett.* **55**, 935 (1985)
- Fälthammar, C.-G.: Magnetosphere-ionosphere interactions: near-earth manifestations of the plasma universe. *IEEE Trans. Plasma Sci.* **14**, 616 (1986)
- Friedman, M., Hammar, D.A.: Catastrophic disruption of the flow of a magnetically confined intense relativistic electron beam. *Appl. Phys. Lett.* **21**, 174 (1972)
- Hallinan, T.J.: Small scale arc distortions. *Planet. Space Sci.* **18**, 1735 (1970)
- Hallinan, T.J.: Aurora spirals 1. Theory. *J. Geophys. Res.* **81**, 3959 (1976)
- Hammer, D.A., Rostocker, N.: *Phys. Fluids* **13**, 1831 (1970)
- Hill, T.W.: Rotationally-induced Birkeland current systems. In: Potemra, T.A. (ed.) *Magnetospheric Currents. Geophysical Monograph*, vol. 28, p. 340. American Geophysical Union, Washington, DC (1984)
- Iijima, T., Potemra, T.A.: Field-aligned currents in the dayside cusp observed by Triad. *J. Geophys. Res.* **81**, 5971 (1976)
- Ivanov, V.S., Kremontsov, S.I., Raizer, M.D., Rukhadze, A.A., Fedotov, A.V.: *Sov. J. Plasma Phys.* **7** 430 (1981)
- Jones, M.E., Mostrom, M.A.: The diocotron instability in annular relativistic electron beams. *J. Appl. Phys.* **52**, 3794 (1981)
- Kapetanacos, C.A.: Filamentation of intense electron beams propagating in dense plasmas. *Appl. Phys. Lett.* **25**, 484 (1974)
- Kapetanacos, C.A., Hammer, D.A., Striffler, C.D., Davidson, R.C.: Destructive instabilities in hollow intense relativistic electron beams. *Phys. Rev. Lett.* **30**, 1303 (1973)
- Keinigs, R., Jones, M.E.: Two-dimensional dynamics of the plasma wakefield accelerator. *Phys. Fluids.* **30** 252–263 (1987)
- Kim, K.-T., Kronberg, P.P., Giovannini, G., Venturi, T.: Discovery of intergalactic radio emission in the Coma-A1367 supercluster. *Nature* **341**, 720 (1989)
- Knauer, W.: Diocotron instability in plasmas and gas discharges. *J. Appl. Phys.* **37**, 602 (1966)
- Knauer, W., Poeschel, J.L.: The diocotron effect in plasmas and gas discharges, in Phenomena. In: Perovic, B., Tosic, D. (eds.) *Ionized Gases*, p. 719. Gradeviska Knjiga Publication, Beograd (1966)
- Krall, N.A., Trivelpiece, A.W.: *Principles of Plasma Physics*, pp. 678. McGraw-Hill, New York (1973)
- Küppers, G., Salat, A., Wimmel, H.K.: Macroscopic equilibria of relativistic electron beams in plasmas. *Plasma Phys.* **15**, 44 (1973)
- Kyhl, R.L., Webster, H.F.: Breakup of hollow cylindrical electron beams. *IRE Trans. Prof. Group Electron Devices* **ED-3**, 183 (1956)
- Lehnert, B.: Experiments on non-laminar flow of mercury in presence of a magnetic field. *Tellus* **4**, 63 (1952)
- Lehnert, B.: An instability of laminar flow of mercury caused by an external magnetic field. *Proc. R. Soc. Lond. Ser. A* **233**, 299 (1955)
- Lerner, E.J.: Magnetic vortex filaments, universal scale invariants, and the fundamental constants. *IEEE Trans. Plasma Sci.* **14**, 690 (1986)

- Levy, R.H.: Diocotron instability in a cylindrical geometry. *Phys. Fluids* **8**, 1288 (1965)
- Levy, R.H., Hockney, M.A.: Computer experiments on low-density crossed-field electron beams. *Phys. Fluids* **11**, 766 (1968)
- Meierovich, B.E.: Electromagnetic collapse, problems of stability, emission of radiation and evolution of a dense pinch. *Phys. Rep.* **104**, 259 (1984)
- Mostrom, M.A., Jones, M.E.: Shear-driven instabilities of annular relativistic electron beams in vacuum. *Phys. Fluids* **26**, 1649 (1983)
- Murty, G.S.: Instability of a conducting cylinder in the presence of an axial current, a longitudinal magnetic field and a coaxial conducting cylinder. *Ark. fr Fys.* **19**, 483 (1961)
- Nardi, V., Bostick, W.H., Feugeas, J., Prior, W.: Internal structure of electron-beam filaments. *Phys. Rev. A* **22**, 2211 (1980)
- Nielsen, D., Green, J., Buneman, O.: Dynamic evolution of a z-pinch. *Phys. Rev. Lett.* **42**, 1274 (1979)
- Peratt, A.L.: A high-power reflex triode microwave source. *IEEE Trans. Plasma Sci.* **13**, 498 (1985)
- Peratt, A.L.: Evolution of the plasma universe 1. Double radio galaxies, quasars, and extragalactic jets. *IEEE Trans. Plasma Sci.* **14**, 639 (1986)
- Peratt, A.L., Green, J.C.: On the evolution of interacting magnetized galactic plasmas. *Astrophys. Space Sci.* **91**, 19 (1983)
- Peratt, A.L., Snell, C.M.: Microwave generation from filamentation and vortex formation within magnetically confined electron beams. *Phys. Rev. Lett.* **54**, 1167 (1985)
- Peratt, A.L., Green, J., Nielsen, D.: Evolution of colliding plasmas. *Phys. Rev. Lett.* **44**, 1767 (1980)
- Pereira, N.R., Davis, J., Rostocker, N. (eds.): *Dense Z-Pinches*. American Institute of Physics, New York (1989)
- Pierce, J.R.: Instability of hollow beams. *IRE Trans. Electron Devices* **ED3**, 183 (1956)
- Potemra, T.A.: *Magnetospheric Currents*. Geophysical Monograph, vol. 28. American Geophysical Union, Washington, DC (1984)
- Rose, D.J., Clark, M.: *Plasmas and Controlled Fusion*. MIT, Cambridge (1961)
- Schönherr, O.: Über die Fabrikation des Luftsalpeters nach dem Verfahren der Badischen Anilin- und Sodafabrik. *Elektro-techn. Z.* **30**, 365 (1909)
- Salingaros, N.: An amended magnetohydrodynamics equation which predicts field-aligned current sheets. *Astrophys. Space Sci.* **137**, 385 (1988)
- Shrafranov, V.D.: On the stability of a cylindrical gaseous conductor in a magnetic field. *J. Nucl. Energy* **5**, 86 (1957)
- Wagner, J.S., Sydora, R.D., Tajima, T., Hallinan, T., Lee, L.C., Akasofu, S.-I.: *J. Geophys. Res.* **88**, 8013 (1983)
- Webster, H.F.: Breakup of hollow beams. *J. Appl. Phys.* **26**, 1386 (1955)
- Webster, H.F.: Structure in magnetically confined electron beams. *J. Appl. Phys.* **28**, 1388 (1957)

- Webster, H.F., Hallinan, T.J.: Instabilities in charge sheets and current sheets and their possible occurrence in the aurora. *Radio Sci.* **8**, 475 (1973)
- Witalis, E.: *Phys. Rev. A* **24**, 2758 (1981)
- Witalis, E.: Hall magnetohydrodynamics and its applications to laboratory and cosmic plasma. *IEEE Trans. Plasma Sci.* **14**, 842 (1986)
- Yonas, G.: Sandia National Laboratory Report, SAND-74-5367 Albuquerque, New Mexico (1974)
- Yu, S.P., Kooyers, G.P., Buneman, O.: Time-dependent computer analysis of electron wave interaction in crossed fields. *J. Appl. Phys.* **36**, 2550 (1965)
- Zmuda, A.J., Martin, J.H., Huerling, F.T.: Transverse magnetic disturbances at 1100 km in the auroral region. *J. Geophys. Res.* **71**, 5033 (1966)
- Zmuda, A.J., Huerling, F.T., Martin, J.H.: Dayside magnetic disturbances at 1100 km in the auroral oval. *J. Geophys. Res.* **72**, 1115 (1967)

## Chapter 3

# Biot-Savart Law in Cosmic Plasma

### 3.1 History of Magnetism

Our knowledge of magnetism and magnetic phenomena is as old as science itself.<sup>1</sup> According to the writings of the Greek philosopher Aristotle (384–322 B.C.), the attractive power of magnets was known by Thales of Miletus, whose life spanned the period 620–546 B.C. It was not until the sixteenth century, however, that any significant experimental work on magnets was performed. During this century the English physician Gilbert (1544–1603) studied the properties of magnets, realized that a magnetic field existed around the earth, and even magnetized an iron sphere and showed that the magnetic field around was similar to that around the earth. Several other workers also contributed to the knowledge of magnetism during this same period.

The eighteenth century was a period of considerable growth for the theory and understanding of electrostatics. It is therefore not surprising to find that in the eighteenth century the theory of magnetism developed along lines parallel to that of electrostatics. The basic law that evolved was the inverse-square law of attraction and repulsion between unlike and like magnetic poles. Indeed, it would have been difficult for the theory to develop along any other path since batteries for producing a steady current were nonexistent. With the development of the voltaic cell by Volta (1745–1827), it was not long before the magnetic effects of currents were discovered by Oersted in 1820. This was followed by the formulation by Biot (1774–1862) and Savart (1791–1841), of the law for the magnetic field from a long straight current-carrying wire. Further studies by Ampère (1775–1836) led to the law of force between conductors carrying currents. In addition, Ampère's studies on the magnetic field from current-carrying loops led him to postulate that magnetism itself was due to circulating currents on an atomic scale. Thus the gap

---

<sup>1</sup> There are many indications that magnetism played a role at far earlier times. For example, small magnetized metal foils 'fishes' floating in a bowl of oil may have been used as compasses by Asian and Pacific sailors.

between the magnetic fields produced by currents and those produced by magnets was effectively closed.

Today it is expedient to base our entire theory of magnetism and static magnetic fields on the work of Biot, Savart, and Ampère. A formulation in terms of fields produced by currents or charges in motion can account for all known static magnetic effects. The magnetic effects of material bodies is accounted for by equivalent volume and surface currents. The main effort of the following sections will be devoted to the magnetic effects of currents, since this provides us with a general foundation for the understanding of all static magnetic phenomena. Ampère's law of force between two closed current-carrying conducting loops will be elevated to the position of the fundamental law or postulate from which we shall proceed (Elliot 1966; Fujimoto 1987; Krause et al. 1989a,b; Panofsky and Phillips 1962; Plonsey and Collin 1961; Smythe 1950; Stratton 1941; Acuña and Ness 1975; Thompson and Luessen 1986; Voigt 1988 and Woltjer 1958).

### 3.2 The Magnetic Interaction of Steady Line Currents

The magnetic interaction of currents is best described in terms of an experimentally established interaction in vacuum that is analogous to the electrostatic Coulomb's law. The mathematical generalization of the results of Ampère's experiments, which gave the force between two current-carrying elements, as shown in Fig. 3.1, is

$$F_{21} = \frac{\mu_0}{4\pi} \oint_{c1,c2} \frac{I_2 dl_2 \times (I_1 dl_1 \times \hat{r})}{R^2} \quad (3.1)$$

The vector force  $F_{21}$  (newtons) is the force exerted on the conducting loop  $C_2$  by  $C_1$ , as caused by the mutual interaction of the currents  $I_1$  and  $I_2$ . The vector distance from  $dl_1$  to  $dl_2$  is  $r_2 - r_1 = R\hat{r}$ , where  $\hat{r}$  is a unit vector directed from  $x_1, y_1, z_1$  to  $x_2, y_2, z_2$  and

$$R = [(x_2 - x_1)^2 + (y_2 - y_1)^2 + (z_2 - z_1)^2]^{1/2}.$$

Equation (3.1) reveals the inverse-square-law relationship. The differential element of force  $dF_{21}$  between  $I_1 dl_1$  and  $I_2 dl_2$  may be regarded as given by the integrand in Eq. (3.1) and is

$$dF_{21} = \frac{\mu_0 I_1 I_2}{4\pi R^2} dl_2 \times (dl_1 \times \hat{r}) \quad (3.2)$$

The triple-vector product may be expanded to give

$$dF_{21} = \frac{\mu_0 I_1 I_2}{4\pi R^2} [(dl_2 \cdot \hat{r}) dl_1 - (dl_2 \cdot dl_1) \hat{r}] \quad (3.3)$$

One should note that Eqs. (3.2) or (3.3) do not correspond to a physically realizable condition since a steady-current element cannot be isolated. All steady currents must flow around continuous loops or paths since they have a zero divergence.

A further difficulty with relation (3.2) or (3.3) is that it is not symmetrical in  $I_1 dl_1$  and  $I_2 dl_2$ . This superficially appears to contradict Newton's third law, which states that every action must have an equal and opposite reaction (i.e., the force exerted on  $I_2 dl_2$  by  $I_1 dl_1$  is not necessarily equal and opposite to the force exerted on  $I_1 dl_1$

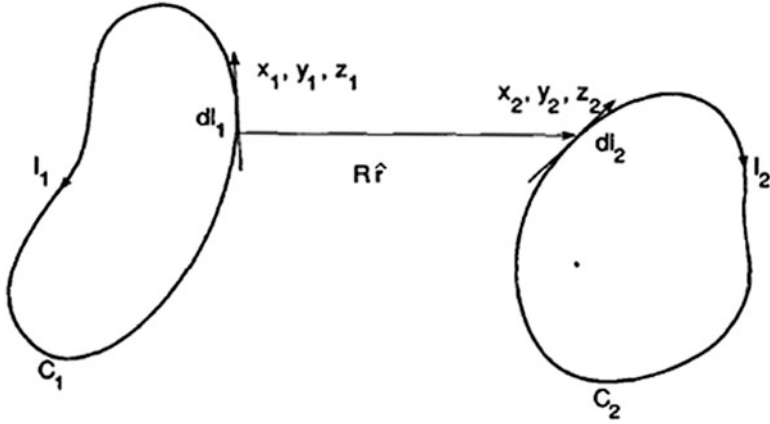


Fig. 3.1 Illustration of Ampère's law of force

by  $I_2 dl_2$ ). However, if the entire closed conductor, such as  $C_1$  and  $C_2$ , is considered, no such difficulty arises and Newton's law is satisfied.

### 3.3 The Magnetic Induction Field

Equation (3.1) can be separated into a field force and a field,

$$F_{21} = \oint_{C_2} I_2 dl_2 \times B_{21} \quad (3.4)$$

$$B_{21} = \frac{\mu_0}{4\pi} \oint_{C_1} \frac{I_1 dl_1 \times \hat{r}}{R^2} \quad (3.5)$$

Equation (3.1) may be thought of as evaluating the force between current-carrying conductors through an action-at-a-distance formulation. In contrast, Eq. (3.4) evaluates the force on a current loop in terms of the interaction of this current with the magnetic field  $B$ , which in turn is set up by the remaining current in the system. The current-field interaction that produces  $F_{21}$  in Eq. (3.4) takes place over the extent of the current loop  $C_2$ , while the magnetic field  $B_{21}$  depends only on the current and geometry of  $C_1$  which sets up the field.

One of the advantages of the field formulation of Eq. (3.5) is that when  $B$  is known, this relation permits one to evaluate the force exerted on a current-carrying conductor placed in the field  $B$  without consideration of the system of currents which give rise to  $B$ . Equation (3.5) is the law based on the experimental and theoretical work of Biot and Savart and is therefore usually called the Biot-Savart law. Since this law may also be extracted from Ampère's law of force, it is sometimes referred to as Ampère's law as well.

A charge  $q$  moving with a velocity  $v$  is equivalent to an element of current  $Idl = qv$  and hence in the presence of a magnetic field experiences a force  $F$  given by

$$F = qv \times B \quad (3.6)$$

This force is called the Lorentz force, and Eq. (3.6) is often taken as the defining equation for  $B$ .

In practice, one does not always deal with currents flowing in thin conductors, and hence it is necessary to generalize the defining equation (3.5) for  $B$  so that it will apply for any arbitrary volume distribution of current. The steady-current flow field does not diverge, and all flow lines form closed loops. If the direction is associated with a current density  $j$ , rather than a short length  $dl$ , then the total current is  $j dS$ , where  $dS$  is the differential cross-sectional area through which the current flows. The total current contained in a volume  $V$  will therefore produce a field  $B$  given by

$$B = \frac{\mu_0}{4\pi} \int_V \frac{j \times \hat{r}}{R^2} dV \quad (3.7)$$

where the integration is over all source coordinates  $x, y$ , and  $z$  and  $dV$  is an element of volume  $dSdl$ . For a surface current  $jS$  amperes per meter flowing on a surface  $S$ , a similar derivation shows that the field produced is given by

$$B = \frac{\mu_0}{4\pi} \int_S \frac{j_S \times \hat{r}}{R^2} dS \quad (3.8)$$

The use of Eqs. (3.4), (3.5), (3.7), or (3.8) is mathematically cumbersome for all but the simplest geometries. For this reason, three-dimensional computer codes utilizing Eqs. (3.4) and (3.5) are generally called upon to determine the forces and magnetic fields associated with complex conductor geometries. A particularly useful technique for solving magnetostatic problems having cylindrical geometry makes use of Ampère's circuital law,

$$\int_S \nabla \times B \cdot dS = \int_S \mu_0 j \cdot dS = \oint_C B \cdot dl \quad (3.9)$$

This equation states that the line integral of  $B \cdot dl$  around any closed contour  $C$  is equal to  $\mu_0$  times the total net current passing through the contour  $C$ .



### 3.3.1 Field from an Infinite Conductor of Finite Radius

Consider an infinite conductor of radius  $a$  with total current  $I$  (Fig. 3.2). The current density  $j$  is equal to  $I/\pi a^2$  and is uniform over the cross section of the conductor. From symmetry considerations the field  $B$  only has a component  $B_\phi$ , which is a function of  $r$  only. Using Ampère's circuital law equation (3.9) and integrating around a circular contour of radius  $r$  gives

$$\oint_C B_\phi dl = \int_0^{2\pi} B_\phi r d\phi = \mu_0 \int_0^r \cdot \int_0^{2\pi} j r d\phi dr = \frac{\mu_0 I}{\pi a^2} \int_0^r \cdot \int_0^{2\pi} r d\phi dr, \quad r \leq a$$

or

$$B_\phi = \frac{\mu_0 I r}{2\pi a^2}, \quad r \leq a \quad (3.10)$$

For  $r \leq a$ , the total current enclosed is  $I$ , so

$$\int_0^{2\pi} B_\phi r d\phi = \mu_0 I$$

or

$$B_\phi = \frac{\mu_0 I}{2\pi r}, \quad r \geq a \quad (3.11)$$

A plot of the intensity of  $B_\phi$  as a function of  $r$  is given in Fig. 3.3.

### 3.3.2 Force Between Two Infinite Conductors

Consider two thin infinite conductors which are parallel and spaced at a distance  $d$ . The currents flowing in the conductors are  $I_1$  and  $I_2$  as in Fig. 3.4. From Eq. (3.11) the magnetic field at  $C_2$  due to  $C_1$  has a  $\phi$  component only and is given by

$$B_\phi = \frac{\mu_0 I_1}{2\pi d} \quad (3.12)$$

The force exerted on  $C_2$  per unit length is given by Eq. (3.4) and is

$$F_{21} = I_2 \hat{z} \times B_\phi \hat{\phi} = \frac{-\mu_0 I_1 I_2}{2\pi d} \hat{r} \quad (3.13)$$

When  $I_1$  and  $I_2$  are in the same direction, the two conductors experience an attractive force. When  $I_1$  and  $I_2$  are oppositely directed, the conductors repel each other.

The fact that two straight parallel conductors exert forces of attraction or repulsion on one another is made the basis of the definition of the ampere in the mks system. The ampere is defined as follows:

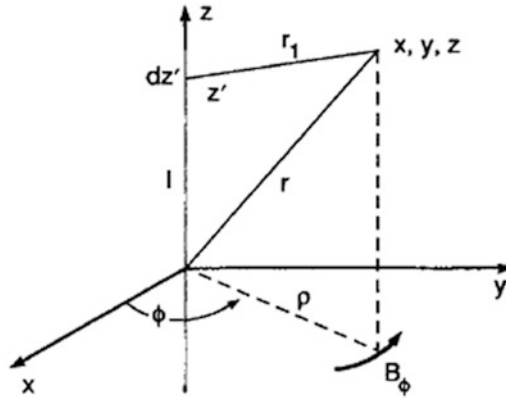


**Fig. 3.2** An infinitely long wire with a current  $I$  and self-consistent field  $B_\phi$

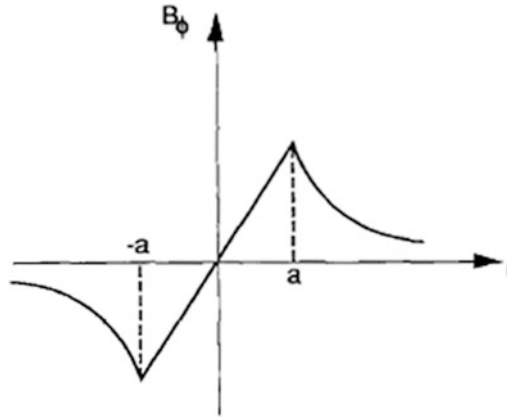


**Fig. 3.3** Magnetic field variation across a plasma filament of radius  $2a$

One ampere is that unvarying current which, if present in each of two parallel conductors of infinite length and one meter apart in empty space, causes each conductor to experience a force of exactly  $2 \times 10^{-7}$  newtons per meter of length.

It follows from this definition that the numerical value of  $\mu_0$  in the rationalized mks system, is exactly  $4\pi \times 10^{-7}$  or, to four significant figures,  $\mu_0 = 12.57 \times 10^{-7}$  webers/amp-m.

### 3.4 The Vector Potential

If, in Eq. (3.7), we replace  $\hat{r}/R^2$  by  $-\nabla(1/R)$ , the integrand becomes  $-j \times \nabla(1/R)$ . The vector differential operator  $\nabla$  affects only the variables  $x, y$ , and  $z$ , and since  $j$  is a function of the source coordinate  $x', y', z'$  only, this latter relation may also be

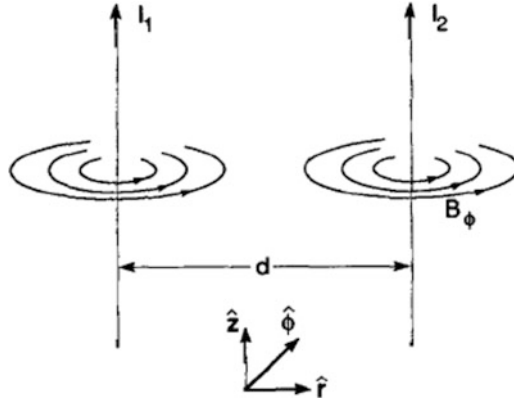


**Fig. 3.4** Two parallel current-carrying filaments

written as follows:  $-j \times \nabla (1/R) = \nabla \times (j/R)$  [and  $\nabla \times (j/R) = (1/R) \nabla \times j - j \times \nabla (1/R) = -j \times \nabla (1/R)$ ] since  $\nabla \times j = 0$ . Thus, in place of Eq. (3.7) we may write

$$B(x, y, z) = \nabla \times \frac{\mu_0}{4\pi} \int_V \frac{j(x', y', z')}{R} dV \quad (3.14)$$

Equation (3.14) expresses the field  $B$  at the point  $(x, y, z)$  as the curl of a vector potential function given by the integral. From Eq. (3.14), the definition of the vector potential function, denoted by  $A$ , is

$$A(x, y, z) = \frac{\mu_0}{4\pi} \int_V \frac{j(x', y', z')}{R} dV \quad (3.15)$$

The integral for  $A$  is a vector integral and must be evaluated by decomposing the integrand into components along the coordinate axis. Having computed  $A$ , the field  $B$  is obtained by taking the curl of  $A$ :

$$B = \nabla \times A \quad (3.16)$$

The integral for  $A$  is easier to evaluate than the original expression equation (3.7) for  $B$ , and since the curl operation is readily performed, the use of Eq. (3.15) as an intermediate step provides us with a simpler procedure for finding  $B$ .

### 3.4.1 Field from a Circular Loop and Force Between Two Circular Loops

Consider a circular conducting loop carrying a current  $I$ . The radius of the loop is  $a$  and it is located in the  $xy$  plane at the origin, as in Fig. 3.5. Of course a seat of electromotive force (emf) is necessary to maintain the current, and one may either

imagine the turn cut and a small seat of emf inserted, or consider that current is led into and out of the turn through two wires side by side. Using Eq. (3.15), we must evaluate the following integral:

$$A = \frac{\mu_0 I}{4\pi} \oint_C \frac{dl'}{r_1} \quad (3.17)$$

where in this case

$$dl' = \hat{\phi} a d\phi' = (-\hat{x} \sin \phi' + \hat{y} \cos \phi') a d\phi' \quad (3.18)$$

$$r_1 = \hat{x}(x - a \cos \phi') + \hat{y}(y - a \sin \phi') + \hat{z}z \quad (3.19)$$

The expression for  $r_1$  is

$$\begin{aligned} r_1 &= [(x - a \cos \phi')^2 + (y - a \sin \phi')^2 + z^2]^{1/2} \\ &= (x^2 + y^2 + z^2 + a^2 - 2ax \cos \phi' - 2ay \sin \phi')^{1/2} \\ &\cong r \left( 1 - \frac{2ax}{r^2} \cos \phi' - \frac{2ay}{r^2} \sin \phi' \right)^{1/2} \end{aligned} \quad (3.20)$$

since  $r^2 \gg a^2$ . For  $r_1^{-1}$  we have approximately

$$r_1^{-1} = r^{-1} \left( 1 + \frac{ax}{r^2} \cos \phi' + \frac{ay}{r^2} \sin \phi' \right) \quad (3.21)$$

by using the binomial expansion and retaining only the leading terms. The integral for  $A$  becomes

$$A = \frac{\mu_0 I \pi a}{4\pi r} \int_0^{2\pi} (-\hat{x} \sin \phi' + \hat{y} \cos \phi') \left( 1 + \frac{ax}{r^2} \cos \phi' + \frac{ay}{r^2} \sin \phi' \right) d\phi' \quad (3.22)$$

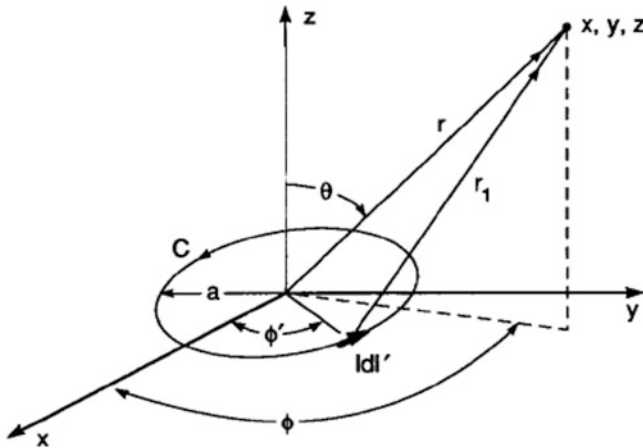


**Fig. 3.5** A circular current loop

and integrates to give

$$A = \frac{\mu_0 I (\pi a^2)}{4\pi r^3} (-\hat{x}y + \hat{y}x) \quad (3.23)$$

Referred to a spherical coordinate system,  $A$  is given by

$$A = (A \cdot \hat{r}) \hat{r} + (A \cdot \hat{\phi}) \hat{\phi} + (A \cdot \hat{\theta}) \hat{\theta} = \frac{\mu_0 I (\pi a^2)}{4\pi r^2} \sin \theta \hat{\phi} = A_\phi \hat{\phi} \quad (3.24)$$

so that, from Eq. (3.16)

$$B = \frac{\mu_0 I (\pi a^2)}{4\pi r^3} (\hat{r} 2 \cos \theta + \hat{\theta} \sin \theta) \quad (3.25)$$

### 3.4.2 Force Between Two Circular Loops Lying in a Plane

In the plane of the loops,  $\theta = \pi/2$ , so that  $B_{21} = \hat{\theta} \mu_0 I a^2 / 4r^3$ , and Ampère's law of force gives

$$F_{21} = I_2 \times B_{21} = \hat{\phi} I_2 \times \left( -\hat{\theta} \frac{\mu_0 I_1 a^2}{4r^3} \right) = \hat{r} \frac{\mu_0 I_1 I_2 a^2}{4r^3} \quad (3.26)$$

## 3.5 Quasi-stationary Magnetic Fields

To complete a discussion of magnetostatics, it is necessary to derive an expression for the stored magnetic energy in a cosmic network. This will then make a full discussion of inductance and also a more powerful technique for determining forces between current-carrying circuits, possible. In order to determine an expression for stored magnetic energy due to time-stationary currents, it is necessary to know something about time-varying currents and time-varying magnetic fields. Consequently, this section starts with a statement about Faraday's law of induction.

### 3.5.1 Faraday's Law

If we consider any closed stationary path in space which is linked by a changing magnetic field, it is found that the induced voltage around this path  $s$  is equal to the negative time rate of change of the total magnetic flux through the closed path. Let  $C$  denote a closed path as in Fig. 3.6. The induced voltage around this path is given by the line integral of the induced electric field around  $C$  and is

$$\varphi = \oint_C \mathbf{E} \cdot d\mathbf{l} \quad (3.27)$$

The magnetic flux through  $C$  is given by

$$\psi = \oint_S \mathbf{B} \cdot d\mathbf{S} \quad (3.28)$$

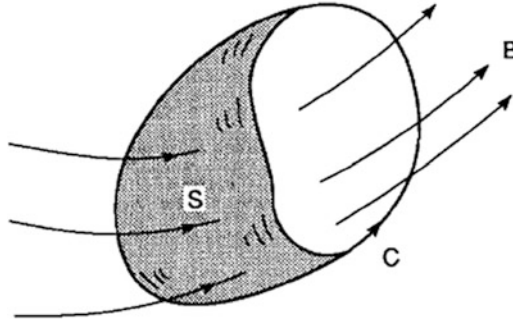


**Fig. 3.6** Illustration of Faraday's law

where  $S$  is any surface with  $C$  as its boundary. Thus the mathematical statement of Faraday's law is

$$\oint_C \mathbf{E} \cdot d\mathbf{l} = -\frac{\partial}{\partial t} \oint_S \mathbf{B} \cdot d\mathbf{S} \quad (3.29)$$

Basically, the law states that a changing magnetic field will induce an electric field. The induced electric field exists in space regardless of whether a conductor exists or not. When a conducting path is present, a current will flow, and we refer to this current as an induced current. Faraday's law is the principle on which most electric generators operate. Note that the electric field set up by a changing magnetic field is nonconservative, as Eq. (3.29) clearly indicates. The changing magnetic field becomes a source for an electric field.

### 3.5.2 Motion Induced Electric Fields

Whenever a conductor moves through a static magnetic field, a voltage is induced across the conductor. This voltage is in addition to that calculated by Eq. (3.29). The magnitude of this voltage may be found from the Lorentz force equation (3.6). The force is seen to act in a direction perpendicular to both  $\mathbf{v}$  and  $\mathbf{B}$ . The interpretation of the Lorentz force gives rise to the concept that an observer moving through

a static magnetic field also sees, in addition to the magnetic field, an electric field. A unit of charge moving with the observer appears to be stationary, and any force experienced by that charge is ascribed to the existence of an electrostatic field. But a force is experienced and is given by Eq. (3.6). Consequently, in the moving reference frame, this fact is interpreted as revealing the existence of an electric field  $E$  given by

$$E = \frac{F}{q} = v \times B \quad (3.30)$$

Equation (3.30) gives an alternative and more general method of evaluating the induced voltage in a moving conductor. As an example consider a cylindrical conductor moving with a velocity  $v$  through a uniform field  $B$ , as in Fig. 3.7, where  $B$  is orthogonal to  $v$ . Each electron in the conducting medium experience a force  $F = -evB$  which tends to displace the electrons along the conductor in the direction shown. When an equilibrium state is reached, the process stops, and the conductor is left polarized as shown with an electrostatic force equal and opposite to the Lorentz force. In this case,  $E = -vB$ . The induced voltage between the ends of the conductor is defined by

$$\phi = \int_{P1}^{P2} E \cdot dl \quad (3.31)$$

The induced voltage caused by motion of a conductor through a magnetic field is called motional emf.

### 3.5.3 Faraday Disk Dynamo

The Faraday disk dynamo is illustrated in Fig. 3.8. It consists of a circular conducting disk rotating in a uniform magnetic field  $B$ . Brushes make contact with the disk at the center and along the periphery. The magnitude of the induced voltage is found from the Lorentz force, Eqs. (3.30) and (3.31). An electron at a radial distance  $r$  from the center has a velocity  $\omega r$  and hence experiences a force  $e\omega rB$  directed radially outward. The electric field acting on the electron at equilibrium is also  $\omega rB$  but is directed radially inward. The potential from the center to the outer rim of the disk is thus

$$\phi = \int_0^d E(r) dr = -\omega B \int_0^d r dr = -\frac{\omega B d^2}{2} \quad (3.32)$$

The value computed from Eq. (3.32) is the open-circuit voltage of the Faraday disk dynamo and therefore also represents the emf of the generator.

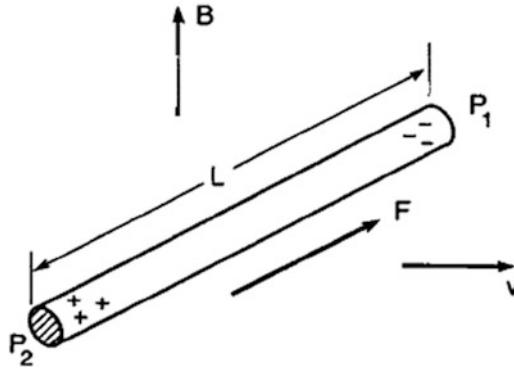


**Fig. 3.7** Induced voltage (potential drop between  $P_2$  and  $P_1$ ) in a conductor moving across a magnetic field

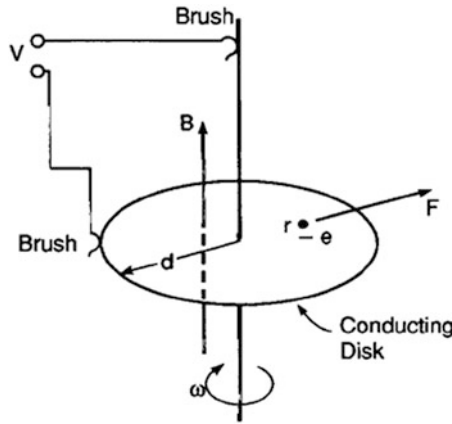


**Fig. 3.8** The Faraday disk dynamo. A potential  $\phi = V$  is produced at the terminals

### 3.6 Inductance

Consider a single current-carrying loop in which a constant current has been established. This current produces a magnetic field. If the current is caused to change, so will the magnetic field. But this means that the total flux linking the loop also changes and, by Faraday's law, a voltage is induced in the loop. The self-induced voltage always has a polarity that tends to oppose the original change in current. For example, if the current begins to decrease, the induced voltage acts in a direction to offset this decrease. This property of a single circuit is known as self-inductance. The similar effect of a changing current in one circuit producing an induced voltage in another circuit is known as mutual inductance. Mathematically, inductance may be defined in terms of flux linkages. If  $\psi_{12}$  is the magnetic flux linking circuit  $C_2$  due to a current  $I_1$  flowing in circuit  $C_1$  (Fig. 3.9), the mutual inductance  $L_{12}$  between circuit  $C_1$  and  $C_2$  is defined by



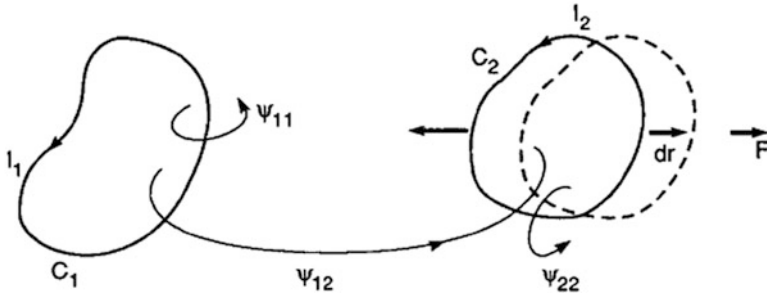


**Fig. 3.9** Illustration of two circuits and their relative displacement ( $L_{12}$  negative)

$$L_{12} = \frac{\text{flux linking } C_2 \text{ due to current in } C_1}{\text{current in } C_1} = \frac{\Psi_{12}}{I_1} \quad (3.33)$$

The self inductance  $L_{11}$  of circuit  $C_1$  is defined in a similar way; that is,

$$L_{11} = \frac{\text{flux linking } C_1 \text{ due to current in } C_1}{\text{current in } C_1} = \frac{\Psi_{11}}{I_1} \quad (3.34)$$

The mutual inductance between  $C_1$  and  $C_2$  may be defined by

$$L_{21} = \frac{\Psi_{21}}{I_2} \quad (3.35)$$

It can be shown that  $L_{12} = L_{21}$  so that Eqs. (3.33) and (3.35) are equivalent. This is a statement of the reciprocity theorem. The above definition of inductance is satisfactory only for quasi-stationary magnetic fields where the current and the magnetic field have the same phase angle over the whole region of the circuit. At high frequencies the magnetic field does not have the same phase angle over the whole region of the circuit because of the finite time required to propagate the effects of a changing current and field through space. A more general definition in terms of the magnetic energy associated with a circuit will be given in the following section.

## 3.7 Storage of Magnetic Energy

### 3.7.1 Energy in a System of Current Loops

The energy  $W_B$  stored in the magnetic field of  $N$  current filaments is given by

$$W_B = \frac{1}{2} \sum_{i=1}^N \sum_{j=1}^N L_{ij} I_i I_j \quad (3.36)$$

or, in terms of the magnetic flux, by

$$W_B = \frac{1}{2} \sum_{i=1}^N \psi_i I_i \quad (3.37)$$

where  $I_i$  is the current flowing in the  $i$ th filament and  $\psi_i$  is the flux linking the  $i$ th filament due to all the other current filaments in the current loop. This in turn is given by

$$\psi = \frac{1}{2} \sum_{\substack{j=1 \\ j \neq i}}^N L_{ij} I_j \quad (3.38)$$

In terms of field energy, the inductance may be defined by the equation

$$W_B = \frac{1}{2} L I^2 \quad (3.39)$$

so that

$$L = \frac{2W_B}{I^2} \quad (3.40)$$

This definition is often easier to apply in practice in order to evaluate  $L$  than the original definition in terms of flux linkages. The quality of a circuit that allows the storage of magnetic energy is called inductance. In terms of the field integral the magnetic energy equation (3.39) is

$$W_B = \frac{1}{2} \int_V B \cdot H dV = \frac{1}{2\mu} \int_V H \cdot H dV \quad (3.41)$$

### 3.7.2 *In Situ Storage in Force Free Magnetic Field Configurations*

The storage of energy in the force-free magnetic field (Sect. 1.7.2) can be thought of as a slow process where the field evolves through a sequence of force-free configurations, each time ending up in a higher energy state (Tandberg-Hanssen and Emslie 1988). An example of this slow process is in the photosphere and lower chromosphere of the Sun, where the energy of the plasma motion dominates the magnetic energy and, therefore, the field is swept passively along with the plasma. This situation is characterized as a high- $\beta$  plasma; i.e., the parameter

$$\beta = \frac{\text{gas pressure}}{\text{magnetic pressure}} = \frac{2\mu_0 n k T}{B^2} \quad (3.42)$$

is large ( $\beta \gg 1$ ). Higher up in the corona where the density is so small that the magnetic pressure dominates, we have a low- $\beta$  plasma, and the magnetic field must take on a force-free character (Gold 1964) as it slowly evolves. This

magnetohydrodynamic (MHD) process is possible since the timescale for the “wind-up” is days or weeks, while the field adjustment at any stage takes place with the Alfvén speed equation (2.19), leading to timescales of the order of seconds. If  $\alpha$  is constant in time and space, we can take the curl of Eq. (1.12) and find

$$\nabla^2 B + \alpha^2 B = 0 \quad (3.43)$$

which is the vector Helmholtz equation. This linear problem then is completely solvable (Chandrasekhar and Kendall 1957; Ferraro and Plumpton 1966; Nakagawa and Raadu 1972). Using Eq. (3.43) and the observed boundary conditions in the form of the value of the longitudinal magnetic field (from magnetograph observations), we can compute the structure of the force-free field and the resulting stored magnetic energy. In these cases,  $\alpha$  is adjusted until reasonable agreement is obtained with observations. With the availability of complete vector magnetic field observations, the field calculations have improved since  $\alpha$  can be determined with higher precision from Eq. (1.12) with the expression

$$\alpha = \frac{(\nabla \times B) \cdot B}{B^2} \quad (3.44)$$

In general, the parameter  $\alpha$  is not constant in space and time, that is

$$\alpha = \alpha(r, t) \quad (3.45)$$

so that Eq. (3.43) is nonlinear, and the problem must be solved by computer simulation.

### 3.8 Forces as Derivatives of Coefficients of Inductance

The force between separate current-carrying loops or circuits may be evaluated by Ampère’s law of force. However, an alternative method that is much easier to apply in many cases may also be used. This alternative method essentially consists of evaluating the derivatives of mutual-inductance coefficients with respect to arbitrary virtual displacements of the circuits with respect to each other (see, e.g., Fig. 3.9). When circuits are displaced relative to each other, the mutual inductance, and hence the energy stored in the magnetic field, changes. The change in the magnetic energy is in turn related to the work done against the forces of the field in displacing the circuits. If we have  $N$  circuits and displace the  $j$ th circuit by an amount  $dr_j$ , the force  $F_j$  exerted on  $C_j$  by all the other circuits is given by

$$F_j = \sum_{\substack{n=1 \\ n \neq j}}^N I_j I_n \frac{dL_{jn}}{dr_j} \quad (3.46)$$

where  $F_j$  is the component of force along  $dr_j$  acting on the  $j$ th circuit.

**Example 3.1. Force on two parallel filaments.** Consider two thin infinitely long conducting filaments as in Fig. 3.4. The filaments are separated by a distance  $D$ . The currents in the two filaments are  $I_1$  and  $I_2$ . The flux linking  $C_2$  due to the current  $I_1$  in  $C_1$  is

$$\psi_{12} = \frac{\mu_0 I_1}{2\pi} \int_D^{\infty} \frac{dx}{x}$$

per unit length.

From Eq. (3.46) the force per unit length exerted on  $C_2$  by  $C_1$  is

$$F = I_1 I_2 \frac{dL_{12}}{dD} \Big|_{I=\text{constant}} = I_2 \frac{d\psi_{12}}{dD} = -\frac{\mu_0 I_1 I_2}{2\pi D}$$

in accord with Eq. (3.13) obtained using Ampère's law.

### 3.9 Measurement of Magnetic Fields in Laboratory Plasmas

**B-Dot Probes.** The simplest way to measure the magnetic field in the vicinity of a point in space is to use a small coil of wire (Fig. 3.10). In a uniform, time-varying magnetic field, the voltage induced in the coil is

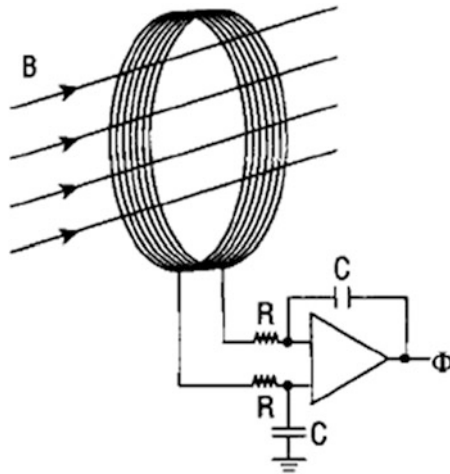


**Fig. 3.10** B-Dot probe and integrating circuit

$$\Phi = NA \frac{dB}{dt} \equiv NAB\dot{B}$$

where  $N$  is the number of turns in the coil of area  $A$  and the dot denotes the time derivative of  $B$ . If  $B$ , rather than  $\dot{B}$ , is the desired quantity, an integrating circuit may be used to obtain a voltage proportional to the field

$$\Phi = \frac{NAB}{RC}$$

where  $RC$  is the time constant of the integrator.

**Rogowski Coil.** Many different variations of the B-dot probe are available. One of the most widespread is the Rogowski coil. This is a solenoidal coil whose ends are brought around together to form a torus as shown in Fig. 3.11a. Consider a coil of uniform cross sectional area  $A$  with a constant number of turns per unit length  $n$ . If the magnetic field varies little over a one-turn spacing, i.e.,  $|\nabla B|/B \ll n$ , the total flux linkage by the coil equation (3.28) can be written as an integral over the individual turns:

$$\psi = n \oint_l \int_A B \cdot d\mathbf{l} dA$$

where  $d\mathbf{l}$  is the line element along the solenoidal axis as depicted in Fig. 3.11b. The purpose of the return wire threading the loops is to exclude the contribution of flux passing through the torus center. Changing the order of integration and using Eq. (3.9) gives

$$\psi = nA\mu_0 I$$

The signal voltage from the Rogowski coil is then

$$\phi = \frac{d\psi}{dt} = nA\mu_0 \dot{I}$$

The Rogowski coil provides a direct measurement of the total current, particle and displacement, flowing through its center. Its signal is independent of the distribution of the current within the loop. The merit of the Rogowski coil is that it need not come into contact with the current whose field it measures. This is an important consideration for intense relativistic electron beams.

**Internal Magnetic Field Probes.** It is often possible to use internal sensing coils in tenuous nonenergetic plasmas. Stenzel and Gekelman (1981) have used such probes with great success to measure the time evolution of magnetic fields in all three dimensions in plasmas contained in large vacuum chambers.

### 3.10 Particle-in-Cell Simulation of Interacting Currents

The basic geometry under study is shown in Fig. 3.12. This figure depicts two current-conducting plasma filaments aligned along a magnetic field  $B_0$  and separated by a distance comparable to the diameters of the filament. The plasma is charge neutral  $n_e = n_i$  and initially thermalized at a temperature  $v_{thx} = v_{thy} = v_{thz}$

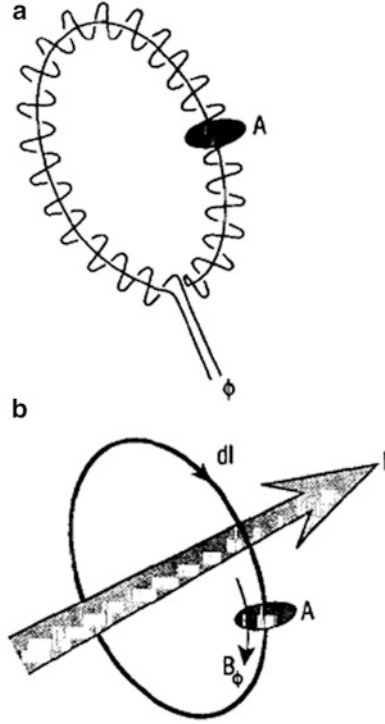


**Fig. 3.11** (a) Rogowski coil. (b) Equivalent geometry for the integral form of flux through a Rogowski coil

for both ions and electrons. The density distribution across a column may either be a flat profile, a Bennett profile, a Gaussian profile, or any arbitrary profile  $n_{e,i}(r)$ . The conduction of current is initiated by placing an electric field  $E = E_0$  along each column. This then produces a current which increases with time. Whether or not a filament pinches, or is simply confined by the self-consistent azimuthal magnetic field  $B_\phi$ , depends on the strength of  $E_0$ . Solution of the relative motion of the two filaments and their reconfiguration by the Biot-Savart forces requires a 3D particle-in-cell treatment. The codes SPLASH and TRISTAN have been applied to this geometry (Chap. 10).

### 3.10.1 Simulation Setup

We choose a temperature typical of cosmic Birkeland filaments, a few kiloelectronvolts, by setting the initial dimensionless simulation parameters (Sect. 10.8) to  $\omega_p dt = 0.25$ ,  $\lambda_D/\Delta = 0.25$ , and  $cdt/\Delta = 1.0$ . A field-aligned Birkeland filament is established by means of the parameter  $\omega_{c0}/\omega_p = 1.5$ . For this choice of parameters,

$\beta_{th} = 0.0625$  (Eq. (10.19)) and, for  $T_e = T_i, \beta_p = 0.0069$  (Eq. (10.20)). Current flow within the filaments is initiated by setting  $E_z/B_z = 0.01c$ , so that  $0 \leq \beta_z \leq 1$  (Eq. (10.18)). For SPLASH, the radius of each filament is  $3\Delta$  and the center-to-center separation is  $11\Delta$ , while for TRISTAN the radius and separation are  $12\Delta$  and  $44\Delta$ , respectively. (Because of the spline interpolation technique, the particle space-time resolution is approximately eight times better than the cell width  $\Delta$ .)

### 3.10.2 Initial Motion of Current Filaments

Initially, the Biot-Savart force between filaments conducting currents can be approximated by Eq. (3.13). However, because of the axial magnetic field  $B_0$ , the particles spiral as they drift or accelerate in the  $z$ -direction, thereby producing a generalized current  $I = \hat{z}I_z + \hat{\phi}I_\phi$ . The force between the  $I_\phi$  currents can be approximated by Eq. (3.26). Figure 3.13 illustrates the total Biot-Savart force as a function of the spacing between helical current filaments. As shown, the electromagnetic forces between filaments are ordered as  $-R_{12}^{-1}$  (long-range attractive) and  $+R_{12}^{-3}$  (short range repulsive). During long-range attraction, the motion of either filament may be approximately described by the equation 111

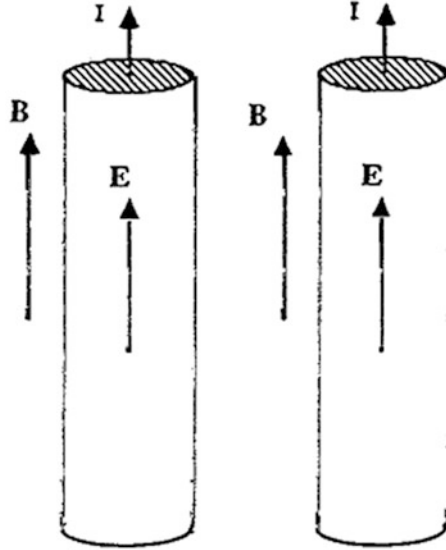


**Fig. 3.12** Basic geometry under analysis: two parallel Birkeland currents formed by the tendency of charged particles to follow magnetic lines of force  $B$  and to pinch due to their own induced magnetic field

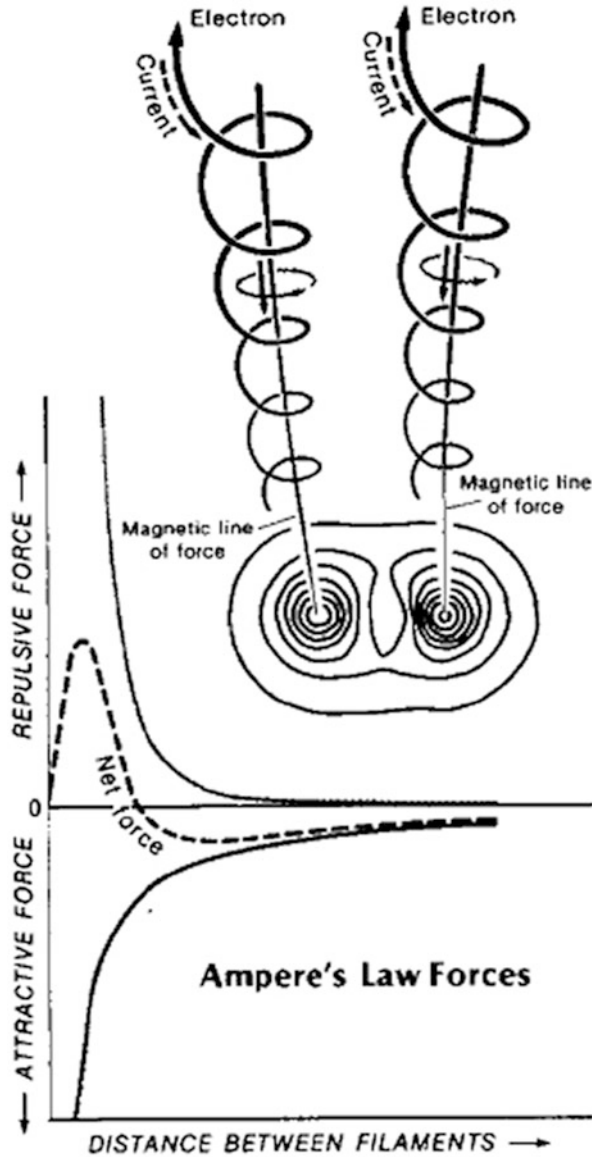


**Fig. 3.13** The forces between two adjacent Birkeland currents. The parallel components of current (*dark gray lines*) are long-range attractive, while the counter-parallel azimuthal currents (*light gray rings*) are short-range repulsive. A third force, long range electrostatic repulsion, is found if the electrons and ions are not present in equal numbers. These forces cause the currents to form sheets, filaments, or “magnetic ropes” and they can be found far from the source region. A projection of the current-induced magnetic fields is shown above the graph



$$F = Ma = M \frac{d^2 r}{dt^2} = \frac{\mu_0 I_z^2 L}{4\pi(a-r)} \quad (3.47)$$

whose velocity solution is

$$v = M \frac{dr}{dt} = I_z \left( \frac{\mu_0 L}{2\pi M} \right)^{1/2} \left[ \ln \left( \frac{a}{a-r} \right) \right]^{1/2} \quad (3.48)$$

where  $L$  is the length of the filament region involved in Biot-Savart attraction,  $M$  is the total mass,  $2a$  is the distance of separation between filaments. If the filaments are sufficiently separated so that the logarithmic correction is of order unity, Eq. (3.48) is approximately given by

$$v \approx I_z \left( \frac{\mu_0 L}{2\pi M} \right)^{1/2}, \quad \left\{ v \approx I_z \left( \frac{2L}{c^2 M} \right)^{1/2} = \frac{B_\phi d}{2} \sqrt{\frac{2L}{M}} \right\}_{cgs} \quad (3.49)$$

In dimensionless gaussian simulation units, Eq. (3.49) is

$$\bar{v} = \frac{\bar{B}_f \bar{d}}{2} \sqrt{\frac{2\bar{L}}{\bar{M}}} \quad (3.50)$$

where  $\bar{M} = N_c (n_e/\Delta^3) (m_i/m_e + 1) \pi \bar{r}_c^2 \bar{L}$  and  $N_c$  are the total simulation mass and number of interacting simulation filaments, respectively. The parameter  $\bar{d} = d/\Delta$  is the distance between filaments and  $\bar{r}_c = r_c/\Delta$  is the radius of a filament, both given in cell widths.

### 3.10.3 Polarization Forces

In the presence of an axial field  $B_0$ , the electrons gyrate in a counter clockwise direction while the ions gyrate in a clockwise direction. The relationship between the ion and electron gyroradii is  $r_{Li} = (m_i/m_e) r_{Le} \gg r_{Le}$ . In addition to the gyration, the charged particles experience a polarizing force caused by the net motion of the plasma filaments across the guide field  $B_0$ . The net motion derives from Eq. (3.49) which causes a  $\mathbf{v} \times \mathbf{B}$  force, primarily in the  $\pm y$ -directions in adjacent filaments as shown in Fig. 3.14a. As a result, the electrons in columns 2 and 1 are accelerated in the  $\pm y$ -directions, respectively. This leaves a net excess of the heavier ions in the original filament positions, and thereby produces, via Eq. (1.3), an electric field which opposes a further diffusion of electrons. The electrons can separate from the ions about a Debye length  $\lambda_D = \sqrt{\epsilon_0 kT/n_e e^2}$  before they are restrained by the ions. The ions then follow the electrons in a process known as ambipolar diffusion (Rose and Clark 1961). It is evident that the dimensions of the plasma be much larger than the Debye length for ambipolar diffusion to take place. Figure 3.14b depicts the displacement of the currents in the filaments (because of excess of axial

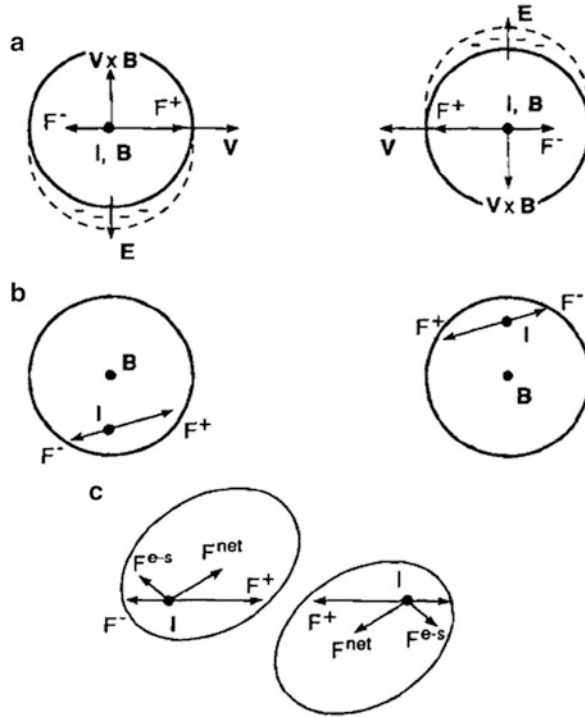


**Fig. 3.14** Net motion between adjacent Birkeland currents. (a) Polarization fields  $E$  due to  $v \times B$  forces. (b) Net forces at early time (c) net forces during filament distortion

current-conducting electrons at the  $\pm y$  surfaces) caused by the inward motion of the filaments across  $B_0$ . The net result of the juxtapositioned currents  $I_z$  is a clockwise torque on the plasma filaments (Fig. 3.14c).

### 3.10.4 Magnetic Energy Distribution and Magnetic Isobars

The two parallel axial currents produce the magnetic energy isobars (through Eq. (1.2)) shown in the time sequence of Fig. 3.15. At  $T = 9$ , the contours of  $B^2$  are very nearly symmetric about each filament. Since the currents increase with time (because of the constant field  $E_z$ ), the  $B^2$  isobars move out from each filament until a linear superposition of isobars produce a magnetic minimum (“sump”) or core between the two filaments (Figs. 3.15 and 3.16). The core has the shape of an ellipse. The effect of the net inward motion is already seen at timestep 16 with the juxtapositioning of the  $B^2$  isobaric peaks associated with the axial currents. In addition to the magnetic peaks and core, two narrow magnetic channels form on either side of the core (Fig. 3.17). At  $T = 255$ , the field strength squared in the vicinity of

the core is  $B^2 = 0.33$ . The field induced pressure is

$$p_B = (2\mu_0)^{-1} B^2 \quad (3.51)$$

At time  $T = 255$ , a channel exists only on the right-hand-side of Fig. 3.17 with length  $9\Delta'$  and width  $0.5\Delta' - 2.0\Delta'$  (The channel alternates from right to left with the passage of time (Peratt 1986a)). The velocity of the isobars toward the core is, approximately, 0.032 cells per timestep, or

$$v_{comp} = 0.032\Delta'/dt' \quad (3.52)$$

Because of the inward traveling isobars, plasma external to the two conducting currents is swept into both the channel and the core. Part of this external plasma derives from unpinched plasma which conducts the current before the Bennett relation equation (1.9) is established.

The phenomena described in the simulation is observed in the laboratory. Figure 3.18 shows laser Schlieren photographs taken at two different times of two interacting Z pinches. The Z pinches were created by stringing two 2 cm long wires between an anode and cathode of a pulsed power generator (Fig. 2.9), which then exploded into plasma pinches with the conduction of 250 kA current. Figure 3.18a ( $t = 40$  ns) shows that the Bennett relation has been established and the conducting paths are confined to circular (but filamentary) cross-sections. At time  $t = 60$  ns, the second frame shows that, in addition to the plasma flowing off the filaments, plasma external to the pinches has been compressed into the central core and also into a channel on the right-hand-side of the core. For the parameters of this experiment, (10 cm/ms). Figure 3.18b shows the time evolution (of wire midsections) as they explode into Z pinched plasmas. Each filament undergoes about a dozen pinch oscillations the first 40 ns (Felber and Peratt 1980), followed by the appearance of inward “jets” of plasma toward the core. The jets of plasma coalesce in the core at about 80 ns. However, with regard to radiation in the axial direction: This continues to come from the intense electron currents in two hot spots at the outer locations. This phase is followed by the rotation of the filaments into a spiral structure. A half-rotation is observed to take about 100 ns, corresponding to a rotation velocity of about 15 km/s.

The radiation burst is an extremely transient phenomena, lasting for only about 5 ns. This appears to be correlated with the constriction of the single Z pinches to very small diameters, but is intense only when two Z pinches are present.

### 3.10.5 Net Motion

The long term motion between the filaments is nonlinear and involves a reconfiguration of their cylindrical cross-sections. This motion is shown in Fig. 3.19 for simulation time up to  $T = 1,700$ . As shown, the initially circular cross-sections are deformed into ovals that then take on a “jelly-bean-like” profile prior to forming

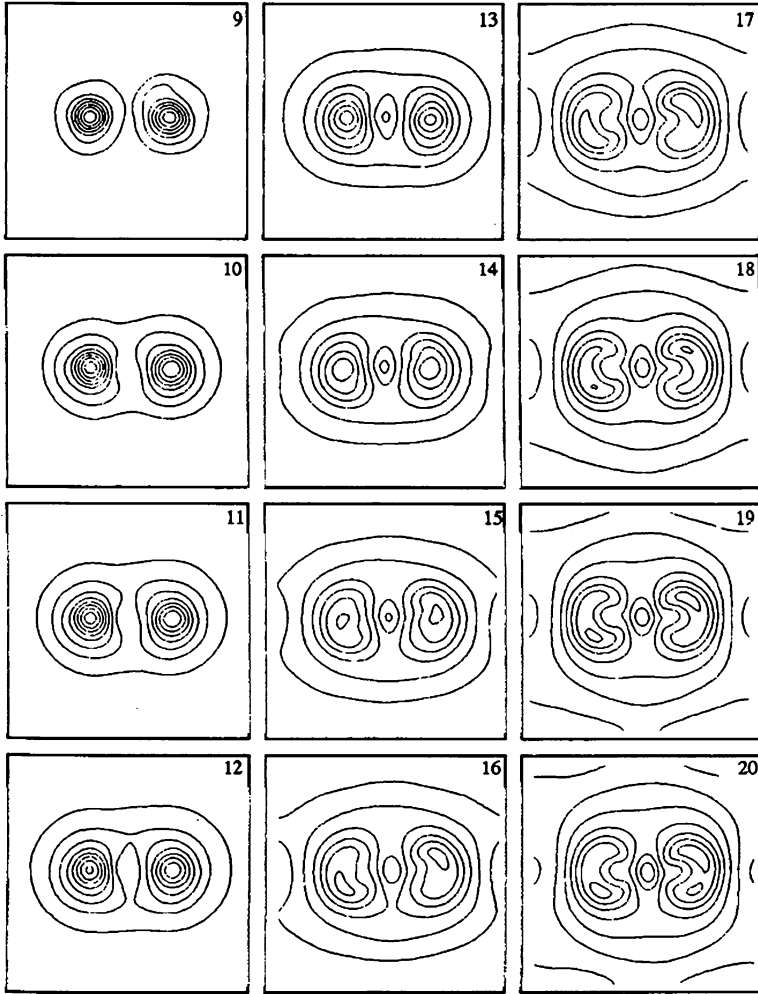


**Fig. 3.15** Contours of magnetic energy  $B^2$  about two adjacent filaments at the simulation cross-section.  $T = 9 - 20$  in  $1 \Delta T$  steps. The contours at the locations of the two filaments correspond to energy maxima while the central ellipse is an energy minimum. “Hot spots” in azimuthal field energy feeding synchrotron radiation are beginning to become noticeable in later time frames

embryonic spiral arms. Once formed, the arms become thin as they trail out behind the rotating center.<sup>2</sup> Not shown in this sequence is plasma confined in the core, onto which the outer plasmas converge, which tends to obscure the nuclear region.

Since  $E \parallel B$  is out of the plane of the page, the column electrons spiral downward in counter-clockwise rotation while the column ions spiral upward in clockwise

<sup>2</sup> Bostick (1957) was the first to observe the formation of spiral structures produced by interacting plasmoids crossing magnetic field lines.

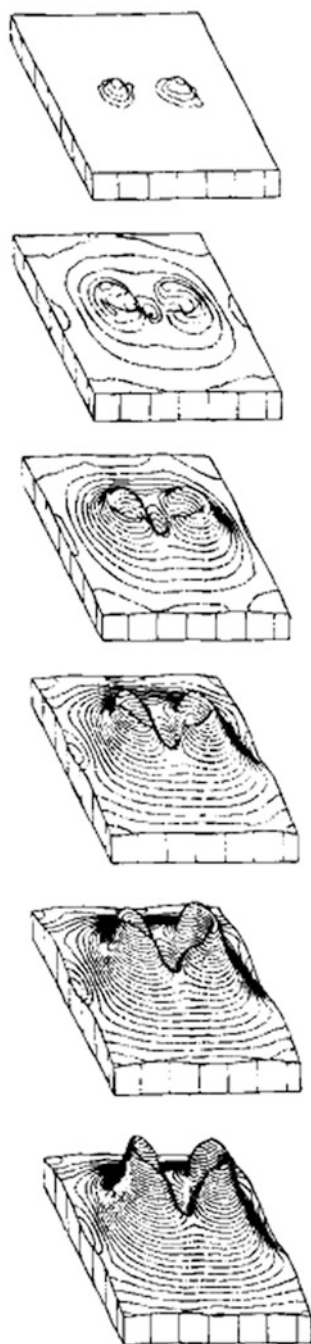


**Fig. 3.16** Isometric view of magnetic energy contours of Fig. 3.15. Time increases from top to bottom

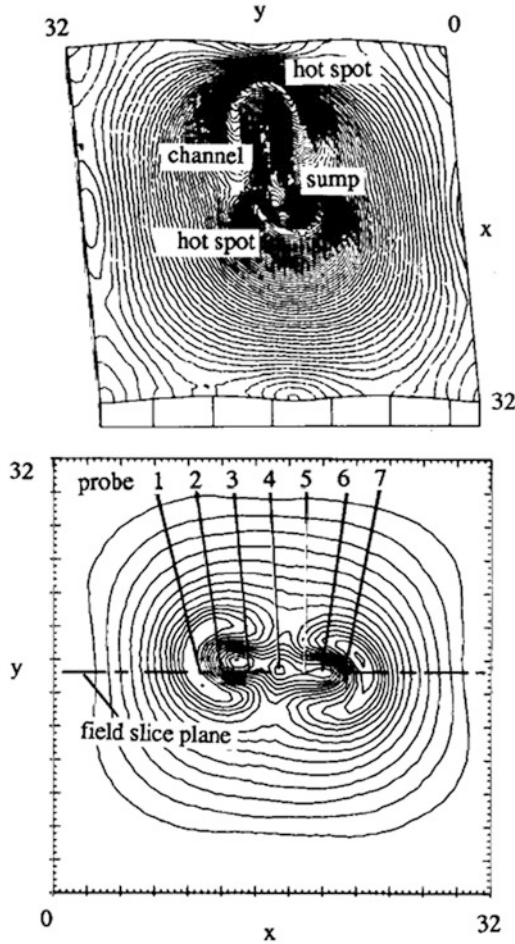


**Fig. 3.17** Isometric and planar views of self-consistent magnetic fields at  $T = 255$  showing elliptical core and one-sided isobaric channel between energy maxima. Peak field squared = 1.5 units, 0.1 units/contour

rotation. The current density is  $j = n_e q_e v_e + n_i q_i v_i$ . A polarization induced charge separation (Sect. 3.10.3) also occurs in each arm, which, as it thins out, produces a radial electric field across the arm. Because of this field, the arm is susceptible to the diocotron instability (Sect. 1.7.3). This instability appears as a wave motion in each arm and is barely discernable in the single frame photographs in Fig. 3.19 at late times. However, the instability is readily apparent in the spiral rotational velocity curve. Figure 3.20 is the rotational velocity curve for the spiral configuration shown in the last frame of Fig. 3.19.

The velocity essentially consists of a linearly increasing component due to a central body undergoing rigid rotation, with two “flat” components on either side of  $r = 0$  due to the trailing arms. The diocotron instability modulates the

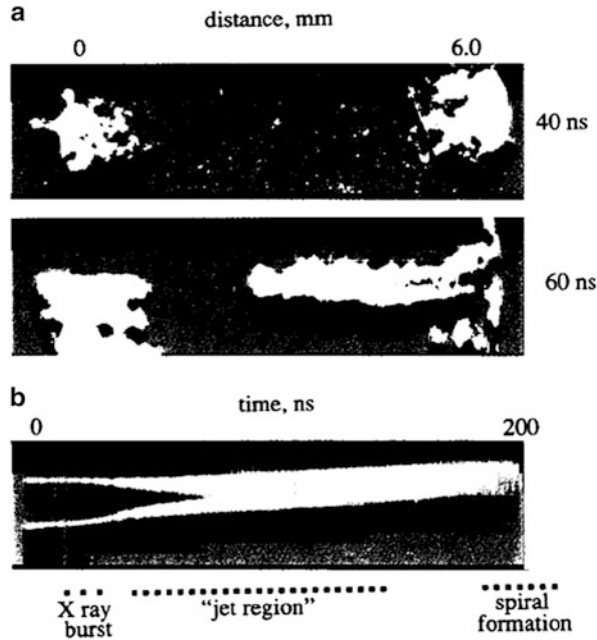


**Fig. 3.18** (a) Schlieren photographs of plasma light from of two interacting current-carrying plasma filaments (Z pinches) at times 40 and 60 ns, respectively (end view). The pinches are produced by exploding two parallel, 15 mm diameter, stainless steel wires with 250 kA of current. The two space frames show that plasma from the right-hand side filament has been channeled towards the central core, by the magnetic field isobars, at a velocity of about 100 km/s. The process is slightly asymmetrical: plasma from the right-hand side filament has reached and filled the core at time 60 ns, whereas the plasma from the left-hand side filament has not yet started to move inward. (b) Streak camera photograph showing time evolution of interacting Z pinches conducting 667 kA (side view). A slit focused the midsections of the wires onto the film (cf., Fig. 6.21). Three distinct regions are recorded: a radiation burst lasting about 5 ns, a “jet” region lasting about 50 ns, where plasma from the exploded wires is channeled inwards (as well as change in the circular cross sections (Fig. 3.19)) and then, a spiral region, where the filaments rotate about each other. Reference is made to Fig. 1.15 for a similar radiation pattern in astrophysical plasma

“flat” components at the strong-magnetic-field, low-density instability wavelength equation (1.16).

### 3.10.6 “Doubleness” in Current-Conducting Plasmas

The  $r^{-1}$  dependency of the Biot-Savart force law between current-conducting filaments leads to a curious phenomena: a pairing of filaments (cf. Sect. 2.6). This pairing leads directly to a “twoness” or “doubleness” when many filaments are present in plasmas in which the magnetic field plays a major role. As an example,

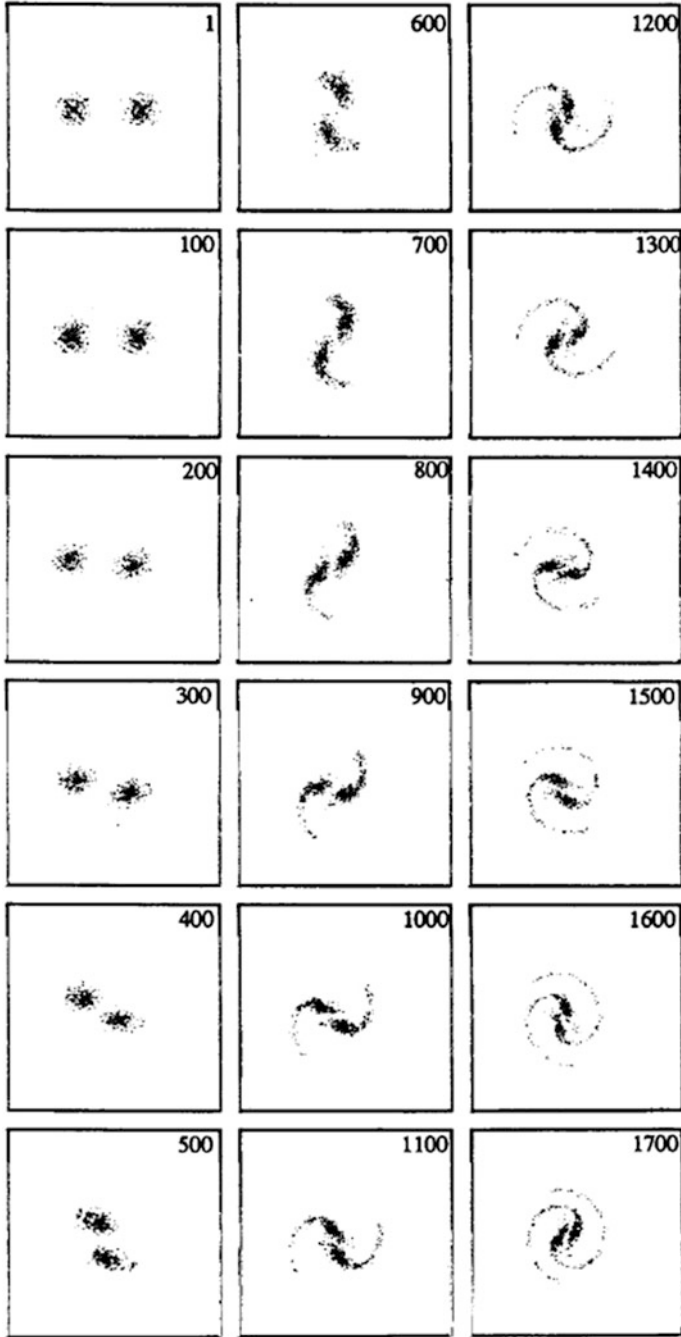


**Fig. 3.19** Single frame stills of plasma in the simulation of two adjacent Birkeland filaments:  $\omega_b/\omega_p = 3.0$ ,  $T_{e0} = T_{i0} = 32$  keV,  $T = 1 - 1,700$ , and acceleration field = 62 mV/m. Not shown is the plasma trapped in the elliptical core at the geometric center of the simulation. The plasma tends to obscure the coalesced region



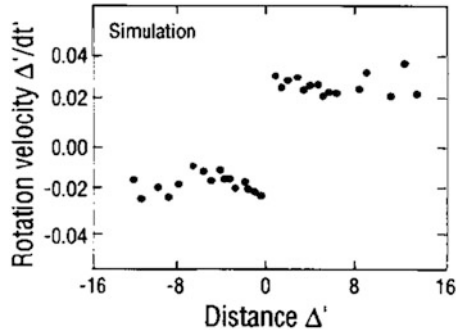


**Fig. 3.20** Rotational velocity of two adjacent Birkeland filaments. Note the fine scale structure due to the diocotron instability (Sect. 1.7.3) on the “flat” portions of the velocity curves. The velocity is given in simulation units

Fig. 3.21 shows the evolution of three plasma filaments having parameters identical to those of Sect. 3.10.1 but spaced  $3 \Delta'$  and  $6 \Delta'$  apart. The two closest interact strongly to form a spiral while the third filament remains relatively quiescent. Examples of pairing in the filaments formed in the dense plasma focus (Sect. 4.6.2) is given by Bernard et al. (1975) and Bostick (1986).

## 3.11 Magnetic Fields in Cosmic Dimensioned Plasma

### 3.11.1 Measurement of Galactic Magnetic Fields

Interstellar magnetic fields in spiral galaxies can be observed indirectly in the optical and radio range. In recent years observations of the linearly polarized radio continuum emission led to a significant improvement of the data. Extensive reviews of the observational methods have been published (Heiles 1976; Spoelstra 1977; Verschurr 1979; Sofue et al. 1986) and the results reviewed by Wielebinski (1989). The methods used to measure magnetic fields in galaxies include the following:

1. **Optical Polarization.** Elongated paramagnetic dust particles become oriented perpendicular to the interstellar magnetic field lines by the effect of paramagnetic relaxation, first discussed by Davis and Greenstein (1951). Extensive observations of several thousand stars revealed regular features of the magnetic field in our Galaxy with the distance range of the observed stars. The field strength and the degree of uniformity of the field, however, can only be determined with limited accuracy because too little is known about the size, shape, temperature, and magnetic properties of interstellar grains.
2. **Zeeman Splitting of Radio Lines.** Spectral lines are split up when the emitting atoms enter a magnetic field. The amount of splitting in a longitudinal field is

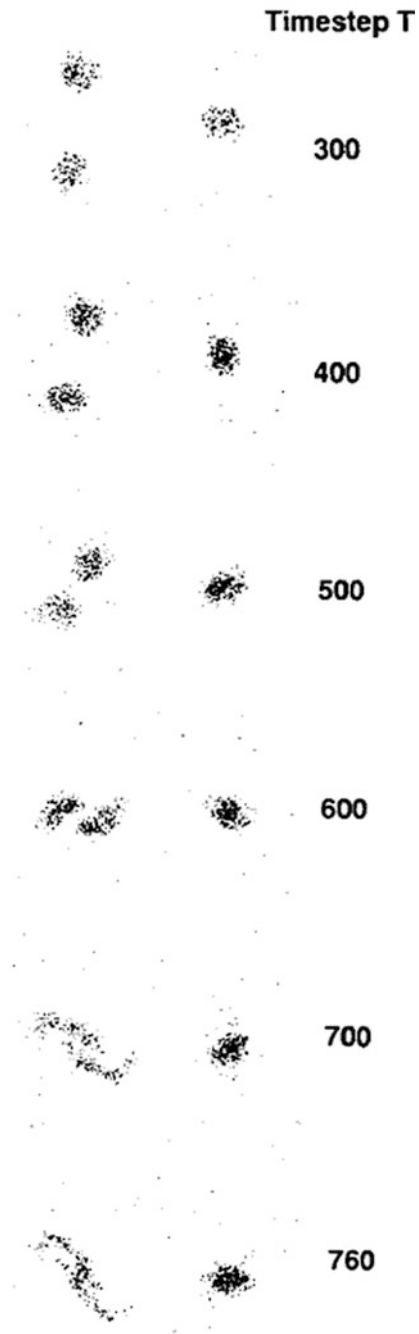


**Fig. 3.21** Interaction of three Birkeland filaments. Same parameters as Fig. 3.19

2.8 Hz/mG for the neutral hydrogen (HI) and 3.3 Hz/mG for the OH radio line and has been observed in several Galactic clouds (Verschurr 1979).

3. **Faraday Rotation of Polarized Radio Emission.** Continuous radio emission is observed from interstellar plasma clouds (HII regions) which radiate by interaction of thermal particles (free-free emission), and/or by synchrotron emission. Thermal radio emission is unpolarized, and synchrotron radiation is partly polarized.

The plane of polarization of a linearly polarized radio wave is rotated when the wave passes through a magnetized plasma according to Eq. (B.14). For an electron plasma, positive (counterclockwise) Faraday rotation occurs if the magnetic field is directed towards the observer; negative (clockwise) Faraday rotation occurs if the field points away from the observer. For a positron plasma, the situation is reversed. From Eq. (B.14), the rotation angle  $\xi$  increases with the integral of  $n_e B_{\parallel}$  over the line of sight (where  $B_{\parallel}$  is the magnetic field component along the line of sight) and with  $\lambda^2$  ( $\lambda$  = wavelength of observation). The quantity  $\Delta\xi/\lambda^2$  is called the “rotation measure” (RM).

An accurate determination of RM requires observations at (at least) three wavelengths because the observed direction of the polarization vectors is ambiguous by  $\pm 180^\circ$ .

4. **Synchrotron Radiation.** The average field strength  $B_{\text{perp}}$  can be estimated from the average synchrotron intensity equation (6.94) since the intensity depends on the field strength and the density of cosmic-ray electrons in the relevant energy range. However, to make this estimation, an equipartition between the energy densities or pressure equilibrium of the magnetic field and cosmic rays is assumed. Since the strength of the magnetic field and the local star formation rate are related quantities, equipartition is not valid, and the field strengths estimated are too small (Beck 1990).

### 3.11.2 Milky Way Galaxy

In the solar neighborhood, the strength of the magnetic field has been determined with rather high accuracy, applying methods in both the optical and the radio range. From the rotation and dispersion measures of 38 pulsars within 2 kpc from the sun, the strength of the uniform field has been found to be  $|B_{\parallel}| = 2.2 \pm 0.4 \mu\text{G}$ . The total synchrotron radiation radio emission in the anticenter direction yields an effective total field strength of  $6 \pm 1 \mu\text{G}$ . A uniform field of  $3 \mu\text{G}$  plus a turbulent field of a similar strength yields a total field strength of  $\sim 4 \mu\text{G}$  which is sufficient to account for the minimum Galactic radio emission between spiral arms, using the local cosmic-ray electron density (Phillips et al. 1981). The maximum effective field in spiral arms has to be stronger; its strength depends on the clumpiness of the field along the line of sight. If magnetized plasma clouds occupy 5 % of the line of sight, the mean strength in the plasma clouds must be  $\sim 45 \mu\text{G}$ .

The observations are roughly consistent with this value. Zeeman splitting of HI lines revealed field strengths up to  $50 \pm 15 \mu\text{G}$  in Orion A (Harnet 1984). The OH lines allow measurements with higher accuracy. In a molecular cloud in NGC 2024 the field strength is  $B_{\parallel} = -38 \pm 1 \mu\text{G}$  (Crutcher and Kazés 1983). Faraday rotation of radio waves from background sources reveal field strengths of a few microgauss in HII regions and up to  $50 \mu\text{G}$  in molecular clouds (Heiles et al. 1981).

Measurements of the Zeeman effect have now been made in HI clouds (Verschurr 1987), OH molecular clouds (Crutcher et al. 1987), and in  $\text{H}_2\text{O}$  masers (Fiebig and Güsten 1988). These data indicate that the magnetic fields in the Galaxy are along the local spiral arm (i.e., azimuthal). For example, Vallée (1988) shows that any deviations of pitch angle of the field from the spiral arm are slight, possibly less than  $6^\circ$  (Fig. 3.22). Vallée also deduces a field reversal in the Sagittarius arm. This could support claims that the galactic magnetic field is bisymmetric (Sofue and Fujimoto 1983).

High resolution radio continuum VLA observations at 6 and 20 cm wavelengths (Yusef-Zadeh et al. 1984) reveal numerous plasma filaments in the inner 60 pc ( $3 \times 10^{18}$  m or 317 light years) of the Galaxy,  $\sim 0.3$  pc in diameter by 10–60 pc in length (Fig. 1.14). The filaments are highly polarized, indicating a synchrotron origin for the radio emission. The filaments are aligned roughly perpendicular to the galactic plane so that the magnetic field is poloidal in a cylindrically force-free configuration. The polarization structure near the Galactic center has been recorded with the Effelsberg 100 m telescope by Seiradakis et al. (1985) at 6.3 cm (4.75 GHz) and 2.8 cm (10.7 GHz). Figure 3.23 shows a radiograph of the intensity of polarized emission at 10.7 GHz and depicts two radio lobes on either side of a core. Seiradakis et al. note that the “core-lobe” structure is the same as that of a classical double radio source. Seiradakis’s results have been substantiated by 9 mm (33 GHz) observations of Reich (1988), who finds that in the galactic center the magnetic field runs exactly perpendicular to the galactic plane (Wielebinski 1989). The strength of the field is 1 mG. An azimuthal (toroidal)/poloidal galactic field of about 1 mG strength was observed earlier in plasma simulations of spiral galaxies (Peratt 1984).

### 3.11.3 Spiral Galaxies

During the last decade, radio polarization observations have revealed large-scale magnetic fields in spiral galaxies (Peratt 1990). For example, the Effelsberg radio telescope has collected polarization data from about a dozen spiral galaxies at 6–49 cm wavelengths (Beck 1990). Rotation measures show two different large-scale structures of the interstellar fields: Axisymmetric-spiral and bisymmetric-spiral patterns (Krause et al. 1989). Figure 3.24 illustrates two cases of bisymmetric spiral structure in the large-scale magnetic field of spiral galaxies (Harnet et al. 1989; Horellou et al. 1990).

The orientation of the field lines is mostly along the optical spiral arms. However, the uniform field is often strongest outside the optical spiral arms. In IC 342

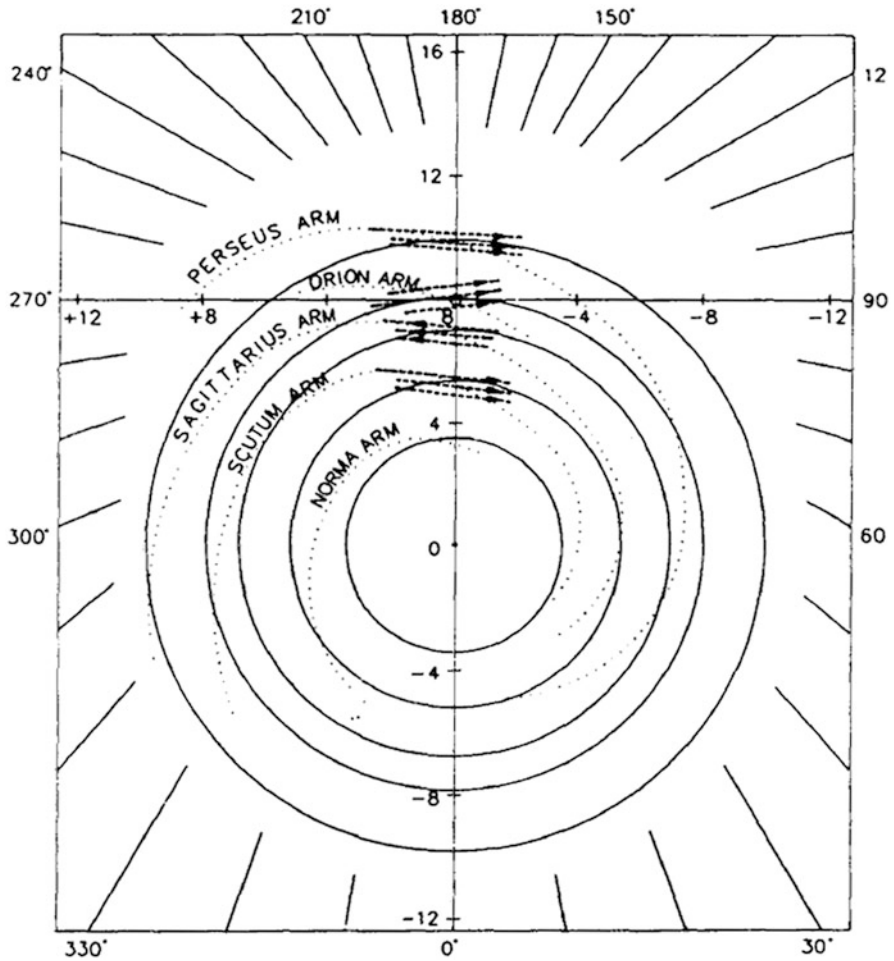


**Fig. 3.22** Model of the magnetic field in our Galaxy (Courtesy of R. Beck)

two filamentary structures are visible in the map of polarized intensity (Fig. 3.25). Their degree of polarization of  $\sim 30\%$  indicates a high degree of uniformity of the magnetic field on the scale of the resolution ( $\sim 700$  pc). These filaments extend over a length of  $\sim 30$  kpc and hence are the most prominent magnetic-field features detected in normal spiral galaxies so far.

A detailed analysis of the rotation measure distribution in a spiral arm southwest of the center of the Andromeda galaxy M31 (Beck 1990) shows that the magnetic field and a huge HI cloud complex are anchored together. The magnetic field then inflates out of the plane outside the cloud. The tendency for the magnetic field to follow the HI distribution has been noted in several recent observations. Circumstantial evidence has accumulated which suggests that there is a close connection between rings of CO and  $H_{\alpha}$  seen rotating in some galaxies and the magnetic fields

in the nuclear regions. This is particularly apparent in observations of spiral galaxies viewed edge-on. This scenario has also been invoked for our Galaxy (Wielebinski 1989).

Neutral hydrogen is detected from galaxies via the van de Hulst radio-emission line at 21.11 cm (1.420 GHz), which arises from the transition between the hyperfine-structure sublevels of the ground state of a hydrogen atom (Kaplan and Pikelner 1970). This is the sole procedure for the direct observation of neutral hydrogen in galaxies. High-resolution observation of neutral hydrogen in irregular and spiral galaxies usually reveal extended HI distributions. Contour maps of the HI typically show a relative lack of HI in the cores of spiral galaxies but high HI content in the surrounding region, usually in the shape of a “horseshoe” (Rogstad et al. 1974; Bosma et al. 1977a,b; Bosma 1981a,b; Hummel and Bosma 1982; Van Woerden et al. 1983). This region is not uniform but may have two or more peaks in neutral hydrogen content. Figure 3.26 shows several examples of HI distributions in spiral galaxies.

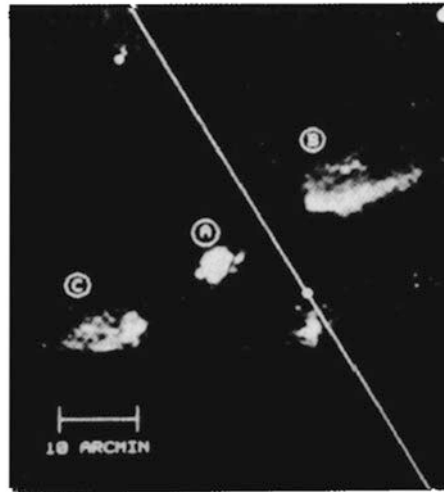


**Fig. 3.23** Polarized intensity radiograph (linear scale) of Galactic center at 10.7 GHz. The peak polarized flux density of components A, B and C is 690, 310, and 140 mJy, respectively (Courtesy of R. Beck 1986)

**Example 3.2. Bisymmetric magnetic field distribution in a simulated spiral galaxy.** For the simulated galaxy we choose  $\Delta' = 1.66 \times 10^{20}$  m,  $dt' = 5.87 \times 10^{11}$  s, a mass per unit length of  $10^{41}$  kg/ $10^{21}$  m ( $10^{44}$  g/35 kpc), and  $B_\phi = 2.5 \times 10^{-8}$  T (cf., Example 6.3, Sect. 6.6.2). Figure 3.27 shows the plasma spiral formed in this simulation overlayed on its magnetic field line (squared) isobars. The diameter of the spiral is about 50 kpc with a mass of  $10^{41}$  kg, i.e., a size and mass of that observed from spiral galaxies. A direct comparison to observations is made by superimposing

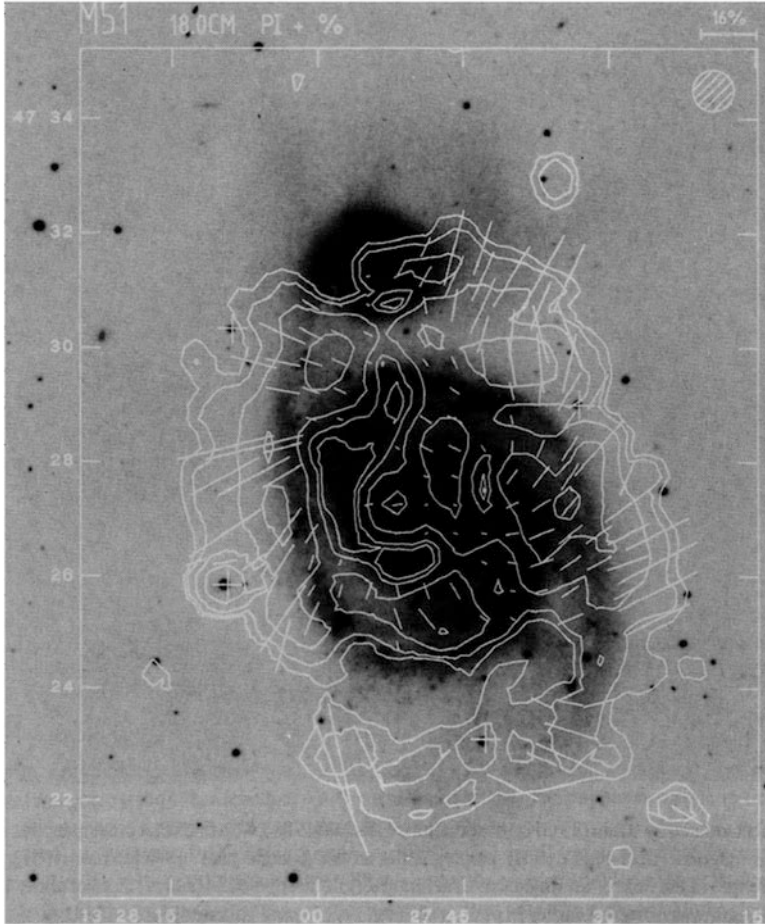


**Fig. 3.24** Bisymmetric spiral structure in the linearly polarized radio emission from spiral galaxies. (Above) Flux density of M51 at 1.66 GHz (18.0 cm). The sensitivity is 30 mJy per beam area (p. 126) Flux density of the linearly polarized emission of NGC 6946 at 4.75 GHz (6.3 cm) superimposed on an optical photograph. Contours are drawn at 0, 1, ..., 5 mJy/beam area. The lengths of the **E** vectors are proportional to the degree of linear polarization. The *ellipses* indicate radial distances of 6 and 12 kpc (Courtesy of R. Beck 1986)

the HI distribution in NGC 4151 on its optical photograph (Fig. 3.27b). The observation shows two peaks in neutral hydrogen surrounding a void. The void is orientated towards one of the arms. The simulation allows the two peaks to be traced back to their origin. Both are found to be the remnants of the originally extended components (i.e., cross-sections of the original Birkeland filaments). As discussed in Sect. 4.6.3, the accumulation and neutralization of hydrogenic plasma is expected in strong magnetic field regions. The hydrogen deficient center is the remnant of an elliptical galaxy formed midway between the filaments, in the magnetic null (Sect. 3.11.4).



### 3.11.4 Rotational Velocities of Spiral Galaxies

Rotational velocities of spiral galaxies are obtained by measuring the doppler shift of the  $H_\alpha$  line emitted by neutral hydrogen in the spiral arms. If the galaxy is canted toward earth, the emission-line in the arm moving away from earth is red-shifted while the line in the arm moving towards earth is blue-shifted. Figure 3.28 shows six radial velocity versus radius curves typical of spiral galaxies. These data show (1) a nearly linear solid-body rotation for the galaxy center (the first few arcminutes from center), (2) a nearly radially independent velocity profile in the spiral arms, and (3) distinct structure in the spiral arms that appears on the so-called flat portion of the velocity curve (beyond the first few arcminutes or, equivalently, the first few kiloparsecs).

**Example 3.3. Rotational velocity of a simulated spiral galaxy.** Using the scaling of Example 3.2, the rotational velocity given in Fig. 3.30 can be converted to physical units. The average velocity for the flat portion of the curve is  $v = 0.0213 \Delta' / dt'$ , or, in time-compressed units,  $6 \times 10^3$  km/s. Applying the mass correction factor 10.7 (Sect. 10.6.3) and the electric field correction factor 2.5,<sup>3</sup> the rotational velocity is 226 km/s. This curve is replotted in the last frame of Fig. 3.28 and is in good agreement with the observations. Concomitant with the lengthening of the arms is a thinning of the arms as shown in Fig. 3.19. As discussed in Sect. 3.10.5, a diocotron instability is produced. This instability shows up in both the cross-sectional views of the spiral arms and in the velocity profile, where a distinct vortex “saw-tooth”

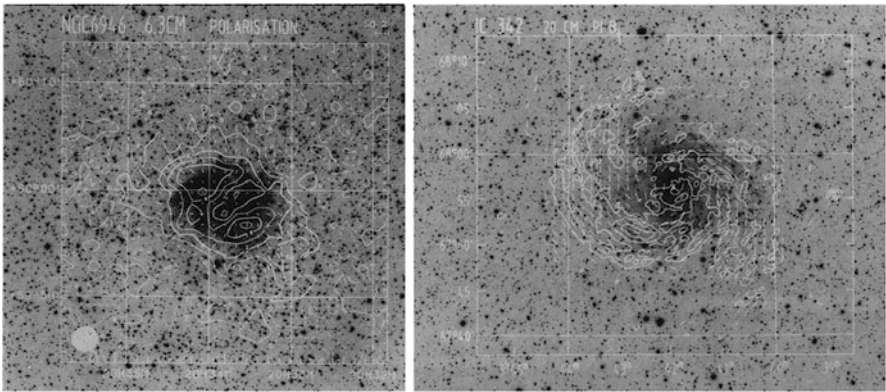


**Fig. 3.25** Orientation of the observed  $\mathbf{B}$  vectors in IC 342 with an angular resolution of  $2''.45$ , corrected for Faraday rotation as derived from data at 6.3 and 20 cm. The vectors have arbitrary lengths and are superimposed onto a contour map of the linearly polarized intensity at 20 cm (Courtesy of R. Beck 1986)

<sup>3</sup> To reduce the computation time to spiral formation, the acceleration field  $E_z$  was increased 2.5 times, from 12 to 30 mV/m. A field strength  $\sim 1\text{--}10$  mV/m is consistent with that associated with double layers in the near-earth plasma (Sect. 4.4). It should be noted that over the axial extent of a spiral galaxy,  $\sim 10$  kpc, a millivolt per meter field strength corresponds to a potential of  $3 \times 10^{17}$  V (Sect. 5.6.4).



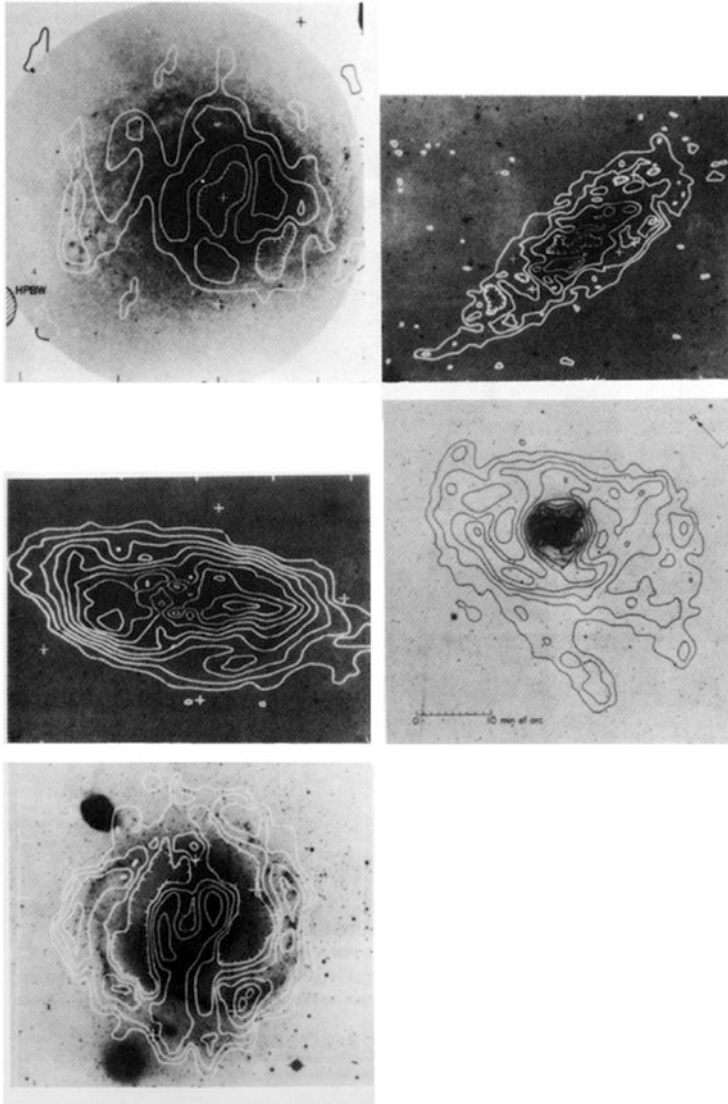


**Fig. 3.26** (*Opposite*) HI distributions superimposed on optical photographs of galaxies. (*Left column*) NGC 4736, NGC 5033, and NGC 4151. (*Right column*) NGC 3198 and M83 ([Peratt 1986a](#))

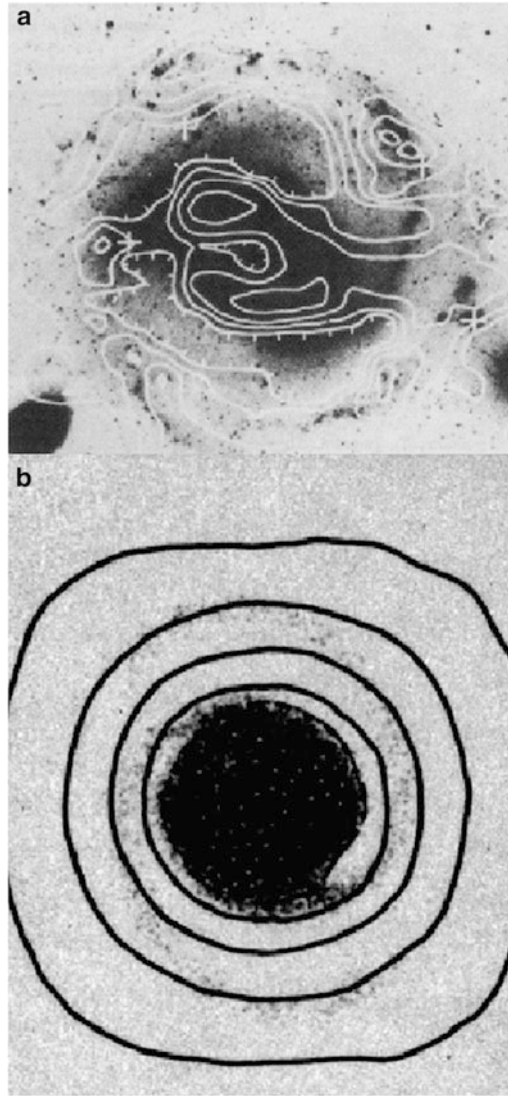


**Fig. 3.27** (a) HI distribution superimposed on an optical photograph of NGC 4151. (b) Simulation magnetic energy density superimposed on simulated spiral galaxy. See Fig. 13.9

pattern is measured. Good examples of this instability are found in the Sc-type galaxies M101, NGC 253, and NGC 2998 (Arp 1986). Figure 3.29, NGC 3646, is an example of a very large diocotron instability, similar to that observed in auroras, in the spiral arms.

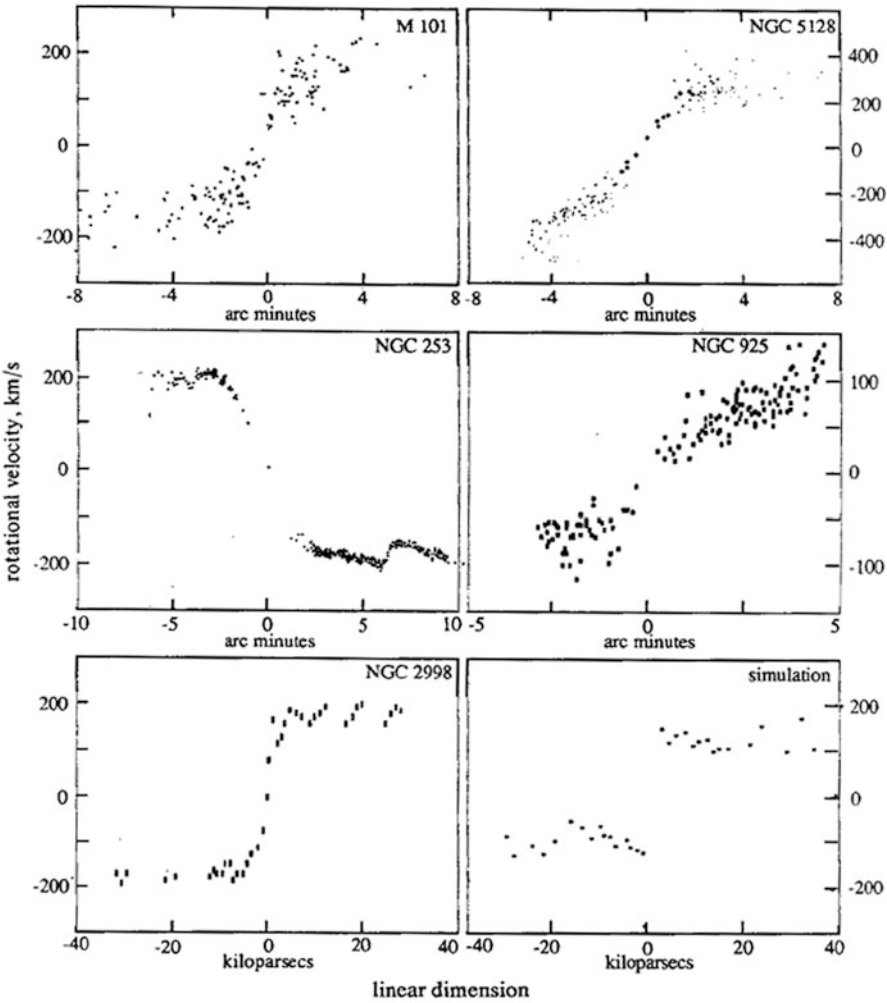


**Fig. 3.28** Spiral galaxy rotational velocity characteristics. The *bottom right-hand-side curve* is the simulation result taken from Fig. 3.20

### 3.11.5 Elliptical Galaxies

Elliptical (E) galaxies, as distinct from peculiars, irregulars, and spirals, are characterized by a very smooth texture, a bright nucleus, and a tenuous outer envelope of large extent (sensitive photographic plates show that the visible envelope may be 20 times the diameter of the nucleus, Fig. 3.30). Ellipticals are most often found midway between the extended radio components of double radio galaxies and radioquasars. Figure 3.31 is an example of this geometry. Like S0 galaxies



**Fig. 3.29** Optical photograph of NGC 3646. Note the well-defined diocotron instability in the spiral's arm

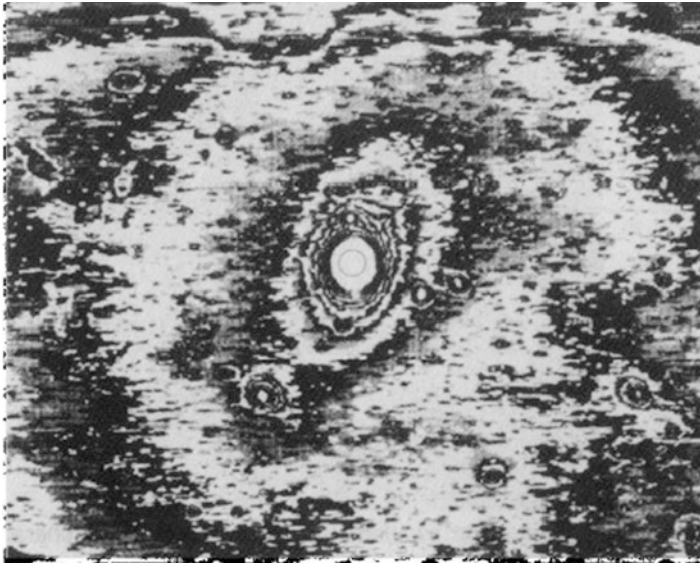


**Fig. 3.30** Isodensitometer tracing of the elliptical galaxy M87, made from a 60 min exposure with the 1.2 m Palomar Schmidt telescope. The inner circle is the diameter given in the Shapely-Ames catalogue, while the outer ellipse spans as much as 70 arcmin. The horizontal extent of the image frame is 500 arcmin. Note that the inner isophotes have vertical major axes, but the outer isophotes show noticeable clockwise twisting

(galaxies with little or no evidence of star-forming activity) E galaxies are found most frequently in regions characterized by high galaxy density (i.e., areas most susceptible to interactions).

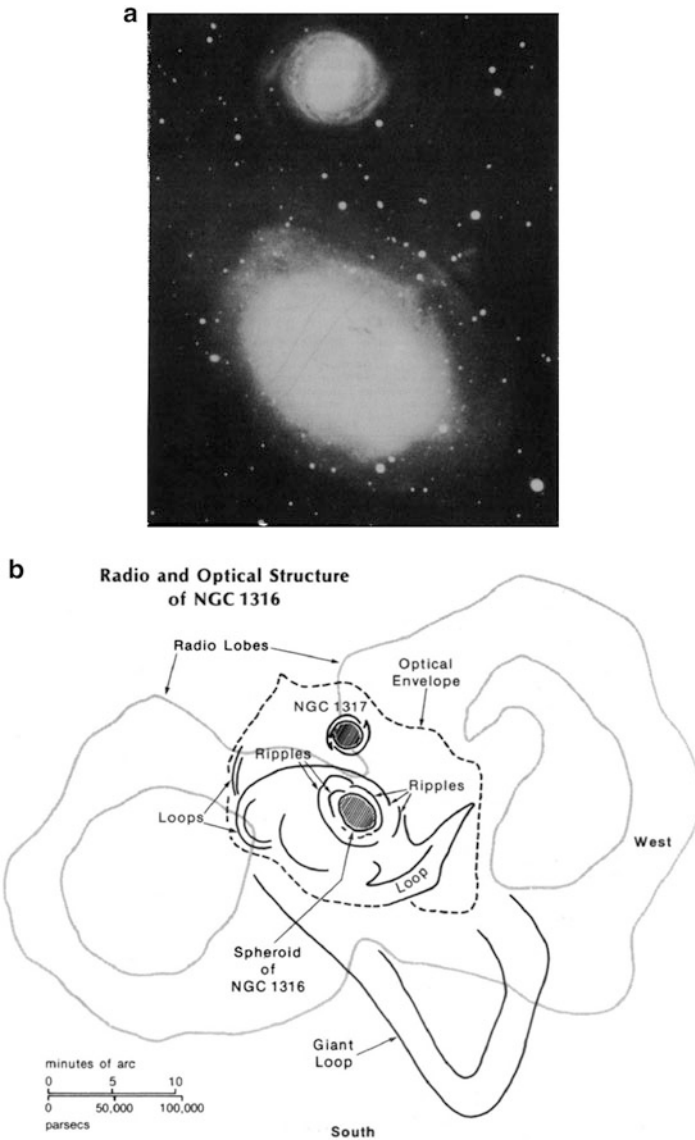


**Fig. 3.31** (a) Optical photographs of the elliptical galaxy NGC 1316 and the spiral galaxy NGC 1317. (b) Radio and optical structure of NGC 1316

The resolution of the magnetic energy density is insufficient to resolve the magnetic field structure in the simulation spiral arms. (galaxies with little or no evidence of star-forming activity) E galaxies are found most frequently in regions characterized by high galaxy density (i.e., areas most susceptible to interactions).

Diffuse elliptical galaxies are also found midway between the synchrotron emitting galactic simulation filaments. These galaxies are characterized by a twisting of their outer isophotes. Elliptical galaxies have weak or no magnetic fields.

**Example 3.4. Simulated elliptical galaxy.** Figures 3.15 and 3.17 depict the elliptical core formed in a plasma galaxy simulation. In physical units, the bottom frame of Fig. 3.16 corresponds to an elapsed time of 20 Myr from the start of the filament interaction. At this time, the field strength squared in the vicinity of the core (approximately midway up the figure) is  $B_\phi = 0.592 \times 10^{-8} \text{ T}$ . The field induced pressure defining the boundary of the core at this time is  $p_B = (2\mu_0)^{-1} B_\phi^2 = 1.4 \times 10^{11} \text{ Pa}$  ( $1.4 \times 10^{-10} \text{ dyn/cm}^2$ ). This isobar extends some 50 kpc and can balance the thermokinetic pressure of a  $10^4 \text{ m}^{-3}$  ( $10^{-2} \text{ cm}^{-3}$ ) 6 keV plasma compressed into the core. The magnetic field is null at the core center. As is the case with elliptical galaxies, the simulated elliptical plasma galaxy shows only a slight twist of rotation (Fig. 3.17), caused by the start of a clockwise rotation of filaments beginning a Biot-Savart force law interaction (Sect. 3.10.3).

### 3.11.6 Intergalactic Magnetic Fields

A large-scale intercluster magnetic field with an estimated strength of 0.3–0.6  $\mu\text{G}$  located between the Coma cluster of galaxies and the Abell 1367 cluster was discovered in 1989 (Kim et al. 1989) (Sect. 2.6.6).

## References

- Acuña, M.H., Ness, N.F.: The Pioneer XI high field fluxgate magnetometer. *Space Sci. Instrum.* **1**, 177 (1975)
- Arp, H.: The persistent problem of spiral galaxies. *IEEE Trans. Plasma Sci.*, **PS-14** (1986)
- Beck, R.: Interstellar magnetic fields. *IEEE Trans. Plasma Sci.* **14**, 740 (1986)
- Beck, R.: Magnetic fields in spiral galaxies. *IEEE Trans. Plasma Sci.* **18**, 33 (1990)
- Beck, R., Buczylowski, U.R., Harnett, J.I.: Polarized radio emission from NGC 6946. In: Beck, R., Kronberg, P.P., Wielebinski, R. (eds.) *Galactic and Intergalactic Magnetic Fields*, pp. 213. Kluwer Acad., Dordrecht (1990)
- Bernard, A et al: Experimental studies of the plasma focus and evidence for non-thermal processes. *Phys. Fluids* **18**, 180 (1975)
- Bosma, A., Goss, W.M., Allen, R.J.: The giant spiral galaxy M101. VI-The large scale radial velocity field. *Astron. Astrophys.*, **93**, 1–2 (1981)
- Bosma, A.: 21-cm line studies of spiral galaxies. I. Observations of the galaxies NGC 5033, 3198, 5055, 2841, and 7331. *Astron. Astrophys.* **86**, 1791 (1981a)

- Bosma, A.: 21-cm line studies of spiral galaxies. II. The distribution and kinematics of neutral hydrogen in spiral galaxies of various morphological type. *Astron. Astrophys.* **86**, 1825 (1981b)
- Bosma, A., Ekers, R.D., Lequeux, J.: A 21-cm study of the Seyfert galaxy NGC 4151. *Astron. Astrophys.* **57**, 97 (1977a)
- Bosma, A., van de Hulst, J.M., Sullivan, W.T., III: A neutral hydrogen study of the spiral galaxy NGC 4736. *Astron. Astrophys.* **57**, 373 (1977b)
- Bostick, W.H.: Simulation of astrophysical processes in the laboratory. *Nature* **179**, 214 (1957)
- Bostick, W.H.: What laboratory-produced plasma structures can contribute to the understanding of cosmic structures both large and small. *IEEE Trans. Plasma Sci.* **14**, 703 (1986)
- Chandrasekhar, S., Kendall, P.C.: On force-free magnetic fields. *Astrophys. J.* **126**, 457 (1957)
- Crutcher, R.M., Kazés, I.: The magnetic field of the NGC 2024 molecular cloud - Detection of OH line Zeeman splitting. *Astron. Astrophys.* **125**, L23 (1983)
- Davis, L., Greenstein, J.L.: The polarization of starlight by aligned dust grains. *Astrophys. J.* **114**, 206 (1951)
- Elliot, R.S.: *Electromagnetics*. McGraw-Hill, New York (1966)
- Felber, F.S., Peratt, A.L.: Self-similar oscillations of a Z pinch. *Bull. Am. Phys. Soc.* **25**, (1980)
- Ferraro, V.C.A., Plumpton, C.: *An Introduction of Magneto-Fluid Mechanisms*. Clarendon Press, Oxford (1966)
- Fiebig, D., Güsten, R.: Strong magnetic fields in interstellar H<sub>2</sub>O maser clumps. *Astron. Astrophys.* (1988)
- Fujimoto, M.: Bisymmetric spiral magnetic fields in spiral galaxies. In: Beck, R., Gräve, R. (eds.) *Interstellar Magnetic Fields*. Springer, Berlin (1987)
- Gold, T.: In: Hess, W.N. (ed.) *AAS-NASA Symposium on Physics of Solar Flares*, Greenbelt. NASA SP-50, p. 389 (1964)
- Harnet, J.I.: *Monthly Notices. R. Astron. Soc.* **210**, 12 (1984)
- Harnet, J.I., Wielebinski, R., Haynes, R.F., and Klein, U.: Polarized radio emission from NGC 4945. *Astron and Astrophys* **216**(1–2), 39–43 (1989)
- Heiles, C.: The interstellar magnetic field. *Annu. Rev. Astron. Astrophys.* **14**, 1 (1976)
- Heiles, C., Chu, Y.-H., Troland, T.H.: Magnetic Field Strengths in the H II Regions S117, S119, and S264. *APJ.* **247**, L77–L80 (1981)
- Horellou, C., Beck, R., Klein, U.: Polarized radio emission from M 51. In: Beck, R., Kronberg, P.P., Wielebinski, R. (eds.) *Galactic and Intergalactic Magnetic Fields*, pp. 211. Kluwer Acad., Dordrecht (1990)
- Hummel, E., Bosma, A.: Radio continuum observations of the spiral galaxies NGC 2841, NGC 5055, and NGC 7331. *Astron. J.* **87**, 242 (1982)
- Kaplan, S.A., Pikelner, B.: *The Interstellar Medium*. Harvard University Press, Cambridge (1970)
- Kim, K.-T., Kronberg, P.P., Giovannini, G., Venturi, T.: Discovery of intergalactic radio emission in the Coma-A1367 supercluster. *Nature* **341**, 720 (1989)

- Krause, M., Beck, R., Hummel, E.: The magnetic field structure in two nearby galaxies. I. The bisymmetric field structure in M81. *Astron. Astrophys.* **217**, 4 (1989)
- Krause, M., Beck, R., Hummel, E.: The magnetic field structure in two nearby galaxies. I. The bisymmetric spiral magnetic field in M81. *Astron. Astrophys.* **217**, 17 (1989a)
- Krause, M., Hummel, E., Beck, R.: The magnetic field structure in two nearby galaxies. I. The axisymmetric spiral magnetic field in IC 342. *Astron. Astrophys.* **217**, 4 (1989b)
- Nakagawa, J., Raadu, M.A.: On practical representation of magnetic field. *Solar Phys.* **25**, 127 (1972)
- Panofsky, W.K.H., Phillips, M.: *Classical Electricity and Magnetism*. Addison-Wesley, Reading (1962)
- Peratt, A.L.: Simulating spiral galaxies. *Sky Telesc.* **68**, 118 (1984)
- Peratt, A.L.: Evolution of the plasma universe I. Double radio galaxies, quasars, and extragalactic jets. *IEEE Trans. Plasma Sci.* **14**, 639 (1986a)
- Peratt, A.L.: Evolution of the plasma universe II. The formation of systems of galaxies. *IEEE Trans. Plasma Sci.* **14**, 763 (1986b)
- Peratt, A.L.: 3-dimensional particle-in-cell simulations of spiral galaxies. In: Beck, R. (ed.) *IAU Symposium*, 140 (1990)
- Peratt, A.L., Green, J.C.: On the evolution of interacting magnetized galactic plasmas. *Astrophys. Space Sci.* **91**, 19 (1983)
- Phillips, S., Kearsy, S., Osborne, J.L., Haslam, C.G.T., Stoffel, H.: Distribution of galactic synchrotron emission. I. *Astron. Astrophys.* **98**, 286 (1981)
- Plonsey, R., Collin, R.E.: *Principles and Applications of Electromagnetic Fields*. McGraw-Hill, New York (1961)
- Reich, W.: Observations of linear polarization at 32 GHz of the galactic center arc. In: Morris, M. (ed.) *The Galactic Center*. D. Reidel, Dordrecht (1988)
- Rogstad, D.H., Lockart, I.A., Wright, M.C.H.: Aperture synthesis observations of the HI in the galaxy M85. *Astrophys. J.* **193**, 309 (1974)
- Rose, D.J., Clark, M.: *Plasmas and Controlled Fusion*. MIT, Cambridge (1961)
- Seiradakis, J.H., Lasenby, A.N., Yusef-Zadeh, F., Wielebinski, R., Klein, U.: A new symmetrical polarization structure near the galactic center. *Nature* **317**, 697 (1985)
- Smythe, W.R.: *Static and Dynamic Electricity*. McGraw-Hill, New York (1950)
- Sofue, Y., Fujimoto, M.: A bisymmetric spiral magnetic field and the spiral arms in our galaxy. *Astrophys. J.* **265**, 722 (1983)
- Sofue, Y., Fujimoto, M., Wielebinski, R.: Global structure of magnetic fields in spiral galaxies. *Annu. Rev. Astron. Astrophys.* **24**, 459 (1986)
- Spoelstra, T.A.T.: The galactic magnetic field. *Sov. Phys. Usp.* **20**, 336 (1977)
- Stenzel, R.L., Gekelman, W.: Magnetic field reconnection experiments 1. Field topologies. *J. Geophys. Res.* **86**, 649 (1981)
- Stratton, J.A.: *Electromagnetic Theory*. McGraw-Hill, New York (1941)
- Tandberg-Hanssen, E., Emslie, A.G.: *The Physics of Solar Flares*. Cambridge University Press, New York (1988)



- Thompson, J.E., Luessen, L.H. (eds.): Fast Electrical and Optical Measurements. Volume 1: Current and Voltage Measurements. Martinus Nijhoff Publishers, Dordrecht (1986)
- Vallée, J.P.: Can the large-scale magnetic field lines cross the spiral arms in our Milky Way galaxy? *Astron. J.* **95**, 750 (1988)
- Van Woerden, H., Van Driel, W., Schwarz, U.J.: Distribution and motions of atomic hydrogen in lenticular galaxies. In: Athanassoula, E. (ed.) *Internal Kinematics and Dynamics of Galaxies*, p. 99. American Astron. Union, Washington, DC (1983)
- Verschurr, G.L.: Observations of the Galactic magnetic field. *Fund. Cosm. Phys.* **5**, 113 (1979)
- Verschurr, G.L.: The strength of the interstellar magnetic field and its possible role in HI cloud dynamics. In: Beck, R., Gräve, R. (eds.) *Interstellar Magnetic Fields*, p. 154. Springer, Berlin (1987)
- Voigt, G.-H.: Quasi static MHD processes in earth's magnetosphere. *Laser Part. Beams* **6**, 525 (1988)
- Wielebinski, R.: Magnetic fields in the galaxy. Max-Planck-Institut für Radioastronomie Preprint Series No. 347 (1989)
- Woltjer, L.: A theorem on force-free magnetic fields. *Proc. Natl. Acad. Sci.* **44**, 489 (1958)
- Yusef-Zadeh, F., Morris, M., Chance, D.: Large, highly organized radio structures near the galactic centre. *Nature* **310**, 557 (1984)

## Chapter 4

# Electric Fields in Cosmic Plasma

Electric fields play a crucial role in cosmic plasmas. Electric fields can accelerate charged particles to high energies and cause currents to flow, generate and “un-freeze” magnetic fields in plasmas, cause plasma to pinch into filaments, separate chemical elements, and initiate the collapse of plasma to the condensate and neutral state of matter.

Until fairly recent times, electric fields were thought impossible, first in space (because the conductivity  $\sigma$  was thought to be zero), and then in cosmic plasma (because the conductivity  $\sigma$  was thought to be infinite and the plasma thought to be uniform). For these reasons, other mechanisms were sought to explain the existence of highly-relativistic charged particles which, in terrestrial laboratories, are produced only by accelerators with high potential gradients (i.e., electric fields).

The discovery of magnetic-field-aligned (“parallel”) electric fields in space above the aurora has profoundly changed our concepts of particle energization and plasma dynamics in the magnetosphere Fälthammar. It may also have far-reaching implications for the understanding of other space and astrophysical plasmas. The parallel electric field itself is hard to measure directly, but concurrent evidence of its existence has come from measured particle distributions—electrons as well as ions—both outside and inside the regions of parallel electric fields. Thus the existence of parallel electric fields with voltages of several kilovolts is now beyond doubt, but their distribution in space is still incompletely known.

Section 4.1 briefly mentions how electric fields occur. The methods of measuring electric fields are discussed (Sect. 4.2), followed by the mechanisms that lead to parallel electric fields in the magnetosphere (Sect. 4.3). A review of the data obtained from satellite and rocket measurements is then presented in Sect. 4.4. The fruit of these efforts is knowledge that is fundamental to our understanding of plasma-related phenomena in the rest of the universe, which will forever lie beyond the reach of in situ measurement. Sections 4.5–4.6 start the application of this knowledge to these regions of the universe.

## 4.1 Electric Fields

Maxwell-Hertz-Heaviside's equations (1.1) and (1.3),

$$\nabla \times E = -\frac{\partial B}{\partial t}$$

$$\nabla \cdot E = \rho/\epsilon_0 = -e(n_e - n_i)/\epsilon_0$$

tell us that electric fields derive from either of two mechanisms: time-varying magnetic fields or charge separation. These two equations are deceptively simple and convey no information about the multitude of mechanisms whereby a time-varying magnetic field arises or charges separate. Two examples of the former are given in Sects. 3.5.2 and 3.5.3. Charge separation can occur from plasma instabilities (Sect. 1.7.3), gyrations in a magnetic field, magnetic field and temperature gradients, diffusion, drifts, and radiation forces. Intense, high-frequency radiation nearly always produces free charges in dielectrics which lead to potential gradients  $\nabla\phi$  from which an electric field  $E = -\nabla\phi$  derives.

In electromagnetism, understanding the physical system under study is incomplete without the knowledge of the electric field. For this reason, field maps of  $E$  are highly sought after in laboratory and space plasmas. However, in contrast to the relative simple measurement of magnetic fields, electric fields are far harder to measure (Block et al. 1987).

## 4.2 Measurement of Electric Fields

A wide variety of techniques for measuring electric fields with strengths ranging from millivolts per centimeter to megavolts per centimeter have been developed. In pulsed energy applications, E-dot (or V-dot) probes, resistive dividers, and electrooptic crystals are used. In space plasmas, spherical double probes, radar, electron beams, and ion detectors find employment. The mapping of electric fields in space plasma is also possible by following the motions of rocket released ionized barium clouds, observing the paths that whistler waves take, and from the convection of ions in space regions (Helliwell 1967). Rydberg states may also be used for the measurement of electric fields in space and astrophysical plasmas (Garscadden 1986).

**V-Dot Detectors.** A V-dot detector is the electric field analog to the B-dot detector (Chap. 3). This detector can be as simple as a chopped-off coaxial cable with its tip exposed to the voltage that is to be measured. A slightly modified design uses a coaxial cable with a small metal sphere or a plate attached to increase sensitivity. The exposed tip can then be inserted through one electrode or conductor into the medium in which an electric field is present. The detector will capacitively couple to the opposite electrode or conductor, producing a signal proportional to the area of the detector times the rate of change of the voltage between conductor elements.

Figure 4.1 illustrates how a V-dot detector is used to measure the field component normal to the probe plate. The current density  $J$  consists of two parts: a conduction current dependent on the field  $E$  and the conductivity of the medium  $\sigma$ , and a displacement current that is proportional to the permittivity  $\epsilon$ ,

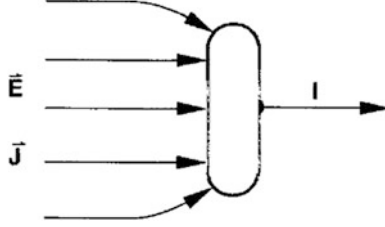


**Fig. 4.1** V-dot detector geometry

$$J = J_{cond} + J_{disp} = \sigma E + \epsilon_0 \frac{\partial E}{\partial t} \quad (4.1)$$

The total current coming out of the probe plate is

$$I = \int_S J \cdot dS = \frac{\phi}{R} + C \frac{\partial \phi}{\partial t} \quad (4.2)$$

where the resistance is defined as,

$$R = \frac{\phi}{\sigma \int E \cdot dS} \quad (4.3)$$

the capacitance is  $C \equiv \epsilon / \sigma R$ , and the voltage is

$$\phi = \int_L E \cdot dl \quad (4.4)$$

for an electric field over length  $L$ . With these definitions Eq. (4.2) can be rewritten as

$$\frac{d\phi}{dL} + \frac{\phi}{RC} = \frac{\phi_0}{R_0C} \quad (4.5)$$

where  $\phi_0$  is the signal voltage produced across a calibration resistance  $R_0$ ,  $\phi_0 = I/R_0$ . The solution to Eq. (4.5) is given by

$$\phi(t) = \frac{1}{R_0C} e^{-t/RC} \int_0^t e^{t'/RC} \phi_0(t') dt' \quad (4.6)$$

The accuracy of Eq. (4.6) depends in large part on how well the parameters  $R, R_0$ , and  $C$  are known.

**Electro-Optic Crystals.** The electrically induced birefringence in electrooptic crystals can be used to measure electric fields directly. The experimental

arrangement is shown in Fig. 4.2. A beam of laser light is directed through an input polarizer whose polarization axis is parallel to the crystal's  $x$ -axis. An output polarizer is placed after the crystal as shown. When placed in an electric field  $E$ , the crystal experiences a potential drop  $\phi = EL$  across its length  $L$ . The ratio of the laser light intensity, output to input, is then given by

$$\frac{I_0}{I_1} = \sin^2 \left[ \frac{\pi}{2} \frac{\phi}{\phi_\pi} \right] \quad (4.7)$$

where  $\phi_\pi$  is the potential which produces a light retardation of  $\pi$  radians, given by

$$\phi_\pi = \frac{\lambda}{2n_0^3 r_{63}} \quad (4.8)$$

where  $\lambda = 2\pi c/\omega$  is the free space wavelength of the laser light,  $n_0$  is the index of refraction of the crystal (typically, 1.5–3.3), and  $r_{63}$  is the crystal electrooptic coefficient ( $10^{-30} \times 10^{-12}$  m/V). For a KD\*P crystal,  $\phi_\pi$  is 3.3 kV. The number of variations measured in  $I_o/I_i$  gives the ratio  $\phi/\phi_\pi$ , from which the strength of  $E$  aligned along the major axis of the crystal can be obtained. Electrooptic crystals find application in laboratory regions where high electric field strengths exist. For example, a 10 kV/m field strength is required to produce  $\sim 10^{-3}$  variation in  $I_o/I_i$ .

**Spherical Double Probes.** Spherical double probes often find application in measuring electric fields in space, where field strengths may be of the order of a millivolt per meter. A spherical double probe consists of two spherical sensors mounted at the ends of wire booms that spin with the satellite as shown in Fig. 4.3. The potential

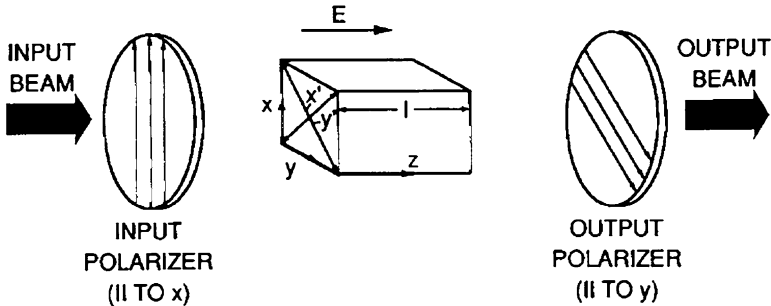
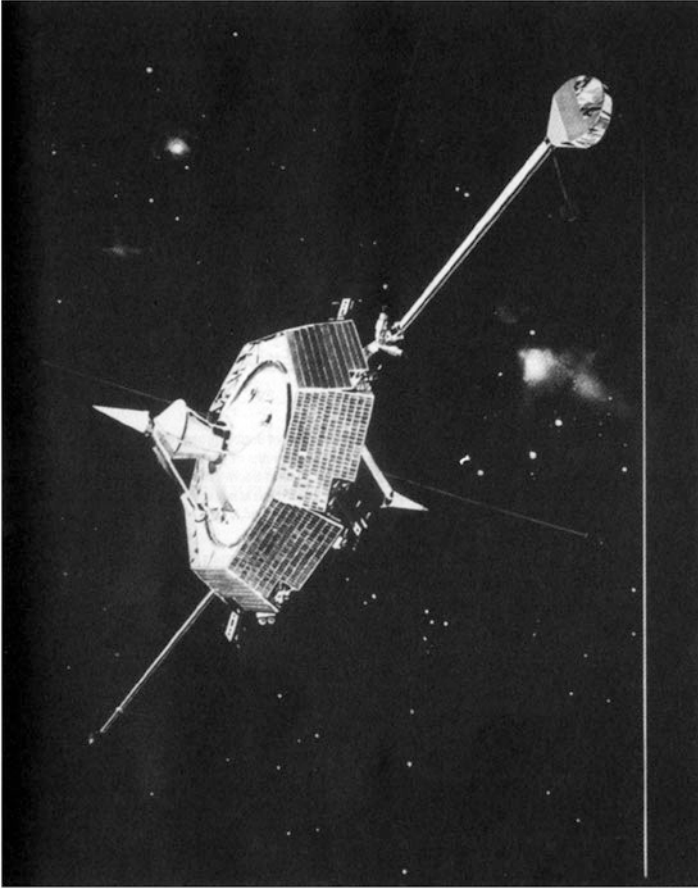


Fig. 4.2 Electrooptic-crystal electric field detector

difference is measured between the sensors that are typically spaced tens of meters apart. For example, ISEE-1 utilized a 73.5 m probe-to-probe boom length while the GEOS probe-to-probe separation was 42 m (Fig. 4.4).

The spherical sensors, each several centimeters in diameter, are constructed of vitreous carbon to ensure uniform work function and photo-emission properties. Unlike magnetic field sensors, probe biasing is necessary to obtain a balance between currents from escaping photo-electrons along the boom with currents from



**Fig. 4.3** The Viking spacecraft with magnetometers and electric field double probes

impinging ambient electrons. Often electron guns are necessary for controlling the satellite potential in order to achieve a satisfactory balance.

In the presence of an electric field, the resulting spin modulation signal between the probes will provide the direction and magnitude of the spin averaged, spin plane component of the electric field. The full electric field vector  $E$  can be constructed from the measured data under conditions (Fälthammar et al. 1987).

**Ion Detectors.** An ion detector in a uniform plasma can measure the bulk velocity components  $v_{\parallel}$  or  $v_{\perp}$ , parallel and perpendicular to  $B$ , respectively. In the hydro-magnetic approximation the gyrocenter drift is  $u_E = E \times B/B^2$ , and in a uniform plasma it is  $u_E = v$ . This allows checking of electric field double probe measurements against a plasma experiment (e.g., in the solar wind where  $u_E = v_{\perp}$  is the solar wind velocity component perpendicular to the instantaneous magnetic field vector  $B$ ).

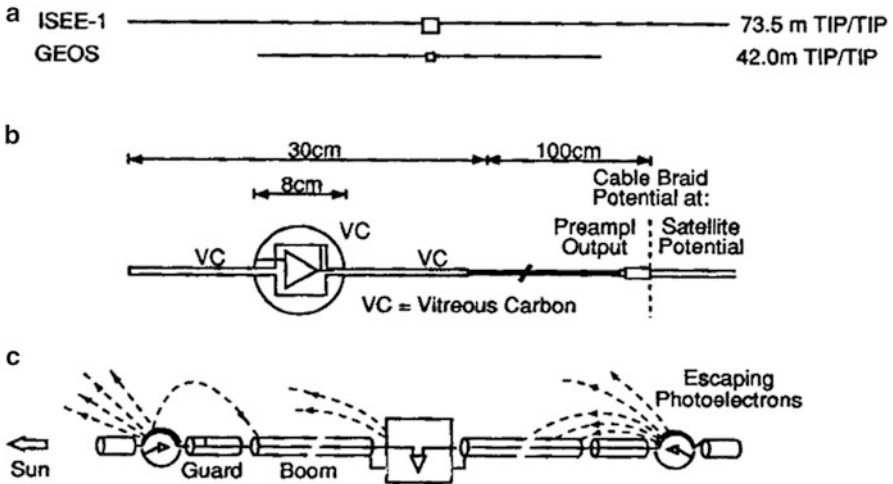


**Fig. 4.4** Electric field double probes. (a) The relative dimensions of double probes on the GEOS and ISEE satellites. (b) Sensor arrangement. (c) Overall configuration and the paths of photoelectrons which influence the electric field measurements. This figure shows the GEOS-1 guard-boom arrangement. On GEOS-2 the cable braid (100 cm) between probe inner tip and plug could be controlled at negative potentials of a few volts. On ISEE-1 the whole wire boom outer braid potential could be controlled

**Electron Beams.** Electron beams emitted from an electron gun may also be used to measure the electric field. The electrons emitted perpendicular to the local magnetic field  $B$  gyrate around the field and return to their point of origin, provided no other external forces act on them. The actual beam has dispersion causing the electrons to spread in the plane perpendicular to  $B$ . Their orbits average after each revolution at the point of origin, which acts as a focal point for detection. When an electric field that is perpendicular to  $B$  is present the electrons undergo a drift motion which results in a shift of the focal point from the origin. This process is identical to the  $E \times B$  drift of electrons in a magnetron or along a cathode that is magnetically insulated (Fig. 4.5). The displacement perpendicular to the beam  $s$  amounts to

$$s = v_{\perp} t_H = \left( \frac{2\pi}{e/m} \right) \frac{E \cos \omega t}{B^2} \quad (4.9)$$

where  $v_{\perp}$  is the drift velocity of the electrons perpendicular to the beam,  $t_H$  is the gyrotime, and  $\omega t$  is the momentary angle between  $E$  and the direction of the beam. Thus measurement of  $s$  and  $B$  allows the determination of  $E$  through Eq. (4.9).

As an example, for a satellite in stationary orbit about the earth (34,000 km), the magnetic field  $B \sim 100 \gamma$  (100 nT) so that a measured 3 m displacement at the satellite would yield  $E \sim 1$  mV/m. The gyroradius is about 1 km, so that the electrons spend most of their flight time away from the satellite and its disturbed surroundings.

## 4.3 Magnetic Field Aligned Electric Fields

### 4.3.1 Collisionless Thermoelectric Effect

The average force that a charge carrier experiences from a turbulent time-varying wave field will be different for particles of different energy. In a collision-dominated plasma the friction force decreases rapidly with energy. This is the ordinary thermoelectric effect, which is capable of supporting a dc electric potential between plasmas of different temperatures without requiring a net electric current. In the classical case we can write the magnetic-field-aligned component of the electric field

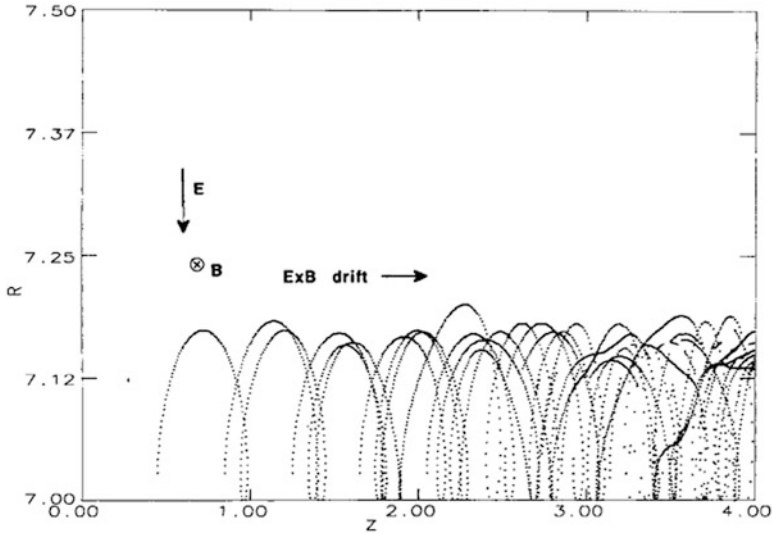


**Fig. 4.5** Trajectories of electrons in the presence of an electric and magnetic field. The electrons are emitted from a metallic surface located at an arbitrary radius  $R = 7.0$

$$E_{||} = \frac{k}{n_e e} T_e^{-\gamma_h/2} \frac{d}{ds} \left( n_e T_e^{1+\gamma_h/2} \right) \quad (4.10)$$

where  $\gamma_h$  is the thermal diffusion coefficient, which has the value 1.4 for singly charged particles in a fully ionized plasma, and  $d/ds$  is the derivative along the magnetic field. The thermoelectric field vanishes only if the density  $n_e$  and temperature  $T_e$  vary in a manner that keeps  $n_e T_e^{1+\gamma_h/2}$  constant.



### 4.3.2 Magnetic Mirror Effect

Parallel electric fields supported by the magnetic-mirror force were proposed by [Alfvén and Fälthammar \(1963\)](#) with application to magnetically trapped particles in the absence of net currents. Subsequently, the existence of this mechanism in laboratory plasmas was verified by [Geller et al. \(1974\)](#).

In the case of currents flowing out of the ionosphere, the effect of the magnetic-mirror force becomes particularly pronounced, because the downward flow of current-carrying electrons is inhibited except for those in the loss cone (Fig. 4.6).

To outline the basic physical characteristics of mirror-supported parallel fields due to upward Birkeland currents, we note that the electron current density  $j_{\parallel}$  at ionospheric altitude is related to the total field-aligned potential drop  $\phi_{\parallel}$  by the relation ([Knight 1973](#); [Lemaire and Scherer 1974](#))

$$j_{\parallel} = n_e e \sqrt{\frac{kT_e}{2\pi m_e}} \frac{B_i}{B_{\phi\parallel}} \left[ 1 - \left( 1 - \frac{B_{\phi\parallel}}{B_i} \right) \exp \left( \frac{e\phi_{\parallel}}{kT_e (B_i/B_{\phi\parallel} - 1)} \right) \right] \quad (4.11)$$

where  $T$  and  $n$  are the electron temperature and density of the magnetospheric source plasma,  $B_i$  is the ionospheric magnetic field strength, and  $B_{\phi\parallel}$  is the magnetic field strength at the top of the potential variation along field lines. This result will apply provided the electron loss cone in the source plasma is always replenished, otherwise the current can be choked to arbitrarily low values, approaching the idealized case described by Alfvén and Fälthammar. [Lemaire and Scherer \(1983\)](#) have extended Eq. (4.11) to account for both cold and warm electrons as well as ions.

Among the features of Eq. (4.11) is a wide range of voltages for which there is a linear relationship between voltage and current density. It is to be noted that current densities commonly observed above the auroras require potential drops of several kilovolts. Comparisons of the energy flux derived for magnetic-mirror-supported parallel fields to the measured energy flux from rocket flights are in excellent agreement ([Lundin and Sandahl 1978](#)).

### 4.3.3 Electrostatic Shocks

Electrostatic shocks are nonlinear solutions of the coupled time-independent Poisson-Vlasov equations (Eqs. (1.3) and (2.1), in the absence of collisions). They are characterized by an electrostatic potential jump supported by space charges of electrons and ions in the shock region.

Electrostatic shocks in the magnetosphere are limited regions of strong (several hundred mV/m) transverse electric fields (Fig. 4.7).

In earth's magnetosphere electrostatic shocks are reasonably uniformly distributed in local time, with a slight preference for the cusp, and scarcity in the post-midnight (0–6 h) region. Electrostatic shocks have been seen as far out as about  $7 R_e$ . Large shocks occur preferentially above 5,000 km and in the 16–22 h

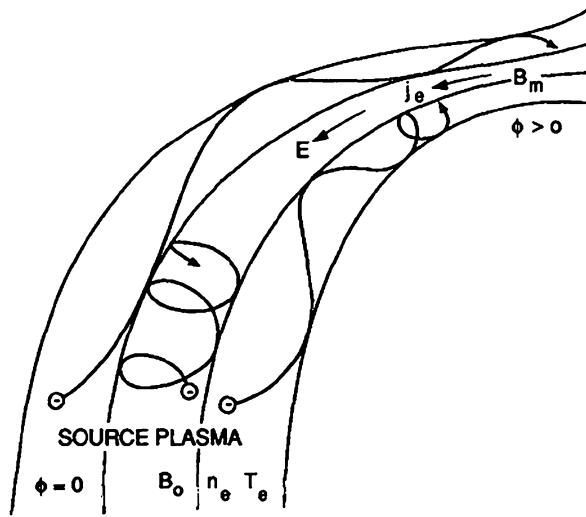


**Fig. 4.6** The magnetic mirror force restricts the motion of the charge carriers and makes a certain voltage  $\phi$  necessary in order to carry a given current density  $j_e$  through the throat of the mirror

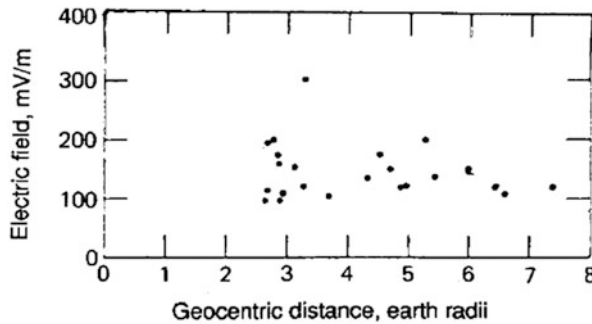


**Fig. 4.7** Peak electric field strengths in electrostatic shocks observed with ISEE-1 (Courtesy of C.-G. Fälthammar)

local-time region. However, parallel electric fields related to electrostatic shocks probably extend down below 1,100 km (Mozer et al. 1980). Upward pointing parallel electric fields of the order of 100 mV/m and extent of 2 km have been measured at an altitude of 7,950 km.

#### 4.3.4 Electric Double Layers

The electric double layer is a thin (tens of Debye lengths) space-charge structure sometimes observed in laboratory experiments of current-carrying plasmas. Between the two sheaths of equal but opposite charges that constitute the double layer there is a strong electric field, but not in the plasma outside it.

The characteristics of the classical double layer are such that for space plasmas electric field strengths as large as 1 V/m are possible. However, this field should have a very narrow altitude range of the order of 100 m, and should therefore be very hard to detect. Instead of a single strong double layer, satellite measurements and numerical simulations reveal the existence of numerous weak double layers, whose total contribution can lead to significant energy gains by the accelerated particles. For example, S3-3 and Viking satellite data indicate that field-aligned potential drops are made up of hundreds or thousands of weak double layers.

Although both wave and dc electric fields can accelerate particles, only a dc field, such as that found in double layers, can accelerate electrons and ions in the opposite directions to about the same energy. Because this mechanism is observed in space, laboratory, and simulation plasmas, in association with strong electric fields, the topic of double layers is covered in detail in Chap. 5.

## 4.4 Magnetospheric Electric Fields

### 4.4.1 *The Plasmasphere*

The plasmasphere is populated by a collision-dominated plasma for which the generalized Ohm's law (Sect. 2.4.1) can be expected to hold. It is therefore, electro-dynamically, the least complicated part of the magnetosphere (Lyons and Williams 1984). At least in the inner parts of this region one would expect a corotational electric field simply mapped from the corresponding areas of the ionosphere. The measurements with GEOS-1 and 2 and ISEE-1 have confirmed this but have also shown interesting deviations. Thus, the average quiet-time electric fields largely agree with what has been expected from Whistler results and theoretical considerations. However, the instantaneous electric field is highly variable and shows considerable deviations from simple corotation. An example of the plasmaspheric electric field is shown in Fig. 4.8. Inside 3.3 Earth radii there is a very good agreement with the expected corotational electric field, but further out considerable deviations from corotation are found.

During disturbed conditions, large deviations from corotation are observed near the plasmapause (Fig. 4.9). Just inside the dusk side of the plasmapause, electric fields many times stronger than the corotational field, and oppositely directed, have been observed with GEOS-2. During a substorm very strong electric fields were recorded adjacent to and just outside the plasmapause. The field strength projected to the ionospheric level exceeded 100 mV/m, and the event was accompanied by significant penetration of the convection electric field inside the plasmapause.

### 4.4.2 The Plasmasheet

Unlike a largely homogeneous and steady dawn-to-dusk electric field, the actual electric field in the plasmasheet has proved to be extremely variable, not only in time but also in space. During geomagnetically quiet times the electric field is too weak to be measured with the double probes flown so far (i.e., less than a few tenths of millivolts per meter). Finite small values (0.1–0.3 mV/m) have, however, been measured with the electron beam technique of the GEOS spacecraft.

During the substorm active phase, the electric fields are both strong and variable. As induction electric fields are important during times of extreme variability, there does not even exist an electric potential on the global scale. An example of electric fields measured in the plasmasheet is given in Fig. 4.10. Field strengths up to several tens of mV/m have been recorded near the plasmasheet boundary.

Two-point measurements of the electric field components taken by GEOS 2 and ISEE-1 show a time delay between observed pulses (Fig. 4.11). The direction of propagation was usually toward the earth with a velocity of the order of the average Alfvén velocity.

Occasionally, strong electric fields associated with “electrostatic shocks” were seen by ISEE. Figure 4.7 illustrates the peak electric field recorded versus earth radii. As shown, these fields are of the order of a few hundreds of mV/m and extend from 2.5 to 7.5  $R_e$ .

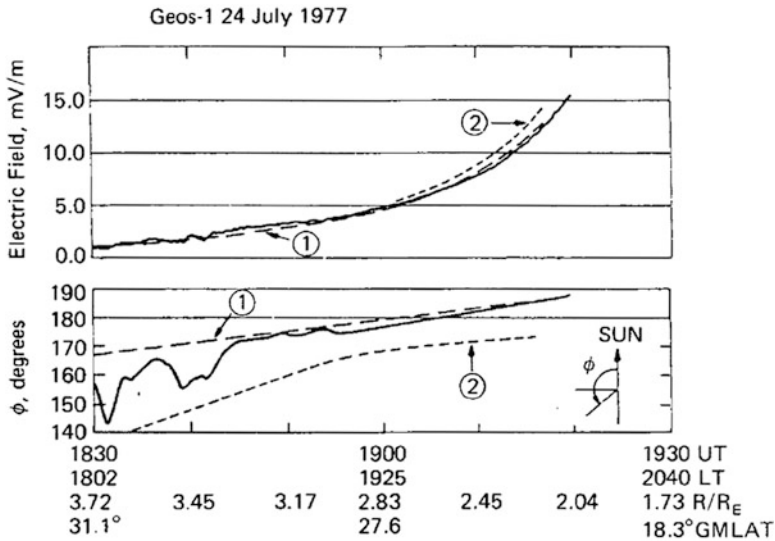


**Fig. 4.8** Magnitude and direction of GEOS-1 spin plane component of the electric field for an inbound pass through the plasmasphere. *Curve 1* is a model field representing perfect corotation. *Curve 2* is model field without any corotation (Courtesy of C.-G. Fälthammar)

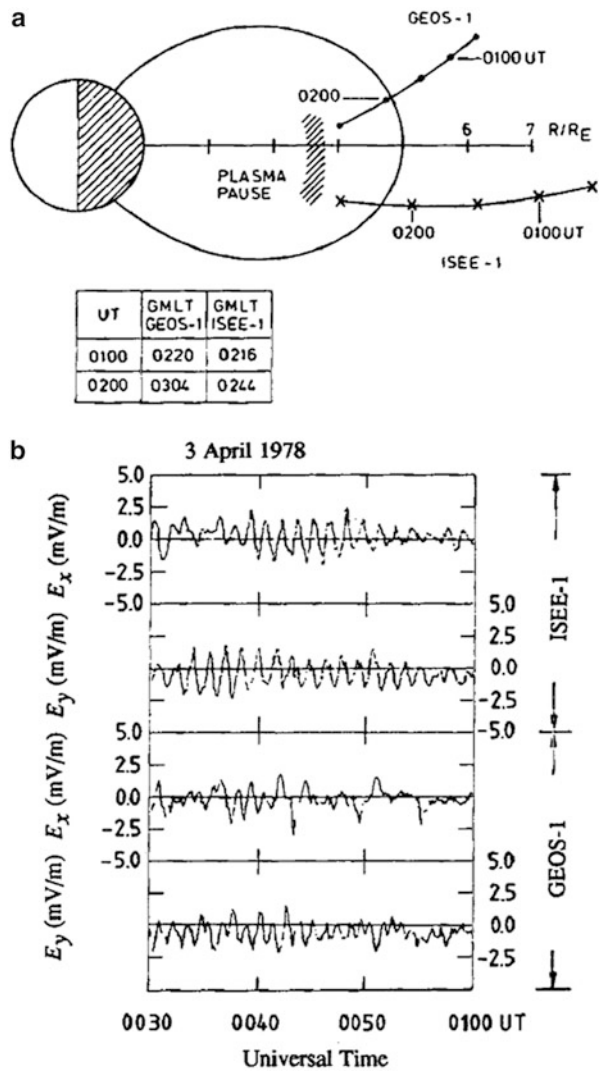


**Fig. 4.9** (a) The probe locations and universal times. (b) Comparisons of  $E_x$  and  $E_y$  during disturbed conditions observed by GEOS-1 and ISEE-1 (Courtesy of C.-G. Fälthammar)

### 4.4.3 The Neutral Sheet

At quiet times, the electric field strength in the neutral sheet is typically less than 0.5 mV/m. At active times, the field can reach 6 mV/m (Fig. 4.12).

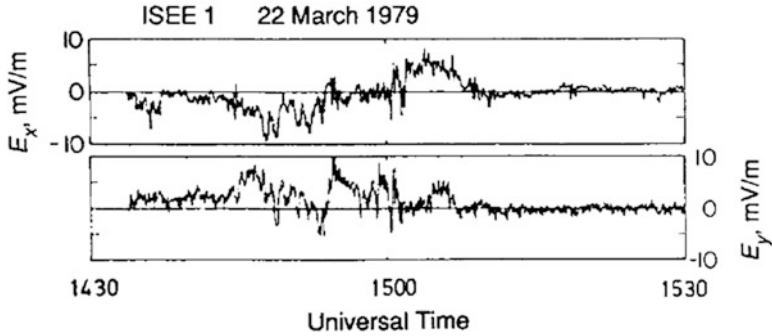


**Fig. 4.10** The field  $E$  measured in the plasmasheet during a substorm active phase (Courtesy of C.-G. Fälthammar)

#### 4.4.4 The Magnetotail

Double probe measurements in the central tail lobes have proven unsatisfactory because of low plasma densities. However, in other regions of the tail, measurements have been possible. Information about the electric field have also been drawn from plasma flow detected through anisotropies in measured particle fluxes. One result of the latter kind, is the occurrence of velocity fields with a nonvanishing vorticity (Fig. 4.13).

#### 4.4.5 The Magnetopause

Electric fields in the magnetopause are characterized by violent fluctuations with field strengths as high as 10 mV/m. The surprisingly large amplitudes of these fluctuations probably overshadow any dc fields that were expected from early models of the magnetopause. Also, the fluctuations are probably important for the penetration of plasma into the magnetosphere, as suggested by several investigators.

#### 4.4.6 The Auroral Acceleration Region

Probably the most interesting electric field observations of all are those made in the auroral acceleration region (Fig. 4.14). The first electric field measurements in this region were made with the S3-3 satellite. It led to two major discoveries: “electrostatic shocks” and multiple electric double layers.

Electrostatic shocks with field amplitudes of hundreds of mV/m were measured by S3-3 in the altitude range up to the S3-3 apogee of 8,000 km. Other measurements were made by ISEE-1 and by Viking, which extended the measurement of electric fields up to 13,527 km (Fälthammar et al. 1991). An example of the electrostatic shock type observed with Viking is shown in Fig. 4.15.

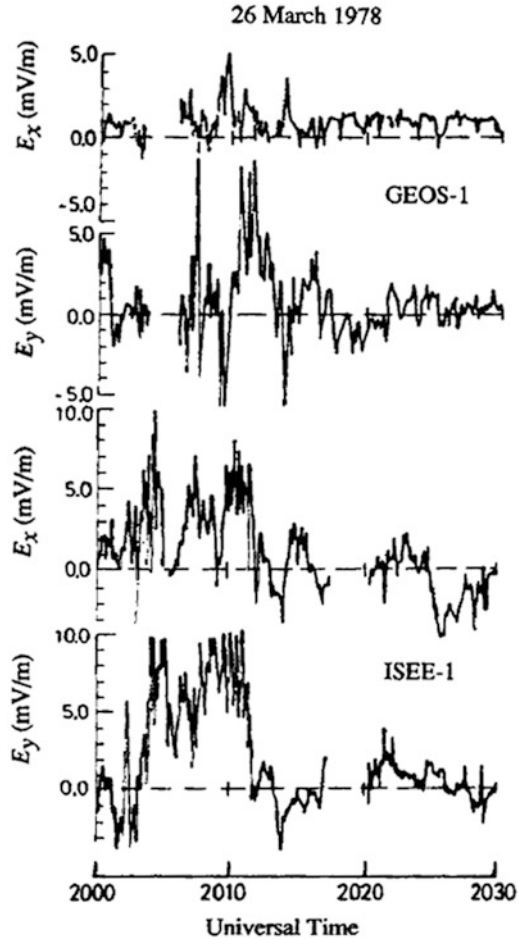


**Fig. 4.11** Two-point measurements of electric field pulse by ISEE-1 and GEOS-1 (Courtesy of C.-G. Fälthammar)

A typical feature of the Viking electric field data is the prevalence of extremely strong and irregular electric fields above the auroral oval. The occurrence of such electric fields is correlated with regions of electron precipitation. The transition from quiet, several mV/m electric fields at subauroral latitudes to the hundreds of mV/m auroral type oval fields has been found to be very sharp.

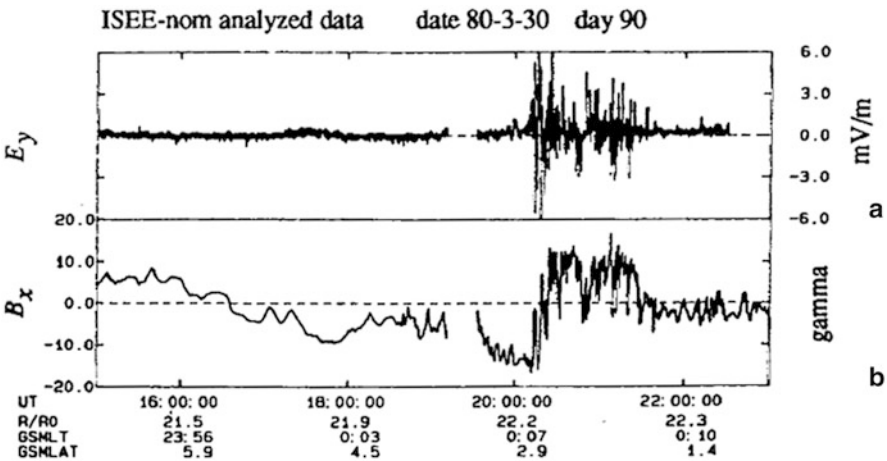


**Fig. 4.12** (a) Dawn-to-dusk component of the electric field and (b) sunward magnetic field in the neutral sheet. A quiet condition crossing at 16.30 UT with unobservably small electric fields is followed by a disturbed condition crossing in the 20.00–21.30 time interval with large and irregular electric fields (Courtesy of C.-G. Fälthammar)

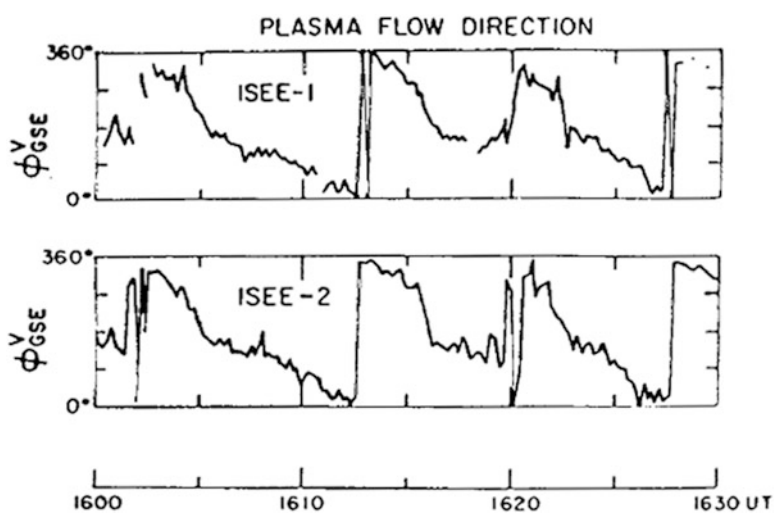


**Fig. 4.13** The occurrence of velocity fields with a nonvanishing vorticity is shown in this graph taken in the magnetotail (Courtesy of C.-G. Fälthammar)

### 4.4.7 Global Distributions of Auroral Electric Fields

In situ measurements in the magnetosphere have, by necessity, a limited time and space coverage. Measurements are taken along satellite orbits that are traversed at intervals of more than an hour for low orbits, and many hours for high orbits. However by combining (1) in situ measurements with (2) remote-sensing information



such as the Viking UV pictures of the whole auroral oval, as well as (3) ground-based data relevant to these measurements, and (4) a quantitative mathematical model of the electrodynamics of the auroral ionosphere, rather detailed information can be obtained of the “instantaneous” distribution of auroral electric fields and currents.

Figure 4.16 shows an example of the “instantaneous” global electric potential in the ionosphere as calculated from the Marklund-Blomberg model and the electric field measured in situ with Viking and projected down to the ionosphere.<sup>1</sup>

The instantaneous global electric potential pattern calculated by Marklund and Blomberg shows, as it should, a general but not detailed agreement with average patterns calculated for the same geophysical conditions. An example is shown in Fig. 4.17. The calculated pattern has also been projected to the equatorial plane and compared to the average plasmapause. The instantaneous demarcation line between open and closed equipotentials of the instantaneous potential distribution shows, as it should, a general but not detailed agreement with the average plasmapause.

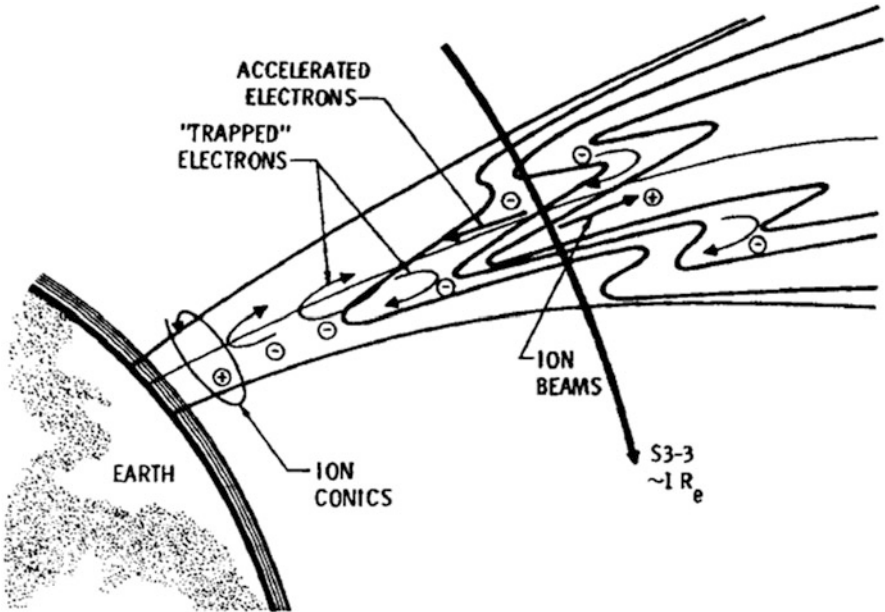


**Fig. 4.14** Schematic representation of electric equipotentials in the auroral acceleration region

<sup>1</sup> To facilitate comparison, the Viking electric field is represented by means of the  $E \times B$  vectors, which should be tangent to the electric potentials.

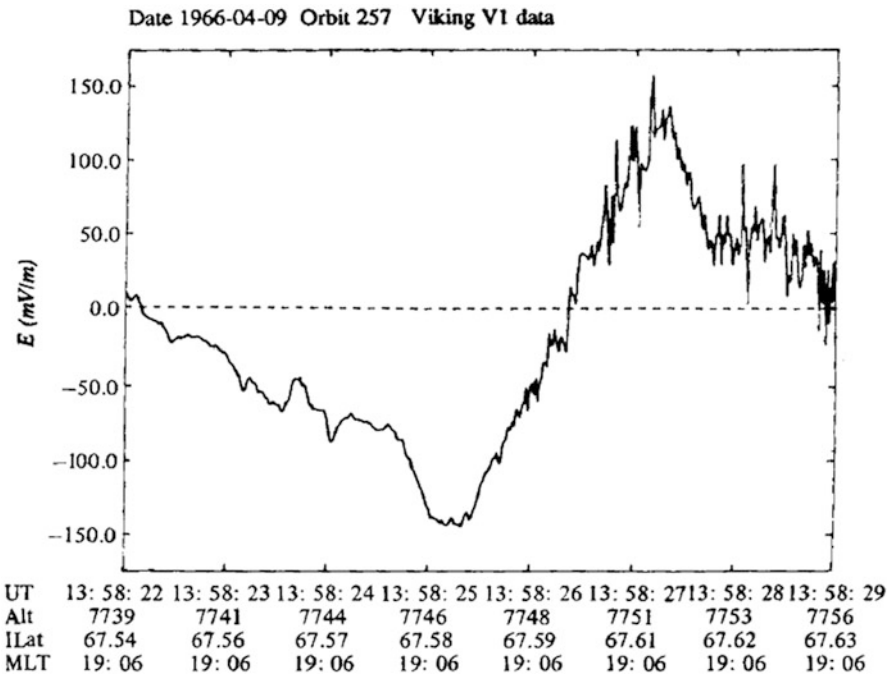


**Fig. 4.15** Close-up of an electrostatic shock observed with the Viking satellite. The structure of the double electric field spike is shown with enough time resolution to show fine detail. Electric fields with a strength of 150 mV/m are directed inward from both sides (Courtesy of C.-G. Fälthammar)

### 4.5 Outstanding Questions

The earth’s magnetosphere still poses a number of unsolved problems that involve electric fields in a fundamental way. The way in which plasma enters the magnetosphere, both from the solar wind and from the ionosphere, is still far from fully understood. More direct measurements are needed to solve the problem of plasma entry (Nishida 1988).

The earth’s own ionosphere is an important source of magnetospheric plasma. The expulsion of ionospheric plasma is the result of complex interactions between the ionosphere and the magnetosphere. In these interactions, electric fields, including magnetic field-aligned electric fields, seem to play an important role.

The auroral acceleration region still holds a number of unanswered questions. They concern, for example, the existence, distribution, and other properties of field-aligned electric fields, and their role in auroral acceleration. These are questions that are also relevant to the understanding of cosmic plasmas in general, which are known to have a remarkable capability of energizing charged particles (Fälthammar 1977, 1978, 1979, 1983, 1988).

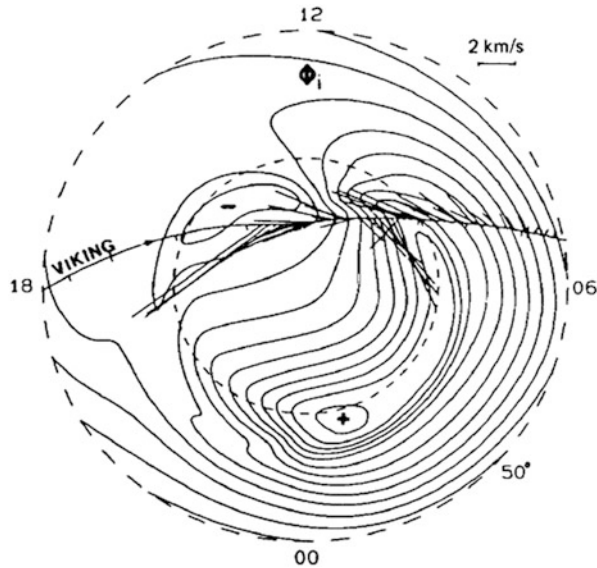


**Fig. 4.16** Comparison of “instantaneous” global ionospheric potential as calculated with Marklund-Blomberg model and the in situ electric field measurements at the Viking spacecraft. For convenience of comparison, the Viking electric field, projected down to the ionosphere, is represented by vectors, which should be tangential to the equipotentials. The equipotentials are given in steps of 5 kV (Courtesy of C.-G. Fälthammar)

## 4.6 Phenomena Associated with Electric Fields

### 4.6.1 Surface Discharges

Surface discharges are produced by large electric fields that develop between the surface and subsurface layers in dielectric materials as a consequence of energetic charged-particle deposition. For example, when spacecraft dielectrics are exposed to bursts of kiloelectronvolt particles during magnetic substorms, the particles penetrate a few micrometers to a few millimeters, building up field strengths which may be of the order of hundreds of kilovolts per centimeter. A schematic representation of this process is shown in Fig. 4.18.

If the material is a conductor or a semiconductor, a conduction current will flow in response to the charge deposition and will effectively neutralize the field. If the material is an insulator, the space charge will build up at a rate faster than the local relaxation time, and the associated electric field will increase. When the field reaches a critical value that depends on the material, surface smoothness, and porosity, a surface discharge will occur. This is a problem that often occurs in laboratory pulsed-power and, in fact, is the limiting constraint on how much power can flow in laboratory transmission lines. Figure 4.19 illustrates the “Lichtenberg figures” recorded

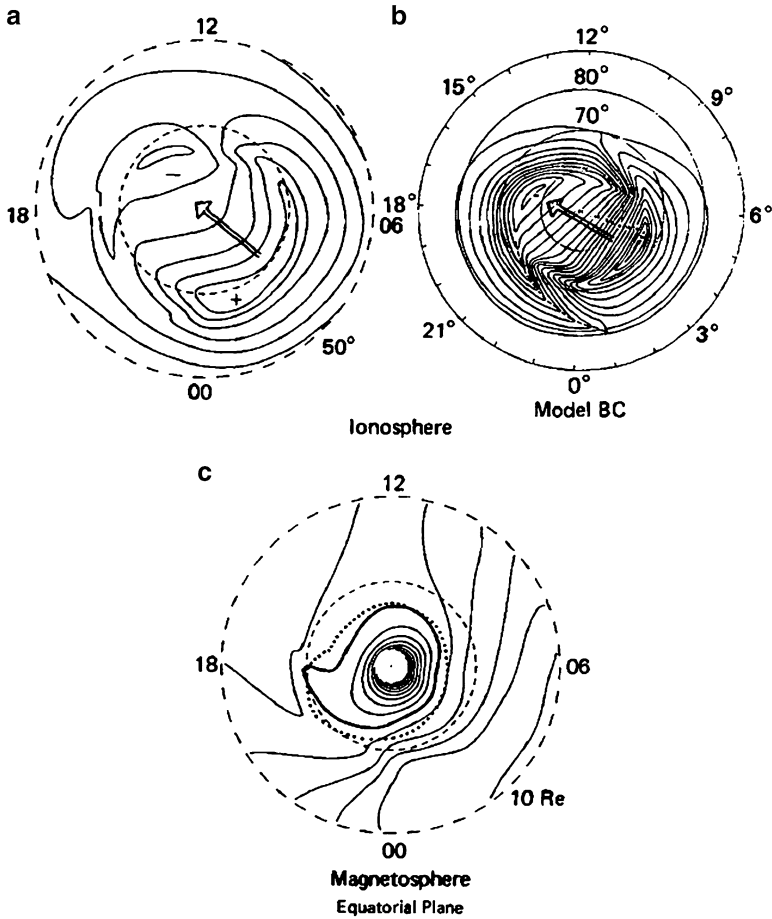


**Fig. 4.17** Comparison between instantaneous and average potential distributions. (a) Instantaneous ionospheric electric potential pattern calculated with the Marklund-Blomberg model. (b) Average potential pattern according to Heppner and Maynard (1987) for the same conditions. (c) The same pattern projected to the equatorial plane. Also shown, for comparison, is the average plasmapause (heavy line) as deduced from the Whistler data (Carpenter 1966) (Courtesy of C.-G. Fälthammar)

just below the surface of an acrylic transmission line spacer. Voltage breakdown at dielectric interfaces nearly always results in the formation of these dendrite-type streamers.<sup>2</sup>

Surface discharges will also occur on natural dielectrics in the solar system when these surfaces are exposed to large fluxes of energetic particles. This condition can be found, for example, where magnetospheric currents interact with the surfaces of the giant planets and their satellites.

<sup>2</sup> For thick acrylic pulse-line spacers, of the order of 10 cm wide, Lichtenberg figures are *three-dimensional* and can extend over the width of the insulator.

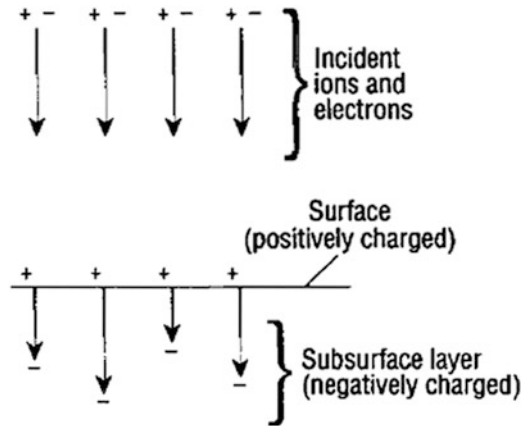


**Fig. 4.18** A schematic illustration of how a subsurface layer of charged particles forms when a dielectric material is exposed to energetic particles. In general, ions do not penetrate significantly below the surface, but electrons can penetrate to depths ranging from a few micrometers to a few millimeters, depending on their energy and the type of target material. When the electric field that develops between the surface and subsurface layers reaches a critical breakdown value, a surface discharge will occur

#### 4.6.2 Plasma Gun Arc Discharges

The plasma gun or dense plasma focus is one of the most “physics-rich” devices in plasma science. Characteristically, it is one of the least understood. The annihilation of magnetized plasma in a pinch results in the collective acceleration of ions to very high energies and the prodigious production of neutrons. In the late 1950s and early 1960s this device saw application in explaining the origin of the planets and satellites (Alfvén 1960; Alfvén and Wilcox 1962). Today, the dense plasma focus forms one of the most promising alternatives (to Tokamaks) in magnetic fusion (Gratton et al. 1990).

The plasma gun or plasma focus (Alfvén 1958, 1981; Lindberg et al. 1960; Lindberg and Jacobsen 1961; Filippov et al. 1962; Alfvén and Fälthammar 1963; Mather 1971; Bostick et al. 1975) is a plasma discharge consisting of a short but finite Z pinch (Sect. 6.6.1) which forms near or at the end of a coaxial plasma discharge. In the laboratory, the coaxial discharge is formed by switching a charged capacitor bank between a center electrode and an outer conducting tube electrode (Fig. 4.20). The discharge is manifested by a current sheath, called a penumbra, that forms between the inner and outer electrodes when the inner electrode is at a positive potential (i.e., an anode) and the outer electrode is at ground (i.e., a cathode). The current sheath is equally well defined whether the inner electrode is at a positive or negative potential but ion and neutron production at the focus are observed only when the inner electrode is an anode. Part of the stored magnetic energy in the tube and external circuit is rapidly converted to plasma energy during the current sheath’s collapse to-

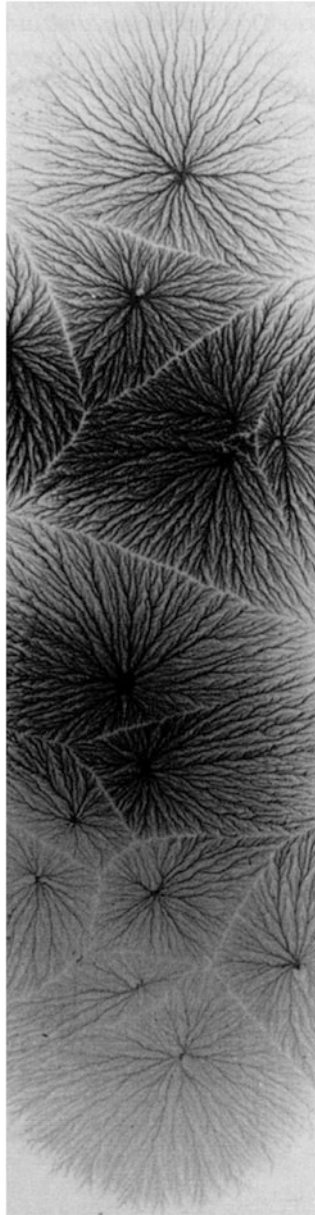


**Fig. 4.19** Lichtenberg figures recorded on the surface of an acrylic insulator used in a terawatt pulsed-power generator

ward the axis. The current flow convergence is largely due to the self-constricting nature of the current filament, whereas the heating and compression from the  $r, z$  implosion on the axis are due both to the magnetic forces of the current-carrying

plasma filament and to inertial forces. Partial conversion of the kinetic energy of the imploding axisymmetric current to internal heat energy may occur during the implosive phase owing to self-collision.

Development of the plasma current leading to the formation of a plasma focus at the center electrode terminus can be conveniently subdivided into three main phases. First is the initial gas breakdown and the formation of a parabolic current front. Second is the hydromagnetic acceleration of a current sheath toward the open end. Third is the rapid collapse of the azimuthally symmetric current sheath toward the axis to form the plasma focus.

**Breakdown Phase.** The breakdown has a radial, striated light pattern with a definite multifilamentary structure (Fig. 4.21). This structure, except for its obvious radial striation, appears cylindrically symmetric (Figs. 4.20 and 4.22). As the current increases, the terminus of this visible pattern moves radially outward until it

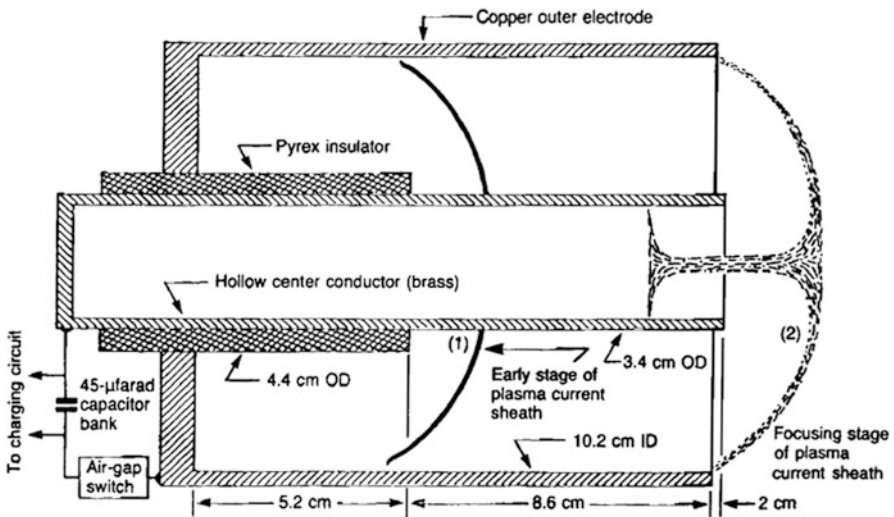


**Fig. 4.20** Typical plasma gun apparatus. A capacitor bank is discharged through two coaxial electrodes forming a plasma current sheath between inner and outer electrodes. The  $j \times B$  force accelerates the sheath outward to the ends of the electrodes where the inner sheath radius is forced inwards forming a columnar pinch or “focus” on axis. Also depicted on the diagram is the “penumbra”, the long-lived state of the current sheath at the muzzle of the plasma gun (Courtesy of W. H. Bostick)

reaches the outer electrode. The current front motion is best described as an unpinch or inverse process (i.e., the  $(j \times B)_r$  body force is exerted outward between the center electrode surface and the plasma current sheath). During this inverse phase, the sheath remains stable because of the stability of the inverse pinch process (the  $B_\theta$  lines are convex).

The filamentary structures within the focus, rather than blending together, form a finite number of intense radial spokes (“spider legs”). These spokes appear to

retain their identity throughout the acceleration phase and finally coalesce or focus on the axis beyond the end of the center electrode, forming a thin circular annulus (Fig. 4.21).

**Acceleration Phase.** The current sheath across the annulus  $\Delta r$  is not planar, but canted backward from the anode to the cathode owing to the radial dependence of the magnetic pressure gradient. The total acceleration force  $j \times B$  acting perpendicular to the current boundary leads to radial and axial motion. The  $(j \times B)_r$  radial component is outward and forces the current sheath to be annular at the outer electrode. The axial force  $(j \times B)_z$  varies as  $r^{-2}$  across the annulus and leads to higher sheath velocities near the surface of the center electrode. In the laboratory, fast image converter photographs distinctly show a parabolic current front. Owing to the parabolic current boundary, plasma flows centrifugally outward from anode to cathode along the current boundary as the acceleration continues. Plasma is seen to progress radially outward and beyond the outer electrode diameter as the current front accelerates downstream.

The overall time for plasma sheath acceleration to the end of the center electrode is related to the discharge potential across the annulus and the mass density of the background gas. For the case in which the current sheath pushes the gas ahead of the sheath, the sheath velocity is

$$v_s = \left[ \frac{E^2}{\mu_0 \rho_{m0}} \right]^{1/4} \quad (4.12)$$

where  $E$  and  $\rho_{m0}$  are the discharge field strength and initial mass density, respectively.

**Collapse Phase.** The third phase encompasses the rapid convergence of the axisymmetric current sheath to the axis and the conversion of stored magnetic energy to plasma energy in the focus. The  $r, z$  convergence is due to the  $j \times B$  pinch force. With this configuration, there is no equilibrium along the axis; hence the plasma may readily escape axially in either direction. By the very nature of the convergence, much of the gas that the sheath encounters during collapse is ejected downstream and lost. The gas trapped in the focus is estimated as  $\sim 10\%$  of that originally present.

The pinch effect is perhaps the most efficient way of heating and compressing a plasma. As the pinch induced implosion velocity of the current boundary imparts the same velocity to both ions and electrons, and because of the ion-electron mass difference, most of the energy appears as kinetic energy of the ions. In pinch devices, the ions are preferentially heated.

**Dynamic Behavior of the Current Sheath.** The dynamic behavior of the plasma current sheath can be analyzed using the measured time dependent values of the voltage  $\phi(t)$  across the electrodes, the tube current  $I(t)$ , and the sheath resistance  $R(t)$ .



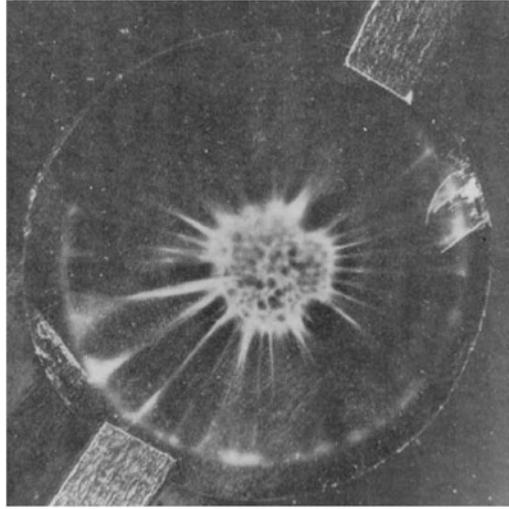


**Fig. 4.21** End-on recording of the plasma gun penumbra (Courtesy of W. H. Bostick)

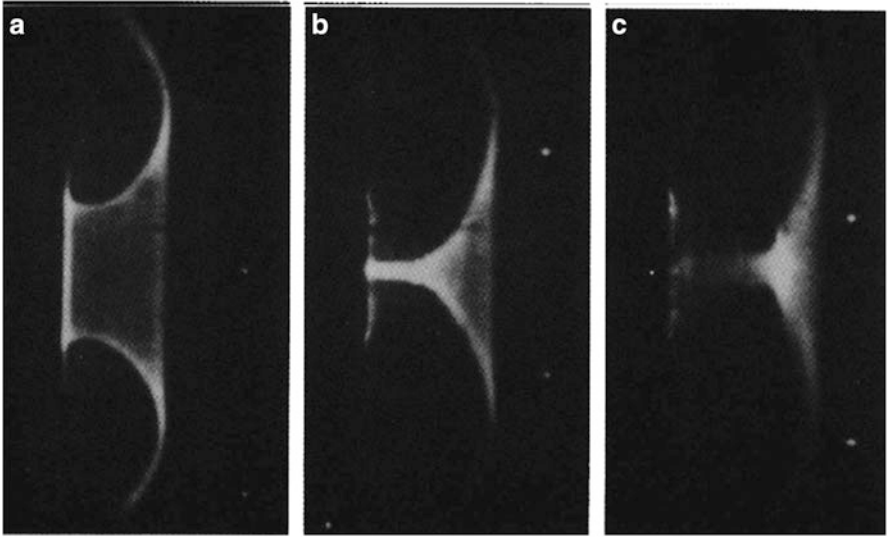


**Fig. 4.22** Side-on image converter photographs of the plasma penumbra. (a) Before columnar collapse or pinch. (b) and (c) During pinch or “focus”

The circuit equation representing the voltage across the electrodes  $ab$  in the equivalent electrical circuit (Fig. 4.23) is

$$v_s = \left[ \frac{E^2}{\mu_0 \rho_{m0}} \right]^{1/4} \quad (4.13)$$

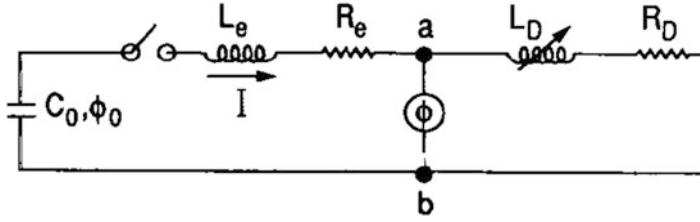


**Fig. 4.23** Equivalent electrical circuit of the plasma gun discharge. The subscripts  $e$  and  $D$  denote external and discharge circuit elements, respectively

The part of the circuit to the left of  $ab$  in Fig. 4.23 represents the electrical discharge and external circuit resistance  $R_e$  and external parasitic inductance  $L_e$ . The circuit to the right of  $ab$  represents the discharge inductance  $L_D(t)$  and resistance  $R_D(t)$ .

Using Eq. (4.13), the following quantities are calculated.

1. Discharge inductance:

$$L(t) = \frac{1}{I(t)} \int_0^{t'} [\phi(t) - I(t)R(t)] dt \quad (4.14)$$

2. Magnetic energy storage Eq. (3.39):

$$W_B(t) = \frac{1}{2} (L_e + L_D) I^2 \quad (4.15)$$

3. Mechanical energy of the sheath:

$$W(t) = \frac{1}{2} \int_0^{t'} \dot{L}_D I^2 dt \quad (4.16)$$

where  $d/dt(L_D) = \dot{L}_D$  is obtained from Eq. (4.13); and

4. Pinch voltage during collapse:

$$\phi_p(t) = \dot{L}_D I + I R_D \quad (4.17)$$

The instantaneous mass of the plasma sheath can be estimated using the momentum equation (2.13)  $\rho_m \partial v / \partial t = j \times B$ ,

$$m_o(t) = \frac{10^{-7}}{v} \int_0^{t_c} I^2 \ln \left( \frac{r_o}{r_i} \right) dt \quad (4.18)$$

where  $v = v_s$  is the sheath velocity and  $r_o/r_i$  the ratio of the outer to inner electrode radii. The upper integration limit  $t_c$  is the time to inner penumbra plasma collapse or pinch on axis.

**Example 4.1 Electric arcs on the Jovian satellite Io.** The satellite Io was observed by the spacecraft Voyager 1 and Voyager 2 to be covered with volcanoes (Morabite et al. 1979; Smith et al. 1979; Strom et al. 1979; Strom and Schneider 1982). Nine active volcanoes were observed during the Voyager 1 encounter, eight of which were still active during the Voyager 2 flyby 4 months later. Detailed pictures of the plumes from one of these volcanoes were rather striking in that the plume material was ejected in a well-defined cone whose geometry showed converging (rather than diverging) matter at large lateral distances from the vent, and the plume material was concentrated into striations. Thus, we have a volcanic vent with exit velocities of about 0.5 km/s, but with the volcanic effluent concentrated into a cone with a half angle initially less than about  $25^\circ$  to the vent axis. Furthermore, the material in the cone tends to concentrate into filaments that terminate on a narrow, well-defined, concentric annulus (Strom and Schneider 1982). The possibility that details of the volcanic discharge are a manifestation of a plasma arc at the volcanic vent were initially suggested by Gold (1979).

The dominant electric field in the Jovian magnetosphere is one that is associated with the corotational motion of plasma. This is given by  $E = -(\Delta\omega \times R) \times B = -\Delta v \times B$ , where  $R$  is the position vector from the center of Jupiter and  $\omega$  is the angular velocity vector of Jupiter's rotation. The electric field is directed outwards where  $\delta\omega = \omega'$  is the difference between  $\omega$  and the angular velocity  $\omega'$  of Io's motion.

Plasma in Jupiter's magnetosphere injected from Io (the Io plasma torus) flows past Io with a speed of about 57 km/s. The magnetic field from Jupiter at Io is 1,900 nT. The  $v \times B$  voltage induced across Io (3,630 km) is therefore 400 kV, and approximately  $10^6$ . A was observed to be flowing out of the satellite (Acuna et al. 1981; Southwood et al. 1980). It would seem plausible that the current would tend to concentrate in the volcanic plumes, which would give the current easy access to the highly conducting molten interior of Io. We would suppose that the crust, consisting of sulfur and frozen sulfur dioxide, would be a relatively poor conductor, thus directing the current to the volcanic vents. If we assume the available power ( $\sim 0.4$  TW) is equally divided between the four largest volcanic plumes, we have  $\sim 10^{11}$  W of continuous power available for each volcanic plasma arc. This is roughly equal to the kinetic energy flux of material issuing from a volcanic vent. A small fraction of this power can account for the faint auroral glow reported by Cook et al. (1981).

Figure 4.24 illustrates the basic geometry at hand. Viewed from the north Jovian and Ionian poles, Jupiter's dipole magnetic field is into the plane of the figure while the plasma flow within the torus is counterclockwise toward Io. With this orientation, the electric field is directed from Jupiter to Io. Volcanic activity on Io generally occurs within an equatorial band of  $\pm 30^\circ$  latitude.

Figures 4.25 and 4.26 are photographs of the particularly well-developed volcanic plume Prometheus (latitude  $-2.9^\circ$ , longitude  $153^\circ$ ) taken at two different aspect angles by Voyager 1. The height and width of this plume is 77 and 272 km, respectively (Strom and Schneider 1982) while the vent velocity of the gaseous material ejected is 0.49 km/s. The current flow is outward from Prometheus (i.e., the vent of Prometheus is an anode). To relate these pictures to the plasma-arc process,

we must explicitly assume that the fine particulate matter that makes the volcanic plumes visible is entrained by the plasma. Thus, as the plasma moves to form filaments, we assume that the plasma carries with it the small solid particles.

While an exact calculation of the breakdown field associated with a volcanic arc discharge requires precise knowledge about the region where the breakdown occurs,<sup>3</sup> an estimate can be made in the following way (Peratt and Dessler 1988). For a sufficiently large separation between anode and cathode electrodes, the breakdown field strength in air, nitrogen, freon, and sulfur hexafluoride is (Miller 1982),

$$E_{br} = 2.64pF^{-1} \text{ (MV/m)} \quad (4.19)$$

where  $p$  is the pressure of the ambient gas in atmospheres and  $F$  represents a field enhancement factor of order unity that depends on the shapes of the anode and cathode. Applying Eq. (4.19) to  $\text{SO}_2$ , the most common gas on Io, while setting  $F = 1$  and taking an ambient pressure of the gas near the vapor-liquid transition (the triple point for  $\text{SO}_2$  is 0.0163 atmospheres), yields  $E_{br} = 0.044 \text{ MV/m}$  (0.4 kV/cm). This value is to be compared to the breakdown field strength for lightning on earth (0.44 MV/m (4.4 kV/cm)).

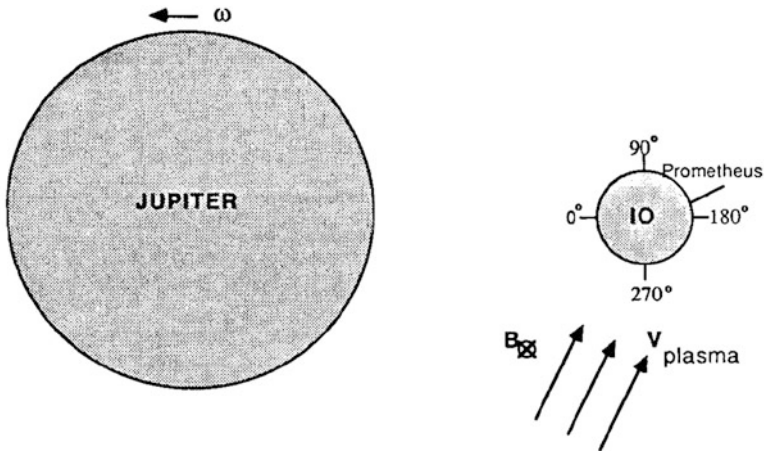


**Fig. 4.24** The Jupiter-Io system (north pole view). The rotational period of Jupiter is approximately 9 h 50 m. The orbital (synchronous) period of Io is 1.770 days. The relative velocity of the plasma torus flowing past Io is 57 km/s. Io's radius of orbit is  $4.22 \times 10^5 \text{ km}$  (Diagram is not to scale)

Substituting  $E = 0.044 \text{ MV/m}$  and into Eq. (4.12), we obtain a parabolic sheath velocity of  $v_s = 0.893 \text{ km/s}$ , close to that observed for Prometheus (0.49 km/s). It is at this velocity that gas and plasma are pushed into Io's upper atmosphere by means of the arc discharge mechanism. The volcanos effluent is concentrated into a

<sup>3</sup> Comparison of the side-on penumbra morphology (Figs. 4.20 and 4.22) to the side-on plume morphology (Fig. 4.26) suggests that the location of the electrical discharge may be well below the surface of Io.

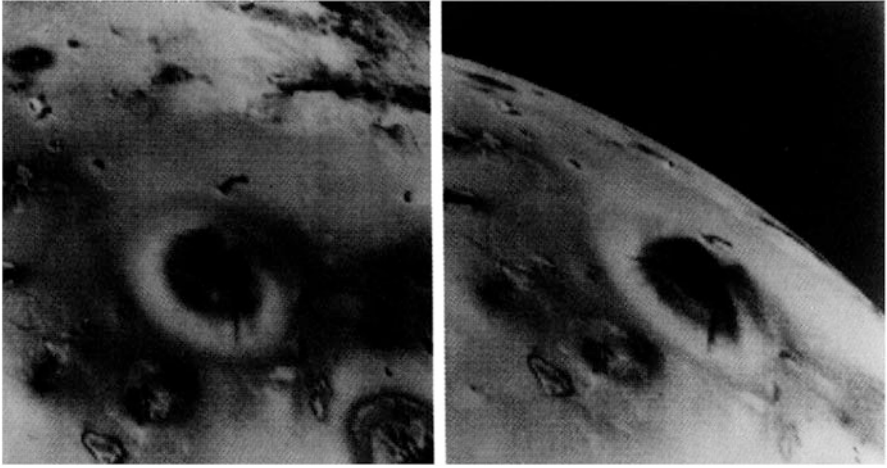


**Fig. 4.25** Voyager 1 oblique views of Prometheus's plume. The *left-hand image* was taken 2.3 h before the *right-hand image*

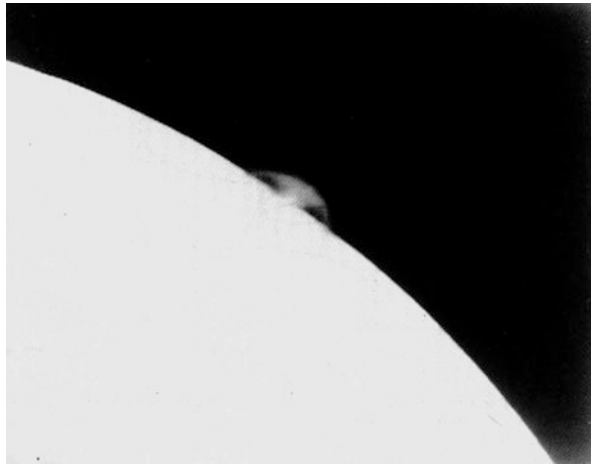


**Fig. 4.26** Horizon view of Prometheus's plume

penumbra whose morphology differs from those of ballistic or shock models in two ways. The first is the radial striations resulting from the electromagnetic pinch and accretion of matter into filaments (Figs. 4.21 and 4.25). The second is the termination of the penumbra on a narrow cathode annulus (Figs. 4.22 and 4.26).

### 4.6.3 Marklund Convection and Separation of Elements

When an electric field is present in a plasma and has a component perpendicular to a magnetic field, radial inward convection of the charged particles is possible. This situation is depicted in Fig. 4.27. Under the influence of the  $E \times B$  force, both the electrons and ions drift with the velocity

$$\mathbf{v} = (\mathbf{E} \times \mathbf{B}) / B^2 \quad (4.20)$$

so that the plasma as a whole moves radially inward. This mechanism provides a very efficient convection process for the accumulation of matter from plasma. The material should form as a filamentary structure about the twisted magnetic flux tubes, the lines of which are commonly referred to as “magnetic ropes” because of their qualitative pattern (Fig. 4.28). Magnetic ropes should tend to coincide with material filaments that have a higher density than the surroundings (this is also the case for the filaments in the current sheath of the plasma focus). The cosmic magnetic flux tubes are not directly observable themselves, but the associated filaments of condensed matter can be observed by the radiation they emit and absorb.

When a plasma is only partially ionized, the electromagnetic forces act on the non-ionized components only indirectly through the viscosity between the ionized and non-ionized constituents. From Eq. (4.20), the inward drift of matter is at a velocity  $|\mathbf{v}_r| \approx E_z / B_\phi$ . Hence, at a large radial distance  $r$ , the rate of accumulation of matter, per unit length, into a filament is

$$\frac{dM}{dt} = 2\pi r v_r \rho_m = (2\pi r)^2 \rho_m \frac{E_z}{\mu_0 I_z} \quad (4.21)$$

If the electric field is antiparallel to the current, the drift is outwards.

Marklund (1979) found a stationary state when the inward convection of ions and electrons toward the axis of a filament was matched by recombination and outward diffusion of the neutralized plasma (Fig. 4.29). The equilibrium density of the ionized component normally has a maximum at the axis. However, because of the following mechanism, hollow cylinders, or modifications of hollow cylinders of matter, will form about the flux tubes.

Because of the radiated loss of energy, the filaments cool and a temperature gradient is associated with the plasma. As the radial transport depends on the ionization potential of the element, elements with the lowest ionization potentials are brought closest to axis. The most abundant elements of cosmical plasma can be divided into groups of roughly equal ionization potentials as follows:  $H_e$  (24 eV);  $H, O, N$  (13 eV);  $C, S$  (11 eV); and  $F_e, Si, Mg$  (8 eV) (Table 1.7). These elements can be expected to form hollow cylinders whose radii increase with ionization potential. Helium will make up the most widely distributed outer layer; hydrogen, oxygen, and nitrogen should form the middle layers, while iron, silicon, and magnesium will make up the inner layers. Interlap between the layers can be expected and, for the case of galaxies, the metal-to-hydrogen ratio should be maximum near the center and decrease outwardly. Both the convection process and the luminosity increase with the field  $E_z$ .

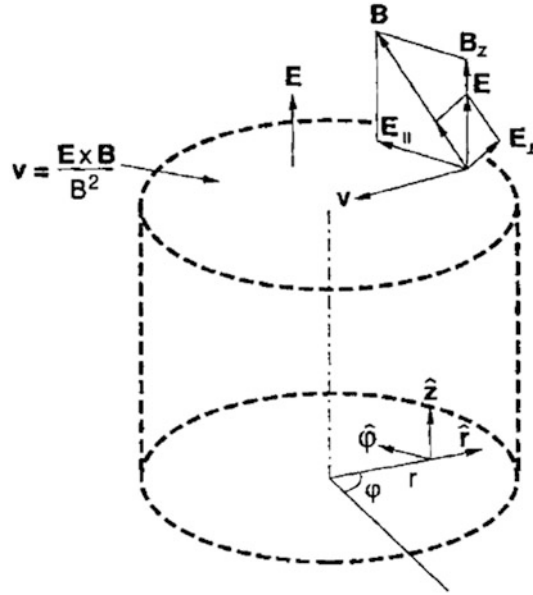


**Fig. 4.27** When the pressure is negligible the plasma acquires a drift velocity  $v$  such that the electric field in the moving plasma is parallel to  $B$ . Therefore, current flows only along the magnetic lines of force

For the case of a fully ionized hydrogenic plasma, the ions drift inwards until they reach a radius where the temperature is well below the ionization potential and the rate of recombination of the hydrogen plasma is considerable. Because of this “ion pump” action, hydrogenic plasma will be evacuated from the surroundings and neutral hydrogen will be most heavily deposited in regions of strong magnetic flux. Examples of this convection for galaxies are given in Sect. 3.11.3. In addition, [Mirabel and Morras \(1984\)](#) have detected the inflow of neutral hydrogen towards our own galaxy.

#### 4.6.4 Particle Acceleration and Runaway

The equation of motion of an electron in a region of plasma in which there is an external electric field  $E$  is (cf. Eq. (C.1))

$$m_e \dot{v} = -eE - \nu_c m_e v \quad (4.22)$$

where  $\nu_c$  is the electron-electron collision frequency associated with the so-called dynamical friction from Coulomb scattering ([Rose and Clark 1961](#)), given by

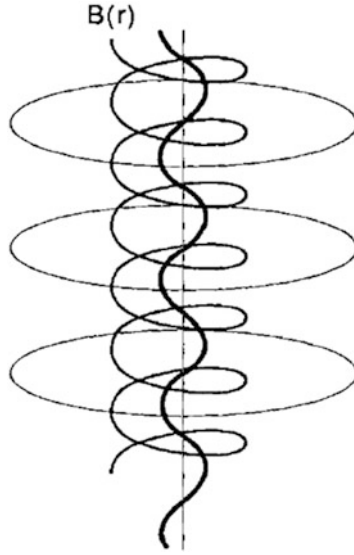


**Fig. 4.28** A “magnetic rope” with magnetic field lines shown at three different radii

$$v_c = \frac{e^4 n_e \ln \Lambda}{2\pi \epsilon_0^2 m_e^2 v^3} \quad (4.23)$$

where

$$\Lambda = \frac{12\pi (\epsilon_0 kT / e^2)^{3/2}}{n_e^{1/2}} \quad (4.24)$$

Considering only the case of electron velocities along the electric field, we may utilize the scalar form of Eq. (4.22) and write

$$\dot{v} = \frac{e}{m_e} E = \frac{e^4 n_e v \ln \Lambda}{2\pi \epsilon_0^2 m_e^2 v^3} \quad (4.25)$$

Equation (4.25) is the dual of the sum of a uniform field plus the field of a point charge.

To gain some insight into the meaning of Eq. (4.25), consider two electrons, one with initial velocity  $v(0)$  small and the other with initial velocity  $v(0)$  large. For the former, if

$$v(0) < v_{crit} = \left[ \frac{e^3 n_e \ln \Lambda}{2\pi \epsilon_0^2 m_e E} \right]^{1/2} \quad (4.26)$$

the right-hand side of (4.25) is negative and the electron eventually decelerates to a stop. For the latter,  $v(0) > v_{crit}$ , and the electron accelerates. Since Eq. (4.23) decreases with the inverse cube of the velocity, the drag force decreases as the electron accelerates, causing the electron acceleration to increase still further.



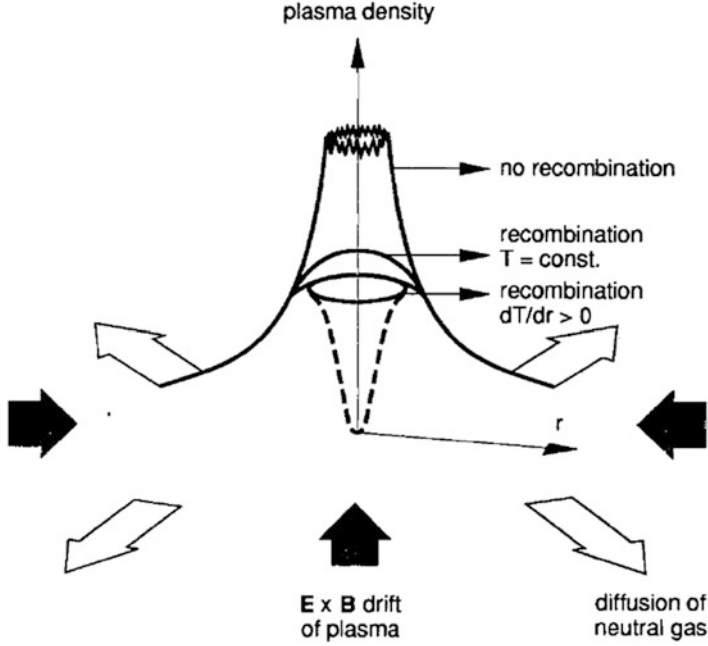


**Fig. 4.29** Plasma density profile as a function of radius sketched qualitatively for three cases: No recombination, recombination with  $T = \text{const.}$ , and recombination with a lower central temperature

This phenomenon is known as electron runaway. Electrons with an initial velocity above the threshold velocity gain speed indefinitely (within the limits of relativity), so long as the electric field is present, and “run away”, while initially slow electrons come to rest.

To determine what portion of an electron population undergoes runaway, we rewrite the critical velocity equation (4.26) in form of the kinetic energy

$$\frac{m_e v_{crit}^2}{2e} = \frac{e^2 n_e \ln \Lambda}{4\pi \epsilon_0^2 E} = 2.6 \times 10^{-17} \frac{n_e \ln \Lambda}{E}, \text{ eV} \quad (4.27)$$

We note that the threshold velocity equals the electron thermal velocity  $v_{the}$  for a field

$$E = E_D = \frac{e^3 n_e \ln \Lambda}{2\pi \epsilon_0^2 m_e v_{the}^2} = \frac{e^3 n_e \ln \Lambda}{2\pi \epsilon_0^2 kT} \quad (4.28)$$

This field is called the Dreicer field. In terms of the  $E_D$ , the critical velocity is

$$v_{crit} = v_{the} \left( \frac{E_D}{E} \right)^{1/2} \quad (4.29)$$

so that large fields  $E$  imply low  $v_{crit}$  and a large population of runaway electrons.

**Example 4.2 Runaway electrons in fusion and cosmic plasmas.** Consider a fusion plasma  $n_e = 10^{20} \text{ m}^{-3}$ ,  $E = 10 \text{ V/m}$ , and  $\ln \Lambda = 20$ . Substituting these values into Eq. (4.27) shows that electrons with energies above 5 keV will run away. Consider a cosmic plasma  $n_e = 10^3 \text{ m}^{-3}$ ,  $E = 10^{-6} \text{ V/m}$ , and  $T = 3 \text{ keV}$ . For these values, electrons with energies greater than  $0.5 \mu\text{eV}$  will run away. Thus, electrons in cosmic plasmas are readily accelerated to high energies in the presence of even very small electric fields.

Equation (4.22), and the runaway process, will be modified if a magnetic induction  $B$  is present. However, if  $E$  and  $B$  are parallel, the runaway condition is not altered. In addition, the body of electron population which attracts electrons of less than runaway speed is eroded by the escape of electrons brought up to critical speed. If the electric field persists long enough, all the electrons will eventually run away in energy.

#### 4.6.5 Field-Aligned Electric Fields as the Source of Cosmic Rays

Cosmic rays are extraordinarily isotropic on earth, having a degree of anisotropy of about 0.1 for low energy particles, then decreasing to  $\pm 5 \times 10^{-4}$  for particles approaching energies of  $10^{20} \text{ eV}$ . At one time, it was generally believed that cosmic rays were born in the shock waves produced by supernovae. However, it is now realized that the degree of anisotropy that would be produced by such shocks is far larger than that observed.

**Example 4.3 The anisotropy of charged particle fluxes from supernovae produced shock waves.** Consider the number of supernovae in our Galaxy capable of subtending a cone of cosmic ray flux of solid angle  $(D/R_{gal})^2$  on earth where  $D \sim 10^2 - 10^3 \text{ pc}$  is the size of the shock accelerating medium and  $R_{gal} \sim 10^4 \text{ pc}$ . This number is

$$N_{sn} = f_{sn} \tau_{sn} (D/R_{gal})^2$$

where the frequency of supernovae events is  $f_{sn} \sim 1/100$  years, and the duration  $\tau_{sn} \sim 10^7$  years. Thus,  $10 \leq N_{sn} \leq 500$  and the degree of anisotropy defined by  $an \equiv (2N_{sn})^{-1/2}$  is large,  $0.03 \leq an \leq 0.3$ .

Colgate (1990) points out that because of the high anisotropy of any shock wave acceleration together with the complete lack of any laboratory evidence that shock-wave/charge particle acceleration actually exists, that field-aligned electric fields are the most plausible mechanism for producing cosmic rays. This mechanism is addressed in Sect. 5.6.4.

## References

- Acuña, M.H., Neubauer, F.M., Ness, N.F.: Standing Alfvén wave current system at IO: Voyager 1 observations. *J. Geophys. Res.* **86**, 8513 (1981)
- Alfvén, H.: In: *Proceedings of the 2nd International Conference on Peaceful Uses of Atomic Energy*, Geneva, vol. 31, p. 3. United Nations, Geneva (1958)
- Alfvén, H.: *On the Origin of the Solar System*. Oxford University Press, See also *Rev. Mod. Phys.* **32**, 710. New York (1960).
- Alfvén, H.: *Cosmic Plasma*. D. Reidel, Dordrecht (1981). Chap. IV
- Alfvén, H., Fälthammar, C.-G.: *Cosmic Electrodynamics*. Oxford University Press, New York (1963)
- Alfvén, H., Wilcox, J.M.: On the origin of satellites and planets. *Astrophys. J.* **136**, 1016 (1962)
- Block, L.P., Fälthammar, C.-G., Lindqvist, P.-A., Marklund, G., Mozer, F.S., Pedersen, A., Potemra, T.A., Zanetti, L.J.: Electric field measurements on Viking: first results. *Geophys. Res. Lett.* **14**, 435 (1987)
- Bostick, W.H., Nardi, V., Prior, W.: Production and confinement of high-density plasmas. *Ann. N. Y. Acad. Sci.* **251**, 2 (1975)
- Carpenter D.L.: Whistler studies of the plasmopause in the magnetosphere IO. *J. Geophys. Res.* **71**, 693 (1966)
- Colgate, S.: E-parallel acceleration of cosmic rays, twisted magnetic fields, and collimated radio sources. Los Alamos Astrophysics Seminar, December 1990 **5**. (1990)
- Cook, A.F., Shoemaker, E.M., Smith, B.A., Danielson, G.E., Johnson, T.V., Synnott, S.P.: Volcanic origin of the eruptive plumes on IO. *Science* **211**, 1419 (1981)
- Fälthammar, C.-G.: Problems related to macroscopic electric fields in the magnetosphere. *Rev. Geophys. Space Phys.* **15**, 457 (1977)
- Fälthammar, C.-G.: Generation mechanisms for magnetic-field-aligned electric fields in the magnetosphere. *J. Geomagn. Geoelectr.* **30**, 419 (1978)
- Fälthammar, C.-G.: Non-resistive electric potential drops in cosmical plasmas. In: Arons, J., McKee, C., Max, C. (eds.) *Particle Acceleration Mechanisms in Astrophysics*. American Institute of Physics, New York (1979)
- Fälthammar, C.-G.: Magnetic-field-aligned electric fields. *ESA J.* **7**, 385 (1983)
- Fälthammar, C.-G.: Laboratory and near-earth space plasmas as a key to the plasma universe. *Laser Part. Beams* **6**, 437 (1988)
- Fälthammar, C.-G., Block, L.P., Lindqvist, P.-A., Marklund, G., Pedersen, A., Mozer, F.S.: Preliminary results from the D.C. electric field experiment of Viking. *Ann. Geophys. A* **5**, 171 (1987)
- Fälthammar, C.-G., Bohm, M., Brenning, N.: A new mechanism for parallel electric fields in space and laboratory plasmas. In: *Conference Record, IEEE International Conference on Plasma Science*, Williamsburg (1991)
- Filippov, N.V., Filippova, T.I., Vinogradov, V.P.: Dense, High-temperature plasma in a non-cylindrical Z-pinch compression, *Nucl. Fusion Suppl. Pt. 2* (1962)

- Garscadden, A.: Rydberg states: properties and applications to electrical discharge measurements. In: Proud, J.M., Leussen, L.H. (eds.) *Radiative Processes in Discharge Plasmas*. Plenum Publ. Co., New York (1986)
- Geller, R., Hopfgarten, N., Jacquot, B., Jacquot, C.: Electric fields parallel to the magnetic field in laboratory plasma in a magnetic mirror field. *J. Plasma Phys.* **12**, 467 (1974)
- Gold, T.: Electrical origin of the outbursts on IO. *Science* **206**, 1071 (1979)
- Gratton, F.T., Nardi, V., De Chiara, P., Gnani, G.: On the possibility of chaotic motion and acceleration of ions in oscillating plasma structures. IV Latin American Workshop on Plasma Physics, Buenos Aires, July 1990. Contributed papers
- Helliwell, R.A.: *Whistlers and Related Ionospheric Phenomena*. Stanford University Press, Stanford (1967)
- Heppnard, J.P., Maynard, N.C.: Empirical high-latitude electric field models. *J. Geophys. Res. Space Phys.* **92**(A5), 4467–4489 (1978–2012)
- Knight, S.: Parallel electric fields. *Planet. Space Sci.* **21**, 741 (1973)
- Lemaire, J., Scherer, M.: Ionosphere plasma-sheet field-aligned currents and parallel electric fields. *Planet. Space Sci.* **22**, 1485 (1974)
- Lemaire, J., Scherer, M.: Field-aligned current density versus electric potential characteristic for magnetosphere flux tubes. *Ann. Geophys.* **1**, 91 (1983)
- Lindberg, L., Jacobsen, C.T.: On the amplification of the poloidal magnetic flux in a plasma. *Astrophys. J.* **133**, 1043 (1961)
- Lindberg, L., Jacobsen, C.T.: Studies of plasma expelled from a coaxial plasma gun. *Phys. Fluids Suppl.* **7**, S44 (1964)
- Lindberg, L., Witalis, E., Jacobsen, C.T.: Experiments with plasma rings. *Nature* **185**, 452 (1960)
- Lundin, R., Sandahl, J.: Some characteristics of the parallel electric field acceleration of electron over discrete auroral arcs as observed from two rocket flights. *ESA Spec. Publ.* **SP-135**, 125 (1978)
- Lyons, L.R., Williams, D.J.: *Quantitative Aspects of Magnetospheric Physics*. D. Reidel, Dordrecht (1984). Chap. 4
- Marklund, G.T.: Plasma convection in force-free magnetic fields as a mechanism for chemical separation in cosmical plasmas. *Nature* **277**, 370 (1979)
- Mather, J.W.: In: Lovberg, R.H., Griem, H.R. (eds.) *Plasma Physics*, Chap. 15. Academic, New York (1971)
- Miller, R.B.: *Intense Charged Particle Beams*. Plenum, New York (1982). Chap. 1
- Mirabel, I.F., Morras, R.: Evidence for high velocity inflow of neutral hydrogen toward the galaxy. *Astrophys. J.* **279**, 86 (1984)
- Morabite, L.A., Synnott, S.P., Kupferman, P.N., Collins, S.A.: Discovery of currently active extraterrestrial volcanism. *Science* **204**, 972 (1979)
- Mozer, F.S., et al.: Satellite measurements and theories of low altitude auroral particle acceleration. *Space Sci. Rev.* **27**, 155 (1980)
- Peratt, A.L., Dessler, A.J.: Filamentation of volcanic plumes on the Jovian satellite Io. *Astrophys. Space Sci.* **144**, 451 (1988)
- Peratt, A.L., Snell, C.M., Thode, L.E.: A high power reflex triode microwave source. *IEEE Trans. Plasma Sci.* **13**, 498 (1985)

- Smith, B.A., Soderblom, L.A., Johnson, T.V., Ingersoll, A.P., Collins, S.A., Shoemaker, E.M., Hunt, G.E., Masursky, H., Carr, M.H., Davies, M.E., Cook, A.F., 2Nd; Boyce, J., Danielson, G.E., Owen, T., Sagan, C., Beebe, R.F., Veverka, J., Strom, R.G., Mccauley, J.F., Morrison, D., Briggs, G.A., Suomi, V.E. Soderblom, Johnson, Ingersoll, Collins, Shoemaker, Hunt, Masursky, Carr, Davies, Cook, Boyce, Owen, Danielson, Sagan, Beebe, Veverka, Mccauley, Strom, Morrison, Briggs, Suomi: The jupiter system through the yes of Voyager 1. *Science* **204**(4396), 951–972 (1979)
- Smith, B.A., et al.: The jupiter system through the yes of Voyager 1. *Science* **204**, 945 (1979a)
- Smith, B.A., Shoemaker, E.M., Kieffer, S.W., Cook, A.F.: The role of SO<sub>2</sub> in volcanism on Io. *Nature* **280**, 738 (1979b)
- Southwood, D.J., Kivelson, M.G., Walker, R.J., Slavin, J.A. (1980): IO and its plasma environment. *J. Geophys. Res.* **85**, 5959
- Strom, R.G., Schneider, N.M.: In: Morrison, D. (ed.) *Satellites of Jupiter*, p. 598. University Arizona Press, Tucson (1982)
- Strom, R.G., Terrile, R.J., Masursky, H., Hansen, C.: Volcanic eruption plumes on IO. *Nature* **280**, 733–736 (1979)

## Chapter 5

# Double Layers in Astrophysics

Double layers were discovered by Irving Langmuir; (who called them “double sheathes”) in his experiments with low-pressure discharges in the 1920s. Subsequently, they were observed by nearly all the pioneers in experimental plasma physics (Tonks 1931; Schönhuber 1958; Crawford and Freeston 1963; Babic et al. 1971). The double layer consists of two thin and close regions of opposite charge excess which give rise to a potential drop, and therefore an electric field, across the layer. H. Alfvén first advocated the existence of double layers in cosmic settings (1958), but proof of their existence in the earth’s magnetosphere did not come until potential probes on earth satellites made in situ measurements two decades later.

### 5.1 General Description of Double Layers

The basic phenomena under study in this chapter is illustrated in Fig. 5.1. Electrons and ions counterflow with velocities  $v_{e0}$  and  $v_{i0}$ , respectively, or with a relative drift velocity  $V_0 = v_{e0} + v_{i0}$ . Because of this counterflow, an instability or instabilities are set up within the current. The net result is a reconfiguration of the current carrying charges over a narrow region so as to cause a potential drop. Because of the potential drop a beam of electrons with instantaneous velocity  $v_{eb}$  is accelerated to the right while a beam of ions with instantaneous velocity  $v_{ib}$  is accelerated to the left. The phenomenon responsible for this behavior is called a double layer.

The classic double layer (DL) (Tonks 1958; Williams 1987; Langmuir 1929) is therefore an electrostatic structure which can appear within a current carrying plasma and sustain a significant net potential difference. The thickness is of the Debye length scale and can be very small compared to the dimensions of the region in which the DL is embedded. Internally the DL is not charge neutral and must contain at least two layers of opposite net charge (hence the term “double layer”) associated with an internal electric field (Biskamp and Chodura 1971; Carpenter and Torven 1987).

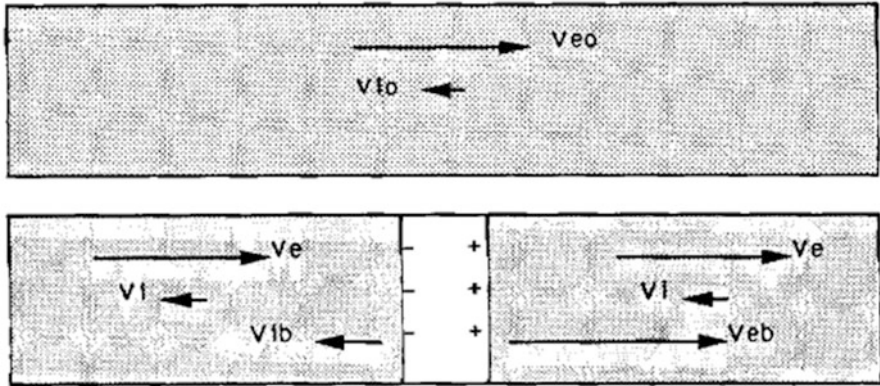


**Fig. 5.1** (Top) Condition for the development of a double layer. (Bottom) A double layer

Four populations of particles are required to produce the space-charge distribution needed to support the double layer potential. These are (i) the current-carrying streaming electrons, (ii) the current-carrying streaming ions, (iii) trapped electrons on the downstream side of the streaming electrons, and (iv) trapped ions on the downstream side of the streaming ions.

Figure 5.2 is a sketch of the potential profile, the four-particle populations, and their contributions to the space-charge distribution to support the double layer potential. The streaming electrons and ions are present because the field-aligned current is an essential ingredient of a double layer. Due to the acceleration of the streaming particles by the double layer potential, the density of each streaming particle population decreases on the downstream side. Therefore, trapped particles must be produced to ensure overall charge neutrality.

Because electrical currents in astrophysical settings are often aligned along magnetic fields, the internal electric field has a component parallel to the magnetic field. Thus, the DL is a region where ideal magnetohydrodynamics breaks down. As a whole the DL has no net charge and the surrounding plasma may be perturbed by extended presheaths matching the conditions at the edges of the DL to those in the undisturbed plasma.

A basic property, which is of particular interest for applications to astrophysics, is that particles traversing the DL are directly accelerated by the net potential difference,  $\phi_{DL}$ . The DL acts as an electrical load dissipating energy at a rate  $I\phi_{DL}$  (where  $I$  is the total current through the DL), which is transformed to the directed kinetic energy of accelerated particles. Thus, the DL exhibits inertial resistance. This should be contrasted with the effect of ohmic or anomalous resistance, which is to transform electrical energy to thermal or random particle motions. Since the DL acts as a load, there has to be an external source maintaining the potential difference  $\phi_{DL}$  and driving the current  $I$ . In the laboratory this source is usually an electrical power supply, whereas in space it may be the magnetic energy stored in an extended current system Eq. (3.36), which responds to a change in current with an inductive voltage. The material in this chapter is based primarily on the in-depth reviews of Block (1978), Carlqvist (1982, 1986), Borovosky (1984a), Borovosky and Joyce (1983) and Raadu (1989).

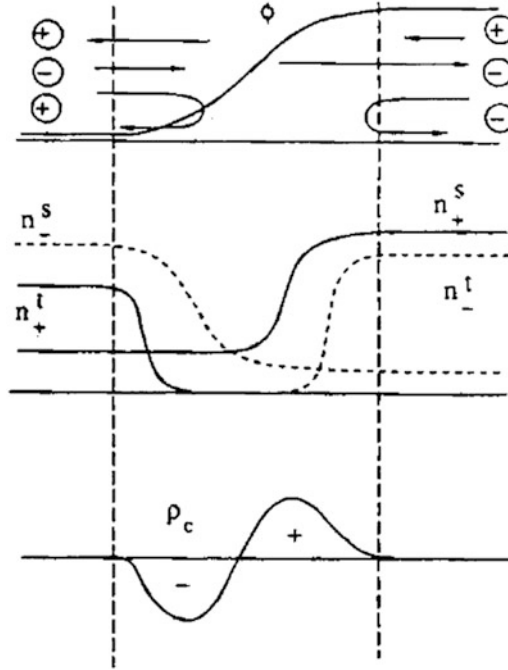


**Fig. 5.2** A sketch of the double layer potential  $\phi$ , the trapped and streaming ions and electrons, the space charge due to each of the four populations of particles, and the net space charge required to support the double layer potential

## 5.2 The Time-Independent Double Layer

### 5.2.1 One-Dimensional Model

It is instructional to first consider a one-dimensional, time-independent model of a double layer with a high potential drop (Carlqvist 1986). In this model the layer is situated between the cathode boundary at  $x = 0$  and the anode boundary at  $x = d$  (Fig. 5.3). The potential is set  $\phi = 0$  at  $x = 0$  and  $\phi = \phi_{DL}$  at  $x = d$  so that the potential drop across the layer is  $\phi_{DL}$ . Electrons and ions are emitted with zero velocity from the cathode boundary and anode boundary, respectively. The ions and electrons inside the double layer are accelerated in opposite directions along the magnetic field by the electric field. The ions accelerate towards the cathode while the electrons accelerate towards the anode. Since the initial velocity of the particles is zero, conservation of energy dictates the potential energy be balanced by the kinetic energy so that

$$Ze\phi' = m_i c^2 (\gamma - 1) \quad (5.1)$$



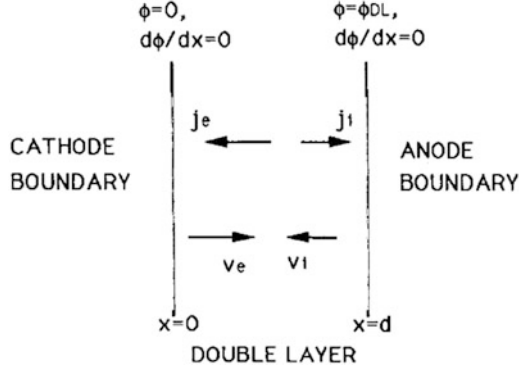


**Fig. 5.3** Schematic of a one-dimensional double layer model. The DL has the thickness  $d$  and sustains a potential drop  $\phi_{DL}$ . Ions and electrons are emitted with zero velocity from the anode boundary and cathode boundary, respectively, and accelerated in opposite directions by a strong electric field

for the ions, and

$$e\phi = m_e c^2 (\gamma_e - 1) \quad (5.2)$$

for the electrons, where  $Ze$  is the ion charge and the Lorentz factors are  $\gamma_i \equiv (1 - \beta_i^2)^{-1/2}$ , and  $\gamma_e \equiv (1 - \beta_e^2)^{-1/2}$  for ion and electron velocities  $\beta_i$  and  $\beta_e$  (Eq. (10.18)), respectively. At the potentials  $\phi_i$  and  $\phi_e$ ,  $\beta_i$  and  $\beta_e$  are given by

$$\beta_i = \frac{(\phi'^2 + 2\phi_i\phi')}{\phi_i + \phi'} \quad (5.3)$$

and

$$\beta_e = \frac{-(\phi^2 + 2\phi_e\phi)}{\phi_e + \phi} \quad (5.4)$$

where  $\phi_e = m_e c^2 / e = 511 \text{ kV}$  is the rest mass energy of electrons,  $\phi_i = m_i c^2 / Ze = 0.939 \text{ GV}$  is the rest mass energy of ions, and  $\phi' = \phi_{DL} - \phi$ . The current densities of the ions and electrons are

$$j_i = Zen_i \beta_i c$$

and

$$j_e = -en_e \beta_e c$$

respectively. Combining Eqs. (5.1) and (5.2) with Eqs. (5.3) and (5.4) and inserting the particle densities in Poisson's equation, we find

$$\frac{d^2 \phi}{dx^2} = \frac{e(Zn_i - n_e)}{\epsilon_0} = \frac{j_e}{\epsilon_0 c} \frac{\phi_e + \phi}{(\phi^2 + 2\phi_e\phi)^{1/2}} - \frac{j_i}{\epsilon_0 c} \frac{\phi_i + \phi'}{(\phi'^2 + 2\phi_i\phi')^{1/2}} \quad (5.5)$$

Multiplying both sides of Eq. (5.5) with  $2d\phi/dx = -2d\phi'/dx$  and integrating, yields,

$$\left(\frac{d\phi}{dx}\right)^2 = \frac{2j_e}{\epsilon_0 c} (\phi^2 + 2\phi_e \phi)^{1/2} + \frac{2j_i}{\epsilon_0 c} (\phi'^2 + 2\phi_i \phi')^{1/2} - C_1 \quad (5.6)$$

This equation describes the momentum balance in the layer and may be cast in a more familiar form

$$n_i \gamma_i m_i v_i^2 + n_e \gamma_e m_e v_e^2 - \frac{1}{2} \epsilon_0 E^2 = C_1$$

The constant of integration  $C_1$  is obtained by inserting the boundary conditions  $d\phi/dx = 0$  for  $\phi = 0$  and  $\phi = \phi_{DL}$  in Eq. (5.4). This is given by

$$C_1 = \frac{2j_e}{\epsilon_0 c} (\phi_{DL}^2 + 2\phi_e \phi_{DL})^{1/2} = \frac{2j_i}{\epsilon_0 c} (\phi_{DL}^2 + 2\phi_i \phi_{DL})^{1/2} \quad (5.7)$$

### 5.2.2 Ratio of the Current Densities

From Eq. (5.7) the ratio of the ion current density to the electron current density is

$$\frac{j_i}{j_e} = \left( \frac{\phi_{DL} + 2\phi_e}{\phi_{DL} + 2\phi_i} \right)^{1/2} \quad (5.8)$$

For the nonrelativistic double layer  $\phi_{DL} \ll \phi_e \leq \phi_i$  and Eq. (5.8) reduces to [Carlqvist \(1982\)](#)

$$\frac{j_i}{j_e} \approx Z^{1/2} \left( \frac{m_e}{m_i} \right)^{1/2} \quad (5.9)$$

Equation (5.9) is referred to as the Langmuir condition. For relativistic double layers ( $\phi_{DL} \gg \phi_i \geq \phi_e$ ), and Eq. (5.8) reduces to

$$\frac{j_i}{j_e} = 1 - \frac{\phi_i}{\phi_{DL}} + \frac{\phi_e}{\phi_{DL}} \approx 1 \quad (5.10)$$

### 5.2.3 The Potential Drop

We can integrate Eq. (5.6) to find the potential drop of the double layer as a function of the total current density  $j = j_i + j_e$  and the thickness of the layer  $d$ . For nonrelativistic double layers, [Langmuir \(1929\)](#) found by numerical integration

$$\phi_{DL} = \left\{ \frac{9}{4\epsilon_0 C_2} \left( \frac{m_e}{2e} \right)^{1/2} \left[ 1 + \left( Z \frac{m_e}{m_i} \right) \right]^{-1} j d^2 \right\}^{2/3} \quad (5.11)$$

Here  $C_2$  is a constant having the value 1.865 (Raadu 1982). For relativistic double layers a direct integration of Eq. (5.6) yields

$$\phi_{DL} = \left( \frac{\phi}{4\epsilon_0 c} j d^2 \right)^{1/2} \quad (5.12)$$

The potential drop of both the nonrelativistic and relativistic double layers depend on the product  $j d^2$ . Note also that the relativistic double layer is strongly influenced by the mass-to-charge ratio of the ions. In Fig. 5.4 the double layer potential  $\phi_{DL}$  has been plotted as a function of  $j d^2$  for double layers carrying electrons and two kinds of ions ( $H^+$ ,  $F_e^+$ ). Included in the figure is also a layer which, instead of ions, carries positively charged dust grains (Appendix C). The mass and charge chosen for the grains are  $m_g = 10^{-20}$  kg and  $Z_g e = 10^2 e$ , respectively, being constant with a radius  $r_g = 1.4 \times 10^{-8}$  m, a density of  $\rho_{mg} = 10^3$  kg m $^{-3}$ , and a potential  $\phi_g = 10^4$  V of the grains.

### 5.2.4 Structure of the Double Layer

The charge distributions in the relativistic double layer are illustrated in Fig. 5.5. The density of the positive charges  $Zn_i$  shows a spike close to the anode surface and is almost constant in the rest of the double layer. The spike is caused by rapid ion acceleration away from the anode. A similar variation is found for the electron density  $n_e$  near the cathode surface. The negative spike is much thinner than the positive spike because of the smaller mass of the electrons. In order for charge neutrality to prevail in the layer as a whole, the almost constant charge level of the electrons must be slightly larger than that of the ions. The charge distribution in the layer consists, approximately, of a positive surface charge at the anode surface and a small and uniform negative charge density in the rest of the layer. For a constant current density, the density of the surface charge remains constant and independent of the thickness of the relativistic layer (Goldsworthy et al. 1986; Jones and Gisler 1986; Peratt and Jones 1986).

### 5.2.5 Kinetic Description

Mathematically, double layers are a subset of the Bernstein-Greene-Kruskal (BGK) solutions (Bernstein et al. 1957; Ichimaru 1973) of the Poisson-Vlasov equations for constant-profile electrostatic potential structures, moving at a constant speed or stationary in a plasma. The BGK solutions include double layers, electrostatic shocks, ion-acoustic solitons, and nonlinear wave trains of any potential form. In the moving frame of a constant-profile constant-speed potential structure, the Vlasov equation (Eq. (2.1) in the absence of collisions) becomes time independent and can be written as

$$v \frac{\partial f_s}{\partial x} - \frac{q_s}{m_s} \frac{\partial \phi}{\partial x} \frac{\partial f_s}{\partial v} = 0 \quad (5.13)$$

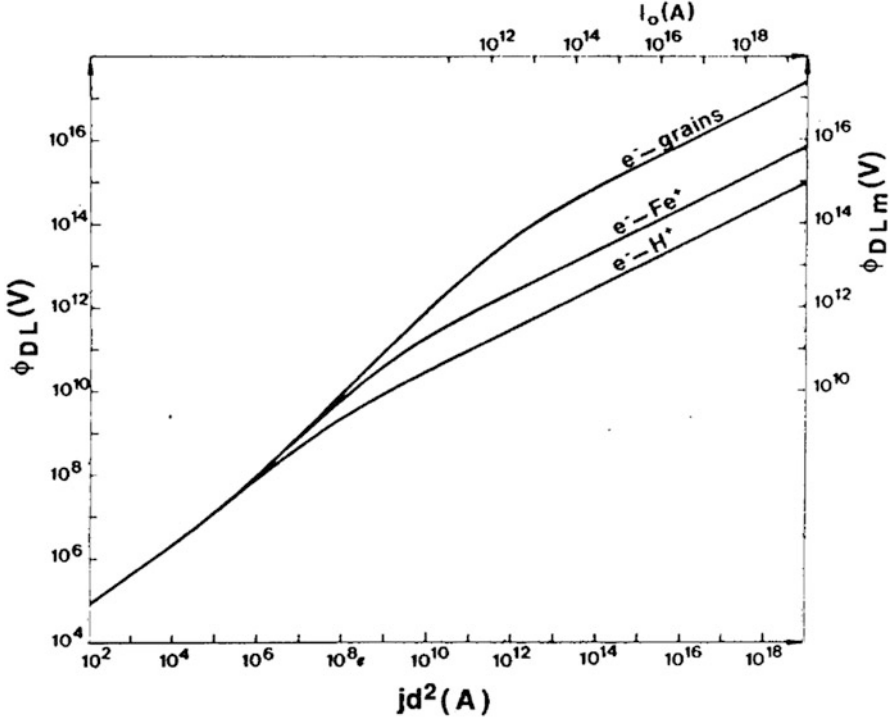


**Fig. 5.4** Potential drop  $\phi_{DL}$  (left-hand vertical scale) as a function of  $jd^2$  (lower horizontal scale) shown for three strong one-dimensional double layers consisting of (1) electrons and protons, (2) electrons and singly ionized iron ions, and (3) electrons and dust grains of mass  $m_g = 10^{-20}$  kg and positive charge  $10^2 e$ . Notice that the three curves practically coincide in the nonrelativistic regime but differ significantly in the relativistic regime. The diagram also illustrates the maximum potential drop  $\phi_{DLm}$  (right-hand vertical scale) as a function of the filamentary current  $I_0$  (upper horizontal scale) for relativistic double layers in a current filament (Courtesy of P. Carlqvist)

where the subscript denotes the particle species  $f_s$  is the distribution function, and  $\phi$  is the electrostatic potential. Solutions of the time-independent Vlasov equation,  $f_s$ , can be any function of the constants of particle motion. In an unmagnetized plasma, a constant of the motion is the total energy (i.e., the sum of the kinetic and potential energies). Hence a general solution of Eq. (5.13) can be written as

$$f_s = f_s(v^2 + 2q_s\phi/m_s) \quad (5.14)$$

The number densities of the electrons and ions can be calculated from the distribution function  $f_s$ . Thus, using Eq. (2.2) in velocity space, Poisson's equation (1.3) can be written as (Kan and Akasofu 1989; Akasofu 1988)

$$\frac{\partial^2 \phi}{\partial x^2} = \frac{e}{\epsilon_0} \left[ \int_{-\infty}^{\infty} d^3v f_e - \int_{-\infty}^{\infty} d^3v f_i \right] \quad (5.15)$$

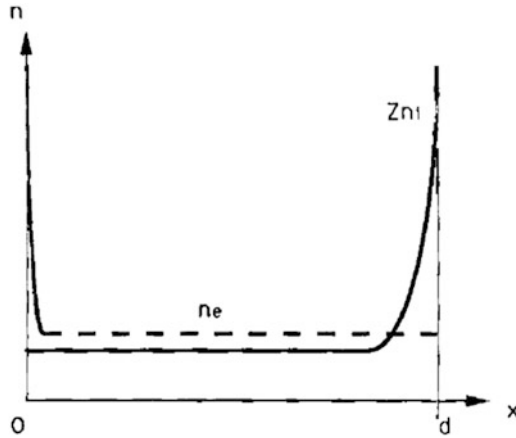


**Fig. 5.5** Schematic diagram illustrating the densities of positive ion charges  $Zn_i$ , and of negative charges (electrons)  $n_e$  as a function of  $x$  for a one-dimensional DL. The resulting charge distribution may roughly be described as a positive surface charge at the anode boundary  $x = 0$ , and an equal but negative charge distributed uniformly in the rest of the DL

$$\begin{aligned}
 &= \frac{e}{\epsilon_0} [n_e(\phi) - n_i(\phi)] \\
 &= \Psi(\phi)
 \end{aligned}$$

where the number densities  $n_e$  and  $n_i$  are functions of the electrostatic potential  $\phi$ , as can be seen from Eq. (5.14) upon integration over the velocity space. The third equality is just a further simplification in notation. A standard method for solving the nonlinear differential of the type of Eq. (5.15) is to treat it as an equation of motion for the fictitious particle in a pseudo potential  $\Psi$ , in which “ $\phi$ ” is taken to be the “coordinate” and “ $x$ ” is taken to be the “time.” The double layer solution to Eq. (5.15) exists if  $\Psi(\phi)$  has the appropriate form as shown in Fig. 5.6. In this case, the fictitious particle which starts from point A will roll down the potential well  $\Psi$  and climb back up to stay at point B. As the fictitious particle moves from A to B in Fig. 5.6, the electrostatic potential  $\phi$  makes a monotonic transition from  $\phi_A$  to  $\phi_B$  as required by the double layer. To ensure that  $\phi_A$  and  $\phi_B$  are asymptotic states of the double layer potential,  $\Psi$  must be maxima at points A and B. To ensure that the transition from A to B can take place,  $\Psi$  must have a minimum between A and B. Thus, the conditions for the existence of double layer solutions are

$$(1) \Psi < 0, \phi_A < \phi < \phi_B \quad (5.16)$$

$$(2) \Psi_A = 0, \Psi'_A = 0, \Psi_B = 0, \Psi'_B = 0, \quad (5.17)$$

$$(3) \Psi''_A < 0, \Psi''_B < 0, \quad (5.18)$$

Double layer solutions are guaranteed if the electron and ion distribution functions are such that the resulting  $\Psi$  satisfies Eqs. (5.16)–(5.18).

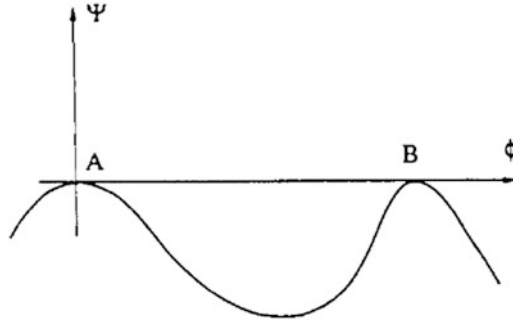


**Fig. 5.6** A sketch of the pseudo potential  $\Psi$  as a function of the double layer potential  $\phi$

### 5.3 Particle-in-Cell Simulation of Double Layers

By their very nature, double layers are nonuniform in density and produce particle beams with non-Maxwellian velocity distributions. Moreover, the formation of double layers is a time-dependent problem. For these reasons, the evolution of double layers is often studied by numerical simulation.

Numerical simulation has certain advantages over laboratory experiment and space-satellite observation. Numerical diagnostics do not perturb the system. Additionally, the orbits of the particles and their phase-space densities, easily obtained from simulations, are nearly impossible to obtain from real plasmas, and instantaneous multi-point measurements are impractical in space plasmas and strongly perturbing in the laboratory. Moreover, the electrons and ions can be delineated in a simulation and help to unfold the physical mechanisms at work. This is impossible in real plasmas. The basic problems of double layers that simulations hope to solve are as follows

1. What is their geometry and structure and how is this related to the plasma parameters?
2. What is their generation mechanism?
3. What are their stability properties?

Double layers have been simulated by two types of computer programs: particle codes and Vlasov codes. In particle codes large numbers of particles are moved according to Eqs. (1.1)–(1.5) (Chap. 8). Vlasov simulations manipulate particle distribution functions  $f(x, v)$  which are resolved on a position-velocity grid.

These two methods are equivalent in the limits of infinite numbers of particles, vanishingly small time-steps, and infinite spatial resolution. Each type of simulation has its advantages: boundary conditions on the distribution functions being easier to implement with the Vlasov method and magnetized and multi-dimensional plasmas being easier to analyze with the particle method. We utilize the particle approach throughout; the Vlasov method is reviewed by Borovsky (1984).

### 5.3.1 Simulations of the Two-Stream Instability

Since current-conducting plasma can form double layers once a threshold in current density is passed, it is of some interest to examine the events leading up to double layers in current flows. The flow of electrons through ions is subject to the Buneman (two-stream) instability as given by the linear treatment of Sect. 2.7.2. As the formation of a double layer involves trapped populations of electrons and ions, an extension of the linear analysis to quasilinear and nonlinear regimes is necessary.

Some indication that the Buneman instability might lead to double layers is given by the fact that plasma is unstable to an electron-ion two stream instability if the drift velocity of the electrons exceeds the electron thermal velocity,  $V_0 > 1.3v_{Te}$  (Buneman 1959), while theory (Block 1972; Carlqvist 1972) and experiments (Torvén and Andersson 1979) have shown the threshold for strong double layers<sup>1</sup> is  $V_0 > v_{Te}$ .<sup>2</sup> Additionally, both phenomena are electrostatic in nature.

The nonlinear evolution of the Buneman instability was studied by Hirose and Langdon (1981) who employed a one-dimensional PIC simulation model of a force-free plasma ( $E_z = 0$ ). Under the condition  $V_0 \gg v_{Te}$  the Buneman instability can develop with the maximum growth rate and frequency,

$$\Gamma = \frac{\sqrt{3}}{2} \left( \frac{m_e}{2m_i} \right)^{1/3} \left[ 1 - \frac{1}{2} \left( \frac{m_e}{2m_i} \right)^{1/3} \right] \omega_{pe} \quad (5.19)$$

$$\omega = \frac{1}{2} \left( \frac{m_e}{2m_i} \right)^{1/3} \left[ 1 + \frac{1}{2} \left( \frac{m_e}{2m_i} \right)^{1/3} \right] \omega_{pe} \quad (5.20)$$

at resonance  $kV_0 = \omega_{pe}$ . The Buneman instability is “strong” (i.e.,  $\Gamma > \omega$ ). However, the linear regime cannot persist more than a few growth periods because of strong nonlinear effects. These nonlinear effects are (i) the deceleration of the electron beam (anomalous resistivity), (ii) consequent electron heating, (iii) modification of  $\Gamma$  and  $\omega$ , and (iv) electron trapping.

There are two time scales of interest in the nonlinear evolution of the Buneman instability. The first is the time at which the exponential growth  $\exp^{\gamma t}$  terminates (Fig. 5.7). The second is the time when electron trapping sets in. Figure 5.7 shows that after electron trapping begins, the electric field energy density oscillates at twice the ion plasma frequency. (The oscillation has the nature of a standing wave; the electric field and ions exchange energy at this frequency. It is not a complete standing wave since neither field nor ion kinetic energy become zero.) This oscillation is

<sup>1</sup> A DL is said to be “strong” if the energies acquired by the ions and electrons accelerated by the potential difference  $\phi_{DL}$  are very large compared to the energies of the incoming and reflected particles. The internal DL structure is then determined by the accelerated particles, which may be treated approximately as cold beams.

<sup>2</sup> This *Bohm Criterion* is a condition for existence of strong double layers with a Maxwellian distribution of trapped ions (Bohm and Torven, 1987).

a manifestation of strong ion oscillations at the nonlinear stage of the instability. The role of the Buneman instability is to create large amplitude ion density perturbations at a wavelength that corresponds to the most unstable mode.

The following sequence of events lead to electron trapping. When the field energy reaches a saturation plateau, the electron drift velocity  $V_0$  approaches zero and then takes on negative values. When this occurs, the linear assumption of electrons freely streaming through ions is no longer valid. The electrons begin to reflex in the axial coordinate and rotate in phase space. This is depicted by the phase space vortices as shown in Fig. 5.8. The phenomena observed resembles that associated with the Kelvin-Helmholtz fluid instability.

The trapped electrons follow different orbits with different periods due to the nonadiabatic nature of the trapping. This causes the phase space “smearing” seen at later times in the simulation. The region for which  $V_0 = 0$  and a substantial number of electrons are reflected backwards is called a virtual cathode. Hirose et al. did not observe reflexing in ion motion but did note that the kinetic energy of the ions acquired 10 % of the initial electron drift energy.

Boris et al. (1970) studied the two-stream instability when  $E_z \neq 0$ . In their simulation a current was driven by imposing a axial electric field in the simulation region. They simulated an electron-positron plasma with periodic boundary conditions in both one and two dimensions. The electrons leaving the simulation region to the right, or the positrons leaving to the left, were re-introduced at the opposite boundary at the same exit vertical position (2D) and same exit velocity. Since  $m_i = m_e$ , the growth rate is large Eq. (5.19) and phase space vortices rapidly appear. Because

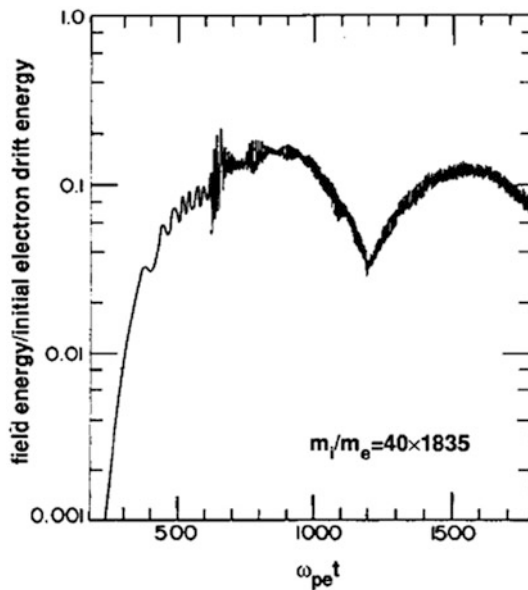


**Fig. 5.7** Time evolution of electric field energy density for an argon plasma obtained by computer simulation. The system length in the simulation was chosen as one wavelength of the most unstable mode (After Hirose and Langdon 1981)



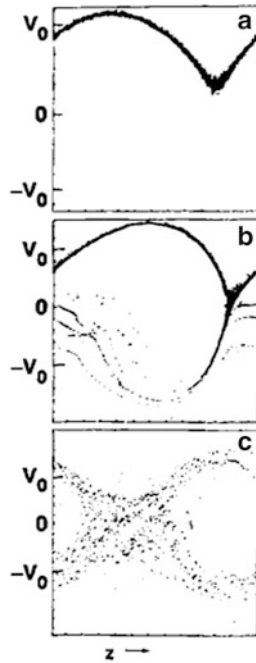


**Fig. 5.8** Electron phase space diagram. (a)  $t = 38$ . (b)  $t = 56$ . (c)  $t = 68$

of the periodic boundary conditions and the axial electric field, collective runaway of some of the electrons was observed. One of their observations was that electron heating by the two-stream instability tended to conserve the condition  $v_{Te} \approx V_0$  as the drift velocity increased.

### 5.3.2 Simulations of Double Layers

Simulations of double layers may involve one or two dimensions in space. The one dimensional system requires far less central processor time but suffers from excluding transverse particle motions associated with expansion or contraction, heat loss at surfaces, and a realistic magnetic field strength (the magnetic field strength may be taken as infinite in a 1D simulation since there can be no transverse losses). Two dimensional simulations may be run with or without the presence of a magnetic field.

To date, almost all PIC simulations of double layers have been electrostatic; again the cost of running a fully electromagnetic simulation is a major consideration.

In PIC simulation, boundary conditions must be specified for both the fields and the particles. For field conditions, one may either specify a particular boundary as being metallic (with tangential electric fields set to zero), wave transmitting as in

free-space, or an axis of symmetry. Conductors may be placed at or within the boundaries and their potentials fixed or allowed to float with respect to some reference conductor. The conductors are often made “transparent” to act as grids, so that particles may accelerate through potential gradients. Sometimes a periodic field or potential boundary condition is specified. For this case  $\phi(0) = \phi(L)$ , where  $L$  is the dimension of the system. Since a double layer has a potential drop, periodic field boundary conditions may only be used when the double layer is small compared to the system length.

The particle boundary conditions may be reflecting, absorbing, or periodic. If periodic,  $v_{e,i}(0) = v_{e,i}(L)$ . Much has been learned about the nature of double layers from periodic boundary conditions. However, since the electron and ion beam velocities are unidirectional, the double layer can be simulated only for times shorter than a particle transit time. For this reason, periodic particle boundary conditions do not allow the full growth of double layers.

In nonperiodic simulations neither the potential or the particle velocity vectors are periodic. Nonperiodic simulations can either have a floating or self-adjusting potential, or else have a fixed potential, across the system. The first case corresponds to a constant current source; the second case is a constant voltage source. Both are appropriate to study double layers which appear as elements in an electric circuit.

## 5.4 Double Layers in Current Filaments

Observations show that electric currents in cosmic plasmas often tend to flow in thin filaments or sheets. Particularly in filaments, the current density may reach comparatively high values. Hence, as suggested by laboratory experiments, the conditions for double layer formation in filaments are optimal.

A double layer that occurs in a current filament cannot, however, be strictly one-dimensional but must constitute a two-dimensional or three-dimensional structure. To clarify the physics of such a layer as studied in 2D simulations, we shall consider the following simple model.

Consider an electric circuit which contains a plasma filament. The filament has the radius of cross section  $a$  and carries a current density  $j_0$  so that the total filamentary current is  $I_0 = \pi a^2 j_0$ . The length scale of the circuit is  $l$  implying an inductance of the order  $L \approx \mu_0 l$ . Hence, the magnetic energy Eq. (3.39)

$$W_B = \frac{1}{2} L I_0^2 \approx \frac{1}{2} \mu_0 l I_0^2 \quad (5.21)$$

is stored in the circuit.

We now assume that a double layer with the potential drop  $\phi_{DL}$  is formed in the filament. Inside the layer, stored magnetic energy is released as kinetic energy of the particles accelerated through the layer. The power developed by the layer is

$$P_{DL} \approx I_0 \phi_{DL} \quad (5.22)$$

Hence, we obtain the time constant for the release of the stored energy

$$\tau_B = \frac{W_B}{P_{DL}} \approx \frac{\mu_0 I_0}{2\phi_{DL}} \quad (5.23)$$

The ions and electrons accelerated in the double layer form beams when leaving the layer (Fig. 5.1). These beams exert a pressure upon the plasma surrounding the layer. As a result of this, the double layer may expand (or explode). The expansion leads to a growing potential drop across the layer and even larger beam pressures.

As long as the double layer has a thickness  $d$  that is small compared with its radial extension  $a$ , the one-dimensional theory is approximately applicable. However, if the thickness grows larger, a two-dimensional treatment becomes necessary.

In order to get an idea of what the potential drop of the double layer may be in this latter case we consider a capacitor consisting of two circular plates of radius  $a$  separated by the distance  $d$ . The two plates are charged with the constant surface charge densities  $+\sigma_C$  and  $-\sigma_C$ . When  $d \ll a$  the potential drop between the plates is

$$\phi_C = \sigma_C d / \epsilon_0 \quad (5.24)$$

(i.e., the same as in a purely one-dimensional geometry). The potential  $\phi_C$  is then proportional to the separation  $d$ . For larger separation,  $\phi_C$  grows more slowly with  $d$ . Finally, when  $d \gg a$  the potential drop tends to the constant and maximum value

$$\phi_{Cm} = \sigma_C a / \epsilon_0 \quad (5.25)$$

Notice that Eq. (5.25) may be formally obtained from the potential drop in the one-dimensional case by putting  $d = a$ .

The charge distribution in the relativistic double layer is in several respects similar to the charge distribution in the capacitor considered above. In both cases there is a pronounced charge separation while the total charge is equal to zero. Furthermore, the positive “surface” charge density at the anode boundary of the relativistic double layer appears to be independent of the thickness of the layer, just as the surface charge density of the capacitor is independent of the separation between the plates. Hence, when the thickness of the double layer  $d$  is much larger than the radius  $a$  we should expect the potential drop of the layer to approach the maximum value

$$\phi_{DLm} = \left( \frac{\phi_i j_0 a^2}{4\epsilon_0 c} \right)^{1/2} \quad (5.26)$$

corresponding to the one-dimensional potential drop given by Eq. (5.12) with  $d = a$  and  $j = j_0$ . In terms of the filamentary current  $I_0$ , Eq. (5.26) may be rewritten as

$$\phi_{DLm} = \left( \frac{\phi_i I_0}{4\pi\epsilon_0 c} \right)^{1/2} \quad (5.27)$$

Thus, the maximum potential drop of the relativistic double layer is a function of the *total current* rather than of the current density. In Fig. 5.4  $\phi_{DLm}$  is shown as a function of  $I_0$  in the relativistic regime.

The potential  $\phi_{DLm}$  as described by Eq. (5.27) constitutes the maximum potential drop that can be sustained by the double layer. One condition for to be approached is, as we have seen above, that the double layer expands so that its thickness becomes larger than its radius. There is, however, another condition which depends on the circuit that also has to be fulfilled if  $\phi_{DL}$  is to approach  $\phi_{DLm}$ . Due to the fact that the magnetic energy stored in the current filament cannot be released faster than the Alfvén travel time Eq. (2.22) along the filament, there is an upper limit to the power that can be supplied by the circuit. For  $\phi_{DLm}$  to be reached, this power has to be at least equal to the maximum power of the double layer  $I_0\phi_{DLm}$ . This condition seems to be well met in cosmic circuits.

## 5.5 Basic Properties of Double Layers

### 5.5.1 Double Layers as a Surface Phenomena

If an electrical discharge is produced between an anode and a cathode (Fig. 5.9), a cathode sheath forms near the cathode and serves to accelerate electrons that carry a current through the plasma. This sheath, a “virtual cathode,” is one layer of the double layer. Similarly, a “virtual anode” is set up near the anode, protecting the plasma from this electrode. Again, a space charge layer constitutes the border between the double layer and the plasma. The double layers carry electric currents.

The lateral limitation of the plasma is also produced by double layers, which reduce and slow the escape of fast electrons and also accelerate ions outwards, so that ambipolar diffusion is established (no net current). The walls of an enclosing vessel take on a negative charge while a positive space charge layer forms to act

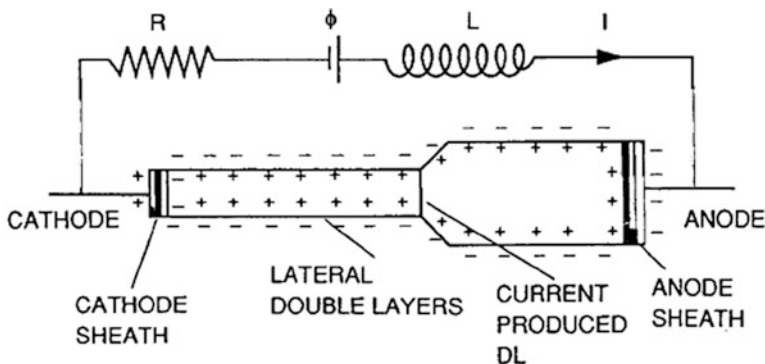


Fig. 5.9 Sheaths and double layers associated with an electric discharge

as a border between the double layer and the contained plasma. If the discharge constricts itself, the walls can be removed (without removing the space charge), and the net electric current is zero in the lateral double layers.

If the plasma is inhomogeneous in chemical composition, density, and electron temperature, double layers may form to “cellularize” the plasma into regions which are, more or less, homogeneous. For example, Birkeland currents flowing between the ionosphere and magnetosphere may produce a series of double layers as the currents flow through regions with different densities.

There are innumerable variations and complications of the cases we have discussed, just as biological cell walls show innumerable variations. Another example of this is the formation of a double layer when the current through a plasma is increased by increasing the applied voltage. The double layer so formed takes up part of the voltage and thereby “clamps” the current to some threshold value. Hence, the plasma divides itself into two cells, analogous to what a biological cell does when it gets a large energy input.

The voltage difference  $\Delta\phi$  over a double layer is usually of the order 5–10 times the equivalent of the temperature  $kT_e/e$ . However, if there are two independent plasmas produced by two different sources, the energy may be as high as 100–1,000  $kT_e/e$  in the double layer produced between the plasmas.

### 5.5.2 Noise and Fluctuations in Double Layers

Concomitant with double layers are noise and rapid fluctuations. [Lindberg \(1982\)](#) found that noise (i.e., rapid variations within a broad spectral band) was associated with a broadening of the energy spectrum of the electrons. The effect of noise is to scatter the electrons in the beam that is produced within a double layer so that plasma expansion across the confining magnetic field is possible. The noise scattering mechanism can greatly exceed the scattering due to collisions between electrons.

### 5.5.3 Exploding Double Layers

Since double layers form in electrical currents, the double layer itself can be considered an element within the complete electrical circuit. Figure 5.10 depicts a simple series circuit in which a current  $I$  flows that contains a generator, motor, resistance, inductance, and a double layer.

If  $\phi > 0$ , we have a generator transferring plasma power  $\phi I$  into the circuit; if  $\phi < 0$  we have a motor transferring circuit energy into kinetic energy of the plasma. The circuit also has a resistance  $R$  which dissipates power  $I^2 R$  into heat, and an inductance  $L$  in which circuit energy is stored (Eq. (3.39)).

In most cosmic plasma situations the individual circuit elements must be replaced with elements that are distributed over cosmic distances. Thus, even the conducting

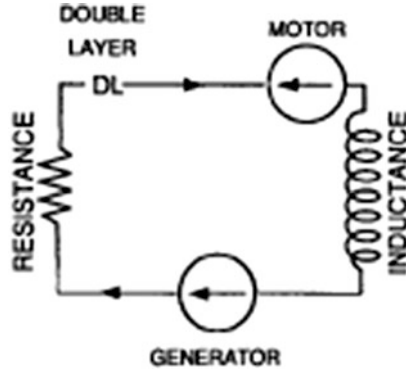


**Fig. 5.10** Series circuit containing a voltage source, resistance, inductance, motor, and double layer. Circuit energy in the “motor” is used to accelerate the plasma

“wire” itself, connecting the circuit elements, must be replaced by a transmission line representation of the current-carrying, field-aligned, pinched cosmic plasma filament conductors (Appendix A).

Every circuit that contains an inductance  $L$  is intrinsically explosive. The inductive energy Eq. (3.39) can be tapped at any point of the circuit. Any interruption of the current  $I$  results in the transfer of the inductively stored energy to the point of interruption. By its nature, this point is most often a double layer which then releases energy at a rate

$$P = I\phi_{DL} \quad (5.28)$$

where  $\phi_{DL}$  is the voltage drop across the double layer. This energy is mainly used for accelerating charged particles, with a small percent released in the generation of noise. Secondary effects associated with the particle acceleration include localized heating and radiation.

#### 5.5.4 Oblique Double Layers

In space, double layers are often associated with magnetic fields, and the trajectories of the double layer electrons and ions are influenced by  $B$ . When the double layer field  $E$  is not parallel to  $B$ , the magnetized double layer is referred to as an oblique double layer (Fig. 5.11) (Borovsky 1984).

Magnetized double layers usually have scale thicknesses of approximately  $20\lambda_D$  (where  $\lambda_D$  is the Debye length of the hottest species of particles passing through the DL), regardless of their orientation with respect to  $B$  (an exception occurs if  $E$  is not precisely perpendicular to  $B$ ). Depending on the properties of the plasma on either side of the DL, the oblique magnetized DL will drift at velocities up to the ion acoustic speed. Owing to the transfer of momentum from the beam to the electrons in the high-potential plasma via two-stream instabilities, the predominant direction

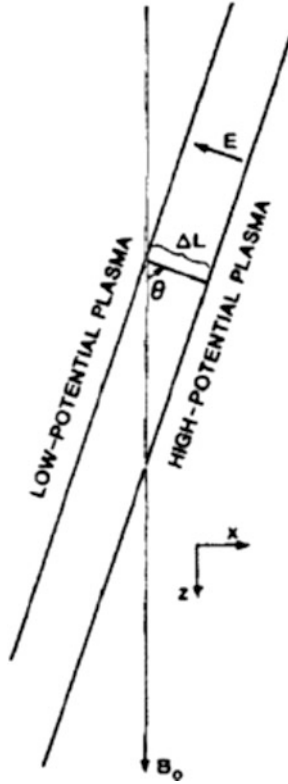


**Fig. 5.11** The coordinate system of an oblique double layer. The angle between the double layer normal and  $B_0$  is denoted as  $\theta = \theta_{DL}$

of the DL drift is in the direction of the emitted electron beam. The orientation of fields in Fig. 5.11, when applied to a sheet beam geometry, makes the oblique DL a naturally occurring analog of the smooth bore magnetron (Sect. 1.7.3).

## 5.6 Examples of Cosmic Double Layers

### 5.6.1 Double Layers in the Auroral Circuit

The auroral circuit is by far the best known of all cosmic circuits (Alfvén, 1986). It is derived from a large number of measurements in the magnetosphere and in the ionosphere. A simplified schematic of the picture that has evolved of the auroral circuit is shown in Fig. 5.12. Magnetospheric convection produces an emf  $\phi_0$  which drives a field aligned current  $j_{||}$ . The ionosphere is represented by a resistance  $R$ .

DLs form in the plasma region to produce a field-aligned electric field which accelerates electrons and ions in opposite directions.

On auroral field lines, the current-carrying electrons and the oppositely streaming ions are governed by conditions external to the double layer and therefore can be specified fully as boundary conditions for simulations. The trapped ions on auroral field lines are mostly plasma-sheet thermal ions of keV energy on the low-potential side of the double layer; therefore the distribution function of the trapped ions can be specified externally as a boundary condition. On the other hand, the trapped electrons on auroral field lines with sufficient energy to penetrate deep into the double layer are produced mostly by the backscattering of the streaming electrons due to charge-neutral collisions in the ionosphere on the downstream side of the double layer; or are a combination of both. The ionospheric electrons of energy less than 1 eV are of no consequence because they are unable to contribute to the space charge inside the double layer. Therefore, the trapped electrons can not be prescribed as a boundary condition (Singh et al. 1986).

Since the trapped ions and the streaming electrons and ions on auroral field lines can be specified as boundary conditions, one can determine the density of the trapped electrons as a function of  $\phi$  from Eqs. (5.16) to (5.18) for  $\psi$  for the existence of double layer solutions. This result provides an explicit constraint on the distribution function of the trapped electrons, but still cannot answer the question on realizability of the solution. To answer this question unambiguously, one must treat the double layer formation as an initial value problem so that the production of the trapped electrons can be followed in time. The transition from a localized DL to an extended DL has been shown to depend predominantly on the energy of the trapped electrons (Kan and Akasofu 1989).

An immediate question that comes to mind is what controls the field-aligned scale length of a double layer? The boundary conditions on the ionospheric side of the auroral double layer are uniquely different from the classic double layer. First, the converging geomagnetic field is favorable for retaining the trapped particles on the ionospheric side. Secondly, the partially ionized ionosphere is a source of trapped particles due to the backscattered primary and secondary electrons produced

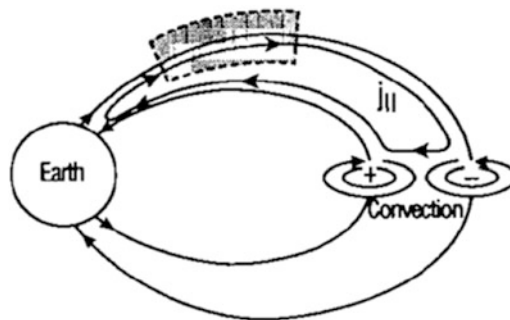


**Fig. 5.12** A model of coupled magnetosphere-ionosphere system. (adapted from Sato and Okuda 1981)



by the auroral electrons. This is in contrast to the classic double layer in which the trapped particles can only be produced by instabilities, and with no magnetic mirror to help maintain the trapped-particle population.

Figure 5.14 shows the double layer simulations results of Yamamoto and Kan (1985). The field-aligned scale length  $L_{\parallel}$  of a double layer varies from (a) localized to about a ten Debye lengths in the absence the backscattered primary electrons and the hot magnetospheric ions, to (b) a partially extended in the presence of the backscattered primary electrons, and (c) to become fully extended across the entire simulation domain if both the backscattered primary electrons and the magnetospheric hot ions are present. Figure 5.14d shows that the fully extended double layer remains fully extended under the same condition as in Fig. 5.14c except that the length of the simulation domain is double in length. This result clearly indicates that the field aligned scale length of a double layer is controlled by the energy of the trapped-particle populations. The scale length increases as the energy of the trapped-particle population increases.

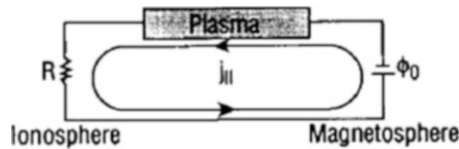


**Fig. 5.13** Equivalent circuit representation of the Earth-convection system shown in diagram Fig. 5.12 (adapted from Sato and Okuda 1981)

Oblique DLs (Sect. 5.5.4) have been suggested as causes of ion conics (beams of ions whose angular distributions have a minima in the field-aligned direction), and auroral kilometric radiation (Borovsky 1984, 1988).<sup>3</sup> Figure 5.15 illustrates the trajectories of various magnetized initially magnetic field-aligned ions passing through an oblique DL. In unmagnetized DLs, the ion motion is along  $E$ . As the strength of the magnetic field increases, the ion trajectories become increasingly aligned along  $B$ . In studying ion conics, Borovsky finds a transition between electric field alignment and magnetic field alignment in the parameter range  $2.18 \leq \omega_{ci} \tau_{cr} \leq 8.72$ , where  $\tau_{cr}$  is the time required for an ion to be accelerated across the oblique DL.

<sup>3</sup> Auroral kilometric radiation (AKR) (Sect. 1.8.1) is bursty electromagnetic emission originating in the dusk and evening auroral zone at geocentric radii of 2–4  $R_e$ . The radiation is believed to be emitted at frequencies near the local electron cyclotron frequency. The power levels of AKR emission are highest during times of geomagnetic activity, and the emission is correlated with the presence of precipitating high-energy electrons, with the presence of Birkeland currents, and with the presence of auroral arcs. The radiation is believed to be emitted with wave vectors that are nearly perpendicular to the terrestrial magnetic field, but tilted slightly earthward. It is also thought that the extraordinary mode dominates in AKR. Because of the rising or falling in frequency of the bursts, the source region is envisioned to move down or up the terrestrial magnetic field at approximately the local ion acoustic speed.

Simulations of oblique DLs show electromagnetic wave properties similar to that of AKR (Borovsky 1988). The emitted waves have frequencies slightly above and slightly below the local electron cyclotron frequency ( $f_{ce} \sim 30$  kHz,  $\lambda_{ce} \sim 10$  km), and the waves are emitted primarily in the north-south (constant longitude) direction. In the auroral zone, the DL drift in the electron sheet beam direction, carries it along the terrestrial magnetic field, toward the poles (Fig. 5.16). Borovsky (1988) finds a power of  $P \sim 1.2 \times 10^6$  W per discrete auroral arc element. The observation that a typical arc consists of 5 elements requires the presence of 16–160 arcs in the auroral zone to produce 100 MW–1 GW of AKR. The total efficiency of auroral arc electron kinetic energy into electromagnetic radiation is  $\sim 0.5\%$  (smooth bore magnetrons typically achieve efficiencies of a few percent).

### 5.6.2 Solar Flares

Solar flares are the result of a sudden irreversible release of energy in the corona and chromosphere of the sun. These lead to particle acceleration observed mainly in the range  $10^4$ – $10^5$  eV, and to a transient heating of the chromosphere (to  $\approx 1$  eV ( $10^4$  K)) and corona (to  $\approx 10^3$  eV ( $10^7$  K)). Electromagnetic radiation is produced over an extremely broad range from radio up to X and even  $\gamma$  ray frequencies.

A typical flare passes through a sequence of phases. There is an initial preflare or preheating phase lasting around 10 min characterized by a slow optical brightening with an accompanying rise in the extreme ultraviolet (EUV) and soft X ray emission. This is followed by a short explosive or impulsive phase ( $\sim 1$  min) during which there are impulsive emissions of hard X rays, EUV, and microwaves (i.e., the most energetic nonthermal events). There is a rise to maximum brightness and emission in soft X rays and EUV during the 5–15 min flash phase, followed by a slow decline in the main phase ( $\sim 1$  h). Flashes occur mainly in active regions, containing sunspots and a generally enhanced magnetic field, and are believed to derive their energy through this field. There are strong arguments for the storage of energy in the magnetic field [i.e., as inductive energy in an extended current system (Sect. 3.7)].

Estimates of the energy release due to changes in the magnetic field topology are of the right order of magnitude. The total energy released in a flare is in a range extending over more than three orders of magnitude, from  $\approx 10^{22}$  J for a typical subflare to  $\approx 3 \times 10^{25}$  J in the most energetic cases. For large flares this energy is roughly equally divided between electromagnetic radiation, energetic particles, and shock waves propagating outward into the solar wind region (Priest 1982). Flare “areas” are reported for the extent of the  $H\alpha$  emission at maximum intensity and range from less than  $3 \times 10^8$  km<sup>2</sup> for subflares, and from  $7.5 \times 10^8$  km<sup>2</sup> to over  $3.6 \times 10^9$  km<sup>2</sup> for major flares. High-resolution observations reveal small (diameter  $\sim 3,000$ – $6,000$  km) impulsive flare kernels with enhanced brightness associated with the X ray bursts. Small-scale “compact” flares may take the form of simple loops accompanied in some cases by surges. The much larger “two-ribbon” flares, so called from the pair of  $H\alpha$  emission regions in the form of long ribbons observed

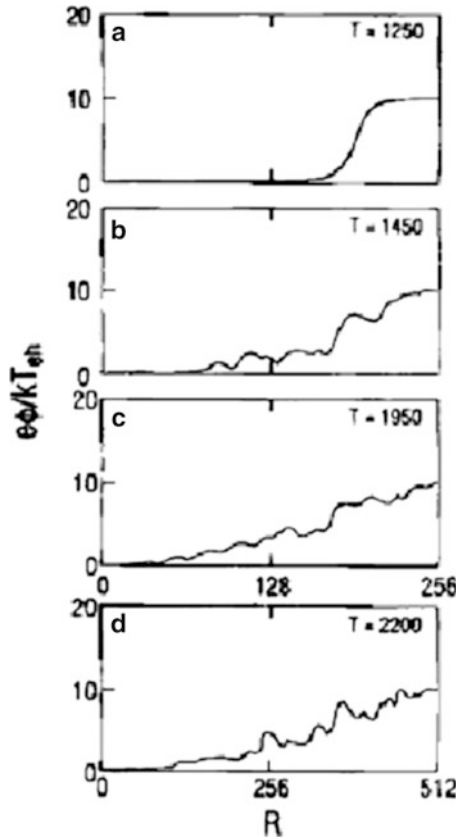


**Fig. 5.14** Simulation results on the variation of the field-aligned scale length of a double layer. The right hand potential is fixed at 10.0

during the flash phase, are closely associated with a prior filament destabilization and eruption ([Bernstein et al. 1957](#)).

Currents in the solar atmosphere are inferred from magnetic field measurements. If the magnetic field  $B$  is known, the current density  $j$  can be derived from Eq. (1.2),  $\nabla \times \mathbf{B} = \mu_0 \mathbf{j}$ . By measuring the transverse component of the magnetic field [Severny \(1965\)](#) found that vertical currents of the order of  $10^{11}$  A exist in the neighborhood of sunspots.

[Moreton and Severny \(1968\)](#) have pointed out a remarkable coincidence between the bright knots appearing during the initial phase of flares and spots with a vertical current density larger than  $8 \times 10^{-3} \text{ A m}^{-2}$ . The currents can either flow outward or inward from the spots. The measured diameter of the spots is comparable with the observational resolution  $\approx 7''$  corresponding to a distance  $\sim 5 \times 10^6$  m on the sun. With a current density  $j = 8 \times 10^{-3} \text{ A m}^{-2}$  and with a diameter of the current elements of  $5 \times 10^6$  m one obtains a total current of  $I \sim 2 \times 10^{11}$  A.

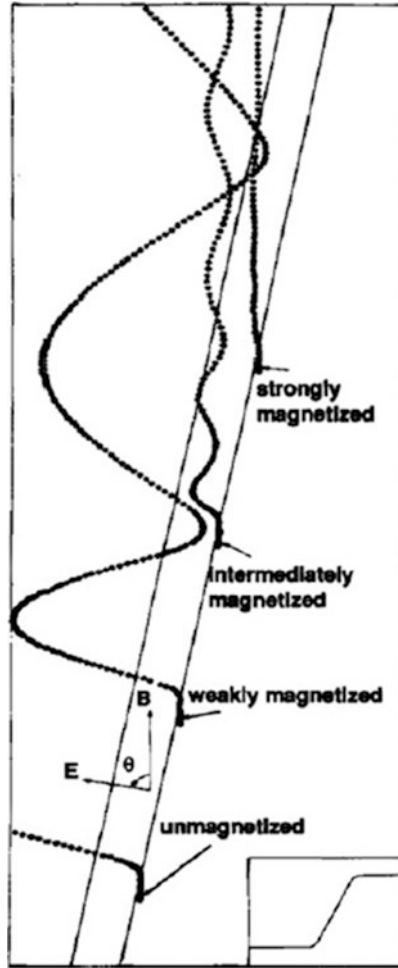


**Fig. 5.15** The trajectories of variously magnetized initially field-aligned ions passing from the high-potential plasma through an oblique ( $\theta_{DL} = 79.7^\circ$ ) double layer. The functional form of the double layer is contained in the inset to the bottom right

Since the apparent diameters of the spots are of the same order as the resolution it is possible that the real diameter might be still smaller. This would lead to an enhanced current density compared with the measured one.

In the corona and in most of the chromosphere the magnetic pressure  $p_B = B^2/2\mu_0$  far exceeds the kinetic pressure of the plasma as soon as the magnetic field is larger than  $\approx 10^{-3}$  T (10 G). This implies that any stationary current system inducing magnetic fields larger than  $\approx 10^{-3}$ , must be nearly force-free with the current almost parallel to the magnetic field. Otherwise kinetic pressure forces cannot balance the  $j \times B$  forces. For example, a current of the order of  $2 \times 10^{11}$  A, constricted to an area with a diameter equal to or less than  $5 \times 10^6$  m, must be force-free since it induces a magnetic field larger than  $10^{-2}$  T ( $10^2$  G).

As shown in Sect. 1.7.2, a force-free current system has a tendency to form a narrow filament with most of the total current and magnetic flux confined within it. Inside the filament the magnetic-field lines will assume helical shapes.

The results obtained by Moreton and Severny (1968) indicate that such a current filament can pass from one point in a sunspot group through the chromosphere and through the lower corona and then back again to another point in the same group (Fig. 5.17). Hence, the length of the filament  $l$  should be comparable with the typical dimension of a sunspot group  $\sim 10^7 - 10^8$  m. The current circuit might finally be closed in the deeper layers of the solar body where non-force-free conditions prevail.

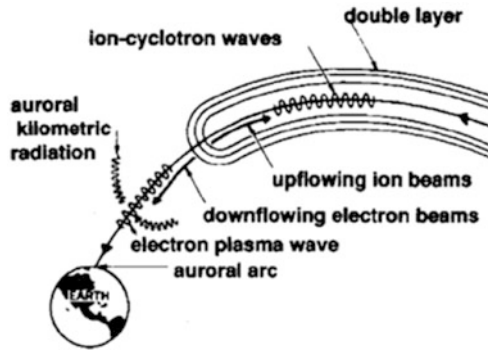


**Fig. 5.16** Schematic (not to scale) of an auroral double layer and some of the phenomena it produces. An actual auroral double layer is only a few kilometers in north-south (constant latitude) extent, and may be one in a chain of many double layers

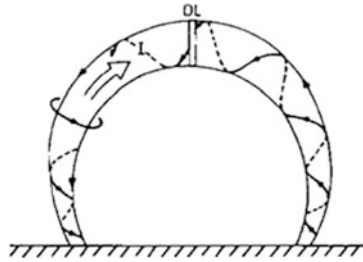


**Fig. 5.17** Model of a solar flare. The lower boundary is the high-density photosphere. The energy stored in a twisted magnetic flux loop in the corona is released by a double layer

**Example 5.1 Electrical properties of solar flares.** The magnetic energy stored in a current system is given by Eq. (3.36). It is convenient to use the inductance  $L = L_{int} + L_{ext}$  and derive the energy from

$$W_B = \frac{1}{2}LI^2 = \frac{1}{2}L_f I^2 + \frac{1}{2}L_{ext} I^2$$

where the first and second terms correspond to the magnetic energy stored inside and outside the filament, respectively (Akasofu 1988; Carlqvist 1969).

For a circular current loop of radius  $R$  consisting of a current channel of radius  $a$ , the internal and external inductances in vacuum are

$$L_{int} = \frac{11}{24} \mu_0 R$$

and

$$L_{ext} = \mu_0 R \left[ \ln \frac{8R}{a} - 2 \right], \quad R \gg a$$

The distribution of the current density is assumed to be  $j \propto (a^2 - r^2)$  for  $r \leq a$  resembling that of the force-free filament.

We can now use the circular loop as a model of the current filament in the solar atmosphere in order to estimate the inductance of the filament. Because of the high conductivity of the solar atmosphere it is likely that a considerable part of the magnetic field outside the filament will be screened by the plasma. The external inductance of the filament may therefore be much reduced compared with the vacuum case. On the other hand, the internal inductance of the current filament would be comparable with the internal inductance of the circular current loop. With a radius of the current filament  $\approx l/2 \approx 5 \times 10^6 - 5 \times 10^7$ , we then obtain an inductance of the filament of the order of  $L \approx 3 - 30$  H.

The total filamentary current needed to produce a stored magnetic energy comparable with the energy of a flare  $W_f = LI^2/2 \approx 10^{21} - 10^{25}$  J is in the range  $I \approx 10^{10} - 10^{12}$  A.

If we assume that the filamentary current is mainly carried by electrons and protons, the maximum potential drop of a double layer in the filament is, according to Eq. (5.27),  $\phi_{DLm} \approx 9 \times 10^{10}$  V (90 GV). The time constant for energy release connected with this potential drop is from Eq. (5.23)  $t_B \approx 2 \times 10^2$  s. It is to be noticed that both  $W_B$  and  $\tau_B$  in Example 5.1 are of the same magnitudes as the total energy and the time constant of solar flares, respectively. Hence, the double layer constitutes a mechanism that is capable of releasing the flare energy during the brief explosive phase observed.

The analysis of observations from the Solar Maximum Years have led to an improved understanding of the build-up phase of solar flares and of the energy release. Hard X ray and microwave bursts have been found to have fine structure on time scales of a few tens of milliseconds. During the impulsive phase, hard X ray emission is observed at the foot of loops with microwave emission from the tops. Of particular interest for models with acceleration by strongly relativistic DLs is the observation of energetic neutrons (50–500 MeV, where the upper limit is uncertain and may be much greater) produced during the impulsive phase. The DL model is able to meet the rather stringent requirements for the acceleration mechanism set by the observations, both as regards to the time scale and number of high-energy protons which produce the neutrons (Carlqvist 1986). Further evidence of acceleration to very high energies comes from observations of g ray emission due to protons

(Ryan et al. 1983). In the context of these results the DL has the advantage of accounting for the acceleration to very high energies and allowing extremely rapid time variations, since its structure can vary on the local ion transit time scale.

### 5.6.3 Double Radio Galaxies and Quasars

Double layers produce beams of electrons and, on astrophysical scales, these beams are relativistic. The beams are also directed along  $B_0$  so that the expected loss mechanism for the beam kinetic energy is synchrotron radiation. The formation of a series of DLs in a network of current-conducting plasmas thus leads to an interesting problem regarding total synchrotron intensity, background radiation levels, and isophotal patterns. This problem is addressed in some detail in Chap. 6.

### 5.6.4 Double Layers as a Source of Cosmic Radiation

It is of interest to compare the cosmic particle acceleration discussed in Sect. 5.6.2 with some energetic cosmic particle observations. Very energetic particles—primarily protons—are recorded on earth following large solar flares. The proton energies can be many tens of GeV after such an event.

It has been demonstrated by Chupp et al. (1982) that the sun also emits neutrons of high energy. Just after a solar  $\gamma$  ray impulsive burst, indicating the onset of a strong (1B) flare, neutrons with energies at least as high as  $6 \times 10^8$  eV were detected at the earth. The production of such neutrons requires that protons be accelerated to GeV energies, probably within a 20 s time interval corresponding to the impulsive phase. As pointed out by Chupp et al., this short time imposes a strong constraint on the properties of the particle accelerator operating in the flare region.

In Sect. 5.6.2 we found that a double layer in a solar filament carrying the current  $I = 3 \times 10^{11}$  can sustain a maximum potential drop of about  $\phi_{DLm} \approx 9 \times 10^{10}$ . This means that such a layer is capable of accelerating particles to energies that correspond to the highest solar cosmic ray energies observed.

As regards the high-energy neutron event detected by Chupp et al., a solar double layer seems to meet the very special requirements on the acceleration mechanism imposed by the observations. First, the double layer is able to accelerate a fairly large flux of protons,  $\psi_p \approx 10^{30} \text{ s}^{-1}$ . Second, the time of acceleration of each particle in the layer is very short—only a fraction of a second. Hence, the total number of protons  $N_{20} = 20\psi_p = 2 \times 10^{31}$  of GeV energy can be directly produced by the double layer during the 20 s time interval of the impulsive burst. In addition to this, it is likely that many more particles of lower energy are generated by the primary particles through secondary processes in the solar atmosphere.

**Example 5.2 Electrical properties of galactic pinches.** Consider a double layer in a galactic filament conducting  $10^{20}$  A (Example 6.7). For a proton-electron plasma,

Fig. 5.4 gives a value  $\phi_{DL} \approx 3 \times 10^{17}$  V in the relativistic regime. If the voltage is actually distributed over a series of double layers extending for 10 kpc in the filament, the average electric field strength is 1 mV/m. The total energy of an ion that has been accelerated through the double layers is  $3 \times 10^{17}$  eV. This energy is similar to that derived by Vlasov et al. (1989) for pinched plasma currents as a source of cosmic rays. The time constant for the release of energy Eq. (5.22) is  $T_B = 2 \times 10^9$  years. The time rate of energy release Eq. (5.28) is  $3 \times 10^{37}$  W.

## References

- Akasofu, S.-I.: An electric-current description of solar flares. *Astrophys. Space Sci.* **144**, 303 (1988)
- Alfvén, H.: Proceedings of the 2nd Int. Conf. on Peaceful Uses of Atomic Energy (United Nations, Geneva) **31**, 3 (1958)
- Alfvén, H.: Double layers and circuits in astrophysics. *IEEE Trans. Plasma Sci.* **14**, 779 (1986)
- Babić, M., et al.: The growth of a space charge structure in a low density discharge plasma. In: Tenth International Conference on Phenomena in Ionized Gases, Oxford. The growth of a space charge structure in a low density discharge plasma (1971)
- Bernstein, I.B., Greene, J.M., Kruskal, M.D.: Exact nonlinear plasma oscillations. *Phys. Rev.* **108**, 546 (1957)
- Biskamp, D., Chodura, R.: Computer simulation of anomalous dc resistivity. *Phys. Rev. Lett.* **23**, 1553 (1971)
- Block, L.P.: Cosmic electrodynamics, **3** (1972)
- Block, L.P.: A double layer review. *Astrophys. Space Sci.* **55**, 59 (1978)
- Bohm, M., Torven, S.: Electric fields along the magnetic field in a collision free laboratory plasma. *Int. Conf. Plasma Phys. (Kiev)*, TRITA-EPP-86-11, Roy. Inst. Tech., Stockholm (1987)
- Boris, J.P., Dawson, J.M., Orens, J.H., Roberts, K.V.: Computations on anomalous resistance. *Phys. Rev. Lett.* **25**, 706 (1970)
- Borovsky, J.E.: A review of plasma double-layer simulations. In: Schrittwieser, R., Eder, G. (eds.) *Second Symposium on Plasma Double Layers and Related Topics*, Innsbruck (1984a)
- Borovsky, J.E.: The production of ion conics by oblique double layers. *J. Geophys. Res.* **89**, 2251 (1984b)
- Borovsky, J.E.: Production of auroral kilometric radiation by gyrophase-bunched double-layer-emitted electrons: antennae in the magnetospheric current regions. *J. Geophys. Res.* **93**, 5727 (1988)
- Borovsky, J.E., Joyce, G.: Numerically simulated two-dimensional auroral double layers. *J. Geophys. Res.* **88**, 3116 (1983)
- Buneman, O.: Dissipation of currents in ionized media, *Phys. Rev.* **115**, 503 (1959)
- Carlqvist, P.: Current limitation and solar flares. *Sol. Phys.* **7**, 377 (1969)



- Carlqvist, P.: On the formation of double layers in plasmas. *Cosm. Electrodyn.* **3**, 377 (1972)
- Carlqvist, P.: On the physics of relativistic double layers. *Astrophys. Space Sci.* **87**, 1–2, 21–39 (1982)
- Carlqvist, P.: On the acceleration of energetic cosmic particles by electrostatic double layers. *IEEE Trans. Plasma Sci.* **14**, 794 (1986)
- Carpenter, R.T., Torven, S.: The current-voltage characteristic and potential oscillations of a double layer in a triple plasma device. *Laser Part. Beams* **5**, 325 (1987)
- Chupp, E.L., et al.: A direct observation of solar neutrons following the 0118 UT flare on 1980 June 21. *Astrophys. J.* **263**, L95 (1982)
- Crawford, F.W., Freeston, I.L.: In: *VIe Conférence Internationale sur les Phénomènes d'Ionisation dans les Gaz*, Paris, vol. I (1963)
- Goertz, C.K., Joyce, G.: Numerical simulation of the plasma double layer. *Astrophys. Space Sci.* **32**, 165 (1975)
- Goldsworthy, M.P., Green, F., Lalouis, P., Stening, R.J., Eliezer, S., Hora, H.: Hydrodynamic analysis of the high electric fields and double layers in expanding inhomogeneous plasmas. *IEEE Trans. Plasma Sci.* **14**, 823 (1986)
- Hirose, A., Langdon, B.A.: Nonlinear saturation of the Buneman instability, *Phys. Rev. Lett.*, **44**, 1404–1407 (1981)
- Ichimaru, S.: *Basic Principles of Plasma Physics*. W.A. Benjamin, Reading (1973)
- Jones, M.E., Gisler, G.: *Bull. Am. Phys. Soc.* **31**, 1398 (1986)
- Kan, J.R., Akasofu, S.-I.: Electrodynamics of solar wind-magnetosphere-ionosphere interactions. *IEEE Trans. Plasma Sci.* **17**, 83 (1989)
- Langmuir, I.: The interaction of electron and positive ion space charges in cathode sheaths. *Phys. Rev.* **33**, 954 (1929)
- Lindberg, L.: In: Michelsen, P., Rasmussen, J.J. (eds.) *Proceedings of the Symposium on Plasma Double Layers* Michelsen and Rasmussen (eds). Risø Nat. Lab., Roskilde, Denmark (1982)
- Moreton, G.E., Severny, A.B.: Magnetic fields and flares in the region CMP, 20 September 1963. *Sol. Phys.* **3**, 282 (1968)
- Peratt, A.L., Jones, M.E.: Particle-in-cell simulations of heavy ion plasma double layers. In: *IEEE Conference on Record, IEEE International Conference on Plasma Science*, Saskatoon (1986)
- Priest, E.R.: *Solar MHD*. D. Reidel, Dordrecht (1982)
- Raadu, M.A.: Relativistic effects in electrostatic double layers, in *Symposium on plasma double layers*, Risø National Laboratory, Denmark, June 16–18 (1982)
- Raadu, M.A.: Relativistic effects in electrostatic double layers. In: *Symposium on Plasma Double Layers*. Risø National Laboratory, Denmark (1982)
- Ryan, J.M., Chupp, E.L., Forrest, D.J., Matz, S.M., Rieger, E., Reppin, C., Kanbach, G., Share, G.H.: *Astrophys. J.* **272**, L61 (1983)
- Sato, T., Okuda, H.: *J. Geophys. Res.* **86**, 3357 (1981)
- Schönhuber, M.J.: *Quecksilber-Niederdruck-Gasenladung*. Lachner, München (1958)
- Severny, A.B.: *Astron. Zh.* **42**, 217 (1965)

- Singh, N., Thiemann, H., Schunk, R.W.: Plasma processes driven by current sheets and their relevance to the auroral plasma. *IEEE Trans. Plasma Sci.* **14**, 805 (1986)
- Tonks, L.: Kinetic model of Tonks-Dattner resonances in plasma columns, *Phys. Rev.* **37**, 1458 (1931)
- Tonks, L.: Theory and phenomena of high current densities in low pressure arcs. *Trans. Electrochem.* **72**, 167 (1958)
- Torvén, S., Andersson, D.: Observations of electric double layers in a magnetized plasma column. *J. Phys. D: Appl. Phys.* (1979)
- Vlasov, V.P., Zhdanov, S.K., Trubnikov, B.A.: Plasma pinch as a source of cosmic rays. *JETP Lett.* **49**, 667 (1989)
- Williams, A.C.: General Bohm and Langmuir conditions for a strong double layer in space plasmas. *IEEE Trans. Plasma Sci.* **14**, 800 (1986)
- Williams, A.C.: Double layers in astrophysics. *Laser Part. Beams* **5** (1987)
- Yamamoto, T., Kan, J.R.: The field-aligned scale length of one-dimensional double layers. *J. Geophys. Res.* **90**, 1553 (1985)

## Chapter 6

# Synchrotron Radiation

Electromagnetic waves propagated in cosmic space derive from a variety of mechanisms. The major contribution in the optical region of the spectrum is from radiation resulting from bound-bound electron transitions between discrete atomic or molecular states, free-bound transitions during recombination, and free-free transitions in the continuum. In the latter case, when for transitions between levels, radiation classified as bremsstrahlung results from the acceleration of electrons traveling in the vicinity of the atom or ion.

In addition, there are other mechanisms of considerable importance operating in the radio region. In particular, there are noncoherent and coherent mechanisms connected with the existence of sufficiently dense plasmas which are responsible for radiation derived from plasma oscillations, such as the sporadic solar radio emissions. This radiation cannot be attributed to the motion of individual electrons in a vacuum but is due to the collective motion of electrons at the plasma frequency

$$\frac{\omega_{pe}}{2\pi} = \frac{1}{2\pi} \sqrt{\frac{n_e e^2}{m_e \epsilon_0}} = 9\sqrt{n_e}, \text{ Hz} \quad (6.1)$$

for an electron density  $n_e$  ( $\text{m}^{-3}$ ). This often occurs in cosmic plasma when electron beams propagate through a neutralizing plasma background (Sect. 2.9).

When a plasma is subjected to a magnetic field there is yet another mechanism which plays an extremely important role in radio astronomy. The frequency and angular distribution of the radiation from free electrons moving in the presence of a magnetic field undergoes dramatic changes as the electron energy is increased from nonrelativistic to extreme relativistic energies. Essentially three types of spectra are found. Names such as cyclotron emission and magnetobremsstrahlung are used to describe the emission from nonrelativistic and mildly relativistic electron energies, whereas the name synchrotron radiation is traditionally reserved for highly relativistic electrons because it was first observed in 1948 in electron synchrotrons.

Synchrotron radiation is characterized by a generation of frequencies appreciably higher than the cyclotron frequency of electrons (or positrons) in a magnetic field,

a continuous spectra whose intensity decreases with frequency beyond a certain critical frequency, highly directed beam energies, and polarized electromagnetic wave vectors.

In astrophysics, nonthermal (nonequilibrium) cosmic radio emission is, in a majority of cases, synchrotron radiation. This is true for general galactic radio emission, radio emission from the envelopes of supernovae, and radio emission from double radio galaxies and quasars (continuum spectra). Synchrotron radiation also appears at times as sporadic radio emission from the sun, as well as from Jupiter. In addition, optical synchrotron radiation is observed in some instances (Crab nebula, the radiogalaxy and “jet” in M87-NGC 4486, M82, and others). This apparently is also related to the continuous optical spectrum sometimes observed in solar flares. Synchrotron radiation in the X ray region can also be expected in several cases, particularly from the Crab nebula.

When cosmic radio or optical emission has the characteristics of synchrotron radiation, a determination of the spectrum makes possible a calculation of the concentration and energy spectrum of the relativistic electrons in the emission sources. Therefore, the question of cosmic synchrotron radiation is closely connected with the physics and origin of cosmic rays and with gamma- and X ray astronomy.

Synchrotron radiation was first brought to the attention of astronomers by [Alfvén and Herlofson \(1950\)](#), a remarkable suggestion at a time when plasma and magnetic fields were thought to have little, if anything, to do in a cosmos filled with “island” universes (galaxies).<sup>1</sup> The recognition that this mechanism of radiation is important in astronomical sources has been one of the most fruitful developments in astrophysics. For example, it has made possible the inference that high-energy particles exist in many types of astronomical objects, it has given additional evidence for the existence of extensive magnetic fields, and it has indicated that enormous amounts of energy may indeed be converted, stored, and released in cosmic plasma.

## 6.1 Theory of Radiation from an Accelerated Charge

In this section we give, for reference purposes, a series of formulas relating to the energy spectrum of an accelerated charge. For detailed evaluation of the equations the reader is referred to texts such as [Panofsky and Phillips \(1962\)](#).

Consider a charge  $e$  in vacuum whose instantaneous position  $P'(t')$  is given by the vector  $r(t')$  and whose instantaneous velocity is  $v(t')$  (Fig. 6.1);  $t'$  is the time at which the signal propagated at velocity  $c$  is emitted at  $P'(t')$  to arrive at the position of the observer  $P(t)$  at a time  $t$ . The “retarded” time  $t'$  is related to  $t$  through

$$t' = t - \frac{R(t')}{c} \quad (6.2)$$

where  $R(t')$  is the distance between  $e$  and the observer.

---

<sup>1</sup> The “island universes” concept was introduced by the philosopher Kant (1724–1804).

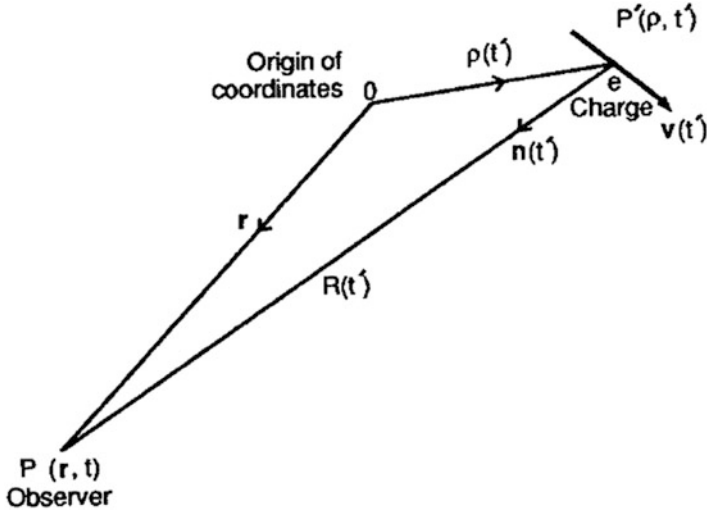


Fig. 6.1 Vector diagram of formulation quantities

Deriving the electromagnetic fields of the accelerated electron are a straightforward, but lengthy calculation. These are, Jones (1964)

$$E(r, t) = \frac{e}{4\pi\epsilon_0} \left[ \frac{(1 - \beta^2)(n - \beta)}{(1 - n \cdot \beta)^3 R^2} + \frac{n \times \{(n - \beta) \times \dot{\beta}\}}{(1 - n \cdot \beta)^3 cR} \right]_{t'} \quad (6.3)$$

$$H(r, t) = \eta n \times E$$

where  $\eta = \sqrt{\epsilon_0}/\mu_0$  is the intrinsic impedance of the propagation medium  $\beta = v/c$  and  $[\dots]_{t'}$  denotes that the quantity within the brackets is to be evaluated at the retarded time  $t'$  defined by Eq. (6.2). For nonrelativistic motion  $\beta \rightarrow 0$ .

Equation (6.3) consists of two field components. The almost static (induction) near-field can be identified with the first term of Eq. (6.3) which shows it to be independent of the acceleration of the moving charge.<sup>2</sup> The second term of Eq. (6.3) represents the far field or “radiation” field. The far fields  $E$  and  $H$  vary linearly with  $\beta$ , exhibit a  $1/R$  fall-off with distance, and are orthogonal to the radius vector. Delineation of the induction and wave zones is given in Fig. 6.2.

<sup>2</sup> A time frame study of the fields shows that the strength of the “static” component does vary slightly in time.

### 6.1.1 The Induction Fields

We first consider the importance of the induction field in the problem of radiation from an accelerated charge. In the immediate neighborhood of the charge

$$E \sim E_{ind} = \frac{e}{4\pi\epsilon_0} \left[ \frac{(1 - \beta^2)(n - \beta)}{(1 - n \cdot \beta)^3 R^2} \right] \quad (6.4)$$

$$H \sim H_{ind} = H_0 + \eta \frac{e}{4\pi\epsilon_0} \left[ \frac{(1 - \beta^2)(\beta \times n)}{(1 - n \cdot \beta)^3 R^2} \right] \quad (6.5)$$

where  $\mathbf{H}_0$  is the external magnetic intensity about which the charge spirals. Confining ourselves to the nonrelativistic case, we may then write (for  $R$  small in comparison to the radiation wavelength)

$$E_{ind} = \frac{e}{4\pi\epsilon_0} \frac{(n - \beta)}{R^2} \quad (6.6)$$

$$H_{ind} = H_0 + \eta \frac{e}{4\pi\epsilon_0} \frac{(\beta \times n)}{R^2} \quad (6.7)$$

Neglecting  $\beta$  in Eq. (6.6) leads to

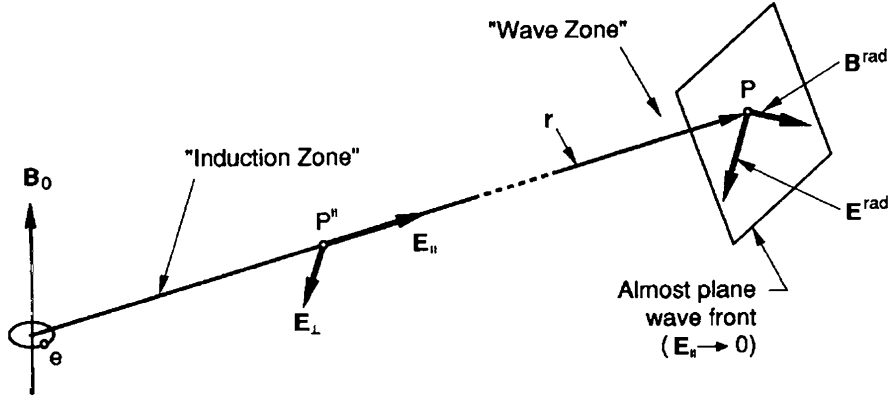


Fig. 6.2 Delineation of induction (near-field) and wave (far-field or radiation) zones

$$E = \frac{e}{4\pi\epsilon_0} \frac{n}{R^2} \quad (6.8)$$

where  $\mathbf{n}$  is a unit vector in the direction of  $R$ . Thus, we have recovered the electrostatic or Coulomb field. Similarly, since a charge  $e$  moving with velocity  $v$  is equivalent to an element of current  $Idl = e\beta c$ , Eq. (6.7) gives

$$dB = \frac{\mu_0}{4\pi} \frac{Idl \times n}{R^2} \quad (6.9)$$

Equation (6.9) is simply the Biot-Savart law equation (3.5). Thus, the electromagnetic fields generated by an accelerated electron give rise to a strong near-field which can be identified with the Biot-Savart law as well as weaker, but propagating, radiation fields. It will be shown that the strong near-fields determine the morphology of the radiating region in a plasma, which is then conveyed to an observer a great distance away via the radiation fields.

### 6.1.2 The Radiation Fields

The remainder of Sects. 6.1–6.6 are mainly concerned with the radiation fields. The observation point is assumed to be far away from the charge, so that  $\mathbf{n}$  and  $R$  change negligibly during a small acceleration interval.

The instantaneous energy flux is given by Poynting's vector

$$S = E \times H = |E|^2 n \quad (6.10)$$

This means that the power radiated per unit solid angle is

$$\frac{dP(t)}{d\Omega} = R^2 S \cdot n = |RE|^2 \quad (6.11)$$

or, in terms of the charge's own time

$$\frac{dP(t')}{d\Omega} = R^2 S \cdot n \frac{dt}{dt'} = \frac{e^2}{16\pi\epsilon_0 c} \frac{\left| n \times \left\{ (n - \beta) \times \dot{\beta} \right\} \right|_{t'}^2}{(1 - n \cdot \beta)^5} \quad (6.12)$$

In deriving Eq. (6.12), the change of variable

$$dt = \frac{\partial t}{\partial t'} dt' = (1 - n \cdot \beta) dt' \quad (6.13)$$

has been used. For a nonrelativistic particle, Eq. (6.12) yields

$$\frac{dP(t')}{d\Omega} = \frac{e^2}{16\pi\epsilon_0 c^3} |n \times \{n \times \dot{v}\}|^2 \quad (6.14)$$

A comparison of Eqs. (6.11) and (6.14) shows that  $E$  lies in the plane containing  $n$  and  $\dot{v}$ ; when we choose  $\dot{v}$  as the polar axis and  $\Theta$  as the angle between  $n$  and  $\dot{v}$ , it follows that

$$\frac{dP(t')}{d\Omega} = \frac{e^2}{16\pi\epsilon_0 c^3} |\dot{v}|^2 \sin^2 \Theta \quad (6.15)$$

and the polar pattern of the emitted radiation is typically that of an electric dipole (Fig. 6.3). This limit is referred to as the *dipole approximation*.

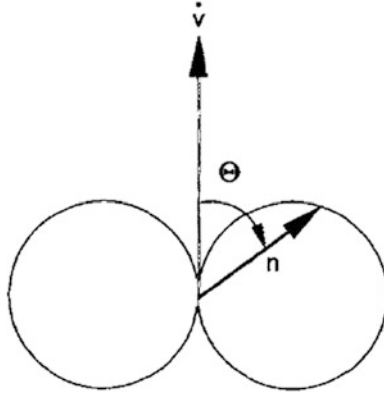


**Fig. 6.3** Angular distribution of radiation field of a nonrelativistic electron. The pattern is symmetric about the axis  $\dot{v}$

**Example 6.1. Total radiation field from an ensemble of charge emitters when  $\lambda \gg L$ .** Consider a plasma region of radiating charges of dimension  $L$  (Fig. 6.4). Let  $\Delta t$  be the time required for an appreciable change in particle motion. If  $r_c$  is a characteristic scale of the particle's orbit and  $v$  is its velocity, then  $\Delta t \sim r_c/v$ . The condition  $\Delta t \gg L/c$  then implies  $v/c \ll r_c/L$ . Since  $r_c < L$ , the nonrelativistic condition  $v \ll c$  is apropos. Under this approximation equation (6.3), for a single electron, is

$$E^{rad}(r, t) = \frac{e}{4\pi\epsilon_0} \frac{n \times (n \times \dot{v})}{c^2 R} \quad (6.16)$$

For an ensemble of point charges the total radiation field is a linear superposition of the radiated field from each charge emitter

$$E^{rad}(r, t) = \frac{1}{4\pi\epsilon_0} \sum_i \frac{e_i}{R_i} \frac{n \times (n \times \ddot{r})}{c^2} \quad (6.17)$$

We shall have a need for the electric dipole moment which, by definition (Stratton 1941), is

$$p^{(1)} = \int \rho(r) r dV \quad (6.18)$$

In this notation, the total charge is

$$p^{(0)} = Ne = \int \rho(r) dV \quad (6.19)$$



For  $N$  point charges, the electric dipole moment of the distribution equation (6.18) is

$$p^{(1)} = \sum_{i=1}^N e_i r_i \quad (6.20)$$

where  $r_i$  are the differential lengths of the dipole elements associated with the emitters  $e_i$ . If the variation of the dipole moment is caused by an oscillation,  $p^{(1)} = \sum e_k r_k e^{-i\omega t}$ , so that  $\sum e_k \ddot{r}_k = -\omega^2 p^{(1)}$ . Substituting this into Eq. (6.17) and using Eq. (B.7) gives

$$E^{rad}(r, t) = -\frac{1}{4\pi\epsilon_0 R} k \times (k \times p^{(1)}) \quad (6.21)$$

In deriving Eq. (6.21), use has been made of the fact that in the far-field,  $R_i \rightarrow R$ . The current in the dipole is

$$I = \frac{dq}{dt} = \frac{p^{(1)}}{r_i} = -\frac{i\omega p^{(1)}}{r_i} \quad (6.22)$$

so that  $p^{(1)} = I r_i / (-i\omega)$ . For a cosinusoidal current distribution aligned along the polar axis,  $e\ddot{r} = -\hat{z}\omega^2 p \cos(\omega t) = -\omega^2 p^{(1)}$ , and

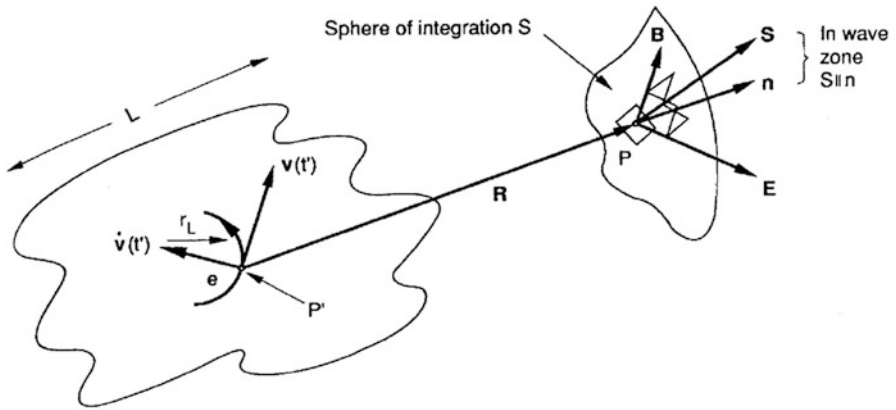


Fig. 6.4 Orientation of field vectors from a region  $L$  of radiating electrons

$$E^{rad}(r, t) = E_{\theta}^{rad}(r, t) = -k^2 \frac{p \cos(\omega t) \sin \theta}{4\pi\epsilon_0 R} \quad (6.23)$$

The total field equation (6.3) in the limit  $\beta \rightarrow 0$ , with induction and radiation components, can be cast in terms of the dipole moment (Panofsky and Phillips 1962):

$$E_R^{rad} = \frac{p^{(1)} \cos \theta}{2\pi\epsilon_0 R^2} \left( \frac{1}{R} - ik \right) e^{ikR} \quad (6.24)$$

$$E_{\theta}^{rad} = \frac{p^{(1)} \sin \theta}{4\pi\epsilon_0 R} \left( \frac{1}{R^2} - \frac{ik}{R} - k^2 \right) e^{ikR} \quad (6.25)$$

$$H_{\phi}^{rad} = \frac{-i\omega p^{(1)} \sin \theta}{4\pi} \left( \frac{1}{R^2} - \frac{ik}{R} \right) e^{ikR} \quad (6.26)$$

The electric fields Eqs. (6.24) and (6.25) can be plotted as a function of space and time and a single time frame of  $E(r, t)$  is shown in Fig. 6.5a.

**Example 6.2. Radiation from two dipole elements.** Consider two oscillating dipole moments  $p_1^{(1)}$  and  $p_1^{(2)}$  spaced a distance  $L$  apart as shown in Fig. 6.6. Both oscillate at a frequency  $\omega$ . The total radiation field seen by an observer is then

$$E_{\theta}^{rad} = \frac{-k^2}{4\pi\epsilon_0 R} \left[ p_1^{(1)} \cos \omega t + p_2^{(1)} \cos \omega(t - \Delta t) \right] \sin \theta \quad (6.27)$$

where  $\Delta t = (\delta/c) \sin \theta$ . When  $L \ll \lambda$ , Eq. (6.27) is

$$E_{\theta}^{rad} = \frac{-k^2}{4\pi\epsilon_0 R} \left[ p_1^{(1)} + p_2^{(1)} \right] \cos \omega t \sin \theta \quad (6.28)$$

Figure 6.5b shows the radiation pattern for the case  $L = 1/8\lambda$ . The radiation is now beamed to the upper right. When properly phased, an array of dipole moments will produce a pencil-like beam of radiation. The total power radiated in all directions is obtained by integrating equation (6.12) over the solid angle, with the result, called *Lienard's formula*:

$$P^T = \frac{e^2}{6\pi\epsilon_0 c} \left[ \frac{\beta^2 - (\boldsymbol{\beta} \times \dot{\boldsymbol{\beta}})^2}{(1 - \beta^2)^3} \right] \quad (6.29)$$

In the dipole approximation equation (6.29) reduces to the familiar Larmor formula for a nonrelativistic, accelerated charge:

$$P^T = \frac{e^2}{6\pi\epsilon_0 c} |\dot{\mathbf{v}}|^2 \quad (6.30)$$

The total energy radiated is obtained by integrating equation (6.30)

$$W_R^T = \int_{-\infty}^{\infty} P^T dt = \frac{1}{6\pi\epsilon_0 c^3} \int_{-\infty}^{\infty} |\dot{\mathbf{v}}(t)|^2 dt \quad (6.31)$$

To find the frequency spectrum of the radiated energy we Fourier-analyze making use of the Fourier-transform pair

$$V(\omega) = \int_{-\infty}^{\infty} e^{-i\omega t} V(t) dt \quad (6.32)$$

$$V(t) = (2\pi)^{-1} \int_{-\infty}^{\infty} e^{i\omega t} V(\omega) d\omega \quad (6.33)$$

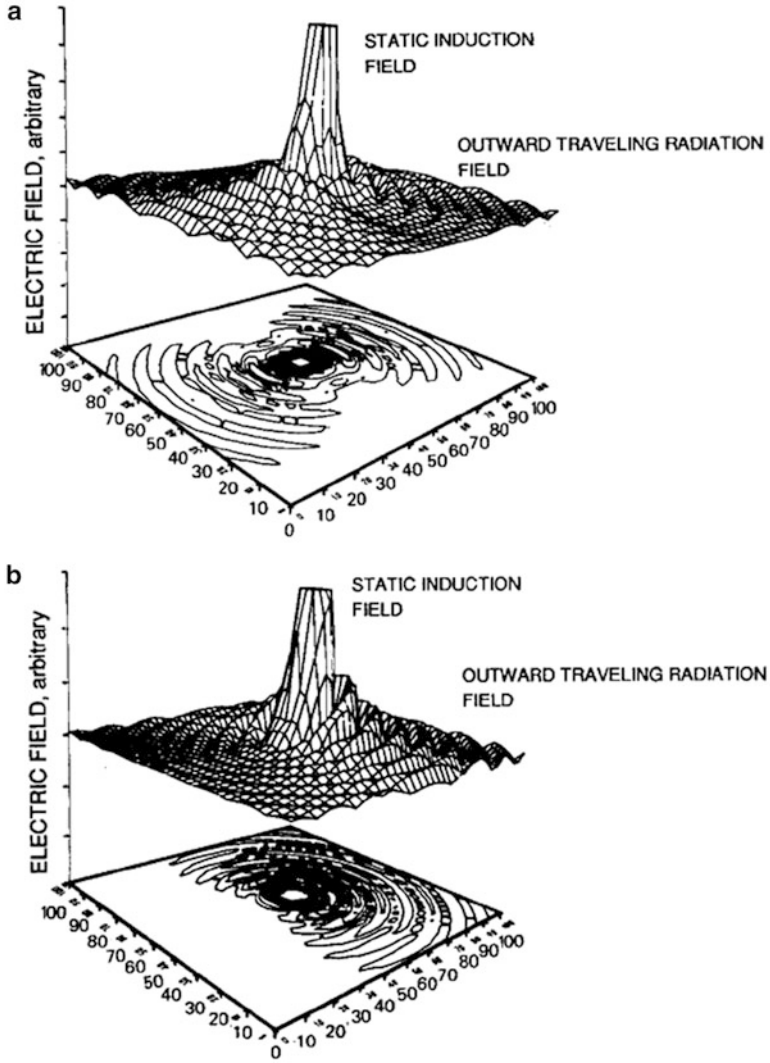


**Fig. 6.5** Induction and radiation fields  $E$ . (a) Single dipole radiator, (b) two dipoles spaced  $\delta = \lambda/8$  apart. The dipoles are oriented in the plane along axes running from the *upper left* to the *lower right*

and Parseval's theorem for the Fourier components of a function  $V(t)$ :

$$\int_{-\infty}^{\infty} |V(t)|^2 dt = \pi^{-1} \int_{-\infty}^{\infty} V(\omega) V^*(\omega) d\omega = \int_0^{\infty} W(\omega) d\omega \quad (6.34)$$

where  $\omega$  is only defined over positive values,  $V(\omega)$  is the Fourier transform of  $V(t)$ , and  $W(\omega)$  defines the spectral energy density. We then find that  $W(\omega, \Omega)$  (which has units of joules per unit solid angle per  $d\omega$ ) is

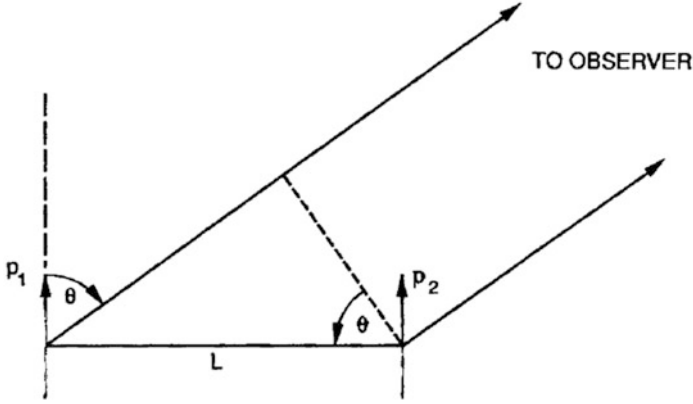


**Fig. 6.6** Two dipole elements separated by a distance  $L$

$$W(\omega, \Omega) = \frac{e^2}{16\pi^3 \epsilon_0 c} \left| \int_{-\infty}^{\infty} e^{i(k \cdot \rho - \omega t')} \frac{n \times \{(n - \beta) \times \dot{\beta}\}}{(1 - n \cdot \beta)^2} dt' \right|^2 \quad (6.35)$$

where  $t$  has been transformed to  $t'$  by Eq. (6.2) and the large distance  $R(t')$  has been approximated by  $r - n \cdot \rho(t')$ . Now the unit vector  $n$  is essentially independent of time and points from the origin of coordinates to the point of observation  $P$ . Equation (6.36) can be transformed to read

$$W(\omega, \Omega) = \frac{e^2 \omega^2}{16\pi^3 \epsilon_0 c} \left| \int_{-\infty}^{\infty} e^{i(k \cdot \rho - \omega t')} n \times \{n \times \dot{v}\} dt' \right|^2 \quad (6.36)$$

where this form is obtained by integrating equation (6.36) by parts. Note that  $\omega$  is the frequency measured in the observer's own time scale. The polarization of the radiation is given by the direction of the vector integral of Eq. (6.36) or Eq. (6.37).

### 6.1.3 Radiation of an Accelerated Electron in a Magnetic Field

The motion of a particle of charge  $e$  and mass  $m$  in a uniform static magnetic field  $B_0$  is illustrated in Fig. 6.7. The equation of motion Eq. (1.5) is

$$\frac{dp}{dt} = e(v \times B_0) \quad (6.37)$$

where

$$p = \gamma m_0 v; \gamma \equiv \frac{1}{\sqrt{1 - \beta^2}} = \frac{W}{mc^2} = \frac{W}{511 \text{ keV}}; \beta^2 = \left(\frac{v_{\parallel}}{c}\right)^2 + \left(\frac{v_{\perp}}{c}\right)^2 \quad (6.38)$$

and  $v_{||}$  and  $v_{bot}$  are the instantaneous particle velocities along and perpendicular to  $B_0$ , respectively. A solution of equation (6.38) for the particle velocity  $v$  and displacement  $r$  (e.g., [Rose and Clark 1961](#), Chap. 10) gives

$$v = \hat{x}v_{\perp} \cos \omega_{\gamma}t + \hat{y}v_{\perp} \sin \omega_{\gamma}t + \hat{z}v_{||} \quad (6.39)$$

$$\rho = \hat{x}\frac{v_{\perp}}{\omega_{\gamma}} \sin \omega_{\gamma}t - \hat{y}\frac{v_{\perp}}{\omega_{\gamma}} \cos \omega_{\gamma}t + \hat{z}v_{||}t \quad (6.40)$$

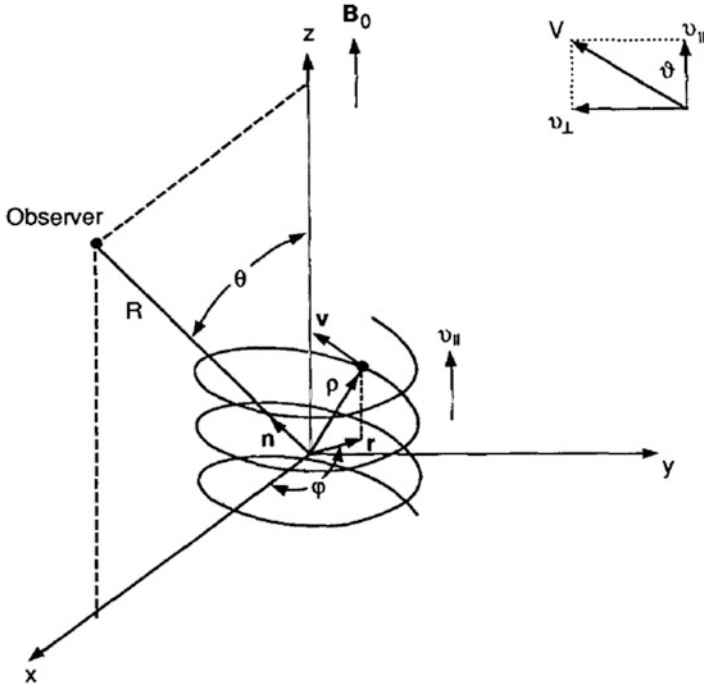


**Fig. 6.7** Vector diagram for an electron in helical motion in a uniform magnetic field

where

$$\omega_b = -\frac{eB_0}{m_0}; \quad \omega_{\gamma} = -\frac{eB_0}{m_0\gamma} \quad (6.41)$$

and  $\omega_{\gamma}$ , the relativistic cyclotron frequency, takes account of the relativistic mass charge while  $\omega_b$  is its value in the limit of zero particle speed. The path of the particle is a circular helix of radius and pitch angle  $J$  given by  $\tan^{-1}(2\pi r\omega_{\gamma}/v_{||})$ . The rotation for an electron is counterclockwise when viewed opposite to the direction of  $B_0$ .

From Eq. (6.38)  $\dot{v} \propto v \times B_0$ , which shows that  $\dot{v}$  is perpendicular to  $v$  (and  $B_0$ ) with

$$\begin{aligned} v_{\perp} &= r\omega_{\gamma} \\ \dot{v}_{\perp} &= v_{\perp}\omega_{\gamma} \end{aligned} \quad (6.42)$$

Figure 6.8 is the circular motion analog of Fig. 6.1 and shows the orientation of the radiation field equation (6.16). The effect of the parallel motion  $v_{||}$  is a component of the radiation field arising from the motion of the charge along  $B_0$ . This is illustrated in Fig. 6.9.

If the motion is circular so that  $v_{||} = 0$  and  $v_{bot} = v$ , and if the electron is ultra-relativistic, the electron will be shown to radiate only in the plane of the orbit. An observer located in the plane of rotation would see pulses of radiation corresponding to those instants when the electron is moving precisely towards the observer. The periodicity of the pulses is then

$$T' = \frac{2\pi}{\omega_\gamma} = \frac{2\pi m_0 \gamma}{eB_0} \quad (6.43)$$

The duration of each pulse is [Ginzburg and Syrovatskii \(1965\)](#)

$$\Delta T' = \frac{m_0}{eB_0} \frac{1}{\gamma^2} \quad (6.44)$$

Figure 6.10 depicts the pulse characteristic for this idealized, single particle case. For the helical motion case when  $v_{||} \neq 0$ , a pitch angle correction is required in  $\omega_\gamma$ . This was first brought out by [Epstein and Feldman \(1967\)](#). For helical motion with pitch angle  $\vartheta$  (Fig. 6.7), the Doppler-shifted time interval between pulses is (Fig. 6.11)

$$T_{DS} = T' (1 - \beta_{||} \cos \vartheta) \approx T' (1 - \cos^2 \vartheta) = (2\pi/\omega_\gamma) \sin^2 \vartheta \quad (6.45)$$

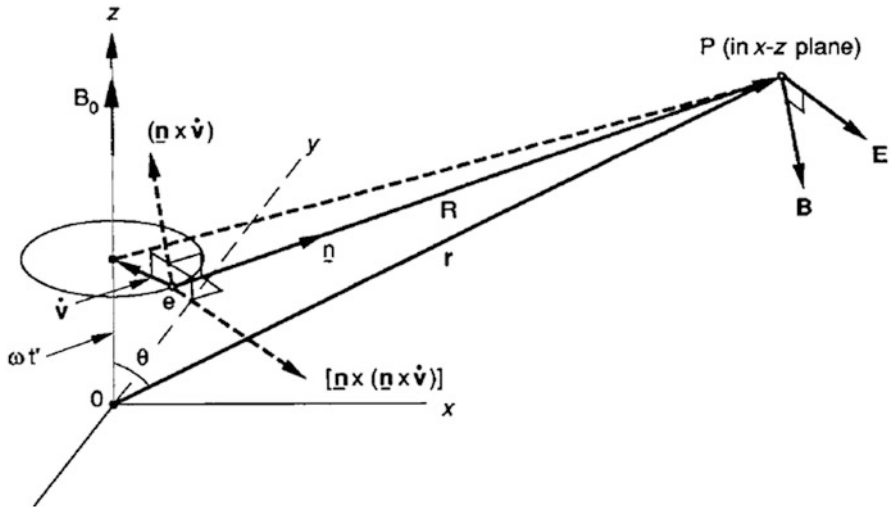
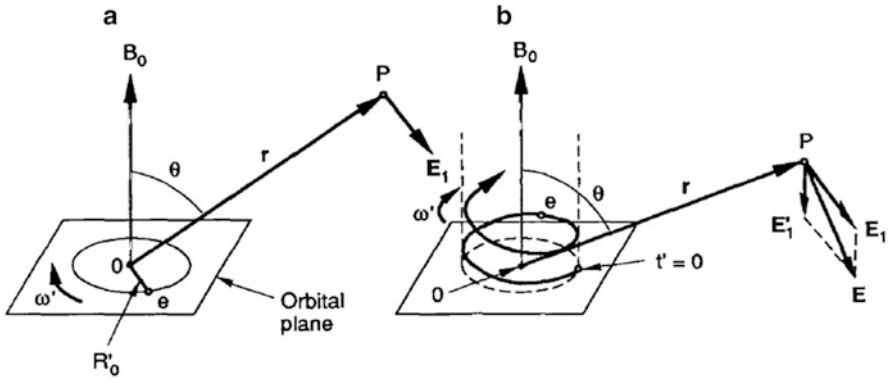
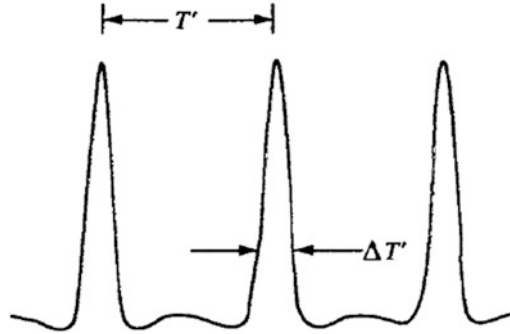


Fig. 6.8 Orientation of far-field vectors for an electron in circular motion

For an ultrarelativistic electron the radiation is very nearly in the direction of its instantaneous motion so that the velocity polar angle  $\vartheta = \theta$ , the coordinate polar angle.



**Fig. 6.9** Polarization of radiation field  $E$ . (a) Plane circular orbit. (b) Helical orbit



**Fig. 6.10** Electric field in the wave zone as a function of time for a particle undergoing circular motion in a magnetic field

Thus, the radiation field of the electron consists of harmonics of the angular frequency

$$\omega_{\gamma DS} = \frac{2\pi}{T_{DS}} \approx \frac{\omega_{\gamma}}{\sin^2 \vartheta} \quad (6.46)$$

In the formulation that follows, we shall let  $T' \rightarrow T_{DS}$  and  $\omega_{\gamma} \rightarrow \omega_{\gamma DS}$  in order to include the pitch angle correction when the trajectory is helical.

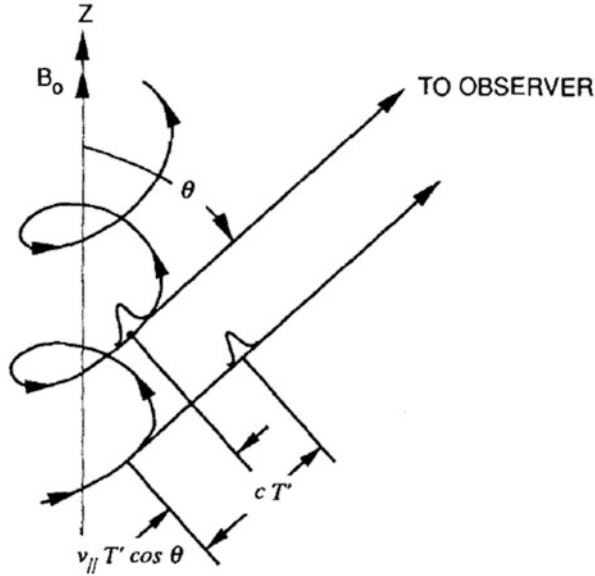


**Fig. 6.11** Doppler shift of synchrotron radiation emitted by a particle moving towards the observer

#### 6.1.4 Angular Distribution of the Radiation

The electromagnetic field seen by an observer situated in the radiation zone of Fig. 6.2 is periodic with period

$$T = T' (1 - n \cdot \bar{\beta}) \quad (6.47)$$

where

$$\bar{\beta} = \frac{1}{T'} \int_{T'} v(t')/c dt' \quad (6.48)$$

From Eq. (6.12), the mean power emitted by the electron per solid angle in the direction  $n$  is defined by

$$\frac{dP}{d\Omega} = R^2 (S \cdot n) \frac{T}{T'} \quad (6.49)$$

where  $\langle \rangle$  denotes time averaging over the period  $T$ . Thus

$$\frac{dP}{d\Omega} = \frac{e^2}{16\pi^2 \epsilon_0 c} \frac{1}{T'} \int \frac{\left| n \times \left\{ (n - \beta) \times \dot{\beta} \right\} \right|^2}{(1 - n \cdot \beta)^5} dt' \quad (6.50)$$

Integration of this power over the solid angle gives the total mean power  $P^T$  emitted by the electron. Lienard's formula equation (6.29) for a periodic velocity motion is then



$$P^T = \frac{e^2}{6\pi\epsilon_0 c} \frac{1}{T'} \int \frac{\dot{\beta}^2 - (\boldsymbol{\beta} \times \dot{\boldsymbol{\beta}})^2}{(1 - \mathbf{n} \cdot \boldsymbol{\beta})^3} dt' \quad (6.51)$$

Equation (6.51) reduces to the integral

$$\frac{dP(\theta)}{d\Omega} = \frac{e^2 \omega_b^2}{32\pi^3 \epsilon_0 c} (1 - \beta^2) \beta_{\perp}^2 \times \int_0^{2\pi} \frac{(\cos \theta - \beta_{\parallel})^2 + \beta_{\perp}^2 \sin^2 \theta + 2g_{\parallel} \beta_{\perp} \sin \theta \sin \phi + (1 - \beta_{\parallel}^2) \sin^2 \theta \sin^2 \phi}{[g_{\parallel} + \beta_{\perp} \sin \theta \sin \phi]^5} d\phi \quad (6.52)$$

where  $\varphi = \omega_b t'$  and  $g_{\parallel} = g_{\parallel}(\theta) = 1 - \beta_{\parallel} \cos \theta$ . After integrating (Johner 1988), Eq. (6.53) reduces to

$$\frac{dP(\theta)}{d\Omega} = \frac{e^2 \omega_b^2}{32\pi^3 \epsilon_0 c} (1 - \beta^2) \beta_{\perp}^2 F(\beta_{\parallel}, \beta_{\perp}, \theta) \quad (6.53)$$

where

$$F(\beta_{\parallel}, \beta_{\perp}, \theta) = \frac{4g_{\parallel}^2 [(1 - \beta_{\parallel}^2)(1 - \cos^2 \theta) - 4\beta_{\parallel} \cos \theta] - (1 - \beta_{\parallel}^2 + 3\beta_{\perp}^2) \beta_{\perp}^2 \sin^4 \theta}{4(g_{\parallel}^2 - \beta_{\perp}^2 \sin^2 \theta)^{7/2}} \quad (6.54)$$

Equation (6.55) reduces to Landau's result (Landau and Lifshitz 1962) when  $\beta_{\parallel} = 0$ . In a way analogous to the directivity of an antenna, the gain  $G(\theta)$  is defined as

$$G(\theta) = \frac{dP(\theta)/d\Omega}{P_{\text{circular}}^T/4\pi} \quad (6.55)$$

where we have chosen to normalize to the total circular power radiated by an electron. Substituting Eq. (6.43) into Eq. (6.52) while neglecting the time integration gives

$$P_{\text{circular}}^T = \frac{e^2 \omega_b^2}{6\pi\epsilon_0 c} \frac{\beta_{\perp}^2}{1 - \beta^2} \quad (6.56)$$

From Eqs. (6.54)–(6.57), we get

$$G(\beta_{\parallel}, \beta_{\perp}, \theta) = \frac{3}{4} (1 - \beta^2) F(\beta_{\parallel}, \beta_{\perp}, \theta) \quad (6.57)$$

The gain  $G(\theta)$  is plotted in polar coordinates in Figs. 6.12–6.14 for various values of  $\beta_{\parallel}$  and  $\beta_{\perp}$ . Noteworthy in  $G(\theta)$  is the inversion of gain direction between the cases  $\beta_{\parallel} = 0$  as  $\beta_{\perp}$  increases and the essentially forward emission in the relativistic case when  $\beta_{\parallel}/\beta_{\perp}$  is large.

### 6.1.5 Frequency Distribution of the Radiation

The energy  $W(\omega, \Omega)$  emitted per unit solid angle per frequency interval  $d\omega$  is given by Eq. (6.37). To evaluate the exponent appearing in the equation we assume, without loss of generality, that the propagation vector lies in the  $x-z$  plane (see Fig. B.2). Thus,

$$n = \hat{x} \sin \theta + \hat{y}(0) + \hat{z} \cos \theta \quad (6.58)$$

and it follows from Eq. (6.41) that

$$\begin{aligned} \exp i(k \cdot \rho - \omega t) &= \exp i \left( \frac{\omega}{\omega_\gamma} \beta_\perp \sin \theta \sin \omega_\gamma t + \omega t \beta_\parallel \cos \theta - \omega t \right) \\ &= \sum_{-\infty}^{\infty} J_m \left( \frac{\omega}{\omega_\gamma} \beta_\perp \sin \theta \right) \exp i (m \omega_\gamma t + \omega t \beta_\parallel \cos \theta - \omega t) \end{aligned} \quad (6.59)$$

(e.g., see Higher Transcendental Functions, Vol.II. Bateman Manuscript Project, p. 7). Substituting Eq. (6.60), the cross product  $n \times (n \times v)$ , and Eq. (B.7) into Eq. (6.37), leads to integrals of the form

$$\int_{-\infty}^{\infty} \{1; \sin \omega_\gamma t; \cos \omega_\gamma t\} \exp [i(x \sin \theta + \omega t \beta_\parallel \cos \theta - \omega t)] dt \quad (6.60)$$

with solutions

$$2\pi \sum_{-\infty}^{\infty} \left[ J_m[x]; -i \frac{dJ_m[x]}{dx}; \frac{1 - \beta_\parallel \cos \theta}{\beta_\perp \sin \theta} J_m[x] \right] \delta[y] \quad (6.61)$$

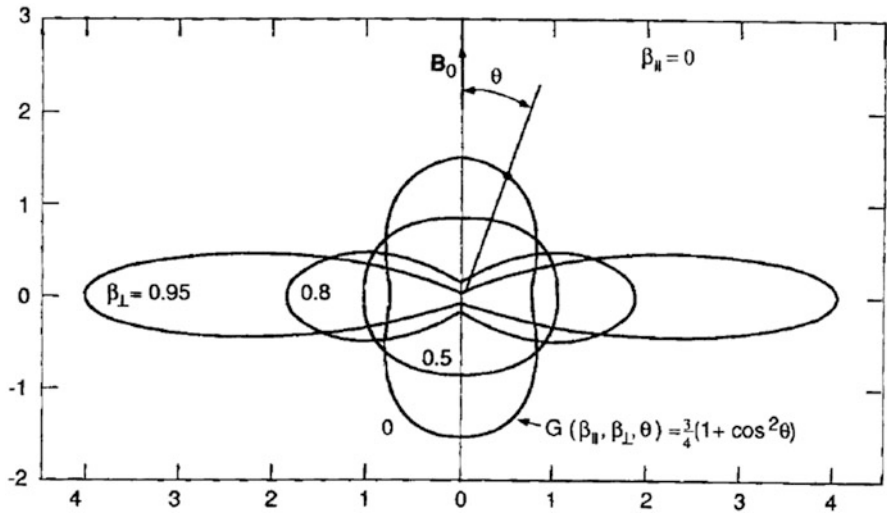


**Fig. 6.12** Gain patterns for  $\beta_\parallel = 0$  when  $\beta_\perp = 0.5, 0.8$ , and  $0.95$

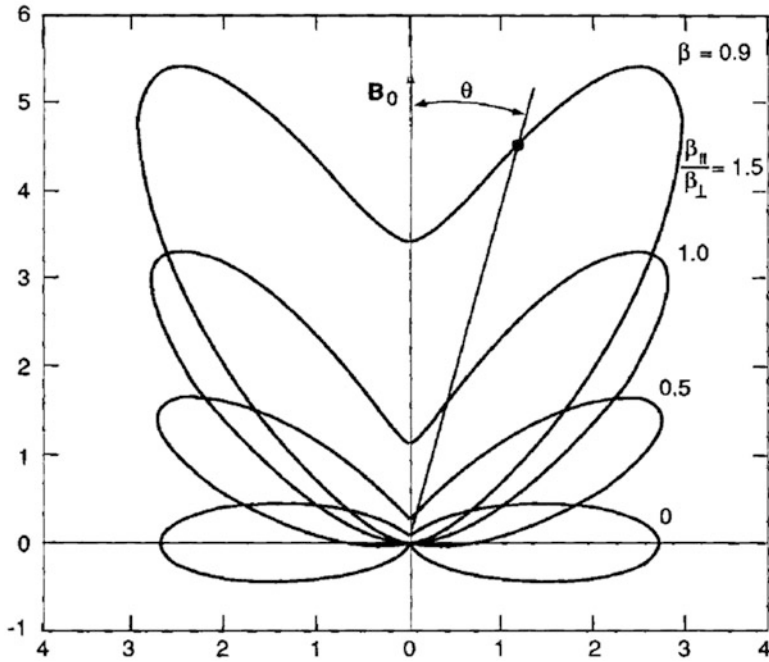


**Fig. 6.13** Gain patterns for  $\beta = 0.9$  and  $\beta_{||}/\beta_{\perp} = 0, 0.5, 1.0$ , and  $1.5$

where

$$x = \frac{\omega}{\omega_{\gamma}} \beta_{\perp} \sin \theta \quad (6.62)$$

$$y = m\omega_{\gamma} - \omega (1 - \beta_{||} \cos \theta) \quad (6.63)$$

We see that by setting the argument of the delta function in Eq. (6.62) to zero, that the radiation spectrum consists of spectral lines occurring at frequencies

$$\omega = \frac{m\omega_{\gamma}}{1 - \beta_{||} \cos \theta} = \frac{m\omega_b \sqrt{1 - \beta_{||}^2 - \beta_{\perp}^2}}{1 - \beta_{||} \cos \theta} \quad (6.64)$$

As shown in Fig. 6.11, the term  $\beta_{||} \cos \theta$  ( $\propto v_{||} \cos \theta$ ) represents the Doppler shift of the observed radiation.

The emitted energy  $W(\omega, \Omega)$  is obtained by inserting Eqs. (6.61) and (6.62) in Eq. (6.37). The result has the form  $W(\omega, \Omega) = \sum |\dots|^2 \delta^2(y)$ . The emitted power is

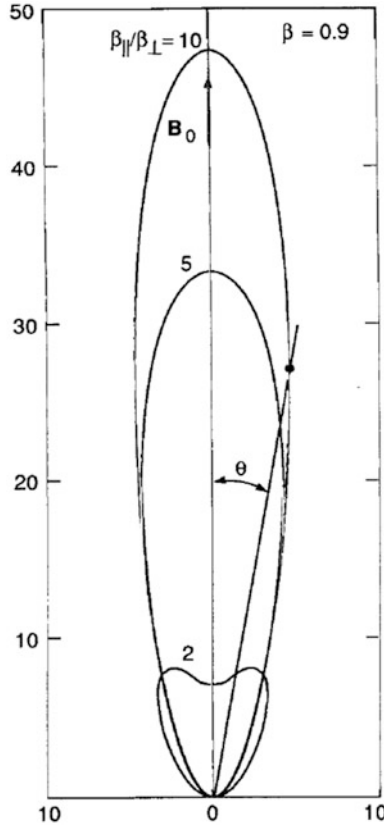


**Fig. 6.14** Gain patterns for  $\beta = 0.9$  and  $\beta_{\parallel}/\beta_{\perp} = 2, 5$ , and  $10$

found by dividing  $W$  by the “total time of radiation” given by  $\int_{-\infty}^{\infty} \exp(-i\gamma t) dt = 2\pi\delta^2(y)$ .<sup>3</sup> The quantity obtained is the coefficient of spontaneous emission (Bekefi 1966)

$$P_{\omega}(\omega, \beta, \theta) = \frac{e^2 \omega^2}{8\pi^2 \epsilon_0 c} \sum_1^{\infty} \left| \begin{array}{c} -\hat{x} \frac{\cos \theta}{\sin \theta} (\cos \theta - \beta_{\parallel}) J_m(x) \\ -\hat{y} i \beta_{\perp} \frac{dJ_m(x)}{dx} \\ \hat{z} (\cos \theta - \beta_{\parallel}) J_m(x) \end{array} \right|^2 \delta(y) \quad (6.65)$$

The electric field is oriented in the vector direction of Eq. (6.66). The magnitude of Eq. (6.66) is

$$P_{\omega}(\omega, \beta, \theta) = \frac{e^2 \omega^2}{8\pi^2 \epsilon_0 c} \left[ \sum_1^{\infty} \left( \frac{\cos \theta - \beta_{\parallel}}{\sin \theta} \right)^2 J_m^2(x) + \beta_{\perp}^2 J_m'^2(x) \right] \delta(y) \quad (6.66)$$

<sup>3</sup> The function  $\delta^2(y)$  is to be interpreted as  $\delta(y)T/2\pi$  where  $T$  is the period of revolution.

In the two foregoing equations the terms of the series  $m = 0, -1, -2, \dots$  were eliminated as not meaningful because of the argument of the delta function.

The total radiation in a given harmonic  $m$  is obtained by integrating a single term of the right-hand side of Eq. (6.67) over frequency  $\omega$  and solid angle  $d\Omega = 2\pi \sin \theta d\theta$ . The result is [Schwinger \(1949\)](#);

$$P_m^T = \frac{e^2 \omega_b^2}{2\pi \epsilon_0 c} \frac{1 - \beta_0^2}{\beta_0} \left[ m \beta_0^2 J'_{2m}(2m\beta_0) - m^2 (1 - \beta_0^2) \int_0^{\beta_0} J_{2m}(2mt) dt \right] \quad (6.67)$$

where  $\beta_0 = \beta_{\perp} / \sqrt{1 - \beta_{\parallel}^2}$ .  $P_m^T$ , given by Eq. (6.68), is the total emission in all directions, but the emission is anisotropic and depends on the direction of the observer. With the use of Bessel function conversion formulas (*Handbook of Mathematical Functions*, Dover Publications, 1965), Eq. (6.68) can be written, for the case of relativistic electrons  $\gamma \gg 1$  and  $m \gg 1$ , as

$$P_m^T = \frac{e^2 \omega_b^2}{4\pi^2 \sqrt{3} \epsilon_0 c} \frac{\beta_0 (1 - \beta_0^2)}{\gamma^2} m \times \left[ 2K_{23} \left( \frac{2m}{3\gamma^3} \right) - \frac{\gamma^2 (1 - \beta_0^2)}{\beta_0^2} \int_{2m3\gamma^3}^{\infty} K_{13}(t) dt \right] \quad (6.68)$$

Replacement in Eq. (6.69) of  $m$  by  $\omega/\omega_{\gamma}$  and then dividing by  $\omega_{\gamma}$ , gives the total emission per unit radian frequency interval rather than per harmonic:

$$P_{\omega}^T = \frac{\sqrt{3} e^2 \omega_b}{8\pi^2 \epsilon_0 c} \times \left\{ \beta_0 (1 - \beta_0^2) \gamma^2 \frac{\omega}{\omega_c} \left[ 2K_{23} \left( \frac{\omega}{\omega_c} \right) - \frac{\gamma^2 (1 - \beta_0^2)}{\beta_0^2} \int_{\omega \omega_c}^{\infty} K_{13}(t) dt \right] \right\} \quad (6.69)$$

where, by definition,

$$\begin{aligned} \omega_c &= \frac{3}{2} \omega_{\gamma} \gamma^3 = \frac{3}{2} \omega_b \gamma^2 \\ &= 2.64 \times 10^7 B_0 \text{ Gauss} \left( \frac{W_{\text{keV}}}{511 \text{ keV}} \right) \text{ rad/s} \end{aligned} \quad (6.70)$$

Figure 6.15 plots the characteristic frequencies versus  $\gamma$ . For example, an electron with  $\gamma = 10$  (5 MeV) in the presence of a  $10^{-4}$  G field, has a “critical frequency”  $\omega_c/2\pi \sim 42$  kHz ( $\alpha = \pi/2$ ) whereas a  $\gamma = 100$  electron (50 MeV) has a “critical frequency”  $\sim 4.2$  MHz. It will be shown that the critical frequency is located near the frequency at which the spectrum has its maximum value. Otherwise, the “critical frequency” is only a mathematical artifice and has no physical meaning. The actual oscillatory frequency of the gyrating electron for these two cases is 28 and 2.8 Hz, respectively.

Only for the special case  $\beta_{\parallel} = 0$  and  $\beta_{\perp} \rightarrow 1$ , is the recurrence relation  $2K'_{2/3}(\xi) + K_{1/3}(\xi) = -K_{5/3}(\xi)$  applicable so that Eq. (6.70) reduces to the well-known circular orbit, highly relativistic synchrotron function

$$P_{\omega}^T = \frac{\sqrt{3} e^2 \omega_b}{8\pi^2 \epsilon_0 c} \left\{ \frac{\omega}{\omega_c} \int_{\omega/\omega_c}^{\infty} K_{5/3}(t) dt \right\} \quad (6.71)$$

The special functions in Eqs. (6.70) and (6.72) are plotted in Fig. 6.16.

With the substitution  $\omega_\gamma \rightarrow \omega_{\gamma DS}$  (Eq. (6.47)), the total radiated power from a single electron at frequency  $\omega$  (Eq. (6.72)) is divided by the factor  $\sin^2 \theta$ . However this factor is cancelled out if we consider the time average of the power emitted from a fixed volume element. Consequently, such a correction is unnecessary for the interpretation of synchrotron emission from radio sources (Scheuer 1968).

The spectrum  $P_\omega^T$  for arbitrary  $\beta_{||}$  and  $\beta_\perp$  may be determined by numerically evaluating the ... term in Eq. (6.70). The results of these calculations are shown in Fig. 6.17.

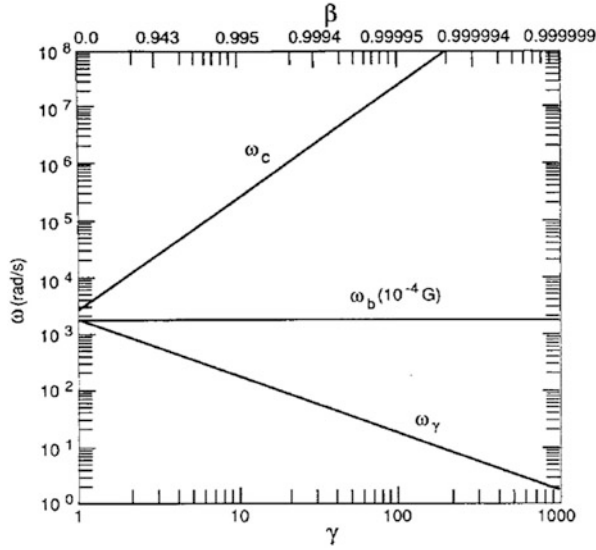


Fig. 6.15 The frequencies  $\omega_b$  and  $\omega_\gamma$  vs.  $\gamma$  or  $\beta$

## 6.2 Field Polarization

### 6.2.1 Polarization in the Plane of Rotation

Two independent modes of propagation, ordinary and extraordinary (Appendix B), are identifiable in Eqs. (6.66) and (6.67) when  $\theta = \pi/2$ . The ordinary mode emissivity component ( $E_{||B}$ ) is

$$P_\omega^{(o)}(\pi/2) = \frac{e^2 \omega^2}{8\pi^2 \epsilon_0 c} \sum_{m=1}^{\infty} \beta_{||}^2 J_m^2(m\beta_\perp) \delta(m\omega_\gamma - \omega) \quad (6.72)$$

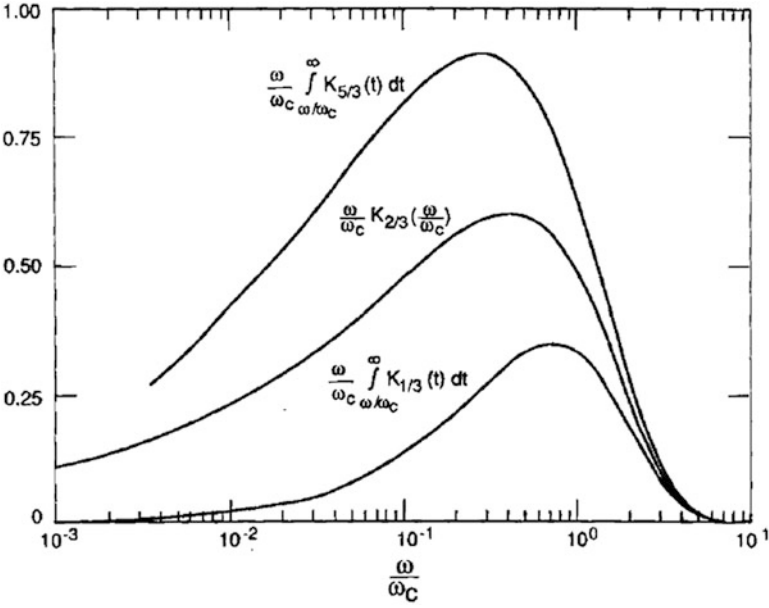


Fig. 6.16 Special functions vs.  $\omega/\omega_c$ .

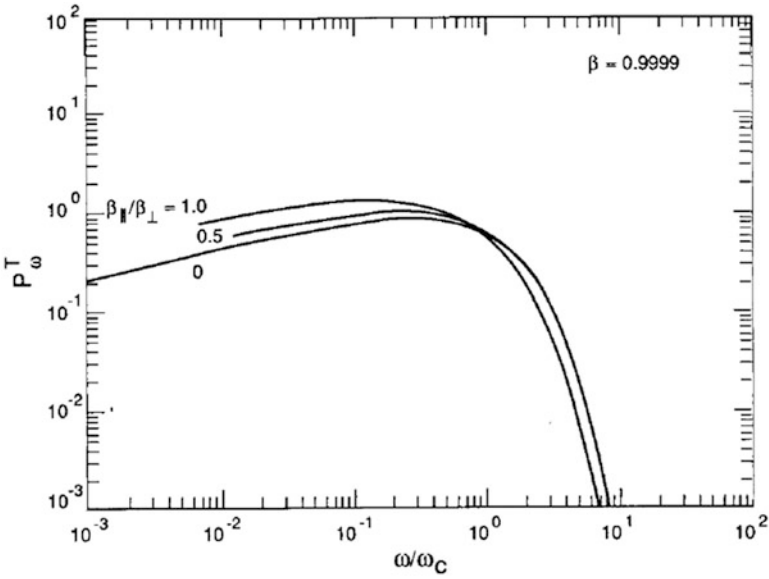


Fig. 6.17 Spectrum  $P_\omega^T$  vs.  $\omega/\omega_c$  for  $\beta = 0.9999$  and  $\beta_\parallel/\beta_\perp = 0.9999, 0.5$ , and  $1.0$ .

while the extraordinary mode component ( $E \perp B$ ) is

$$P_{\omega}^{(X)}(\pi/2) = \frac{e^2 \omega^2}{8\pi^2 \epsilon_0 c} \sum_1^{\infty} \beta_{\perp}^2 J_m'^2(m\beta_{\perp}) \delta(m\omega_{\gamma} - \omega) \quad (6.73)$$

The existence of the ordinary wave is due solely to  $\beta_{\parallel} \neq 0$ . As shown in Fig. B.3, the ordinary wave is linearly polarized along  $B_0$  while the extraordinary wave circumscribes an ellipse in the plane transverse to  $B_0$  as it propagates. Since the angle of propagation (and observation) is  $\theta = \pi/2$ , Eqs. (6.73) and (6.74) are linearly polarized:  $P_{\omega}^{(O)}$  along  $B_0$  and  $P_{\omega}^{(X)}$  perpendicular to  $B_0$ . The Poynting vector equation (7.2), and therefore the strength of  $P_{\omega}^{(X)}$ , is maximum when  $E^{(X)}$  is oriented perpendicular to  $n$ . When  $E^{(X)}$  rotates sufficiently to have a component along the line-of-sight, a longitudinal plasma wave exists. The mode conversion properties of an oblique wave propagating in magnetized, nonuniform plasma (i.e., a characteristic of most cosmic plasmas) is beyond the scope of this book and is covered elsewhere (Peratt and Kuehl 1972).

### 6.2.2 Polarization for Arbitrary Angles of Observation

The expression for the power radiated into the  $m$ th harmonic in Eq. (6.67) may be written as the sum of two parts,

$$P_{\omega}(\omega, \beta, \theta) = P_{\omega}^{(1)} + P_{\omega}^{(2)} \quad (6.74)$$

where

$$P_{\omega}^{(1)}(\theta) = \frac{e^2 \omega^2}{8\pi^2 \epsilon_0 c} \sum_1^{\infty} \left\{ \frac{\cos \theta - \beta_{\parallel}}{\sin \theta} J_m(x) \right\}^2 \delta(y) \quad (6.75)$$

$$P_{\omega}^{(2)}(\theta) = \frac{e^2 \omega^2}{8\pi^2 \epsilon_0 c} \sum_1^{\infty} \{ \beta_{\perp} J_m'(x) \}^2 \delta(y) \quad (6.76)$$

whose orthogonal field vectors  $E_m^{(1)}$  and  $E_m^{(2)}$  ( $p_{\omega} \sim E_m^2$ ) lie parallel and perpendicular, respectively, to the projection of  $B_0$  on the plane normal to the line of sight  $[B_0^{\perp n} = B_0 - (B_0 \cdot n)n]$  as shown in Fig. 6.18.<sup>4</sup> The easiest way to determine the polarization of the  $m$ th harmonic is to take the ratio of the field amplitudes in Eqs. (6.76) and (6.77),

$$R_m = -\frac{E_m^{(1)}}{E_m^{(2)}} = -\left( \frac{\cos \theta - \beta_{\parallel}}{\beta_{\perp} \sin \theta} \right) \frac{J_m(\psi m)}{J_m'(\psi m)} \quad (6.77)$$

where  $\psi = \beta_{\perp} \sin \theta / (1 - \beta_{\parallel} \cos \theta)$ . The parameter  $R_m$  defines the ellipticity of the propagating wave in the direction  $\theta$ . When  $|R_m| = 1$ ,  $R_m = 1$ , the wave is circu-

<sup>4</sup> While  $P_{\omega}^{(O)}$  has no rotation,  $P_{\omega}^{(1)}$  does rotate.



larly polarized while when  $R_m = 0$ , the wave is linearly polarized. When  $0 < R_m < 1$ , the wave is elliptically polarized in the ratio of the field amplitudes oriented along the minor and major axes of the ellipse. The polarization of the extraordinary mode rotates in the same sense as does the radiating electron.

Figure 6.19a depicts  $R_1$  for the fundamental  $m = 1$  mode versus  $\psi$  for the case  $\theta = \pi/2$ . As shown, when  $\psi = 0$  ( $\theta = \pi/2$ ),  $P\omega_{(1)} = P\omega_{(0)} = 0$ , and the existing extraordinary wave is linearly polarized. When  $\psi \neq \pi/2$ ,  $P\omega_{(1)}$  is finite and the wave is elliptically polarized.

Figure 6.20 depicts  $R_m$  for higher order harmonics as the angle of observation  $\theta$  is decreased. As shown, the polarization remains more closely circular over a larger range of  $\psi$  when  $m \gg 1$ . A rapid change in the sense of polarization also occurs when  $m \gg 1$ . When  $\theta \rightarrow 0$ , this change occurs for larger values of  $\beta_{||}$ .

## 6.3 Radiation from an Ensemble of Electrons

### 6.3.1 Velocity-Averaged Emissivity

The emissivity averaged over all velocity components is defined by

$$\langle P_{\omega}^{(2,1)} \rangle = (4\pi)^{-1} \int_0^{\pi} P_{\omega}^{(2,1)} d\beta = (4\pi)^{-1} \int_0^{\pi} P_{\omega}^{(2,1)} (\beta_{\perp}, \beta_{||}) 2\pi \sin \vartheta d\vartheta \quad (6.78)$$

where  $\beta_{\perp} = \beta \sin \vartheta$  and  $\beta_{||} = \beta \cos \vartheta$ .

For the special case  $\theta = \pi/2$ , Eq. (6.79) can be written as

$$\begin{aligned} \langle P_{\omega}^{(X,O)} \rangle &= (4\pi)^{-1} \int_0^{\pi} P_{\omega}^{(X,O)} (\beta_{\perp}, \beta_{||}) 2\pi \sin \vartheta d\vartheta \\ &= \frac{e^2 \omega^2}{8\pi^2 \epsilon_0 c} \sum_1^{\infty} A_m^{(X,O)} (\gamma) \delta(m\omega_{\gamma} - \omega) \end{aligned} \quad (6.79)$$

where Eqs. (6.73) and (6.74) have been used, and the functions  $A_m^{(X,O)}$  embody the pertinent integration over  $J$ . Trubnikov (1958) has derived expressions for  $A_m^{(X,O)}$  in three distinct energy regimes: nonrelativistic, mildly relativistic, and relativistic,

$$A_m^{(X,O)} (\gamma) = \begin{cases} \frac{(m\beta)^{2m}}{(2m+1)!} \left[ 1; \frac{\beta^2}{2m+3} \right] & m\beta \ll 1 \\ \frac{e^{2m/\gamma}}{\sqrt{16\pi m^3} \gamma} \left( \frac{\gamma-1}{\gamma+1} \right)^m \left[ 1; \frac{\gamma(\gamma^2-1)}{2m} \right] & \gamma^3 \ll m \\ \frac{1}{4\sqrt{3}\pi m \gamma^2} \left[ \int_{2m/3\gamma^3}^{\infty} K_{5/3}(t) dt \pm K_{2/3}(2m/3\gamma^3) \right] & \gamma, m \gg 1 \end{cases} \quad (6.80)$$

Consider the case of relativistic electrons. Because the harmonics are closely spaced in this energy range, the summation in Eq. (6.80) can be replaced by an integration over  $dm$ . Thus

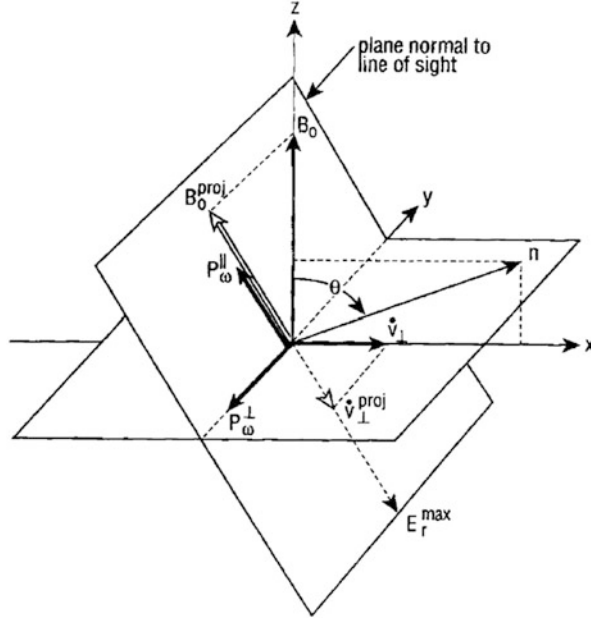


**Fig. 6.18** Orientation of the quantities  $P_{\omega}^{\perp}$  and  $P_{\omega}^{\parallel}$

$$\sum_1^{\infty} A_m^{(X,O)}(\gamma) \delta(m\omega_{\gamma} - \omega) \rightarrow \int_1^{\infty} A_m^{(X,O)}(\gamma) \delta(m\omega_{\gamma} - \omega) dm = \frac{1}{\omega_{\gamma}} \left[ A_m^{(X,O)} \right]_{m=\frac{\omega}{\omega_{\gamma}}} \quad (6.81)$$

with the result

$$\langle P_{\omega}^{(X,O)} \rangle = \frac{\sqrt{3}e^2\omega_b}{64\pi^3\epsilon_0 c} \left( \frac{\omega}{\omega_c} \right) \left[ \int_{2m/3\gamma^3}^{\infty} K_{5/3}(t) dt \pm K_{2/3}(2m/3\gamma^3) \right] \quad (6.82)$$

For arbitrary angles  $\theta$ , the degree of polarization  $\Pi(\theta)$  may be defined as

$$\Pi(\theta) = \left| \frac{\langle P_{\omega}^{(1)} \rangle - \langle P_{\omega}^{(2)} \rangle}{\langle P_{\omega}^{(1)} \rangle + \langle P_{\omega}^{(2)} \rangle} \right| \quad (6.83)$$

where, in general, the superscripts 1 and 2 denote two independent modes of propagation at angle  $\theta$ . For  $\theta = \pi/2$ , the two independent modes of propagation are the ordinary and extraordinary waves. Substituting Eq. (6.83) into Eq. (6.84) gives

$$\Pi(\pi/2) = \left| \frac{\langle P_{\omega}^{(O)} \rangle - \langle P_{\omega}^{(X)} \rangle}{\langle P_{\omega}^{(O)} \rangle + \langle P_{\omega}^{(X)} \rangle} \right| = \left| \frac{K_{2/3}(\omega/\omega_c)}{\int_{\omega/\omega_c}^{\infty} K_{5/3}(t) dt} \right| \quad (6.84)$$

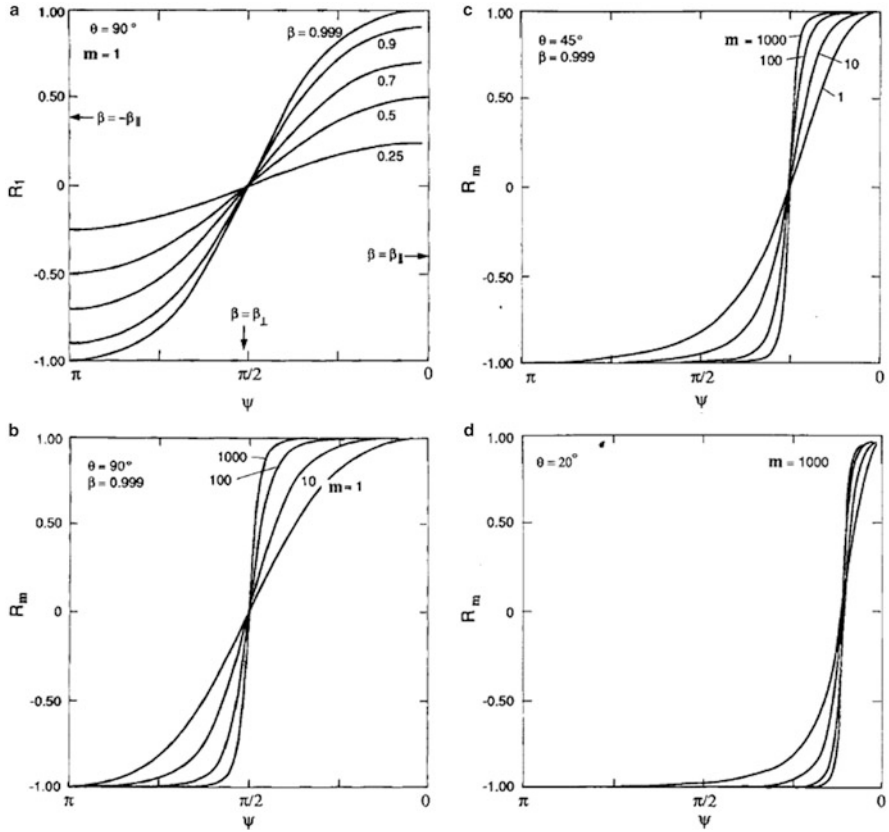


**Fig. 6.19** (a)  $R_I$  vs.  $\psi$  for  $\theta = 90^\circ$ ,  $\beta = 0.25, 0.5, 0.7, 0.9$ , and  $0.999$ . (b)  $R_n$  vs.  $\psi$  for  $\theta = 90^\circ$ ,  $\beta = 0.999$ , for  $m = 1, 10, 100$ , and  $1,000$ . (c)  $R_n$  vs.  $\psi$  for  $\theta = 45^\circ$ ,  $\beta = 0.999$ , for  $m = 1, 10, 100$ , and  $1,000$ . (d)  $R_n$  vs.  $\psi$  for  $\theta = 20^\circ$ ,  $\beta = 0.999$ , for  $m = 1, 10, 100$ , and  $1,000$

Figure 6.20 shows Eqs. (6.84) and (6.85a) versus  $\omega/\omega_c$  for various angles of  $\theta$ . As shown, the maximum degree of polarization is obtained when  $\theta = \pi/2$ , when the difference between the amplitudes of the orthogonal modes is maximum. For this case,  $\Pi \sim 1/2$  for  $\omega/\omega_c \ll 1$  and  $\Pi \sim 1$  for  $\omega/\omega_c \gg 1$ . For oblique angles of observation the degree of polarization falls rapidly for  $\omega/\omega_c > 1$ . However, for oblique angles the independent modes can no longer be delineated into purely ordinary and extraordinary components.

### 6.3.2 Emission from an Ensemble of Electrons

We now wish to determine the total power radiated by all electrons which have a Maxwellian distribution of energies. First, the emission coefficient  $j_\omega$  is defined as the sum  $P_\omega$  over an ensemble of electrons,

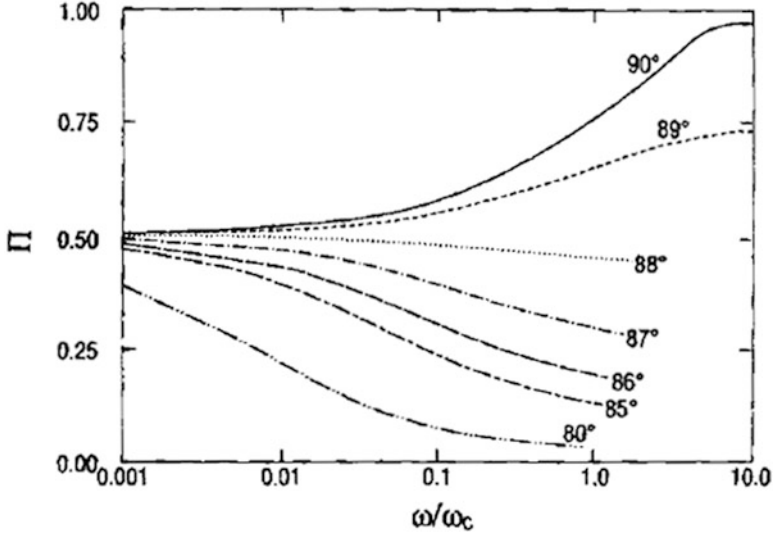


Fig. 6.20 Polarization factor  $\Pi$  vs.  $\omega/\omega_c$

$$j_{\omega}^{(2,1)} = \int_0^{\infty} \langle P_{\omega}^{(2,1)} \rangle f(p) d^3 p = \int_0^{\infty} \langle P_{\omega}^{(2,1)} \rangle f(p) 4\pi p^2 dp \quad (6.85a)$$

The total emission  $j_{\omega}^T$  associated with Eq. (6.85b) is

$$j^T = \int_0^{\infty} P^T(p) f(p) 4\pi p^2 dp \quad (6.85b)$$

where  $P^T(p)$  is the total emissivity integrated over all frequencies. Substituting Eq. (6.43) into Eq. (6.29) gives

$$P^T(v) = \frac{e^4 B^2 v_{\perp}^2}{6\pi\epsilon_0 m^2 c^2 (1 - v^2/c^2)} \quad (6.86)$$

or, in terms of momentum,

$$P^T(p) = \frac{e^4 B^2 p_{\perp}^2}{6\pi\epsilon_0 m^4 c^3} \quad (6.87)$$

Since  $f(p)$  is isotropic and since there are two directions associated with  $p_{\perp}$ , but only one associated with  $p_{\parallel}$ , we have

$$p_{\perp}^2 = 2\bar{p}^2/3 \quad (6.88)$$

The Maxwellian distribution function is

$$f(p) = C_p \exp(-W/kT) \quad (6.89)$$

where

$$W(p) = (p^2 c^2 + m^2 c^4)^{1/2} = \gamma m c^2 \quad (6.90)$$

is the total energy of the particle. The normalization constant can be found from the requirement that

$$\int_0^\infty f(p) 4\pi p^2 dp = C_p \int_0^\infty \exp\left\{-\frac{mc^2}{kT} \sqrt{1 + (p/mc)^2}\right\} 4\pi p^2 dp = 1 \quad (6.91)$$

This integral can be evaluated by setting  $\xi = \sqrt{1 + (p/mc)^2}$  and using the Hankel function  $H_1^{(1)}(\xi)$ , the derivative relation for these functions, and the definition of the modified Bessel function  $K_2(\xi)$ . We find

$$C_p = [4\pi kT m^2 c K_2(mc^2/kT)]^{-1} \quad (6.92)$$

Finally, from Eqs. (2.2), (6.85bb), (6.87), (6.89), and (6.92),

$$j^T = \frac{e^4 B^2 [K_2]^{-1}}{9\pi \epsilon_0 m^6 c^4 kT} \int_0^\infty p^4 \exp\left\{-\frac{mc^2}{kT} \sqrt{1 + (p/mc)^2}\right\} dp \quad (6.93)$$

which reduces to

$$j^T = \frac{e^4 B^2}{3\pi \epsilon_0 m^2 c} \left(\frac{n_e kT_e}{mc^2}\right) \frac{K_3(mc^2/kTe)}{K_2(mc^2/kTe)} \text{ W/m}^3 \quad (6.94)$$

Equation (6.94) is the total power radiated by all the electrons which have a relativistic Maxwellian distribution of energies. A more practical expression may be obtained by expanding the modified Bessel functions in a power series, so that

$$\begin{aligned} j^T &= \frac{e^2 \omega_p^2}{3\pi \epsilon_0 c} \left(\frac{n_e kT_e}{mc^2}\right) \left(1 + \frac{5}{2} \frac{kT_e}{mc^2} + \dots\right) \\ &= 6.2 \times 10^{-17} B_{\text{Tesla}}^2 n_{\text{cm}^{-3}} T_{\text{keV}} [1 + T_{\text{keV}}/204 \text{ keV} + \dots] \text{ W/m}^3 \end{aligned} \quad (6.95)$$

More restrictively, if the radiating filaments are in a thermal/magnetic pressure balance, so that from Eq. (10.20)  $\beta_p = 2\mu_0 n_e k(T_e + T_i)/B^2 = 1$ , then Eq. (6.95) becomes

$$j^T = 5.0 \times 10^{-38} n_{\text{cm}^{-3}}^2 T_{\text{keV}}^2 [1 + T_{\text{keV}}/204 \text{ keV} + \dots] \text{ W/m}^3 \quad (6.96)$$

From either Eq. (6.95) or Eq. (6.96), the total radiated power  $j^T V$  over a volume  $V$  can be computed.

## 6.4 Synchrotron Radiation from Z Pinches

Charged particle beams held together or pinched by their self-magnetic fields have been of general interest since their earliest investigation by [Bennett \(1934\)](#). Confinement in the simple cylindrical pinch is a result of the axial, or  $z$ , directed current  $I_z$ ; hence, the name “Z” or “zed” pinch, often used in place of Bennett pinch. The macroscopic picture of such a beam is that of a self-consistent magnetic confinement or compression against the expansion due to thermal pressure equation (1.9). On the microscopic scale, the individual particle orbits include radial oscillations due to the Lorentz force equation (1.5) superimposed on the drift in the direction of mean flow. Since they imply particle acceleration, there is electromagnetic radiation associated with them. Because the force is a  $\mathbf{v} \times \mathbf{B}$  force, the radiation from the relativistic electrons is synchrotron radiation.

Manifestations of the pinch effect appear to the laboratory observer as a rapidly occurring phenomena. A burst of radiation from high-current discharges (with current densities of the order  $10^{11}$  A/cm<sup>2</sup>), such as low-inductance vacuum sparks, plasma focus devices, and exploded wires, is found over a broad spectral range: the microwave region to the hard X ray region. Recorded data show that the radiation bursts are correlated with dips in the current waveform. The microwaves observed are attributed to the synchrotron radiation of electrons in the magnetic field of the proper current. The hard X ray quanta are attributed to synchrotron radiation from the electrons at the transitions between Landau levels in this same current-induced magnetic field ([Meirovich 1984](#); [Peratt and Koert 1985](#); [Trubnikov 1958](#)).

This phenomena may be similar to that of impulsive solar microwave bursts which are believed to be produced by the synchrotron radiation of electrons accelerated in solar flares ([Takakura 1960](#); [Kawabuta 1964](#); [Kai 1965](#)).

Z pinches as sources of synchrotron radiation in the laboratory have been studied by [Meirovich \(1984\)](#) and by [Newberger \(1984\)](#), who used the Los Alamos PHERMEX Facility. PHERMEX produces a 30 MeV ( $\gamma \sim 57$ ), 1 kA electron beam that is synchrotron-loss limited in energy. Like the sun, which generates synchrotron radiation and solar radio outbursts at microwave frequencies (1–10 GHz), PHERMEX experiments also produce bursts of microwaves at gigahertz frequencies ([Mack et al. 1987](#)).

### 6.4.1 X Ray Emission

Moderately high atomic number plasma pinches with temperatures in the kilovolt range have been produced in discharges with megavolt electron energies and currents up to 5 mA. Figure 6.21 shows a typical experimental setup used to produce and measure X rays. One or more metallic or glass wires are strung between the cathode and anode of a pulse power generator diode (Fig. 2.9). Typically, the wires have diameters of 15  $\mu\text{m}$ , are 3 cm long, and are on a 20 mm array diameter. Streak and framing cameras and laser shadowgraphy follow the behavior of the plas-

mas produced when the  $\sim 100$  ns pulse of energy explodes the wires into Bennett pinches. The self-consistent magnetic field is tens of megagauss in the 0.1–1 mm pinches.

If more than one wire is exploded, or if a jet of gas is injected between the cathode-anode gap, copious amounts of X ray radiation are produced. For example, neon (atomic number 10) produces  $\sim 55$  kJ of K-line X rays at  $h\nu \sim 1$  keV at frequency  $\nu$  while titanium (atomic number 22) plasmas can produce  $\sim 10$  kJ of K-line emission up to  $h\nu \sim 10$  keV. Figure 6.22 depicts the radiation energy as a function of the number of exploded wire filaments. As shown, an order of magnitude enhancement in X rays may be expected if at least two plasma filaments are present.

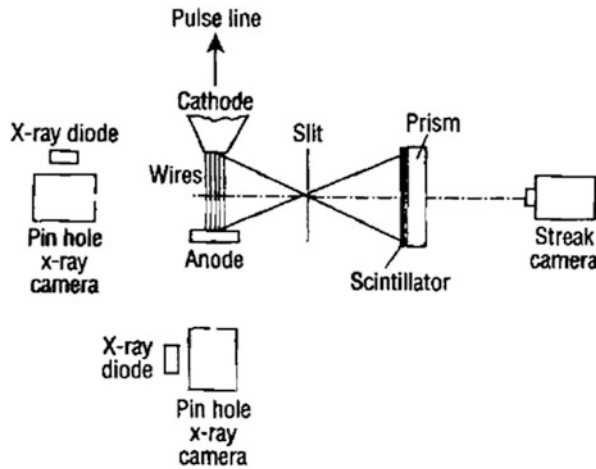


**Fig. 6.21** Experimental arrangement used to obtain X ray streak and frame photographs of the X ray source as it evolves in time. The X rays are imaged through a slit onto a strip of scintillator, which is then viewed by the streak camera through a prism (Reference is made to Figs. 2.9, 2.12, and 3.18)

### 6.4.2 X Ray Spectroscopy

X ray pinhole photographs and the spatial correlation of spectral emission show three types of emission emanating from exploded Z pinches. These are (a) hot-plasma thermal emission, (b) cool plasma thermal emission, and (c) nonthermal (synchrotron) emission.

The X ray emission from high-ionization states are recorded as narrow lines (using a curved crystal spectrograph) corresponding to the excited states of the elements present in the plasma. The high-temperature emission emanates from pinched regions along the plasma which emit X rays predominantly in the less than 3.5 keV energy region. Figure 6.23 shows the spectra produced by a titanium plasma.

Thermal X ray emission is also found from cooler-plasma regions with temperatures between 50 and 200 eV.

In addition to hot- and cool-plasma emission, X rays are also produced by relativistic electrons in the exploded-wire discharges. These X rays may have energies as high as  $\sim 8$  keV and measurements of the shape and location of the radiating plasmas as a function of time show that the nonthermal X rays have time histories of longer duration than the pinches. The hard X ray emission produced by the energetic electrons generally begins about 20 ns after the beginning of the low energy X ray emission from pinches and lasts for the duration of the pulse discharge.

### 6.4.3 Morphology of the Thermal X Ray Source

Time integrated pinhole camera photography is used to acquire information on the size and shape of the radiating plasma. A pinhole camera may consist of a metal box containing the X ray film, with a number of pinholes covered by a graded aluminum foil material to increase the film latitude.

A contour plot made from a pinhole photograph is shown in Fig. 6.24 and shows that the intense X rays originate from hot spots along the plasma that is confined between the Bennett-pinch exploded wires.<sup>5</sup> The dimensions of the X ray hot spots are  $< 100$  mm in diameter; with cores often between 25 and 75 mm diameter. For a typical pinhole photograph with five hot spots of  $\sim 100$  mm diameter emitting 10 kJ of X rays, the energy density per hot spot is  $3.8 \times 10^{15}$  J/m<sup>3</sup> ( $3.8 \times 10^{16}$  ergs/cm<sup>3</sup>), making the exploded wire the most copious energy density producer known of X rays from either laboratory or astrophysical plasmas.

The variability of the thermal X ray radiation, based on the “spikedness” of the XRD signal, is tens of picoseconds (i.e., corresponding to the speed of light dimensions of the emitting regions). The energy, of course, is supplied by the Marx bank via the transmission line (Fig. 2.9), both of which are invisible in electromagnetic emission.

The plasma characteristics determined from the distribution of excitation states in the exploded-wire spectra corresponds well with those from other high-energy-density generating devices, namely, the vacuum spark and the plasma focus (Sect. 4.6.2).

---

<sup>5</sup> Long after the thermal plasma X ray burst, streak photographs show the Bennett-pinch exploded wire plasmas converging onto the centrally confined plasma because of the Biot-Savart attraction. The pinhole camera placed in front of the anode records a single “dot” of X rays.



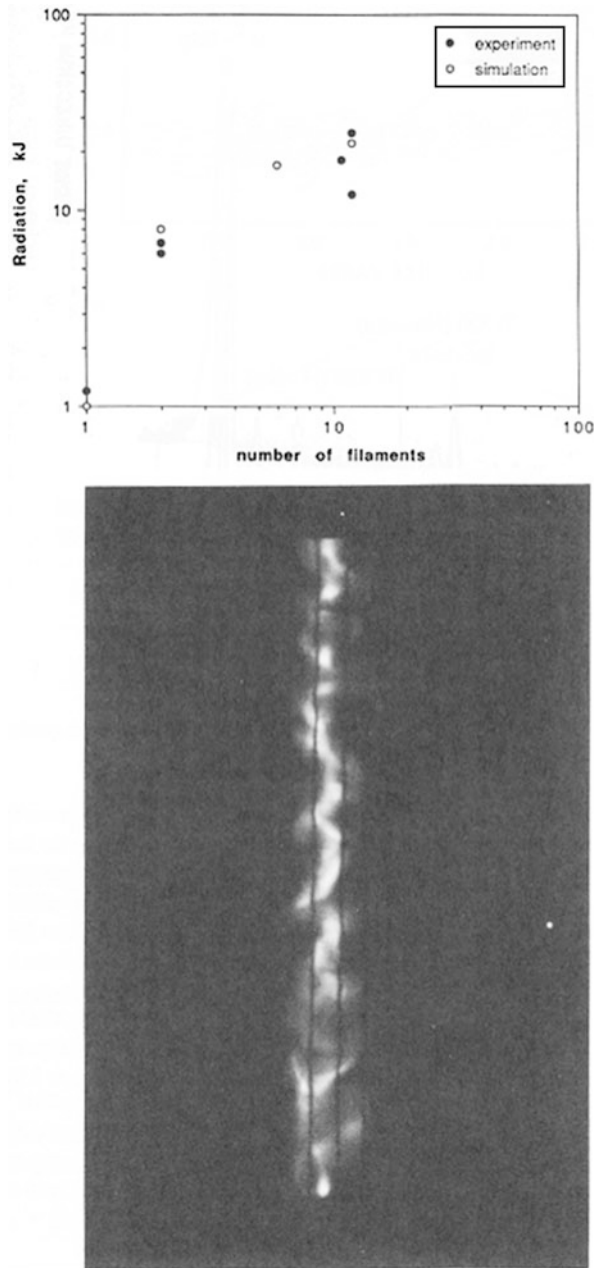


**Fig. 6.22** (Top) Radiated energy versus number of exploded wire filaments for a 1 mV, 1.3 mA pulse delivered to titanium wires. (Bottom) Side-on X ray pinhole photograph of the plasma confined between the Bennett-pinch exploded wires (seen in absorption)

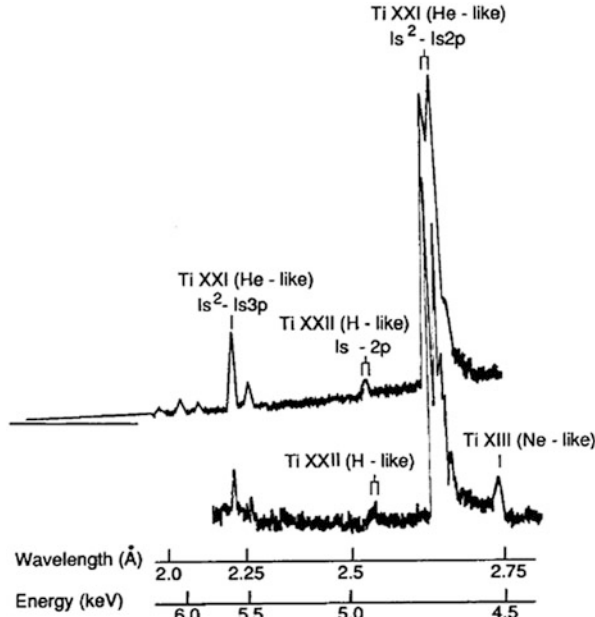


**Fig. 6.23** X ray spectra from titanium plasma (Fig. 6.22) collected with a curved-crystal spectrograph

## 6.5 Particle-in-Cell Simulation of Synchrotron Processes

### 6.5.1 Simulated Z Pinches

Since  $I_z$  is often driven by a potential difference across a plasma column, an axial field component  $E_0 = \hat{z}E_z$  may be present. Chapter 5 dealt with naturally occurring magnetic-field-aligned electric fields in current columns or filaments. Because of  $E_0$ , the formulation given in the previous sections must be modified to include the acceleration of electrons parallel to  $B_0$ . For this case  $\dot{\beta} = \dot{\beta}_\perp + \dot{\beta}_\parallel$ ,  $\beta \times \dot{\beta} \neq 0$ , (cf. Eqs. (6.29) and (6.52)) and the equation of motion Eq. (1.5) is

$$\frac{dp}{dt} = e(E_0 + v \times B_0) \quad (6.97)$$

Because of the added complexity to the analysis of Sects. 6.1–6.5, and because of geometrical complexities (Sect. 6.5.2), we choose instead to “brute-force” a solution via three-dimensional (three spatial dimensions), fully-electromagnetic (static and radiation fields), particle-in-cell simulations (Chap. 10).

### 6.5.2 Synchrotron Bursts from Simulated Z Pinches

An enhancement of radiated power equation (6.29) or Eq. (6.52) is achieved when the sum of the  $v \times B$  radial forces seen by the relativistic electrons is increased, as is the case when the azimuthal magnetic fields of neighboring pinches are present (Fig. 3.13). Whenever the attractive force between simulation columns causes their separation to be reduced to a distance such that the repulsive force equation (3.26) starts to become comparable to the attractive force equation (3.13), a burst in the radiation occurs (Fig. 6.25). For the parameters used in these simulations, this distance is of the order of several pinch radii. As shown in Fig. 6.25, the radiation from the kiloelectronvolt particles is polarized in the transverse plane and the synchrotron enhancement (burst) is detected in the  $x$  and  $y$  electric radiation energies ( $W_{ERx}, W_{ERy}$ ) and the  $z$  magnetic radiation energy ( $W_{BRz}$ ). The burst lasts until the induced axial magnetostatic energy  $W_{Bz}$ , due to the azimuthal current  $I_\phi$ , is depleted (because the counterparallel azimuthal current force equation (3.26) brakes the azimuthal electron flow in both filaments). For some simulation parameters,  $W_{Bz}$  can build-up and discharge again in the form of additional bursts of synchrotron radiation. The long-time, slowly varying increase in radiation in  $W_{ERx}$  and  $W_{ERy}$  is due to the buildup of electrostatic energy from charge separation in the particle number and size constrained simulation model.

The total power emitted as synchrotron radiation during the burst (simulation time  $T \sim 90$ ) is

$$P^T = \frac{W_{rad}^T}{\tau_{burst}} \text{ AEU/time step} \quad (6.98)$$

where  $W_{rad}^T$  is the total radiated power in arbitrary energy units (AEU) and  $\tau_{burst}$  is the burst duration in simulation time steps. Equation (6.98) may be converted to watts by scaling the simulation magnetostatic energy in AEU to a physical magnetostatic field in Tesla (the spatial dimensions and time in seconds are known quantities in a simulation):

$$P^T = \frac{W_{rad}^T \left[ (2\mu_0)^{-1} B_\phi^2 V / W_{ms} \right]}{\tau_{burst \text{ seconds}}} \text{ W} \quad (6.99)$$

For this case,  $W_{rad}^T = W_{ERx} + W_{ERy} + W_{ERz} = 2.1$  AEU and  $W_{ms} = 350$  AEU. The radiation burst lasts  $\sim 20dt'$  in the compressed simulation time frame (Sect. 10.6.3). Since time compression is achieved by using light ions,  $m_i/m_e = 16$ , the actual burst time in seconds is

$$\tau_{burst} = 20dt' \sqrt{1,836/16} \quad (6.100)$$

Hence,

$$P^T = 2.8 \times 10^{-5} \frac{B_\phi^2 V}{2\mu_0 dt'} \text{ W} \quad (6.101)$$

### 6.5.3 Synchrotron Source Radiation Patterns

When  $\beta_{||} > \beta_{\perp}$ , interacting Z pinches beam a double-lobed radiation pattern in a direction close to  $B_0$ . The basic shape is shown in Figs. 3.13–3.17, which depict the magnetic isobars that confine the radiating electrons within the filaments. The isobars during the peak of the microwave burst are shown in Fig. 6.26a. Because of the Biot-Savart forces between filaments, the currents in each filament have taken on a C-shaped cross-section from their original circular cross-sections. The most intense currents are confined to narrow regions within the C-shaped lobes. These are shown as spots in Fig. 6.26a, which are found to be diagonally juxtapositioned in the two lobes. This juxtaposition marks the start of the rotation of filaments (Fig. 3.14).

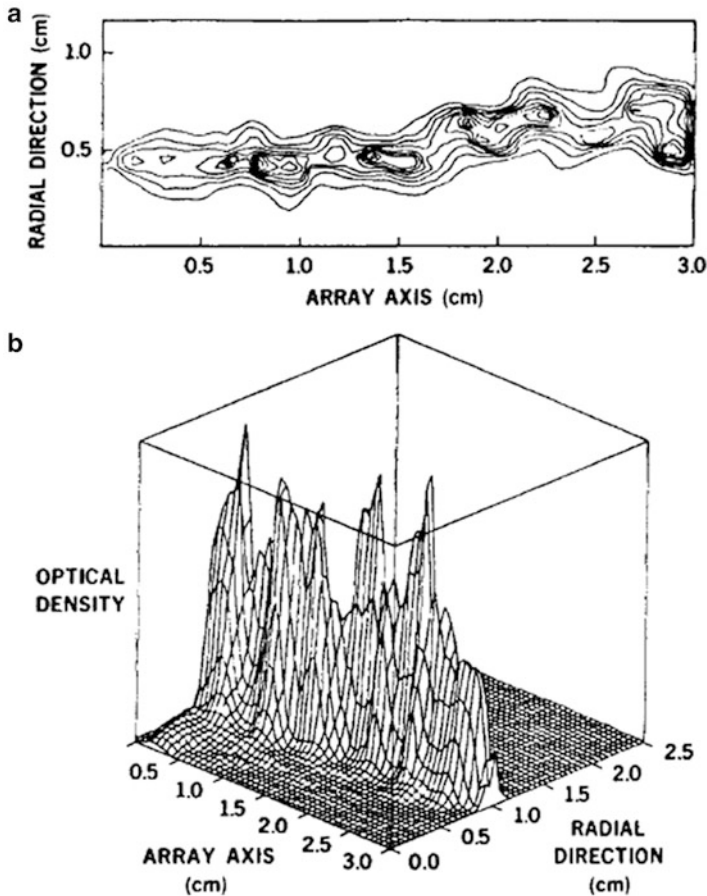


**Fig. 6.24** (a) Planar contour plot of a pinhole photograph from a titanium plasma. (b) Isometric plot of the optical density

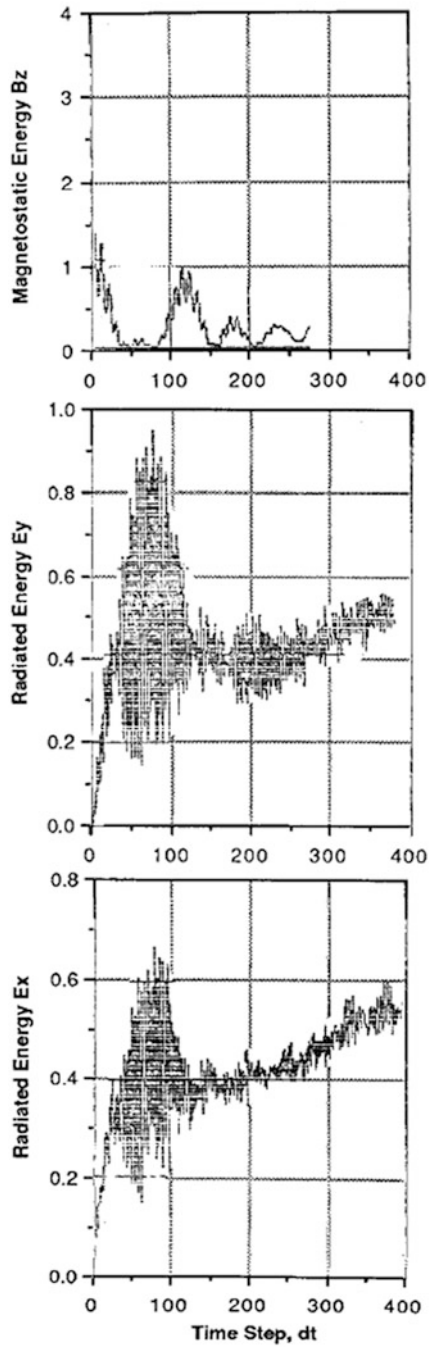


**Fig. 6.25** (a) Self-consistent axially-directed magnetic field vs. time in  $\delta t'$  time steps. (b) and (c) Synchrotron radiation energy in the  $x$  and  $y$  electric field components, respectively. The ordinates are in arbitrary energy units (AEU)

The two lobes represent regions of strong synchrotron emission while the radiation is most intense from the spots within the lobes.

Examples of isophotes of the generated electric field strength (squared) over a time span which includes the microwave burst are shown in Fig. 6.27a. These isophotes show where the acceleration fields are strongest, and therefore depict the radiation patterns of the forward-beamed synchrotron emission (cf. Eq. (6.58)). As shown, the isophotes tend to be more complex than the isophotes and often show additional filamentation in each radiating lobe. At early times, before and during the microwave burst, the acceleration fields tend to be strongest at the outer edges of the lobes. At later times, maxima migrate inward within the filaments, eventually producing a “butterfly” like radiation pattern. The fourth frame of Fig. 6.27 shows the vectors  $B$  overlaid on , giving information on the polarization properties of the radiation from the filaments. In general, the  $B$  vectors are maximum where they lie transverse to  $|E|^2$ .

## 6.6 Synchrotron Radiation from Cosmic Sources

### 6.6.1 Gross Radio Properties of Galaxies

Most cosmological objects, including galaxies, are emitters of synchrotron radiation, over a relatively wide band encompassing radio frequencies through optical frequencies. The radio power  $L$  of galaxies, integrated from 10 MHz to 100 GHz, ranges from about  $10^{30}$  W to about  $10^{38}$  W, and relative to their optical luminosity, from less than  $10^{-6}$  to about 1 (Perola 1981). The distribution in power is described by means of the Radio Luminosity Function (RLF) which represents the number of radio emitting galaxies per unit volume as a function of the monochromatic power at a certain frequency. Figure 6.28 illustrates the RLF at 1.4 GHz at the present cosmological epoch, the “local” RLF.

The RLF suggests a continuity in the morphological types of radioemitting galaxies. Above  $10^{26}$  W/Hz, the main contribution comes from quasars and classical double radio galaxies. In the region  $10^{23}$ – $10^{26}$  W/Hz, the elliptical galaxies dominate while below  $10^{23}$  W/Hz (about an order of magnitude greater than the power of our Galaxy) the power comes principally from spiral galaxies.

In the region  $10^{21}$ – $10^{23}$  W/Hz, an overlap of spiral and elliptical galaxies occurs. The “ellipticals” are in fact a hybrid class, containing bona fide ellipticals along with  $N$  galaxies (a bright nucleus surrounded by a faint nebosity) to that of  $cD$  galaxies (giant ellipticals with very extended radio “halos”). Noteworthy in Fig. 6.28 is a “break” in synchrotron power from ellipticals at  $10^{24.5}$  W/Hz and another at  $10^{21.3}$  W/Hz for spirals.

The size of the radioemitting regions in galaxies spans a very wide range. At powers larger than about  $10^{23}$  W/Hz at 1.4 GHz the radio emission is generally dominated by an extended component, whose size goes from tens of kiloparsecs (e.g.,

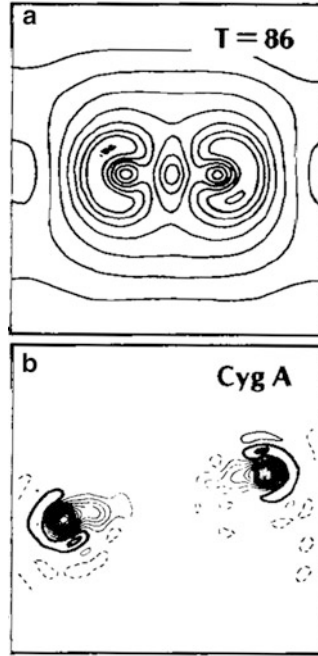


**Fig. 6.26** (a) Magnetic energy isobars  $B^2$  in the plane perpendicular to the axial field-aligned currents at time of peak burst of synchrotron radiation. The most intense fields are the “hot spots” in the radiation lobes. A  $B^2$  minima exists between the two outflowing currents. (b) Isophotal contours of synchrotron radiation at 150 MHz from Cyg A. An elliptical galaxy is situated midway between the two radio lobes

Cygnus A) to tens of megaparsecs (e.g., 3C236). Often a very compact central radio component is present, whose power ranges from  $10^{22}$  up to  $10^{25}$  W/Hz, and which may be seen to vary with time. Extended and central radio components are typically found also in quasars.

At powers less than about  $10^{23}$  W/Hz, the size of the radio region in elliptical galaxies is generally measured in kiloparsecs and often reduces to a compact central component. In spiral galaxies, the next stage of a suggested epochological sequence in Fig. 6.28, the situation is different. Apart from the radical change in morphology between elliptical and spiral, the spiral galaxies not only have a compact nuclear component (of radio dimension between 0.1 and 1 kpc) but also a component of size  $\sim 10$  kpc, coincident with the spiral disk.

Overlapping the powerful radio ellipticals (with Seyfert-like nuclear spectra) and spiral galaxies are the Seyfert-spirals themselves, comprising 1 % of all spiral types. In contrast to the ellipticals, spiral galaxies rarely have compact nuclear sources and are unassociated with extended radio lobes. Table 6.1 delineates the properties of galactic radio sources.

Figure 6.29 shows the positions of the radio sources, both extended and compact on a linear-size, radio-luminosity plot. As seen, the bulk of the classical double radio galaxies possessing an elliptical galaxy have a spatial extent between a few

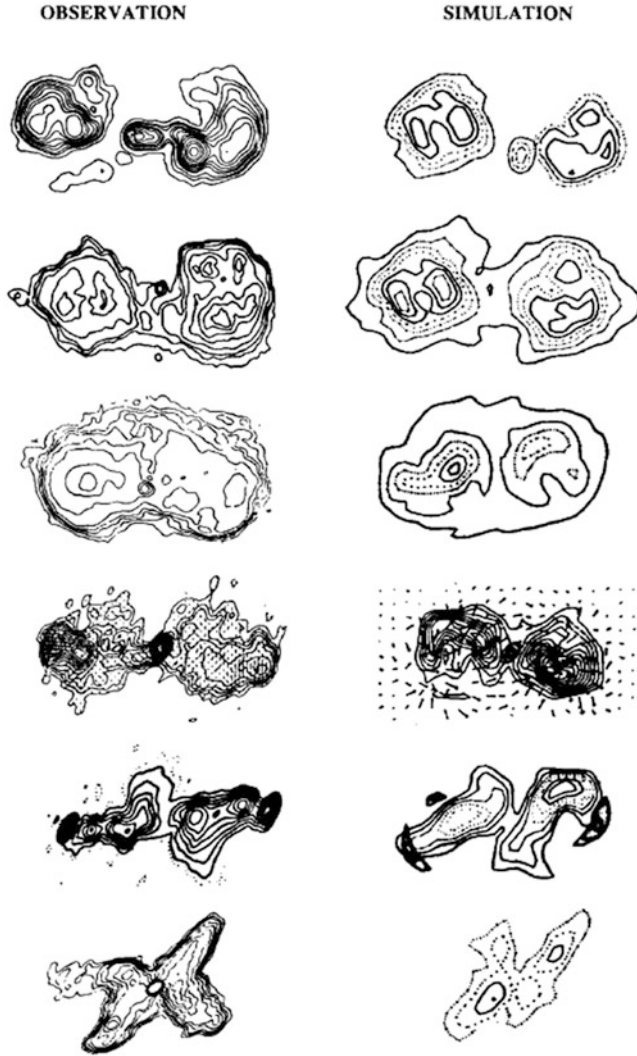


**Fig. 6.27** (a) Electric energy isophotes  $E^2$ . Top to bottom: simulation times  $T = 51, 52, 236, 237, 280$ , and  $288 \delta t'$ , respectively. (b) Synchrotron isophotes (various frequencies) of double radio galaxies and quasars. Top to bottom: 0844+319, Fornax A, 3C310, 2355+490, 3C192, and 3C315



tens of kiloparsecs to many hundreds of kiloparsecs, with radio luminosities of  $L \sim 10^{35} - 10^{39}$  W. Some transitional radiogalaxies, 8–80 kpc, and  $L \sim 10^{34}$  W, are also present. The radioquasars appear in two distinct populations; extended sources with dimensions of several kiloparsecs to several hundreds of kiloparsecs ( $L \sim 10^{37} - 10^{39}$  W), and compact sources  $\sim 2$ –8 parsecs ( $L \sim 10^{37} - 10^{39}$  W). Most of the spiral galaxies are found to be clustered according to a size-luminosity of  $\sim 10$ –80 kpc, and  $L \sim 10^{31} - 10^{32.5}$  W.

Finally, unlike their other properties, the radio spectra of the spiral galaxies are similar to those of the radio galaxies. The nuclear component of our galaxy, for example, is a miniature replication of a classic double radio galaxy (Fig. 3.23).

### 6.6.2 Double Radio Galaxies

The discovery of discrete radio sources dates back to the pioneering survey of [Reber \(1944\)](#), who found areas of enhanced radio intensity in the constellations Cygnus and Cassiopeia. Many excellent reviews of double radio sources are available in the literature ([Shklovsky 1960](#); [Pacholczyk 1977](#); [Miley 1980](#); [Perola 1981](#)), as are a number of models of sources. However, regardless of whatever ingredients are postulated as necessary in models used to “explain” their existence, what is observed from any radio source is synchrotron radiation, that requires only relativistic electrons in the presence of a magnetic field.

One of the first low-resolution radio maps made of a radio galaxy was the strong source Fornax A (Fig. 6.30). The pattern depicted in this figure is that of two radio emitting regions (thus giving “double” radio galaxies their name) situated on either side of an elliptical galaxy (NGC 1316). Improvements in radio telescope technology led to higher resolution maps such as that of Cygnus A shown in Fig. 6.26b. Cygnus A, the brightest radio source in Cygnus, has proved to be the “prototype” of double radio galaxies and models of double radio galaxies are usually based on the characteristics of this source. As shown in Fig. 6.26, Cygnus A consists primarily of two radio lobes of dimension  $l \cong w \cong 35$  kpc ( $10^{21}$  m) separated on either side of an elliptical galaxy by a distance  $a \cong 80$  kpc ( $1.22 \times 10^{21}$  m). Cygnus A is thought to be characterized by the parameters  $B \times 10^{-9} - 10^{-7}$  T ( $10^{-5} - 10^{-3}$  G),  $T \sim 1$ –10 keV,  $n_e \sim 10^2 - 10^4$  m $^{-3}$  ( $10^{-4} - 10^{-2}$  cm $^{-3}$ ),  $L \sim 1.6 - 4.4 \times 10^{37}$  W, with a total source energy of  $10^{50} - 10^{57}$  J. The average energy of the relativistic electrons is estimated to be 100–158 Mev ([Perola 1981](#)).

**Example 6.3. Double radio galaxy simulation model and parameters.** To simulate a radio galaxy, the results of Sect. 6.6.2 are used and the simulation geometry is that shown in Fig. 3.12 scaled to double radio galaxy dimensions (the reason for two filaments is discussed in Sect. 3.10.6). In analogy to Cygnus A, the two filaments are taken to have a width of 35 kpc with a separation of 80 kpc. Assuming that the total plasma mass  $M$  over a length  $L$  ( $\sim 10^{21}$  m) of filament involved in Biot-Savart attraction is of the order of that observed in Galaxies,  $M \cong 10^{41}$  kg, while setting the velocity between galactic filaments to 1,000 km/s ([Peratt and Green 1983](#)) in

**Table 6.1** General properties of galactic radio sources

Source type	Power, W/Hz	Geometry and dimension	Redshift, $z$
Quasars, double radio galaxies	$10^{26} - 10^{29}$	Two extended radio lobes separated tens of kpc to Mpc; oftentimes a central component is present	0.3–3.8 0.01–1.8
Elliptical galaxies:	$10^{23} - 10^{26}$	Kiloparsecs to decaparsecs, devoid of any magnetic field	
cD		Giant ellipticals with very extended haloes	$\sim 1$
N		Bright nucleus surrounded by faint nebulosity	
	$10^{24.5}$	Break in RLF	
	$10^{26}$	Seyfert-like spectra	
Seyfert spiral galaxies		Elementary spirals of a few tens of kpc extent; most active nuclei	0.01–0.09
Spiral galaxies	$< 10^{23}$	Two radio components coincident with spiral disk, kpc-sized nuclear region	0.003–0.5 <sup>a</sup>
	$10^{21.3}$	Break in RLF	

<sup>a</sup> Andromeda is blueshifted

(3.49), yields  $I_z \cong 2.15 \times 10^{19}$  A and  $B_\phi = \mu_0 I_z / w \cong 2.5 \times 10^{-8}$  T ( $2.5 \times 10^{-4}$  G). (The quantities  $I_z$  and  $B_\phi$  are physically nonsensitive to the actual mass distribution, depending only on the square-root of the mass per unit length).

To convert simulation results to dimensional form, it is sufficient to fix the value of one physical quantity (e.g.,  $B_\phi$ ). Since we are scaling to the strong radio source Cygnus A, the value of  $B_\phi$  is applied at time step 90 in Fig. 6.25, the peak of the synchrotron burst energy. At this time the simulation shows that  $B_\phi$  has grown comparable in strength to  $B_{z0}$  so that the pressure ratio has decreased to about  $\beta_p = 0.0034$  from the setup values of Sect. 3.10.1. For  $B_\phi = 2.5 \times 10^{-8}$  T, the magnetostatic energy equation (6.99)  $W_{ms} = 350$  AEU =  $2.5 \times 10^{53}$  J, or 1 AEU =  $7.1 \times 10^{50}$  J.

Counting and plotting the thermal velocities of the electrons at time  $T = 90$  shows a Maxwellian velocity distribution with a corresponding temperature  $T_\perp \approx 2.8$  keV. Substituting  $\beta_p$ ,  $T_\perp$ , and  $B$  into Eq. (8.20) yields a mean plasma density  $n_e = 1.79 \times 10^3$  m<sup>-3</sup> ( $1.7 \times 10^{-3}$  cm<sup>-3</sup>). Since  $\omega_{c0}/\omega_p = 1.5$  (Sect. 3.10.1), the axial magnetic field strength is  $B_{z0} = 2.0 \times 10^{-8}$  T ( $2.0 \times 10^{-4}$  G). These parameter values characterize Cygnus A and are in close agreement with many previous

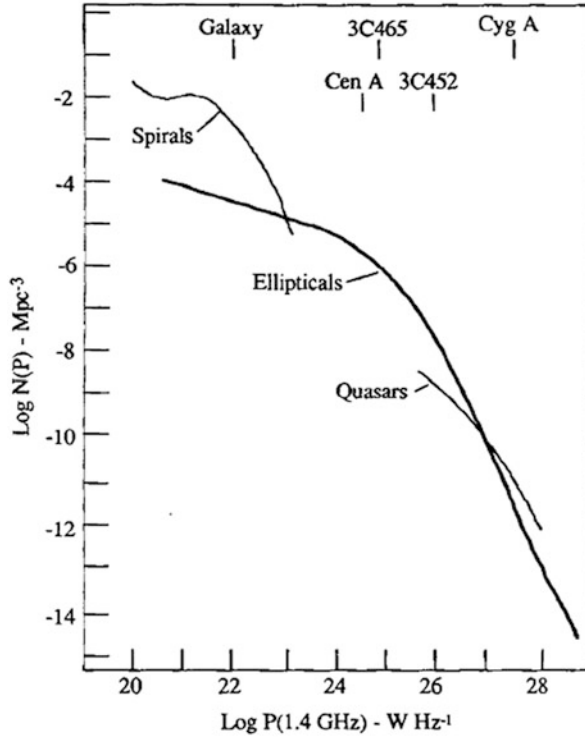


**Fig. 6.28** The radio luminosity function of galaxies and quasars (Adapted from Fanti and Perola 1977)

estimates using independent means. Additionally, from the simulation parameter  $E_{z0}/B_{z0} = 0.002c$ , the acceleration field within a filament is  $E_{z0} = 12 \text{ mV/m}$ .

To scale the simulation spatial and temporal setup dimensions,  $\Delta = 4\lambda_D = 2.97 \times 10^4 \text{ m}$  and  $dt = (4\omega_p)^{-1} = 1.04 \times 10^{-4} \text{ s}$ , to Cygnus A requires a size/time multiplication factor equation (10.21) of  $\alpha = 5.6 \times 10^{15}$ , so that  $3\Delta' = 35 \text{ kpc}$ . Hence,  $\Delta' = \alpha\Delta = 1.66 \times 10^{20} \text{ m}$  and  $dt' = \alpha dt = 5.87 \times 10^{11} \text{ s}$  are the galactic equivalent cell and time step, respectively.

**Example 6.4. Radiated power from a simulated double radio galaxy.** An estimate of the total power emitted as synchrotron radiation follows directly from the results of Sect. 6.6.2. From Fig. 3.15,  $B\phi$  is seen to be largely constrained to the volume of the plasma filaments so that  $V_p \sim (10^{21} \text{ m})^3 = 10^{63} \text{ m}^3$ . Substituting  $B\phi$ ,  $V_p$ , and  $dt'$  into Eq. (6.101) gives a total power emitted in synchrotron radiation of  $1.16 \times 10^{37} \text{ W}$ , which is to be compared with the radio luminosity of Cyg A of  $1.6 - 4.4 \times 10^{37} \text{ W}$ . Table 6.2 compares the simulation and estimated parameters for Cyg A. The agreement between the model predictions and the estimated parameters are generally quite good. For comparison purposes, the synchrotron isophotes of several radio galaxies and quasars are arrayed against their simulation counterparts in Fig. 6.27.

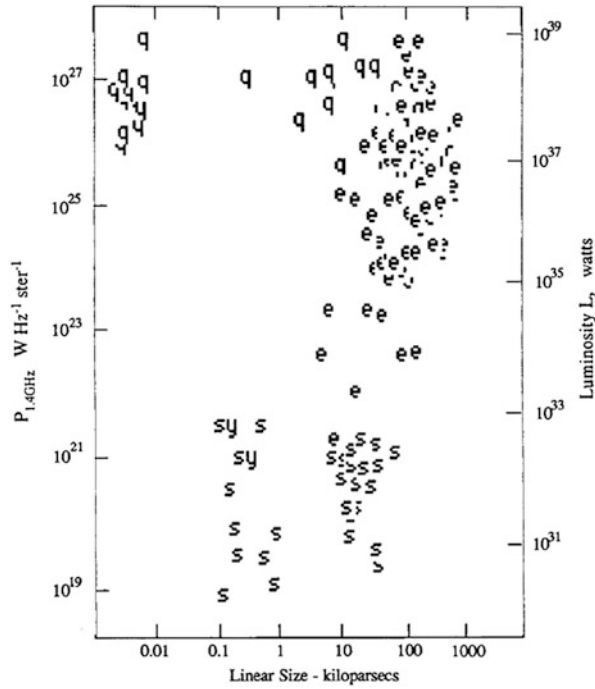


**Fig. 6.29** Plot of the monochromatic radio power at 1.4 GHz versus linear size for classes of extragalactic radio sources. The symbol *e* denotes extended radio sources associated with an elliptical galaxy core while *q*, *sy*, and *s* denote quasars, Seyferts, and spiral galaxies, respectively (Adapted from [Ekers 1974](#))

**Example 6.5. Synchrotron spectrum.** The total kinetic energy of the electrons during burst is  $W_{KE} = 8.78 \times 10^4 \text{ AEU} = 6.26 \times 10^{55} \text{ J}$ . The total number of electrons is  $N = n_e V_p = 1.79 \times 10^{66}$ , so that the average kinetic energy per electron is  $\bar{W} = 218 \text{ MeV}$  ( $1 \text{ J} = 6.242 \times 10^{18} \text{ eV}$ ).

The most probable energy associated with the electron energy distribution is  $W_0 = 2/3\bar{W} = 145 \text{ MeV}$  and, based upon the velocity distribution of the simulation superparticles, the electron energies range from 20.3 to 406.5 MeV ([Peratt and Green 1983](#)). The critical frequencies associated with these energy bounds equation (6.71) are 1.35 and 541 MHz, respectively. The total incoherent spectrum follows from Eq. (6.72) and is shown in Fig. 6.31 (solid line). This curve is a superposition of the individual electron spectra and includes the contribution of each spectra to ten times its critical frequency.

This spectrum may be directly compared to the spectrum of Cygnus A as compiled from a number of independent flux-frequency measurements as shown in Fig. 6.31 (crosses). Beyond 1 GHz, the fall-off on the simulation spectrum is due to the neglect of a smaller number of higher energy, run-away, electrons. The run-away electrons can attain energies as high as  $3 \times 10^{17} \text{ eV}$  over an axial distance of 10 kpc with a millivolt per meter electric field.

6.6.3 “Jets” and Superluminosity

The term jet was first used in astrophysics by Curtis (1918) to describe an elongated optical feature protruding from the core of the elliptical galaxy M87. Later Baade and Minkowski (1954) suggested that such a jet might actually correspond to matter ejection after some active phase of the core. Jets have been mapped in about 200 radio sources. Jets are found not only in double radio galaxies and quasars, but also in central compact radio sources located in the nucleus of associated (optical) galaxies. They are measured from the synchrotron radiation they emit, from centimeter wavelengths to X rays. However, in spite of improved resolution and statistics of observations, definitive direct evidence that ordered streaming motions are present in jets or radiosources is still missing. Moreover, uncertainty exists in identifying structures as either “jets” or “bridges.”

Table 6.2 Comparison of simulation and estimated radio galaxy parameters

Parameter	Simulation value (Cygnus A)	Estimate (model/object dependent)	Author <sup>a</sup>
Galactic current, $I_z$ , A	$2.15 \times 10^{19}$	$10^{17} \times 10^{19}$	Alfvén (1981)
Galactic magnetic field, G	$2.5 \times 10^{-4} (B_\phi)$ $2.0 \times 10^{-4} (B_z)$	$10^{-5}$ $3.16 \times 10^{-4}$ $3 \times 10^{-4}$ $1.2 \times 10^{-4}$ $10^{-5} \times 10^{-3}$	Perley <i>et al.</i> (1979) Mills and Sturrock(1970) de Young and Axford(1967) Hargrave and Ryle(1974) Perola(1981)
Plasma temperature, $T_\perp$ , keV	2.8	1 – 10 10	Miley (1980) Gisler and Miley (1979)
Plasma density, $n_e$ , $\text{cm}^{-3}$	$1.79 \times 10^{-3}$	$4 \times 10^{-3} - 2 \times 10^{-2}$ $10^{-4} \times 10^{-3}$ $0.6 \times 10^{-3}$	Perley et al. (1979) Miley (1980) Gisler and Miley (1979)
Density of synchrotron emitting elections, $n_e$ , syn $\text{cm}^{-3}$	$6.9 \times 10^{-9}$	$10^{-9}$ $1.5 \times 10^{-8}$	Shklovsky (1960) Ginzburg and Szyrovatskii (1965)
$P_{syn}$ , W	$1.16 \times 10^{37}$	$1.16 \times 10^{37}$ $4.4 \times 10^{37}$	Moffet (1975) Shklovsky (1960)
$t_{syn}$ , year	$4 \times 10^6$	$10^4 \times 10^6$ $> 3 \times 10^7$ $5 \times 10^6$	Sturrock and Barnes (1972) de Young and Axford (1967) Ryle and Windram (1968)
Total source energy, J	$6.3 \times 10^{55}$	$10^{57}$ $> 10^{54}$	Strurock and Barnes (1972) de Young and Axford (1967)
Average energy per , MeV election, $T_\parallel$	218	$> 100$ 158	Perola (1981)

<sup>a</sup> Adapted from A. Peratt (1986)

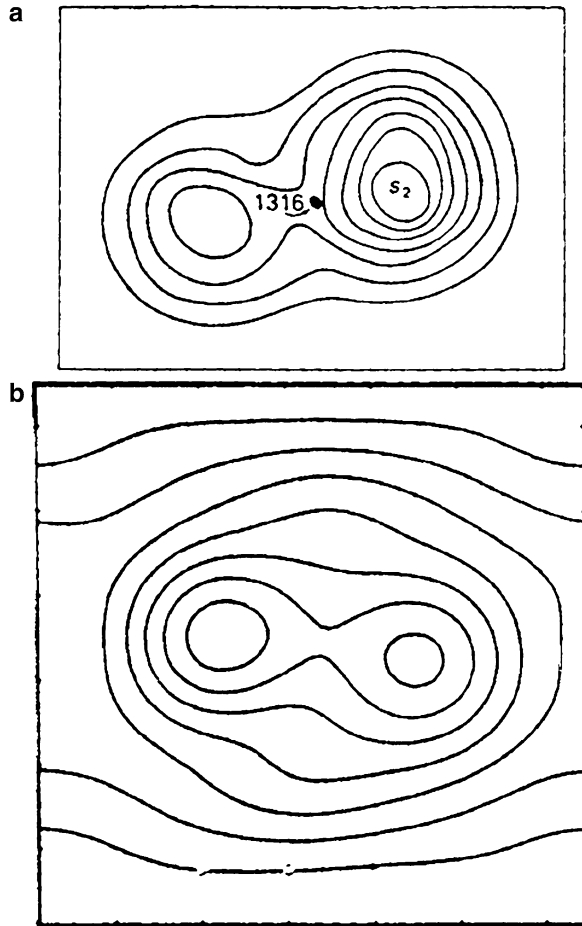


**Fig. 6.30** (a) Low resolution intensity contours of the double radio galaxy Fornax A. The peculiar galaxy NGC 1316 is shown between the radio lobes. (b) Low resolution magnetic isobars of interacting Birkeland currents during synchrotron burst era

Figure 6.32 shows VLA observations of radio quasars having jets (7 out of 26 quasars in a 966 MHz Jodrell Bank survey) and three quasars with faint jets. The general morphology is that of a filamented structure in emission that is connected to a core located midway between two strong radio lobes.

Comparison of the integrated magnitude of the jet in M87 over the period 1934–1980 shows that the jet is variable and has been fading, more or less uniformly, by about 0.8 mag per decade between 1964 and 1980. The data imply that over the period 1952–1980, the total jet intensity fell by at least 2.5 mag. Comparisons of isophotes taken in 1964 and 1979 show no obvious differences in overall shape, apart from effects of variation and noise. This indicates that the fading has affected the whole channel uniformly since 1964 (i.e., the “knots” or hot spots in the

jet (Fig. 6.33a–c) have not been seen to move). However, between 1934 and 1956, knots A and B became significantly brighter than C.

At a distance of 11.4 Mpc, the channel length of M87 is 30 arcsec in the plane of the sky, or 5,400 light years across. For this reason, and because side-on photographs of charged particle beams display different morphologies, the explanation of observable jet fading based on side ejected matter models is untenable.

**Example 6.6. Simulated emission bridges between radio lobes and core.** Plasma confined in the core and channel connecting one of the current filaments by magnetic isobars has been discussed in Sect. 3.10.4. Using the scaling of Example 6.3, the length of the channel is  $9\Delta' = 1.5 \times 10^{21}$  m (49.8 kpc) while the width varies from about 0.5 (2.8 kpc) to 2 (11 kpc). At time  $T = 255$  ( $1.6 \times 10^{15}$  s or 51 Myr), the confining field  $B_\phi$  (from Fig. 3.17) is  $2 - 2.5 \times 10^{-8}$  T, so that the pressure (Eq. (3.51)) is  $2.5 \times 10^{-9}$  Pa, allowing the confinement of a  $10^9 \text{ m}^{-3}$  ( $10^3 \text{ cm}^{-3}$ ) 2 eV plasma. The inwards magnetobaric velocity equation (3.52) is 8,990 km/s, about 9 times faster than the Biot-Savart attraction velocity between synchrotron radiating filaments. Through Eq. (1.1), the time varying  $B_\theta$  produces an axial  $E_z$  field within the plasma, accelerating the electrons in one direction and the ions in the other. Figure 6.34 shows the induced electric field variation at the mid-sections of the two filaments (the radio lobes), the core, and within the channel on either side of the core (Peratt 1986). From top to bottom, the most intense electric field activity occurs earlier in the outer filaments at time  $T \sim 180 - 270$ , then later at time  $T \sim 320 - 390$  in the core. Whether or not an observer can see synchrotron radiation depends on his orientation with respect to the polarity of the electric field. A positive value for  $E_z$  accelerates electrons in the  $-z$  direction, which is also the direction of the gain pattern equation (6.58). An observer in the  $+z$  direction, or out of the gain pattern, would observe radiation only from the thermal plasma, which may be the case for some radio quiet quasars.

The rapid spatial variation of the induction field, as well as the changing field polarity along the channel, causes an apparent “superluminosity” effect as the field sweeps the channel confined plasma. Figure 6.33d, e shows the simulated plasma and its magnetic field. Rather than being core ejected material, the simulated “jet” is a sheet electron beam (Sect. 2.7.1) accelerating out of the plane of the page.

#### 6.6.4 Quasars and Active Galaxy Nuclei

Quasars can be delineated into two classes, radio quasars and radio-quiet quasars (Fig. 6.29). However, there is little to distinguish between a double radio galaxy and a radio quasar. In a redshift range 0.1–0.5, both are found in equal numbers with matched radio luminosities and spectral indices. The quasars appear to be the larger radio sources; with strong cores of flat spectral index; the strongest radio lobe sources are radio galaxies. Hutchings (1987) finds that nearly 70 % of the radio quasars and over 80 % of the radio galaxies are interacting objects, the median separation being 20 kpc for quasars and 12 kpc for radio galaxies. From

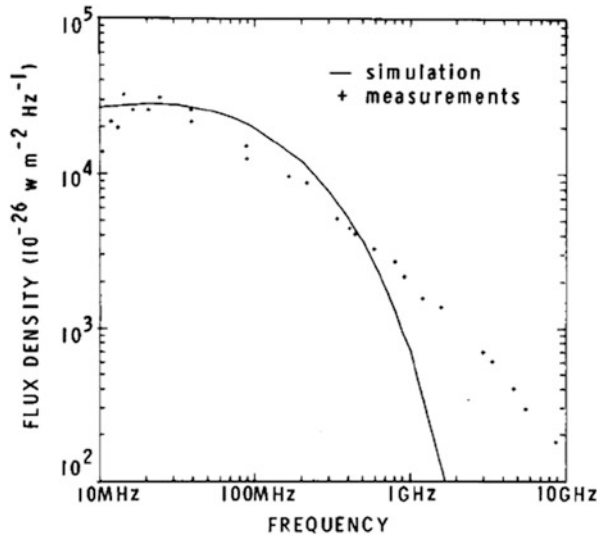


**Fig. 6.31** The radio spectrum of Cygnus A. The absolute results of the electromagnetic particle simulations and measurements are shown

this he infers a relative velocity of 1,000 km/s (identical to the value determined in Example 6.3) and deduces an upper limit of  $10^8$  year for radio activity (Eq. (6.100) yields  $4 \times 10^6$  year). Approximately 30 % of all objects have an elliptical, or a disturbed elliptical galaxy located between the radio lobes; none has spiral. The median source size for the radio quasars is  $10^4$  kpc compared to 60 kpc for radio galaxies.

There is a major difference between the radio quasars and the double radio galaxies: Quasars all have strong nuclear cores while radio galaxies all have very weak cores.

Radio quiet quasars lack the double lobe radio structure but retain the characteristic core signatures: emission lines of hydrogen and other light elements. In addition, unlike radio quiet quasars, radio quasars often have a compact radio component coinciding with the core. Radio variability is shown by this component, in the same way as the quasar varies optically. The time-scales of the variability for the optical and core radio components are of the order of 1 year.

The optical spectra of quasars are similar to those of Seyfert galaxies. Both are strong infrared emitters, but quasars are intense emitters at X ray and gamma wavelengths (Fig. 6.35). For example, NGC 4151 (Fig. 3.27b), the brightest of Seyfert galaxies, shows strong emission lines of hydrogen, helium, carbon, and magnesium. The short wavelength continuum of NGC 4151's spectrum indicates a temperature of about 3 eV. The variability of the lines and the continuum varies greatly on time scales from days to months. From the point of view of spectroscopy, quasars cannot be distinguished from Seyfert galaxies. The continuity in spectra for a quasar, Seyfert, narrow emission line galaxy, and a normal spiral galaxy is shown in Fig. 6.36.



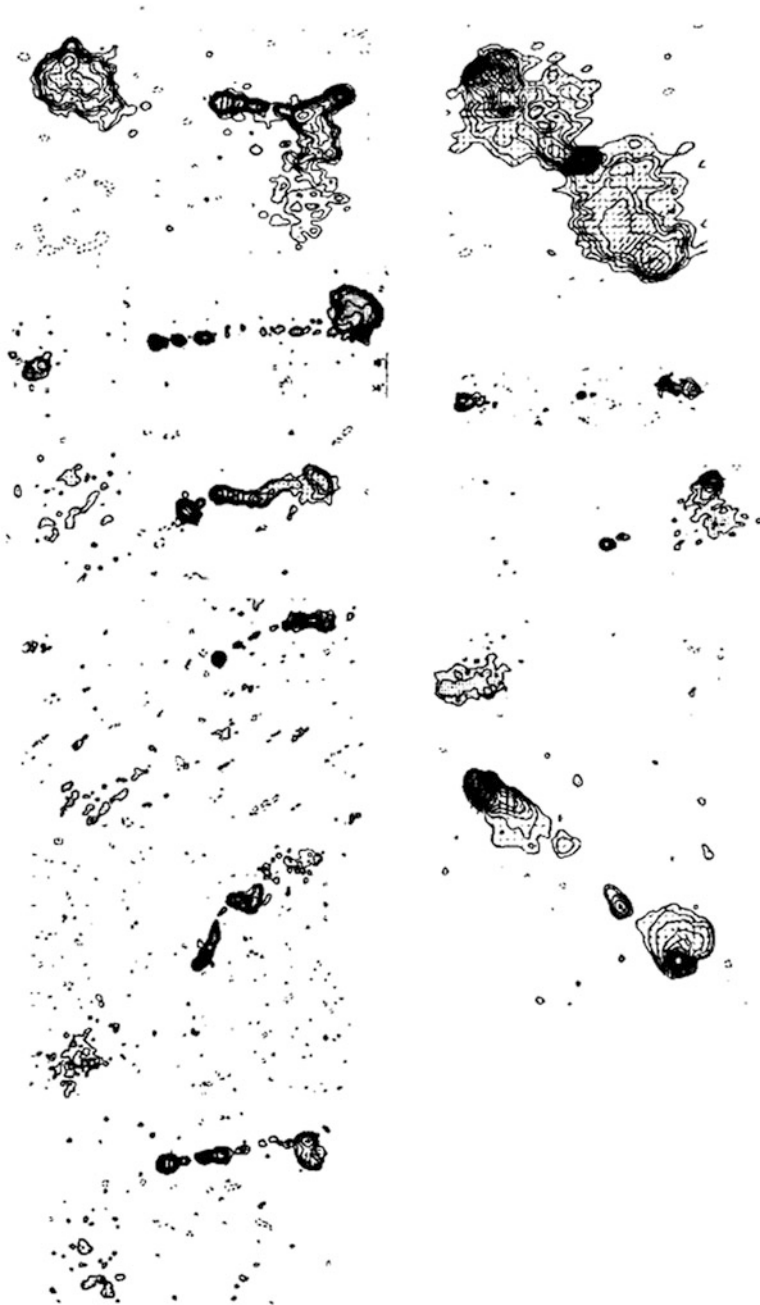


**Fig. 6.32** Ten examples of very large array observations of radio quasars having jets. The general morphology is that of a filamented structure in emission that is connected to a core located midway between two strong radio emitting plasmas. The bottom three sources in the right-hand column are designated as “faint” jets

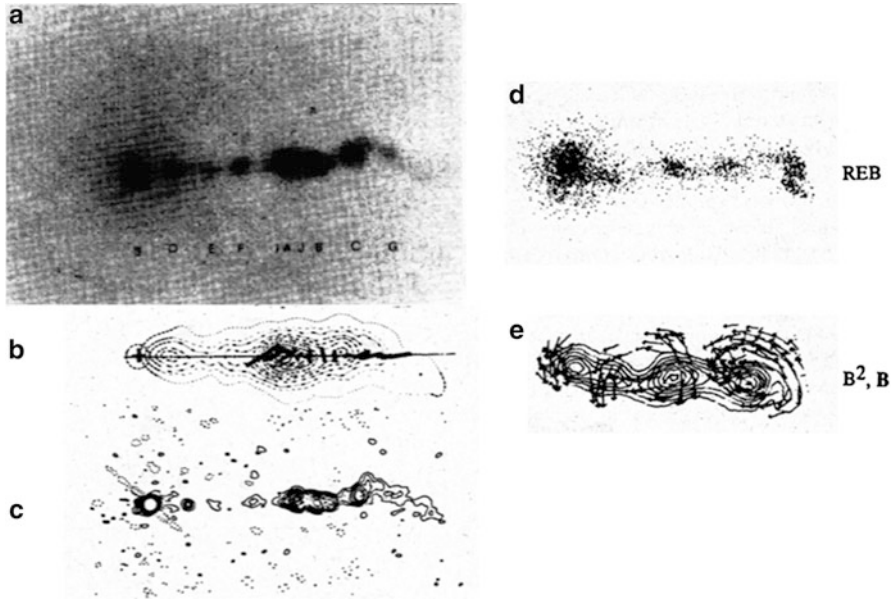


**Fig. 6.33** (a) Optical synchrotron radiation from the “jet” in M87. (b) Isophotes and projected magnetic field vectors. (c) “Knots” within the jet. (d) Relativistic electrons in a jet simulation (the sheet beam electrons are inductively accelerated out of the plane of the page). (e) Magnetic energy contours and vectors from simulation

**Example 6.7. Simulated quasar evolution.** Figures 3.15 and 3.19 (morphology evolution), Fig. 6.25 (temporal characteristic of synchrotron radiation), and Fig. 6.34 (time-space history of the accelerating field  $E_z$ ) allows the study of the morphological and radiation history of a simulated quasar. At early time (5–10 Myr) in the interaction of two current-carrying filaments (scaled to the parameters of Example 6.3) only synchrotron radiation from the two sources (precisely, the cross-sections of the interacting filaments where the double-layer  $E_z$  field occurs) can be seen in the gain pattern. At about 20 Myr, the intensity reaches some  $10^{37}$  W while diffuse inter-filament plasma has been collected into the elliptical core and channel regions. The plasma in the channel can radiate via the synchrotron mechanism (Example 6.6), albeit a much lower intensity than the outer sources. The thermal plasma compressed into the core, in analogy to Sect. 6.5.2, might be expected to also display a two-temperature spectral profile: a continuum and excitation lines of light elements. After  $\sim 50$  Myr, the synchrotron burst era comes to a close with a fall in the intensity of radiation from the filament sources. In spite of this, the current conducted by the filaments continues to increase from  $2 \times 10^{19}$  to  $4 \times 10^{20}$  A (because of the constant  $E_z$ ). This compresses the plasma in the core and reduces its dimension from about 50 kpc in extent to 10 kpc or less at much later time. The heated core plasma is eventually enveloped by the source plasmas which spiral inward to mimic the morphology of a Seyfert galaxy (Fig. 3.27a). The two original

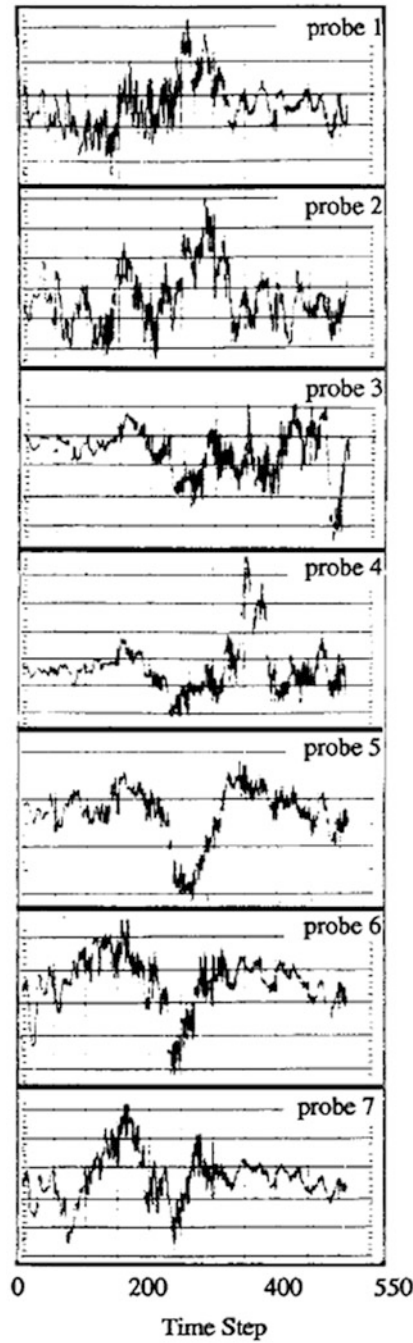


**Fig. 6.34** Induction electric field  $E_z$  from field probes indicated in Fig. 3.17

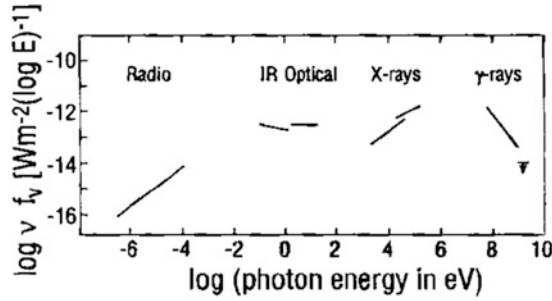


**Fig. 6.35** The continuum spectrum of the quasar 3C273 plotted as  $\nu F_\nu$  against frequency  $\nu$  in electronvolts

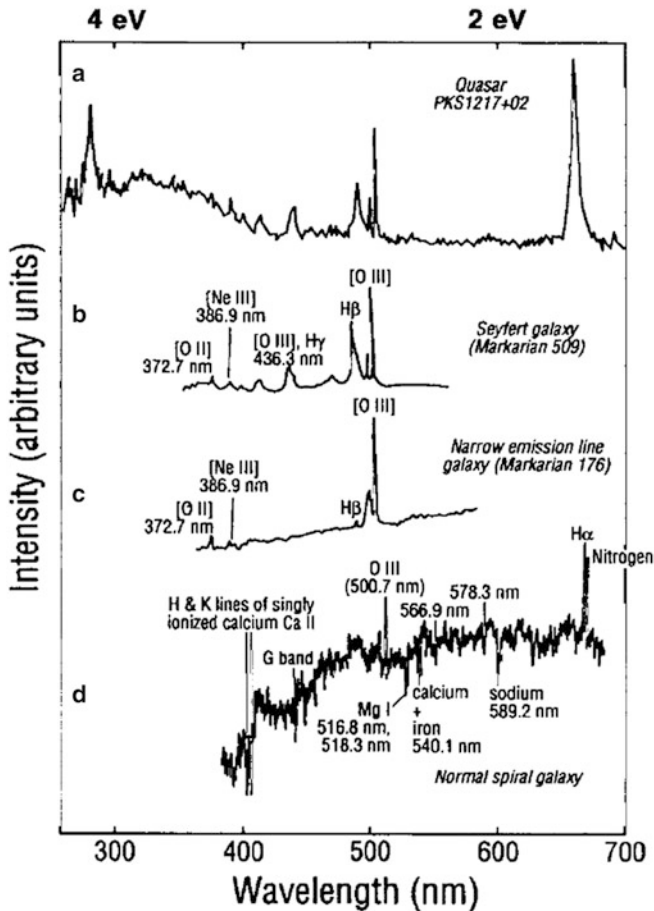


**Fig. 6.36** (a) Spectra of the nearby ( $z = 0.2$ ) quasar PKS 1217+02. (b) Spectra of the Seyfert galaxy Markarian 509. This spectra is similar in all respects to (a). The Balmer lines  $H\beta$ ,  $H\gamma$  are very wide while the forbidden lines such as  $[OIII]$  are narrow and are comparable to the  $H\alpha$  line in a normal spiral galaxy. (c) Spectra of the narrow-emission line galaxy Markarian 176. Compared to Seyferts, this class of galaxy does not have active nuclei. (d) Spectra of a normal spiral galaxy. Spectra are plotted versus wavelength, nm (bottom), and energy, eV (top)

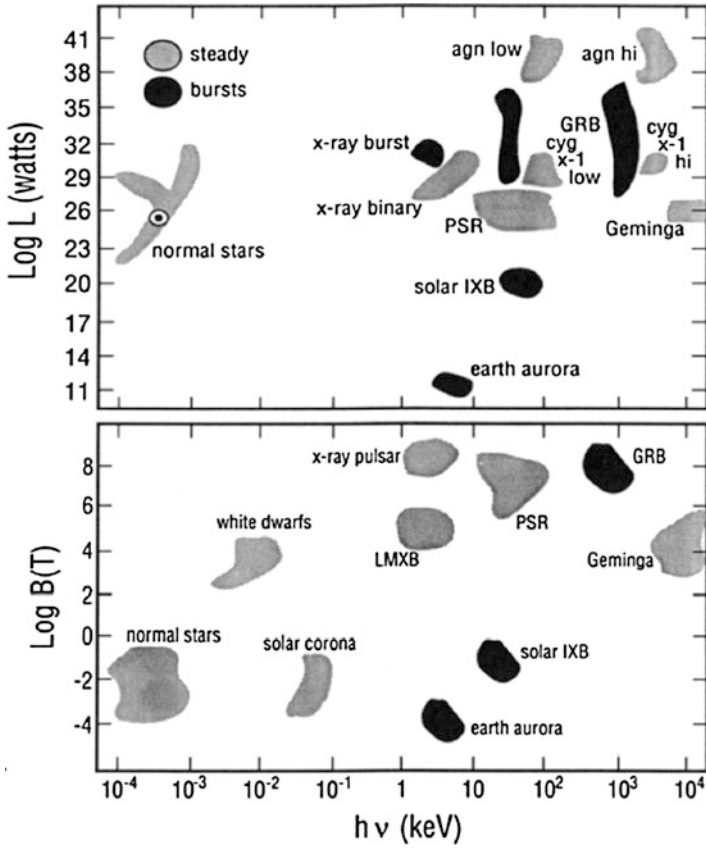


**Fig. 6.37** The location of various classes of steady and burst astrophysical sources in luminosity  $L$  and magnetic field  $B$  in keV (Adapted from Liang 1989)

hot spots which marked the most intense regions of axial current flow and which are the sources of synchrotron radiation, now reside within the core of the galaxy.

### 6.6.5 X Ray and Gamma-Ray Sources

Figure 6.37 plots the luminosity  $L$  and magnetic field  $B$  versus frequency  $\nu$  in keV for a number of classes of astrophysical objects having both steady and “burst” emissions. Liang (1989) has pointed out the suggestive trend linking the so-called classical gamma ray bursters with two other impulsive phenomena, namely, the aurora from geomagnetic storms (Sect. 2.9.8) and impulsive solar X ray flares (Sect. 5.6.2). Like the aurora and solar flares, X ray and gamma ray sources are likely to have their radiative energies supplied by electrical currents (Sect. 6.5).

## References

- Alfvén, H., Herlofson, N.: Cosmic radiation and radio stars. *Phys. Rev.* **78**, 616 (1950)
- Baade, W., Minkowski, R.: Identification of the radio sources in Cassiopeia, Cygnus A, and Puppis A. *Astrophys. J.* **119**, 206 (1954)
- Bekefi, G.: *Radiation Processes in Plasmas*. Wiley, New York (1966)
- Bennett, W.H.: Magnetically self-focussing streams. *Phys. Rev.* **45**, 890 (1934)
- Ekers, R.D.: Radio observations of the nuclei of galaxies. In: Shakeshaft, J.R. (ed.) *The Formation and Dynamics of Galaxies (IAU Symposium 58)*, Canberra, p. 257 (1974)
- Epstein, R.I., Feldman, P.A.: Synchrotron radiation from electrons in helical orbits. *Astrophys. J.* **150**, L109 (1967)
- Ginzburg, V.L., Syrovatskii, S.I.: Cosmic magnetobremssstrahlung. *Ann. Rev. Astron. Astrophys.* **3**, 297 (1965)
- Hutchings, J.B.: What is the difference between radio galaxies and radio quasar galaxies? *Astrophys. J.* **320**, 122 (1987)
- Johner, J.: Angular distribution of the total cyclotron radiation of a relativistic particle with parallel velocity. *Phys. Rev. A* **36**, 1498 (1988)
- Jones, D.S.: *The Theory of Electromagnetism*. Pergamon Press, New York (1964)
- Kai, K.: Polarization characteristics of type IV bursts. *Publ. Astron. Soc. Jpn.* **17**, 294 (1965)
- Kawabata, K.: Transfer of the gyro-resonance radiation. *Publ. Astron. Soc. Jpn.* **16**, 30 (1964)
- Landau, L.D., Lifshitz, E.M.: *The Classical Theory of Fields*. Pergamon, Oxford (1962). Chap. 9
- Liang, E.P.: Gamma ray bursts: confrontation between theory and observational data. In: Johnson, W.N. (ed.) *Proceedings of the GRO Science Workshop, Greenbelt*, pp. 4–397. Naval Research Laboratory, Washington, DC (1989)
- Mack, J.M., Peratt, A.L., Gisler, G.R.: Microwave signatures from circulating electron rings. *Bull. Am. Phys. Soc.* **32**, 1721 (1987)
- Meirovich, B.E.: Electromagnetic collapse, problems of stability, emission of radiation and evolution of a dense pinch. *Phys. Rep.* **104**, 259 (1984)
- Miley, G.: The structure of extended extragalactic radio sources. *Ann. Rev. Astron. Astrophys.* **18**, 165 (1980)
- Newberger, B.S. et al: Synchrotron radiation from Bennett beams, *Bull. Amer. Phys. Soc.* **29**, 1435 (1984)
- Pacholczyk, A.G.: *Radio Galaxies*. Pergamon Press, New York (1977)
- Panosfsky, W.K., Phillips, M.: *Classical Electricity and Magnetism*. Addison-Wesley, Reading (1962)
- Peratt, A.L., Kuehl, H.H.: Transmission and reflection of a wave obliquely incident on a nonuniform magnetized plasma, *Radio Sci.* **7**, 309 (1972)
- Peratt, A.L.: Evolution of the plasma universe: I. Double radio galaxies, quasars, and extragalactic jets. *IEEE Trans. Plasma Sci.* **14**, 639 (1986)

- Peratt, A.L., Green, J.C.: On the evolution of interacting magnetized, galactic plasmas. *Astrophys. Space Sci.* **91**, 19 (1983)
- Peratt, A.L., Koert, P.: Pulsed electromagnetic acceleration of exploded wire plasmas. *J. Appl. Phys.* **54**, 6292 (1985)
- Perola, G.C.: Radio galaxies: observations and theories of their extended components. *Fundam. Cosmic Phys.* **7**, 59 (1981)
- Reber, G.: Cosmic static. *Astrophys. J.* **100**, 279 (1944)
- Rose, D.J., Clark, M.: *Plasmas and Controlled Fusion*. MIT, Cambridge (1961)
- Scheuer, P.A.G.: Synchrotron radiation formulae. *Astrophys. J.* **151**, L139 (1968)
- Schwinger, J.: On the classical radiation of accelerated electrons. *Phys. Rev.* **75**, 1912 (1949)
- Shklovsky, I.S.: *Cosmic Radio Waves*. Harvard University Press, Cambridge (1960). Chap. VI
- Stratton, J.A.: *Electromagnetic Theory* McGraw-Hill, New York (1941)
- Takakura, T.: Synchrotron radiation from intermediate energy electrons in helical orbits and solar radio bursts at microwave frequencies. *Publ. Astron. Soc. Jpn.* **12**, 352 (1960)
- Trubnikov, B.A.: Plasma radiation in a magnetic field, *Sov. Phys. Doklady* **3**, 136 (1958)

## Chapter 7

# Transport of Cosmic Radiation

The theory of electromagnetic radiation was first derived by James Clerk Maxwell in 1873. He showed that both magnetic and electric fields propagate in space and the velocity of propagation, from purely magnetic and electrical measurements, was very nearly  $3 \times 10^8$  m/s. Within the limits of experimental error, this was equal to the velocity of propagation of light. Within 15 years of Maxwell's discovery, Heinrich Hertz succeeded in producing electromagnetic radiation at microwave frequencies by installing a spark gap (an oscillating high-potential arc discharge across two conductors separated by a short gap) at the center of a parabolic metal mirror. While the induction field was significant in Hertz's measurements (1.5 m transmitter-receiver separations), Guglielmo Marconi succeeded in demonstrating true electromagnetic energy transport, first at separations of 9 m, then 275 m, then 3 km, and then, in 1901, across the English Channel. Finally, in 1901, Marconi's transmissions bridged the Atlantic Ocean—a distance of 3,200 km.

Like radiation at optical wavelengths, that can be decomposed into a spectrum of constituent components (reds to violets) by a prism or grating, radiation at other wavelengths is also resolvable into a spectrum, another discovery by Hertz who showed that electromagnetic waves possessed all the properties of light waves—they could be reflected, refracted, focused by a lens, and polarized.

The electromagnetic spectrum corresponds to waves of various frequencies and wavelengths, related by the equation  $\lambda f = c$ , where  $c = 3 \times 10^8$  m/s is the free space velocity of light. In principle, it was found that knowledge of the radiation pattern recorded by an antenna system, and the distribution of the radiation in a frequency spectrum, could give precise information about the distant source of the radiation—its location, size, mechanism, energy, etc.

However, a complication arises when the propagation medium is no longer free space, but instead is plasma. The plasma may be dilute—such as the interstellar or intergalactic medium (Chap. 1), or it may be dense—for example, pinched plasma filaments that may even be the source of the radiation (Sect. 6.5). In both cases



the properties of the radiation are altered, in the dilute case over long propagation distances and in the dense case over short propagation distances.<sup>1</sup>

The first complication results from a modification of the wavelength-frequency relation,  $\lambda f = c/n$ , where  $n$  is the refractive index of the plasma (Appendix B). Since  $n$  depends on the wave frequency, magnetic field strength and orientation, plasma temperature, plasma constituency, and collision frequency, these parameters must be taken into account when an attempt is made to unfold the nature of the distant sources such as those responsible for the spectrum shown in Fig. 1.24. Additionally, linearity is no longer preserved if the wave field  $E$  is intense enough to modify the physical properties of the medium through which it propagates, by accelerating the plasma electrons and ions which may then collide with neutrals to heat the medium (e.g., Sect. 1.2.5).

This chapter starts with an outline of the mathematical description of energy transport in plasma. This is followed by a description of geometrical optics in radiation transfer—its applications and limitations. Blackbody radiation, the source function, and Kirchoff’s law are covered for the case of Maxwellian particle velocity distributions, and the classical definition of radiation temperature is given. The absorption of radiation by plasma filaments, the large-scale random magnetic field approximation, and the generalization of radiation transport to anisotropic velocity distributions, finish the chapter.

## 7.1 Energy Transport in Plasma

A power-energy conservation relationship may be developed by expanding the divergence of the vector product  $\mathbf{E} \times \mathbf{H}$ , and using the Maxwell-Hertz-Heaviside curl equations (1.1) and (1.2) to obtain

$$\begin{aligned}\nabla \cdot (\mathbf{E} \times \mathbf{H}) &= -\mathbf{E} \cdot \left( \mathbf{j} + \frac{\partial \mathbf{D}}{\partial t} \right) + \mathbf{H} \cdot \left( -\frac{\partial \mathbf{B}}{\partial t} \right) \\ &= -\mathbf{E} \cdot \mathbf{j} - \frac{1}{2} \frac{\partial}{\partial t} (\epsilon E^2 + \mu H^2)\end{aligned}\quad (7.1)$$

Equation (7.1) is in the form of a conservation theorem and can be recast in the form

$$\nabla \cdot \mathbf{S} + \frac{\partial}{\partial t} (w_{E \cdot j} + w_E + w_B) = 0 \quad (7.2)$$

where

$$\mathbf{S} = \mathbf{E} \times \mathbf{H}$$

is the Poynting vector,

$$w_{E \cdot j} = \int \mathbf{E} \cdot \mathbf{j} dt$$

---

<sup>1</sup> The discovery that radio waves could “follow” the curvature of the earth caused O. Heaviside and A. Kennelly to simultaneously suggest, in 1901, the existence of a plasma ionosphere which would cause the waves to reflect or “skip” between the earth and this layer.

is the particle energy density in the fluid approximation,

$$w_E = \frac{1}{2} \epsilon E^2$$

is the electric field energy density, and

$$w_B = \frac{1}{2} \mu H^2$$

is the magnetic field energy density.

By applying the divergence theorem to Eq. (7.2), it is seen that the outward flux of the vector  $\mathbf{S}$  from a volume  $V$  is accounted for by a time rate of change within that volume of the electromagnetic to mechanical energy conversion term plus the electromagnetic field energy density

$$\oint_s \mathbf{S} \cdot d\mathbf{s} = -\frac{\partial}{\partial t} \int_V (w_{E \cdot j} + w_E + w_B) dV \quad (7.3)$$

Although Eq. (7.2) is rigorous at every instant of time, our interest will only be in the averaged quantities. Following a procedure outlined by Bekefi (1966, p. 10), utilizing the time and space Fourier transforms of Eqs. (1.1)–(1.4), we obtain

$$k_i \cdot [\bar{\mathbf{S}} + \bar{\mathbf{T}}] = \omega_i (\bar{w}_B + \bar{w}_{E+p}) + \bar{p}_{E \cdot j} \quad (7.4)$$

where  $k_i$  and  $\omega_i$  are the imaginary components of

$$k = k_r + ik_i \quad (7.5)$$

$$\omega = \omega_r + i\omega_i \quad (7.6)$$

and the time-averaged flux,

$$\bar{\mathbf{S}} = \frac{1}{2} \Re(\mathbf{E} \times \mathbf{H}^*) \quad (7.7)$$

the nonelectromagnetic energy flux of particles flowing coherently with wave,

$$\bar{\mathbf{T}} = -\frac{1}{4} \epsilon_0 \mathbf{E} * \cdot \frac{\partial \omega K}{\partial k} \cdot \mathbf{E} \quad (7.8)$$

the time-averaged magnetic energy density,

$$\bar{w}_B = \frac{1}{4} \mu_0 |\mathbf{H}|^2 \quad (7.9)$$

the time-averaged electric energy density plus kinetic energy of particles coherent with wave, and

$$\bar{w}_{E+p} = \frac{1}{4} \epsilon_0 \mathbf{E} * \cdot \frac{\partial \omega K}{\partial \omega} \cdot \mathbf{E} \quad (7.10)$$

the time-averaged rate of power absorption.

$$\bar{p}_{E \cdot j} = \frac{1}{4} \epsilon_0 \mathbf{E} * \cdot (\omega_r K_a) \cdot \mathbf{E} \quad (7.11)$$

The time-averaged Poynting vector  $\bar{S}$  represents the flux of electromagnetic energy. The quantity  $\bar{T}$  is the nonelectromagnetic energy flux due to the coherent motion of the charge carriers. In a cold plasma, where the charge carriers oscillate about fixed positions,  $\bar{T} = 0$ . In a hot plasma, bodily transport of density, velocity, and energy fluctuations by the free-streaming particles lead to finite values for  $K_a = (K - K^*)/2i$ .

The dissipation of energy from the wave enters through the anti-Hermitian part of the equivalent dielectric tensor. When the medium is not time-dispersive, takes on a more familiar form  $\bar{w}_{E+p} = \frac{1}{4}\epsilon_0 \mathbf{E}^* \cdot \mathbf{K} \cdot \mathbf{E}$ .

**Example 7.1 Total energy density of a transverse electromagnetic wave propagating in an isotropic medium.** From Eq. (B.2), since  $B_0 = 0$ , all diagonal tensor elements reduce to  $K = P = 1 - \omega_p^2/\omega^2$  and Eq. (7.10) is

$$\bar{w}_{E+p} = \frac{1}{4}\epsilon_0 |E|^2 (1 + \omega_p^2/\omega^2) \quad (7.12)$$

Since  $H = \sqrt{\epsilon_0/\mu_0}n \times E$ , where  $n$  is given by Eq. (B.7) and  $n^2 = P$  Eq. (B.11),

$$\bar{w}_B = \frac{1}{4}\epsilon_0 |E|^2 (1 - \omega_p^2/\omega^2)$$

The total energy density is therefore

$$\bar{w}_B + \bar{w}_{E+p} = \frac{1}{4}\epsilon_0 |E|^2 \quad (7.13)$$

**Example 7.2 Total energy density of a longitudinal wave in warm magnetized plasma near the second electron cyclotron harmonic.** A transverse electromagnetic wave  $E = E^{inc} e^{i(k \cdot r - \omega t)}$  is incident on a warm magnetized plasma slab (Fig. 7.1) Trubnikov and Yakubov (1963). The propagation vector is  $k = \hat{x}k_x + \hat{y}k_y$ , and  $k/k_y = \sin \xi_i$ , where  $\xi_i$  is the angle of incidence, and the plasma extends in the  $x$  direction. Since the electric field of the longitudinal wave is predominantly along its direction of propagation, it follows from a simple geometrical consideration that in the plasma

$$E_x^L = -\frac{c}{\omega} \frac{k_x}{\sin \xi_i} E_y^L \quad (7.14)$$

so that  $|E_x^L| \gg |E_y^L|$ . Neglecting, Eq. (7.8) can be written

$$\bar{T}_x = -\frac{\omega\epsilon_0}{4} \frac{\partial K_{xx}}{\partial k_x} |E_x^L|^2 \quad (7.15)$$

The element  $K_{xx}$  of the dielectric constant in warm magnetized plasma is (Peratt and Kuehl 1972)

$$K_{xx} = 1 - \frac{\omega^2}{\omega^2 - \omega_c^2} + \frac{c^2 k_x^2}{\omega^2} \left( \frac{\omega^2}{\omega^2 - \omega_c^2} \right) \left( \frac{\omega^2}{4\omega_c^2 - \omega^2} \right) \frac{3\bar{v}_x^2}{c^2} \quad (7.16)$$

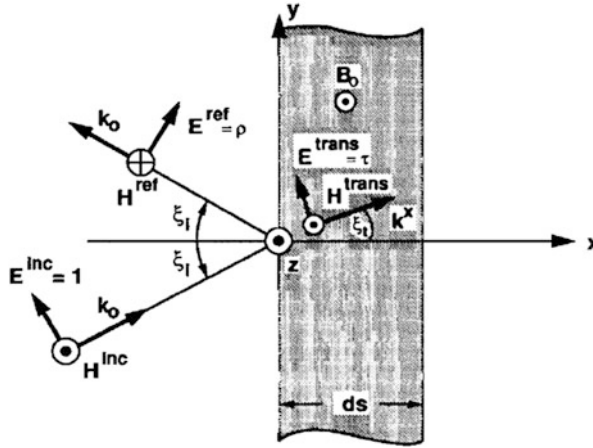


**Fig. 7.1** Incident, reflected, and transmitted wave vectors for a transverse electromagnetic wave obliquely incident upon a magnetized plasma

Differentiating Eq. (7.16) and inserting in Eq. (7.15) gives the final result

$$\bar{T}_x = +\frac{1}{2} \sqrt{\frac{\epsilon_0}{\mu_0}} \frac{ck_x}{\omega} \left( \frac{\omega^2}{\omega^2 - \omega_c^2} \right) \left( \frac{\omega^2}{4\omega_c^2 - \omega^2} \right) \frac{3\bar{v}_x^2}{c^2} \quad (7.17)$$

where the sign of Eq. (7.17) has been reversed since the phase velocity is in the opposite direction from that assumed in the derivation of Eq. (7.15).

### 7.1.1 Group Velocity

The velocity at which energy in the wave propagates, the group velocity, is defined as

$$v_g = \frac{\text{total time - averaged flux}}{\text{time - averaged energy density}} \quad (7.18)$$

or, from Eq. (6.70),

$$v_g = \frac{\partial \omega}{\partial k} = \frac{\bar{S} + \bar{T}}{\bar{w}_B + \bar{w}_{E+p}} \quad (7.19)$$

where

$$\frac{\partial \omega}{\partial k} = \hat{x} \frac{\partial \omega}{\partial k_x} + \hat{y} \frac{\partial \omega}{\partial k_y} + \hat{z} \frac{\partial \omega}{\partial k_z} \quad (7.20)$$

The group velocity vector  $\mathbf{v}_g$  associated with the wave has a magnitude  $v_g$  and a direction given by the angles  $\xi$  and  $\eta$  (Fig. 7.2). In spherical coordinates

$$\omega = \omega(k, \theta, \phi) \quad (7.21)$$

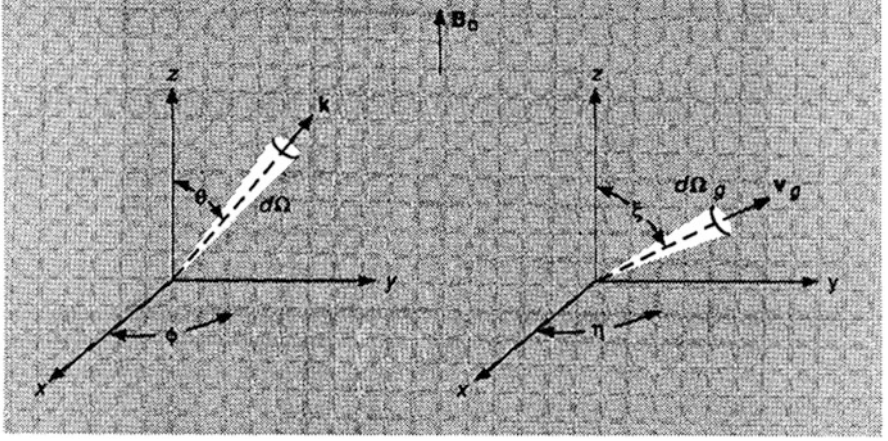


**Fig. 7.2** Coordinate system showing the propagation vector  $\mathbf{k}$  and the associated group-velocity vector  $\mathbf{v}_g$

and Eq. (7.20) is

$$\begin{aligned} \frac{\partial \omega}{\partial k} &= \hat{k} \frac{\partial \omega}{\partial k_x} + \hat{\theta} \frac{1}{k} \frac{\partial \omega}{\partial \theta} + \hat{\phi} \frac{1}{k \sin \theta} \frac{\partial \omega}{\partial \phi} \\ &= \hat{k} v_{gk} + \hat{\theta} v_{g\theta} + \hat{\phi} v_{g\phi} \end{aligned} \quad (7.22)$$

and

$$\begin{aligned} v_{gk} &= \left( \frac{\partial k}{\partial \omega} \right)^{-1} \\ v_{g\theta} &= \frac{\partial k}{\partial \theta} \left( \frac{\partial k}{\partial \omega} \right)^{-1} \\ v_{g\phi} &= \frac{1}{k \sin \theta} \frac{\partial k}{\partial \phi} \left( \frac{\partial k}{\partial \omega} \right)^{-1} \end{aligned} \quad (7.23)$$

The transformations Eq. (7.23) can be simplified if an axis of symmetry  $B_0 = \hat{z}B_0$  is chosen. Thus,  $\partial k / \partial \phi = 0$  and

$$\begin{aligned} v_{gk} &= v_g \cos(\theta - \xi) \\ v_{g\theta} &= -v_g \sin(\theta - \xi) \\ v_{g\phi} &= 0 \end{aligned} \quad (7.24)$$

From Eqs. (7.23) and (7.24)

$$\tan(\theta - \xi) = -\frac{v_{g\theta}}{v_{gk}} = \frac{1}{k} \left( \frac{\partial k}{\partial \theta} \right)_{\omega} \quad (7.25)$$

where  $(\theta - \xi)$  is the angle between the direction of wave propagation  $k$  and the direction of energy propagation  $\mathbf{v}_g/v_g$ . The differentiation of  $k$  in Eq. (7.25) is done at fixed frequency  $\omega$ .

Consider, for example, a wheel lemniscoid wave-normal surface (which is representative of the compressional Alfvén wave) as shown in Fig. 13.6. One may use wave-normal surfaces to find the direction of  $\mathbf{v}_g$ . Let the origin represent an

instantaneous constructive interference maximum for a group of waves which are of the same frequency but which differ slightly in direction. At a later unit time, the wave fronts which had passed through the origin will lie on the surfaces which are perpendicular to and which contain the tip of the  $\omega/\mathbf{k}$  radius vector. The new point of constructive interference occurs where these wavefronts again coincide. The coinciding wave fronts form an envelope for a second surface, which is called the ray surface when the medium is nondispersive.

For dispersive media, only the direction of the wave is given correctly by the construction of Fig. 13.6. One must then consider the constructive interference of waves not only with different directions, but also with different frequencies, and the length of the  $\mathbf{v}_g$  vector is changed accordingly.

**Example 7.3 Whistler mode propagation through the ionosphere.** A famous example of group velocity relations in anisotropic dispersive plasma is furnished by the whistler mode. Whistlers, which were first reported in 1919 by H. Barkhausen, are electromagnetic disturbances initiated by lightning discharges in the upper atmosphere, particularly the electromagnetic radiation with frequencies of 300 Hz–30 KHz. The waves cannot be heard directly but are converted into audible sound waves of the same frequency by an audioamplifier. They are propagated from one hemisphere to another in the ionosphere and follow the earth's dipole magnetic field lines. In propagation through the ionosphere the group velocity is proportional to the square-root of the frequency so that the received signal is a descending tone lasting a few seconds. We write the index of refraction in the form

$$n^2 = 1 - \frac{2(A - B + C)}{2A - B \pm \sqrt{B^2 - 4AC}} \quad (7.26)$$

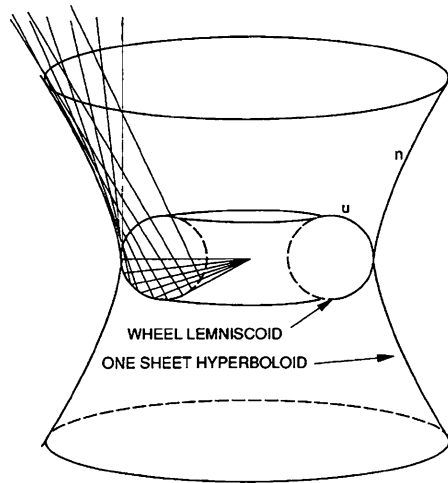


**Fig. 7.3** Wheel lemniscoidal normal surface and partial construction of its one sheet hyperboloidal ray surface. These shapes are representative of the compressional Alfvén wave

Using the “quasi-longitudinal” approximation

$$\omega_p^2 \sin^4 \theta \ll 4\omega^2 (1 - \omega_p^2/\omega^2) \cos^2 \theta \quad (7.27)$$

in addition to the approximation

$$\omega_p^2 \sin^2 \theta \ll |2\omega^2 (1 - \omega_p^2/\omega^2)| \quad (7.28)$$

we arrive at the quasi-longitudinal right-hand index of refraction equation

$$n^2 = 1 - \frac{\omega_p^2/\omega}{\omega - \omega_b \cos \theta} \quad (7.29)$$

In his analysis of this mode, [Storey \(1953\)](#) simplified Eq. (7.29) to obtain the approximate form

$$n^2 = 1 - \frac{\omega_p^2}{\omega \omega_b \cos \theta} \quad (7.30)$$

which is valid where  $|\omega_b \cos \theta| \gg |\omega|$  and when  $n^2 \gg 1$ . Thus, the frequency and group velocity are

$$\frac{\partial \omega}{\partial k} = \frac{2kc^2 \omega_b}{\omega_p^2} \cos \theta = \frac{2c}{\omega_p} \sqrt{\omega_b \cos \theta} \sqrt{\omega} \quad (7.31)$$

$$\tan(\theta - \xi) = 1/2 \tan \theta \quad (7.32)$$

From Eqs. (7.25) and (7.30),  $\tan(\theta - \xi) = \frac{1}{2} \tan \theta$ . Solving for  $\xi$  gives

$$\xi = \tan^{-1} \left( \frac{\sin \theta \cos \theta}{1 + \cos^2 \theta} \right) \quad (7.33)$$

The maximum possible value of  $\xi$  is found by differentiating Eq. (7.33) with respect to  $\theta$  and setting it equal to zero. After some manipulation we find that

$$\xi_{\max} = \tan^{-1} 2^{-3/2} = 19^\circ 29' \quad (7.34)$$

where  $\xi$  is the angle between the ray direction and the earth’s dipole magnetic field lines. This angular limitation on the group-velocity direction accounts for the tendency of whistlers to follow the lines of force of the earth’s magnetic field. The frequency dependence of the group velocity accounts for the whistler’s characteristic descending tone since the higher frequency components of the disturbance arrive first.

An example of a 500 Hz whistler-mode ray path obtained using a ray tracing program is shown in Fig. 7.4 ([Kimura 1966](#)).

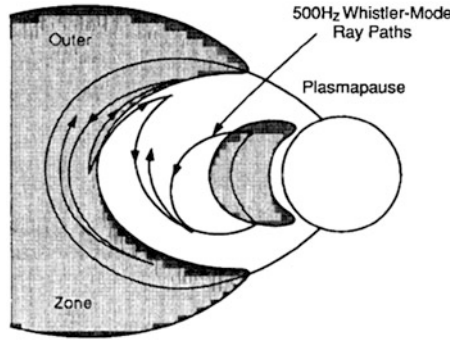


**Fig. 7.4** Example of 500 Hz whistler-mode ray paths, obtained from a ray tracing program, that illustrates how wave energy generated in the outer region of the plasmasphere can propagate across magnetic field lines so as to fill the plasmasphere with waves

### 7.1.2 Time Rate of Decay of Wave Oscillations

The time-averaged rate of power absorption divided by the time-averaged electromagnetic energy density in the waves gives the time rate of decay of the oscillations, that is,

$$\tau = \left[ \frac{\bar{P}_{E \cdot j}}{\bar{w}_E + \bar{w}_B} \right]^{-1} \quad (7.35)$$

An alternate way of expressing the time rate of decay and spatial absorption of a plane wave is through the complex values of  $\omega$  (Eq. (7.5)) and  $\mathbf{k}$  (Eq. (7.6)). The relaxation time for the oscillations is  $(-\omega_i)^{-1}$ ; therefore the relaxation time for energy is

$$\tau = (-2\omega_i)^{-1} \quad (7.36)$$

Likewise, the spatial damping is  $(\mathbf{k}_i)^{-1}$ ; therefore the absorption is

$$\alpha_\omega = 2k_i \quad (7.37)$$

However, the absorption coefficient must be corrected to include the direction of wave propagation  $\mathbf{k}$  with respect to its group velocity  $\partial\omega/\partial\mathbf{k}$ . This correction is (Fig. 7.2)

$$\alpha_\omega = 2k_i \cos(\theta - \xi) \quad (7.38)$$

## 7.2 Applications of Geometrical Optics

Geometrical optics assumes that the medium varies slowly with position and the scale length of the variations is much longer than the wavelength of the radiation in the medium. The radiation can then be considered as being transported along bundles of curves or rays (Fig. 7.5). In plasma, the various bundles may belong



to the different characteristic plasma modes of propagation. Nevertheless, unlike the mode conversion processes described in Appendix B, in geometrical optics the bundles do not interact with one another.

### 7.2.1 Basic Principle and Limitations of Geometrical Optics

Consider for a moment a loss-free plasma ( $\bar{p}_{E \cdot j} = 0$ ) under steady state conditions ( $\omega = 0$ ,  $\nabla \leftrightarrow i\mathbf{k}$ ) so that Eq. (7.4) may be expressed as

$$\nabla \cdot \bar{F}_\omega = 0 \quad (7.39)$$

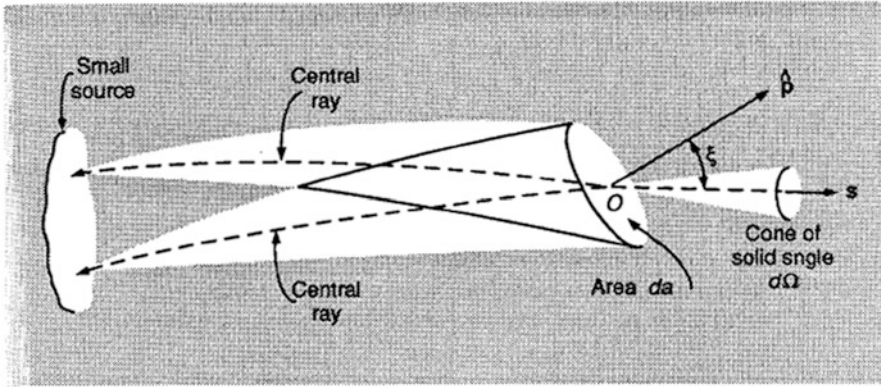


Fig. 7.5 Bundles of rays emanating from a small source crossing an element of area  $da$

The quantity  $\mathbf{F}_\omega$  is called the spectral flux and consists of both the electromagnetic flux and the flux of particles

$$\bar{F}_\omega + \bar{S}(\omega) = \bar{T}(\omega) \quad (7.40)$$

Since Eq. (7.39) is valid for each possible mode supported by the plasma separately of any other mode, the flux  $\bar{F}_\omega$  is the total flux for a single mode.

The problem of flux flow is handled as follows. Let  $da$  be a small area in plasma whose outward normal is along  $\mathbf{B}_0$ . Each element of the source sends through  $da$  a tube of rays, and the central rays of the tubes fill a cone of solid angle  $d\Omega$ . For a sufficiently small cone angle the fluxes from the individual elements travel essentially in the same direction. If the sources are assumed to radiate incoherently with respect to one another, the total flux is the scalar sum of the individual fluxes. The magnitude of this flux is then

$$dF_\omega \cdot \hat{z} = dF_\omega \cos \xi = I_\omega(s) \cos \xi d\Omega \quad (7.41)$$

where  $I_\omega$  is a constant of proportionality. The time-averaged power  $P_\omega$  in the spectral range  $d\omega$ , crossing the elementary area  $da$  and confined to the cone  $d\Omega$  is

$$dP_\omega = I_\omega(s) \cos \xi \, d\Omega \, da \, d\omega \quad (7.42)$$

The scalar quantity  $I_\omega$  is known as the specific intensity of radiation or, simply, the intensity. If  $I_\omega$  at a point is independent of direction, the radiation is isotropic.

To obtain the total flux crossing unit area  $da$  (Fig. 7.6), Eq. (7.41) must be integrated over  $4\pi$  steradians:

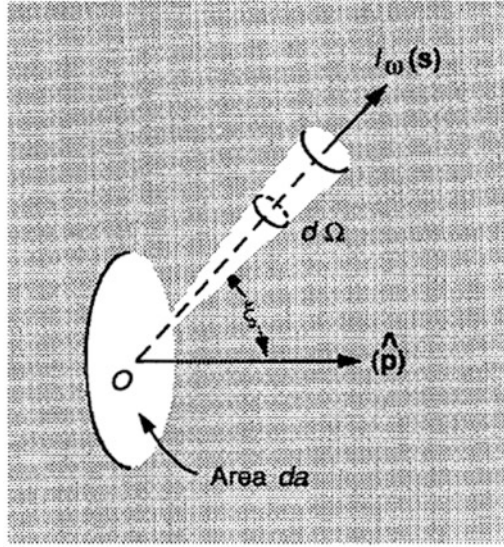


**Fig. 7.6** Vector diagram for radiation flowing across a small area  $da$

$$F_\omega = \int_{0 < \xi < \pi} I_\omega(s) \cos \xi \, d\Omega \quad (7.43)$$

In radio astronomy the measurement of the flux takes place at a large distance from the radiating body and, since the body subtends a sufficiently small solid angle at the position of the observer, Eq. (7.43) can be approximated by

$$F_\omega = \int_{0 < \xi < \pi} I_\omega(s) \, d\Omega \quad (7.44)$$

Consider an infinitesimal volume element of the plasma in the form of a pill-box as shown in Fig. 7.7. A pencil with radiation intensity  $I_\omega$  and solid angle  $d\omega_1$  enters one face at an angle  $\xi$  to the normal  $\hat{z}$ . The radiation in the outgoing beam

of intensity  $I_\omega + dI_\omega$  leaves within a solid angle  $d\omega_2$ . If the plasma is simple and slightly inhomogeneous, it causes a bending of the rays, so that  $\xi_1 \neq \xi_2$ . If the medium is also loss-free then, in accordance with Eq. (7.42)

$$(I_\omega + dI_\omega) \cos \xi_2 d\Omega_2 da d\omega - I_\omega \cos \xi_1 d\Omega_1 da d\omega = 0 \quad (7.45)$$

which is the energy conservation equation for radiation propagating along a bundle of rays. For a simple plasma, Snell's law of refraction may be employed which states

$$n \sin \xi = \text{constant along the ray} \quad (7.46)$$

where  $n$  is the real part of the refractive index Eq. (B.7). We then find that

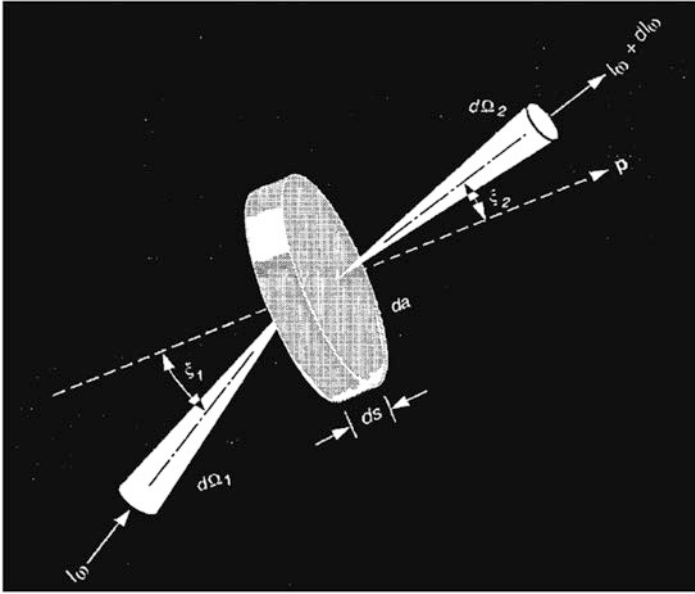


**Fig. 7.7** Radiation entering a small volume of plasma and leaving it after having suffered a small amount of refraction due to a difference in refractive indices on the two sides of the elementary pillbox

$$n^2 da \cos \xi d\Omega = \text{constant} \quad (7.47)$$

$$I_\omega / n^2 = \text{constant along the ray} \quad (7.48)$$

In magnetized, anisotropic, and inhomogeneous plasma, the rigorous solution of the ray trajectory problem is beset with the same basic difficulty of geometrical optics: the wavelength must be short compared to the distance over which the refractive index changes appreciably. This requirement is often violated in cosmic plasma, where transition regions define abrupt changes in plasma density, temperature, and

magnetic field strength. In addition, plasma wave theory shows that the refractive index may change rapidly even though the plasma density or magnetic field changes gradually (Fig. B.1).

**Example 7.4 Absence of a Brewster's Angle in anisotropic plasma.** Referring to Fig. 7.1, where  $\mathbf{E} \perp \mathbf{B}_0$ , the sum of the incident and reflected waves at the plasma boundary may be written as

$$E_y = (1 + \rho) \cos \xi_i \quad (7.49)$$

$$\sqrt{\frac{\mu_0}{\epsilon_0}} H_z = (1 - \rho) \quad (7.50)$$

Within the plasma half-space,  $\mathbf{E} \perp \mathbf{B}_0$ , so that the field is extraordinary and consists of components both perpendicular and parallel to  $\mathbf{k}$ ,

$$E_y^{(X)} = E_\perp \cos \xi_t + E_\parallel \sin \xi_t \quad (7.51)$$

where  $\xi_t$  is given by Snell's law  $\sin \xi_i = n^{(X)} \sin \xi_t$ . A relationship between  $E_\perp$  and  $E_\parallel$  may be obtained by briefly considering the case  $\xi = 0$ . In this case  $E_x = E_\parallel$  and  $E_y = E_\perp$ . From the vector wave equation (6.70),  $SE_x - iDE_y = 0$ , or

$$E_\parallel = -i \frac{\omega_b}{\omega} \frac{\omega_p^2 / (\omega_b^2 - \omega^2)}{\omega_p^2 / (\omega_b^2 - \omega^2) - 1} E_\perp \quad (7.52)$$

Since Eq. (7.52) is independent of coordinate rotation, it is valid at angle  $\xi_t$ . Substituting Eq. (7.52) into Eq. (7.51)

$$E_y^{(X)} = E_\perp \left[ \cos \xi_t - i \frac{\omega_b}{\omega} \frac{\omega_p^2 (\omega_b^2 - \omega^2)}{\omega_p^2 (\omega_b^2 - \omega^2) - 1} \sin \xi_t \right] \times \exp \left\{ i \sqrt{(n^X)^2 - \sin^2 \xi_t} \frac{c}{\omega} x \right\} \quad (7.53)$$

$$H_z^{(X)} = n^X E_\perp \exp \left\{ i \sqrt{(n^X)^2 - \sin^2 \xi_t} \frac{c}{\omega} x \right\} \quad (7.54)$$

The two unknowns  $\rho$  and  $\tau = E_\perp$  are obtained by matching Eqs. (7.49) and (7.50) to Eqs. (7.53) and (7.54) at the vacuum-plasma interface. We obtain

$$\rho = \frac{\cos(\xi_t + \xi_i) \sin(\xi_t - \xi_i) + i(\omega/\omega_b) [a/(a-1)] \sin^2 \xi_t}{\sin(\xi_t + \xi_i) \cos(\xi_t - \xi_i) + i(\omega/\omega_b) [a/(a-1)] \sin^2 \xi_t} \quad (7.55)$$

$$\tau = \frac{2 \cos \xi_i \sin \xi_t}{\sin(\xi_t + \xi_i) \cos(\xi_t - \xi_i) + i(\omega/\omega_b) [a/(a-1)] \sin^2 \xi_t} \quad (7.56)$$

where  $a = \omega_p^2 / (\omega^2 - \omega_b^2)$ . When  $\omega_b = 0$ , Eq. (7.55) reduces to the well-known Fresnel equation for reflection from a dielectric with  $E$  in the plane of incidence (Slater and Frank 1947). For  $\omega_b = 0$ , we may therefore have  $\rho = 0$  at the "Brewster angle", but if  $\omega_b \neq 0$ , Eq. (7.55) shows that  $\rho$  never vanishes, so there is no "Brewster angle" for anisotropic plasma.

**Example 7.5 Absorption due to collisions.** Collisional effects such as wave damping caused by particle interactions can play an important role in the propagation of electromagnetic waves through cosmic plasma (Peter and Peratt 1988). For example, collisions are particularly important for longitudinal wave propagation because of their slow group velocity. Collisional processes become important for the propagation of an extraordinary wave near a resonance. The effect of collisions can be included in the formulation of Example 7.4 with the frequency replacement Eq. (7.6) (this is usually carried out in the derivation of the current density  $j$ ). The quantity  $\omega_i$  is considered a “collisional frequency” (Kuehl et al. 1970) whose magnitude is determined by the type of particles in collision. With this substitution, the absorption is

$$\alpha_\omega = 1 - |\rho|^2 - |\tau|^2 \quad (7.57)$$

None of the wave conversion, wave matching, or collisional damping carried out in Examples 7.4 and 7.5 exist in geometrical optics. Nevertheless, in spite of the inadequacies of the procedure, especially at longer wavelengths, we shall continue to confine ourselves to applications of geometrical optics.

### 7.2.2 Equation of Transfer

In the presence of dissipation, Eq. (7.39) takes the form

$$\nabla \cdot \bar{F}_\omega = (\bar{p}_{E \cdot j})_\omega \quad (7.58)$$

where  $(p_{E \cdot j})_\omega$  represents the spectral density of  $(p_{E \cdot j})_t$ . The effect of dissipative processes is the appearance of absorption which, in the geometrical optics formalism, is described by

$$- \alpha_\omega ds I_\omega \cos \xi d\Omega da d\omega \quad (7.59)$$

The pillbox is also a source of radiation. For an emission coefficient  $j_\omega$  Eq. (6.70), the power generated is

$$j_\omega ds \cos \xi d\Omega da d\omega \quad (7.60)$$

Summing Eq. (6.70), placing the sum on the right-hand side of Eq. (7.45), and using Eq. (7.47), leads to the Equation of Transfer<sup>2</sup>

$$n^2 \frac{d}{ds} \left( \frac{I_\omega}{n^2} \right) = -\alpha_\omega I_\omega + j_\omega \quad (7.61)$$

Equation (7.61) refers to one mode of propagation. There are as many first-order differential equations like Eq. (7.61) as there are characteristic modes in the plasma Sobolev (1963). The following are special cases where the solution to Eq. (7.61) is simple:

<sup>2</sup> The operator  $d/ds$  represents  $\hat{s} \cdot \nabla$  where  $\hat{s}$  is a unit vector along the ray direction  $s$ .

1. Emission only:  $\alpha_\omega = 0$

$$n^2 \frac{d}{ds} \left( \frac{I_\omega}{n^2} \right) = j_\omega, \quad \frac{I_\omega(s)}{n^2(s)} = \frac{I_\omega(s_0)}{n^2(s_0)} + \int_{s_0}^s \frac{j_\omega}{n^2} ds \quad (7.62)$$

2. Absorption only:  $j_\omega = 0$

$$n^2 \frac{d}{ds} \left( \frac{I_\omega}{n^2} \right) = -\alpha_\omega I_\omega, \quad \frac{I_\omega(s)}{n^2(s)} = \frac{I_\omega(s_0)}{n^2(s_0)} \exp \left\{ - \int_{s_0}^s \alpha_\omega ds \right\} \quad (7.63)$$

3. Thermodynamic equilibrium: For complete equilibrium of the radiation with its surroundings, the intensity is described by the Planck function at equilibrium temperature  $T$ .

$$n^2 \frac{d}{ds} \left( \frac{I_\omega}{n^2} \right) = 0, \quad \frac{I_\omega(s)}{n^2(s)} = B_0(\omega, T) \quad (7.64)$$

where  $B_0(\omega, T)$  is the Planck law (Sect. 7.3) Abromwitz et al. 1965.

In general, to solve Eq. (7.61) we define two quantities. The first

$$S_\omega = \frac{1}{n^2} \frac{j_\omega}{\alpha_\omega} \quad (7.65)$$

is known as the *ergiebigkeit* or *source function*. The second is the optical depth  $\tau_\omega$

$$d\tau_\omega = -\alpha_\omega ds \quad (7.66)$$

In terms of these quantities, Eq. (7.61) becomes

$$\frac{d}{d\tau_\omega} \left( \frac{I_\omega}{n^2} \right) = \frac{I_\omega}{n^2} - S_\omega \quad (7.67)$$

The solution of Eq. (7.67) is obtained by first multiplying by  $\exp(-\tau_\omega)$  and then partially integrating over  $\tau_\omega$ .

$$\begin{aligned} \int_0^{\tau_\omega(0)} e^{-\tau_\omega} \frac{dI_\omega n^2}{d\tau} d\tau_\omega &= \left. \frac{I_\omega}{n^2} e^{-\tau_\omega} \right|_0^{\tau_\omega(0)} \\ + \int_0^{\tau_\omega(0)} \frac{I_\omega}{n^2} e^{-\tau_\omega} d\tau_\omega &= \int_0^{\tau_\omega(0)} \left( \frac{I_\omega}{n^2} - S_\omega \right) e^{-\tau_\omega} d\tau_\omega \\ \frac{I_\omega}{n^2} \tau_\omega(0) e^{-\tau_\omega(0)} - \frac{I_\omega}{n^2} \tau_\omega(s_0) e^{-0} &= \int_0^{\tau_\omega(0)} S_\omega e^{-\tau_\omega} d\tau_\omega \end{aligned}$$

or, finally,

$$\frac{I_\omega}{n^2} = \frac{I_\omega(0)}{n^2(0)} + \int_0^{\tau_\omega(0)} S_\omega e^{-\tau_\omega} d\tau_\omega \quad (7.68)$$

Because of the definition Eq. (7.66),  $\tau_\omega$  decreases as  $s$  increases as shown in Fig. 7.8. Thus if  $l$  is the length of the ray,

$$\tau_{\omega} = - \int_l^s \alpha_{\omega} ds \quad (7.69)$$

Equation (7.68) expresses the fact that the intensity is the sum total of the emission at all interior points, reduced by the factor  $\exp(\tau_{\omega})$  that allows for the absorption by the intervening plasma, to which must be added the intensity of radiation incident on the back side of the plasma, reduced by the absorption in traversing the plasma.

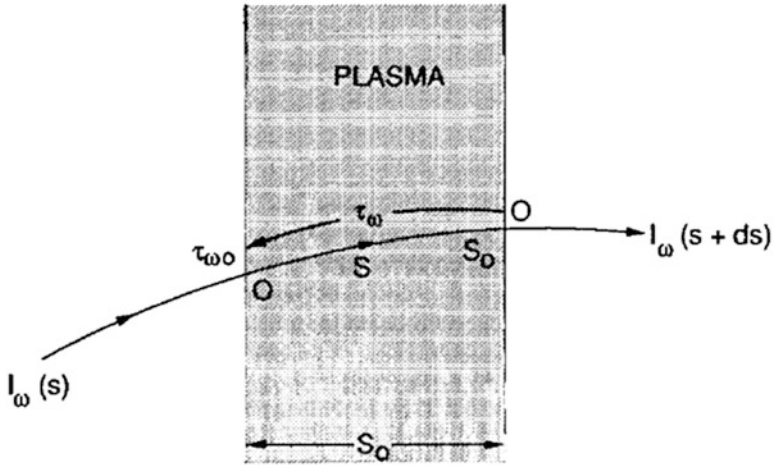


**Fig. 7.8** A ray passing through plasma. The optical depth  $\tau_{\omega}$  is measured from  $s_0$ , the point of emergence of the ray (Stix 1962)

The emission at a given frequency has two characteristic regimes, depending on the value of the total optical depth  $\tau_{\omega 0}$ :

1. When  $\tau_{\omega 0} \ll 1$ , the radiation seen by the observer suffers negligible absorption during its passage through the plasma. The plasma is said to be transparent to the radiation.
2. When  $\tau_{\omega 0} \gg 1$ , then  $I^2 \rightarrow n^2 S_{\omega}$  and the intensity depends on the refractive index and the source function. The plasma is opaque. If the plasma is isotropic and in thermal equilibrium such that  $T_r = T$ , where  $T$  is the true temperature of the radiators, the plasma emits as a black body (Sect. 7.4).

For a plasma of sufficiently large optical depth, most of the radiation seen by the external observer Eq. (7.68) comes from the outer layer of thickness  $\tau_{\omega} \sim 1$ .

### 7.3 Black Body Radiation

The spectral distribution of the radiation of a black body in thermodynamic equilibrium, for a single polarization, is given by the Planck formula

$$B_0(\omega, T) = \frac{\hbar \omega^3}{8\pi^3 c^2} \frac{1}{e^{\hbar \omega / kT} - 1} \quad (7.70)$$

which is plotted for various temperatures  $T$  in Fig. 7.9. On integrating Eq. (7.70) over all frequencies  $\omega$  (see e.g., Reif (1965, Section A. 11)), and multiplying by 2 to include both polarizations, we obtain Stefan's law for the total brightness of a black body

$$B_0(T) = \frac{2\pi^5 k^4 T^4}{15c^2 h^3} = \sigma T^4 \quad (7.71)$$

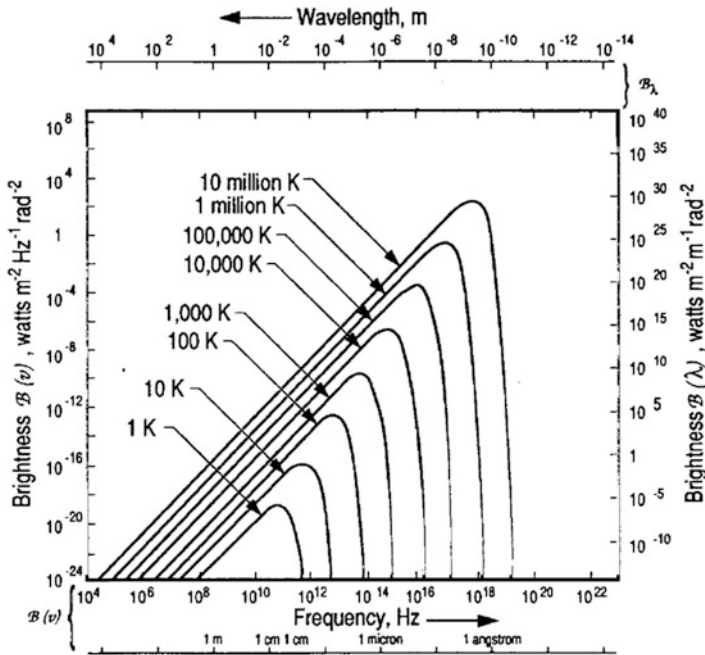


**Fig. 7.9** Planck-radiation-law curves at various temperatures with frequency increasing to the right (Adapted from J.D. Krauss 1986)

where  $\sigma = 5.67 \times 10^{-8} \text{ W m}^{-2} \text{ K}^{-4}$  is the Stefan-Boltzmann constant. The frequency at which the intensity reaches its maximum is found by solving the equation  $\partial B_0(\omega, t) / \partial \omega = 0$ . The final result is



$$\left(\frac{\hbar\omega}{kT}\right)_{\max} = 2.822 \quad (7.72)$$

or

$$\left(\frac{\hbar\omega}{kT}\right)_{\max} = 2.822 \quad (7.73)$$

which is known as Wien's displacement law. Approximations to Eq. (7.70) can be found in the following limiting cases.

1.  $\hbar\omega \ll kT$ : Rayleigh-Jeans law (long wavelength case),

$$B_0(\omega, T) = \frac{\omega^2}{8\pi^3 c^2} kT \quad (7.74)$$

This is the classical limit since it does not contain Planck's constant.

2.  $\hbar\omega \gg kT$ : Wien's law (short wavelength case),

$$B_0(\omega, T) = \frac{\hbar\omega^3}{8\pi^3 c^2} e^{-\hbar\omega/kT} \quad (7.75)$$

## 7.4 The Source Function and Kirchoff's Law

From the theory of spontaneous and stimulated emission (Bekefi 1966), the absorption coefficient finds yet another definition:

$$\alpha_\omega = \frac{8\pi^3 c^2}{n^2 \hbar \omega^3} \int P_\omega(p') [f(p) - f(p')] d^3 p' \quad (7.76)$$

where  $p$  is the momentum corresponding to energy  $W - \hbar\omega$ . Substituting Eqs. (6.70) and (6.70) into Eq. (7.65), gives

$$\alpha_\omega = \frac{8\pi^3 c^2}{n^2 \hbar \omega^3} \int P_\omega(p') [f(p) - f(p')] d^3 p' \quad (7.77)$$

Equation (7.77) is a form of Kirchoff's law for anisotropic, nonthermal plasma. When the particle distribution is Maxwellian,  $f(p)$  is given by Eq. (6.70) and

$$[f(p) - f(p')] = C_p e^{-(W-\hbar\omega)/kT} - C_p e^{-W/kT} = f(p) (e^{-\hbar\omega/kT} - 1) \quad (7.78)$$

Hence, Eq. (7.76) becomes

$$(\alpha_\omega)_{\text{Maxwellian}} = \frac{8\pi^3 c^2}{n^2 \hbar \omega^3} (e^{-\hbar\omega/kT} - 1) \int P_\omega(p') f(p) d^3 p' \quad (7.79)$$

or, from the definition Eq. (6.70)

$$(\alpha_\omega)_{\text{Maxwellian}} = \frac{8\pi^3 c^2}{n^2 \hbar \omega^3} \left( e^{-\hbar\omega/kT} - 1 \right) j_\omega \quad (7.80)$$

Using Eqs. (7.65) and (7.70), the source function for a Maxwellian distribution is

$$(S_\omega)_{\text{Maxwellian}} = \frac{1}{n^2} \left( \frac{j_\omega}{\alpha_\omega} \right)_{\text{Maxwellian}} = B_0(\omega, T) \quad (7.81)$$

Thus, when the particle distribution is Maxwellian, the source function equals the vacuum black-body intensity  $B_0(\omega, T)$ . The quantity  $T$  refers to the temperature of the emitting electrons; neither the energy nor the distribution function of any other species of plasma particles enters into Eq. (7.81). For example, the velocity distribution of streaming electrons or background (or collectively accelerated ions) within the plasma may be non-Maxwellian and their mean energy different from the value  $3kT/2$ . For tenuous plasma  $n \rightarrow 1$  and Eq. (7.81) reduces to what is generally considered to be the classical form of Kirchoff's law.

By analogy with vacuum black-body radiation we may write that  $S_\omega = (n^2 \hbar \omega^3 / 8\pi^3 c^2) (e^{\hbar\omega/kT} - 1)^{-1}$ , where the radiation temperature  $T_r$  now plays the role of the true temperature  $T$  of equilibrium radiation. Equating this to Eq. (7.77) defines  $T_r$ :

$$kT_r = \hbar\omega \left[ \frac{\int P_\omega(p') f(p) d^3 p'}{\int P_\omega(p') f(p') d^3 p'} \right]^{-1} \quad (7.82)$$

It is noted that  $T_r$  is a fictitious temperature and depends on the particle distribution, the frequency of observation, and the direction of propagation.

#### 7.4.1 Classical Limit of the Emission, Absorption, and Source Functions

This book is primarily concerned with the classical range of frequencies  $\hbar\omega \ll$  particle energy, and this limit is applied to the previous equations. We first consider the case in which  $f(p)$  is isotropic (i.e., a function only of  $p^2 = p_x^2 + p_y^2 + p_z^2$ ).

At our low frequencies of interest, we shall use the fact that the energy states of the particle are closely spaced. Writing that  $p = p' + \Delta p$  and using Eq. (6.90) with the energy conservation equation,

$$W' - W = \hbar\omega \quad (7.83)$$

gives

$$\Delta p = \frac{W \Delta W}{c^2 p} = \frac{\hbar\omega W}{c^2 p} \quad (7.84)$$

We now expand  $f(p') = f(p + \Delta p)$  in a Taylor series and keep only the leading terms. It follows that

$$f(p') = f(p) + \hbar\omega \frac{\partial f}{\partial W} \quad (7.85)$$

Substitution into Eqs. (6.70), (7.76) and (7.77) gives the desired equations:

$$j_\omega = \int P_\omega(p) f(p) d^3p \quad (7.86)$$

$$\alpha_\omega = -\frac{8\pi^3 c^2}{n^2 \omega^2} \int P_\omega(p) \frac{\partial f(p)}{\partial W} d^3p \quad (7.87)$$

This equation was derived by [Trubnikov \(1958\)](#) for  $n = 1$  for the study of cyclotron radiation from fusion plasmas. Often, Eqs. (7.86) and (7.87) are expressed in terms of the distribution of energy rather than through the distribution of momenta [Trubnikov \(1961\)](#). The two are related as follows:

$$dN = f(p) 4\pi p^2 dp = N(W) dW \quad (7.88)$$

with the result that

$$j_\omega = \int P_\omega(W) N(W) dW \quad (7.89)$$

$$\alpha_\omega = -\frac{8\pi^3 c^2}{n^2 \omega^2} \int \left\{ \frac{d}{dW} [N(W)/W^2] \right\} W^2 P_\omega(W) dW \quad (7.90)$$

From the definitions of  $S_\omega$  and  $T_r$  we also obtain from Eqs. (7.86) and (7.87)

$$kT_r = -\frac{\int P_\omega(p) f(p) d^3p}{\int P_\omega(p) (\partial f(p) / \partial W) d^3p} \quad (7.91)$$

$$S_\omega = \frac{\omega^2}{8\pi^3 c^2} kT_r \quad (7.92)$$

When  $f$  is a Maxwellian distribution,  $T_r$  equals the electron temperature  $T$  and  $S_\omega$  is the Rayleigh-Jeans limit of the Planck function.

## 7.5 Self Absorption by Plasma Filaments

Cosmic plasma is often filamentary, caused by the electrical currents it conducts. Since these currents are the source of synchrotron radiation, it is of interest to determine the absorption caused by the filaments themselves. The problem at hand is illustrated in Fig. 7.10. We first consider the absorption of a single filament. Applying the initial condition  $I_\omega = 0$  to Eq. (7.68), we obtain

$$\frac{I_\omega(s)}{n^2(s)} = S_\omega \left(1 - e^{-\tau_w(0)}\right) \quad (7.93)$$

Making the simplifying assumption that  $n^2 \sim 1$  and using Eq. (7.66),

$$I_{\omega 1} = S_\omega (1 - e^{-\alpha_w L}) \quad (7.94)$$

where  $I_{\omega 1}$  is the intensity of a single filament of width  $L$ . If there are now two filaments a distance  $d$  apart the radiation intensity seen by an observer is

$$I_{\omega 2} = S_\omega (1 - e^{-2\alpha_w L}) \quad (7.95)$$

We have used the initial conditions for the second filament  $I_{\omega 2}(x = L + \delta) = I_{\omega 1}$ . Similarly, for  $M$  filaments a distance  $d$  apart, the radiation intensity can be shown to be equal to

$$I_{\omega M} = S_\omega (1 - e^{-M\alpha_w L}) \quad (7.96)$$

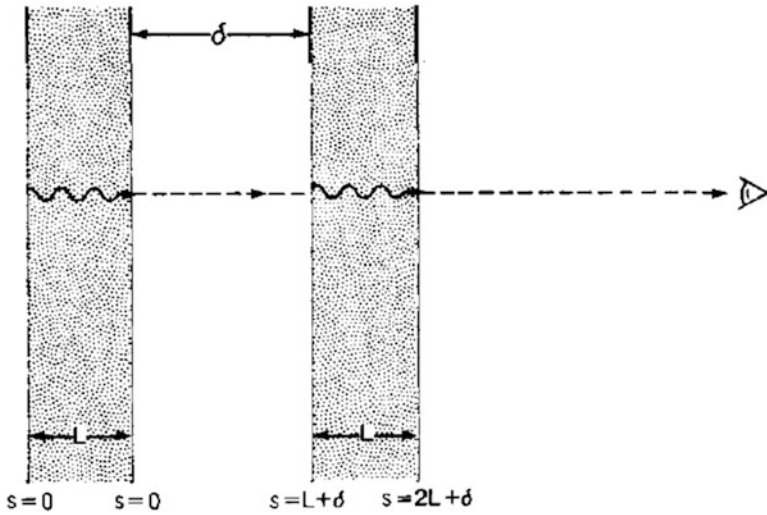


**Fig. 7.10** Radiation intensity seen by an observer through two successive Birkeland currents of width  $L$

Note that the radiation intensity increased for larger  $M$  because of each additional filament current source. If the plasma electrons in a current filament are in equilibrium with a Maxwellian distribution, the absorption coefficient  $\alpha_w$  is given by Eq. (7.87) with  $n^2 = 1$ . Substituting Eqs. (6.67), (6.89), and (6.92) into Eq. (7.87), the absorption coefficient at  $\theta = \pi/2$  is (Trubnikov 1958)

$$\alpha_\omega = \frac{\omega_p^2}{\omega_b c} \sum \Phi_m(\omega/\omega_b, \mu) \quad (7.97)$$

The quantities  $\Phi_m = \Phi_m(\omega/\omega_b, \mu)$  are defined by

$$\Phi_m = \sqrt{2\pi} \frac{\mu^{5/2}}{(\omega\omega_b)^4} m^2 \sqrt{m^2 - (\omega\omega_b)^2} e^{-\mu[m(\omega\omega_b)-1]} A[m(\omega\omega_b)] \quad (7.98)$$

where  $\mu = m_0 c^2 / kT$ . The quantities  $A_m = A_m(\gamma)$  are given by Eq. (6.70). The optical depth for  $M$  Birkeland currents is  $\tau_\omega = \alpha_\omega M L$  or

$$\tau_\omega = \left( \frac{\omega_p^2 L M}{\omega_b c} \right) \sum_m \Phi_m \quad (7.99)$$

The spectral characteristics of the emission are contained in the function  $\Phi$ . Figure 7.11 shows a plot of  $\Sigma P h_i m$  for the first one hundred harmonics as a function of  $\omega/\omega_b$  for  $T = 30$  keV. This value is typical of the thermal temperatures in a plasma filament but is appreciably less than the energies of particles in a relativistic beam. Only the extraordinary wave is considered; the contributions from the ordinary wave are usually small.

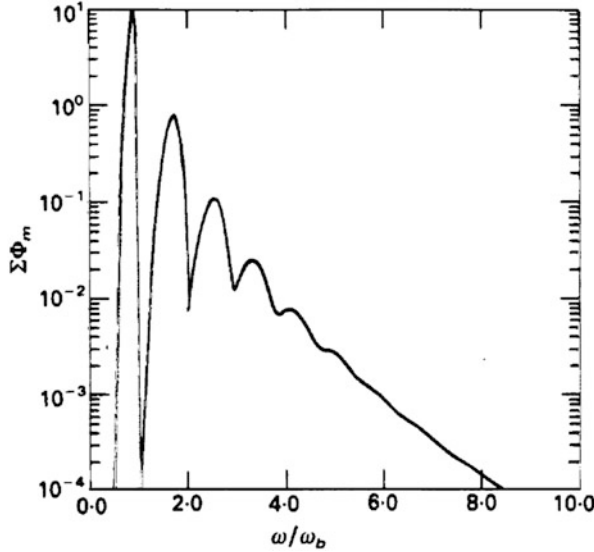


**Fig. 7.11** Calculated spectrum of radiation emitted by a plasma with electron temperature of 30 keV. Self-absorption effects are included

The broadening of the individual lines is due to the relativistic change of mass. A given line contributes only to frequencies  $\omega \leq m\omega_b$  with the highest energy elec-

trons being responsible for the emission at the lowest frequency. The smearing of the successive harmonics produces an almost monotonically decreasing spectrum at higher frequency. For  $T = 30$  keV,  $m \sim 5$  is the harmonic above which smearing prevails. To a fair approximation, the total intensity leaving the filaments is

$$I(\theta = \pi/2) \cong \int_0^{\omega^*} B_0(\omega, T) d\omega = \frac{\omega_b^3 kT}{24\pi^3 c^2} (m^*)^3 \quad (7.100)$$

where  $m^* = \omega^* / \omega_b$  is the harmonic number beyond which the emission effectively ceases to be black-body. An empirical relation for  $m^*$  for mildly relativistic plasma has been derived by [Trubnikov \(1958\)](#); and modified to the case of  $M$  filaments,

$$(m^*)^6 = 0.57 \left( \frac{20\omega_p^2}{3\omega_b c} \right) LMT \quad (7.101)$$

Equation (7.101) is valid under the approximation  $mc^2 \gg kT$ .

**Example 7.6 Number of filaments required to produce a blackbody spectrum up to 100 GHz.** Consider filaments of density  $n_e = 2 \times 10^{-3} \text{ cm}^{-3}$ , magnetic field  $B_0 = 2.5 \times 10^{-4} \text{ G}$ , temperature  $T_e = 30 \text{ KeV}$ , and width  $L = 10^{21} \text{ m}$ . From Eq. (7.101),  $m^* = 1.8 \times 10^8$ , hence  $M = 3.4 \times 10^{31}$  filaments (Fig. 7.12). This geometrical optics calculation neglects, of course, all possible reflections and resonant absorption effects.

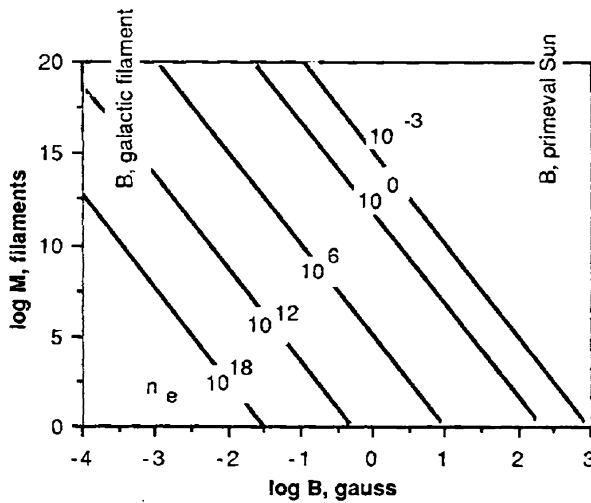


**Fig. 7.12** Number of filaments of average density  $n_e \text{ cm}^{-3}$  required to produce a blackbody spectrum to 100 GHz versus magnetic field. The graph pertains to mildly relativistic electron temperatures

## 7.6 Large-Scale, Random Magnetic Field Approximation

Magnetic fields in cosmic plasmas are generally ordered on a global scale, possessing an overall axis of alignment with components that are delineable into recognizable metrics, such as toroidal and poloidal. Nevertheless, cosmic magnetic fields often present a tangled, almost random appearance on the size scale of interest for synchrotron radiation. Figure 1.2 illustrates this situation in Fig. 7.11. Calculated spectrum of radiation emitted by a plasma with electron temperature of 30 keV. Self-absorption effects are included. a laboratory plasma where current filaments generally flow in a preferred direction but flare, twist, and kink to produce a total magnetic field which, for all practical purposes, is “random.”

In the following analyses, a particularly convenient assumption is that the magnetic field lines are essentially uniform on a scale length which is large with respect to the radiating electron gyroradii  $r_L$ , but randomly distributed on scales which are small compared to the size of the filament itself.

Previously we considered the case of a single magnetic field orientation  $\mathbf{B}_0 = \hat{\mathbf{z}}B_0$ . For this case the spectral power radiated by relativistic particles was simply a sum of the different mode polarizations. In a completely random magnetic field, polarization is absent. The spectral power is calculated by averaging the total spectral power for a homogeneous magnetic field Eq. (6.70) over all possible azimuthal and polar (helical-pitch) angles,  $\phi$  and  $\vartheta$ , respectively.

$$\begin{aligned}
 P_\omega(\omega, \gamma) &= \frac{1}{4\pi} \int_0^{2\pi} d\phi \int_0^\pi P_\omega(\omega, \vartheta, \gamma) \sin \vartheta d\vartheta \\
 &= \frac{e^2}{\sqrt{3} 8\pi^2 \epsilon_0 c} \frac{\omega}{\gamma^2} \int_0^\pi d\vartheta \sin \vartheta \int_{x/\sin \vartheta}^\infty dy K_{5/3}(y) \\
 &= \frac{e^2}{\sqrt{3} 8\pi \epsilon_0 c} \frac{\omega}{\gamma^2} C\left(\frac{2\omega}{3\omega_b \gamma^2}\right) \text{ Js}^{-1} \text{ rad}^{-1}
 \end{aligned} \tag{7.102}$$

where  $C(x)$  is the Crusius-Schlickeiser function, defined by

$$C(x) = W_{0,4/3}(x) W_{0,1/3}(x) - W_{1/2,5/6}(x) W_{-1/2,5/6}(x) \tag{7.103}$$

where  $W_{\lambda,\mu}(x)$  denotes the Whittaker function. Based on the properties of  $W_{\lambda,\mu}(x)$  for small and large arguments (Abromwitz and Stegun 1970), asymptotic expansions of  $C(x)$  are

$$C(x) = \begin{cases} a_0 x^{-2/3} & x \ll 1 \\ x^{-1} e^{-x} & x \gg 1 \end{cases} \tag{7.104}$$

where  $a_0 = 2^{4/3} \Gamma(1/3) / 5\pi$ . Figure 7.13 is a plot of Eqs. (7.102) and (6.70).

### 7.6.1 Plasma Effects

The influence of a background plasma on synchrotron emission enters via the refractive index  $n$ . Consider, for simplicity, the case of a transverse electromagnetic wave propagating in an isotropic plasma (Example 7.1),  $n^2 = P = 1 - \omega_p^2/\omega^2$ . Since  $n$  is less than unity the phase velocity of the wave is greater than the speed of light. All  $\gamma$  factors in the synchrotron formulae that are due to retardation effects undergo the following transformation:

$$\gamma' = (1 - v^2/v_{ph}^2)^{-1/2} = (1 - n^2 v^2/\omega^2)^{-1/2} \quad (7.105)$$

For relativistic particles  $v \cong c$  and Eq. (7.105) becomes

$$\gamma' \approx \gamma/t, \quad t = (1 + \gamma^2 \omega_p^2/\omega^2)^{1/2} \quad (7.106)$$

The influence of an isotropic background plasma is manifested by the fact that  $\gamma'$  can be much smaller than the usual Lorentz factor  $\gamma$ . In the plasma Eq. (6.70) has to be changed

$$\omega'_c = \frac{3}{2} \omega \gamma \gamma'^3 / t^3 = \omega_c / t^3 \quad (7.107)$$

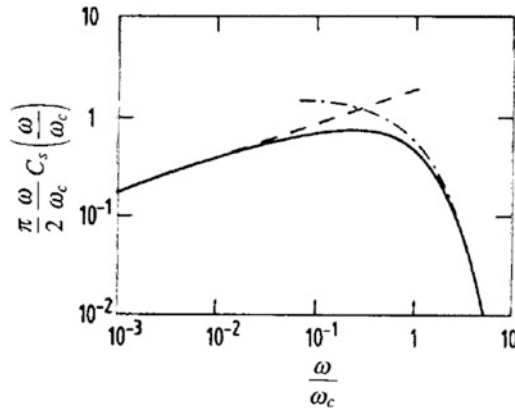


**Fig. 7.13** Emissivity function as a function of normalized frequency  $\omega/\omega_c$ . The dashed curves show the asymptotic results (Crusius and Schlickeiser 1986)

Substituting Eq. (7.107) into Eq. (7.102) leads to

$$P_\omega(\gamma) = \frac{1}{\sqrt{3}} \frac{e^2}{8\pi\epsilon_0 c} \frac{\omega}{\gamma^2} \left[ 1 + \left( \gamma \frac{\omega_p}{\omega} \right)^2 \right] C \left\{ \frac{2\omega}{3\omega_b \gamma^2} \left[ 1 + \left( \gamma \frac{\omega_p}{\omega} \right)^2 \right]^{3/2} \right\}, \quad (7.108)$$

$\text{J s}^{-1} \text{rad}^{-1}$



### 7.6.2 Monoenergetic Electrons

Consider the case of a monoenergetic distribution of relativistic electrons

$$N(W) dW = N(\gamma) d\gamma = N_0 \delta(\gamma - \gamma_0) d\gamma \quad (7.109)$$

Substituting Eqs. (7.108) and (7.109) into Eq. (7.89), we find

$$j_\omega = \int P_\omega(W) N(W) dW = N_0 \int P_\omega(\gamma) \delta(\gamma - \gamma_0) d\gamma \\ = \frac{N_0}{\sqrt{3}} \frac{e^2}{8\pi\epsilon_0 c} \frac{\omega}{\gamma_0^2} \left[ 1 + \left( \gamma_0 \frac{\omega_p}{\omega} \right)^2 \right] C \left\{ \frac{2\omega}{3\omega_b \gamma_0} \left[ 1 + \left( \gamma_0 \frac{\omega_p}{\omega} \right)^2 \right]^{3/2} \right\} \quad (7.110)$$

$$j_\omega = \frac{N_0}{\sqrt{3}} \frac{e^2}{8\pi\epsilon_0 c} \frac{\omega}{\gamma_0^2} f [1 + f^{-2}] C \left\{ \frac{f}{g_0} [1 + f^{-2}]^{3/2} \right\} \quad (7.111)$$

where

$$f = \frac{\omega}{\gamma_0 \omega_p} \quad (7.112)$$

$$g_0 = \frac{3}{2} \left( \frac{\omega_b}{\omega_p} \right) \gamma_0 \quad (7.113)$$

Figure 7.14 illustrates the behavior of the emissivity  $j_\omega$  versus frequency  $f$  for various values of  $g_0$ . The emissivity can be characterized according to the magnetic field/plasma density parameter  $g_0$ . For most cosmic plasma  $\omega_b \leq \omega_p$  so that  $g_0 \gg 1$  corresponds to highly relativistic of electrons  $\gamma_0 \gg 1$ . The spectra of Fig. 7.14 for large frequencies is typical of that generated by relativistic electrons in the absence of plasma effects (cf., Fig. 7.13). This vacuum behavior extends down to a lower frequency  $f \approx g_0^{-1/2}$ . The logarithmic bandwidth of  $j_\omega$  is (Crusius 1988)

$$\Delta \log f \cong 1.5 \log g_0 \quad (7.114)$$

The larger  $g_0$ , the larger the logarithmic bandwidth with its characteristic anisotropy around  $f = 1$ .

When  $g_0 < 1$  ( $\omega_p > \omega_b \gamma_0$ ), Fig. 7.14 shows an exponential suppression for all frequencies when compared to the case of  $g_0 \gg 1$ .

The parameter  $g_0$  may also be written as  
where

$$\gamma_R = \frac{2}{3} \frac{\omega_b}{\omega_p} = \frac{2.1 \times 10^{-10} \sqrt{n_e (m^{-3})}}{B(T)} \quad (7.115)$$

is called the Razin-Lorentz factor in a random magnetic field.

## 7.7 Anisotropic Distribution of Velocities

Only the energy conservation equation was used in the derivation of Eqs. (7.86)–(7.92). However, for an anisotropic distribution function, momentum conservation equations are also needed.

Let  $f(p_{\parallel}, p_{\perp})$  be the distribution of particle momenta where  $p_{\parallel}$  and  $p_{\perp}$  are the components of  $\mathbf{p}$  parallel and perpendicular to  $B_0$ , respectively. We assume for simplicity that  $f(p_{\parallel}, p_{\perp})$  is symmetrical about the  $B_0$  direction, namely, that there is no dependence of  $f(p_{\parallel}, p_{\perp})$  on azimuthal angle  $\phi$ .

Again expanding  $f(p_{\parallel}, p_{\perp})$  in a Taylor series, we obtain

$$f(p'_{\parallel}, p'_{\perp}) = f(p_{\parallel}, p_{\perp}) + \frac{\partial f}{\partial p_{\parallel}} \Delta p_{\parallel} + \frac{\partial f}{\partial p_{\perp}} \Delta p_{\perp} \quad (7.116)$$

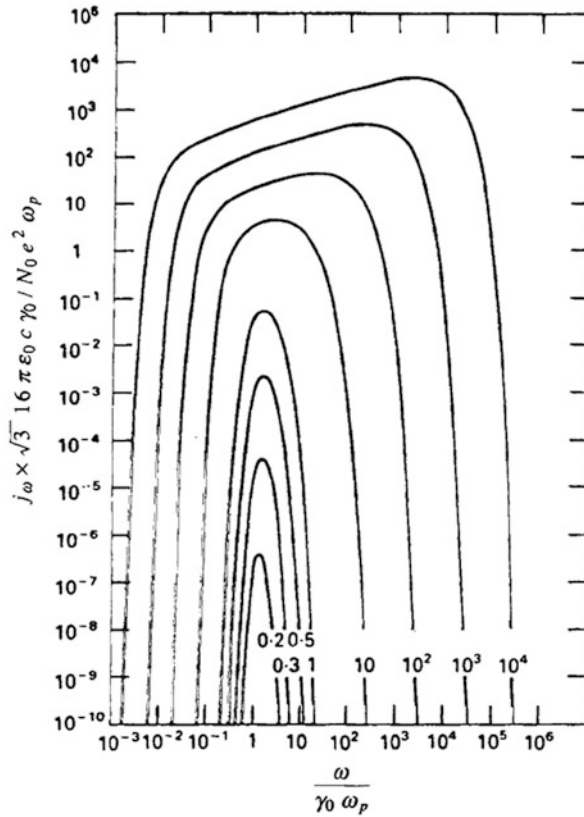


**Fig. 7.14** Emission coefficient  $j\omega$  as a function of the normalized frequency  $f$  for  $g_0 = 0.2, 0.3, 0.5, 1, 10, 10^2, 10^3$ , and  $10^4$  (Crusius 1988)

The determination of  $\Delta p_{||}, \Delta p_{\perp}$  requires use of Eq. (7.83) and the momentum conservation equation for  $p_{||}$

$$p'_{||} - p_{||} = n(\theta) \cos \theta \frac{\hbar \omega}{c} \quad (7.117)$$

The parameters are obtained from the conservation equations (7.116) and (7.117) with the result

$$\begin{aligned} \Delta p_{||} &= n(\theta) \cos \theta \frac{\hbar \omega}{c} \\ p_{\perp} \Delta p_{\perp} &= \frac{W \hbar \omega}{c^2} - p_{||} n(\theta) \cos \theta \frac{\hbar \omega}{c} \end{aligned} \quad (7.118)$$

Using Eqs. (7.116) and (7.118) and the fact that  $d^3 p' \rightarrow dp = 2\pi p_{\perp} dp_{\perp} dp_{||}$ , the emission and absorption coefficients Eqs. (6.85ab) and (7.76) reduce to

$$j_{\omega} = \iint P_{\omega}(p_{||}, p_{\perp}) f(p_{||}, p_{\perp}) 2\pi p_{\perp} dp_{\perp} dp_{||} \quad (7.119)$$

$$\begin{aligned} \alpha_{\omega} &= -\frac{8\pi c^2}{n^2 \omega^2} \iint P_{\omega}(p_{||}, p_{\perp}) \\ &\times \left[ \frac{W}{c^2} \frac{\partial f}{\partial p_{\perp}} - n(\theta) \cos \theta \left( \frac{p_{||}}{c} \frac{\partial f}{\partial p_{||}} - \frac{p_{\perp}}{c} \frac{\partial f}{\partial p_{\perp}} \right) \right] 2\pi p_{\perp} dp_{\perp} dp_{||} \end{aligned} \quad (7.120)$$

It should be noted that Eq. (7.120) contains both the ray refractive index  $n$  and the wave index  $n(\theta)$ . When  $f$  is isotropic Eqs. (7.119) and (7.120) reduce to Eqs. (7.86) and (7.87), respectively. Equation (7.119) has found application in the study of radio bursts of synchrotron radiation at decameter wavelengths from Jupiter for the special case  $n \rightarrow 1, \theta = \pi/2$  (Hirshfield and Bekefi 1963).

## References

- Abromwitz, M., Stegun, I.: Handbook of Mathematical Functions. Dover, New York (1965)
- Abramowitz, M., Stegun, I.A., eds.: Handbook of Mathematical Functions with Formulas, Graphs, and Mathematical Tables, Dover Publications, New York, (1970). ISBN 978-0-486-61272-0
- Bekefi, G.: Radiation Processes in Plasmas. Wiley, New York (1966)
- Crusius, A.: The influence of a thermal plasma on synchrotron radiation. *Laser Part. Beams* **6**, 421 (1988)
- Crusius, A., Schlickeiser, R.: Synchrotron radiation in random magnetic fields. *Astron. Astrophys.* **164**, L16 (1986)
- Hirshfield, J.L., Bekefi, G.: Decameter radiation from Jupiter. *Nature* **198**, 20 (1963)
- Kimura I.: In: Lyons, L.R., Williams, D.J. (eds.) (1984). *Quantitative Aspects of Magnetospheric Physics*. D. Reidel, Dordrecht (1966)
- Krauss, W.: *Jour. Geophys. Research*, **91**, C4, 5061–5074 (1986)

- Kuehl, H.H.: The kinetic theory of waves in a warm plasma excited by a current source by low frequency radiation from an electric dipole in cold anisotropic plasma. USCEC report 82-208 (1970)
- Peratt, A.L., Kuehl, H.H.: Transmission and reflection of a wave obliquely incident on a nonuniform magnetized plasma. *Radio Sci.* **7**, 309 (1972)
- Peter, W., Peratt A.L.: Thermalization of synchrotron radiation from field-aligned currents. *Laser Part. Beams* **6**, 493 (1988)
- Reif, F.: *Fundamentals of Statistical and Thermal Physics*. McGraw-Hill, New York (1965)
- Slater J.C., Frank N.H.: *Electromagnetism*, McGraw-Hill (1947)
- Sobolev, V.V.: *A Treatise on Radiative Transfer*. D. Van Nostrand, Princeton (1963)
- Stix, T.H.: *The Theory of Plasma Waves*. McGraw-Hill, New York (1962)
- Storey, L.R.O.: An investigation of whistling atmospherics. *Philos. Trans. R. Soc. Lond. Ser. A* **246**, 113 (1953)
- Trubnikov, B.A.: Plasma radiation in a magnetic field. *Sov. Phys. Dokl.* **3**, 136 (1958)
- Trubnikov, B.A.: On the angular distribution of cyclotron radiation from a hot plasma. *Phys. Fluids* **4**, 195 (1961)
- Trubnikov, B.A., Yakubov, V.B.: Cyclotron radiation of electrons having a two-dimensional maxwellian distribution. *Plasma Phys.* **5**, 7 (1963)

## Chapter 8

# Critical Ionization Effect in Interstellar Clouds

### 8.1 Critical Ionization Velocity

The concept of a critical ionization velocity (CIV) was first introduced by [Alfvén \(1942, 1954\)](#) as a component of his theory for the formation of the solar system. If a neutral gas and magnetized plasma are in relative motion, a rapid ionization of the neutrals takes place if the kinetic energy of the neutrals relative to the plasma exceeds the ionization potential  $eV_i$  of the neutrals. This then defines a critical velocity for the neutral mass  $M$

$$V_{cr} = (2eV_i/M)^{1/2} \quad (8.1)$$

above which the CIV ionization will take place. This concept was used by Alfvén to explain why the composition of the inner planets differs from that of the outer planets. The idea was that as neutral gas fell toward the Sun, each species present in the gas was preferentially ionized according to its critical velocity and hence trapped by the Sun's magnetic field at a particular distance.

### 8.2 The CIV Process in Laboratory Experiments

The ionization of neutral gas in laboratory experiments ([Brenning 1992a,b](#)) verified that CIV exists and occurs at a threshold near or slightly above that predicted by Eq. (8.1). However, it was discovered that the efficiency of the ionization derives often not from the direct collision of ions with neutrals nor with electrons with neutrals, but rather from a magnetic-field-strength independent plasma instability leading to the transfer of energy from fast ions to background electrons. The resultant distribution function is pseudo-Maxwellian at low energies with a high energy tail containing electrons of energy that exceeds that of the initial ion energy. It is the high energy electrons within the tail  $E > eV_i$  which then ionize the neutrals. The process for generating an ionizing source of fast electrons begins with one of

the most common instabilities in plasma, the two stream instability. The modified two stream instability for cold ions and electrons in the linear approximation is an efficient mechanism leading to fast seed ions in a counterstreaming flow of electrons and ions, such as those produced in a diode in laboratory plasmas, or in space, from a double layer derived longitudinal electric field, [Peratt \(1992\)](#). For cold ions and electrons the linear dispersion relation is, from [Buneman \(1962\)](#)

$$\omega_e^2 \sin^2 \Theta \omega^2 + \omega_e^2 \cos^2 \Theta (\omega^2 - \Omega_e^2) + \omega_i^2 (\omega - kV \cos \Theta)^2 = 1 \quad (8.2)$$

where  $\omega_e$  and  $\omega_i$  are the electron and ion plasma frequencies, respectively,  $\Omega_e$  is the electron gyrofrequency,  $k$  the wave vector,  $V$  the beam ion velocity, and  $\Theta$  the angle between the wave vector and beam ion velocity. The linear-nonlinear evolution of the two stream instability was studied with the 2-1/2 dimensional, fully electromagnetic particle in cell (PIC) code ISIS, [Peratt \(1995\)](#), even for high electron/ion mass ratios; e.g. Argon, [Peratt and Jones \(1986\)](#). A maximum in the growth rate is consistent with the theoretical prediction  $\Theta \sim (m/M)^{1/2}$  and the electrons respond quite rapidly to the electric fields generated by the two-stream instability; with the heating time of the electrons occurring generally in several tens of inverse plasma frequency periods. The interplay of collisional versus collective processes in the ionization of neutrals, including charge exchange and line excitation, has been studied in depth by [McNeil et al. \(1990\)](#). Three dimensional electromagnetic Monte Carlo PIC simulations of CIV experiments in space have been studied by Wang et al. (1994, Private communication).

The randomization and heating of the electrons due to CIV has been reported by [Sherman \(1973\)](#) in laboratory experiments involving cross field  $\mathbf{E} \times \mathbf{B}$  plasma sheath acceleration through a neutral gas background such as found in rail guns and plasma thrusters, [Scheuer et al. \(1994\)](#). Here the CIV effect limits the deuterium, helium, and argon propellant velocities while the heating adversely affects the electrode lifetimes.

### 8.3 The CIV Process in Interstellar Space

While CIV plays an important role in laboratory coaxial gun devices, no agreement has been reached as to whether CIV exists in the natural space environment, primarily based on the study of ionospheric barium releases, [Brenning \(1992b\)](#). However, an effective means for producing CIV in interstellar space involves the cross-field equivalent in space called the Marklund convection mechanism (for a review, see [Peratt \(1992\)](#)). When an electric field is present in a plasma and has a component perpendicular to a magnetic field, radial inward convection of the charged particles is possible. Repeating Eq. (4.20), under the influence of the  $\mathbf{E} \times \mathbf{B}$  force, both the electrons and ions drift with the velocity,

$$\mathbf{v} = \mathbf{E} \times \mathbf{B} / B^2 \quad (8.3)$$

so that a portion of the plasma moves radially inward, Fig. 8.1.

This mechanism provides a very efficient convection process for the accumulation of matter from plasma. The material should form as a filamentary structure about the twisted flux tubes, the lines of which are commonly referred to as “magnetic ropes” because of their qualitative pattern. Magnetic ropes should tend to coincide with material filaments that have a higher density than the surroundings.

A stationary state occurs when the inward convection of ions and electrons toward the axis of a filament is matched by recombination and outward diffusion of neutralized plasma. The equilibrium density of the ionized component normally has a maximum at the axis. However, because of the following mechanism, hollow cylinders, or modifications of hollow cylinders of matter, form about the flux tubes, Fig. 8.1.

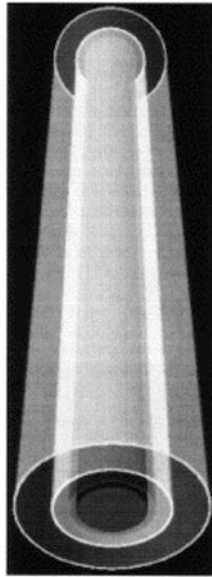


**Fig. 8.1** Idealized picture of hollow cylinders of matter formed about flux tubes; the physical distribution is not so smooth

Because of the radiated loss of energy, the filaments cool and a temperature gradient is associated with the plasma. As the radial transport depends on the ionization potential of the element, elements with the lowest ionization potentials are brought closest to the axis. The most abundant elements of cosmic plasma can be divided into groups of roughly equal ionization potentials as follows: He (24 eV); H, O, N (13 eV); C, S (11 eV); and Fe, Si, Mg, Na, Ca (5–8 eV). These elements can be expected to form hollow cylinders whose radii increase with ionization potential. Helium will make up the most widely distributed outer layer; hydrogen, oxygen, and nitrogen should make up the middle layers, while sodium, calcium, iron, silicon, and magnesium will make up the inner layers. In the classical Marklund picture, the production and diffusion of neutral gas is outwards from the plasma filament. (Note

that the first ionization potential (FIP) is also widely recognized as the determinant of the relative abundance of the elements in the solar corona with respect to the photosphere, [Schmelz et al. \(2012\)](#).)

As noted by [Peratt and Verschuur \(2000\)](#), while the magnetic flux tubes themselves are not directly observable,<sup>1</sup> their existence in the interstellar medium would require both the presence of filamentary structures and a signature of the CIV process. The first condition, that the interstellar medium show a filamentary morphology, was satisfied with the discovery of interstellar neutral hydrogen filaments from high resolution HI data from radio astronomical observations. This is apparent in the Atlas of Galactic Neutral Hydrogen maps, known as the Leiden-Dwingeloo or L-D survey of [Hartmann and Burton \(1997\)](#). Initial analysis of an interstellar HI filament using the Carlqvist relation for Bennett pinched cosmic currents discussed in Chap. 9 suggested such HI filaments originate from axial electrical currents  $I_z \sim 1.4 \times 10^{13}$  A with circumferential magnetic fields  $B_\phi$  of the order 5  $\mu$ G, [Verschuur \(1995\)](#).

The second criterion, that the CIV phenomenon be manifested in interstellar space, is the thrust of this chapter. The cross-field Marklund convection of electrons in the vicinity of a filament, both in the presence of the background plasma and neutral gas, initiates the two stream instability as the electrons flow through the background ions at velocity  $|v_r| = E_z/B_\phi$ , where  $E_z$  is the (longitudinal) component of the electric field within a filament (often thought to be caused by double layers produced by a two-stream instability within the axially directed filament). Collective ion acceleration ([Alfvén and Wernholm 1952](#); [Faehl and Godfrey 1978](#)) is caused by the electrons pull on the ions in the convection flow, thus producing the fast ion beam that imparts its energy on the braking electrons in collisional and collective action. The ions, as do the neutrals, flow unimpeded by the presence of  $\mathbf{B}$ . However, the electrons, deriving both from the background plasma as well as those newly formed from the neutral gas heated by the high-energy tail of the electron distribution function, tend to spiral about  $\mathbf{B}$ .

This imparts a thermal plasma distribution with velocity components in all three spatial directions to the neutral gas. The basic picture, albeit without the 3D electron motion explicitly included in the simulation, is the case studied numerically by [Machida and Goertz \(1986\)](#) who investigated via a one-dimensional electrostatic PIC code the CIV process in high and low neutral particle densities. In their simulation both ions and neutrals were assumed to cross the magnetic flux lines transversely while the electrons spiraled around the lines. Included in their formulation was charge exchange, ion and electron elastic collisions, momentum coupling, electron impact neutral excitation and ionization, cross-field ion beam dynamics, electrostatic wave excitation, and finally, electron heating. Machida and Goertz found that ionization of the neutrals by the fast electrons proceeds effectively by forming a positive feedback loop until thermal saturation limited by the nonlinear energy budget occurs. It is this thermal signature which manifests itself in HI linewidth spectra.

---

<sup>1</sup> Archaeological relics from the Mesopotamian city of Ur suggest otherwise ([Peratt 2003](#)).



One attribute, not possible at the time but currently included, are magnetized ions. This allows a quantitative database whereby particle gyrofrequencies, ionization rates, Alfvén velocity, neutral drift speeds and mean free paths, neutral and plasma densities, self-consistently are available in the post-processed data. These are then matched to the inferred currents and fields estimated from the radiotelescope and satellite observations.

Table 8.1 lists the critical ionization velocities for the most abundant interstellar atomic species. They are grouped into Bands and as will be shown below have distinct HI emission profile line widths associated with them. The most ubiquitous elements in the CIV process in the interstellar medium are Hydrogen and He. Hydrogen has a critical ionization velocity  $V_{cr}$  of 51.2 km/s. This value infers a longitudinal electric field  $E_z$  of about 25  $\mu\text{V/m}$  when the interstellar filament current derived by [Verschuur \(1995\)](#) is used. Most of space, being either fully or partially ionized hydrogenic plasma, is susceptible to the CIV process at this velocity, provided a magnetic field is present, such as that produced by a field-aligned current or magnetic rope. However, observations of neutral hydrogen are unlikely to reveal the CIV signature of H because most of the relevant hydrogen would be ionized. On the other hand, the signature of He with a CIV of  $V_{cr} \sim 34.4$  km/s is common in HI emission line profiles, see below.

After the He CIV band I component, the CIV process then cascades towards ionizing increasingly heavier elements in the neutral background, if these heavy elements are present. As discussed above, these must be progressively closer to the axis of a filamentary flux tube. After CIV band I comes CIV band II with a mean critical velocity of 13.7 km/s. Finally CIV band III should be observable at a mean critical velocity of order 6.5 km/s for the common heavy elements. As noted by Alfvén, overlap between the individual layers should occur and these can be expected to crowd the individual thermal lines. Additionally, because of the ordering, the HI linewidth spectra must show CIV band I, then band II, followed by band III. It is important to note from Table 8.1 that all of the common interstellar elements fall in one of three CIV bands with three delineable HI thermal bandwidths, component families 1, 2, and 3 (see below), from the thermal saturation mechanism discussed above. CIV Band III (associate with narrow HI component 3) is unique in that its region of occurrence must start to coincide with the Marklund pump action close to a filament axis and should then be associated with any dusty plasma forming there.

## 8.4 Neutral Hydrogen Emission Line Data

Neutral hydrogen emission line data can be presented in a variety of ways, each of which reveals some specific aspect of the physical processes that give rise to the emission. In the early days of HI studies (the 1950s and early 1960s) it was

**Table 8.1** Critical velocities

Element	Atomic mass (amu)	Ionization potential (V)	Critical velocity (km/s)
(1)	(2)	(3)	(4)
Band I			
H	1.0	13.6	51.2
Band I and HI broad components			
He	4.0	24.6	34.4
Band II and HI intermediate width			
Ne	20.2	21.6	14.4
N	14.0	14.5	14.2
C	12.0	11.3	13.5
O	16.0	13.6	12.8
Band III and HI narrow components			
Ar	40.0	15.8	8.7
P	31.0	10.5	8.1
S	32.1	10.4	7.9
Mg	24.3	7.6	7.8
Si	28.1	8.2	7.5
Na	23.0	5.1	6.6
Al	27.0	6.0	6.5
Ca	40.1	6.1	5.4
Fe	55.9	7.9	5.2
Ti	47.9	6.8	5.2
Mn	54.9	7.4	5.1
Cr	52.0	6.8	5.0
Ni	58.7	7.6	5.0

common to report emission profile shapes (spectra) which were then discussed in broad terms, at best. Figure 8.2 represents an example in an HI profile drawn from the Leiden-Argentina-Bonn (LAB) HI survey, the most recent incarnation of the L-D Survey ([Hartmann and Burton 1997](#)), in which a Gaussian decomposition reveals the signatures of each of the main HI component families.

When contour mapping hardware and software came available in the late 1960s and early 1970s, a new trend emerged. Maps of HI brightness as a function of velocity and position were published in large numbers. That, in turn, led to the production of area maps of HI brightness temperature or column density as a function of two spatial coordinates being published in catalog form. Figure 8.3 shows HI filament structure at two velocities in an area of sky that was fully mapped by [Verschuur \(2013\)](#) using LAB Survey data. These are but two of more than 50 such maps for this area that shows multiple filaments that in places interact where they intersect.

Area maps of HI properties such as Figure 8.3 are readily compared to photographs or other area representations of astronomical data, such as the brightness of infrared 100 or 60  $\mu$  emission from interstellar cirrus dust. These allow extensive

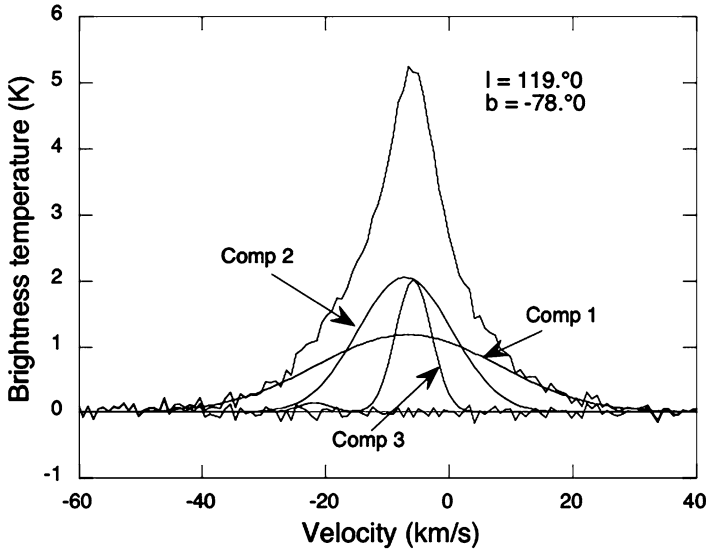


Fig. 8.2 Gaussian fit to the LAB survey profile as discussed below

qualitative comparison between, for example, HI column density molecular clouds, or  $100\mu$  brightness in order to learn about the underlying physics of the regions in which HI and cirrus dust coexist.

## 8.5 The Relationship Between Observed HI Emission and CIV Data

In a number of papers it has been shown that HI Component 1 (He CIV) which is widespread over the sky has a typical line width of 33 km/s (Verschuur 2013; Verschuur and Schmelz 2010; Verschuur and Magnani 1994; Verschuur and Peratt 1999), while Component 2 has a velocity line width of approximately 14 km/s, which appears to be associated with filaments (Verschuur 2013). In addition, Component 3 includes narrow features from 4–6 km/s wide, with a mean around 5.8 km/s, usually superimposed on Component 2. The narrow components are seldom found as isolated profiles away from the velocity range of the broader features. In several cases studied closely, Component 3 appears associated with dust and sometimes molecular structures (see Chap. 9), but this is not always so (Fig. 8.4).

The analysis of the HI structure in directions encompassed by Fig. 8.3 reported by Verschuur (2013) dealt with the possible association with high-frequency continuum sources. Therefor he did not discuss the significance of the apparent association

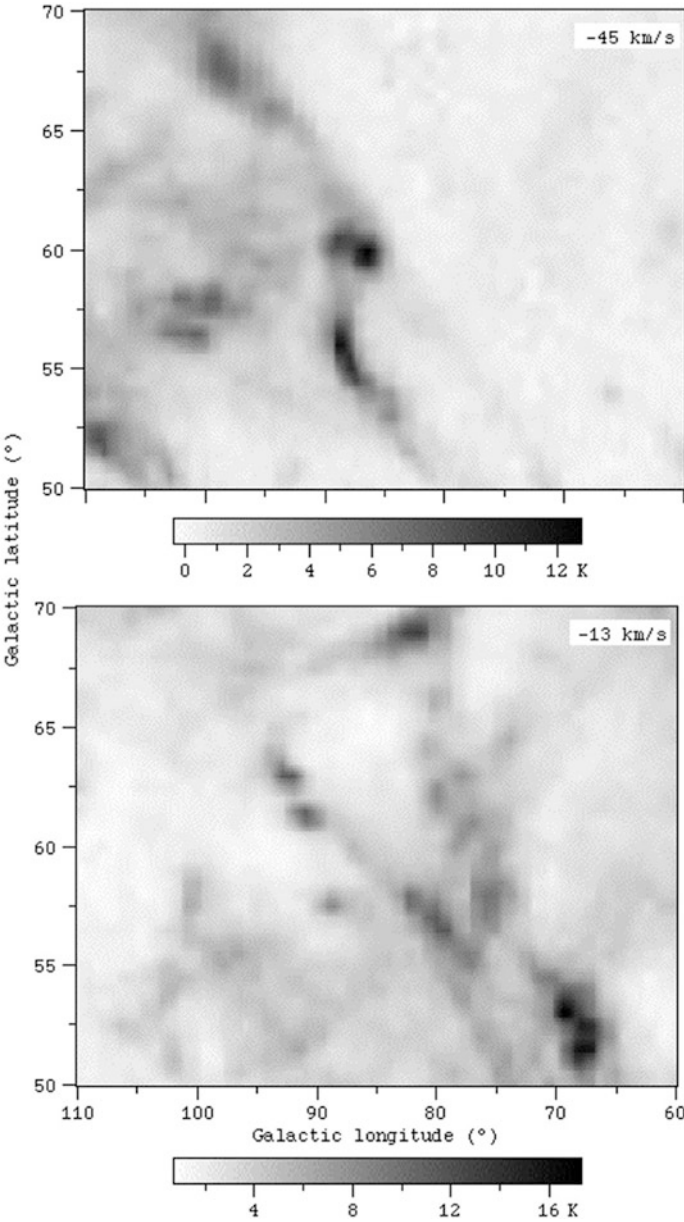


**Fig. 8.3** Large-scale HI filaments threading their way through an area of sky mapped by [Verschuur \(2013\)](#). The upper plot shows the HI brightness at  $-44\text{km/s}$  with respect to the local standard of rest and the lower plot at  $-13\text{ km/s}$ . The bars show the brightness temperature of the HI at each velocity

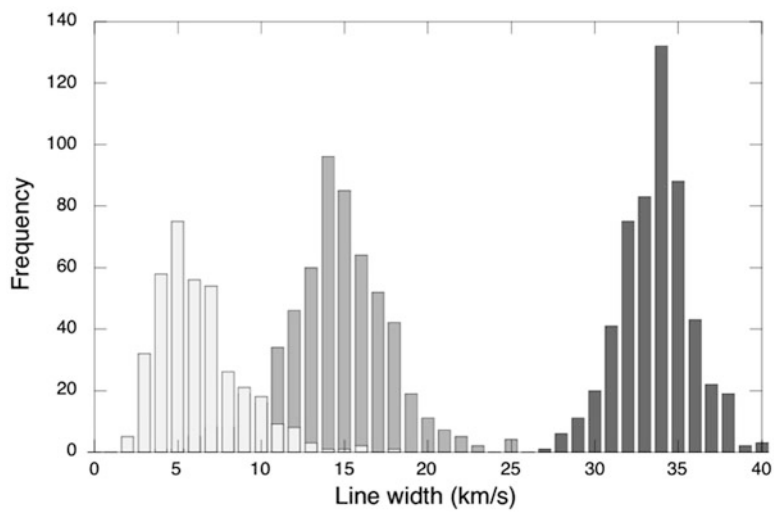


**Fig. 8.4** High resolution observations and the physics of high-velocity cloud A0 (Astrophysical Journal, 766, 113, 2013)

between the average line widths of 18 families of HI components and CIV values, although his line width data were summarized in a table. In Fig. 8.3, kindly made available by Verschuur, the data for major families of line widths are summarized in histogram form. The presence of the three main bands of CIVs is striking. In addition, [Verschuur and Schmelz \(2010\)](#) summarized published data from 10 independent sources and found average values for HI Components 1 & 2. Table 8.2 compares their results with the data from [Verschuur \(2013\)](#) with the average values of the CIVs for the most common interstellar species in those bands are also tabulated. What the data in Table 8.2 show is that the signature of the CIV phenomenon appears to manifest itself in the motion of HI atoms in interstellar space, a topic that deserves a great deal more investigation.

**Table 8.2** Critical velocities

Reference Average line width	Verschuur and Schmelz Verschuur (2010) (km s <sup>-1</sup> )	V(2013) (km s <sup>-1</sup> )	Ave. CIV (km s <sup>-1</sup> )
HI component 1	33.7± 2.4	33.2± 2.1	He 34.4
HI component 2	13.9± 0.9	14.0± 3.2	II 13.7 ± 0.7
HI component 3	5.9± 1.0	5.8± 2.6	III 6.5 ± 1.4

## References

- Alfvén, H.: On the cosmogony of the solar system. *Stockholms Obs. Ann.* **I**, 14, 2.1–2.33 (1942)
- Alfvén, H.: *On the Origin of the Solar System*. Cambridge University Press, Cambridge (1954)
- Alfvén, H., Wernholm, U.: A new type of accelerator. *Ark. för Fys.* **15**, 17 (1952)
- Brenning, N.: Review of the CIV phenomena. *Space Sci. Rev.* **59**, 209 (1992a)
- Brenning, N.: A comparison between laboratory and experiments on Alfvén's critical ionization velocity. *IEEE Trans. Plasma Sci.* **20**, 778 (1992b)
- Buneman, O.: Instability of electrons drifting through ions across a magnetic field. *J. Nucl. Energy, Part C* **4**, 111–117 (1962)
- Faehl, R.J., Godfrey, B.B.: *Phys. Rev. Lett.* **40**, 1137 (1978)
- Hartmann, D., Burton, W.B.: *Atlas of Galactic Neutral Hydrogen*. Cambridge University Press, Cambridge (1997)
- Machida, S., Goertz, C.K.: A simulation study of the critical ionization process. *J. Geophys. Res.* **91**, 11965 (1986)
- McNeil, W.J., Lai, S.T., Murad, E.: Interaction between the ionospheric plasma and a xenon cloud. *J. Geophys. Res.* **95**, 10345 (1990)
- Peratt, A.L.: *Physics of the Plasma Universe*. Springer, New York (1992)
- Peratt, A.L.: Advances in numerical modeling of astrophysical and space plasmas. In: de Gouveia Dal Pino, E.M., Peratt, A.L., Medina Tanco, G.A., Chian, A.C.-L. (eds.) *Kluwer Academic*, Dordrecht, The Netherlands (1995)
- Peratt, A.L.: Characteristics for the occurrence of a high-current z-pinch aurora as recorded in antiquity. *IEEE Trans. Plasma Sci.* **31**, 1192, Fig. 4 (2003)
- Peratt, A., Jones, M.: *IEEE Conference Record, IEEE International Conference on Plasma Science*, Saskatoon (1986)
- Peratt, A.L., Verschuur, G.L.: Plasma experiments in the laboratory and space. *IEEE Trans. Plasma Sci.* **28**, 2122 (2000)
- Scheuer, J.T., Schoenberg, K.F., Gerwin, R.A., Hoyt, R.P., Henins, I., Black, D.C., Mayo, R.M., Moses, Jr., R.W.: A magnetically-nozzled, quasi-steady, multimegawatt, coaxial plasma thruster. *IEEE Trans. Plasma Sci.* **22**, 1015 (1994)
- Schmelz, J.T., Reames, D.V., von Steiger, R., Basu, S.: Elements abundances in solar energetic particles. *Astrophys. J.* **755**, 33 (2012)
- Sherman, V.: *Astrophys. Space Sci.* **24**, 487 (1973)
- Verschuur, G.L.: Neutral hydrogen filaments at high galactic latitudes and the Bennett pinch. *Astrophys. Space Sci.* **227**, 187 (1995)
- Verschuur, G.L.: High-resolution observations and the physics of high-resolution Cloud A0. *Astrophys. J.* **766**, 113 (2013)
- Verschuur, G.L., Magnani, L.: On the nature of 21-cm emission profile, at high galactic latitudes: Implications for the warm neutral medium. *Astrophys. J.* **107**, 287 (1994)
- Verschuur, G.L., Peratt, A.L.: Galactic neutral hydrogen emission profile structure. *Astron. J.* **118**, 1252–1267 (1999)
- Verschuur, G.L., Schmelz, J.T.: A pervasive broad component in HI emission. *Astron. J.* **139**, 2410 (2010)

## Chapter 9

# Neutral Hydrogen Filaments and Dynamics of Galactic Bennett Pinches

### 9.1 Interstellar Filaments

The filamentary nature of the diffuse interstellar neutral hydrogen (HI) is apparent in the Atlas of Galactic Neutral Hydrogen maps, known as the Leiden-Dwingeloo or L-D survey of [Hartmann and Burton \(1997\)](#). This validates the hypothesis by [Carlqvist and Gahm \(1992\)](#) that the existence and stability of galactic filaments is dependent on large-scale cosmic currents.

[Verschuur \(1991a\)](#) has shown that morphological waves with wavelengths of order  $30^\circ$  and amplitude  $\sim 1/8\lambda$  exist in several HI filaments in a 540 square degrees of sky around  $l = 230^\circ$ ,  $b = +40^\circ$ . The extent of the longest filament is greater than  $72^\circ$ , the limit set by the boundaries of the area surveyed. The motion within the filaments, determined by analysis of velocities along their axes, suggests the presence of wave patterns with amplitude 5–6 km/s on an angular scale similar to that seen in the spatial wave-like structure projected on the sky.

In that area of sky, which was fully mapped, every HI cloud is found to be associated with a filament and usually found where the filaments show changes in the orientation of their axes, as if defining kinks in the filaments, [Verschuur \(1991b\)](#). This suggests that a cloud of diffuse interstellar HI, defined by a localized enhancement of HI emission in an area map, may often be a geometric illusion produced where a segment of filament twists into the line of sight, in concordance with that found in very high density plasma experiments and particle-in-cell simulations, [Peratt \(1992\)](#). The name ‘heteromac’ has been given to this geometry, see [Kukushkin and Rantsev-Kartinov \(1998, 1999, 2004\)](#).

Heteromacs, in space, are the coming together of adjacent field aligned currents known as Birkeland currents and their subsequent coiling into helices. Figure 9.1a, b are schematics showing current-carrying (Birkeland) filaments and their evolution to a heteromac. During intense current bursts that may last several centuries, they are visible by the white-light synchrotron light they emit, as predicted by the numerical modeling of the phenomenon. As the giga-amperages subside, the sharpness blurs, and they appear as a ‘cloud’ to the observer. Their occurrence and reoccurrence is

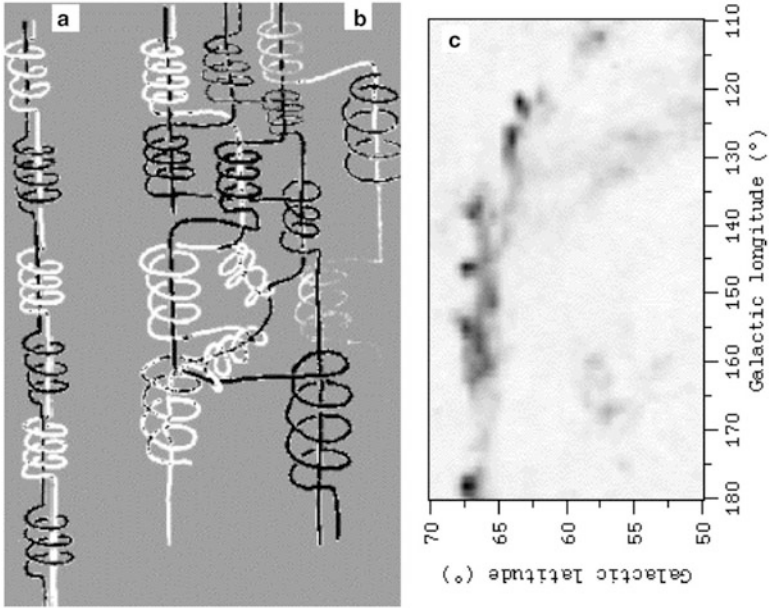


**Fig. 9.1** The schematic shows the internal structure of an intense-current (a) and the evolution of a typical networking of filaments (b). (Courtesy of V. A. Rantsev-Kartinov, National Research Center “Kurchatov Institute”, Moscow). (c) An inverted gray-scale image shows the HI brightness of a segment of an interstellar filament integrated between the velocity limits of 90 and 80 km/s. A loop of weak emission is also found between the two bright spots seen at latitude 66 arcdeg and longitudes 136 and 146 arcdeg

determined by the circuit parameters that determines the ‘sawtooth’ current profile found in the laboratory and in nature as described by [Alfvén \(1981\)](#). Figure 9.1c shows an inverted gray-scale image of the HI brightness of a segment of an interstellar filament integrated between the velocity limits of  $-90$  and  $-80$  km/s (with respect to the local standard of rest). This HI feature, found in the L-D Survey ([Hartmann and Burton 1997](#)), is a corkscrew-like segment of a filament that is here plotted in such a way as to highlight its nature. A loop of weak HI emission links the two bright spots referred to in the figure caption. The overall “corkscrew” shows remarkable similarities to the structures in Fig. 9.1a, b.

Figure 9.2 shows an example of an HI cloud that lies on a filament winding its way through position-velocity phase space. Each frame plots the distribution of the antenna temperature of the HI emission at the velocity indicated at the lower right of the frame (in km/s) using data obtained with a  $10 \hat{\tau}$  resolution by [Verschuur \(1974\)](#) and analyzed by [Verschuur \(1991b\)](#). The lower right frame shows a sketch of the derived filamentary patterns. The numbers in this frame indicate the velocity of the HI emission at various locations along the filament whose morphology is derived by reference to the HI structure in the other frames.



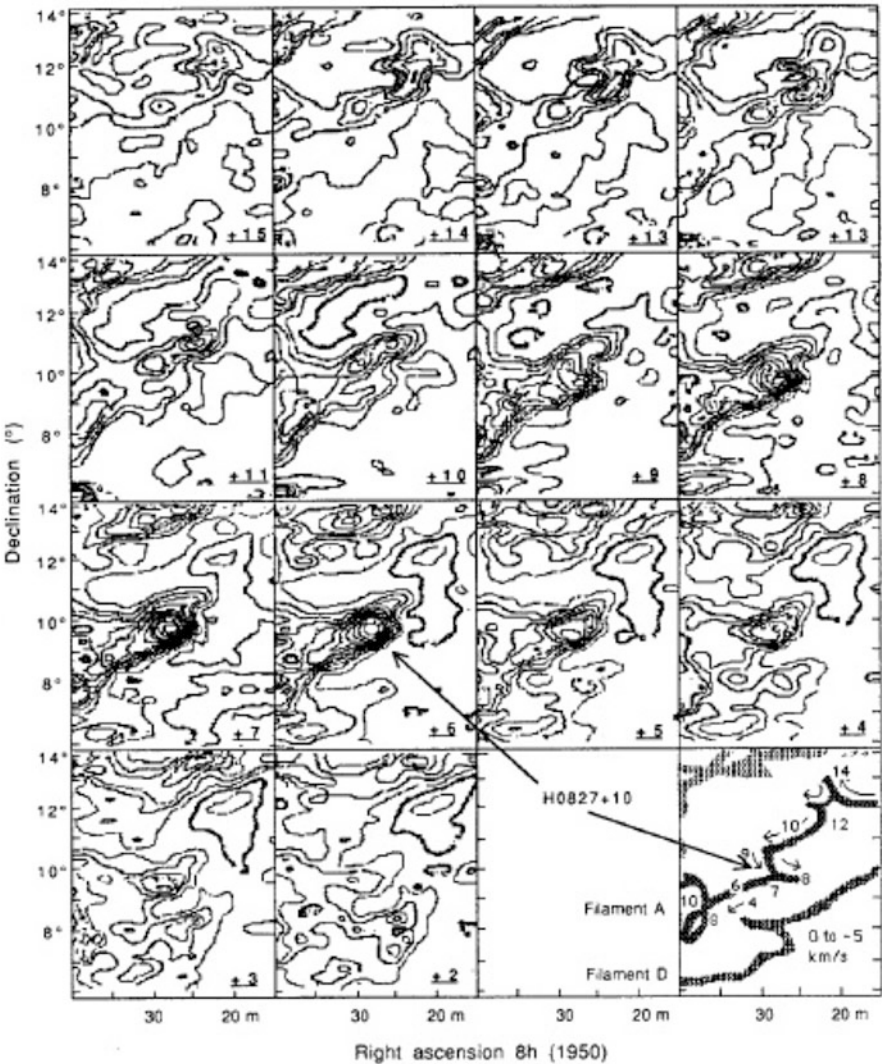


**Fig. 9.2** Neutral hydrogen maps at various velocities of a small area of the sky around the feature labelled H0827+10 (shown by the *arrows*) taken from an area survey. The lower-right frame is a schematic representation of several filaments that cross this field of view. The numbers indicate the velocity of the gas at various locations along Filament A. H0827+10 would traditionally be referred to as a cloud

The bright feature in the center of the various maps is an example of an HI cloud, this one labelled H0827+10. However it appears that H0827+10 may represent a direction in which the filament twists into the line-of-sight. Thus the emission brightness is enhanced in that direction.

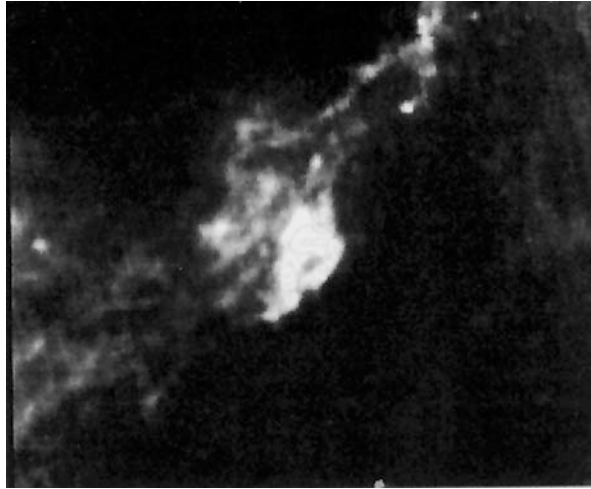


**Fig. 9.3** The  $100\mu$  flux from cool interstellar dust in the direction of the a region of enhanced emission called H0827+10, the bright feature at the center of this map. The presence of filaments, on this scale, are found where the brightest features correspond to filament overlap or where the filament twists into the line-of-sight (From [Verschuur \(1994\)](#))

If cool interstellar HI and dust are associated, one might obtain a better view of the filament geometry by examining the distribution of  $100\mu$  emission from the dust, derived from the IRAS survey of  $100\mu$  emission, which has a resolution of a few arc-seconds, considerably better than most radio telescopes used in the study of interstellar HI structure. Figure 9.3 shows the  $100\mu$  flux from cool interstellar dust in the direction of the EEF H0827+10 based on IRAS data, from [Verschuur \(1994\)](#). Emission from the dust associated with H0827+10 is the bright feature at the center of this map and the structure is seen to have a loop shape.

The Arecibo radio telescope was used to obtain high resolution  $4''$  maps of the HI emission from H0827+10 ([Verschuur 1994](#)). The analysis technique involved the Gaussian decomposition of hundreds of profiles in order to identify families of components. Area maps of each component were made and Fig. 9.4 shows the total HI column density for the most prominent Gaussian components for comparison with the dust data in Fig. 9.3.

Comparison of Figs. 9.3 and 9.4 shows a great deal of similarity, certainly within limits set by the resolution and data display techniques. Noteworthy is the fact that the HI map shows nearly as much detail as is seen in the  $100\mu$  data. Both contain enhanced filamentary structure and the original HI cloud may not be a physically bound, coherent entity at all, but rather follows the principles of a heteromac, where gravity or a magnetic field gathers the plasma into a small, spherically symmetric volume of space. It seems likely that the enhancement in brightness in the HI data in Fig. 9.4 is related mainly to line-of-sight geometrical effects while revealing little

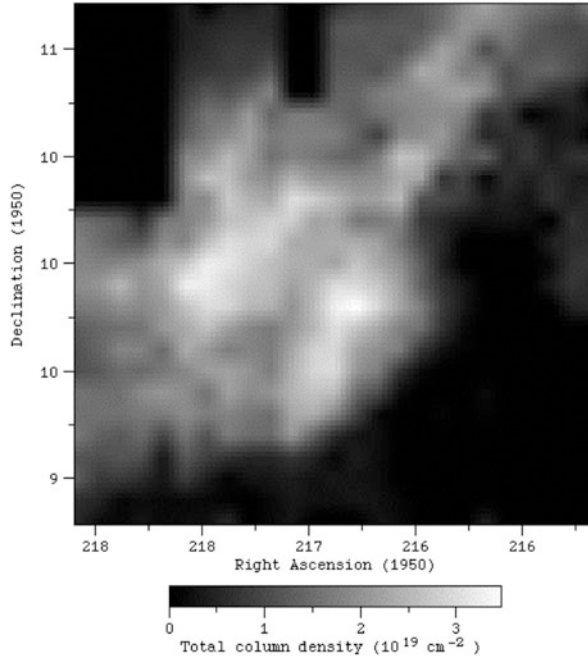


**Fig. 9.4** This figure shows the combined HI column density of cool gas (weakly ionized plasma) found in the brightest Gaussian components defining the emission profiles for H0827+10 (From [Verschuur \(1994\)](#))

about the possible physics involved in creating the structure. It should be noted that the structure seen in these maps is not two-dimensional but has an unknown depth component.

Ideally one would want to detect the signature of a magnetic field in twisted segment of an interstellar filament. In principle, mapping the magnetic field in the direction of an HI cloud using the 21-cm Zeeman effect should provide important evidence on the nature of a twisted field structure. This type of experiment is sensitive to the line-of-sight component of the magnetic field and if a cloud is an illusion produced where a segment of filament twists into the line-of-sight, the magnetic field should appear stronger in the feature than toward its surroundings in the filament where it would be more normal to the line-of-sight. While [Verschuur \(1969\)](#) detected the Zeeman effect signature in several HI clouds seen in absorption, there are no reliable detections of magnetic fields in the  $\mu\text{G}$  range in diffuse HI emission anywhere in the sky ([Verschuur 1995a,b](#)). This does not mean that they such fields do not exist; only that the technology to detect them does not exist yet.

For H0827+10 the Zeeman effect observations did give a value for the limit to the line-of-sight magnetic field strength of  $-0.7 \pm 1.0 \mu\text{G}$  (one sigma error) toward the brightest feature in Fig. 9.4. The average magnetic field for five directions sampled in H0827+10 is  $-0.1 \pm 0.6 \mu\text{G}$ . This implies an upper limit of  $\sim 2 \mu\text{G}$ . Upper limits

of  $1.4 \mu\text{G}$  were also set for two other EEFs, while a third gave  $0.6 \mu$ . Small-scale structure in the magnetic field morphology produced by field reversals within the beamwidth of the telescope would not be detected in the Zeeman effect experiment and could especially hide toroidal magnetic fields with small angular scales.

## 9.2 Interstellar Filaments as Tracers of Current Flow

In the context of plasma physics, nearly neutral HI acts as a tracer of the motion and structure of plasma in interstellar space. Figure 9.5 shows a dramatic HI filament that winds its way through a region of enhanced HI emission based on data obtained with the  $9''$  resolution of the Green Bank Telescope, [Verschuur \(2013b\)](#). In the direction of the bright emission in the map center, the filament appears severely twisted. Also, there is evidence for a clear wave-like pattern in the center velocity along the overall length of the filament. Superimposed on the filamentary feature are several distinct clouds that do not always lie on the filament itself. In order to investigate the stability of the filament, the hypothesis of [Carlqvist \(1988\)](#) was considered.

[Carlqvist \(1988\)](#) and [Carlqvist and Gahm \(1992\)](#) demonstrated that electric currents may generate and maintain interstellar filamentary structure. Key to their discussion is the theory of a generalized Bennett pinch for a cylindrically symmetric plasma filament.

A helical magnetic field with a toroidal component  $B_\phi$  and an axial component  $B_z$  exists in a filament with radius  $a$  inside which a current  $I(a)$  flows. The linear density in the filament,  $N(a)$ , is defined as  $\pi a^2 n$ , where  $n$  is the plasma volume density, which we will take to be the same as the neutral gas volume density,  $n_H$ . The mean mass of the plasma particles is  $m$ , which includes neutrals, electrons, ions and a fraction of helium. For these calculations it is taken to be  $2 \times 10^{-24}$  gm. The neutral gas is assumed to be coupled to the ionized component ([Kahn and Dyson 1964](#)).

From the generalized Bennett (Eq. (2.23)) relationship or the Carlqvist Relation (Eq. (2.52)), we have for a filament in rotation,

$$\frac{\mu_0}{8\pi} I^2(a) + \frac{1}{2} G m^2 N^2(a) = \Delta W_k(a) + \Delta W_{Bz} + \Delta W_{rot}(a) \quad (9.1)$$

The first two terms on the left of Eq. (9.1) represent the pinching forces due to the current and gravity. A current  $I(a)$  in the filament generates a toroidal magnetic field  $B_\phi$  related

$$B_\phi(a) = \frac{\mu_0 I(a)}{2\pi a} \quad (9.2)$$

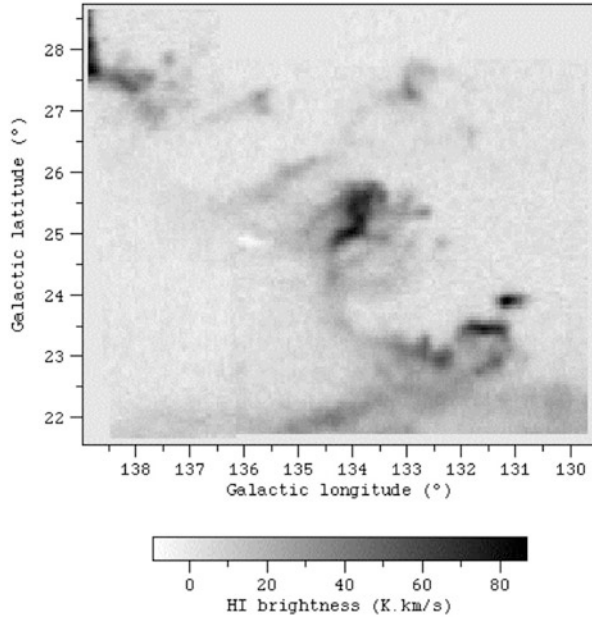


**Fig. 9.5** The twisted filamentary structure of a interstellar HI features known as high-velocity cloud A0 at the center and lower right of the image, which shows the HI brightness integrated between velocity limits of  $-240$  and  $-120$  km/s, from [Verschuur \(2013b\)](#) (The data were obtained with the  $9''$  resolution of the Robert Byrd Green Bank Telescope of the National Radio Astronomy Observatory)

The terms on the right of Eq. (10.1) represent expansive forces, except in the case where the external gas pressure overcomes internal gas pressure in the filament. This follows from the fact that the first term on the right represents the excess kinetic energy in the filament given by

$$\Delta W_k(a) = 2\pi r p_k dr - \pi a^2 p_k(a) \quad (9.3)$$

where

$$p_k(a) = n_W k T_W \quad (9.4)$$

is the kinetic pressure in the warm (here taken to be neutral) gas just outside the filament, and

$$p_k = n_H k T_H \quad (9.5)$$

is the gas pressure inside the filament, whose density and temperature are derived from the HI data.

Depending on the filament distance chosen (usually an unknown parameter), the external gas pressure can be of the order of, or greater than, the internal gas pressure. The filament gas density can be derived from the HI observations if the distance to the filament is known. There is always a critical value for the (unknown) filament distance beyond which the external gas pressure is calculated to be greater than the

internal pressure, so that the relative importance of the Bennett pinch in stabilizing the filament appears to be reduced. It is more than coincidental that the critical distance is usually of the order judged to be reasonable for the filaments, and suggests a new way to obtain this distance.

The excess rotational energy due to angular velocity  $\omega$  is given by

$$W_{rot}(a) = \int_0^a 2\pi r \frac{m\omega^2 r^2}{2} dr \quad (9.6)$$

Interstellar HI filaments are barely resolved in most current observations so that rotation about their axes, which would play an important role in defining emission profile line widths, are difficult to determine unambiguously.

The excess magnetic energy term in Eq. (10.1) Is given by

$$W_{rot}(a) = \int_0^a 2\pi r \frac{B_z^2}{2\mu_0} dr / \pi a^2 B_z^2(a^2) 2\mu_0 \quad (9.7)$$

where  $B_z(a)$  is the axial magnetic field just outside the filament.

Using these equations, [Verschuur \(1995c\)](#) and in a more developed form ([Verschuur 2013b](#)) derived values for the current that would generate a magnetic field necessary to confine a number of interstellar filaments and those data are compared to the results of [Carlqvist and Gahm \(1992\)](#) in Table 9.1. Column 1 lists the filament property for which parameters are derived by [Verschuur \(1995c\)](#) in Column 2, in Column 3 for a filament in Eridanus mapped by [Verschuur et al. \(1992\)](#) and quoted in [Verschuur \(1995c\)](#), and in Column 4 for filament A from [Verschuur \(1995c\)](#). In Column 5 the average values for 9 cuts across the filament in high-velocity cloud A0 mapped by [Verschuur \(2013b\)](#) is listed together with, in Column 6, a single estimate for a segment of filament shaped like an arc that exhibits a large rotation about its axis, also from [Verschuur \(2013b\)](#). Column 7 lists the values for molecular cloud L205 mapped by [Carlqvist and Gahm \(1992\)](#). (In each of the references the authors argue for the choice of certain parameters, such as distance. In addition, for the filament encompassing high-velocity cloud A0, Fig. 9.5, the axial magnetic field strength had to be taken into consideration, and this is included in the calculations summarized in Columns 5 & 6 in Table 9.1. The axial field strength was derived from equating the observed HI emission profile line width over and above that due to thermal motion, with an Alfvén velocity that acts to broaden the emission profiles to an observed value of order 22 km/s. The distribution of component line widths shows no evidence for the CIV signature of helium of Band II elements (see Chap. 8) but those corresponding to Band II are prominent.

**Table 9.1** Bennett pinch in filaments

Summary of parameters that produce equality in the Carlqvist Relation Filament a in the H0297 + 10 region		
Parameter	Value	Comments
<b>Observed</b>		
HI Column density	$0.85 \times 10^{20}$	From HI maps at sides of filament
Angular width	$0.^{\circ}2$	Data from two sides of filament
Angular rotation	$1.63 \text{ km s}^{-1}$	From HI data
Temperature warm, neutral medium	3,000 K	Verschuur and Magnani (1994)
Density of warm medium	$0.3 \text{ cm}^{-1}$	For nonplanar directions <sup>a</sup>
<b>Adjustable</b>		
Aspect ratio	2	Takes into account geometry (los through center = $2 \times$ los through sides of filament)
Distance	100 pc	Assumed (see text)
HI gas temperature	30 K	Set equal to dust temperature
Axial magnetic field in filament	$1.5 \mu \text{ G}$	From pulsar rotation measures and Zeeman effect data (Verschuur 1995c)
Axial magnetic field outside filament	$1.5 \mu \text{ G}$	Same reference. This is the strength of the general interstellar magnetic field
<b>Derived</b>		
Filament $n_H$	$40.4 \text{ cm}^{-3}$	From HI data and distance
Toroidal magnetic field	$5.3 \mu \text{ G}$	Produces equilibrium in filament
Required current	$1.4 \times 10^{13} \text{ A}$	From Eq. (1)

<sup>a</sup> Reynolds (1983) planar data on the warm ionized medium (8,000 K,  $0.1 \text{ cm}^{-3}$ ) produces virtually the same pressure

For the examples of HI filaments summarized in Table 9.1 the authors argued that gravity plays no role in controlling equilibrium. Whether or not external pressure or magnetic fields play a role depends on the distance chosen in evaluating the equations, but for the distances given in Table 9.1 neither plays a role.

The data in Tables 9.1 show good agreement as regards the values of the key parameters; the axial current, from 1 to  $10 \times 10^{13} \text{ A}$ , and the toroidal magnetic field strength, from 5 to  $8 \mu \text{G}$  for the HI filaments. The analysis suggests confirmation of the model proposed by Carlqvist (1988) and Carlqvist and Gahm (1992), that the physics of the generalized Bennett pinch applies to gaseous interstellar filaments. This has far-reaching implications for the study of the properties of interstellar matter. The role of large-scale currents may be very important in defining interstellar structure.

Diffuse interstellar HI is clearly highly filamentary. In low-resolution surveys the pervasiveness of filaments may often be overlooked by labeling localized enhancements in HI brightness as clouds defined as nearly spherically symmetric, bound entities, rather than their being due to line-of-sight enhancements where filaments twist into the line-of-sight, or they may be a manifestation of heteromacs in interstellar astrophysics. This subject is ripe for further exploration.

## References

- Alfvén, H.: Cosmic Plasma, vol. 82, p. 34. D. Reidel, Dordrecht (1981)
- Carlqvist, P.: Cosmic electric currents and the generalized Bennett relation. *Astrophys. Space Sci.* **144**, 73 (1988)
- Carlqvist, P., Gahm, F.: Manifestations of electric currents in interstellar clouds. *IEEE Trans. Plasma Sci.* **20**, 887 (1992)
- Hartmann, D., Burton, W.B.: Atlas of Galactic Neutral Hydrogen. Cambridge University Press, Cambridge (1997)
- Kahn, F.D., Dyson, J.E.: The energy balance and dynamics of the interstellar medium. *Annu. Rev. Astron. Astrophys.* **3**, 47 (1964)
- Kalberla, P.M.W., Burton, W.B., Hartmann, D., Arnal, E.M., Bajaja, E., Morras, R., Pöppel, W.G.L.: The Leiden/Argentine/Bonn (LAB) survey of galactic HI. Final data release of the combined LDS and IAR surveys with improved stray-radiation corrections. *Astron. Astrophys.* **440**, 775 (2005)
- Kukushkin, A.B., Rantsev-Kartinov, V.A.: Formation of a percolating network in dense z-pinch plasmas. *Laser Part. Beams* **16**, 1387 (1998)
- Kukushkin, A.B., Rantsev-Kartinov, V.A.: Self-similarity of plasma networking in a broad range of length scales; from laboratory to cosmic plasmas. *Rev. Sci. Instrum.* **70**, 1387 (1999)
- Kukushkin, A.B., Rantsev-Kartinov, V.A.: Formation of a percolating network in dense z-pinch plasmas. *Laser Part. Beams* **16**, 1387 (2004)
- Peratt, A.L.: Physics of the Plasma Universe. Springer, New York (1992)
- Verschuur, G.L.: Measurements of magnetic fields in clouds of neutral hydrogen. *Astrophys. J.* **156**, 861 (1969)
- Verschuur, G.L.: Studies of neutral hydrogen cloud structure. *Astrophys. J. Supplement* **27**, 65 (1974)
- Verschuur, G.L.: Neutral hydrogen filaments at high galactic latitudes. 2, existence of large-scale waves in interstellar space. *Astrophys. Space Sci.* **185**, 137 (1991a)
- Verschuur, G.L.: Neutral hydrogen filaments at high galactic latitudes. 3. The nature of enhanced emission features. *Astrophys. Space Sci.* **185**, 305 (1991b)
- Verschuur, G.L.: High-resolution images of interstellar cirrus ‘Clouds’. In: Cutri, R.M., Latter, W.B. (eds.) First Symposium on the Infrared Cirrus and Diffuse Interstellar Clouds. vol. 58, pp. 184. Astronomical Society of the Pacific, San Francisco (1994)
- Verschuur, G.L.: Zeeman effect observations of HI emission profiles. I. magnetic field limits for three regions based on observations corrected for polarized beam structure. *Astrophys. J.* **451**, 624 (1995a)
- Verschuur, G.L.: Zeeman effect observations of HI emission profiles. 2, results of an attempt to confirm previous claims of field detections. *Astrophys. J.* **451**, 645 (1995b)
- Verschuur, G.L.: Interstellar neutral hydrogen filaments at high galactic latitudes and the Bennett pinch. *Astrophys. Space Sci.* **227**, 187 (1995c)
- Verschuur, G.L.: Interacting galactic neutral hydrogen filaments and associated high-frequency continuum emission. *Astrophys. J.* (2013a, in Press)



- Verschuur, G.L.: High-resolution observations and the physics of high-velocity cloud A0. *Astrophys. J.* **766**, 113 (2013b)
- Verschuur, G.L., Rickard, L.J., Verter, F., Pound, M.W., Leisawitz, D.: The separation between gas and dust filaments at the edge of the expanding shell in eridanus. *Astrophys. J.* **390**, 514 (1992)

# Chapter 10

## Particle-in-Cell Simulation of Cosmic Plasma

### 10.1 “In-Situ” Observation of Cosmic Plasmas via Computer Simulation

While it is thinkable that our ability to make in situ measurements can perhaps be extended to the nearest stars, most of the universe beyond a few parsecs will be beyond the reach of our spacecraft forever.

From one’s unaided view of the clear night sky, it is tantalizing to believe that the physics of the universe can be unfolded from the observable stars, which may be up to kiloparsecs away, or from the fuzzy “nebula” such as the galaxy M31, nearly a megaparsec away. Our experience in unfolding energetic events in our own solar system suggests otherwise.

The inability to make in situ observations places a severe constraint on our ability to understand the universe, even when the full electromagnetic spectrum is available to us. As outlined in Chap. 1, only after satellites monitored our near-earth environment and spacecraft discovered and probed the magnetospheres of the planets, could we begin to get a true picture of the highly-energetic processes occurring everywhere in the solar system. These processes included large-scale magnetic-field-aligned currents and electric fields and their role in the transport of energy over large distances. The magnetospheres of the planets are invisible in the visual octave (400–800 nm) and from earth cannot even be positively identified in the X ray and gamma ray regions, which cover 10 times as many octaves and have more than 1,000 times the bandwidth as the visual octave. Only in the low frequency radio region is there a hint of the presence of quasi-static electric fields which accelerate charged particles in the magnetospheres of the planets.

As the properties of plasma immediately beyond the range of spacecraft are thought not to change, it must be expected that plasma sources of energy and the transport of that energy via field-aligned currents exist at even larger scales than that found in the solar system. How then are we to identify these mechanisms in the distant universe?

The advent of particle-in-cell (PIC) simulation of cosmic plasmas on large computer systems ushered in an era whereby in situ observation in distant or inaccessible plasma regions is possible. While the first simulations were simple, with many physics issues limited by constraints in computer speed and memory, it is now possible to study the full three-dimensional, fully-electromagnetic evolution of magnetized plasma over a very large range of sizes. In addition, PIC simulations have matured enough to contain Monte Carlo collisional scattering and energy loss treatments, conductor surfaces, dielectric regions, space-charge-limited emission from surfaces and regions, and electromagnetic wave launchers. Since a simulation involves the motion of charge or mass particles according to electromagnetic or gravitational forces, all in situ information is available to the simulationist.

If the simulation correctly models the cosmic plasma object under study, replication of observations over the entire electromagnetic spectrum should be expected, to the extent that the model contains sufficient temporal and spatial resolution.

## 10.2 The History of Electromagnetic Particle-in-Cell Simulation

After the early success of astronomers in rigorously solving the problem of two gravitationally interacting bodies it became quite a disappointment that the notorious “*probleme de trois corps*” could never be solved by elegant, nineteenth century mathematics.<sup>1</sup> Computations were practical (and respectable) only for the evaluation of a series. Finite difference calculus made its way very slowly during the first few decades of this century. Störmer struggled hard calculating orbits of charged particles in the earth’s magnetic field (not even a self-consistent field!) (Størmer 1955).

Strangely, it was a change in physics which brought the next advance: quantum theory changed particle dynamics from ordinary differential equations to partial differential equations, thus putting field and particle dynamics on the same footing. The combination of Schrodinger’s equation for electron density with Poisson’s equation for the electric potential results in coupled nonlinear partial differential equations. As a first step, taken in the 1920s, one eliminated the angle variables and reduced the problem to two nonlinearly coupled ordinary differential equations in the radial variable.

This meant that an efficient integrating machine or procedure was called for and D. R. Hartree built his first “differential analyzer” from an erector set. It used a continuously variable gear and with this device Hartree could solve mechanically self-consistent problems dealing with atomic wave functions and atomic energy levels.

---

<sup>1</sup> The problem of two gravitationally interacting masses was solved when Kepler proved that relative to the center-of-mass the orbits are ellipses or hyperbolae (i.e., “conic sections”). This is exact—and elegant! But this elegance is lost when a third body is added. Only approximate methods exist, all rather ugly. For centuries mathematicians have sought to find an elegant solution to the problem of three gravitationally interacting bodies—without success.

The “magnetron,” a now very familiar microwave generator, had been invented by Boot, Randall, and Sayers in Birmingham. It was of paramount importance to Britain’s defense: its high frequencies could not be jammed. The magnetron (Sect. 1.7.3) is a fine example of “swords into plow-shares.” It is replacing man’s tradition of many millennia to cook food with incandescent heat.

Initially it was something of a mystery exactly how and why the magnetron worked and the scientific staff at the British Admiralty realized that in order to unravel the workings of the magnetron one would have to solve a self-consistent field problem, namely, that of motion of electrons in the electric field which the electrons themselves produce, in addition to the externally applied electric and magnetic fields.

Hartree was given the problem and he initiated classical particle simulation by integrating, numerically, the orbits of a number of particles in a field which was either revised in accordance with the instantaneous charge density at each step, or only occasionally, in the hope of reaching a steady field by iteration. Both one- and two-dimensional simulations were performed by Hartree and his team: Phyllis Nicolson, Oscar Buneman, and David Copley (Nash 1991). “Parallel-processing” was employed by sharing out the several hundred orbits between the three team members.

Operating as human central processing units (CPUs), the team made a number of discoveries including the Crank-Nicolson iteration procedure and the Buneman-Hartree threshold criterion for magnetron operation. The one-dimensional simulations yielded a steady-state but could not account for magnetron operation, or for the observed currents which flow across the magnetic barrier. Only when the technique was taken to two-dimensions did Buneman find an instability, not unlike the Kelvin-Helmholtz in fluid flow. In the transition from one- to two-dimensional simulation, iterative methods were abandoned (in 1944) and Hartree changed to the direct Fourier method (Sect. 10.6.1). It turned out that only a few harmonics were needed for simulation; the fast-Fourier-transform (FFT) was not yet known. Success came in the numerical observation of the four- and six-wheel spokes of electrons that rotate in the magnetron exciting the high frequencies in the resonators.

The numerical simulation by particles of plasma physics began in the 1950s by Dawson at Princeton and Buneman at Stanford, where various plasma phenomena were identified and studied. It should be mentioned that, in the beginning, it was not at all apparent that the technique developed to study pure electron beam propagation in microwave devices could be applied to the plasma state of matter. Unlike the cold electron beam with charges of all one sign, plasmas often consist of thermal distributions with essentially equal density of charges of opposite sign and greatly different masses. In studying cold electron beams, a few dozen particles sufficed to reproduce the essence of the experiment. However, in laboratory plasmas one has scale lengths greater than the Debye length ( $L \gg \lambda_D$ ) and the number of particles in a Debye cube  $N_D \equiv n\lambda_D^3$  is much greater than one ( $N_D \gg 1$ ). For example, the earth’s ionosphere has  $N_D \approx 10^4$  and the literal simulation of it over its scale length appears unfeasible. However the general character of plasmas can often be found

by studying the *collective behavior of collisionless plasmas at wavelengths longer than the Debye length*,  $\lambda \geq \lambda_D$ . It was found that another characterization of such a plasma is that (1) the thermal kinetic energy is much greater than the microscopic potential energy, and (2) the ratio of collision to plasma frequencies is much less than one. Both requirements can be met with rather low values of  $N_D$  (Birdsall and Langdon 1985). Conditions 1 and 2 may be met for finite sized particles called clouds. Clouds occur naturally in simulations which use a spatial grid for interpolation, as well as in simulations which employ spectral methods where the particle profile (usually gaussian) is specified in  $\mathbf{k}$  space.

The term “particle-in-cell” derives from Frank Harlow and his group’s work at Los Alamos in the 1950s in investigating the fluid nature of matter at high densities and extreme temperatures. Modern descriptions of the particle-in-cell technique as related to plasma physics are found in the two texts *Computer Simulation Using Particles* (Hockney and Eastwood 1981) and *Plasma Physics via Computer Simulation* (Birdsall and Langdon 1985).

### 10.3 The Laws of Plasma Physics

The challenge of plasma physics is this: We know with certainty the precise and simple laws of nature that govern the particles and fields in plasmas, yet we are unable to deduce from them how a nontrivial plasma configuration will evolve, nor can we “explain” many of the complicated plasma phenomena which are observed in the laboratory.

Mathematical manipulation of the laws, and intuitive additional assumptions or approximations, have been exploited with only partial success, and often the computer has had to be called upon to “finish the job” in such attempts. The message to be presented here is that one might try to let the computer take us all the way from the basic laws to their macroscopic manifestations. Rather than maximizing intuition and shortcuts which might help the computer get there quicker, let us program the basic laws in their rawest, simplest form and leave all the synthesizing to the computer. Given a big enough computer, this philosophy would justify itself by the demonstration that the computer could not only reproduce all the plasma phenomena which have been observed but also all known theoretical results and, of course, those obtained from more modest simulations on more primitive computers.

In practice, it would be foolish to relinquish theoretical tools, intuition, insight, and past experience entirely in favor of “brute force” computing. Even given a computer that could handle trillions of particles with a resolution of one in a thousand for each dimension at reasonable speed, there would still be some “ $\epsilon$ ” of imperfection to be checked for, and the pressure to get more results per computing dollar would motivate physicists back toward a compromise between traditional theory and highest-power computing.

What is suggested here is a start from the far end: suppose we had that ultracomputer, then how would we do physics with it? And since we haven't got that ultracomputer, what can we do as the next best approximation to that ideal?

We begin our approach by stating the laws of plasma physics in more or less the form which it has been found convenient to program: the equation of motion for the particles with the Lorentz force Eq. (1.5), and the Maxwell-Hertz-Heaviside laws for the electric and magnetic fields Eqs. (1.1)–(1.4).

## 10.4 Multidimensional Particle-in-Cell Simulation

### 10.4.1 Sampling Constraints in Multidimensional Particle Codes

The particle-in-cell technique for the analysis of complex phenomena in science has evolved from 1D through  $1\frac{1}{2}$ D,  $1\frac{2}{3}$ D, 2D,  $2\frac{1}{2}$ D, to 3D particle simulations. While at first one has to face certain limitations of an analytic nature, ultimately the limits are set by data management problems the resolution of which depends critically on the available hardware (Karin et al. 1987).

A trivial reason for the increasing difficulty of higher dimensional particle simulations is their demand for substantially greater particle numbers. With each added dimension the number of sampling particles has to be multiplied by a certain factor.

This also applies to “half-dimensions.” It is customary to denote the inclusion of extra velocity components by referring to them as “half-dimensions.” Typically, a pure 1D simulation simulates the plasma as rigid sheet particles, all parallel to the  $y-z$  plane, say, and moving in the  $x$  direction. It ignores  $y$  and  $z$  motions of the planes. A  $1\frac{1}{2}$ D simulation keeps a record of possible  $y$  motions, uniform within each plane. Then the  $x$ -ward Lorentz force in the presence of a  $z$ -directed magnetic field can be taken into account, as well as the  $y$ -wards Lorentz force due to  $x$  motions. In a  $1\frac{2}{3}$ D simulation,  $dz/dt$  would be recorded as well. In a  $2\frac{1}{2}$ D simulation,  $x, y, dx/dt$ , and  $dz/dt$  are tracked (but not  $z$ ); the particles are rigid straight rods whose motion along their axis is taken into account. One-and-a-half dimensional and  $1\frac{2}{3}$ D simulations have recently found application in space plasma work, namely for simulating the critical ionization phenomenon.

It is reassuring that relatively few samples can often give very good statistics. In many applications the velocity distributions stay close to maxwellian and a modest factor (typically four) in the sample number may suffice to deal with an added half-dimension. One exploits the favorable feature of statistics when initializing thermal velocity distributions: each velocity component is made up as the sum of four random numbers (each uniformly random in a certain interval). The resulting distribution (the “four dice curve,” or cubic spline) is almost indistinguishable from the Gaussian.

However, when incrementing by a full dimension, sampling requirements jump dramatically. It is easily checked that the statistical potential energy fluctuations in

a granular plasma compete with thermal energies when the particles are spaced on the order of a Debye length apart. Such a plasma would be essentially collision dominated. One is mostly interested in collective effects, since fluid codes are adequate for collision-dominated phenomena. Obviously, one needs several particles per Debye length; again, a modest number suffices. Now, most of the interesting phenomena to be resolved by simulation are on the scale of many Debye lengths (hundreds or thousands). Therefore, the addition of each full dimension calls for an increase of the number of particles by, typically, two orders of magnitude. In 1990 a 1D (electrostatic) simulation could barely be squeezed onto a personal computer, a 2D simulation called for a minicomputer or workstation, and a 3D simulation needed a supercomputer (Boris et al. 1970; Cashwell et al. 1959).<sup>2</sup> For comparison to 2012 computers, see Fig. 10.1.

### 10.4.2 Discretization in Time and Space

One-dimensional,  $1\frac{1}{2}$ D, and  $1\frac{2}{2}$ D simulations can be done without discretizing in space. The electrical interaction of sheets is independent of distance and one only needs to order the sheets to calculate their accelerations. Even if the sheets are of finite thickness or if they are “soft” (i.e., they have a smooth density profile across), only a few operations per sheet are needed to move them one time step. This is an effort of order  $N$  where  $N$  is the number of sheets.

However, in all simulations, time must be discretized. By studying the simulation of a simple 1D problem, namely, electrostatic oscillations in a cold plasma, and by Fourier transforming one’s numerical procedure in time, one finds that while a time step  $\delta t = \omega_p^{-1}$  yields the plasma frequency to 5 % accuracy, for  $\delta t > 2\omega_p^{-1}$  one runs into an instability.

To get over this severe limitation of the speed of simulation in cases where the phenomena of interest are much slower than electrostatic oscillations (typically ion responses), one can either use implicit methods, or one can make one’s ions lighter than real ions. Much has been learned from simulations with ion-electron mass ratios as low as 16:1.

The big analytical problems in simulation arise when one advances to two dimensions. Interactions between rods of charge depend on distance, and the many remote rods are as important as the few near ones. For  $N$  rods, one has to calculate  $N^2$  interactions and  $N$  itself might be typically two orders of magnitude larger than for a 1D simulation.

In order to get back to an effort of order  $N$  per step in the particle advance, one tabulates the field over a spatial grid and calculates the self-consistent field from a grid record of the charge and current-densities that each particle contributes.

---

<sup>2</sup> The approximate relationship of supercomputer performance and performance of those in other categories can be shown proportionately. If the performance of contemporary supercomputers is assigned a value of 100, the values in proportion to supercomputers are: minicomputers 0.1–5, workstation 0.1–1.0, and personal computers 0.001–0.1.

The permissible coarseness of the grid mesh becomes a critical issue and the problem of integrating the finite difference version (now in both space and time) of the field equation is far from trivial. Fortunately, both these subjects have been advanced to a state of relative completion and are exhaustively covered in two texts *Computer Simulation Using Particles* (Hockney and Eastwood 1981) and *Plasma Physics via Computer Simulation* (Birdsall and Langdon 1985).

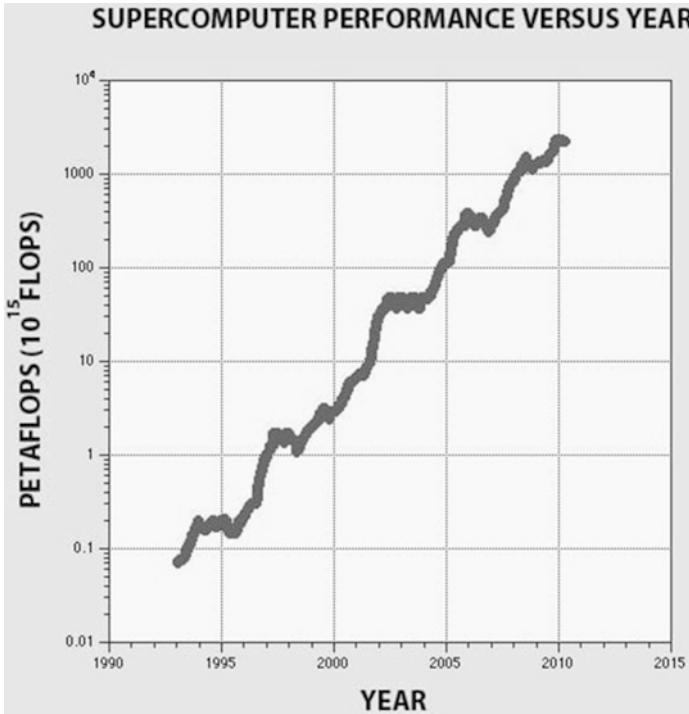


**Fig. 10.1** Supercomputer performance, petaflops versus year, 1993–2012

Very briefly and broadly, one can state that the grid should be fine enough to resolve a Debye length, and that smoothing or filtering of high spatial frequencies should be practiced in order to minimize “aliasing.” This is the stroboscopic phenomenon of high frequencies parading as low frequencies (long wavelengths). Many physical instabilities set in preferentially at long wavelengths and can thus be excited numerically through aliasing. Grid effects can often be studied and checked in 1D where grids are optional. Smoothing can be achieved by particle shaping (i.e., spreading point particles into soft balls with a smooth bell-shaped internal density profile). Likewise, splines and finite-element techniques help.

Regarding the field update from the charge-current record, fast noniterative methods for solving Poisson’s equation over an  $L$ -by- $M$  mesh have been developed. These include cyclic reduction in rows and columns, or Fourier transforming in one



of the two dimensions (say, that of  $M$ ). This is an effort to the order  $LM\log_2 M$ . Two-dimensional simulations go back historically to Hartree who initiated the simulation of the pure electron plasma which circulates in the magnetron. Hartree; also pioneered the time-centered update of the particles from Lorentz's equation (1.5)

$$\frac{dv}{dt} \pm \frac{eB}{m} \times v = \pm \frac{eE}{m} \quad (10.1)$$

using  $(v^{new} + v^{old})/2$  in the second (Lorentz) term and solving the linear equation for  $v^{new}$  explicitly. No limitation of  $\omega_b \delta t = (eB/M) \delta t$  arises from this method except that for large values of  $\omega_b \delta t$  the phases of the gyromotion are misrepresented. For small  $\omega_b \delta t$  one gets the same results as with cycloid fitting (Sect. 8.5), i.e., joining solutions of the type

$$v^\perp = E \times B/B^2 + \text{gyration at frequency } \omega_b \quad (10.2)$$

for the components of the velocity transverse to  $B$ . As regards this particle update, there is no significant increase in effort when advancing from  $1\frac{1}{2}$  to 2D and 3D.

A further time-step limitation is encountered when one wants to integrate the full electromagnetic equations over the grid. Because the Maxwell-Hertz-Heaviside equations (not including Poissons's) are hyperbolic (i.e., they contain a natural  $\partial/\partial t$  or "update" term), they can be solved in an effort which is of the order of magnitude of the number of grid points,  $LM$  in the 2D example discussed earlier. Essentially, one solves the wave equation (B.1). However, this process becomes unstable unless one observes the Courant speed limit  $\delta t < \delta x/c$  in 1D,  $\delta t < \delta x/c\sqrt{2}$  in 2D, and  $\delta t < \delta x/c\sqrt{3}$  in 3D for square and cubic meshes of side  $\delta x$ . In many applications, scales chosen from other considerations are such that  $c$  is a large number and this restriction of  $\delta t$  results in a severe slowdown.

### 10.4.3 Spectral Methods and Interpolation

The Courant condition can be overcome by doing the entire field update in the transform domain. The Maxwell-Hertz-Heaviside laws for the electric and magnetic fields Eqs. (1.1)–(1.4) can be conveniently combined into one equation for the complex field vector  $F = D + iH/c$ . When Fourier transforming, this equation becomes

$$\frac{dF}{dt} - ck \times F = -j \quad (10.3)$$

for the spatial harmonic which goes like  $(\exp ik \cdot r)$ . This field equation is surprisingly similar to that for the particle velocities Eq. (10.1) and has the corresponding solution for the transverse part of  $F$ :

$$F^\perp = j \times k/k^2 (\text{magnetostatic field}) + \text{circularly polarized wave rotating at angular frequency } ck \quad (10.4)$$

The time intervals at which one joins successive solutions of this form are dictated by the rate at which  $j$  changes, not by the magnitude of  $ck$ .<sup>3</sup>

To Eq. (10.1) we should add an initial condition, namely, Poisson's

$$ik \cdot F_k = \rho_k \quad (10.5)$$

Fourier transforming all fieldlike quantities has many advantages. For instance, the longitudinal part of  $F$  (which is just  $D$ ) can be obtained from Poisson's equation as  $k\rho/k^2$ . Of course, transforming in two dimensions rather than only one (as in the fastest Poisson solvers) makes for an effort of the order  $LM(\log_2 L + \log_2 M)$ . On the other hand, the ready availability of well-programmed FFTs and the additional benefits of spectral methods make up for this increase in effort.

In the transform domain one can perform the filtering, the particle shaping, an optimization for the spline fitting process, and the truncation of the interaction to be discussed in the section on boundary conditions. One does not have to use any spatial finite difference calculus for the field equations. However, a grid is still necessary since we have only *discrete* numerical Fourier transforms between  $r$  space and  $k$  space.

This leaves the problem of interpolation in the mesh. By using high-order interpolation, one can greatly reduce aliasing and improve accuracy. Quadratic and cubic splines have been used, but this soon becomes expensive.<sup>4</sup> Linear interpolation is most commonly used. Interpolation is also needed when the particles contribute their charge and current to the  $r, j$  arrays.

Linear interpolation is then, in 2D, equivalent to "area weighting." For 3D, we have cut down the data look-up (or deposit) effort for linear interpolation by using a tetrahedral mesh. Each particle references only the four nearest mesh-point data. The tetrahedra result from drawing the space diagonals into a cubic mesh and introducing cubic center data. Interpolation of currents must be done twice in each step of each practice, once at its old position and once at its new position, since the current is that due to the movement between the two.

## 10.5 Techniques for Solution

The crucial equations, (10.1) and (10.3), are in the "update" form, ideally suited to computers which are themselves devices whose function it is to update the state of their memory continually, albeit not continuously. If the time interval  $\delta t$  between updates is so chosen that during this interval changes of  $\mathbf{E}$  and  $\mathbf{B}$ , as seen by any particle, can be ignored in Eq. (10.1) and changes of  $\mathbf{j}$  can be ignored in Eq. (10.3), each equation can be solved exactly for the entire interval no matter how long this interval is: The Lorentz equation (10.1) then produces cycloidal motion

<sup>3</sup> The wavevector  $k = \pi/\delta x, \pi\sqrt{2}/\delta x$ , or  $\pi\sqrt{3}/\delta x$ , according to the number of dimensions.

<sup>4</sup> In a 3D, EM code, cubic splines would require each particle to look up 384 data points to interpolate the  $\mathbf{E}$  and the  $\mathbf{B}$  that acts on it!

in a plane perpendicular to  $\mathbf{B}$ , composed of a drift and a gyration Eq. (10.2). This may be accompanied by free fall parallel to  $\mathbf{B}$ , generated by a parallel electric field component. Given the initial velocity and position, or given the position and displacement during the preceding time interval, the displacement during any subsequent interval, and the new position, can be computed precisely.

### 10.5.1 Leap-Frogging Particles Against Fields

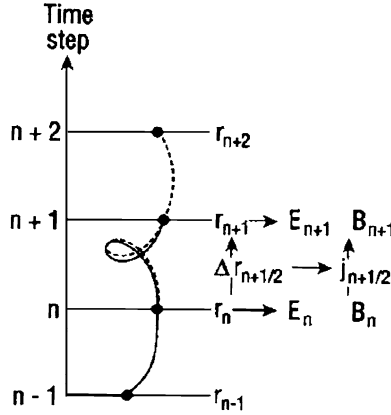


**Fig. 10.2** Leap-frogging particles and fields: At time  $n$ , cycloids with drifts and gyrations due to  $\mathbf{E}_n$  and  $\mathbf{B}_n$  are fitted through  $r_n$  and  $r_{n-1}$ , to be continued through  $r_{n+1}$ . Displacements  $\Delta r_{n+1}$  determine currents  $\mathbf{j}_{n+1/2}$  from which the transverse fields  $\mathbf{E}_n$ ,  $\mathbf{B}_n$  are advanced to  $\mathbf{E}_{n+1}$ ,  $\mathbf{B}_{n+1}$ . The longitudinal  $\mathbf{E}_{n+1}$  is obtained from the  $r_{n+1}$ . Then, at time  $n+1$ , new cycloids (dotted) with drifts and gyrations due to  $\mathbf{E}_{n+1}$  and  $\mathbf{B}_{n+1}$  are fitted through  $r_{n+1}$  and  $r_n$ , to be continued through  $r_{n+2}$ , etc

The average value of the fields  $\mathbf{E}$  and  $\mathbf{B}$  for Eq. (10.1) or the current  $\mathbf{j}$  to be used in Eq. (10.3) is taken to be the actual value at the middle of the time interval (Fig. 10.2). Figure 8.2 shows how the updating from average values proceeds at equal intervals along a time axis. This involves the following:

1. Construct the cycloidal orbit of a particle from  $t_{n-1}$  through  $t_n$  to  $t_{n+1}$  using the known mean values of  $\mathbf{E}_n$  and  $\mathbf{B}_n$  at  $t_n$  (the middle of the interval) and the known particle positions at  $t_{n-1}$  and  $t_n$ .
2. This gives the displacement of the particles from  $t_n$  to  $t_{n+1}$ , and their final positions at  $t_{n+1}$ .
3. The harmonic  $\mathbf{j}_k$  of the mean current flowing during the last interval is obtained by summing all the displacements  $\delta \mathbf{r}$  with phase factors  $\exp i \mathbf{k} \cdot \mathbf{r}$  given by their mean positions, times  $q/\delta t$ .

4. The transverse fields  $\mathbf{F}_k$  are now advanced by  $\mathbf{j}_k$  Eq.(10.3) from  $t_n$  to  $t_{n+1}$  (Sect. 8.5.3).
5. The longitudinal fields  $\mathbf{F}_k$  are obtained from  $\rho_k$  at  $t_{n+1}$  by summing with the new positions  $\mathbf{r}$  at  $t_{n+1}$ .
6. The process is repeated from  $t_n$  through  $t_{n+1}$  and then to  $t_{n+2}$ .

Each time interval is covered by two cycloids for each particle, one with drift and gyrofrequency as given by the fields at the beginning of the interval, the other as given by the fields at the end of the interval. Both cycloids pass through the same points at the termini (Fig. 8.2).

### 10.5.2 Particle Advance Algorithm

The time interval  $\delta t$  must be smaller than  $\sim \omega_p^{-1}$  for proper resolution of electrostatic plasma oscillations, and  $\omega_b \delta t \leq 1$  to account for synchrotron radiation or for  $\nabla B$  drifts. The steps in the solution algorithm are given by Hockney (1966) and Buneman (1967). The interpretation and implementation of this as an electric acceleration followed by a magnetic rotation and another acceleration is due to Boris (1970). The updating of the particle positions and velocities is done using a time-centered second-order scheme, valid for relativistic particle velocities,

$$\frac{v_{new} - v_{old}}{\delta t} = \frac{q}{\gamma m_0} \left[ E + \left( \frac{v_{new} + v_{old}}{2} \right) \times B \right] \quad (10.6)$$

with the scaling<sup>5</sup>

$$E \leftarrow \frac{q \delta t}{2 m_0} E, \quad B \leftarrow \frac{q \delta t}{2 m_0} B, \quad (10.7)$$

Eq.(10.6) is solved by the following sequence,<sup>6</sup>

$$\begin{aligned} \gamma_1 &= (1 - v^2/c^2)^{-1/2} \\ u_1 &= \gamma_1 v_{old} \\ u_2 &= u_1 + E \quad (\text{first half of electric acceleration}) \\ \gamma_2 &= (1 + u_2^2/c^2)^{+1/2} \\ u_3 &= u_2 + \left( \frac{2}{\gamma_2^2 + B^2} \right) (\gamma_2 u_2 + u_2 \times B) \times B \\ u_4 &= u_3 + E \quad (\text{second half of electric acceleration}) \end{aligned}$$

<sup>5</sup>  $\mathbf{E}$  describes half the electric acceleration and the magnitude of  $\mathbf{B}$  is half the magnetic rotation angle during the time step.

<sup>6</sup> The sequence is mathematically concise when  $\gamma = 1$ . The quantity  $u$  is velocity in the sense of momentum per unit restmass. The relativistic  $\gamma$  is obtained from it as the square root of  $1 + (u/c)^2$ . The equation for  $u_3$  is executed by first dividing  $B$  by  $\gamma^2$  and then using “1” in place of  $\gamma^2$ . This accounts for the  $m$  rather than  $m_0$  in the angle.

$$\begin{aligned}
 v_{new} &= u_4 \left[ 1 + (u_4/c)^2 \right]^{+1/2} \\
 x_{new} &= x_{old} + \delta t v_{new}
 \end{aligned}
 \tag{10.8}$$

This process is equivalent to rotating the deviation from the gyrocenter drift through the angle  $2 \arctan(qB\delta t/2m)$  –the “cycloid fitting”–combined with uninhibited electric acceleration along the magnetic field. It is second-order and time reversible.

Since this algorithm now properly accounts for the effects of relativity, particles are automatically restrained from exceeding the speed of light and need not be artificially braked at  $c$ . This limit on the distance traveled by a particle during a single time step plays an important role in particle data management.

### 10.5.3 Field Advance Algorithm

The advance of the fields through one time step of arbitrary length (subject to  $\mathbf{j}_k = \text{constant}$ ) is mathematically just like that of the particles. According to Eq. (10.4),  $\mathbf{F}_k$  consists of a constant component plus a rotating component. The constant part represents the magnetostatic field generated by the currents; the rotating part represents a circularly polarized electromagnetic wave. Again, the advance through any time interval  $\delta t$  is straightforward. The longitudinal (purely electric) component of the field is updated from the record of  $\rho$  at the end of the time step using Eq. (10.5).

We note, so far, we have not invoked finite difference calculus either in the space or time domain and, typically, the advance of the fields from Maxwell-Hertz-Heaviside’s equations is not restricted by any “Courant condition” (Hockney and Eastwood 1981, p. 345).<sup>7</sup> However, in practice,  $\delta t$  is constrained by the fact that  $\mathbf{E}$  and  $\mathbf{B}$  should not change across the range of the orbit excursions during  $\delta t$ .

Equation (10.3) is used to trace the evolution of the transverse field only. The longitudinal, electrostatic field is constructed “from scratch” at the new time, using the charge density records:

$$F_k^{e-s} = ik\rho_k/k^2 \tag{10.9}$$

The longitudinal field, then, need not be held over through the particle move phase: it can be generated directly by Fourier transforming the charges accumulated during that phase. The transverse field is calculated as follows. A particular solution is constructed from  $\mathbf{j}_k$  using

$$F_k^{m-s} = k \times j_k/k^2 \tag{10.10}$$

---

<sup>7</sup> The Courant condition, or Courant-Friedrichs-Lewy condition is a constraint on the maximum size of a timestep in a simulation. It results from a numerical diffusion associated with the size of the spatial mesh (if one is used) in relation to the timestep attempted.

To  $\mathbf{F}_k^{m-s}$  one has to add the rotating “electromagnetic” component

$$F_k^{e-m}(new) = F_k^{e-m}(old) \cos k\delta t - (k/k) \times F_k^{e-m}(old) \sin k\delta t \quad (10.11)$$

The new fields are then reconstructed from the updated pieces according to

$$F_k(new) = F_k^{m-s} + F_k^{e-m}(new) + F_k^{e-s} \quad (10.12)$$

and this is kept on record for the next field update.

The field seen by a particle must then be obtained by summation over the entire available spectrum

$$\begin{aligned} F(r) &= D(r) + iH(r)/c = (2\pi)^{-3} \int_k F_k e^{-ik \cdot r} dk \\ &= (2\pi)^{-3} \sum_{k_x} \sum_{k_y} \sum_{k_z} F_k e^{-ik \cdot r} \end{aligned} \quad (10.13)$$

To calculate  $\mathbf{F}$ , we must introduce a grid over which field values are generated from the spectrum by FFTs, and we must interpolate the local field from the grid record. Likewise, charge and current harmonics must be built up by interpolation into a grid and subsequent FFTs.

Having avoided spatial grids and spatial finite-difference calculus so far, the introduction of a grid to obtain the electromagnetic fields from the spectrum  $F_k$  leads to difficulties associated with grids: inaccuracies and stroboscopic effects. These problems are reduced using higher-order interpolation methods ([Buneman et al. 1980](#)).

## 10.6 Issues in Simulating Cosmic Phenomena

### 10.6.1 Boundary Conditions

A major problem in space applications is to simulate free-space conditions outside the computer domain. Complex Fourier methods (with  $\exp(i\mathbf{k} \cdot \mathbf{r})$ ) imply periodic repeats of the computed domain in all dimensions. If the simulation is to represent phenomena in a rather larger plasma, such repeats are acceptable, but for an isolated plasma of limited extent they become unrealistic. This problem can be overcome by keeping a generous empty buffer zone around the domain containing particles and truncating the interaction between charges beyond a certain radius so that the nonphysical repeats introduced by the Fourier method cannot influence the central plasma. This was first applied to gravitational simulations.

The most elusive boundary problem for space plasmas is the radiation condition. To decide what part of the field in the charge-current-free space outside the plasma is outgoing and what is incoming presents no problem in 1D and the incoming part can be suppressed.

In 2D the decision is more difficult. It requires information not only in the source-free boundary layer at any time but also over its past history. It almost seems as if, in principle, the entire past history is needed for the decision. However, Lindman found

that a fairly short history (such as three past time steps) of the boundary suffices for an algorithm which will suppress all but 1 % of the incoming radiation at all but the shallowest angles of incidence. However, just carrying an absorption layer in an outer envelope seems quite successful. This method, due to Green, simply multiplies the electric and magnetic field by a factor which smoothly approaches zero away from the plasma. A method employing spherical harmonics which should be 100 % effective has been reported (Buneman 1986; Buneman et al. 1994).

### 10.6.2 Relativity

A reason for keeping the mass coupled with the velocities in the update steps is that under relativistic conditions one really updates momenta rather than velocities. Note, however, that in the  $qB\delta t/2m$  terms one needs  $m^{-1} = (m_0^2 + p^2/c^2)^{-1}$  where  $p = mv$ . During the rotation, this magnitude of the momentum does not change, but in the electric acceleration it does. After the full update of momenta, one must again divide by  $m$  in order to get  $\mathbf{v} = \delta\mathbf{r}/\delta\mathbf{t}$ . In practice,  $v$  rather than the momentum is stored for each particle which means that at the beginning of the update one must calculate  $m = m_0(1 - \beta^2)^{-1/2}$ . Thus, there are three separate calls to a reciprocal square root in the relativistic advance of each particle. As system supplied square roots are time consuming and more accurate than needed for particle pushing, a Padé-type rational first approximation, followed by a Newton iteration, is used instead.

### 10.6.3 Compression of Time Scales

The number of steps required to simulate a significant epoch in the evolution of a real plasma configuration would be many million, typically, if  $t$  has to be of the order  $\omega_p^{-1}$  or  $\omega_b^{-1}$ . In order to bring this down to the more acceptable range of several thousand steps, one must compress the time scales. Compressing time scales can be achieved by (1) decreasing the ions' rest mass in relation to the electrons' rest mass, and (2) increasing temperatures so that typical particle velocities get closer to the velocity of light.

For an ion (proton) to electron simulation mass ratio of 16, ion gyrofrequencies  $\omega_{bi} = eB/m_i$  will be high by a factor of  $1,836/16 = 115$ , ion plasma frequencies  $\omega_{pi} = \sqrt{n_i Z^2 e^2 / m_i \epsilon_0}$ , ion thermal velocities  $v_{Ti} = \sqrt{kT_i/m_i}$ , the Alfvén velocity  $v_A = \sqrt{B^2 / \mu_0 n_i m_i}$ , and the relative velocity in Biot-Savart attraction  $v = I_z \sqrt{\mu_0 L / 2\pi \sum m_i}$  will be high by factor of  $\sqrt{1,836/16} = 10.7$ .

The exaggeration of temperatures provides one of several motivations for incorporating relativity into our codes. Note, incidentally, that even a 10-kV electron, a temperature typical of many space plasmas, already moves at  $1/5 c$ .

The exaggeration of “temperatures” of beam or current electrons can also be achieved by exaggerating the external electric field  $E_z$  responsible for accelerating the particles. This technique greatly reduces the number of time steps required to study a phenomenon such as Birkeland current formation and interaction in cosmic plasma. Since the current density is proportional to the electric field (i.e.,  $j_z = I_z/A = n_e e v_z$  ( $n_e e^2/m_e$ )  $E_z t$ ), both the time required for the pinch condition Eq. (1.9) to be satisfied, and the relative velocity between parallel currents (Eq. (3.49)), are linearly related to  $E_z$ .

Of course, when economy necessitates time compression, the time-scales must be “unfolded” upon simulation completion.

### 10.6.4 Collisions

Just as in real plasmas, there are encounters between particles and these give rise to collisional effects which influence the physics of the model. Since computer models are limited to some  $10^6$  particles whereas a laboratory plasma may have  $10^{18}$ – $10^{20}$  particles and a galaxy,  $10^{65}$  particles, each particle in the model is a “superparticle” representing many plasma electrons or ions. Thus the forces between model particles are much larger than in a real plasma and the collisional effects are much greater. Fortunately there is a way to reduce the model collisions to rates comparable with real plasmas. This involves the finite-size particle method (Okuda and Birdsall 1970; Langdon and Birdsall 1970).

The 3D codes discussed in this chapter use a gaussian profile for particles. The shaping is done in  $\mathbf{k}$ -space. This is achieved by first building up  $\rho_k$  and  $\mathbf{j}_k$  for  $|k| < k_{\max}$  (truncation of harmonics at maximum  $k$ ), as if each computer particle were a point and then applying a gaussian filter in  $k$ -space (Buneman et al. 1980). The particle shape is then of the form  $\exp(-r^2 k_p^2/2)$ , where the particle profile factor  $k_p$  is left as a users option: many simulations have used a profile which keeps the spectrum flat up to a fairly large  $k$  and then makes a rapid but smooth slope-off to zero at some desired  $k_{\max}$ .

A limit to the maximum acceptable radius of the finite-sized particles is set by the collective properties of the plasma. If the effective radius of a gaussian particle is increased much beyond the Debye length, it takes over the role of the Debye length, causing collective effects to be altered.

In simulating a physical system, plasma or gravitating, it is usually sufficient to determine if the system models a collisionless one over the simulation time span. Experimental determination of the effective collisional frequency  $\nu_c$  in 2D models closely follows the empirical law (Hockney and Eastwood 1981)

$$\frac{\nu_c}{\omega_p/2\pi} = N_D^{-1} \left[ 1 + \left( \frac{w}{\lambda_D} \right)^2 \right]^{-1}$$



where  $w$  is the width of the particle and  $N_D = n\lambda_D^2$  is the number of particles in a Debye square. In 3D simulations, the reduction of  $nc$  is achieved, without increasing  $N_D$ , by “softening the blow” of collisions—making the particles into fuzzy balls. Okuda (1972) has calculated values  $v_c/\omega_p \approx 10^{-3}$  for gaussian profile particles for  $N_D$  of order unity. This value is consistent with most plasmas, in laboratories or space.

So far we have only considered collisions between particle species that are charged. However, in weakly ionized plasmas where the number of uncharged particles may be hundreds or thousands of times more prevalent, it is often the collision between the massive ions and the massive neutral atoms that cause a redistribution of energy, and concomitant effects, such as plasma heating. Collisions in weakly ionized plasmas have been successfully treated by melding PIC algorithms with MCC—Monte Carlo Collision—algorithms (Kwan et al. 1985; Snell et al. 1990; Birdsall 1991).

PIC codes involve deterministic classical mechanics which generally move all particles simultaneously using the same time step. The only part left to chance is usually limited to choosing initial velocities and positions and injected velocities. The objective for highly-ionized space plasma is usually seeking collective effects due to self and applied fields. On the other hand, MCC codes are basically probabilistic in nature, seeking mostly collision effects in relatively weak fields. For example, let a given charged particle be known by its kinetic energy  $W_{kin}$  and its velocity relative to some target particles. This information produces a collision frequency  $\nu_{coll} = n_{target} \sigma W_{kin} v_{relative}$  and a probability that a collision will occur. This information is then used to describe electron collisions with neutrals (elastic scattering, excitation, and ionization) and ion collisions with neutrals (scattering and charge exchange).

The method is to use only the time step of the PIC field solver and mover,  $\delta t$ , and then to collide as many particles as is probable  $P$  in that  $\delta t$  separately. The actual fraction of particles in collision is  $P = 1 - \exp(-\nu_{coll} \delta t)$ . Note that we have slipped into treating our computer particles as single electrons, not as superparticles; the implication is that with a sufficient number of collisions, the resultant scatter in energy and velocity will resemble that of the single particles.

The end result of current efforts at including collisions in PIC codes due to Monte Carlo methods is the change in velocities of the particles. Thus, the only change from a collisionless run is that the particle velocities are varied in a time step. The last task at the end of a time step is to determine the new (scattered) velocity, and new particle velocities if ionization occurs (if ionization and/or recombination processes have been included in the MCC model). Each process is handled separately. Elastic collisions change the velocity angles of the scattered electrons; charge exchanges decrease ion energy and change velocity angles; ionizations do these and create an ion-electron pair, with new velocities. The effect on the neutral gas is not calculated because the lifetimes of the excited atoms are generally less than a time step.

When recombination rates are high, and if the source of energy to the plasma is terminated, gravitational effects must soon be included in the particle kinematics.

## 10.7 Gravitation

The transition of plasma into stars involves the formation of dusty plasma (Appendix C), the sedimentation of the dust into grains, the formation of stellicals, and then the collapse into a stellar state. While the above process appears amenable to particle simulation, a crude approximation of proceeding directly from charged particles (actually a cloud of charged particles) to mass particles is made. The transition of charge particles to mass particles involves the force constant, that is, the ratio of the coulomb electrostatic force between two charges  $q$  separated a distance  $r$ ,

$$F_q(r) = \frac{q^2}{4\pi\epsilon_0 r^2} \quad (10.14)$$

to the gravitational force between two masses  $m$  separated a distance  $r$ ,

$$F_G(r) = -\frac{Gm^2}{r^2} \quad (10.15)$$

In the particle algorithm this change is effected by the following:

1. Changing all particles to a single species.
2. Limiting the axial extent of the simulation to be of the order of less than the extent or the radial dimension (i.e., about the size of the expected double layer dimension).
3. Setting the axial velocities to zero.
4. Setting the charge-to-mass ratio equal to the negative of the square-root of the gravitational constant ( $\times 4\pi\epsilon_0$ ).

This last change produces attractive mass particles via the transformation  $\varphi_G(r) = \varphi_q(r)$  in the force equation  $F = -\nabla\varphi$ , where

$$\varphi_q(r) = -\frac{q^2}{4\pi\epsilon_0 r} \quad (10.16)$$

and

$$\varphi_G(r) = -\frac{Gm^2}{r} \quad (10.17)$$

are the electrostatic and gravitation potentials, respectively.

## 10.8 Scaling Laws

The scaling of plasma physics on cosmical and laboratory scales generally involves estimates of the diffusion in plasma, inertia forces acting on the currents, the Coriolis force, the gravitational force, the centrifugal force, and the  $\mathbf{j} \times \mathbf{B}$  electromagnetic force (Bostick 1958; Lehnert 1959).

Specification of plasma density, geometry, temperature, magnetic field strength, acceleration field, and dimension set the initial conditions for simulation. The parameters that delineate the physical characteristics of a current-carrying plasma are the electron drift velocity

$$\beta_z = \frac{v_z}{c} \quad (10.18)$$

the plasma thermal velocity

$$\beta_{th} = \frac{v_{th}}{c} = \frac{(\lambda_D/\Delta)(\omega_p \delta t)}{c \delta t / \Delta} \quad (10.19)$$

and the thermal/magnetic pressure ratio

$$\beta_p = \frac{n_e k T_e + n_i k T_i}{B^2 / 2\mu_0} = \frac{(\lambda_D/\Delta)^2 (\omega_p \delta t)^2 4(1 + T_i/T_e)}{(c \delta t / \Delta)^2 (\omega_{c0}/\omega_p)^2} \quad (10.20)$$

where  $n$  is the plasma density,  $T$  is the plasma temperature,  $k$  is Boltzmann's constant, and the subscripts  $e$  and  $i$  denote electron and ion species, respectively. The parameter  $\delta t$  is the simulation time step,  $\Delta$  is the cell size, and  $c$  is the speed of light. All dimensions are normalized to  $\Delta$  and all times are normalized to  $\delta t$ . The simulation spatial and temporal dimensions can be changed via the transformation

$$\frac{c \delta t}{\Delta} = \frac{c \delta t'}{\Delta'} = 1 \quad (10.21)$$

where  $\Delta' = \alpha \Delta$  and  $\delta t' = \alpha \delta t$ , for the size/time multiplication factor  $\alpha$ . The values of  $n, T, B$ , and  $E$  remain the same regardless of whether the simulations are scaled to  $\Delta$  and  $\delta t$  or to  $\Delta'$  and  $\delta t'$ .

One immediate consequence of the rescaling is that, while the dimensionless simulation parameters remain untouched, the resolution is reduced, that is,

$$\omega \delta t = \omega' \delta t' \quad (10.22)$$

where  $\omega' = \omega/\alpha$  rad/s is the highest frequency resolvable.

To convert simulation results to dimensional form, it is sufficient to fix the value of one physical quantity (e.g.,  $B\phi$ ).

## 10.9 Data Management

The management of data is a contemporary problem only for 3D simulations. Using a modest factor of 4 in the total particle number for each velocity dimension and a factor 64 for each spatial dimension, one concludes that 3D simulations ought to employ some  $2^{24}$ , that is, 16 million particles, each requiring six data ( $x, y, z, u, v, w$ ) to be recorded (i.e., 100 million data).

Obviously, there is no hope for doing a plausible 3D simulation without (1) introducing some economies, and (2) storing the particles outside core and calling them in only small batches.

Similarly, the  $64^3$  linear scale range calls for over 1 million field data: Fields cannot reside in core. "Layering" is therefore practiced in 3D codes. In the tridimensional code TRISTAN a grid of  $2 \times 128^3$  points (cubic mesh, plus cube centers) is used for recording field data, and particles are kept ordered into 128 layers. At present, the number of particles is 4 1/2 million. This is currently being increased to 50 million. Only two field layers are in core at any time, and four charge current layers (the latter because after moving, particles can have dropped below or risen above their original layers). Triple buffering is used when the particles of each layer are passed through core for processing, in batches of about 5,000. Images of the batches that straddle layer borders are kept in core, for depositing particles that have dropped or risen. Some sorting of the particles is necessary here.

Fields of the next layer above are brought in when a layer of particles has been completed and the lowest of the four charge-current layers is put out to disk. These two moves are accompanied by Fourier transforming within the layer dimensions (e.g.,  $x$  and  $y$ , when layering is in  $z$ , to  $k_x$  to  $k_y$ ). Filtering of high harmonics at this stage helps with input/output economy.

When all layers have been processed, the original field record on the disks is converted into a charge-current record, indexed in a hybrid manner, namely according to  $k_x$ ,  $k_y$ , and  $z$ .

At this point, field solving can begin, but it will require prior Fourier transforming in  $z$ . The  $j, r$  data have to be read back into core, but in different order, from scattered disk areas. Again, layering must be used, but now according to  $k_y$  (say). TRISTAN uses 16 sectors at this point. Fourier transforming cannot begin until all reading of a sector is complete: Input/output (I/O) cannot be overlapped with computation. A similar bottleneck occurs after the field update when the FFTs in  $z$  have to be completed before the new fields of a sector can be written to disk.

It is difficult to assess the cost of waiting for I/O completion; this depends strongly on the operating system. A time step overall (particle plus field update) in TRISTAN in 1990 took about 2 m on a CRAY-1.

## References

- Birdsall, C.K.: Particle-in-cell charged particle simulations, plus Monte Carlo collisions with neutral atoms, PIC-MCC. *IEEE Trans. Plasma Sci.* **19**, 65 (1991)
- Birdsall, C.K., Langdon, A.B.: *Plasma Physics via Computer Simulation*. McGraw-Hill, New York (1985)
- Boris, J.P., Dawson, J.M., Orens, J.H., Roberts, K.V.: Computations on anomalous-resistance. *Phys. Rev. Lett.* **25**, 706 (1970)
- Bostick, W.H.: Possible hydromagnetic simulations of cosmical phenomena in the laboratory. *Rev. Mod. Phys.* **30**, 1090 (1958)

- Buneman, O.: Multi-dimensional particle codes: their capabilities and limitations for modeling space and laboratory plasma. *IEEE Trans. Plasma Sci.* **14**, 661 (1986)
- Buneman, O., Barnes, C.W., Green, J.C., Nielsen, D.E.: Principles and capabilities of 3D, EM particle simulations. *J. Comp. Phys.* **38**, 1 (1980)
- Cashwell, E.D., Everett, C.J.: *Monte Carlo Method for Random Walk Problems*. Pergamon Press, New York (1959)
- Hockney, R.W., Eastwood, J.W.: *Computer Simulation Using Particles*. McGraw-Hill, New York (1981)
- Karin, S., Smith, N.P.: *The Supercomputer Era*. Hartcourt, Brace, Jovanovich, Boston (1987)
- Kwan, T.J.T., Snell, C.M., Mostrom, M.A., Mack, J.M., Hughes, H.G.: Monte Carlo charged particle and photon transport in particle-in-cell codes. In: *Eleventh International Conference on Numerical Simulation of Plasmas*, Montreal, 25–27 June 1985
- Langdon, A.B., Birdsall, C.K.: *Phys. Fluids* **13**, 2115 (1970)
- Lehnert, B.: Plasma physics on cosmical and laboratory scale. *Nuovo Cimento* **13**(supplement), 59 (1959)
- Lindman, E.L.: *J. Comp. Phys.* **5**, 13 (1970)
- Nash, S.: *History of Scientific Computation* (1991, in press)
- Okuda, H.: *Phys. Fluids* **15**, 1268 (1972)
- Okuda, H., Birdsall, C.K.: *Phys. Fluids* **13**, 2123 (1970)
- Peratt, A.L.: Numerical observatory. *Phys. Today* **37**, 90 (1984)
- Snell, C.M., Kwan, T.J.T., Morel, J.E., Witte, K.H.: Incorporation of atomic physics into particle simulations. *Bull. Am. Phys. Soc.* **35**, 2001 (1990)
- Størmer, C.: *The Polar Aurora*. Clarendon Press, Oxford (1955)

# Chapter 11

## Further Developments in Plasma Simulation

### 11.1 Updates in Three-Dimensional, Electromagnetic Particle Simulation Models

Driven by increased computer capabilities, the original TRISTAN code ([Buneman et al. 1980](#); Peratt A.L., TRISTAN user's manual, Los Alamos National Laboratory, Pulsed Energy Applications, X-10, unpublished report, 1984) has been continuously updated to TRISTAN-PRIME. Starting in 1994, its new features ([Buneman 1994](#)) are:

1. **Updating fields locally:** Poisson's equation and Fourier transforms have been eliminated by updating the fields locally from the curl equations and depositing the particle currents according to charge-conserving formulas (Villasenor and Buneman 1992),
2. **Radiating boundary conditions are applied to the fields:** Radiating boundary conditions are applied to the fields using a first order Lindman approximation (Lindman 1975),
3. **Filtering locally done:** All gaussian  $k$ -space filtering is done locally,
4. **Minimizing data paths:** Localization makes the code ideally suited to modern parallel machines which call for minimizing data paths,
5. **Modest code versions in Fortran:** Code version in Fortran to encourage usage and fully transportable: modest versions run on workstations.

### 11.2 Astrophysical Plasma and Plasma Cosmology

In the past, the TRISTAN code has successfully simulated large scale space plasma phenomena such as the formation of systems of galaxies ([Peratt et al. 1980](#); [Peratt 1988, 1990, 1995a,b, 1997, 1998](#); [Peratt et al. 1990](#); [Peter and Peratt 1990](#); [Snell and Peratt 1995](#)) and addressed the discipline of plasma cosmology ([Buneman et al. 1994a](#)).

The new version of the code has been applied to the study of the dynamics of low- $\beta$  plasma clouds (Neubert et al. 1992), electron-positron plasmas (Zhao et al. 1994a,b and current loop coalescence, Nishikawa et al. 1994, Sakai et al. 1994, Cai et al. 2003, Büchner et al. 2003).

### 11.3 Advancement in Particle/Field Methodology

As pointed out in Sect. 10.9, data management problems dominate the subject of 3D plasma simulation using particles-in-cell. In the novel computer architectures, with their high degree of parallelism, data transport becomes an even more important issue. Computing efficiency depends critically on (topological or physical) data proximity in the basic procedure of a problem. “Local” algorithms, such as finite-difference equations, have preference over “global” algorithms, such as Fourier transforms (Note that the calculation of each single Fourier harmonic requires the entire data-base). With this in mind, new 3D plasma codes have been constructed. In these the particles are advanced just as in Eqs. (10.6)–(10.8), but Maxwell-Hertz-Heaviside’s equations are integrated locally over a cubic mesh in the form:

1. Change of  $\mathbf{B}$ -flux through a cell-face = - circulation of  $\mathbf{E}$  around it.
2. Change of  $\mathbf{D}$ -flux through a cell-face = circulation of  $\mathbf{\Gamma}$  around it – charge flow through it.

The  $\mathbf{E}$ – or  $\mathbf{D}$  data mesh is staggered relative to the  $\mathbf{B}$ – or  $\mathbf{\Gamma}$ – data mesh both in space and time.

This method has the advantage that these need to be satisfied only at the beginning of a run (where it becomes a triviality of initialization): it is automatically carried forward in time by consistent determination of the charge flow between cells. Thus Poisson’s equation does not have to be solved. Poisson’s equation is “global”: The solution anywhere depends on the data everywhere.

For the simulation of solar wind-magnetosphere interaction the following boundary conditions were used for the particles: (1) Fresh particles representing the incoming solar wind (in our test run unmagnetized) are continuously injected across the  $yz$ -plane at  $x = x_{min}$  with a thermal velocity plus a bulk velocity in the  $+x$  direction, (2) thermal solar particle flux is also injected across the sides of our rectangular computation domain, (3) escaping particles are arrested in a buffer zone and redistributed there more uniformly by making the zone conducting in order to simulate their escape to infinity. They are then written off.

For the fields, boundary conditions were imposed just outside these zones: radiation is prevented from being reflected back inward, following Lindman’s ideas 1975. The lowest order Lindman approximation was found adequate: radiation at glancing angles was no problem. However, special attention was given to conditions on the edges of the computational box.

In order to bring naturally disparate time- and space-scales closer together in this simulation of phenomena dominated by ion inertia and magnetic field interaction,

the natural electron mass was raised to 1/16 of the ion mass and the velocity of light was lowered to twice the incoming solar wind velocity. This means that charge separation and anomalous resistivity phenomena are accounted for qualitatively but perhaps not with quantitative certainty. Likewise, radiation related phenomena (e.g. whistler modes) are covered qualitatively only.

## 11.4 Simulation Results

The first test to explore the solar-wind-magnetosphere interaction was carried out on a Cray-YMP at the National Center for Atmospheric Research (NCAR) using a 105 by 55 by 55 grid with 200,000 electron-ion pairs (Buneman et al. 1992). A second test was run on a CRAY-2 using a larger 215 by 95 by 95 grid and about 1,000,000 electron-ion pairs for unmagnetized solar wind (Buneman et al. 1994b). Initially, these fill the entire box uniformly and drift with a velocity  $v_D = 0.5c$  in the  $+x$  direction that represents the solar wind.

The electron thermal velocity is  $v_{th} = 0.02c$  while the magnetic field is initially zero. A circular current generating the dipole magnetic field is increased smoothly from 0 to a maximum value reached at time step 65 and kept constant at that value for the rest of the simulation. The center of the current loop is located at  $(40.5\Delta, 27.5\Delta, 28\Delta)$  with the current in the  $xy$ -plane and the axis in the  $z$ -direction. During initial expansion of the magnetic field cavity, a large fraction of the initial plasma is expelled. The solar wind density is about 0.7 electron-ion pairs per cell, the mass ratio is  $m_i/m_e = 16$ , and  $\omega_{pe}\Delta t = 0.84$ .

The purpose of these runs is to investigate the simulation results with the solar wind with southward or northward interplanetary magnetic field (IMF). Figure 11.1 shows the ion density in the center  $xz$ -layer containing the dipole center at time step 785. (Data were recorded at 128 or 256 step intervals and while no fully steady state was approached, no major change was seen between steps 768 and 1024 (Buneman et al. 1992, 1994b)).<sup>1</sup> The ion density is color coded and the magnetic field component in the plane is shown with arrows at every third grid point. The magnitude of the field has been scaled in order to see the field direction for weak fields. Thus the length of the vectors is not a true representation of the field magnitude. The plasma is flowing through the simulation domain from left to right (low to high  $x$ -values). In the process the dipolar field is compressed at the side facing the plasma wind and is extended to a long tail on the down-wind side, just as the Earth's magnetic field in the solar wind.

Note that in these simulations, the current in the loop creating the dipole, is such that the orientation of the dipole is opposite to that of the earth's field. Or, the orientation of the plane of representation is different for what has been normally chosen in modern times, here with the North Pole down and the South Pole up. However,

<sup>1</sup> At least numerically, some concern was given to these step interval numbers with respect to the numerical and experimental data. No correlation was found and the experimental and astrophysical data instabilities have no connection to the simulation grid and time step parameters.



this orientation is totally consistent with the data in Chaps. 12 and 13 and also with world, southern-hemisphere, and Antarctic charts apparently deriving from very-ancient antiquity.

Some particles have entered the cusp regions and, on the down-wind side (night side), particles have gathered on closed field lines in what could be equivalent to the radiation belt. The particles at the up-wind magnetopause are forming a bow shock. The temperature of these particles is much elevated from the background temperature. Also seen up-wind from the magnetopause is what could be a secondshock or

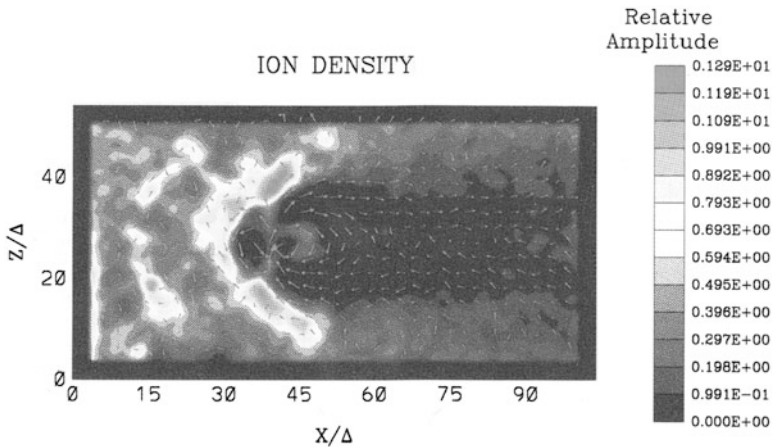


**Fig. 11.1** Ion density in the center  $xz$ -layer containing the dipole axis. “Relative amplitude” on the color bar signifies simulation units

a foreshock. The magnitude of both shocks has a minimum at the sub-solar point and is increasing to a maximum at some distance from the sun-Earth line.

The current density associated with the electron and ion fluxes and the magnetic field are shown in Fig. 11.2. The current density component shown is perpendicular to the  $xy$  plane ( $J_y$ ), with current into the plane (the positive  $y$  direction) colored red and current out of the plane colored blue. Again, the values are for the center layer obtaining the dipole axis. The current densities have been determined from the  $y$  component of the particle fluxes at each cell in the layer.

At the upwind, low-latitude magnetopause the current runs in a direction which cancels the original magnetic field on the upwind side, and doubles the field at the downwind side. At the cusp regions the current changes polarity with the magnetic field, as expected. The magnetopause in the tail also has negative  $J_y$ , with a positive  $J_y$  in the neutral sheath. The current in the neutral sheath is carried by the very few particles located here.

The ion density and magnetic field in the  $yz$  plane are shown in Fig. 11.3. The values are those of the layer which contains the center of the dipole and the dipole axis. The direction of the solar wind is out of the plane toward the viewer. Note that the density is asymmetric, with more ions located at the left side. This is by ions  $\nabla B$

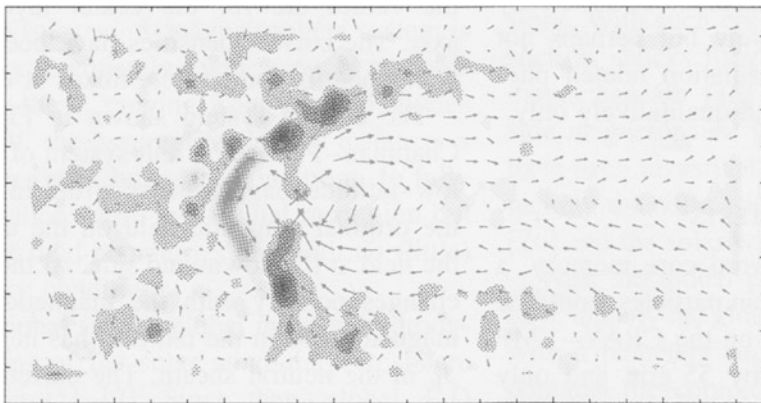


**Fig. 11.2** Current density in the center  $xz$ -layer containing the dipole axis. Positive currents flow into the plane and negative out of the plane

drifting toward this side as they move around the magnetic obstacle. The current density  $J_x$  in the  $yz$  containing the dipole axis (not shown), is running in a belt around the dipole with a polarity that cancels fields on the outside. This is the origin of the magnetopause.

Key parameters are shown in Fig. 11.4 as functions of  $x$ , for center  $y$  and center  $z$  (sun-earth line). These are the ion density (top panel), the ion thermal pressure (second panel), the ion dynamic pressure (third panel), the magnetic pressure (fourth panel), and the ion Larmor radius (bottom panel). The magnetic field is small in the wind and in the tail, and rises to a peak at the location of the dipole center. Upwind, the increase is quite sudden and corresponds to the magnetopause. Upwind of the magnetopause, the density is high and some oscillations in the density are present here. The nature of these oscillations has not yet been investigated. At the magnetopause the density drops, but recovers and reaches a local maximum at  $x = 39$ . This maximum is associated with cusp particles that have penetrated to the center of the dipole (there is no planet to stop them). At  $z = 46$  a second maximum is reached which correspond to the radiation belt – type particles mentioned earlier. Finally, the density increases slowly with distance in the tail.

The thermal pressure increases dramatically in a region upwind of the magnetopause. The location of this maximum corresponds to the location of the third of the three density maxima found upwind. Through the shock, the wind is slowed down, as seen by combining the plots of density and dynamic pressure. Thus the structures at the upwind side of the magnetopause bear much resemblance to the structures of the earth's bow shock. The ion Larmor radius has large variations with location, as does the magnetic field. In the wind and in the tail (we are in the neutral sheath) the Larmor radius is of the order of 10–30, with peaks in places where the magnetic field becomes small. The magnetic fluctuations in the tail are caused by the tail waving like a flag. (In regions of rapidly varying low field strength, “Larmor radius” loses its meaning.)

Improvements to the simulation include finer grids (larger array sizes) while varying the time-dependent IMF's. Also, tilting the magnetic axis, and including an inner conducting surface to better simulate ionosphere.

### ***11.4.1 Advances in the Setup of Geometries for Plasmas in Interstellar Space***

One of the features of TRISTAN-PRIME has been its incorporation of mid-evolution simulation geometries. After decades of PIC simulation on plasma gun and interstellar evolution together with nearly 10,000 z-pinch experiments on a wide range of high energy generators, the thought was to simply redo some of these mid-point in time as verifications, the new execution time being minutes rather than months.

That the first version of TRISTAN (circa 1982) was both fully three-dimensional and operable at 100 teraflops was due to the genius of O. Buneman and his colleagues, accomplished by writing the code in machine assembly language, e.g. CAL, cray assembly language, rather than high-level languages. With regards portability, this proved very unpopular to the PIC simulation community who almost universally continued to analyze physical models with two-dimensional codes.<sup>2</sup>

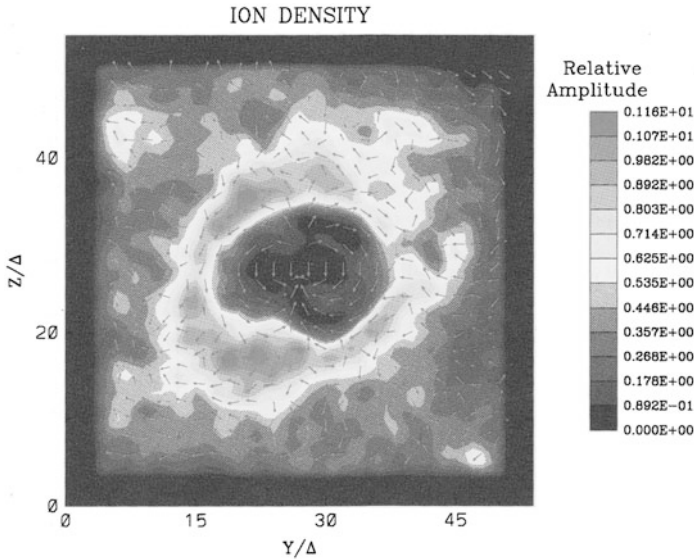


**Fig. 11.3** Current density in the center  $xz$ -layer containing the dipole axis. Positive currents flow into the plane and negative out of the plane

<sup>2</sup> Buneman felt that “programming in Fortran was like playing a piano wearing boxing gloves.”

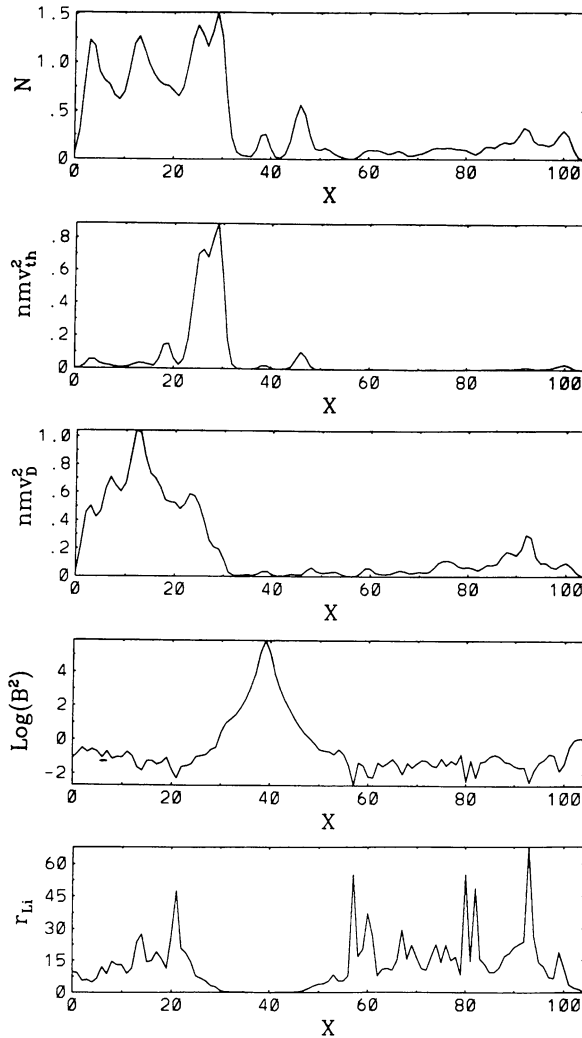


**Fig. 11.4** Current density  $J_x$  in the center  $yz$ -layer containing the dipole axis. Positive currents flow out of the plane and negative into the plane

The new version of TRISTAN had two classes of problems in mind: high power microwave tubes and space plasmas.

By the 1990s high power microwave generation schemes came to be dominated by reflex triodes, vircators, reflex klystron oscillators (RKO's), magnetically insulated transmission line oscillators (MILOs), gyrotrons, and backward wave oscillators (BWO's). These devices are characterized by multiple conductors such as anodes, grids, cathodes, slow wave structures, vanes, and resonant cavities. Unfortunately, conducting boundaries were not permitted in the original versions of TRISTAN.

Nevertheless, TRISTAN remained nearly unused outside of Stanford and Los Alamos. Its lack of widespread acceptance might be traced, in part, to its sparse documentation and the obscure user-unfriendly CAL coding as some of its key algorithms. Nevertheless, a TRISTAN user manual which describes the set up various beam geometries in CAL and operation on a Cray machine was distributed to TRISTAN users (Peratt AL, TRISTAN user's Guide, Los Alamos National Laboratory, Pulsed Energy Applications, X-10, unpublished report, 1984).

Only when machine speeds reached multiple-petaflop, now exaflop speeds, did three-dimensional simulation become readily adopted in the code community. These advances were pioneered by the nuclear energy and space plasma community before reaching the pulse-power analysts.

## References

- Büchner, J., Dum, C.T., Scholer, M.: Plasma interaction between extrasolar planets and their stars. In: *Space Plasma Simulation*, Springer, Berlin/New York (2003)
- Buneman, O.: TRISTAN: the 3-D, E-M particle code. In: Matsumoto, H., Omura, Y. (eds.) *Computer Space Plasma Physics, Simulation Techniques and Software*, pp. 67–84. Terra Scientific, Tokyo (1994)
- Buneman, O., Barnes, C.W., Green, J.C., Nielsen, D.E.: Review: principles and capabilities of 3-d, E-M particle simulations. *J. Comput. Phys.* **38**, 1–44 (1980)
- Buneman, O., Neubert, T., Nishikawa, K.-I.: Solar wind-magnetosphere interaction as simulated by a 3D, EM particle code. *IEEE Trans. PlasmaSci.* **20**, 810–816 (1992)
- Buneman, R., Barker, R.J., Peratt, A.L., Brecht, S.H., Langdon, A.B., Lewis, H.R.: A tribute to Oscar Buneman – pioneer of plasma simulation. *IEEE Trans. Plasma Sci.* **22**, 22–30 (1994a)
- Buneman, R., Barker, R.J., Peratt, A.L., Brecht, S.H., Langdon, A.B., Lewis, H.R.: A tribute to Oscar Buneman – pioneer of plasma simulation. *IEEE Trans. Plasma Sci.* **22**(1), 22–30 (1994b)
- Cai, D., Yaoting, Li, Nishikawa, K.-I., Chijie, X., Xiaoyang, Y., Pu, Z.: Parallel 3-D electromagnetic particle code using high performance fortran: parallel TRISTAN in space plasma simulation. In: Büchner, J., Scholer, M., Dum, C.T. (eds.) *Space Plasma Simulation*. Springer, Berlin/Heidelberg (2003)
- Lindman, E.L.: Free-space boundary conditions for the time dependent wave equation. *J. Comput. Phys.* **18**, 66–78 (1975)
- Neubert, T., Miller, R.H., Buneman, O., Nishikawa, K.-I.: The dynamics of low- $\beta$  plasma clouds as simulated by a 3-dimensional, electromagnetic particle code. *J. Geophys. Res.* **97**, 12,057–12,072 (1992)
- Nishikawa, K.-I., Sakai, J.I., Zhao, J., Neubert, T., Buneman, O.: Coalescence of two current loops with a kink instability simulated by a 3-D EM particle code. *Astrophys. J.* (1994, in press)

- Peratt, A.L.: The role of particle beams and electrical currents in the plasma universe. *Laser Part. Beams* **6**(3), 471 (1988)
- Peratt, A.L.: The evidence for electrical currents in cosmic plasma. *IEEE Trans. Plasma Sci.* **18**, 26 (1990)
- Peratt, A.L.: Introduction to plasma astrophysics and cosmology. In: *Plasma Astrophysics and Cosmology*, pp. 3–11. Kluwer, Dordrecht (1995a)
- Peratt, A.L.: Plasma and the universe: large scale dynamics, filamentation, and radiation. *Astrophys. Space Sci.* **227**(1–2), 97–107 (1995b)
- Peratt, A.L.: Advances in numerical modeling of astrophysical and space plasmas. In: de Gouveia Dal Pino, E.M., Peratt, A.L., Medina Tanco, G.A., Chian, A.C.-L. (eds.) *Advanced Topics on Astrophysical and Space Plasmas*, pp. 93–163. Kluwer, Dordrecht/Boston (1997)
- Peratt, A.L.: Advances in numerical modeling of astrophysical and space plasmas, part II: astrophysical force laws on the large scale. *Astrophys. Space Sci.* **256**, 51–75 (1998)
- Peter, W., Peratt, A.L.: Synchrotron radiation spectrum for galactic-sized plasma filaments. *IEEE Trans. Plasma Sci.* **18**, 49 (1990)
- Peratt, A.L., Green, J., Nielsen, D.: Evolution of colliding plasmas. *Phys. Rev. Lett.* **44**, 1767–1770 (1980)
- Peratt, A.L., Peter, W., Snell, C.M.: 3-dimensional particle-in-cell simulation of spiral galaxies. In: Beck, R., Kronberg, P.P., Wielebinski, R. (eds.) *Galactic and Extragalactic Magnetic Fields. Proceedings of the IAU Symposium*, vol. 140. Kluwer Academic, IEEE Transactions on Plasma Sci. Dordrecht (1990)
- Sakai, J.I., Zhao, J., Nishikawa, K.-I.: Loops heating by D.C. electric current and electro-magnetic wave emissions simulated by a 3-D EM particle code. *Solar Phys.* (1994, in press)
- Snell, C.M., Peratt, A.L.: Rotation velocity and neutral hydrogen distribution dependency on magnetic field strength in spiral galaxies. *Astrophys. Space Sci.* **227**(1), 167–173 (1995)
- Villasenor, J., Buneman, O.: Rigorous charge conservation for local electromagnetic field solvers. *Comput. Phys. Commun.* **69**, 306–316 (1992)
- Zhao, J., Nishikawa, K.-I., Sakai, J.I., Neubert, T.: Study of nonlinear Alfvén waves in an electron-positron plasma with 3-D EM particle code. *Phys. Plasmas* **1**, 103–108 (1994a)
- Zhao, J., Sakai, J.I., Nishikawa, K.-I., Neubert, T.: Relativistic particle acceleration in an electron-positron plasma with a relativistic electron beam. *Phys. Plasmas* (1994b, in press)

## Chapter 12

# Dynamics of Field–Aligned Currents in the Laboratory, Aurorae, and Galactic Space

### 12.1 Formation and Dynamics of Laboratory Currents

#### 12.1.1 Formation and Evolution of Plasma Currents

One of the outstanding properties of electron beam propagation along an axial magnetic field is the breakup of the beam into discrete vortex-like current bundles when a threshold determined by either the beam current or distance of propagation is exceeded (Buneman et al. 1992; Peratt and Snell 1985; Shishlov et al. 2002; Krejci et al. 1993; Dessler 1983; Peratt 1992).

The phenomena, when observed closely, resembles that associated with the Kelvin-Helmholtz fluid dynamical shear instability, in which vortices develop throughout a fluid when a critical velocity in the flow is exceeded, with a large increase in the resistance to flow (Alfvén and Carlqvist 1978).<sup>1</sup>

While structural changes in the azimuthal direction are observed in solid, annular, or sheet beams, it is with thin-sheath hollow electron beams that the vortexing phenomenon is most pronounced. Thin plasma hollow beams are naturally produced and are capable of conducting currents exceeding those given by the characteristic Alfvén value (Alfvén 1981).

For strong magnetic, field low density beams, the *cross-field electron beam parameter* is given by

$$q = \omega_{pe}^2 / \omega_{ce}^2 \quad (12.1)$$

where  $\omega_{pe}^2 = n_e e^2 / m_e \gamma \epsilon_0$ ,  $\omega_{ce} = eB / m_e \gamma$ , and  $\gamma = (1 - \beta^2)^{-1/2}$ , and  $\beta = v_z / c$  for a beam of axial velocity  $v_z$ .

For strong magnetic field low-density beams,  $q < 1$ , and for a beam of thickness  $\Delta r$ , the instability occurs at long wavelengths

$$\lambda \approx (\pi / 0.4) \Delta r \quad (12.2)$$

---

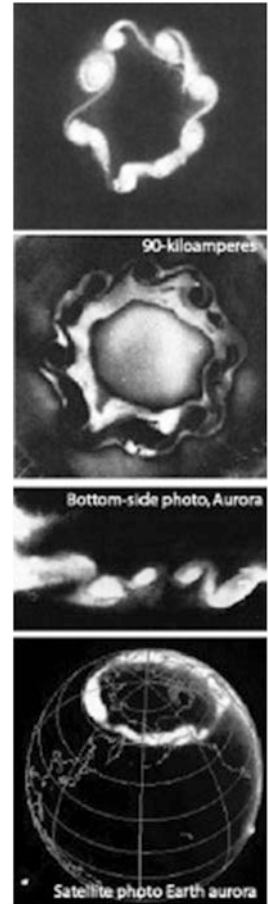
<sup>1</sup> The same is true of proton beams but because of the  $1,836 m_p / m_e$  mass difference, the proton beam evolution is slowed considerably in computational analysis, Chap. 3.

The  $e$ -folding length for instability buildup is

$$L = \lambda C B_z V / I \quad (12.3)$$

where  $C$  is the beam circumference,  $B_z$  is the longitudinal magnetic field,  $V$  is the voltage, and  $I$  is the current in MKS units. [Shishlov et al. \(2002\)](#) have studied the cross-sectional views of hollow beams with conducting currents from  $7\ \mu\text{A}$  to  $6\ \text{MA}$ , over 12 orders of magnitude in current. The onset of the diocotron instability satisfying (3) is shown in Fig. 12.1.

**Fig. 12.1** Frame 1 (*top*):  $58\text{-}\mu\text{A}$  hollow electron beam recorded on a fluorescence screen (Courtesy of H. Webster, General Electric). Frame 2: diocotron instability recorded on a steel witness plate impacted by a hollow  $90\text{-kA}$  beam at Los Alamos National Laboratory. Frame 3: ground view of overhead aurora (approximately  $1\ \text{MA}$ ) from televised frame (Courtesy of T. Hallinan). Frame 4: auroral activity around Arctic on July 15, 2000 (Courtesy of NASA/IMAGE far-ultraviolet archive)





### 12.1.2 Evolution of Field-Aligned Currents

In its simplest, the Biot-Savart Force law states that current filaments or wires running in the same direction attract, while those in opposite directions repulse. For plasmas there is a neutral force region where the filaments do not merge but rather start a rotational motion around each other to form a vortex-like geometry. In the laboratory, this is most often seen for the closest pairs of filaments but also for three and more filaments (Kukushkin et al. 1999).

Figure 12.2 is an artist's illustration of a hollow relativistic charged-particle beam forming individual current filaments while Fig. 12.3 shows their merging sequence.

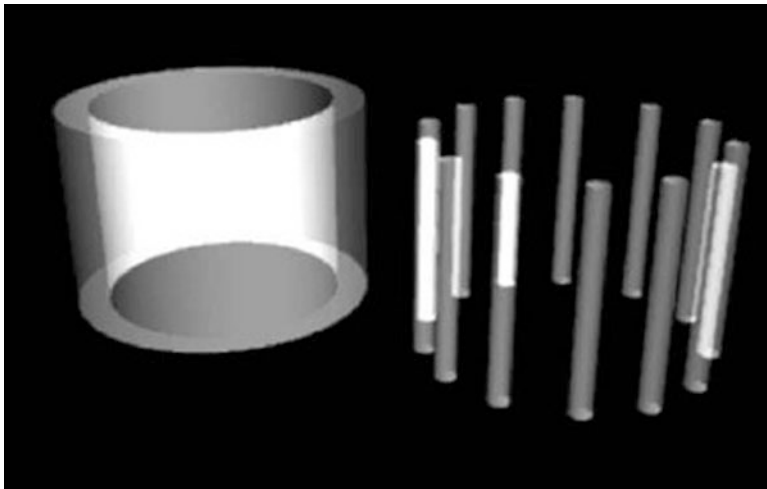
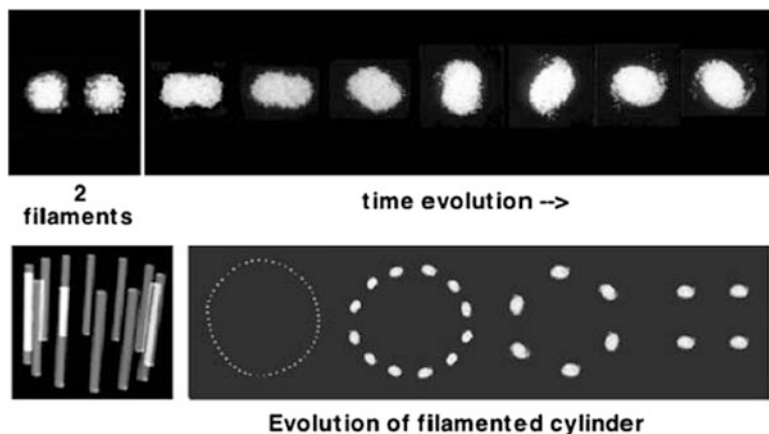


**Fig. 12.2** Basic characteristic of a very thin plasma sheath of relativistic electrons and ions flowing along a longitudinal (vertical) magnetic field; the sheath filaments into 56 current filaments

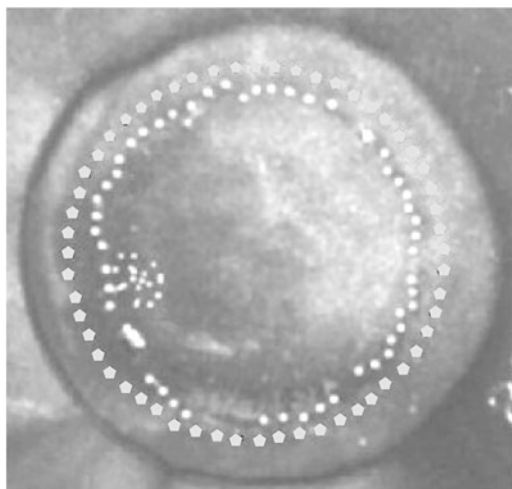
Figure 12.4 shows the pattern of a 90-kA electron beam from a thin circular cathode as recorded on a steel witness plate. The periodicity of the beam filaments impacts into the steel plate (white dots) is 56. For comparison purposes, a circle of 56 evenly spaced outer hexagonal fiducial markers has been superposed onto the witness plate.

Figure 12.5 shows the pattern created on a witness plate of the oppositely directed ion-beam filaments. The outer ring, 75  $\mu\text{m}$  in diameter, numbers 28 filaments. Slightly inside the outer ring is are 28–33 irregular shaped (likely merging or rotating) deposits. Far to the center are four ‘posts,’ a “quadrupole structure”.

The behavior and merging of inflowing filaments is shown in Fig. 12.6 shows a streak camera recording whereby a group of plasma filaments are open-shutter photographed through a slit aperture focused across the array. In Fig. 12.6, time increases from top to bottom. At the top, the photograph shows six filaments (one of the six is shielded by a filament in front of it) in Biot-Savart attraction. In addition,



**Fig. 12.3** *Top:* particle-in-cell time evolution of two adjacent filaments, as shown by the cross sections of the plasma. Two, and sometimes three, filaments are drawn together to form a vortex structure. *Bottom:* rendition of 56 filaments converging to four currents during current increase illustrates the merging of adjacent filaments, starting with 56, to end with four



**Fig. 12.4** Pattern of a 90-kA particle beam from a thin circular cathode as recorded on a steel witness plate (*white dots*). The periodicity of the beam filaments is 56 as determined by the outer circle of pentagon-shape fiducial markers

seen in the early stages of the filaments are micropinches. The filaments converge to a strong pinch (center) where they twist into a helix structure before untwisting back into six filaments (bottom).

A framing camera was used to capture the twisting filaments at maximum pinch. The resulting “helix” is shown in Fig. 12.7.

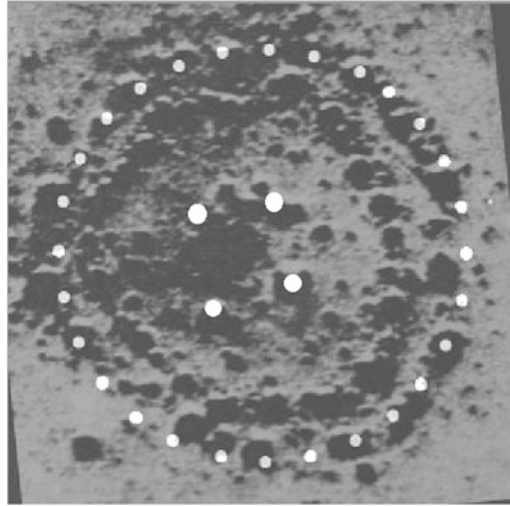


**Fig. 12.5** Pattern of the ion beam filaments (28) deposited on a witness plate in the direction opposite the 90 kA electron beam. At the center is a quadrupole, 4 ion deposits

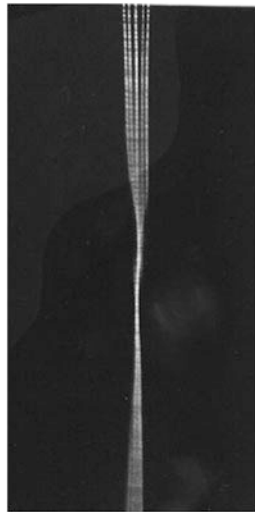


**Fig. 12.6** Streak camera recording with image slit focused across (horizontal direction) six 5-MA current-conducting plasma columns. Time runs from top to bottom, with the columns converging and twisting at the center before separating (A. Peratt, LANL)

As shown in Fig. 12.8, the most common pairing or tripling, as determined from a large collection of observations is 56 (by far the most common), 49, 47, 41, 39, 33, 30, followed by a large number of 28-ray petroglyphs and other structures

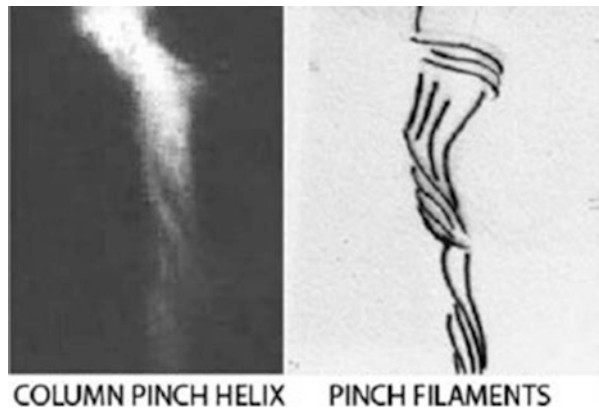


**Fig. 12.7** *Left*: Time-frame, single instant, x-ray photograph of plasma pinch. *Right*, densitometer enhancement reveals six filaments are present in the helical pinch. Converging and twisting are typical of filaments in experimental and simulation filaments

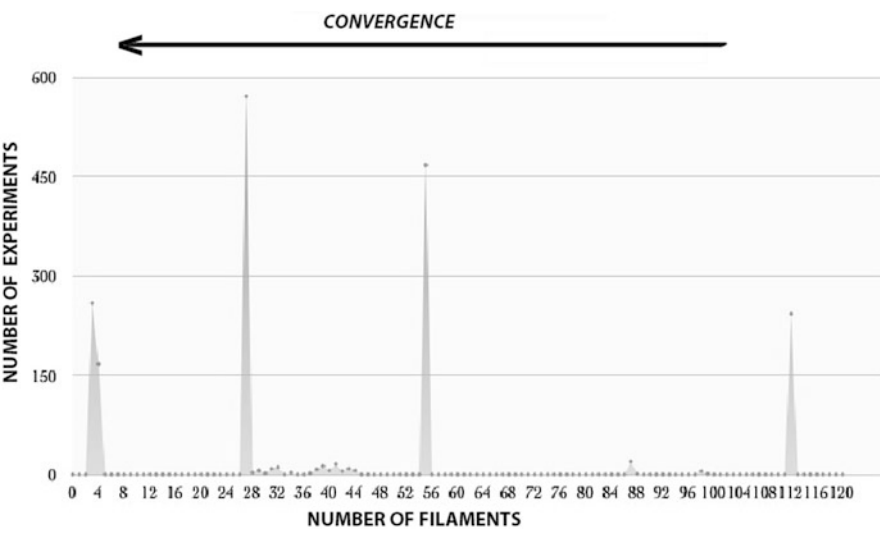


**Fig. 12.8** The most common pairing or tripling, as determined from record surveys, is 224, 112, 56 (by far the most common), 49, 47, 41, 39, 33, 30, followed by a large number of 28-ray recordings and other structures. The convergence of filaments via the Biot-Savart force is to the left and continues through 20, 16, 8, 7, 6, and 4, the latter being the minimum number of Birkeland currents recorded, but in great frequency

(Mountford 1960). The converging continues through 20, 16, 8, 7, 6, and 4, the latter being the minimum number of Birkeland currents recorded but in great frequency.

Also important are 112 ( $2 \times 56$ ) filaments, the number prior to the merging to 56.

## 12.2 Dense Plasma Focus (DPF)

The DPF is among the most interesting of high-energy plasma devices. A capacitor bank, or a highly explosive magnetic-compression generator, is discharged through two coaxial electrodes, called a *plasma gun*, forming a plasma current sheath between the inner and outer electrodes. The  $j \times B$  force accelerates the sheath outward to the ends of the electrodes where the inner sheath radius is forced inwards toward the center electrode forming a columnar pinch or “focus” on axis. The outer sheath, the “penumbra,” is a chalice of current filaments (Milanese and Moroso 2005). The inner electrode is usually the anode.

According to Haines (1981): Many of the earliest experiments in controlled thermonuclear fusion research were Z-pinches. However, they were found to be highly unstable to the  $m = 0$  (sausage) and the  $m = 1$  (kink) MHD instabilities, and to the  $m = 0$  Rayleigh–Taylor instability.

However, as experimentalists were searching for more stable configurations, the plasma focus found other applications other than laboratory fusion and on other scales. Plasma foci since have been found in the solar system, e.g., on the surface of Jupiter’s satellite Io (Chap. 4).

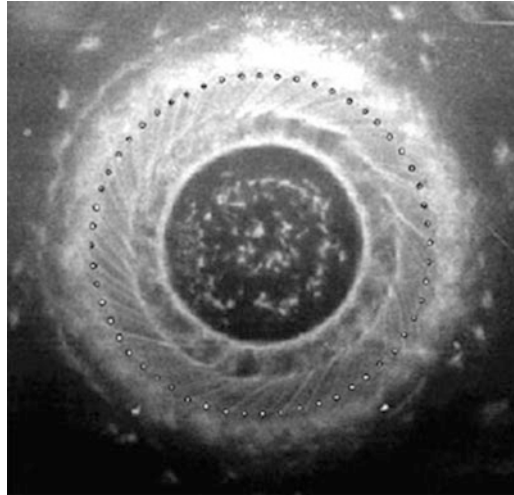


**Fig. 12.9** Penumbra of a DPF from a discharge current of 174 kA. The rotational structure has a periodicity of 56 as shown by the 56-dot overlay pattern

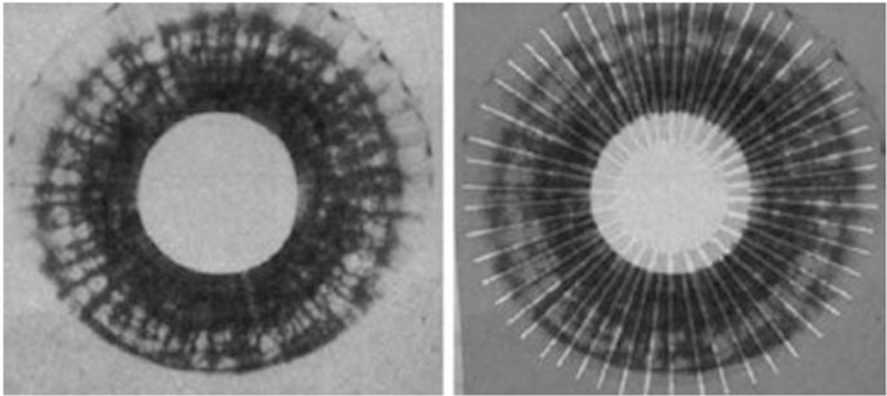


**Fig. 12.10** Penumbra of a 1.8-MA DPF with 56 pairs of filaments as shown by the 56-rayed pattern overlay

Studies of the plasma focus, which after 3-D compression on axis, closely resembles a Z-pinch. Diagnostics show that a plasma of density  $10^{25} \text{ m}^{-3}$  and an electron temperature of 1 keV can be achieved in a narrow filament a few millimeters in diameter and about a centimeter in length. It sometimes can have enhanced stability properties which might be attributable to the effect of the finite ion Larmor radius.

With regard to the DPF, the usual number of filaments formed in the penumbra or “chalice” at the pinch is either 56 or 56-paired filaments. Figure 12.9 shows the penumbra created at pinch in a 174-kA discharge-current DPF. The periodicity of this chalice structure is 56. Figure 12.10 is the penumbra created at pinch in a 1.8-MA discharge-current DPF.

At this higher current, 56 pairs of filaments are discernable in the open-shutter photograph. The figure to the right is an overlay of 56 lines on top of each filament pair. [Milanese and Moroso \(2005\)](#), using a low-power 250-kA DPF, report about 60 filaments recorded by their image converter camera in a series of time-evolution photographs. Figure 12.11 shows the penumbra of a 250-KA DPF.

### 12.3 Evolution of Plasma Filaments via the Biot-Savart Force

As an example, Fig. 12.6 shows a streak camera recording whereby a group of plasma filaments are open-shutter photographed through a slit aperture focused across the array. In Fig. 12.6, time increases from top to bottom. At the top, the photograph shows six filaments (one of the six is shielded by a filament in front of it) in Biot-Savart attraction. In addition, seen in the early stages of the filaments are micropinches. The filaments converge to a strong pinch (center) where they twist into a helix structure before untwisting back into six filaments (bottom).

A framing camera was used to capture the twisting filaments at maximum pinch. The resulting “helix” is shown in Fig. 12.7.

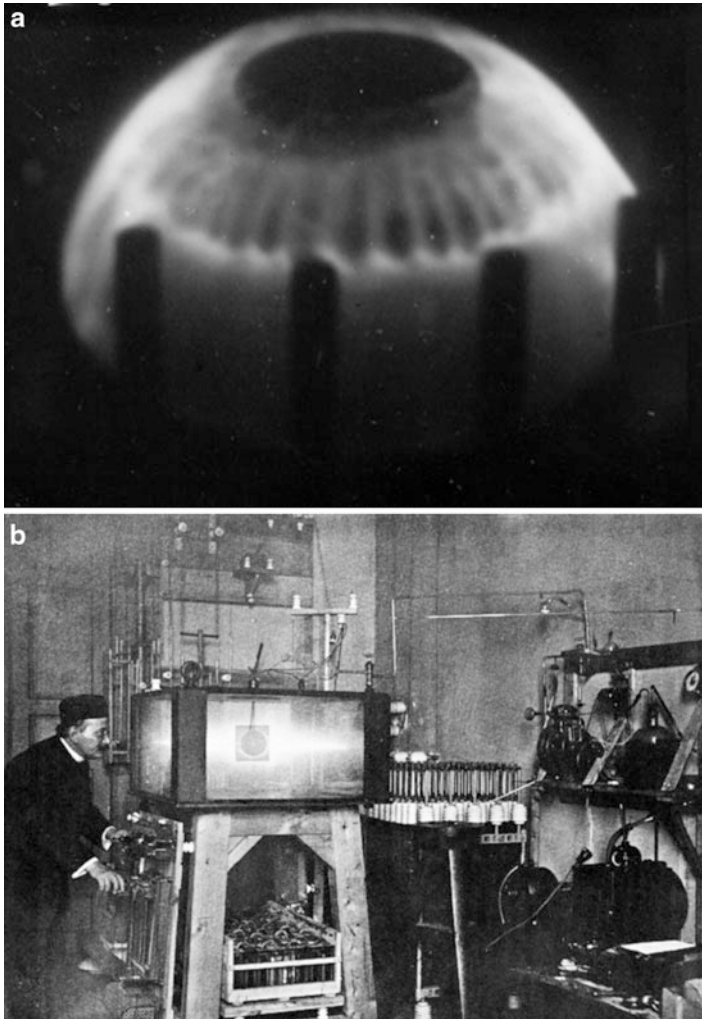


**Fig. 12.11** Penumbra of a 250-kA DPF with approximately 56 pairs of filaments. The outer black objects are the return current posts

## 12.4 Birkeland's Terrella Experiments

As Professor of Physics at the Royal Frederik University in Kristiania (Oslo), Kristian Birkeland laid foundations for our current understanding of geomagnetism and polar auroras (Chap. 2). In 1901, Birkeland initiated a new set of laboratory simulations that he called *Terrella Experiments*.<sup>2</sup> His purpose was to prove incontrovertibly the correctness of his theoretical interpretation of auroral and geomagnetic

---

<sup>2</sup> Terrella, Latin for “Little Earth”.

disturbances. For the first time cosmic phenomena were scaled and simulated in a laboratory. His terrella experiments were at once simple and ingenious. He fully believed that the laboratory experiments would confirm his understanding of auroras. They opened new paths suggesting how electromagnetic forces might operate in the solar system.

Birkeland's life (1867–1917) spanned a watershed period in the understanding of our planet and its environment. Insights about electricity and magnetism, codified by Maxwell (Sect. 1.1, page 1) in the mid-nineteenth century, evolved from theoretical curiosities to become the basis for our electronic technology and eventually what is now called *The Space Age*, the understanding of the geospace environment (Egeland and Burke 2005).

While the Earth's magnetic field had been accurately measured, it was not known if the Sun possessed a magnetic field, and the atmosphere and layers around the Earth were completely hypothetical (Walker 1861).

While many theories existed as to the cause of the Aurora Borealis, the Northern Lights so clearly seen on Earth at high latitudes, Birkeland was the first to systematically study them with modern scientific methodology: hypothesis, mathematical analysis, and finally measurement and observation with world-wide data.

Under the guidance of Henri Poincaré, Birkeland turned to the study of Maxwell's equations and the motions of charged particles in a magnetic monopole field. To prove that there existed charged particles in space and that these followed supposed magnetic fields in space, Birkeland started a series of experiments whose results he would compare to geophysical observations.

To do so, he constructed in his laboratory, a vacuum chamber (a 1,000 L pumped-down aquarium) into which he placed a thin brass globe coated with either phosphorescent paint or oil in order to observe the electron spatial distributions and dynamics. An electromagnet was placed within the brass globe to simulate Earth's geomagnetic dipole field. Within the chamber, the earthed (grounded) globe was bombarded with *cathode rays*, electron beams produced by a cathode placed near a wall of the vacuum chamber.

Given the size and capabilities of his battery bank and electromagnet (to produce the simulated Earth field) and his high-voltage generator (to produce the electrons), his experimental parameters, when scaled, were remarkably close to the what is observed and measured around Earth today. His diagnostics, eight cameras surrounding the dc driven terrella experiment with concomitant recording screens, are completely familiar to pulsed energy physicists today who design multi-megajoule magnetic fusion Z machines (Chap. 2) or record underground nuclear detonations.

Altogether, Birkeland constructed 17 terrella's.<sup>3</sup> These ranged in size from 2–70 cm in diameter.

Birkeland's solar and cosmic phenomena were made at a time when other scientists maintained that the Earth was surrounded by vacuum (Birkeland 1908).<sup>4</sup>

<sup>3</sup> Private communication with A. Egeland.

<sup>4</sup> The ionosphere's existence was not fully established until about 1930 by Sir Edward Appleton (1892–1965) and Douglas R Hartree (1897–1958) in Great Britain.



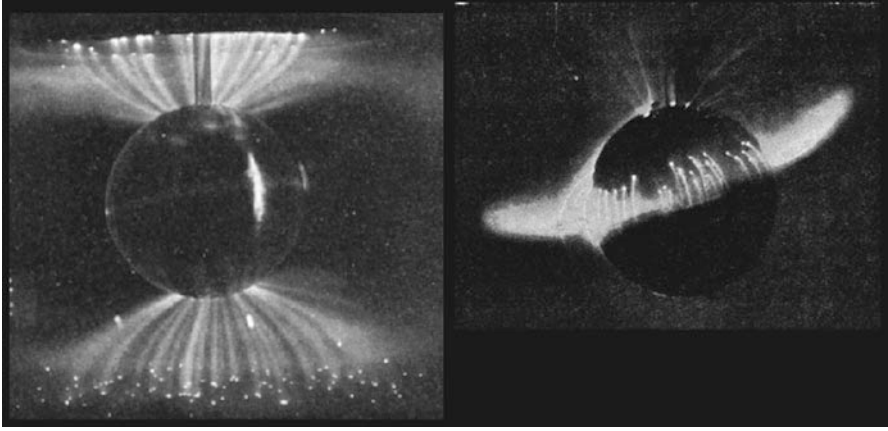


**Fig. 12.12** Birkeland's 8-cm globe. (*Left*): Experiment parameters adjusted such that the inflow-outflow currents are visible. (*Right*): Experiment parameters adjusted such that the ground or atmospheric currents are mostly visible

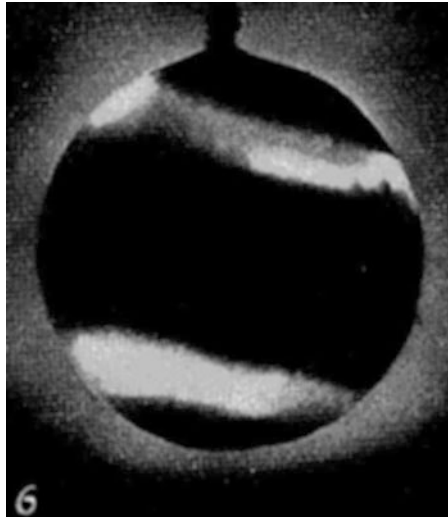


**Fig. 12.13** Birkeland's replication of the aurora borealis and the aurora australis

Figure 12.11b is a photograph of Birkeland and his terrella, a magnetized copper globe. The globe is an anode between two cathode plates in a 320 L vacuum chamber containing 0.013–0.012 mm Hg. His largest current generator could deliver 300 mA at 20 kV.

For distances less than that is given in (3), the filaments are constrained by the generalized Bennett relation (Buneman et al. 1992), or if rotation is ignored, by the Bennett relation  $\mu_0 I^2 / 4\pi = 2NkT$ . Birkeland, using eight cameras and eight screens, was apparently the first to capture the nature of these constrained filaments, as shown in Figs. 12.12 and 12.13. Depicted are currents flowing into and out of a magnetized copper globe along its axis.

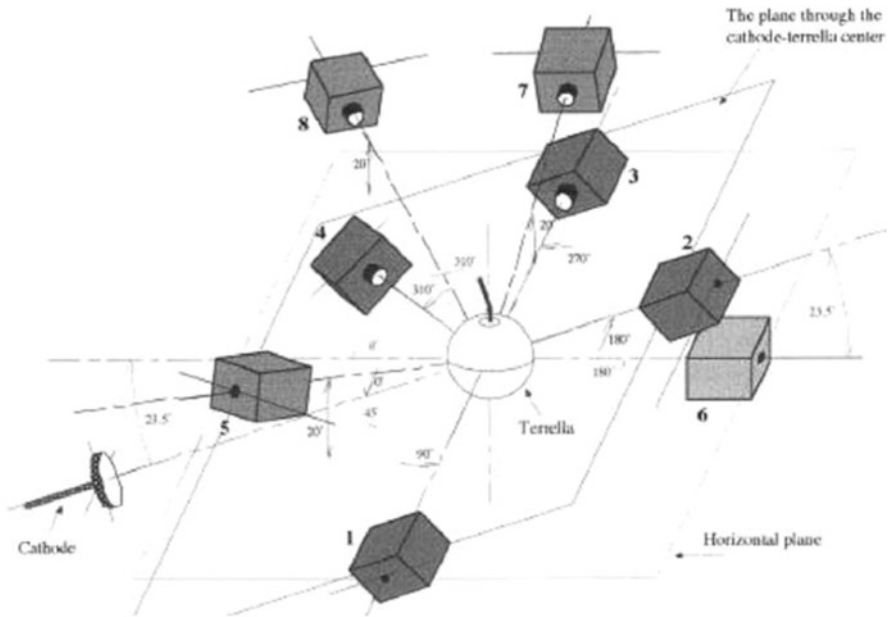


**Fig. 12.14** Birkeland's terrella's experimental setup. Eight cameras projecting light onto eight screens to map the electron trajectories (Courtesy, A. Egeland)

In his other photographs, the filaments (surface currents or ionospheric currents) can be seen running along the surface of the globe.<sup>5</sup>

As current was increased to the electromagnet within the globe to simulate the Earth's magnetic dipolar field, the currents were forced toward the poles of the terrella, eventually satisfying (3) to produce "auroral" rings around each pole. Densitometer scans across the Bennett-constrained currents in his photographs show approximately 56 filaments, many in pairs.

## 12.5 Birkeland's Trips to Egypt

Birkeland had done research in Egypt and Sudan in 1910, moving there in 1913 and remaining for nearly 3 years (Egeland and Burke 2005). The purpose reported was his interest in *zodiacal light*. There is reason to wonder if other observations of *light* in the laboratory raised his interest in this country lying at  $30^\circ\text{N}$  latitude as compared to Oslo at  $70^\circ\text{N}$ . Birkeland had spent much effort preparing a treatise that reportedly was nearly as complete as his earlier treatises.

<sup>5</sup> A terrella is a magnetized sphere in a vacuum chamber; electron beams are shot against the sphere; residual gas in the chamber makes the path of the beams visible as they are bent by the magnetic field of the sphere.



**Fig. 12.15** Birkeland's dilemma: how to travel from Cairo to Oslo in 1917 as WWI raged across Europe and the Ottoman Empire?

Comparison of Figs. 12.15 to 12.12, left and right,<sup>6</sup> suggests that Oslo lies near the Aurora Borealis and that Cairo lies within the atmospheric current region. It seems plausible that Birkeland, beyond compare in the interest of all things physical, would have made note of this. He must also have been aware of Walker's galvanometer "ground-current" measurements of the 1859 event.<sup>7</sup>

In the spring of 1917, Birkeland decided to return home to Norway to celebrate his upcoming 50th birthday. However his return trip was made far more complicated than his 1913 arrival as now WWI was raging in Europe. Birkeland was thus forced to return by travelling across the Indian Ocean, reaching Tokyo in early May where he fell ill, dying June 15, 1917 before his 50th birthday.

As detailed by Egeland and Burke, some time after Birkeland's death word came that the "Peking" carrying Birkeland's belongings, including his Egyptian treatise, was lost off the Korean coast. Thus we might never know what it contained but shall pursue possibilities in Chap. 13.

<sup>6</sup> And taking "north" as "up".

<sup>7</sup> While we have no notes to prove this; supporting evidence is given in Chap. 13.

## 12.6 Macro–Terrella Experiments

To realistically record a topside Birkeland high-current evolution as viewed from a ‘ground’ level, requires a sophisticated experimental setup of a size reasonable for cameras viewing  $4\pi^2$  at the terrella surface (Peratt 1988b).

The need to study high-energy electrons impacting a high-vacuum terella requires more than a tabletop experiment. A relevant experiment would be a terella lowered down-hole with concomitant viewing enclosure and fast diagnostics, subjected to the fluence of a typical nuclear detonation. This would show current filaments flowing systematically over its surface (U.S. Department of Energy, (1993) Announced United States Nuclear Tests, DOE/NV-209, UC-700, pp. 1–104). However, cessation of nuclear testing between the United States and Russia in 1993 now precludes this area of research.

## 12.7 Properties of a Strong Aurora

An estimate for the currents in a strong aurora can be obtained from Alfvén and Carlqvist (1978) who find, for a strong circular aurora of diameter 5,000 km, a total current of about 7 MA. If this pertains to 56 filaments (before the ring is formed), each filament conducts 125 kA. Hence, Eq. (2.60) is satisfied, and the currents remain as pinched filaments.

In an intense aurora, the giga-ampere current flow and concomitant strong magnetic field produces a major change in the auroral-height profile. Because of the intense plasma flow and strong longitudinal magnetic field, the plasma forms a thin but dense sheath or plasma column in its propagation toward Earth.

The in-flowing plasma is a Z-pinch, and as a result, Z-pinch instabilities form as well as intense radiation from the relativistic electrons. The intense radiation consists primarily of X-rays and synchrotron radiation in the visible.

## 12.8 Temporal Occurrence and Properties of Intense Auroras

The properties of intense aurora described by Gold (1962) appear to be similar to the properties of a column of plasma-conducting giga-amperes of current rather than mega-amperes.

According to Gold, a very intense aurora might be expected to occur every several thousand of years or even every 10,000 years.

A 1,000-fold increase of a concurrent aurora is 7 GA, or for 56 filaments, 1.25 MA carried by a filament REB. This is what was seen in antiquity, often carved on granite or recorded in other ways (Chap. 13).

## 12.9 The Carrington Event

The Carrington event, August 27–September 6, 1859, was the most famous solar storm in modern history and, for the first time, verified that the Sun and aurora were connected by strong ionospheric currents (Clark 2007). A significant portion of 200,000 km of telegraph lines on Earth were adversely affected, some made inoperable for 8 h. At its height the Type A aurora was described as blood or deep crimson red that was so bright that one “could read a newspaper by”.

On August 28, 1859 a major solar storm caused spectacular aurora seen all over the globe. It was reported in all the major newspapers, poems were written about it, and famous artists painted its shapes and forms. It also caused severe problems with telegraph networks at the time, which lasted for many hours world-wide. Reports from widely different locations on Earth have been given by Clauer and Siscoe (2006) and Green et al. (2006).

1. Galveston, Texas: “August 28 as early as twilight closed, the northern sky was reddish, and at times lighter than other portions of the heavens. At 7:30 PM a few streamers showed themselves. Soon the whole sky from Ursa Major to the zodiac in the east was occupied by the streams or spiral columns that rose from the horizon. Spread over the same extent was an exquisite roseate tint which faded and returned. Stately columns of light reaching up about 45 degrees above the horizon moved westward. There were frequent flashes of lightning along the whole extent of the aurora. At 9:00 PM the whole of the streaking had faded leaving only a sort of twilight over the northern sky.”
2. London, England: “At 0:15 AM on August 28th the auroral light in the north assumed the form of a luminous arch, similar to daybreak, and in the southwest there was an intense glare of red covering a very large extent of the sky. At 00:20 AM streamers appeared; at 00:25 AM the streamers rose to the zenith and were tinged with crimson at their summits. At 00:45 AM frequent coruscations appeared in the aurora. At 01:20 AM the arch which had partially faded began to reform and the body of the light was very strong but not bright enough to read newspaper print. At 1:30 AM the light had begun to fade. By 2:00 AM the aurora was very indistinct.”

Certainly, these descriptions do not match what is seen during today’s auroras. However, historically, such accounts are found nearly every few centuries; stronger events every century, and cataclysmic events every several millinnea.

A complete picture of the Earth-current environment is made possible from historical eye-witness accounts, telegrapher’s galvanometer needle deflections, and from a number of terrella experiment observations. This is shown in Fig. 12.16: 56 current filaments along a N-S axis enclosing an eastward turning globe whose altitude is determined by the strength of the current driving the filamentation.

This geometry (Fig. 12.16), as observed from different locations on the globe at eye-level will be investigated in Chap. 13.

An artists depiction of the synchrotron emitting atmospheric currents is shown in Fig. 12.17.

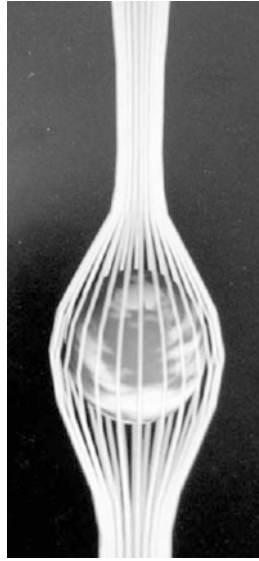


**Fig. 12.16** This figure is the analog of Fig. 12.12 if the left and right (ground or atmospheric currents) were overlaid



**Fig. 12.17** Red auroras were considered a sign of ill omens during medieval times and pilgrimages were organized to avert the wrath of Heaven. Brilliant displays have frightened people as recently as this century in regions where aurora sightings are rare (Courtesy of Zentral Bibliothik, Zurich: from S.-I. Akasofu)

Historical accounts suggest that intense aurora differs from concurrent aurora in several aspects. One Chinese account (translated from Sung-Shih) is,

Red cloud spreading all over the sky, and among the red bands of white vapor like glossed silk penetrating it. They arose from Tzu-wei, invading the Great Dipper and the Wen-Chang, and then dispersed from the southeast.

In Europe during medieval times,

Swords, spears, white vapor, like glossed silk penetrating, candles in the sky, a red sky patterned with white stripes stretching from horizon to horizon.

and in Europe, North America, and other parts of the world in 1859,

A vivid red light on the landscape and 'a thousand fantastic figures, as if painted with fire on a black ground'

## 12.10 THEMIS Mission

THEMIS, Time History of Events and Macroscale Interactions during Substorms, is a European Space Agency (ESA) venture, a quintet of satellites located about 40,000 km above the Arctic pole. THEMIS is the first experiment in the near-Earth plasma to study macroscale physics during auroral substorms and greatly expanded since its initiation in 2007 (Burch and Angelopoulos 2012; Peratt et al. 2009; Rantsev-Kartinov 2006).<sup>8</sup>

The THEMIS spacecraft discovery of large holes in the Earth's magnetosphere explains an anomaly in the global distribution of petroglyphs on our planet (Li 2007). Previously it was reported on the GPS world-wide logging of some four-million of these objects, each a picture of a filamental MHD instability carved in rock (Peratt 2003; Peratt et al. 2007; Qöyawayma and Peratt 2007; Yao and Peratt 2007).

THEMIS researchers have also uncovered what appears to be the earliest records of what was seen in antiquity regarding aurora; 30,000 B.C. Cro-Magnon cave paintings depictions of aurora (Sisco 1976; Eather 1980). Other ancient pictograph recordings, written in 2,600 B.C. in China include "Fu-Pao, the mother of the Yellow Empire Shuan-Yuan (Aurora History 2009)".

NASA, in the 2007 annual meeting of the American Geophysical Union, reported on the time history of events and macroscale interactions during substorms. The

---

<sup>8</sup> An anonymous referee, when asked by the Austrian Science Fund to evaluate a new proposal entitled "TCR evolution and energy transport in the Earth's magnetotail", replied, "This is an excellent topic of inquiry and much needed for continued understanding of our near-Earth plasma environment. The database, to date, is inadequately tapped and should greatly enhance our understanding of the complex phenomena, largely unanticipated but discovered in the THEMIS mission. From a scientific point-of-view, this undertaking is certainly worthy of funding from the scientific agencies."



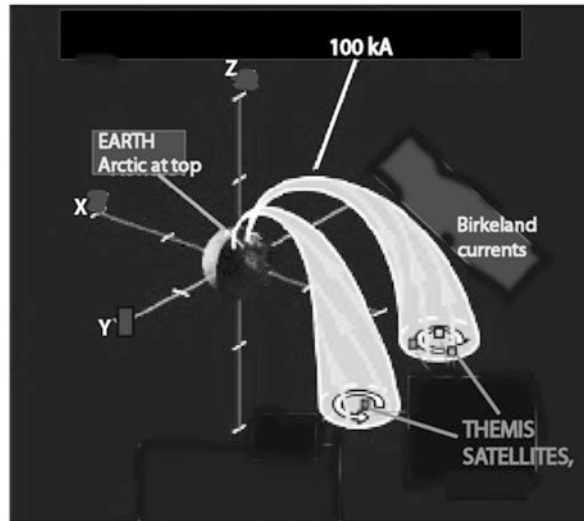


**Fig. 12.18** IBirkeland currents flowing to Earth's arctic as measured by the five THEMIS satellites (probes) above the Arctic. This partial coverage was to investigate the properties of the polar auroras, capturing the twisting nature of two of the 100 kA currents as well as their inflow paths

quintet of THEMIS satellites observed the dynamics of a rapidly developing sub-storm and unequivocally confirmed the existence of giant magnetic ropes in the solar system and near-Earth environment (Fig. 12.18).<sup>9</sup>

## References

- V. Angelopoulos, The THEMIS Mission, *Space Sci. Rev.*, doi: 10.1007/s11214-008-9336-1, (2008)
- Alfvén, H.: *Cosmic Plasma*. Reidel, Dordrecht (1981)
- Alfvén, H., Carlqvist, P.: Interstellar clouds and the formation of stars. *Astrophysics and Space Science* **55**(2), 487–509 (1978)
- Aurora History, THEMIS: THEMIS E/PO, April 27 (2009)
- Birkeland, Kr.: *The Norwegian Aurora Polaris Expedition 1902–1903*. H. Aschehoug, Christiania (1908)
- Buneman, O., Neubert, T., Nishikawa, K.L.: Solar wind magnetosphere interaction as simulated by a 3-D, EM particle code. *IEEE Trans. Plasma Sci.* **20**, 810 (1992)
- Burch, J.L., Angelopoulos, V.: *The THEMIS mission*. *Space Sci. Rev.* **141**(1–4), Springer (2008)
- Clark, S.: *The Sun Kings*. Princeton University Press, Princeton (2007)

<sup>9</sup> The symmetry of the two polar currents suggest that full 360° satellite coverage might reveal the existence six currents.



- Clauer, C.R., Siscoe, G.: The Great Historical Geomagnetic Storm of 1859: A Modern Look, p. 117. Elsevier, Oxford (2006)
- Dessler, A.J.: The evolution of arguments regarding the existence of field-aligned currents. In: Magnetospheric Currents. Geographical Monograph, vol. 48, pp. 22–28. American Geophysical Union, Washington, DC (1983)
- Eather, R.H.: Majestic Lights; the Aurora in Science, History, and the Arts, vol. 34. American Geophysical Union, Washington, DC (1980)
- Egeland, A., Burke, W.J.: Kristian Birkeland, the First Space Scientist. Springer, Dordrecht/New York (2005)
- Gold, T.: Large solar outburst in the past. *Pontificiae Academiae Scientiarum Scripta Varia* **25**, 159–174 (1962)
- Green, J., Boardsen, S., Odenwald, S., Humble, J., Pazamickas, K.: Eyewitness reports of the great auroral storm of 1859. *Adv. Space Res.* **38**(2), 145–154 (2006)
- Haines, M.G.: Dense plasma in Z-pinches and the plasma focus. *Philos. Trans. R. Soc. Lond. A Math. Phys. Sci.* **300**(1456), 649–663 (1981)
- Krejci, A., Raus, J., Piff, V., Golubev, A.V., Platoov, Y.Y., Krousky, E., Renner, O.: Multichannel soft X-ray diagnostics of hot plasma evolution in nitrogen-puff Z-pinch. *IEEE Trans. Plasma Sci.* **21**(5), 584–587 (1993)
- Kukushkin, A.B., Rantsev-Kartinov, V.A.: Self-similarity of plasma networking in a broad range of length scales: from laboratory to cosmic plasmas. *Rev. Sci. Instrum.* **70**(22), 1387–1391 (1999)
- Milanese, M.M., Moroso, R.L.: The first stages of the discharge in a low-energy dense plasma focus. *IEEE Trans. Plasma Sci.* **33**(5), 1658–1661 (2005)
- Mountford, C.P.: Simple rock engravings in Central Australia. *Man* **60**, 145–147 (1960)
- Li, W., Shprits, Y.Y., Thorne, R.M.: Dynamic evolution of energetic outer zone electrons due to wave-particle interactions, **112**(A10) (2007) [onlinelibrary.wiley.com](http://onlinelibrary.wiley.com)
- Peratt, A.L.: Magnetic flux compression generator powered electron beam experiments. In: Fowler, C.M., Caird, R.S., Erickson, D.J. (eds.) *Megagauss Technology and Pulsed Power Applications*. Plenum Press, New York (1988)
- Peratt, A.L.: *Physics of the Plasma Universe*. Springer, New York (1992)
- Peratt, A.L.: Characteristics for the occurrence of a high-current Z-pinch aurora as recorded in antiquity. *IEEE Trans. Plasma Sci.* **31**(6), 1192–1214 (2003)
- Peratt, A.L., Snell, C.M.: Microwave generation from filamentation and vortex formation within magnetically confined electron beams. *Phys. Rev. Lett.* **54**, 1167 (1985)
- Peratt, A.L., van der Sluijs, M.A., McGovern, J., Bustamante, P.: Virtual image reconstruction of an intense Z-pinch aurora at Earth's southern axis from archaic petroglyphs. In: *Proceedings of the IEEE Pulsed Power and Plasma Science Conference*, Albuquerque, p. 623 (2007)
- Peratt, A.L., Yao, W.F., Bustamante, P., Tuki, R.: The THEMIS magnetospheric breach discovery; MHD recorded in antiquity. In: *APS 2009 April Meeting*, Denver, 2–5 May 2009

- Qöyawayma A.H., Peratt, A.L.: The influence of 56 synchrotron radiating Birke-land filaments formed in an archaic auroral sheath on man-made structures and artifacts found worldwide. In: Proceedings of the IEEE Pulsed Power and Plasma Science Conference, Albuquerque, p. 623 (2007)
- Rantsev-Kartinov, V.A.: Observation of the sun self-similarity skeletal structures. In: Proceedings of the Conference on Abstracts IEEE International Conference on Plasma Science, Traverse City, p. 269 (2006)
- Shishlov, A.V., Baksht, R.B., Labetsky, A.Y., Oreshkin, V.I., Rousskikh, A.G., Fedunin, A.V., Chaikovsky, S.A., Kokshenev, V.A., Kurmaev, N.E., Fursov, F.I.: Experimental study of an argon-hydrogen Z-pinch plasma radiation source. IEEE Trans. Plasma Sci. **30**(2), 498–511 (2002)
- Sisco, G.L.: Solar-terrestrial relations: stone age to space age. Technol. Rev. **79**, 26 (1976)
- Walker, C.V.: On magnetic storms and Earth-Currents. Philos. Trans. R. Soc. Lond. **151**, 89 (1861)
- Yao, W.F., Peratt, A.L.: Observations of a quadruple from recordings of an intense aurora in prehistory: three rivers petroglyphs. In: Proceedings of the IEEE Pulsed Power and Plasma Science Conference, Albuquerque, p. 624 (2007)

# Chapter 13

## Plasma Astrophysics

The study of astrophysics in modern times should essentially involve the application of laboratory results to cosmical problems, with help from theoretical physics. In the realm of plasma physics, there appears to be no reason why known basic laws, formulated in the laboratory, should not hold just as well at the astrophysical and cosmological scale.

Hannes Alfvén, *Plasma Physics Applied to Cosmology*, Physics Today, 1971.

### 13.1 The Cosmic–Triple–Jump

From the latter half of the nineteenth century through the twentieth century, research on the plasma state of matter led to a number of discoveries revealing a close tie of the physics of plasmas at the smallest known scale, e.g., the flow of charged particles in crystal lattices, to microampere particle beams, to intense particle beams, to the currents associated with planetary and solar plasmas, to the interstellar medium, to galaxies, and intergalactic plasmas (Alfvén 1971).<sup>1</sup>

Alfvén made note that the plasma, or original state of matter, scaled. It was found experimentally and verified numerically, that the dimensionless parameters were valid regardless of whether the plasma was measured in microns or gigaparsecs (Fig. 13.1).

From this, Alfvén hypothesized a *Cosmic–Triple–Jump* for the state of plasma, scaled according to size but equally valid in other dimensionless parameters. In size he chose  $10^9$ , such that starting with his smallest dimension, laboratory plasma, he could scale in three  $10^9$  m (*giga*)—steps to the Hubble distance (Alfvén 1975, 1983, 1986; Gurnett and Bhattacharjee 2005, 2009; Kukushkin and Rantsev-Kartinov 1999; Suplee 2009).

That 27 orders of magnitude is not beyond human comprehension, the reader should consult T. Eastman (2013) and C. and R. Eames article on powers of 10 (Eames and Eames 2011).

---

<sup>1</sup> A word revealing its antiquity is “space” suggesting emptyness.

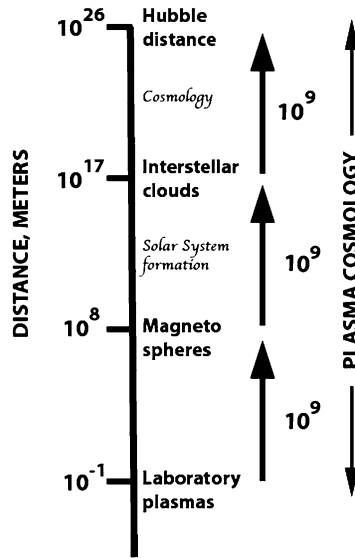


**Fig. 13.1** Cosmic triple jump in the plasma universe. From laboratory experiments to cosmological distances, experiments, simulations, and observations suggest the plasma state and its evolution follows the same laws of physics everywhere

His hierarchy ‘jumped’ from laboratory centimeter sizes<sup>2</sup>; to magnetospheric sizes<sup>3</sup>; to interstellar clouds<sup>4</sup>; to the hubble distance.

## 13.2 Near-Earth Plasma Astrophysics

### 13.2.1 “Earth–Currents”

Again we repeat a sage prediction<sup>5</sup>:

A reason why Birkeland currents are particularly interesting is that, in the plasma forced to carry them, they cause a number of plasma physical processes to occur —. These in turn lead to consequences such as acceleration of charged particles, both positive and negative —. Both of these classes of phenomena should have a general astrophysical interest far beyond that of understanding the space environment of our own Earth.

<sup>2</sup> Laboratory plasma pinches; see Sect. 1.7.1 on page 26.

<sup>3</sup> See Sect. 1.2.2 on page 5.

<sup>4</sup> See Sect. 1.2.5 on page 16.

<sup>5</sup> The sightings of brilliant bands of light across the sky frightened people long before their medieval observation. “Earth–Currents” became known in the western–world with the invention of the compass. Today, both phenomena are known to be caused by Birkeland Currents.

Carl-Gunne Fälthammar, *Near-earth manifestations of the plasma universe, 1986* (Fälthammar 1986)

The general direction of the westward motion of the “Earth-Current” filaments were known as early as 1859 from telegraph galvanometer measurements, e.g., between Red Hill and Brighton in London (Walker 1861). However, there is little need to go through telegraphers (and scientists) current deflection logs to determine the exact current flow as mankind has measured and recorded these for tens of millennia if not longer. During intense events, the current flow is true north-south, or for intense synchrotron light emitting relativistic electrons, towards true north from geophysical south.

### 13.2.2 View of Birkeland Currents from Ica and Palpa, Peru

In South America, flat desert terrain and mesas are sometimes marked by kilometer-long, man-made lines. Most of these cross each other at various angles and others start or end with trapezoidal profiles. Construction techniques involve the up-turning of large amounts of patinated stones to show the light colored ground beneath or in areas covered by flat heavily patinated stones (pavement), flipping the stones to place the whitish under-layer on top—a technique also common to the American southwest (Fig. 13.2).

Markings such as these are found among the Lluta Valley geoglyphs near Arica, Chile, many parts of Brazil, in northern Venezuela (Deutsch and Peratt 1997), and other regions on Earth. The best known cases are the lines at Palpa, south of Ica, Peru (14.7°S, 75.1°W).

What makes the Peruvian lines unique is the sudden flaring of a straight line into a trapezoid geometry (Fig. 13.5). As seen from the ground, the Birkeland currents incoming vertically from the solar plasma above and towards Antarctica suddenly flare upwards to follow Earth’s curvature until exiting in the Arctic region. These were seen as white light on the ground, not moving for perhaps centuries.

Optically stimulated luminescence (OSL) provides a date as to when the feldspar and quartz grains of a stone surface, buried since construction of temples, limestone pyramids, and megalithic structures, gives an age for the event of the last exposure to light. This technique requires a stringent protocol for the evaluation of doses on a stone surface and an exacting extraction of the stone in the absence of any ambient light, e.g., moon, stars, etc., and field/laboratory handling. In a dark laboratory, 660±20 nm, 5–10 μW cm<sup>-2</sup>, the upper-most 2 mm slice of the light-protected stone sample was stimulated with green and blue (when possible) lasers ~ (24 mW cm<sup>-2</sup>) at the sample surface. A construction stone chosen, 20 cm below present ground level of a selected Palpa line, for which the OSL age was determined to be 56.7 ka (Greulich et al. 2005).

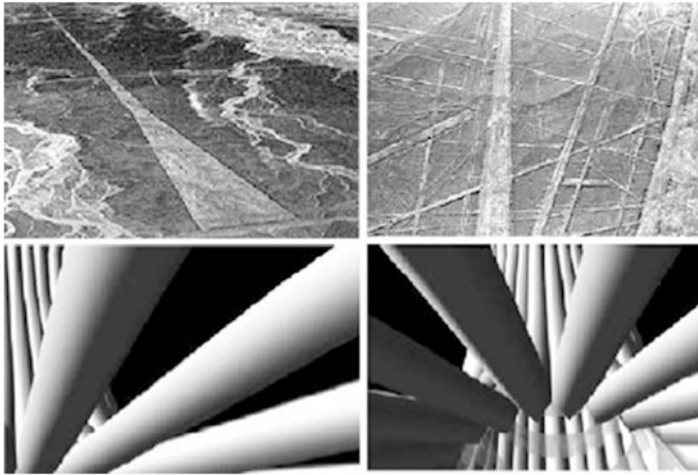


**Fig. 13.2** *Top*: Palpa lines, *Bottom*: Birkeland filaments as seen from ground level at approximately  $14^{\circ}\text{S}$ ,  $75^{\circ}\text{W}$

### 13.2.3 Mandalas or Concentric Circles in the Southern Hemisphere

Near Palpa, along the Panamerican highway to the Cerro Carapo, situated on a mesa overlooking the Rio Viscas, are a set of large 3-concentric mandalas ( $14^{\circ}32'\text{S}$ ,  $75^{\circ}10'\text{W}$ ) oriented approximately in a SW-NE direction. Concentric cairns that number 14, 28, 56, 112, and 224 have been used in their construction. The center mandala has concentric ring diameters of 74.2, 41, 27.4, and 15.3 m. For clarity, we also discuss a second mandala (NE-most), see Fig. 13.3. Aerial and satellite (Quickbird) and Los Alamos imagery were used.

For comparison we show the center mandala Fig. 13.4. The white markings, from center, denote an aerial view of Stonehenge: The stones about the center are, in order, a horseshoe of small inner bluestones, five pairs of 'trilithon' sarsens with a lintel stone atop each pair, a ring of undressed bluestones, an outer sarsen circle with a continuous layer of lintels (30) on top (shown as the continuous white ring), the Z holes (30), the Y holes (30), followed by 56 outer-most Aubrey holes on a 84 m in diameter.

The black markings, the locations of cairns that define the mandala geometry are still visible in spite of their apparent age. The appearance is that of markers seen today melting into the desert pavement. The complexity and apparent effort of construction is noteworthy. Also, the orientation of the overlaid image of Stonehenge and the NE corner of the framing square are exact. While there is no central structure within the outer sarsen circle, the close fit cairns are an exact fit to the circle. The remaining stone portions of Stonehend have no mandala equivalent. Instead 16 rays emanate from the center out to the Z holes. The 16 rays are typical of rayed recordings in South America.

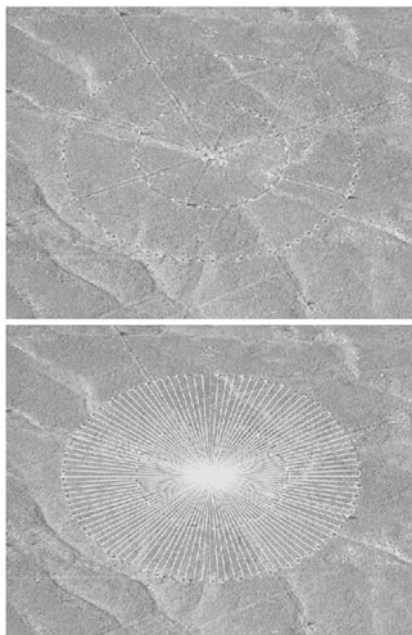


**Fig. 13.3** *Top:* aerial photo of the NE mandala. *Bottom:* overlay of 112 lines each stretching from the center to an outside rock cairn (Photo by A. L. Peratt)

In comparison, one of the mandalas has 224 ( $4 \times 56$ ) outer cairns whereas Stonehenge has 56 Aubrey holes on the outer periphery. The former corresponds to an age where the plasma filaments have not yet merged to 56 or lesser numbers (see Fig. 12.3). Second, the Y and Z rings of Stonehenge, never circular, show the onset of a later time diocotron instability, that is, Buneman's chasing instability (In petroglyphs (Fig. 12.1)).

Many thousands of man-made objects, while of widely varying sizes, replicate the Stonehenge pattern (Peratt 2001, 2003; Qöyawayma and Peratt 2007; Peratt and Yao 2008a,b), all recordings of intense, focused, synchrotron light skyward.

### 13.3 The Cosmic Nebula and Interstellar Clouds

A somewhat larger structure  $60 \times 60$  ly, a molecular cloud at the Galactic center, replicates the same helical z-pinch structure as do high-energy-density laboratory z-pinchs such as shown in Figs. 2.27 and 2.21.

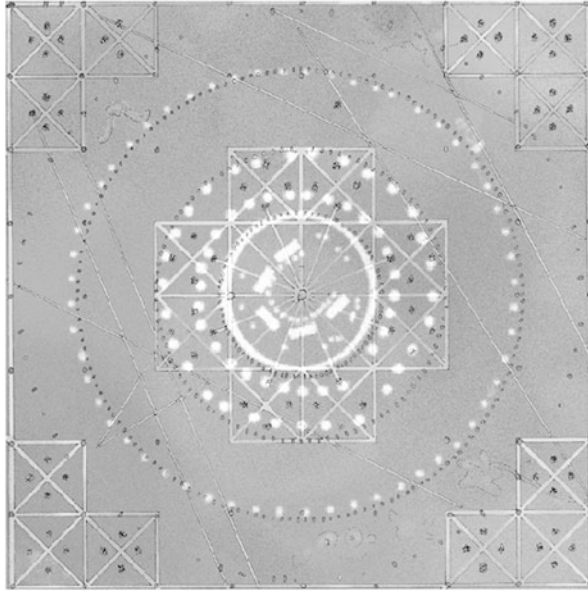


**Fig. 13.4** Overlay of Stonehenge (*white*) on the center Palpa Mandala (*black*). The entire Mandala has been constructed to lie within rectangular blocks, also *white*, a quadrupole

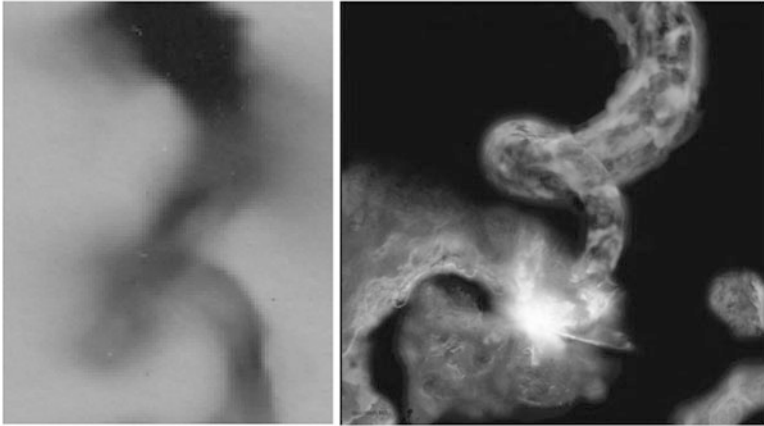


**Fig. 13.5** *Left*: Laboratory z-pinch, 2-cm long, 2 ns. *Right*: Helical molecular cloud at the galactic center. 60 ly by 60 ly, B approx 1milligauss? (S. Matsumura, National Astronomical Observatory of Japan)

Supernova 1987a, that burst upon the scene just prior to the first edition of this book, has now been studied for over 20 years. During this time the 28 filaments in the circular center of the wheel lemniscoid have become better defined with better observing telescopes, Fig. 13.6.



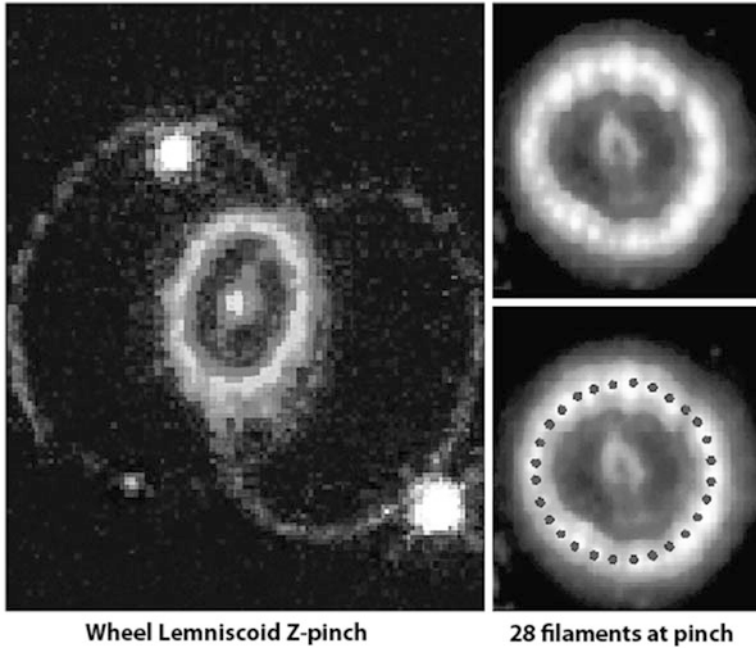


**Fig. 13.6** Supernova 1987A in the Large Magellanic Cloud. (*Left*); The three rings define a plasma sheet hyperboloid with a wheel lemniscoid at the center pinch. (*Right*); 28 filaments are discernable in the z-pinch region. For example, see Figure 13.3

Thus, two-thirds of the way through Alfvén's cosmic-triple-jump, astrophysical entities appear to differ in no appreciable way from their high-energy laboratory counterparts (Fälthammar 1986).

## 13.4 Galaxies in Plasma Cosmic Space

### 13.4.1 Double Radio Galaxies

Among the largest entities detected in the universe, other than multi-megaparsec plasma filaments, are double radio galaxies. In size, these radio sources extend for hundreds of kiloparsecs ( $10^{21}$ – $10^{22}$  m) to a few mega-parsecs ( $10^{21}$ – $10^{22}$  m). Double radio galaxies are thought to have densities of  $10^{-3}$  cm $^{-3}$  and magnetic fields of the order of  $10^{-4}$  G (Figs. 13.8 and 13.9).

The radiation produced by two plasma filaments in proximity replicate both the isophotal and power spectra from double radio galaxies (Fig. 13.7). Time evolves

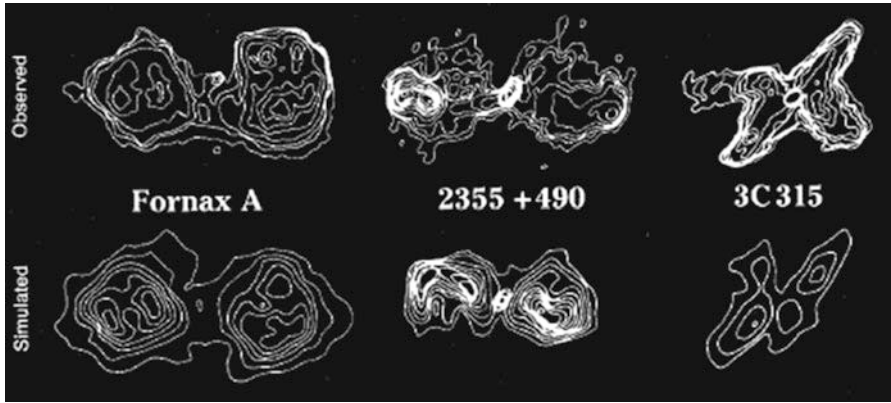


**Fig. 13.7** *Top*: Synchrotron isophotes of double radio galaxies. *Bottom*: Simulation analogs at time 10.4–58.7 Myr. Time increases from left to right

from left to right in this figure, 10.4–58.7 Myr. The rise of this synchrotron pulse was initiated when portions of two megaparsec long plasma filaments became parallel when about 20 kpc apart (Fig. 13.7). The top row shows, from left to right, three radio telescope observations of three different double galaxies taken from three different parts of the sky and reflecting three different radio snapshots of their respective evolution. The bottom row shows the computer simulations of a single laboratory plasma experiment at three different moments of its evolution in physical space-time.

Likely not recognized before Alfvén and Bostick, is the fact that each of the two time intervals between the three different galaxies, at the top, represents a span of time of about 20 million years, while the intervals between the different moments of the laboratory plasma experiment, in the bottom, represents a few microseconds. If the top set of recordings is projected onto the bottom set of recordings, as if through a conical projection of millions of years long, everything is mapped as being the same including the proportional magnitudes of time. One now has the ability to forecast what a double radio galaxy will be like millions of years into the future.

As will be shown, radio galaxy 3C 315 is starting a rotation that will evolve into a spiral galaxy, i.e., NGC 4151 (Fig. 13.9).

### 13.4.2 Spiral Galaxies

In reference to Sect. 3.10 on page 109 and Sect. 6.5.2 on page 237, updated simulations of the spiral magnetic fields and their field strengths are shown in Fig. 13.8.



**Fig. 13.8** Simulation: spiral galaxy circumferential magnetic fields,  $5\text{--}70\,\mu\text{G}$ . The spiral layout of the gray bands gives the circumpolar direction of the galactic magnetic field, while the height of any band provides an estimate of the field strength

The spiral layout of the gray bands gives the circumpolar direction of the galactic magnetic field, while the height of any band provides an estimate of the field strengths,  $5\text{--}70\,\mu\text{G}$ .

Figure 13.9 shows the plasma spiral formed in this simulation overlayed on its magnetic field line (squared) isobars. The diameter of the spiral is about 50 kpc with a mass of  $10^{41}$  kg, i.e., a size and mass of that observed from spiral galaxies. A direct comparison to observations is made by superimposing the HI distribution in NG4151 on its optical photograph. The observation show two peaks in neutral hydrogen surrounding a void. The void is oriented towards one of the galactic arms. The simulation allows the two peaks to be traced back to their origin. Both are found to be the remnants of the originally extended components, i.e., cross-sections of the original Birkeland filaments. The hydrogen deficient center is the remnant of an older elliptical galaxy formed midway between the filaments, in the magnetic null. The velocity consists essentially of a linearly increasing component due to a central body undergoing rigid rotation, with two “flat” components on either side of  $r = 0$  due to the trailing arms.

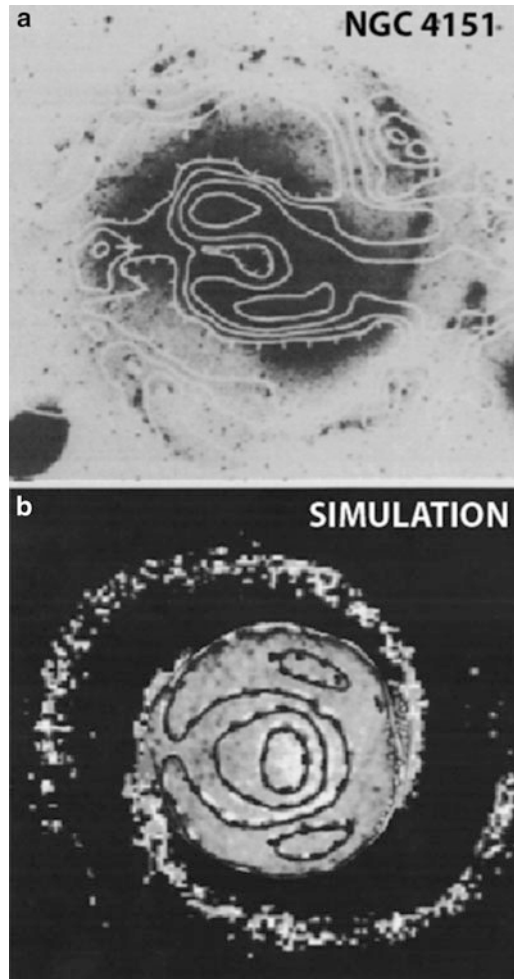


**Fig. 13.9** (*top*) HI distribution superimposed on an optical photograph of NGC4151. (*bottom*) Simulation magnetic energy superposed on simulation galaxy. In both cases a “horse-shoe” cusp, opening towards a spiral arm, surrounds a magnetic field HI/minima core. Within the cusp, two magnetic field/HI peaks are observed

## References

- Alfvén, H.: Plasma physics applied to cosmology. *Phys. Today* **24**(2), 28–33 (1971)  
 Alfvén, H.: Relations between cosmic and laboratory plasma physics. *Ann. N. Y. Acad. Sci.* **257**, 179 (1975)

- Alfvén, H.: On hierarchical cosmology. *Astrophys. Space Sci.* **PS-14**, 629–638 (1983). Springer
- Alfvén, H.: Model of the plasma universe. *IEEE Trans. Plasma Sci.* **89**, 313–324 (1986)
- Deutsch, C., Peratt, A.: A survey of the petroglyphs in Canaima, Venezuela. In: *Latin American Workshop on Plasma Physics*, Caracas, 20–31 Jan 1997. University Simon Bolivar Support Program (1997)
- Eames, C., Eames, R.: <http://www.powersof10.com/film> (2011)
- Eastman, T.E.: <http://www.plasmas.org/powers.htm> (2013)
- Fälthammar, C.-G.: Magnetosphere-ionosphere interactions: near-earth manifestations of the plasma universe. *IEEE Trans. Plasma Sci.* **14**, 616 (1986). rein-grue:2005
- Greulich, S., Glasmacher, U., Wagner G.: Optical dating of granitic stone surfaces. *Archaeometry* **47**, 645 (2005)
- Gurnett, D.A., Bhattacharjee, A.: *Introduction to Plasma Physics with Space and Laboratory Applications*. Cambridge University Press, Cambridge/New York (2005)
- Kukushkin, A.B., Rantsev-Kartinov, V.A.: Self-similarity of plasma networking in a broad range of length scales; from laboratory to cosmic plasmas. *Rev. Sci. Instrum.* **70**, 1387 (1999)
- Peratt, A.L.: Stonehenge, a giant petroglyph? *University of Pennsylvania Almanac* **48**(8) (2001) (update February 18, 2004)
- Peratt, A.L.: Characteristics for the occurrence of a high-current, z-pinch aurora as recorded in antiquity. *IEEE Trans. Plasma Sci.* **31**(6), 1192 (2003)
- Peratt, A.L., Dessler, A.J.: Filamentation of volcanic plumes on the Jovian satellite Io. *Astrophys. Space Sci.* **144**, 1 (1988)
- Peratt, A.L., Yao, W.F.: Characteristics for the occurrence of a high-current, z-pinch aurora as recorded in antiquity. *IEEE Trans. Plasma Sci.* **31**(6), 1192 (2008a)
- Peratt, A., Yao, W.F.: Evidence for an intense solar outburst in prehistory. *Phys. Scr.* **2008**(T131), 014048 (2008b)
- Qöyawayma, A.H., Peratt, A.L.: The influence of 56 synchrotron radiating Birke-land filaments formed in an archaic auroral sheath on man-made structures and artifacts found worldwide. In: *Proceedings of the IEEE Pulsed Power and Plasma Science Conference*, Albuquerque, p. 623 (2007)
- Suplee, C.: *The Plasma Universe*. Cambridge University Press, Cambridge/New York (2009)

# Appendix A

## Transmission Lines

### A.1 Cosmic Filaments as Transmission Lines

The high conductivity of cosmic plasma permits electric currents to flow that constrict the plasma to filaments. These current-carrying filaments form transmission lines which allow electric energy to be transported over large distances. Transmission lines consist of an assemblage of two or more conducting paths. Transmission lines on earth, used for communications and the transport of electric energy, employ conductors that are usually arranged parallel to a common axis. This need not be the case in space and is often not the case in filamentary current-conducting plasma in pulsed-power generators. Nevertheless, a simplification in analysis results if we assume parallel conducting paths. The generalization to nonparallel transmission lines, such as radially converging lines, is a straightforward extension of the theory. For the case at hand, the geometric and physical parameters of the line (the nature of the conductors and of the dielectric) are assumed to be constant everywhere along the line; this is the hypothesis of homogeneity of the line. This assemblage of conductors comprises two groups of at least one conductor each, one group being the forward conductors, and the other the return conductors. The simplified theory of lines that is to be treated here assumes that the lateral dimensions of the line are negligible, or, more precisely, that the time of propagation of the electromagnetic field between the forward and return conductors in a plane perpendicular to the axis of the line is negligible with respect to the duration of the briefest of the phenomena to be studied. This restriction leads to the second fundamental hypothesis, that of the conservation of current across a plane is zero, which is to say that the current through the forward conductors is equal, but in the opposite sense to the current through the return conductors. These two fundamental hypotheses reduce the theory of transmission lines to a problem of partial differential equations in two variables (time and one space variable taken along the axis of the line). The general case would lead to partial differential equations in time and three space variables. With no loss of generality, it can be assumed that the line is composed of only two conductors. This considerably simplifies the definition of per unit length parameters

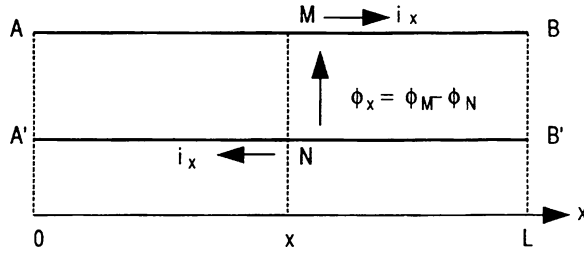


**Fig. A.1** A two-conductor transmission line

of the line. Frequently the additional hypothesis of symmetry of the line is made, motivated by the two-wire line having two identical cylindrical conductors. This hypothesis is by no means necessary, and most lines in space do not have this symmetry and may not even be everywhere cylindrical. Nevertheless, we will appeal to this simplification in establishing the general line equations ([Bekefi 1966](#); [Book 1987](#); [Stix 1962](#)).

## A.2 Definition of the State of the Line at a Point

Let us consider an ideal two-conductor transmission line, having forward and return conductors reduced to straight lines (Fig. A.1). Let  $MN$  be the intersection of the transmission line with a plane perpendicular to the line and located a distance  $x$  along an axis  $Ox$  parallel to the line. Arbitrarily choose  $AB$  to be the forward conductor and  $A'B'$  to be the return conductor. The current in the line at the abscissa  $x$  is defined to be the current flowing in conductor  $AB$  at point  $M$ . It is taken to be positive if it is directed in the sense  $Ox$ , i.e., if it flows from  $M$  toward  $B$ . By the hypotheses of conservation of current, the current at  $N$  is equal and opposite to the current at  $M$ . If  $\phi_M$  and  $\phi_N$  are, respectively, the potentials of points  $M$  and  $N$  with respect to some reference potential, the line voltage at the abscissa  $x$  will be

$$\phi_x = \phi_M - \phi_N \quad (\text{A.1})$$

## A.3 Primary Parameters

We will use the term parameter for the quantities to be defined below, rather than the term constant often used. The latter term arises from the fact that discussions of transmission lines on earth most often consider only sinusoidal waves of a given frequency. On the contrary, we will be especially interested in the pulse regime, which corresponds to a large band of frequencies. (The pulse may be measured in seconds, minutes, or hours; or in days, years, centuries, millenia, or megayears or more, but its duration is  $\delta t = \delta x/c \ll l/c$ , where  $l$  is the total length of the

transmission line). At least two of the parameters of interest are strong functions of frequency: the resistance per unit length, affected by the electromagnetic skin depth,

$$\delta = \sqrt{\frac{2}{\omega \mu \sigma}} \quad (\text{A.2})$$

and the conductance per unit length, affected by the variations of dielectric losses with frequency. Nevertheless, in deriving the equations of interest, we will suppose that these parameters are constants. Since the line is homogeneous, the total resistance of the conductors is proportional to the length of the line. A resistance per unit length  $R$  can thus be defined. In the same way a *self-inductance per unit length*  $L$  can be defined, which is the result of the true self-inductance of the conductors and the mutual inductance between the two conductors. Because of the imperfect properties of the plasma dielectric between conductors (losses in the dielectric that separates the conductors), a uniformly distributed transverse conductance appears. It is thus possible to define a *transverse conductance per unit length*  $G$ . This is the ratio of the charge on a unit length conductor element to the voltage between the two conductors at the element considered. The *capacitance per unit length* is denoted  $C$ .

## A.4 General Equations

### A.4.1 The General Case

Consider a line element of length  $\Delta x$  (Fig. A.2). This element can be compared to a four component discrete circuit ( $AA', BB'$ ) with elements  $R\Delta x$ ,  $L\Delta x$ ,  $G\Delta x$ , and  $C\Delta x$ .<sup>1</sup>

$$\Delta \phi = \phi_B - \phi_A = R\Delta x i - L\Delta x \frac{\partial i}{\partial t} \quad (\text{A.3})$$

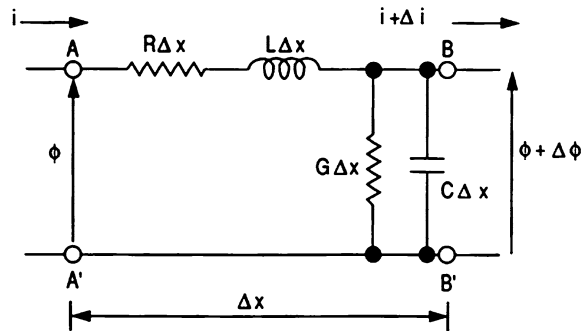


**Fig. A.2** An infinitesimal line element

<sup>1</sup> In rationalized MKS units the actual values of the line constants for a differential length of line are  $L\Delta x$  henrys,  $R\Delta x$  ohms,  $C\Delta x$  farads, and  $G\Delta x$  siemens.



The current  $\Delta i$  flowing into  $B$  from  $B'$  is

$$\Delta i = -G\Delta x(\phi + \Delta\phi) - C\Delta x \frac{\partial}{\partial t}(\phi + \Delta\phi) = -G\Delta x\phi - C\Delta x \frac{\partial\phi}{\partial t} + G\Delta x^2 \left(Ri + L\frac{\partial i}{\partial t}\right) + C\Delta x^2 \left(R\frac{\partial i}{\partial t} + L\frac{\partial^2 i}{\partial t^2}\right) \quad (\text{A.4})$$

Dividing the terms of Eq. (A.1) by  $\Delta x$  and letting  $\Delta x$  go to 0, we obtain the first basic equation:

$$\lim_{\Delta x \rightarrow 0} \left( \frac{\Delta\phi}{\Delta x} \right) = \frac{\partial\phi}{\partial x} - Ri - L\frac{\partial i}{\partial t} \quad (\text{A.5})$$

In the same way, from Eq. (A.2)

$$\lim_{\Delta x \rightarrow 0} \left( \frac{\Delta i}{\Delta x} \right) = \lim_{\Delta x \rightarrow 0} \left\{ -G\phi - C\frac{\partial\phi}{\partial t} + \Delta x \left[ G \left( Ri + L\frac{\partial i}{\partial t} \right) + C \left( R\frac{\partial i}{\partial t} + L\frac{\partial^2 i}{\partial t^2} \right) \right] \right\} \quad (\text{A.6})$$

which results in the second basic equation:

$$\lim_{\Delta x \rightarrow 0} \left( \frac{\Delta i}{\Delta x} \right) = \frac{\partial i}{\partial x} - G\phi - C\frac{\partial\phi}{\partial t} \quad (\text{A.7})$$

Differentiating Eq. (A.3) with respect to  $x$  yields

$$\frac{\partial^2\phi}{\partial x^2} = - \left[ R\frac{\partial i}{\partial x} + L\frac{\partial}{\partial t} \left( \frac{\partial i}{\partial x} \right) \right] \quad (\text{A.8})$$

Replacing  $\partial i / \partial x$  by its value in Eq. (A.4) leads, finally, to

$$\frac{\partial^2\phi}{\partial x^2} = RG\phi + (RC + LG) \frac{\partial\phi}{\partial t} + LC \frac{\partial^2\phi}{\partial t^2} \quad (\text{A.9})$$

The last relation is the *telegrapher's equation*. it can be integrated in certain special cases, e.g., if the voltage  $\phi$  is sinusoidal or in the transient regime using operational calculus. The current equation is of the same form as Eq. (A.5) and can be obtained by differentiating Eq. (A.4) with respect to  $x$ .

#### A.4.2 The Special Case of the Lossless Line

If the parameters  $G$  and  $R$  can be neglected, the fundamental Eqs. (A.3) and (A.4) simplify to

$$\frac{\partial\phi}{\partial x} = -L\frac{\partial i}{\partial t} \quad (\text{A.10})$$

$$\frac{\partial i}{\partial x} = -C\frac{\partial\phi}{\partial t} \quad (\text{A.11})$$

These relations lead to the equation for the propagation of plane waves, which can also be obtained from Eq. (A.5) by setting  $R = 0$  and  $G = 0$ :

$$\frac{\partial^2 \phi}{\partial x^2} = LC \frac{\partial^2 \phi}{\partial t^2} \quad (\text{A.12})$$

Setting

$$u = \frac{1}{\sqrt{LC}} \quad (\text{A.13})$$

in which  $u$  is the *propagation constant*, of the delay per unit length, this equation takes the form

$$\frac{\partial^2 \phi}{\partial x^2} = \frac{1}{u^2} \frac{\partial^2 \phi}{\partial t^2} \quad (\text{A.14})$$

The solution of Eq. (A.10) is of the form

$$\phi(x, t) = \phi^+(x - ut) + \phi^-(x + ut) \quad (\text{A.15})$$

in which  $\phi^+$  and  $\phi^-$  are arbitrary functions. The current in the line can now be found from the relations Eqs. (A.6), (A.7), and (A.11), which yield

$$i(x, t) = \frac{1}{R_c} [\phi^+(x - ut) + \phi^-(x + ut)] \quad (\text{A.16})$$

where

$$R_c = \sqrt{\frac{L}{C}} \quad (\text{A.17})$$

is by definition the *characteristic resistance* of the line.

Formulas for  $R_c$  for a number of transmission-line geometries and configurations are available in the literature [Westman \(1960\)](#).

## A.5 Heaviside's Operational Calculus (The Laplace Transform)

### A.5.1 The Propagation Function

Consider a transmission line such as defined above, having per unit length parameters  $L$ ,  $C$ ,  $R$ , and  $G$ , and of length  $l$ , as shown in Fig. A.3.

At the instant  $t = 0$ , an electromotive force  $\Theta(t)$  arising from a voltage source with internal impedance  $Z_g$ , is applied to the left end, or input, of the line. The right end, or load, is terminated in an impedance  $Z_L$ . The currents and voltages at each point along the line are assumed to be zero prior to the initial time  $t = 0$ . The problem is to calculate the voltage  $\phi(x, t)$  between the two conductors of the line, and the current  $i(x, t)$  flowing in each of these conductors, at each point  $x$  and at each instant  $t$ . The distance  $x$  is taken to be positive in the direction to the left of the origin, or generator side of the line.

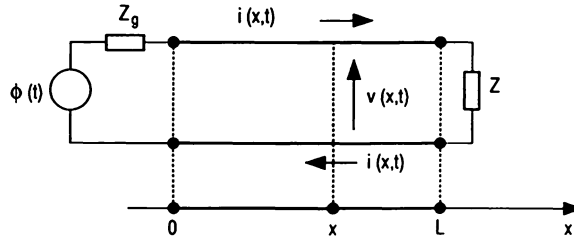


**Fig. A.3** Transmission line circuit under study with current  $i(x,t)$  and voltage  $\phi(x,t) = V(x,t)$

Equations (A.3) and (A.4) can be rewritten in terms of the Laplace transforms of the current and voltage waveforms. To that end consider  $\Phi(x,s) \Leftrightarrow \phi(x,t); I(x,s) \Leftrightarrow i(x,t)$

Using the conditions

$$\frac{\partial \phi(x,t)}{\partial t} \Leftrightarrow s\Phi(x,s) - \phi(x,0^+); \frac{\partial i(x,t)}{\partial t} \Leftrightarrow sI(x,s) - i(x,0^+) \quad (\text{A.18})$$

Since the Laplace transform is defined by

$$\Phi(x,s) = \int_0^{\infty} e^{-st} \phi(x,t) dt$$

we have

$$\frac{\partial \Phi(x,s)}{\partial x} = \int_0^{\infty} e^{-st} \frac{\partial \phi(x,t)}{\partial x} dt \Leftrightarrow \frac{\partial \Phi(x,t)}{\partial x} \quad (\text{A.19})$$

and Eqs. (A.3) and (A.4) in the transform domain become

$$\frac{\partial \Phi(x,s)}{\partial x} = +(R + Ls)\Phi(x,s) = 0 \quad (\text{A.20})$$

$$\frac{\partial I(x,s)}{\partial x} + (G + Cs)I(x,s) = 0$$

Differentiating Eq. (A.15) with respect to  $x$  and using Eq. (A.16) to eliminate  $\partial I(x,s)/\partial x$  from the result, we obtain

$$\frac{\partial^2 \Phi(x,s)}{\partial x^2} - \gamma^2 \Phi(x,s) = 0 \quad (\text{A.21})$$

An analogous relation can be found for the current:

$$\frac{\partial^2 I(x,s)}{\partial x^2} - \gamma^2 I(x,s) = 0 \quad (\text{A.22})$$

where  $\gamma(s) = \sqrt{(R + Ls)(G + Cs)}$  is called the *propagation function*. Note that  $\gamma$  is independent of  $x$  but not of  $s$ .

## A.6 Characteristic Impedance

The differential equation (A.17) has solutions of the form

$$\Phi(x, s) = \Phi_1(s)e^{-\gamma x} + \Phi_2(s)e^{\gamma x} \quad (\text{A.23})$$

where  $\Phi_1(s)$  and  $\Phi_2(s)$  are arbitrary functions of  $s$  only, which will be simply written as  $\Phi_1$  and  $\Phi_2$ .

From Eq. (A.19) there follows

$$\frac{\partial \Phi(x, s)}{\partial x} = -\gamma(\Phi_1 e^{-\gamma x} + \Phi_2 e^{\gamma x}) \quad (\text{A.24})$$

which together with Eq. (A.14) yields

$$I(x, s) = \frac{\gamma}{R + Ls} (\Phi_1 e^{-\gamma x} + \Phi_2 e^{\gamma x}) = \left( \frac{G + Cs}{R + Ls} \right)^{1/2} (\Phi_1 e^{-\gamma x} + \Phi_2 e^{\gamma x}) \quad (\text{A.25})$$

It is convenient to define

$$Z_c(s) = \sqrt{\frac{R + Ls}{G + Cs}} \quad (\text{A.26})$$

This last quantity, which has the dimensions of an impedance, is called the *characteristic impedance* of the line. It is related to the physical properties of the line, i.e., to its dimensions and to its conductive and dielectric properties. It is a function of  $s$ , and hence of time. We will write  $Z_c(s)$  simply as  $Z_c$ .

The general solutions of Eqs. (A.17) and (A.18) are thus

$$\Phi(x, s) = \Phi_1 e^{-\gamma x} + \Phi_2 e^{\gamma x}; I(x, s) = \frac{1}{Z_c} (\Phi_1 e^{-\gamma x} + \Phi_2 e^{\gamma x}) \quad (\text{A.27})$$

## A.7 Reflection Coefficients

The complete solution to Eq. (A.21) is obtained by determining the functions 1 and 2 using the boundary conditions at the ends of the line. In space plasmas, the end of a transmission line may be a planetary ionosphere or wherever else the conductivity between conducting paths becomes large. Arc discharges across dielectrics (Sect. 4.6.1) make excellent terminations.

Let  $\Phi(s) \Leftrightarrow \Phi(t)$  be the transform of the generator voltage. At the input to the line  $x = 0$

$$\Phi(s) = Z_g I(0, s) + \Phi(0, s) = \frac{Z_g}{Z_c} (\Phi_1 - \Phi_2) + (\Phi_1 + \Phi_2) \quad (\text{A.28})$$

From Eqs. (A.21) to (A.22), and the definition of the voltage reflection coefficient at the input to the line

$$\Gamma_g = \frac{Z_g - Z_c}{Z_g + Z_c} \quad (\text{A.29})$$

we obtain

$$\Phi_1 - \Gamma_g \Phi_2 = \Phi(s) \frac{Z_c}{Z_g + Z_c} \quad (\text{A.30})$$

In the same way, at the output of the line ( $x = l$ ), we find

$$\Phi_1 e^{-\gamma l} \Gamma_l - \Phi_2 e^{\gamma l} = 0 \quad (\text{A.31})$$

where is the voltage reflection coefficient at the output of the line. Solving Eqs. (A.24) and (A.25) yields

$$\Gamma_l = \frac{Z_l - Z_c}{Z_l + Z_c} \quad (\text{A.32})$$

$$\Phi_1 = \Phi(s) \frac{Z_c}{Z_g + Z_c} \frac{e^{\gamma l}}{e^{\gamma l} - \Gamma_0 \Gamma_l e^{-\gamma l}} = \Phi(s) \frac{Z_c}{Z_g + Z_c} \frac{1}{1 - \Gamma_g \Gamma_l e^{-2\gamma l}} \quad (\text{A.33})$$

With the aid of the convergent series expansion

$$\frac{1}{1 - \Gamma_g \Gamma_l e^{-2\gamma l}} = 1 + \Gamma_g \Gamma_l e^{-2\gamma l} + \dots + \Gamma_g^n \Gamma_l^n e^{-2n\gamma l} + \dots \quad (\text{A.34})$$

$$\Phi_2 = \Gamma_l \Phi_1 e^{-2\gamma l} = \Phi(s) \frac{Z_c}{Z_g + Z_c} \frac{\Gamma_l e^{-2\gamma l}}{1 - \Gamma_g \Gamma_l e^{-2\gamma l}} \quad (\text{A.35})$$

we arrive at

$$\Phi(x, s) = \Phi(s) e^{-\gamma x} + \Gamma_l e^{-\gamma(2l-x)} \sum_{n=0}^{\infty} \Gamma_g^n \Gamma_l^n e^{-2n\gamma l} \quad (\text{A.36})$$

$$I(x, s) = \Phi(s) \frac{1}{Z_g + Z_c} e^{-\gamma x} + \Gamma_l e^{-\gamma(2l-x)} \sum_{n=0}^{\infty} \Gamma_g^n \Gamma_l^n e^{-2n\gamma l} \quad (\text{A.37})$$

## A.8 Time-Domain Reflectometry

Consider the case of a lossless line  $R=G=0$ . For this case  $Z_c = LC s = u/l s$  and  $Z_c = R_c$ . Taking the inverse Laplace transform of Eq. (A.29) by using the translation identity

$$L^{-1} \left[ \Phi(s) e^{-\gamma(s)} \right] = L^{-1} \left[ \Phi(s) e^{-\frac{x}{u}(s)} \right] = \phi \left( t - \frac{x}{u} \right) \quad (\text{A.38})$$

gives, as parameters for Eqs. (A.11) and (A.12)

$$\phi^+ = \frac{R_c}{R_g + R_c} \sum_{n=0}^{\infty} \Gamma_g^n \Gamma_l^n \phi \{t - t_u [x + 2ln]\} \quad (\text{A.39})$$

$$\phi^- = \frac{R_c}{R_g + R_c} \sum_{n=0}^{\infty} \Gamma_g^n \Gamma_l^n \phi \{t - t_u [x + 2l(n+1)]\} \quad (\text{A.40})$$

Equations (A.11), (A.12), and (A.30) give waveforms in remarkably good agreement with waveforms measured by probes placed within the transmission line. For example, very low resistances caused by dielectric surface flashover in pulsed-power transmission lines can be determined to an accuracy of less than 1 % if waveforms are available for at least two spatial locations in the line. The problem reduces to iterating Eq. (A.30) in  $R_g$  and  $R_l$  until a best fit between calculated and measured waveforms is obtained. Losses in the propagating current and voltage pulses are of course determined by this procedure.

### A.8.1 Cosmic Transmission-Line

Consider for illustration a hypothetical planetary ionosphere-magnetosphere transmission line model (Fig. A.4) that might be applied to the geometry of Figs. 1.9 and 4.24 Allis et al. (1963). Assume a  $-40 \text{ kV}$  and  $250 \text{ ms}$  perturbation at the source. We arbitrarily take a source impedance of  $2 \Omega$ , a characteristic transmission line impedance of  $0.4 \Omega$ , and an ionosphere (load) impedance of  $0.1 \Omega$ . The transmission line length is  $6 \times 10^8 \text{ m}$ . With these parameter values a probe (spacecraft) located at a distance  $10^8 \text{ m}$  from the source would measure the current and voltage transients depicted in Fig. A.5. After a time  $3.3 \text{ s}$  following the peak voltage spike from the perturbation, the probe would measure the first ionospheric reflection signal and, if the source impedance differs from the transmission line impedance, it would also measure a reflected signal from the source  $0.7 \text{ s}$  later. Since the amplitude of the reflections depend on the reflection coefficients Eqs. (A.23) and (A.26), an accurate determination of the source and ionospheric impedance can be made. If probe measurements are available at two spatial locations, the waveforms from Eq. (A.30) are uniquely determined and can be used to ascertain the impedances and their locations. In laboratory application, precise determination of the impedances and positions of high-voltage surface flashovers (Sect. 4.6.1) has been achieved.

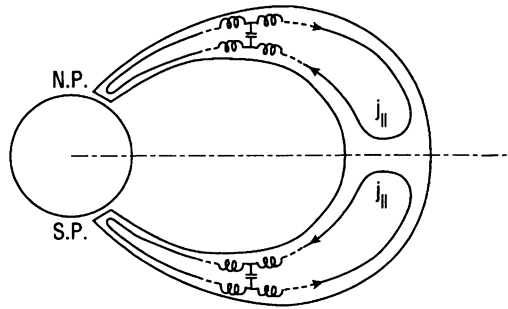


**Fig. A.4** An ionosphere coupling model. The north and south pole transmission lines need not be symmetric (Adapted from Sato 1978)

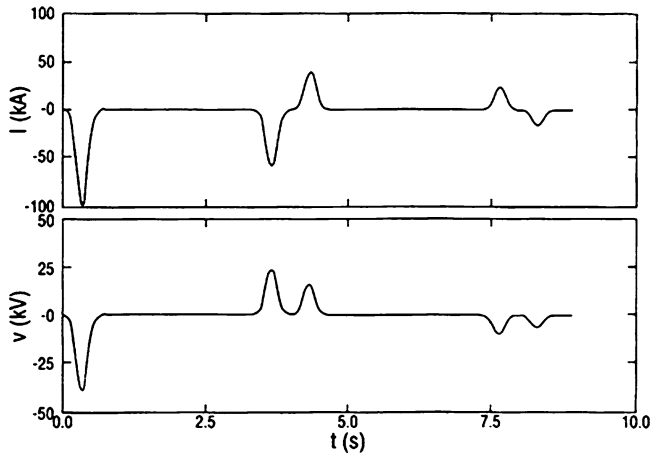


**Fig. A.5** Current and voltage waveforms associated with a  $-40$  kV and  $250$  ms source perturbation on a  $6 \times 10^8$  m,  $-0.4\Omega$  transmission line. The source impedance is  $2\Omega$  and the ionosphere (load) impedance is  $0.1\Omega$ . The probe is located  $1 \times 10^8$  m from the source

## References

- Allis, W.P., Buchsbaum, S.J., Bers, A.: *Waves in Anisotropic Plasmas*. MIT, Cambridge (1963)
- Bekefi, G.: *Radiation Processes in Plasmas*. Wiley, New York (1966)
- Book, D.L.: *NRL Plasma Formulary*. Naval Research Laboratory, Washington, DC (1987)
- Sato, T.: A Theory of quiet auroral arcs, *J. Geophys. Res.* **83** 1042 (1978)
- Stix, T.H.: *The Theory of Plasma Waves*. McGraw-Hill, New York (1962)
- Swanson, G.D.: *Plasma Waves*. Academic, New York (1989)
- Westman, H.P. (ed.): *Reference Data For Radio Engineers*, chap. 20. International Telephone and Telegraph Corporation, New York (1960)

## Appendix B

# Polarization of Electromagnetic Waves in Plasma

A wave equation is derivable from Maxwell-Hertz-Heaviside's equations (1.1)–(1.4)

$$\nabla \times \mathbf{H} = \mathbf{j} - i\omega\epsilon_0\mathbf{E} = -i\omega\epsilon_0 \left[ \mathbf{E} + \frac{i}{\omega\epsilon_0} \mathbf{j} \right] = -i\omega\epsilon_0 \mathbf{K} \cdot \mathbf{E} \quad (\text{B.1})$$

where  $\mathbf{K}$ , the relative dielectric tensor, is given by

$$\mathbf{K} = \begin{bmatrix} S & -iD & 0 \\ iD & S & 0 \\ 0 & 0 & P \end{bmatrix} \quad (\text{B.2})$$

and derives from the solution to the current density  $\mathbf{j}$  (Stix 1962). For cold plasma, the matrix elements are

$$\begin{aligned} S &= \frac{1}{2}(R + L) \\ D &= \frac{1}{2}(R - L) \\ P &= 1 - \sum_k \frac{\omega_{pk}^2}{\omega^2} \\ R &= 1 - \sum_k \frac{\omega_{pk}^2}{\omega^2} \frac{\omega}{\omega - \omega_b} \\ L &= 1 - \sum_k \frac{\omega_{pk}^2}{\omega^2} \frac{\omega}{\omega + \omega_b} \end{aligned} \quad (\text{B.3})$$

The vector fields have been taken to be the sum of a zero (external field) and a first order field (e.g.  $\mathbf{B} = \mathbf{B}_0 + \mathbf{B}_1$ ,  $\mathbf{E} = \mathbf{E}_0 + \mathbf{E}_1$ ) where the first-order quantities vary as  $e^{i(\mathbf{k} \cdot \mathbf{r} - \omega t)}$ . Setting  $\nabla \rightarrow i\mathbf{k}$  in Eq. (B.1) gives

$$\mathbf{k} \times \mathbf{B} = -\omega\mu_0\epsilon_0 \mathbf{K} \cdot \mathbf{E} = -\frac{\omega^2}{c^2} \mathbf{K} \cdot \mathbf{E} \quad (\text{B.4})$$



Likewise, setting  $\partial/\partial t \rightarrow -i\omega$  in Eq. (1.1) gives

$$\mathbf{k} \times \mathbf{E} = \omega \mathbf{B} \quad (\text{B.5})$$

Crossing Eq. (B.5) with  $\mathbf{k}$ , then substituting into Eq. (B.4) yields a wave equation

$$\mathbf{k} \times (\mathbf{k} \times \mathbf{E}) + \frac{\omega^2}{c^2} \mathbf{K} \cdot \mathbf{E} = 0 \quad (\text{B.6})$$

At this point it is convenient to introduce the dimensionless vector  $\mathbf{n}$  which has the direction of the propagation vector  $\mathbf{n}$  and the magnitude of the refractive index

$$\mathbf{n} = \mathbf{k} \frac{c}{\omega} \quad (\text{B.7})$$

The magnitude  $n = |\mathbf{n}|$  is the ratio of light to the phase velocity. The reciprocal of  $n$  is the wave phase velocity divided by the velocity of light. The wave normal surface is the locus of the tip of the vector  $\mathbf{n}^{-1} \equiv \mathbf{n}/n^2$ .

Figure B.1 is a plot of phase velocity surfaces for electromagnetic waves. The ordinate is  $\omega_b^2/\omega^2$  while the abscissa is  $\omega_b^2/\omega^2$ . The symbols L, R, X, and O denote left-hand circularly polarized (LHCP), right-hand circularly polarized (RHCP), extraordinary, and ordinary wave types, respectively. This figure is called a Clemmow-Mullaly-Allis or CMA diagram (Allis et al. 1963) and is to be interpreted as a “plasma pond” for a two-component plasma where cross-sections of the allowable wave normal surfaces are shown. The surfaces are typically in the form of spheres, ellipsoids, and wheel and dumbbell lemniscoids. The diagram is divided up into 13 regions, each of which supports two independent modes.

The significance of the different regions is due to “boundaries” where the refractive indices go either as  $n^2 \rightarrow 0$  ( $v_{ph} \rightarrow \infty$ ) called a “cutoff” condition, or  $n^2 \rightarrow \infty$  ( $v_{ph} \rightarrow 0$ ) called a “resonance” condition (Table B.1). Waves are reflected at cutoffs and absorbed at resonances.

The cross-sections in Fig. B.1 are not to scale, but the speed of light in relation to the velocities lies generally between the two cross-sections in each region. This divides the wave normal surfaces into “fast” and “slow” modes. The various wave types and their locations in Fig. B.1 are delineated in Table B.2.

Substituting Eq. (B.7) into Eq. (B.6) gives a wave equation in terms of  $\mathbf{n}$

$$\mathbf{n} \times (\mathbf{n} \times \mathbf{E}) + \mathbf{K} \cdot \mathbf{E} = 0 \quad (\text{B.8})$$

which, when used for the orientation of the vectors shown in Fig. B.2, becomes

$$\begin{pmatrix} S - n^2 \cos^2 \theta & -iD & n^2 \cos \theta \sin \theta \\ iD & S - n^2 & 0 \\ n^2 \cos \theta \sin \theta & 0 & P - n^2 \sin^2 \theta \end{pmatrix} \begin{pmatrix} E_x \\ E_y \\ E_z \end{pmatrix} = 0 \quad (\text{B.9})$$

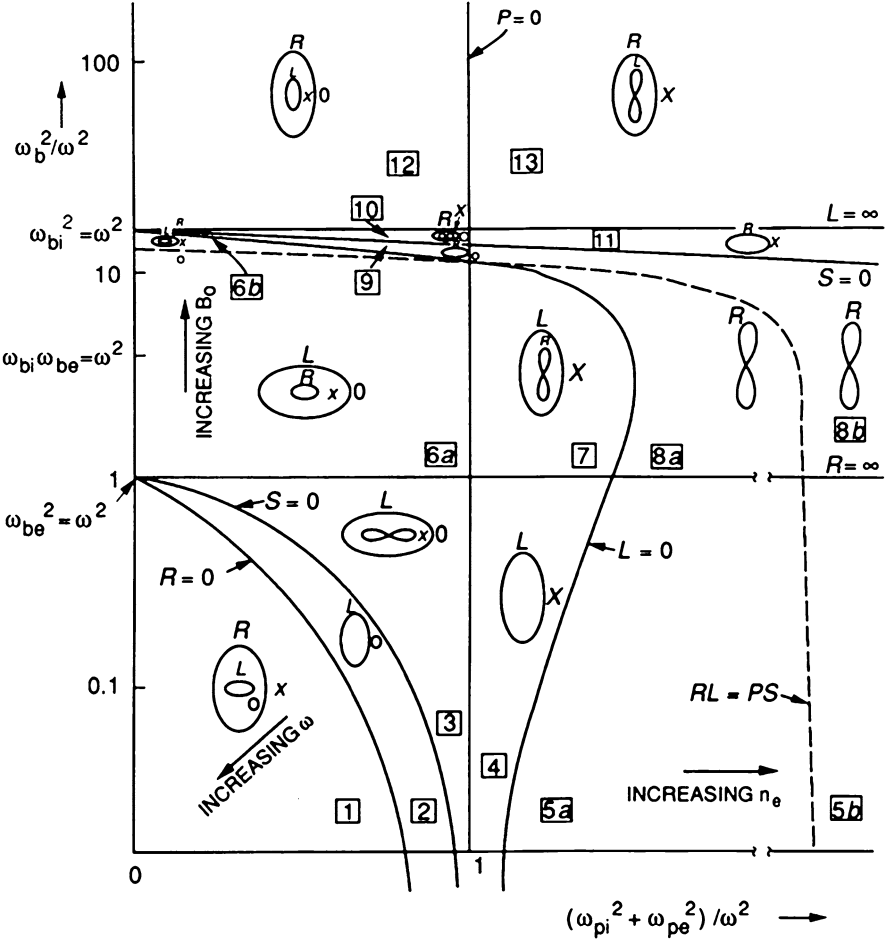


**Fig. B.1** CMA diagram for a two-component plasma with  $m_i/m_e = 4$ . Bounding surfaces appear as lines in the two-dimensional parameter space. Cross sections of wave-normal surfaces are sketched and labeled for each region. For these sketches the direction of the magnetic field is vertical

**Table B.1** Nomenclature for cutoffs and resonances

$P = 0$	Plasma cutoff
$S = 0$	Plasma resonance, $\theta = \pi/2$
$L = 0$	Ion cyclotron cutoff
$R = 0$	Electron cyclotron cutoff
$L = \infty$	Ion cyclotron resonance
$R = \infty$	Electron cyclotron resonance

**Table B.2** Regions of plasma wave types

Type	Region
Ordinary	1,2,3,4,6,7,12,13
Extraordinary	1,2,3,4,6,7,10,11,12,13
RHCP	1,6,7,8,9,10,11,12,13
LHCP	1,2,3,4,6,7,12,13
Whistler	8
Electron cyclotron	7,8
Quasi-transverse ordinary	1,2,3,6,7,8
Alfvén-Astrom waves, ion cyclotron waves	13

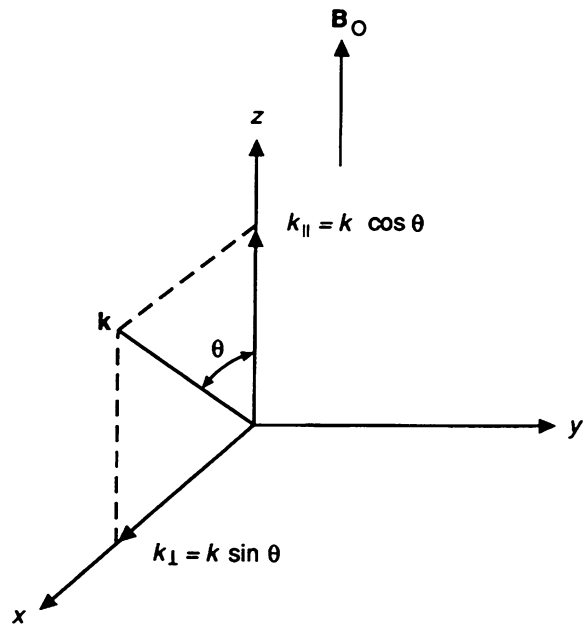


**Fig. B.2** The propagation vector  $\mathbf{k}$  in relation to the static magnetic field  $\mathbf{B}_0$

The condition for a nontrivial solution to Eq. (B.9) is that the determinant of the square matrix be zero. This condition gives the dispersion relation, or the equation for the wave normal surface

$$\begin{aligned} An^4 - Bn^2 + C &= 0 \\ A &= S \sin^2 \theta + P \cos^2 \theta \\ B &= RL \sin^2 \theta + PS(1 + \cos^2 \theta) \\ C &= PRL \end{aligned} \tag{B.10}$$

The solutions of Eq. (B.10) reduce to simple expressions when  $\theta = 0$  and  $\theta = \pi/2$ :

$$\begin{aligned} n^2 &= R, L & \theta &= 0 \\ n^2 &= RL/S, P & \theta &= \pi/2 \end{aligned} \quad (\text{B.11})$$

The polarization relations between the cartesian field components of  $\mathbf{E}$  follow from Eq. (B.10)

$$E_x : E_y : E_z = (S - n^2)(P - n^2 \sin^2 \theta) : -iD(P - n^2 \sin^2 \theta) : -(S - n^2)n^2 \cos \theta \sin \theta \quad (\text{B.12})$$

If  $\theta = 0$ , Eq. (B.12) shows that  $E_z = 0$  ( $\mathbf{E} \perp \mathbf{B}_0$ ) and, if  $n^2 = R$ , then  $E_x/E_y = -i$ . This means that  $E_x$  is  $90^\circ$  ahead of  $E_y$  and, by convention, the polarization is right-hand circular. If  $n^2 = L$ ,  $E_x/E_y = i$  and the polarization is left-hand circular. Figure B.3a illustrates these modes of propagation.

For the case  $\theta = \pi/2$  and  $n^2 = P$ ,  $E_x = E_y = 0$  ( $\mathbf{E} \parallel \mathbf{B}_0$ ). When  $n^2 = RL/S$ ,  $E_z = 0$  ( $\mathbf{E} \perp \mathbf{B}_0$ ). For this case the electric field circumscribes an ellipse in a plane of  $y$ . The modes  $n^2 = P$  and  $n^2 = RL/S$  are called the “ordinary” and “extraordinary” waves, respectively. These terms have been taken from crystal optics; however the terms have been interchanged in plasma physics, since the “extraordinary” mode is affected by  $\mathbf{B}_0$  whereas the “ordinary” mode is not. Figure B.3b illustrates these modes of propagation.

Expressed in spherical coordinates Eq. (B.12) is

$$E_k : E_\theta : E_\phi = (S - n^2)(P - n^2) \sin \theta : -(S - n^2)P \cos \theta : -iD(P - n^2 \sin^2 \theta) \quad (\text{B.13})$$

which shows that  $E_k$  and  $E_\theta$  are in phase while  $E_\phi$  is out of phase by  $90^\circ$ . Figure B.4 shows the orientation of the field vectors. The vector  $\mathbf{E}$  is elliptically polarized in a plane containing the  $y$  direction and the resultant of  $E_k$  and  $E_\theta$ .

**Example B.1 Faraday rotation.** The magnitudes of the RHCP and LHCP propagation vectors are  $k^R = (\omega/c)\sqrt{R}$  and  $k^L = (\omega/c)\sqrt{L}$ . Faraday rotation is given by

$$\tau = \frac{1}{2}(k^L - k^R)$$

At high frequencies where  $\omega \gg \omega_p, \omega_b$ , leading to the approximations,

$$K^{L,R} \approx \frac{\omega}{c} \left[ 1 - \frac{\omega_p^2}{2\omega^2} \left( 1 \pm \frac{\omega_b}{\omega} \right) \right]$$

Hence, the rotation angle of the linearly polarized wave as it propagates through magnetized plasma is

$$\Delta\chi = \tau l = \frac{\omega_p^2 \omega_p}{2c\omega^2} = \frac{e^3}{2m^2 c \epsilon_0} \frac{n_e B_{||} l}{\omega^2} \quad (\text{B.14})$$

where  $B_{||}$  is the magnitude of  $\mathbf{B}$  along the direction of wave propagation through a plasma of length  $l$  (Metzger and Vabre 1969; Sato 1978).

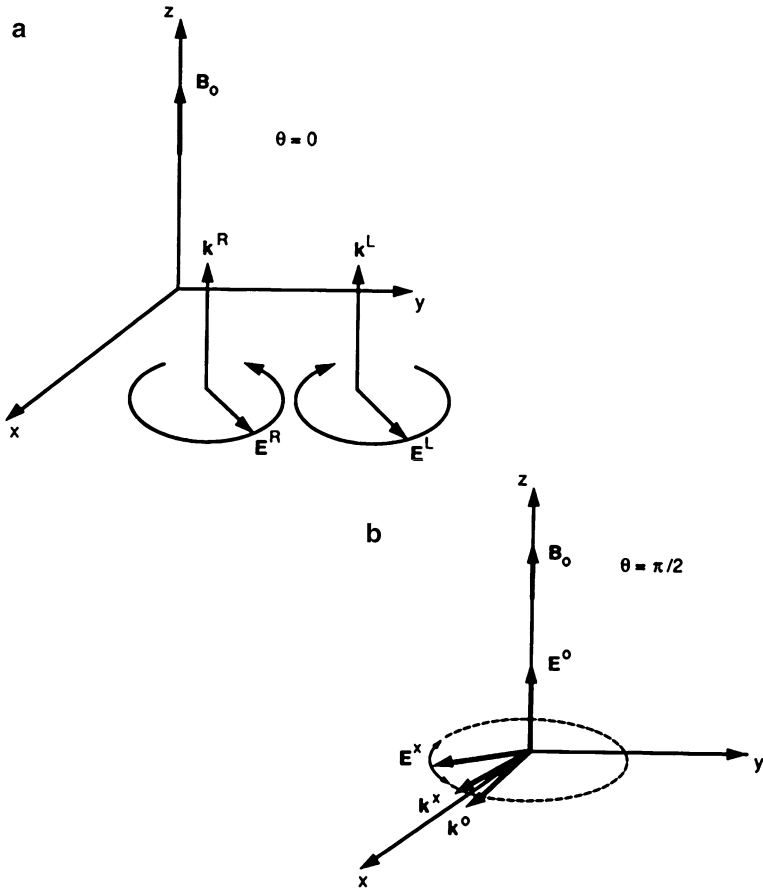


**Fig. B.3** Polarization of independent mode types. (a) Right-hand circularly polarized mode (RHCP) and left-hand circularly polarized mode (LHCP). The electrons (ions) rotate in the same sense as the RHCP (LHCP) mode. (b) Ordinary and extraordinary modes

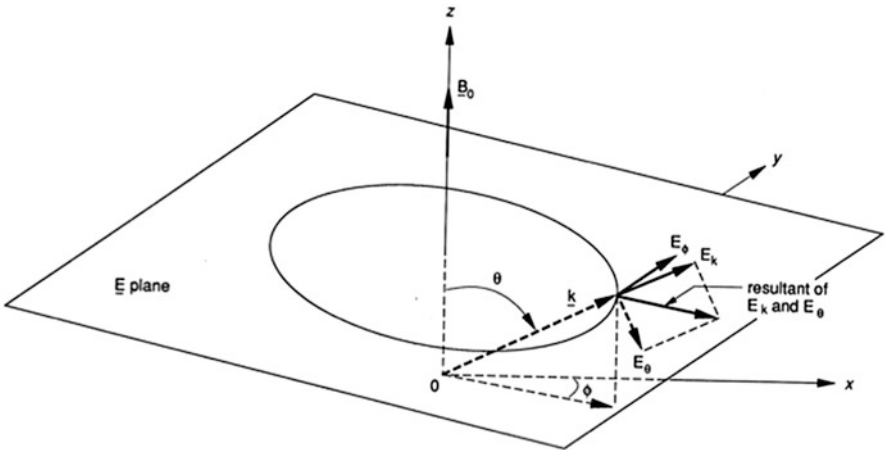


**Fig. B.4** Orientation of wave fields in spherical coordinates

## References

- Allis, W. P., Buchbaum, S. J., Bers, A.: *Waves in Anisotropic Plasma*, M.I.T. Press, Cambridge, Mass (1963)
- Metzer, G., Vabre, J.-P.: *Transmission Lines with Pulse Excitation*. Academic, New York (1969)
- Sato, T.: A theory of quiet auroral arcs. *J. Geophys. Res.* **83**, 1042 (1978)
- Stix, T.H.: *The Theory of Plasma Waves*, McGraw-Hill Lib Congress 62-17376 (1962)

## Appendix C

### Dusty and Grain Plasmas

In general, the motion of a solid particle in a plasma obeys Eq. (2.11)

$$m \frac{d\mathbf{v}}{dt} = m\mathbf{g} + q(\mathbf{E} + \mathbf{v} \times \mathbf{B}) - mv_c \mathbf{v} + \mathbf{f} \quad (\text{C.1})$$

where  $m$  and  $q$  are the mass and the electric charge of the particle, respectively,  $\mathbf{g} = \hat{\mathbf{r}}Gm(r)/r^2$  is the gravitational acceleration,  $-mv_c \mathbf{v}$  is due to viscosity, and  $\mathbf{f}$  is the sum of all other forces, including the radiation pressure.

Depending on the size of the particle, four typical cases are delineable:

1. *Very small particles.* The term  $q(\mathbf{E} + \mathbf{v} \times \mathbf{B})$  in Eq. (C.1) dominates over  $m\mathbf{g}$  and the particle is part of a dusty plasma (Sect. C.1). Under cosmic conditions this is true if the size of the particle is less than 10 nm. In the case of large electric charges the limiting size may rise to 100 nm.
2. *Small Grains.* For this case,  $q/m \approx \sqrt{G}$ . Plasma effects still play a major role in system dynamics (Sect. C.2).
3. *Large Grains.* If the size of the particle is so large that the electromagnetic term is negligible, we have an intermediate case dominated by viscosity and gravity. The particles in this regime are referred to as grains. Their equation of motion is

$$mv_c \mathbf{v} = m\mathbf{g} \quad (\text{C.2})$$

Under conditions in interstellar clouds this may be valid for particles of the order of 10  $\mu\text{m}$ .

4. *Large solid bodies.* For “particles” of the size of kilometers or more, the inertia and gravitational terms dominate. Electromagnetic forces are negligible, and viscous forces can be considered as perturbations which may change the orbit slowly. Depending on the properties of the cosmic cloud, viscous forces become important for meter or centimeter sizes. The equation of motion Eq. (C.1) is then,

$$m \frac{d\mathbf{v}}{dt} = m\mathbf{g} - mv_c \mathbf{v} \quad (\text{C.3})$$

The transition of plasma into stars involves the formation of dusty plasma, the sedimentation of the dust into grains, the formation of stellesimals, and then the collapse into a stellar state (Alfvén and Arrhenius 1976; Alfvén and Carlqvist 1978).

## C.1 Dusty Plasma

An important class of cosmic plasmas are those which are “dusty” (i.e., plasmas that contain solid matter in the form of very small dust grains). These grains are electrically charged and if  $q/m$  is large enough, the dynamics of the dust grain is controlled by electromagnetic forces (Mendis 1979; Hill and Mendis 1979, 1980; Houpis 1987; Azar and Thompson 1989; Horanyi and Goertz 1990).

The temperature of the dust in a cosmic plasma may differ by orders of magnitude from the temperature of the plasma. For example, the temperature of the dust radiating into space through a transparent plasma may be 10 K, the molecular temperature 100 K, the ion temperature  $10^3$  K, and the electron temperature 104 K.

Dusty plasma is characterized by solid particles of mass  $m$ , charge  $q$ , and a charge-to-mass ratio that is much greater than the square-root of the gravitational constant,  $q/m \gg \sqrt{G}$ . The dust grains are charged negatively by impacts from streams of electrons. The loss of negative charge can be due to the photoeffect, field emission, and ion impacts. Normally, the potential of a dust grain may be 1–10 V, positive or negative. However, if the electron stream responsible for the charge is relativistic, the grain can charge up to several kilovolts (Deforest 1972; Reasoner 1976; Mendis 1979).

## C.2 Grain Plasma

Consider a plasma whose dust may have accreted into macroscopic solid matter. For simplicity, the plasma is taken to consist of two components: grains with mass  $m_g$  and charge  $q_g$ , and particles with mass  $m_p$  and charge  $q_p$ . The grains are assumed to be weakly charged with  $q_g/m_g \sim \sqrt{G}$ . The particles may be electrons, ions, dust, or some other unspecified charge mass with the property  $m_p \ll m_g$  (Wollman 1988; Gisler and Wollman 1988).

Consider a spherically symmetric gravitational condensation of the plasma, so that the parameters depend only on the distance  $r$  from the center. The dynamics of the grain fluid are specified by Eqs. (2.13) and (2.15) where  $n_g(r)$  is the number density, and  $N(r)$  and  $M(r)$  are the total grain number and grain mass inside  $r$ , respectively. The total mass and net charge inside radius  $r$  are

$$\begin{aligned} M_T &\equiv M_T(r) \equiv m_g N_g + m_p N_p \\ Q_T &\equiv Q_T(r) \equiv q_g N_g - q_p N_p \end{aligned}$$



If the plasma is tenuous and in thermal equilibrium,  $dv/dt = 0$ ; the electrostatic potential at  $q_g$  is  $\phi = Q_T/4\pi\epsilon_0 r$ , and the gravitational potential at  $m_g$  is  $\phi_G = -GM_T/r$ . Substituting these parameters into Eq. (2.13) while (momentarily) neglecting  $\mathbf{B}$ , gives the following, for grains and particles, respectively:

$$0 = \frac{n_g q_g Q_T}{4\pi\epsilon_0 r^2} - \frac{n_g m_g G M_T}{r^2} - k T_g \frac{dn_g}{dr} \quad (\text{C.4})$$

$$0 = \frac{-n_p q_p Q_T}{4\pi\epsilon_0 r^2} - \frac{n_p \langle \gamma \rangle m_p G M_T}{r^2} - k T_p \frac{dn_p}{dr} \quad (\text{C.5})$$

The particles may be relativistic with mean Lorentz factor  $\langle \gamma \rangle$ .

Equations (C.4) and (C.5) have as solutions

$$n_g(r) = n_{0g} \left( \frac{r_0}{r} \right)^2$$

$$n_p(r) = n_{0p} \left( \frac{r_0}{r} \right)^2$$

Some insight into the meaning of Eqs. (C.4) and (C.5) is possible by considering the special case  $T_g = T_p = T$ , and scale lengths  $n_g^{-1} d n_g / d r = n_p^{-1} d n_p / d r$ , for the grain plasma and particle plasmas, respectively. For these conditions, Eqs. (C.4) and (C.5) reduce to

$$\frac{q_g Q_T}{4\pi\epsilon_0} - m_g G M_T = -\frac{q_p Q_T}{4\pi\epsilon_0} - \langle \gamma \rangle m_p G M_T \quad (\text{C.6})$$

If the grain thermal speed is much less than  $c$ , then  $\langle \gamma \rangle m_p \ll m_g$  and Eq. (C.6) may be written,

$$\frac{q_g}{\sqrt{4\pi\epsilon_0 G m_g}} \frac{Q_T}{\sqrt{4\pi\epsilon_0 G M_T}} = \frac{q_g}{q_g + q_p} \quad (\text{C.7})$$

Now consider the behavior of the particle scale height relative to the grain scale height. The particle scale height parameter  $r_{0p}$  is defined by the relation

$$q_p N_p(r_{0p}) = q_g N_g(r_0)$$

Now write, ignoring the particle mass with respect to the grain mass,

$$\frac{Q_T}{\sqrt{4\pi\epsilon_0 G M_T}} \approx \frac{q_g N_g(r) - q_p N_p(r)}{\sqrt{4\pi\epsilon_0 G m_g N_g(r)}} = \frac{q_g}{\sqrt{4\pi\epsilon_0 G m_g}} \left( 1 - \frac{q_p N_p(r)}{q_g N_g(r)} \right)$$

The ratio of particle numbers is

$$\frac{N_p(r)}{N_g(r)} = \frac{N_p(r_0)}{N_g(r_0)} = \frac{N_p(r_{0p}) N_p(r_0)}{N_g(r_0) N_g(r_{0p})} = \frac{q_g r_0}{q_p r_{0p}}$$

The last identity is due to the fact that for a  $r^{-2}$  density distribution,  $N(r) \propto r$ . Hence,

$$\frac{Q_T}{\sqrt{4\pi\epsilon_0 G M_T}} \frac{q_g}{\sqrt{4\pi\epsilon_0 G m_g}} \left(1 - \frac{r_0}{r_{0p}}\right) \quad (\text{C.8})$$

Combining Eqs. (C.7) and (C.8) yields,

$$\frac{r_0}{r_{0p}} = 1 - \frac{4\pi\epsilon_0 G m_g^2}{q_g^2} \left(\frac{q_g}{q_g + q_p}\right)$$

For an atomic plasma,

$$\frac{q_g^2}{4\pi\epsilon_0 G m_g^2} \gg \left(\frac{q_g}{q_g + q_p}\right)$$

and the radial electrical polarization, due to the separation  $|r_0 - r_{0p}|$ , is negligible. The condition for maximum polarization (i.e., when the particles are removed to infinity so that  $r_{0p} \Rightarrow \infty$ ), is

$$\frac{q_g}{\sqrt{4\pi\epsilon_0 G m_g}} = \sqrt{\frac{q_g}{q_g + q_p}} \quad (\text{C.9})$$

or, since  $q \equiv Ze$ ,

$$m_g = \sqrt{\frac{q_g(q_g + q_p)}{4\pi\epsilon_0 G}} = 1.9 \times 10^{-9} \sqrt{Z_g(Z_g + Z_p)} \quad \text{kg}$$

The grain mass, then, is of the order of micrograms.

It is possible to state the condition for significant large-scale separation. The Jeans wave number  $k_J = 2\pi/\lambda_J$  is from Eq. (2.75),

$$k_J^2 = \frac{4\pi G m_g \rho_m}{KT} \left(\frac{Z_p}{Z_g + Z_p}\right)$$

The particle Debye length is given by

$$\lambda_p^2 = \frac{kT_p/m_p}{n_p q_p^2/m_p \epsilon_0} = \left[ \frac{kT}{4\pi G m_g \rho_m} \right] \frac{4\pi\epsilon_0 G m_g^2}{q_p q_g}$$

Hence, Eq. (C.9) is equivalent to

$$k_J \lambda_p = 1$$

Thus, the condition for maximum polarization can be written

$$\frac{\text{Jeans length}}{\text{Debye length}} = 2\pi \quad (\text{C.10})$$

This analysis is valid insofar as thermalization is efficient, so that the formation of condensation heats the plasma and  $T_p = T_g$ . This increases the Debye length. Then the condition for charge separation is equivalent to the condition for poor shielding of Jeans mass concentrations.

The inclusion of  $\mathbf{B}$  causes a  $\mathbf{E} \times \mathbf{B}$  drift of the low mass component around the axis at the center of the spherical condensation. Strong magnetic fields invalidate the concept of a Jeans mass (Sect. 2.7.1).

## References

- Alfvén, H., Arrhenius, G.: Evolution of the Solar System. NASA Publication, SP-345. NASA, Washington, DC (1976)
- Alfvén, H., Carlqvist, P.: Interstellar clouds and the formation of stars. *Astrophys. Space Sci.* **55**, 484 (1978)
- Azar, M.J., Thompson, W.B.: The role of dust particles with large gyroradii in the 2/3 fall-down process. *IEEE Trans. Plasma Sci.* **17**, 228 (1989)
- Deforest, S.E.: *J. Geophys. Res.* **77**, 651 (1972)
- Gisler, G.R., Wollman, E.R.: *Phys. Fluids* **31**, 1101 (1988)
- Hill, J.R., Mendis, D.A.: *Moon Planets* **21**, 3 (1979)
- Hill, J.R., Mendis, D.A.: Charged dust in outer planetary magnetospheres. *Moon Planets* **22** (1980)
- Horanyi, M., Goertz, C.K.: Coagulation of dust particles in a plasma. *Astrophys. J.* **361**, 155 (1990)
- Houpis, H.L.F., Whipple, E.C.: Electrostatic charge on a dust size distribution in a plasma. *J. Geophys. Res.* **92**, 12057 (1987)
- Mendis, D.A.: *Astrophys. Space Sci.* **65**, 5 (1979)
- Mendis, D.A., Houpis, H.L.F., Hill, J.R.: The gravito-electrodynamics of charged dust in planetary magnetospheres. *J. Geophys. Res.* **87**, 3449 (1982)
- Reasoner, D.L., Lennartsson, W., Chappell, C.R., Rosen, A. (eds.): *Spacecraft Charging by Magnetospheric Plasmas*, p. 89. American Institute of Aeronautics and Astronautics, New York (1976)
- Wollman, E.R.: A grain plasma model of galaxies. *Laser Part. Beams* **6**, 545 (1988)

## Appendix D

### Some Useful Units and Constants

#### Length

meter  $m = 100\text{ cm}$   
kilometer  $km = 10^5\text{ cm} = 10^3\text{ m}$   
millimeter  $mm = 10^{-1}\text{ cm} = 10^{-3}\text{ m}$   
micron  $\mu = \mu m = 10^{-4}\text{ cm} = 10^{-6}\text{ m}$   
angstrom  $\text{\AA} = 10^{-8}\text{ cm} = 10^{-10}\text{ m}$   
femtometer  $fm = 10^{-13}\text{ cm} = 10^{-15}\text{ m}$   
astronomical unit (= mean sun-earth distance)  $AU = 1.49598 \times 10^{11}\text{ m}$   
light year  $ly = 9.46053 \times 10^{15}\text{ m} = 63,240\text{ AU}$   
parsec  $pc = 3.08568 \times 10^{16}\text{ m} = 3.26163\text{ ly}$   
solar radius  $Rs = 6.9599 \times 10^8\text{ m}$   
earth equatorial radius  $Re = 6.3782 \times 10^6\text{ m} = 6,378\text{ km}$

#### Volume

cubic meter  $m^3 = 10^6\text{ cm}^3$   
cubic parsec  $pc^3 = 2.938 \times 10^{49}\text{ m}^3 = 34.7\text{ ly}^3$   
cubic kiloparsec  $pc^3 = 2.938 \times 10^{58}\text{ m}^3 = 3.470 \times 10^{10}\text{ ly}^3$

#### Time

minute  $min = 60\text{ s}$   
hour  $h = 3,600\text{ s} = 60\text{ min}$   
day  $d = 86,400\text{ s} = 24\text{ h}$

sidereal year  $y = 365.256 \text{ d} = 3.15581 \times 10^7 \text{ s}$   
 aeon  $10^9 y$

## Mass

solar mass  $M_s = 1.989 \times 10^{30} \text{ kg}$   
 earth mass  $M_e = 5.976 \times 10^{24} \text{ kg}$   
 atomic mass unit (12C = 12 scale)  $\text{amu} = 1.66056 \times 10^{-27} \text{ kg}$   
 electron mass  $m_e = 9.10953 \times 10^{-31} \text{ kg} = 5.4858 \times 10^{-4} \text{ amu}$   
 proton mass  $m_p = 1.67265 \times 10^{-27} \text{ kg} = 1.00728 \text{ amu} (m_p/m_e = 1,836.15)$   
 mass of 1H atom  $m_H = 1.67356 \times 10^{-27} \text{ kg} = 1.00783 \text{ amu}$

## Energy

joule  $1 \text{ kg m}^2 \text{ s}^{-2}$   
 erg  $1 \text{ erg} = 10^{-7} \text{ J}$   
 calorie  $\text{cal} = 4.1868 \text{ J}$   
 electron volt  $\text{eV} = 1.60219 \times 10^{-19} \text{ J} = 10^{-3} \text{ keV} = 10^{-6} \text{ MeV} = 10^{-9} \text{ GeV}$   
 mass energy of 1 amu  $1.49243 \times 10^{-10} \text{ J} = 931.502 \text{ MeV}$   
 rest mass energy of electron  $m_e c^2 = 511.003 \text{ keV}$   
 wavelength associated with 1 eV  $\lambda = 1.2398 \mu\text{m} = 1,239.8 \text{ nm}$   
 frequency associated with 1 eV  $\nu = 2.4180 \times 10^{14} \text{ Hz}$   
 temperature associated with 1 eV  $11,604 \text{ K}$   
 detonation energy of 1 kt of high explosive  $R_s = 6.9599 \times 10^8 \text{ m}$   
 detonation energy of 1 kt of high explosive  $4.2 \times 10^{12} \text{ J} = 4.2 \text{ TJ}$   
 detonation energy of 1 Mt of high explosive  $4.2 \times 10^{15} \text{ J} = 4.2 \text{ PJ}$   
 detonation energy of 1 Gt (1,000 Mt) of high explosive  $4.2 \times 10^{18} \text{ J} = 4.2 \text{ EJ}$

## Power

watt  $\text{W} = \text{J s}^{-1}$   
 solar luminosity  $L_s = 3.826 \times 10^{26} \text{ W} = 2.388 \times 10^{39} \text{ MeV s}^{-1}$   
 Jansky  $\text{Jy} = 10^{-26} \text{ W m}^{-2} \text{ Hz}^{-1}$

## Velocity

$$\begin{aligned} \text{velocity of light } c &= 2.997925 \times 10^8 \text{ ms}^{-1} = 2.997925 \times 10^4 \text{ cm } \mu\text{s}^{-1} = 2.997925 \\ &\times 10^5 \text{ km s}^{-1} \quad (10 \text{ cm } \mu\text{s}^{-1} = 100 \text{ km s}^{-1}) \end{aligned}$$

## Pressure

$$\text{pascal } P_a, \text{ kg m}^{-1} \text{ s}^{-2}$$

$$\text{bar } 10^5 P_a$$

$$\text{atmosphere } \text{atm} = 1.01325 \text{ bar} = 760 \text{ torr}$$

$$\text{millimeter of mercury } \text{mmHg} = 133.322 P_a = 1.315 \times 10^{-3} \text{ atm} = 1.298 \text{ mbar}$$

## Temperature

$$\text{temperature comparisons } 0^\circ\text{C} = 273.150 \text{ K}; 100^\circ\text{C} = 373.150 \text{ K}$$

## Angle, Solid Angle

$$\begin{aligned} \text{degree } \text{deg} &= 1^\circ = \text{rightangle}/90 = 60 \text{ minutes of arc (60 arcmin)} = 3,600 \\ &\text{seconds of arc (arcsec} = 3,600'') \end{aligned}$$

$$\text{radian } \text{rad} = 57^\circ.29578$$

$$\text{steradian } \text{sr} = 3,282.8 \text{ deg}^2$$

## Angular Momentum

$$\text{quantum unit } 1.0546 \times 10^{-34} \text{ Js} = 6.5822 \times 10^{-16} \text{ eVs}$$

$$\text{Planck's constant } h = 6.6262 \times 10^{-34} \text{ Js}$$

$$\text{Planck's constant } \hbar = h/2\pi = 1.0546 \times 10^{-34} \text{ Js}$$

## Electric Charge

$$\text{Coulomb } C = -6.24145 \times 10^{18} \text{ electrons}$$

$$\text{electron charge } e = 1.60219 \times 10^{-19} \text{ C}$$

## Magnetic Field

tesla  $T = 10^4$  gauss

gauss  $G = 10^{-4} T = 1$  oersted  $= 79.58$  (amp – turn)  $m^{-1}$

gamma  $\gamma = 10^{-9} T = 1$  nT  $= 10^{-5} G$

earth's nominal magnetic field  $0.5 G = 50,000$  nT

## Some Physical Constants

Boltzmann constant  $k = 1.3807 \times 10^{-23} J K^{-1}$

gravitational constant  $G = 6.6726 \times 10^{-11} m^2 s^{-2} kg^{-1}$

gravitational acceleration, earth  $g = 9.8067 ms^{-2}$

permittivity of free space  $\epsilon_0 = 8.8542 \times 10^{-12} F m^{-1}$

permeability of free space  $\mu_0 = 4\pi \times 10^{-7} H m^{-1}$

Stefan-Boltzmann constant  $\sigma = 5.6705 \times 10^{-8} W m^{-2} K^{-4}$

Avogadro number  $N_A = 6.0221 \times 10^{23} mol^{-1}$

# Index

## A

Acceleration, 12, 22, 25–27, 32, 41, 45, 48, 51, 53, 56, 68, 73, 76, 111, 113, 120, 128, 139, 148, 151–155, 158, 160–161, 168–171, 175–178, 184, 187–189, 191, 193–195, 199, 200, 205–224, 236, 240, 245, 252, 260, 277, 290, 292, 311, 316, 321, 328, 347, 362, 391

Adjacent filaments, 113, 116, 120, 121, 344

Akasofu, S.-I., 21, 181, 193, 356

Alfvén, H., 15, 19, 25, 28, 31, 42, 43, 48–50, 53, 61, 63, 76, 78, 107, 146, 149, 158, 175, 189, 206, 264, 265, 289, 292, 293, 300, 306, 324, 341, 354, 361, 367, 368, 392

Alfvén limiting current, 53–55

Aliasing, 317, 319

Ampere, 62, 96–98, 354

Anode, 3, 25, 34, 68, 69, 71, 72, 115, 158, 161, 164, 165, 176–178, 182, 188, 189, 232, 233, 337, 347, 351

Antares, 6

Arcs, 2, 56, 158–166, 194, 195, 259, 306, 379, 399

Arecibo radio telescope, 302

Aristotle, 93

Arrhenius, G., 28, 31, 392

Aurora, 2, 6, 21, 23, 28, 31, 32, 35, 41, 43–46, 59–61, 72–74, 86–87, 130, 139, 146, 151–155, 164, 192–195, 197, 254, 341–358

Aurora australis, 351

Aurora borealis, 350, 351, 353

Auroral kilometric radiation, 35, 194

Auroras, red, 356

Axnäs, I., 29

## B

Barkhausen, H., 265

Barkhausen–Kurz, 33

Beam breakup, filamentation, 78–79

Beam threshold, 27, 341

Beck, R., 123–128

Bennett pinch, 26, 57, 58, 60, 232–235, 292, 299–307

Bennett, W.H., 26, 232

Bernstein–Greene–Kruskal, 180

Biot, 93, 94, 96

Biot–Savart force law, 93–134, 209, 234, 238, 243, 249, 324, 343, 346, 348–349

Birkeland currents, 11, 23, 41–87, 111, 112, 114, 146, 190, 194, 248, 279, 280, 299, 325, 346, 347, 353, 358, 362, 363

Birkeland, Egypt, 352–353

Birkeland, K., v, 41, 43, 349

Blackbody radiation, 260

Block, L.P., 45, 176, 184

Bostick, W., 26, 70, 116, 121, 158, 160, 162, 327, 368

Boundary conditions, 107, 179, 183, 185–187, 193, 319, 323–324, 331, 332, 379

Bow shock, 6, 7, 334, 335

Brenning, N., 29, 289, 290

Budker's parameter, 53

Buneman, O., 28, 67, 290, 313, 323, 325, 331–333, 336, 341, 351

Buneman two-stream instability, 184



**C**

Cairns, 364, 365  
 Carlqvist, P., 48, 56, 57, 59, 60, 177, 179, 199, 299, 304, 306, 307, 354, 392  
 Carlqvist relation, 56, 59–64, 292, 304  
 Carrington event, 355–357  
 Cathode, 3, 25, 68, 69, 71–73, 115, 144, 161, 165, 166, 177, 178, 180, 185, 189, 233, 343, 344, 350  
 Centauri, 6  
 Chalice, 347, 348  
 Chapman, S., 42, 43  
 Chen, F., 48, 49, 67  
 Chromosphere, 11–13, 27, 106, 195, 197, 198  
 Chupp, E.L., 200  
 CIV. *See* Critical ionization velocity (CIV)  
 CMB. *See* Cosmic microwave background (CMB)  
 COBE, 35  
 Colgate, S., 171  
 Collisions, 5, 6, 25, 28, 145, 148, 160, 180, 190, 193, 272, 290, 292, 314, 325–326  
 Columnar pinch, 160, 162, 347  
 Comet, 8, 11, 30  
 Conductivity, 19, 22, 55, 69, 110, 115, 139, 156, 199, 373, 379  
 Conductor, 2, 20, 25, 56, 93, 95–98, 102–104, 140, 156, 164, 187, 191, 337, 373–375, 377  
 Continuity equation, 48, 240, 250  
 Corona, 11–13, 34, 61, 106, 195, 197, 198, 292  
 Cosmic microwave background (CMB), 35  
 Cosmic plasma, 1–37, 41–87, 93–134, 139–171, 187, 190, 191, 205, 206, 270, 278, 282, 284, 311–329, 373, 392  
 Cosmic triple jump, 361–362, 367  
 Coulomb's Law, 94, 168, 327  
 Crank–Nicolson, 313  
 Cray computer, 336, 338  
 Critical ionization velocity (CIV), 28–32, 289–293, 295–297, 306  
 Critical velocity, 27, 170, 289, 293, 294, 297, 341  
 Cro-Magnon, 357  
 Cutler, C.C., 80, 81

**D**

Davis, H., 29  
 Debye-cube, 79, 313  
 Dense plasma focus (DPF), 46, 121, 158, 347–349  
 Density, 2, 45, 96, 141, 176, 205, 261, 291, 299, 312, 333, 341, 365  
 Dessler, A.J., 42, 165

Detectors, 69, 140–143  
 Dimensionless parameters, 110, 328, 361  
 Diocotron, 27, 56  
 Diocotron instability, 27–28, 81–82, 118–119, 121, 130, 132, 342, 365  
 Dipole, 5, 6, 21, 36, 41, 45, 164, 210–214, 265, 333–337, 350  
 Discharge, 4, 5, 10, 22–24, 56, 156–166, 189, 190, 232, 234, 237, 265, 347, 348, 379  
 Discretization, 316–318  
 Displacement current, 20, 52, 113, 141  
 Double layers, 34, 68, 147–148, 151, 175–201, 290  
 DPF. *See* Dense plasma focus (DPF)  
 Dreicer field, 170  
 Drift velocity, 144, 167, 168, 175, 184–186, 290, 328, 333  
 Dust, 1, 4, 34, 121, 180, 181, 293, 295, 302, 327, 391–395

**E**

Earth, 3–9, 12, 19–23, 33, 35–37, 41, 42, 44, 45, 59–61, 128, 148, 149, 155, 171, 200, 311, 333–335, 350, 355, 357, 362–365, 374  
     currents, 355, 362–363  
     markers, 344, 364  
 Eastman, T., 8, 361  
 Eastwood, J.W., 314, 317, 322, 325  
 Einstein, A., 1  
 Ekdahl, C.A., 73  
 Electric field, 2, 23, 25, 37, 45, 48, 54, 74, 77, 85, 89, 102, 103, 110, 118, 128, 139–171, 175, 177, 178, 184–186, 193, 194, 201, 212, 217, 222, 239, 249, 253, 290, 311, 325  
 Electrojet, 41  
 Electron beam, 25, 27–29, 33, 34, 46, 53, 54, 72, 73, 75, 76, 80, 82, 84–86, 109, 144, 192, 232, 313, 325, 341, 343, 345, 350  
 Electron beam parameter, 28  
 Electron runaway, 170  
 Electrons, 1, 45, 103, 139, 175, 205, 260, 289, 304, 312, 332, 341, 363, 388, 392  
 Electron volt, 2, 254  
 Electro-optic crystals, 141–142  
 Elliptical galaxy, 131–134, 240–243, 246, 247, 250, 369  
 Emission, 15, 18, 35, 64, 71, 121, 123, 124, 126–128, 142, 194, 195, 199, 205, 206, 219, 222–224, 229–234, 240, 248–251, 255, 277–278, 285, 293–295, 300–304, 306  
 Emission lines, 128, 250, 255, 293–295, 300

- Emission-line shift, 128
- English Channel, 259
- Evolution of earth-record synchrotron lines, 4, 6
- Exa-speed, 338
- Exploding, 4, 115, 119, 188, 190–191, 232–235
- Extragalactic, 16–17
- F**
- Faehl, R.J., 25, 292
- Fahleson, U., 29
- Falthammar, C.-G., 19, 41, 45, 146, 147, 149–153, 155–158, 363
- Faraday rotation, 69, 123, 124, 128, 380
- Faraday's Law, 101–102, 104
- Felber, F.S., 115
- Feldspar, 363
- Field-aligned currents, 27, 41–42, 46–47, 176, 191, 241, 293, 299, 311, 341–358
- Filamentary, 2, 4, 11, 26, 46, 62, 115, 124–125, 167, 181, 188, 199, 291–293, 299, 300, 302, 304, 305, 307, 373
- Filament pairing, 28, 56, 114, 230
- Filaments, number of, 281, 348
- Fluid equations, 47–49
- Flux
  - ropes, 46
  - tube, 21, 167, 291–293
- Force-free, 26–27, 57, 61, 68, 70, 106–107, 124, 184, 197, 198
- Framing camera, 46, 69–71, 233, 344, 348
- Fusion, 3, 68, 158, 171, 278, 347
- G**
- Galactic, 16–18, 20, 63–64, 121–124, 126, 196, 206, 241, 243–247, 292, 299–307, 341–358
- Galactic pole, 35
- Galaxy rotation, 131
- Galeev, A.A., 30
- Galvanometer measurement, 353, 363
- Gamma ray, 12, 13, 32, 254, 311
- Gas, 1–3, 19, 26, 28, 50, 55, 56, 65, 66, 69, 71, 161, 164, 165, 289–292, 301, 303–305, 307
- Gauss, 14, 19
- Gaussian components, 302, 303
- Gekelman, W., 109
- Generalized Bennet relation, 50–59, 351
- Generator, 4, 6, 20, 23, 25, 46, 61, 68–71, 73, 102, 115, 159, 190, 232, 313, 336, 347, 350, 373
- Geophysics, 263
- Geomagnetic, 8, 41–42, 44, 45, 149, 193, 254, 349–350
- Geometrical optics, 260, 267–274
- Geophysical, 154, 350, 357, 363
- Gilbert, 93
- Gold, T., 30, 106, 164, 354
- Grains, 1, 121, 180, 181, 327, 363, 391–395
- Green Bank, 36, 304, 305
- Green flash, 324
- Green, J., 64, 243, 246, 355
- Grid, 72, 183, 187, 314, 316–319, 323, 329, 333, 336
- Ground currents, 353
- Gyro-radius, 113, 144, 282
- H**
- Hartree, D.R., 312, 313, 318, 350
- Heating, 12, 22, 27, 159, 161, 184, 186, 189, 195, 290, 292, 326
- Heaviside, O., 1, 47, 140, 260, 315, 318, 322, 332, 377–378, 383
- Hertz, H., 1, 47, 140, 259, 260, 315, 318, 322, 332, 383
- Heteromacs, 299, 307
- Histogram, 297
- Hollow beams, 341, 342
- Hubble distance, 361, 362
- I**
- Instability, 12, 26–33, 41, 55, 64–68, 73, 78–80, 82, 84, 86, 118, 119, 121, 130, 132, 140, 175, 184–186, 191–192, 194, 289, 290, 292, 313, 316, 317, 333, 341, 342, 347, 354, 356, 365
- Interstellar, 2, 11–16, 20, 30, 37, 46, 57, 62–63, 121, 123, 124, 259, 289–297, 299–307, 336–338, 361, 362, 365–367, 391
- Interstellar clouds, 46, 57, 62, 289–297, 362, 365–367, 391
- Inverted V events, 46
- Io, 8, 10, 11, 21, 30, 164–166, 347
- Ion beam, 187, 290, 292, 343, 345
- Ionization, 1, 3–6, 8, 11, 16, 17, 19, 22, 26, 28–32, 45, 47, 48, 69, 71, 140, 145, 167, 168, 181, 193, 233, 289–297, 303, 304, 307, 315, 325, 326
- Ionosphere, 5–7, 20, 30, 35, 42, 44–46, 146, 148, 154–156, 190, 192, 193, 260, 265–267, 313, 336, 350, 379, 381, 382
- Ions neutrals, 1, 28, 50, 52, 55, 67, 289, 290, 292, 320

**J**

Jeans's criterion, 57  
 Johnston Island, 4, 6  
 Jones, M., 73, 77, 207, 290  
 Jovian, 21, 30, 164–166  
 Jupiter, 4, 8, 10, 11, 21, 35, 164, 165, 206, 286, 347

**K**

KC-135, 6  
 Keinigs, R., 77  
 Kelvin-Helmholtz instability, 185, 313  
 Kink instability, 55, 68  
 Kirchhoff, 12, 20, 260, 276–278  
 Kohoutek, 11  
 Krauss, J.D., 275  
 Kuehl, H.H., 226, 262, 272  
 Kurchatov Institute, 300

**L**

Langmuir, I., 2, 175, 179  
 Leap-frogging, 320–321  
 Leiden-Dwingeloo, 292, 299  
 Lemniscoid, 264, 265, 366, 367, 384  
 Lichtenberg figures, 156, 157, 159  
 Lightning, 2, 4, 5, 20, 22, 165, 265, 355  
 Lindman, E., 323–324, 331, 332  
 Liquid, 2, 3, 165  
 London, 355, 363  
 Lorentz, 25, 28, 41, 96, 102, 103, 178, 232, 283, 284, 315, 318, 319, 393  
 Los Alamos, 5, 6, 232, 314, 331, 338, 342, 364  
 Lundquist number, 49–50  
 Lundquist parameter, 19, 21, 49, 66

**M**

Magnetic diffusivity, 49, 50, 55  
 Magnetic field, 55–56, 80–86, 101–104, 106–109, 121–134, 145–148, 214–218, 282–284, 400  
 Magnetic-mirror, 146, 147, 194  
 Magnetic Reynolds number, 49–50  
 Magnetism, 16, 93–94, 350  
 Magnetohydrodynamics, 47–50, 176  
 Magnetopause, 6, 151, 334, 335  
 Magnetosphere, 5–10, 14, 19–21, 23, 36, 37, 41, 45, 46, 59–61, 139, 146, 148, 151, 153, 155, 164, 175, 190, 192, 193, 311, 332, 333, 357, 381  
 Magnetotail, 151, 153, 357  
 Magnetron, 28, 33, 144, 192, 195, 313, 318  
 Mandala, 364–366

Maps, Antarctic charts, 334

Markings, 363, 364

Marklund, 154, 156, 157, 167–168, 290–293

Marx-bank, 68, 69, 234

MASER. *See* Microwave amplification by stimulated emission of radiation (MASER)

Matter, 1, 2, 12, 26, 37, 64, 70, 139, 165–167, 247, 249, 291, 313, 314, 319, 361, 392

Maxwell, 1, 44, 47, 140, 259, 260, 315, 318, 322, 332, 350, 383

Medical science, 2

Meirovich, 232

Meteorites, 36

Microwave, 13, 22, 27, 28, 33–36, 67–69, 71, 73, 82, 84, 195, 199, 232, 238, 240, 259, 313, 337

Microwave amplification by stimulated emission of radiation (MASER), 34, 124

Milky Way galaxy, 123–124

Monte-Carlo, 290, 312, 326

Moon, 10, 22, 363

Mostrom, M., 73

Multidimensional PIC, 315–319

**N**

NASA, 11, 13, 17, 22, 23, 33, 342, 357

National Center for Atmospheric Research (NCAR), 333

NCAR. *See* National Center for Atmospheric Research (NCAR)

Near-earth, 5–8, 37, 357, 358, 362–365

Neutral hydrogen (HI), 16, 123–127, 129, 130, 292–297, 299–307, 369, 370

Nishikawa, K.-I., 332

Nuclear, 4, 6, 11, 12, 20, 25, 116, 126, 241, 243, 250, 338, 350, 354

Numerical grid, 316, 317, 319

**O**

Occurrence of strong auroras, 354

Oersted, H.C., 93

Ohm's law, 49, 148

Optically stimulated luminescence (OSL), 363

OSL. *See* optically stimulated luminescence (OSL)

Oslo, 349, 352, 353

**P**

Palpa, Peru, 363–364

Parallel fields, 27, 44, 46, 54, 63, 72, 79, 111, 139, 146, 147, 168, 176, 191, 197, 216, 226, 271, 320

Particle-in-cell (PIC), 25, 73–87, 109–121,  
183–187, 236–240, 290, 292, 299,  
311–329, 332, 336, 344

Penumbra, 158, 162, 163, 166, 347–349

Peratt, A.L., 34, 64, 68, 81, 115, 124, 129, 165,  
226, 243, 246, 249, 262, 290, 292, 299,  
331, 338, 341, 345, 354, 357, 365

Peter, W., 331

PIC. *See* Particle-in-cell (PIC)

Pinch, 20, 22, 25–32, 50, 52–61, 63, 64, 68–72,  
74, 76–79, 86, 110, 111, 115, 119, 158,  
160–163, 196, 232–238, 299–307, 344,  
346–348, 354, 365–367

Pinhole camera, 46, 234

Plasma, 1, 41, 98, 139, 175, 205, 259, 289,  
299, 311, 331, 341, 361  
cosmology, 331–332  
dimension, 3, 14, 16, 21, 24, 46, 76, 113,  
121–134, 183–185, 210, 252, 361  
fluid equations, 47–49  
focus, 25, 46, 121, 158, 160–162, 167, 232,  
234, 347–348  
gun, 70, 158–166, 290, 336, 347  
lifetime, 3  
sheathes, 147, 160, 161, 163, 165, 167, 189,  
290, 343, 347, 354

Plasmasphere, 8, 148, 149, 267

Plasma universe, 2–17, 19, 32, 47, 139, 206,  
362

Plasmoid, 68, 70, 72

Plumes, 46, 164–166

Poincaré, H., 350

Poisson's equation, 65, 67, 146, 178, 180, 181,  
312, 317, 319, 331, 332

Poles, 8, 15, 35, 44, 93, 164, 165, 195, 333,  
343, 345, 350, 352, 357

Potemra, T., 15, 44

Potentials, 5, 20, 21, 23, 25, 28, 31, 48, 69,  
98–101, 103, 104, 139, 140, 142–146,  
148, 149, 154, 156–158, 161, 167, 168,  
175–183, 187–189, 191–193, 196, 199,  
200, 236, 259, 289, 291, 292, 312, 314,  
315, 327, 374, 392, 393

Probes, 21, 36, 37, 108, 109, 140–144,  
149–151, 175, 253, 311, 358, 381

Prominences, 13, 46

Propagation, 27, 54–57, 66, 75–78, 84–86,  
149, 207, 220, 224, 226, 228, 259, 260,  
262, 264, 265, 267, 268, 272, 277, 341,  
354, 373, 377–378, 384–387

Proton beams, 341

Pulsar, 37, 123

Pulsed-power, 3, 4, 19, 20, 22, 25, 68–70, 115,  
156, 159, 373, 381

## Q

Quadrupole, 343, 345

Quasars, 200, 206, 240–242, 245–255

Quasi-longitudinal, 266

## R

Raadu, M.A., 107, 176, 180

Radiation, 2, 4, 16, 20, 22, 32–37, 48, 64,  
68, 69, 75, 80–82, 85, 115, 116, 119,  
123, 140, 167, 191, 194, 195, 200–201,  
205–254, 259–286, 321, 323–324,  
332–335, 354, 367, 391

Radio  
emission, 18, 35, 123, 124, 126, 127, 206,  
240  
frequency, 25, 240  
galaxy, 16, 18, 20, 34, 46, 89, 131, 200, 206,  
240–245, 247–250, 367–368  
telescope, 124, 243, 302, 368  
waves, 6, 35–36, 123, 124, 260

Rantsev-Kartinov, V.A., 299, 300

Rayleigh-Jeans, 35, 276, 278

REB. *See* Relativistic electron beam (REB)

Reber, G., 36, 37, 243

Red Hill, 363

Red skies, 355, 357

Relativistic electron beam (REB), 12, 33, 34,  
53, 58, 68, 84–86, 109, 354

Rogowski coil, 109, 110

Rotation, 15, 50, 51, 53, 56, 69, 74, 80, 87,  
115, 116, 118, 121, 123–125, 128–131,  
134, 164, 165, 215, 216, 224–226, 238,  
271, 304, 306, 321, 324, 343, 347, 351,  
368, 369, 387–388

## S

Sagittarius, 124

Satellite Probe, 8, 14, 22, 28, 30, 32, 35, 42,  
44, 45, 59, 144, 148, 151, 153, 155, 157,  
164, 175, 293, 347, 357

Saturn, 4, 8, 21, 35

Savart, 93, 94, 96

Schlieren, 115, 119

Screen, 28, 29, 46, 72, 199, 342, 350–351

Seyfert galaxy, 250, 252, 255

Shanahan, W.R., 25

Shannahan, R., 78

Sheet, 8, 14, 15, 27, 56, 59, 72, 73, 150–151,  
153, 187, 192, 195, 249, 252, 265, 315,  
316, 341, 367

Simulation-codes, 75, 79, 338

Size, 3–17, 46, 47, 57, 63, 64, 121, 171, 237,  
240, 241, 245, 246, 250, 255, 259, 282,  
314, 322, 327, 350, 354, 361, 362, 391

Snell, C.M., 326, 331, 341,  
 Solar, 6–8, 11–17, 20–21, 23, 30, 33, 61, 62,  
     196, 198, 199, 292, 347, 355, 363  
     flares, 12, 61, 195, 198, 199, 206, 232, 254  
     system, 8–11, 13, 14, 36, 157, 289, 311,  
     347, 350  
     wind, 5–8, 13, 21, 30, 36, 42, 45, 143, 195,  
     332–334  
 Solid, 2, 3, 27, 33, 73, 78, 128, 165, 171, 209,  
     212, 213, 218, 220, 223, 246, 268–270,  
     391, 392  
 Spectral methods, 314, 318–319  
 Spectrum, 32–36, 69, 78, 190, 205, 206, 212,  
     221, 223–225, 246, 250, 259, 260,  
     280–282, 311  
 Spicules, 46  
 Spiral, 13, 15, 23, 45, 70, 84, 115, 116, 118,  
     121, 123–128, 130–133, 240, 241, 292,  
     368–369  
 Spiral galaxy, 121, 124–131, 133, 240, 241,  
     243, 246, 250, 255, 368–370  
 SPLASH, 79, 81, 110, 111  
 Starfish, 4, 6  
 Stars, 1, 2, 14, 16, 19, 32–34, 70, 121, 311,  
     327, 363, 392  
 Stenzel, R., 109  
 Storey, L.R.O., 266  
 Streak camera, 46, 69, 119, 233, 343, 345, 348  
 Streamers, 6, 12, 13, 46, 66–68, 157, 176, 177,  
     184–186, 191–193, 262, 277, 290, 292,  
     355, 392  
 Streamers/sky filaments, 36, 249, 296, 297,  
     299  
 Structure, 2–4, 8, 11, 18, 26, 27, 33, 41, 46, 76,  
     80, 107, 115, 116, 121, 124–128, 133,  
     155, 160, 167, 180, 183, 184, 187, 200,  
     235, 247, 248, 250, 251, 291, 292, 294,  
     295, 299, 300, 302–305, 307, 337, 341,  
     344–348, 363, 365  
 Sun, 2, 8, 11–13, 15, 19, 27, 33, 34, 36, 41,  
     46, 61, 63, 106, 123, 195, 196, 200, 206,  
     232, 289, 334, 335, 350, 355, 397  
 Sunspots, 11–13, 19, 27, 195, 196, 198  
 Synchrotron  
     emission, 6, 35, 75, 123, 134, 224, 233, 240,  
     283, 363  
     light, 299, 363, 365  
     radiation, 4, 48, 80, 116, 123, 200, 205–254,  
     278, 282, 286, 321, 354  
  
**T**  
 Terella, 352, 354  
 Thales of Miletus, 93

THEMIS mission. *See* Time History of Events  
     and Macroscale Interactions during  
     Substorms (THEMIS) mission  
 Thode, L., 78  
 Time History of Events and Macroscale In-  
     teractions during Substorms (THEMIS)  
     mission, 357–358  
 Time-scales, 107, 184, 199, 214, 250, 325  
 Tonks, L., 175  
 Transmission line, 20–23, 33, 68, 156, 157,  
     234, 337, 373–382  
 TRISTAN, 110, 111, 329, 331, 336–338  
 TRISTAN prime, 331, 336  
 Trubnikov, B.A., 227, 278, 279, 281  
 Two-fluid equation, 48

## U

Ultraviolet, 12, 32, 154, 195, 342

## V

Van Allen, J.A., 4  
 Veil Nebula, 17, 46  
 Verschuur, G., 292–297, 299, 300, 302–307  
 Very large array (VLA), 18, 36, 124, 248, 251  
 VLA. *See* Very large array (VLA)  
 Volta, 93  
 Vortices, 27–29, 31, 41, 46, 72, 80–84, 87,  
     128, 185, 341, 343, 344  
 Voyager spacecraft, 8, 21, 164, 166

## W

Waves, 12, 19, 33, 35, 41, 42, 65–67, 73, 80,  
     118, 123, 140, 148, 171, 180, 184, 186,  
     194, 195, 205–208, 217, 226–228, 250,  
     255, 259–265, 267, 271, 272, 280, 283,  
     286, 290, 292, 299, 304, 312, 318, 322,  
     337, 374, 377, 383–388, 394  
 Webster, H.F., 29, 72, 73, 82, 342  
 Welding, 2  
 Whirl stabilization, 56  
 Whistler, 140, 148, 157, 265–267, 333  
 White light, 22, 299, 363  
 Wien's displacement law, 276

## X

X-rays, 346, 354

## Y

Yao, F.Y., 357, 365  
 Yonas, G., 53

## Z

Zeeman effect, 303, 304  
 Zeeman splitting, 121–123  
 Zmuda, A.J., 42